Insights into Rockfall from Constant 4D Monitoring

JACK GORDON WILLIAMS

Insights into Rockfall from Constant 4D Monitoring

Jack Gordon Williams

Department of Geography

Durham University

A thesis submitted in partial fulfilment of the requirements for the University of Durham for the degree of Doctor of Philosophy

February 2017

Statement of Copyright

Cover image: Aerial photo of the toe of East Cliff, Whitby, UK, taken during an airborne LiDAR survey in 2014. The rock armour revetment and foreshore platform are visible at low tide, with a ramp that leads onto East Pier at the top of the photo. At the end of this pier stands the lighthouse that houses the 4D monitoring system presented in this research.

Abstract

Current understanding of the nature of rockfall and their controls stems from the capabilities of slope monitoring. These capabilities are fundamentally limited by the frequency and resolution of data that can be captured. Various assumptions have therefore arisen, including that the mechanisms that underlie rockfall are instantaneous. Clustering of rockfall across rock faces and sequencing through time have been observed, sometimes with an increase in pre-failure deformation and pre-failure rockfall activity prior to catastrophic failure. An inherent uncertainty, however, lies in whether the behaviour of rockfall monitored over much shorter time intervals (T_{int}) is consistent with that previously monitored at monthly intervals, including observed failure mechanisms, their response to external drivers, and pre-failure deformation.

To address the limitations of previous studies on this topic, 8 987 terrestrial laser scans have been acquired over 10 months from continuous near-real time monitoring of an actively failing coastal rock slope ($T_{int} = 0.5$ h). A workflow has been devised that automatically resolves depth changes at the surface to 0.03 m. This workflow filters points with high positional uncertainty and detects change in 3D, with both approaches tailored to natural rock faces, which commonly feature sharp edges and partially occluded areas.

Analysis of the resulting rockfall inventory, which includes $> 180\,000$ detachments, shows that the proportion of rockfall < 0.1 m^3 increases with more frequent surveys for $T_{int} <$ *ca.* 100 h, but this trend does not continue for surface comparison over longer time intervals. Therefore, and advantageously, less frequent surveys will derive the same rockfall magnitude-frequency distribution if captured at *ca.* 100 h intervals as compared to one month or even longer intervals. The shape and size of detachments shows that they are more shallow and smaller than observable rock mass structure, but appear to be limited in size and extent by jointing. Previously explored relationships between rockfall timing and environmental and marine conditions do not appear to apply to this inventory, however, significant relationships between rockfall and rainfall, temperature gradient and tides are demonstrated over short timescales.

Pre-failure deformation and rockfall activity is observed in the footprint of incipient rockfall. Rockfall activity occurs predominantly within the same *ca.* 100 h timescale observed in the size-distribution analysis, and accelerated deformation is common for the largest rockfall during the final 2 h before block detachment. This study provides insights into the nature and development of rockfall during the period prior to detachment, and the controls upon it. This holds considerable implications for our understanding of rockfall and the improvement of future rockfall monitoring.

Acknowledgements

There are many people to whom I owe a debt of thanks – I sincerely hope that this gratitude has been expressed during the course of my Ph.D.. First and undoubtedly foremost, I would like to thank Dr Nick Rosser. Nick has an incredible ability to conceive and conduct novel and interesting research, and this Ph.D. would not have been possible without this. Nick is able to examine any plot and extract every possible trend, implication, and potential for development, even if you think it is as good as it can be or shows nothing at all. Nick's supervisions have ensured that I take a step back from my research and examine datasets from a broader, alternative perspective. This, combined with his unwavering patience and enthusiasm, has been the driver behind the results presented here. Nick has placed a lot of faith in my capabilities, often to an extent that I would consider overestimation. During my Ph.D., I was fortunate to work alongside Nick on a NERC-Urgency project following the 2015 Nepal earthquakes, and on a foreshore-monitoring project in London. I am sincerely grateful for these opportunities. While I am one of many students to acknowledge Nick's support from an academic perspective, it may not be too bold to say that I can offer my own fairly unique points of gratitude. These include, but are by no means limited to, driving for an hour and a half to pull me out of what I insisted was a ditch, but admittedly more closely resembled a patch of grass; helping me to navigate Kathmandu's Tribhuvan International Airport while I was a little worse for wear; and for the fluffy pink dice that he thought would be an excellent addition to my new Vauxhall Corsa. Thanks also for taking such a keen interest in my dress sense. There have been numerous raised eyebrows and off the cuff comments regarding the pastel palette of choice in my clothing. This has since largely disappeared, but walking into a supervision to the sound of 'what on earth are you wearing?' at least provided me with an indication that there was an impending tirade of mockery subsumed within the guise of a supervisory meeting.

Second, I would like to thank Dr Rich Hardy. Rich and I tend to meet for impromptu supervisions when the weekend's football has been in favour of Rich's team and, all too often, to the detriment of mine. Indeed, while Rich has provided a large number of insightful comments on the thesis, these are 'dependent on the weekend's results'. Rich has offered some truly fantastic advice throughout my Ph.D., in particular relating to statistics, data handling and MATLAB. He has also done his upmost to ensure that work does not get the better of my social life, sense of humour and ability to be mocked. Thank you, Nick and Rich. On a joint note, thank you also for contributing to my skills and approach to independent research, having told me in our first ever meeting to 'read the manual', or words to that effect.

The initial stages of this Ph.D. ran alongside a knowledge transfer partnership between Durham University and 3D Laser Mapping (3DLM). Central to this was Dr Ashraf Afana, a research associate at the time who remains a very good friend. Ashraf's knowledge of scanners

and associated software has been a fantastic resource, and I have learnt a great deal from him. Ashraf and I spent two 24 h periods manually scanning targets and slopes repeatedly. Thanks for the help and company! Ashraf also provided considerable assistance in developing and maintaining the 4D monitoring system.

The slope monitoring system was created with help from 3DLM. Their monitoring software, *SiteMonitor4D*, scheduled and defined scan areas. 3DLM were great to be alongside during the Slope Stability 2013 conference, Brisbane. Ashraf and 3DLM helped to organise a two-week trip to an open pit mine in the Dominican Republic. Here, I collected repeat scan data that was critical for the methodological development of this project. I thank Sean Jefferies of Barrick and his survey team at the time, who provided a large amount of help in the scanning and a great insight into industry applications, which formed the basis for the initial stages of this Ph.D.. Thanks also to Sean for playing devil's advocate regarding the use of TLS monitoring in open-pit mines, relative to radar and Structure from Motion. Justifying my work to someone with Sean's experience and expertise was both challenging and rewarding.

I also extend sincere thanks to John Davis of NavStar Geomatics. NavStar's *GeoExplorer* software was incredibly useful in synthesising the weather station, web cam, and scan schedule data. John's expertise in *SiteMonitor4D* during his time at 3D Laser Mapping, in *GeoExplorer* within his current role at NavStar, and his vast knowledge of slope monitoring systems around the world have been critical throughout my Ph.D. and in helping with the Whitby lighthouse system. John also organised a visit to the China Clay mines of St Austell, U.K., where I was able to meet Prof. John Coggan and present my work.

The maintenance and development of the system's fuel, electronics, and data transfer would not have been possible without Dave Hodgson and Sam Waugh of the Department of Geography. I hope that this thesis shows that the effort has been worthwhile! Considering the many unique aspects of our system, it is both character building and humbling to have realised that the two weather stations that we installed failed to record rainfall correctly. Chris Carvell, who has operated his own weather station in Whitby for over a decade, was immensely helpful in filling this data gap with his own excellent weather station data.

The postgraduate community in the Department of Geography comprises a wonderfully diverse set of people that provides a constant source of humour. Dr John Morris was a fantastic, humorous housemate for two years, with legendary cooking abilities that I most certainly made the most of. Siobhan Whadcoat began her Ph.D. just after me. Working on similar topics over the same period has formed a unique friendship. Dr Mark Kincey has been a source of constant wit, sarcasm, and unbounded geomatics knowledge. Hannah, Sophie, Naomi – thank you all.

Finally, I thank Jess and my family. Jess has tolerated me, set an immensely high standard, been a huge source of encouragement, and known how to handle me perfectly during the final stages of my thesis. I am sure that many families only receive Ph.D. progress updates

when it isn't going quite to plan or there seems an insurmountable volume of work left to do. Mum, Dad, Evie, Uncle David and, of course, Nana and Grandad; thanks for all your patience. You have been on the end of the phone after late nights in the Department, and listened to a jumbled set of thoughts on a topic that is fairly niche. I appreciate it greatly.

This Ph.D. was funded as a studentship from the Department of Geography, Durham University, provided by the Engineering and Physical Sciences Research Council (EPSRC). The British Society for Geomorphology supported costs associated with attendance at the AGU Fall Meeting 2014, through a postgraduate travel grant.

Contents

List of Figures

Chapter 6

Chapter 7

List of Tables

Chapter 1

Introduction

1.1 Rationale for research

Brittle failure in tension or in shear that occurs through rockfall is normally viewed as a near-instantaneous phenomenon (Rose and Hungr, 2007). However, the ability to monitor hard rock slopes, particularly from a face-on perspective, has yielded an increasing body of evidence that indicates precursors to final rockfall failure, bringing into question the treatment of failure as instantaneous. Such evidence includes acoustic emissions due to internal cracking (Eberhardt *et al.*, 1999; Netaji and Ghazvinian, 2014), microseismic ground motions recorded by accelerometers or seismometers (Amitrano *et al.*, 2005; Helmstetter and Garambois, 2010; Burjánek *et al.*, 2012), joint dilation that induces pre-failure deformation (Travelletti *et al.*, 2008; Oppikofer *et al.,* 2009; Abellán *et al.*, 2010; Royán *et al.*, 2015; Collins and Stock, 2016), and pre-failure rockfall activity within the footprint of incipient rockfall scars (Rosser *et al.*, 2007a,b; Pedrazzini *et al.*, 2010; Stock *et al.*, 2012; Royán *et al.*, 2015). Pre-failure deformation and pre-failure rockfall activity have been identified using repeat photography from both terrestrial and airborne platforms, as well as terrestrial LiDAR.

In the laboratory, pre-failure deformation of samples has been observed through a process of brittle cracking, which increases in rate as microfractures coalesce and the area of unsheared material at the shear zone deceases exponentially (Kilburn and Petley, 2003; Petley *et al.*, 2005; 2008). This suggests that pre-failure deformation in brittle materials can develop in a time-dependent, progressive manner rather than instantaneously. The progression of a slope towards failure can therefore be considered as much a function of strain as it is of stress, which emphasises the importance of developing an understanding of strain that includes time as a critical parameter. Similar time-dependent behaviour has been observed prior to large rockfall, in which both the size and frequency of rockfall increase prior to failure. This process may indicate either accelerated deformation towards catastrophic failure (Rosser *et al.*, 2007a), or a process through which accumulated strain is released and the slope reverts to a new equilibrium state (Leroueil, 2001; Pedrazzini *et al.*, 2010).

While anecdotal observations of precursory rockfall activity have been captured in videos during the final minutes before failure, this is unlikely to capture the full evolution of pre-failure deformation and quantifying this pattern remains complex. A number of studies have opted to use terrestrial laser scanning (TLS) to measure the evolution of rockfall, however, due

to technical, logistical, and financial constraints, such studies rarely survey slopes within a month of the previous survey (Abellán *et al.*, 2014). Since exponential accelerations in brittle failure have been observed in the laboratory, accurately capturing the path to failure not only requires monitoring over a sustained period, but also over short time intervals. While processes such as microcrack growth are observed in lab testing or through the analysis of acoustic emissions from the rock mass, these processes occur at depth. However, if the surface expression of deformation is assumed to have propagated through brittle materials from the rupture plane, then monitoring at high precision becomes critical in relating rock slope deformation to *in situ* damage accumulation.

Drivers that are external to the slope can prepare it for failure by inducing strength changes within the rock mass. These include, but are not limited to, thermal cycling, which may induce permanent damage to the rock mass (Gunzburger *et al.*, 2005; Gischig *et al.*, 2011a; Collins and Stock, 2016; Eppes *et al.*, 2016), and changing pore water pressure, which can weaken the rock mass itself and induce permanent, irreversible deformation. If small detachments of material are assumed to constitute part of the progressive failure of hard rock slopes, then external drivers may act as both triggers of small rockfall, and factors that prepare the slope for failure in the longer-term (Iverson, 2000; Schuster and Wieczorek, 2002; Selby, 2005). In order to examine these drivers as triggers of rockfall, rockfall should be detected at a rate that is consistent with the timescales of variability in external driving forces.

1.2 A novel approach to slope monitoring

Frequent and precise monitoring enables the identification of rockfall over timescales that are sufficiently short to overcome coalescence and superimposition when rockfall are spatially contiguous. This in turn enables a more realistic appraisal of the size distribution of rockfall events, which holds implications for the prediction of future rates of erosion, understanding of the mechanisms of failure evolution, and the sensitivity of the size distribution to scale of the discontinuity network. In addition to controls that are *in situ* in the rock mass, continuous high frequency monitoring (≤ 1 h) may provide the additional benefit of relating the timing of rockfall, which may or may not precede larger incipient failures, to external forcing such as environmental or marine conditions. While previous studies have attempted to establish relationships between the two, these have required considerable time-averaging of conditions and assume that: (a) a linear relationship between rockfall and environmental conditions is most appropriate; (b) the average conditions, or some measure of the distribution of conditions during a monitoring epoch, are those which are best placed to explain rockfall occurrence; and (c) such relationships can be resolved by treating the datasets as a direct cause-effect relationship. High frequency monitoring enables rockfall to be examined with respect to chronological sequences of

weather conditions, but also allows rockfall timings to be resampled relative to any cyclical occurrence in the environmental factors, such as diurnal temperature cycles and tide cycles.

1.3 Aim, research questions, and objectives

The overarching aim of this research is *to use high frequency continuous monitoring to understand the mechanisms and nature of rockfall*. The conceptual basis that underpins this aim is that precursory displacement and rockfall constitute part of the progressive failure of rock slopes. Within this model, failure is not exclusively driven by external conditions; instead, damage accumulation within the rock mass dictates catastrophic failure (Rosser *et al.*, 2007a; Petley *et al.*, 2008). A series of research questions has been designed in order to achieve this aim:

(1) Does the observed power-law behaviour of rockfall extend to its occurrence over short timescales?

This question has been formulated in response to the uncertainties around the influence of rockfall coalescence and superimposition on the size distribution of rockfall from actively failing slopes. This holds implications for the accurate estimation of cliff retreat, the actual probability of rockfall of any given size, as well as understanding the relative significance of small rockfall in the progression of a slope towards catastrophic failure. This question also highlights the need to understand rockfall size distributions, in order to more accurately categorise the relationships between rockfall, environmental drivers and structural controls by rockfall size.

(2) To what extent does the visible persistence of discontinuities determine the permissible size of failures?

Knowledge of the shape and size of rockfall enables insight into their release relative to the geometry of the rock surface and, therefore, the control that it exerts on failures that occur. Interpreting this relationship requires measurements of rockfall, and the rock mass, that are precise and of high spatial resolution.

(3) Are environmental conditions significant as triggers of rockfall occurrence and, if so, which conditions promote failure?

External drivers of rock slope failure can include environmental conditions and, depending on its setting, marine conditions and seismicity. These conditions vary at a range of timescales, with

environmental and marine conditions at the sub-daily, daily and seasonal timescales. Previous studies have presented variable correlation strengths between such variables and the timing of rockfall, which themselves may relate to variations in the lithology, structure, and local climate of the rock slope, or the spatial and temporal resolution of monitoring. Monitoring at a high frequency and a high spatial resolution allows the nature of the response of hard rock slopes to be examined, including whether this response is lagged, without the uncertainty attributed to the frequency of monitoring and the time-averaging of weather conditions that this necessitates.

(4) Can 4D monitoring detect precursory rockfall or deformation of the rock mass at timescales below those previously observed for rockfall?

This research question has been devised to examine the patterns of precursory rockfall that precede larger scale failure, here considered as those with volumes > 0.1 m^3. This provides a means to assess whether rockfall promote or stabilise the rock face for further failure, the conditions under which they may do so, and whether patterns of accelerated rockfall activity previously observed at time intervals of one month to several months are valid over shorter timescales.

In order to answer these research questions. The following objectives have been established:

(1) To develop a method capable of handling large numbers (10^3 - 10^4) of sequential terrestrial laser scans, which involves pre-processing them to increase their precision, and accurate 3D change detection.
(2) To assess the use of 4D data in providing reliable volume estimates for erosion prediction.
(3) To develop an understanding of the size distribution of rockfall, necessary to categorise analysis on the role of external drivers and the visible persistence of discontinuities.
(4) To examine failure of the slope over a range of monitoring intervals, in order to identify the benefit of near-real time monitoring and examine the temporal scales of failure based on varying rockfall size distributions.
(5) To develop techniques to examine rockfall timing with respect to environmental conditions.
(6) To examine patterns of both rockfall and precursory creep within incipient failure scars prior to failure, and in relation to environmental conditions.

1.4 Thesis structure

This thesis comprises nine chapters. Their relation to the objectives and research questions are presented in Figure 1.1.

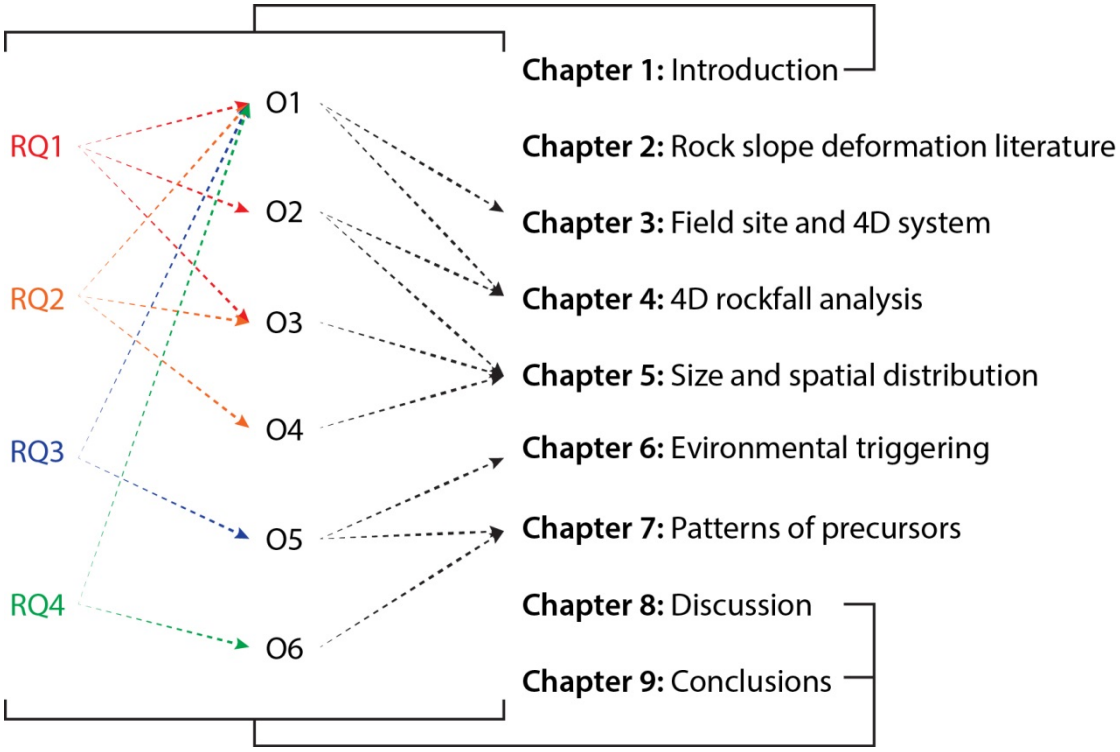

Figure 1.1: *Schematic overview of the thesis structure with respect to the research questions and their objectives.*

Chapter 2 reviews current understanding of the development of failure through brittle mechanisms of microcrack growth, and introduces literature surrounding the concept of progressive, time-dependent failure. The final stage of failure, commonly referred to as the tertiary phase, is related to both deformation of rock slopes and rockfall from them, and is shown to follow accelerating, and potentially predictable patterns. Previous research into the role that environmental conditions play in triggering rockfall is also examined, highlighting the importance of monitoring their occurrence at a similar interval to environmental data. Background literature that considers the magnitude-frequency distribution of rockfall and landslides is also presented, which introduces the scale invariant nature of mass-movements but also the fact that this pattern appears to break down for the smallest monitored events. A brief summary of current approaches to slope instability monitoring is then provided. This chapter highlights the need to advance slope deformation monitoring beyond current practices of data processing and analysis, in order to provide a more robust understanding of the nature of rockfall.

Chapter 3 introduces the rock slope that is monitored in this study, including its setting, lithology, previous observations of rockfall and erosion at the site, and local environmental and marine conditions. The second half of this chapter concerns the installation of the continuous near-real time monitoring system. This includes a system design as well as details of the system setup, including scan schedule and point spacing.

Chapter 4 begins with a review of current techniques and workflows for processing TLS-acquired point cloud data to derive surface change. The chapter outlines the methods and workflows adopted in order to pre-process the large number of scans and, in doing so, to increase the precision of each scan for the detection of change. This comprises the filtering of unreliable points between successive scans, based on their topographic position and radiometric return, and accurate batch alignment. This is followed by the development of an adaptation of the widely adopted Multiscale Model-to-Model Cloud Comparison algorithm (M3C2; Lague *et al.*, 2013), which reduces uncertainty in detection of change between scan pairs.

Chapter 5 is the first of three chapters of results. It builds on *Chapter 4* by addressing the uncertainty attached to volume estimates within the acquired rockfall inventory. This highlights the importance of the magnitude-frequency distribution of rockfall events in determining the overall uncertainty in material loss estimates, since small events have the highest volumetric uncertainty. The magnitude-frequency distribution is also used to infer the timescales over which the process of rockfall occurs, and hence the potential uses for monitoring over different timescales. The chapter ends with an examination of the scale of rockfall with respect to the scale of visible persistence of joints in the cliff rock mass, derived in 3D from the scan data. This compliments an analysis of the shape of rockfall in suggesting that rockfall are both shallow and below the scale of persistent discontinuities.

Chapter 6 examines the temporal distribution of rockfall through the 10-month monitoring period, providing a general assessment of the relationship between rockfall and stormy conditions throughout the period. This is followed by a linear regression approach that has previously been adopted to establish the strength of a cause-effect relationship between environmental conditions as triggers and the occurrence of rockfall. The chapter concludes with a number of analyses designed to examine the occurrence of rockfalls with respects to cycles of environmental and marine conditions, at the sub-daily (tide cycle) and daily (temperature cycle) scales.

Chapter 7 draws upon the combined high spatial and temporal resolution of the dataset in order to observe both pre-failure deformation and pre-failure rockfall before catastrophic failure, here defined as failure that follows an exponential increase in activity within its footprint. Due to the size of the inventory, this is undertaken for a small proportion of the recorded detachments. This chapter builds upon *Chapter 5*, by examining the timescales over

which pre-failure rockfall occur, and *Chapter 6* by examining the onset of final failure with respect to environmental conditions.

Chapter 8 discusses the key findings made through the thesis. Initially, this constitutes an appraisal of the key considerations that are required in undertaking a continuous near-real time monitoring campaign. Following this, the implications of some of the novel and key findings in this study are discussed with regard to the insight that can be gained from high frequency monitoring. A conceptual model of the path to failure that rockfalls can take is discussed.

Chapter 9 presents the major findings of the study in relation to the research questions outlined above. Here, the most novel findings are identified alongside areas of future research and development of the project.

Chapter 2

Rock Slope Deformation and Monitoring

2.1 Introduction

Chapter 1 introduced the concept of progressive failure, which is commonly used to describe time-dependent failure mechanisms that act within unstable rock masses, and the insights into the nature and controls upon this process that may be drawn from high-resolution, near-constant rock slope monitoring. These relate to: (1) the timescales and mechanisms through which rockfall evolve; (2) the controls on this evolution (both structural and exogenic); and (3) the nature of accelerated rockfall activity prior to failure. These themes have conventionally been examined for landslides and large rock slope failures to a greater extent than for rockfall (for example, Eberhardt *et al.*, 2004; Gischig *et al.*, 2011a;b). This is due in part to the comparative ease with which larger landslides can be discerned from aerial and satellite sensors, as well as with which they are instrumented *in situ* at the surface (such as extensometers) and at depth via boreholes (such as piezometers, inclinometers, and calipers). However, with the advent of new remote monitoring technology, in particular those from ground-based platforms, rockfall from near-vertical rock faces have been recorded with increasing frequency and precision (Abellán *et al.*, 2014; 2016; Eitel *et al.*, 2016).

This study focuses upon rockfall monitoring; however, in order to define the underlying rationale and technical specification of the monitoring approach that is developed, an examination of progressive rockfall failure is required. The chapter therefore reviews existing understanding concerning the failure mechanics and dynamics of rockfall, and does not seek to review the technologies of monitoring this process, with the exception of a short description at the end. A thorough appraisal of the slope instability monitoring techniques is provided by Jaboyedoff *et al.* (2012) and Abellán *et al.* (2014). The chapter begins with a review of first-time progressive failure in brittle slopes, and highlights examples of this process in material shedding prior to catastrophic rockfall. This is the most-likely failure mechanism that underpins the rockfall observed in this study, and has been previously inferred on similar slopes (Rosser *et al.*, 2007a;b; Lim *et al.*, 2010; Rosser *et al.*, 2013; Brain *et al.*, 2014). Failure-time prediction, which makes use of patterns of increasing strain-rate during the final phases of failure, or derivatives therein, is then discussed. *Section 2.3* reviews the relationship between exogenic controls, viewed

both as preparatory factors and triggers, and the timing of landslides and rockfall. *Section 2.4* highlights the importance of quantifying the size distribution of rockfall in inventories, and then examines the role of new monitoring technologies in capturing these distributions. The chapter concludes by identifying current deficits in the understanding of rockfall development, interpreted from the size distribution of detachments, the influence of environmental conditions on failure, and the applicability of strain-rate based acceleration to failure models.

2.2 Progressive failure

The setting of the rock slope monitored within this study is the North Yorkshire coastline, UK. Failures that develop through time have previously been observed in the setting of this study (Rosser *et al.*, 2007a;b;2013). However, the nature and controls of this development are not clearly understood. A review of the potential mechanisms, controls and paths to failure is therefore provided below with the aim of devising a monitoring approach that is tailored to progressive rockfall failure. There is widespread recognition that first-time brittle slope failures develop in three discrete phases of movement (Petley *et al.*, 2002). These are commonly referred to as primary, secondary and tertiary creep (Varnes, 1978) and are characterised by a gradual equalisation of the ratio of resisting forces to driving forces known as the Factor of Safety (Bjerrum, 1967; Main, 2000; Zavodni, 2000). The time-dependent nature of this behaviour is defined in this study as deformation that follows a characteristic pattern through time, which is independent of everything but time. This time-dependence is often termed progressive failure and can be observed in the surface and subsurface deformation of many natural (e.g. Eberhardt *et al.*, 2004) and engineered slopes (e.g. Zavodni, 2000), as well as underground excavations (e.g. Kemeny, 2005). Micro-mechanical changes that occur in each phase play a distinct role in failure evolution, ultimately allowing failure without the shear surface mobilising peak strength (Bjerrum, 1967; Scholz, 1968; Martin and Chandler, 1994). An understanding of this process is integral to the prediction of likely surface deformation and acceleration prior to collapse. Two mechanisms have been proposed for the observed failure evolution: (1) the slider block friction model (Helmstetter *et al.*, 2004); and (2) damage accumulation by microcrack growth (Main, 2000; Petley *et al.*, 2005).

2.2.1 The slider block friction model

The slider block friction model proposed by Helmstetter *et al.* (2004) assumes a rigid landslide block governed by the state- and rate-dependent friction law (Dietrich, 1978; Ruina, 1983; Scholz, 1998), in which resistance to movement is predicted to decrease with strain-rate (Figure 2.1). When the block is at an incline, the shear strength τ (kPa) is:

$$\tau = \sigma \cdot \tan\phi + c \qquad \text{[Eq. 2.1]}$$

where σ is the effective normal stress, $\tan\phi$ defines the friction of coefficient at a slope incline of ϕ, and c is the cohesion (Selby, 2005). However, the force necessary to cause sliding between solid surfaces in (dry) frictional contact typically exceeds the force required to sustain sliding (Putelat and Dawes, 2015). This behaviour requires a distinction to be made between the static and dynamic coefficients of friction. The concept of rate-and-state friction considers the complex evolution of asperities during sliding by drawing upon the logarithmic time variation of the static coefficient of friction and variation of the dynamic coefficient with velocity (Putelat and Dawes, 2015). The solid friction coefficient, μ, between the block and surface is state- and rate-dependent, determined by the slip velocity V and the state variable ϑ.

$$\mu = \mu_0 + A \ln\frac{V}{V_0} + B \ln\frac{V_0\theta}{D_C} \qquad \text{[Eq. 2.2]}$$

where μ_0 is the steady-state friction at a reference sliding velocity V_0. D_C is the critical slip distance, which usually reflects the size of asperities and is related to the evolution of the state variable through time by:

$$\frac{\delta\theta}{\delta t} = 1 - \frac{\theta V}{D_C} \qquad \text{[Eq. 2.3]}$$

As reviewed by Scholz (1998), the transition between an initial velocity V_0 and a higher velocity, V_A yields an increased frictional response of A.

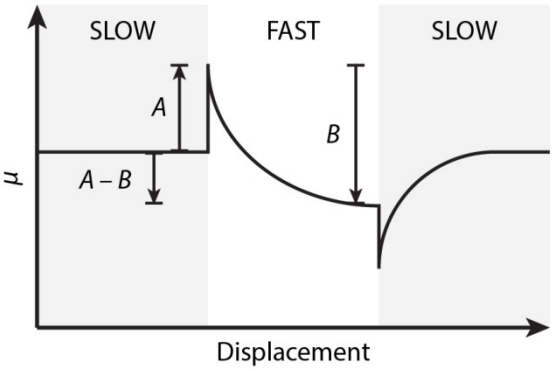

Figure 2.1: *Experimentally observed frictional response to an exponential increase in sliding velocity, followed by an exponential decrease in sliding velocity. During the initial velocity increase, a direct increase in friction (A) occurs, known as the direct velocity effect. An evolutionary decrease in friction (B) then occurs. Adapted from Scholz (1998:37).*

At a constant velocity of V_A, there is a decrease in friction, B, with displacement of the material. At steady-state, the friction μ_S is:

$$\mu_s = \mu_0 + (A - B) \ln \frac{V}{V_0} \quad \text{[Eq. 2.4]}$$

A–B is therefore the derivative of μ_S with respect to the log of the reduced slip velocity. When $A>B$, friction increases with slip velocity resulting in a stable slide. When $A<B$, however, unstable acceleration can occur as friction decreases with velocity. In a landslide, the shearing of gouge at the sliding surface is such that A is greater than B if the material is poorly consolidated, though this difference decreases as the material is subjected to higher pressures (Helmstetter *et al.*, 2004; Handwerger *et al.*, 2016). Sornette *et al.* (2004) showed that a gradual decrease in frictional resistance with strain-rate could provide a physical explanation for the hyperbolic acceleration of the 1963 Vaiont failure. However, this model does not account for fluctuations in friction associated with variable pore-water pressure (Iverson, 2005) or the development of Coulomb stress at asperities (Brückl and Parotidis, 2005).

2.2.2 Microcrack growth

An alternative mechanism that can explain the presence of time-dependent failure evolution, as well as discrepancies in this development by brittle and ductile failure mechanisms, is microcrack growth. Bjerrum (1967) suggested that, for a shear surface to grow in cohesive materials, the shear zone must undergo a shift from peak to residual strength, resulting in a drop in resistance and the redistribution of shear stresses from the base of an incipient landslide. A landslide may therefore fail without the shear surface mobilising peak strength (Scholz, 1968; Martin and Chandler, 1994). This model assumes the existence of 'recoverable strain energy', which is released from elastic materials at the landslide base as interparticle bonds break under stress, instigating localised plastic deformation. In a uniform material under tension, stress is passed from one atom to another in a series of parallel lines orientated in the stress direction (Selby, 2005). Strain energy is diffused evenly within the material and, if it is held by surrounding bodies, no strain energy can escape. If a crack is initiated, however, stress trajectories gather at the crack tip and the material on either side relaxes, releasing its stored energy, which becomes available for crack propagation. This gradual loss of shear resistance with increasing strain after peak strength, also known as s*train-softening*, occurs in both rupture surface and microcrack growth. *Strain-hardening* mechanisms represent reduced strain-rates due to dislocating movements within the crystal lattice (Callister and Rethwisch, 2007; Figure 2.2).

Main (2000) developed a hybrid model relating subcritical crack growth to the existence of primary and tertiary creep, mediated by a phase of 'steady-state' secondary creep (Figure

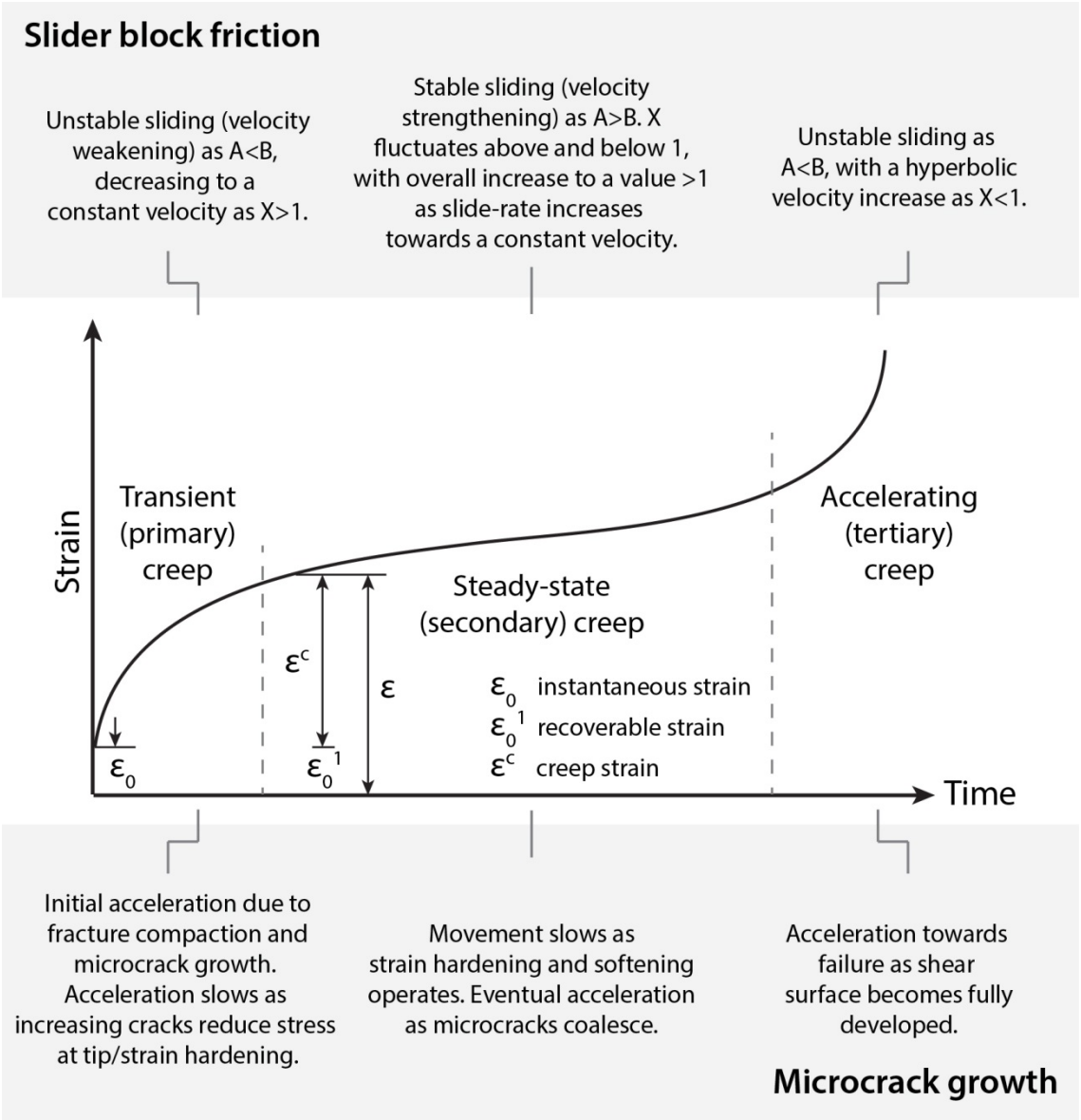

Figure 2.2: *Schematic plot of the time-dependent strain component on a rock sample, exhibiting three phases of movement known as transient, steady-state and accelerating. Parameters A, B and X of the slider block friction model account for observed variation (top). Microcrack growth (bottom) in conjunction with strain hardening and softening is also displayed.*

2.2). During primary creep, strain hardening dominates and causes crack lengths to increase while inducing stress reduction at crack tips, a negative feedback manifest by initially high but decreasing strain rates. During secondary creep, the superimposition of both hardening and softening mechanisms produces a relatively constraint strain-rate, with the overall increase in strain-rate reflecting a gradual shift towards the latter process. At a critical inflection point, this shift marks the beginning of the tertiary phase in which strain softening mechanisms induce a hyperbolic acceleration towards final failure (Petley *et al.*, 2008). Reches and Lockner (1994) suggested that this inflection point reflects the interaction of adjacent microcracks when a critical crack density is reached, further dilating each crack. The interaction of multiple cracks propagates into adjacent intact rock, eventually resulting in shear surface development at the

centre of the damaged rock mass. Petley *et al.* (2005) developed a more synthesised understanding of this process, noting that Bjerrum's (1967) shear surface growth is achieved by brittle cracking that can be described in similar terms to the Varnes (1978) three-stage creep model (Table 2.1) and so-called *'Saito'* linearity or acceleration (see *Section 2.3*).

If the growing crack in Bjerrum's (1967) model is replaced with the progressive growth of a shear surface, a zone of stress concentration is created within the unsheared material (Figure 2.3). As the area of this zone reduces to zero, the shear stress acting upon it (the force exerted by the weight of the failing material divided by the unit area) tends to infinity, thereby explaining a hyperbolic 'Saito' acceleration (Petley *et al.*, 2008). Conversely, an asymptotic trend is exhibited by ductile deformation along existing rupture surfaces (with already destroyed interparticle bonds) in plastic materials (Kilburn and Petley, 2003), a difference that is not explained by the rate-dependent friction proposed by Helmstetter *et al.* (2004).

A positive feedback defines the growth of shear cracks by their interaction and nucleation through stress concentrations around crack tips. Based on this, the time-dependent crack-growth models by Main (2000) and Petley *et al.* (2005) are synonymous with a progressive failure mechanism. This section therefore raises two key points: (1) final failure can be characterised by a precursory period of slope deformation; and (2) such deformation operates in a time-dependent manner and is therefore independent of exogenic forcing. Assuming that such deformation propagates to, and can be monitored at, the slope surface, which is probable in a rigid material such as rock, it is this latter tertiary period of progressive failure that offers opportunities for strain-rate based failure prediction.

Table 2.1: *The three phases of creep identified by Varnes (1978) and modified by Petley et al. (2005)* in relation to *brittle cracking. Of note is the influence of pore-water pressure that, although triggering microcrack development, becomes increasingly unconnected to landslide development especially within the tertiary phase where microcracks accelerate towards full shear surface growth.*

Varnes (1978)	**Petley *et al.* (2005)**	**Description of Microcrack Growth by Petley *et al.* (2005)**
Primary Creep	1	Varying pore-pressures cause FoS fluctuation. At a critical FoS, shear surface begins to develop due to stress concentrations on, and growth of, microcracks. Slope is stable.
Secondary Creep	2	Microcrack interaction begins at a critical density, leading to crack coalescence and shear surface growth.
Tertiary Creep	3	Shear stress is loaded on unsheared area of shear zone, the rate of which increases exponentially at the beginning of the tertiary phase.
	4	Hyperbolic acceleration causes a catastrophic acceleration to failure.

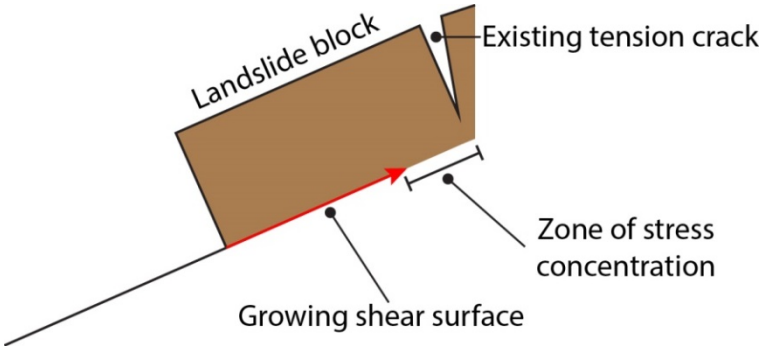

Figure 2.3: *Modified Bjerrum (1967) model to account for Saito linearity. A proposed explanation for shear surface growth is one in which microcrack growth reduces the area of unsheared material (stress concentration) to zero. This growth is shown by the red arrow and induces a hyperbolic increase in shear stress responsible for Saito acceleration. Petley et al. (2008) suggest that a tension crack, or a shear surface moving towards the surface, creates the zone of stress concentration in the unsheared material that ultimately develops into the growing crack proposed by Bjerrum (1967). Adapted from Figure 12 in Petley et al. (2008:870).*

2.3 Accelerating strain rates prior to failure

The final stage of time-dependent failure presented above has previously been characterised by a hyperbolic acceleration in strain rate. As discussed in this section, however, this acceleration can take the form of both pre-failure deformation (creep), and of pre-failure rockfall activity. Examining the nature of this activity prior to rockfall is necessary in order to establish a monitoring system tailored to the failure mechanism.

Three approaches have been implemented to examine creep within geological materials (Crosta and Agliardi, 2003). Micromechanical approaches (e.g. Mitchell *et al.*, 1968; Kuhn and Mitchell, 1993; Murad *et al.*, 2001) observe changes in particle-level processes that accompany and promote creep. Kuhn and Mitchell (1993) showed that strain rate is partially defined by particle rearrangement that occurs with movement of the mass along the shear surface. Rapid decreases in strain rate were observed when particles were rearranged, such that a greater proportion of deviatoric stress was accommodated by forces normal to particle contacts, rather than tangential forces (Kuhn and Mitchell, 1993). Rheological-mechanical approaches create models of the deformation behaviour of specific materials by fitting numerical constants that correspond with idealised models, such as viscous, elastic, plastic and combinations of each (Shea and Kronengburg, 1992; Vauchez *et al.*, 1998). Tests are conducted in the laboratory, often using soil shear box and triaxial compression apparatus, which can be used to quantify the conditions under which materials fail. The final approach is the empirical measurement of strain rates in laboratory tests, scale models or through site-specific monitoring of the slope itself. Unlike the above approaches, empirical approaches based on monitoring directly address failure timing. In practice, surface displacements are recorded over time and examined to identify

accelerations that may precede final failure. This approach is adopted here and assumes that surface deformation is directly proportional to subsurface deformation at the shear surface. Owing to the hard rock composition of the slope in question and the shallow depth of previously observed failures (Rosser *et al.*, 2007a), this assumption is considered likely to be valid.

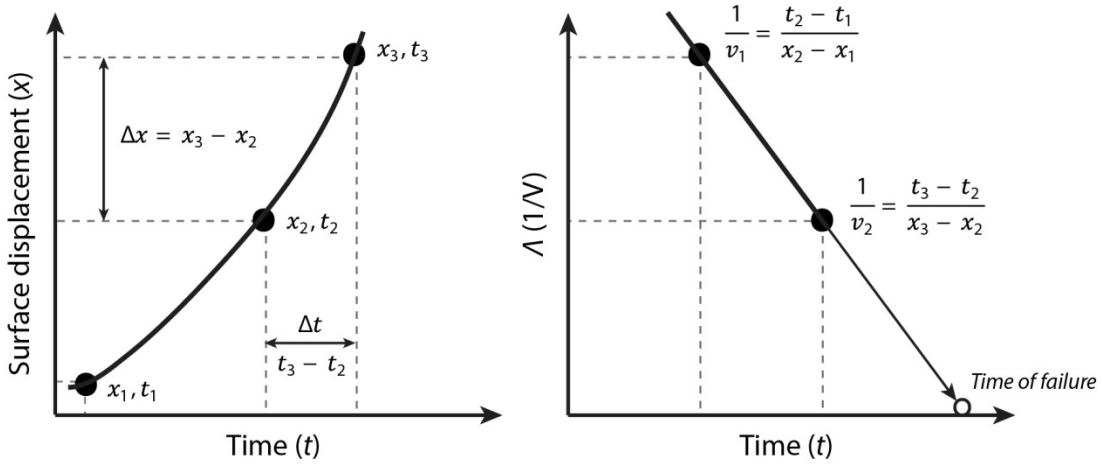

Figure 2.4: *Left. Hyperbolic acceleration of surface displacements prior to failure. Here velocity is measured using the displacement at each measurement interval. Right: For the same displacement, the reciprocal of velocity, Λ, also termed 'Inverse Velocity' is shown. Extrapolating to the point where 1/V is approximately zero provides an estimate of failure time.*

2.3.1 Pre-failure deformation

Saito (1965) first quantified pre-failure accelerations during the tertiary phase of landslide movement, observing linearity in log time-log strain rate immediately prior to collapse:

$$\dot{\varepsilon}(t_f - t) = a \qquad \text{[Eq. 2.4]}$$

where $\dot{\varepsilon}$ is the strain rate, t_f is the time of failure, t is the time of the strain rate measurement, and α is a dimensionless parameter, typically in the range of 1.7 – 2.2. Equation 2.4 shows that the strain rate is inversely proportional to the time to failure at which it is measured. If the initial strain ε_0 at t_0 is zero, integrating the above equation provides the strain measurement ε at t:

$$\varepsilon = a \cdot \ln \frac{t_f - t_0}{t_f - t} \qquad \text{[Eq. 2.5]}$$

The time to failure is hence:

$$t_f = \frac{0.5(t_2 - t_1)^2}{(t_2 - t_1) - 0.5(t_3 - t_1)} + t_1 \qquad \text{[Eq. 2.6]}$$

where t_3 is the time of the last survey, and t_2 and t_1 are time values selected at the same displacement interval as t_3 and t_2 (Federico *et al.*, 2012; Figure 2.4). Based upon the observation of accelerating creep, Fukuzono (1985) described this acceleration in terms of displacement:

$$\frac{d^2x}{dt^2} = A\left(\frac{dx}{dt}\right)^{\alpha} \qquad \text{[Eq. 2.7]}$$

where x is displacement, (dx/dt) is velocity, and acceleration is (d^2x/dt^2). A is a dimensionless parameter, typically $1 \times 10^{-4} - 1 \times 10^{-3}$. Using this differential function, Saito's (1965) observation can be represented using the reciprocal of velocity, Λ, which is manifest by a straight line in Λ-t space (Fukuzono, 1985) and elsewhere termed 'Saito' linearity:

$$\Lambda = [A(\alpha - 1)]^{(\alpha-1)^{-1}}(t_f - t)^{(\alpha-1)^{-1}} \qquad \text{[Eq. 2.8]}$$

where Λ is conventionally termed 'inverse velocity' $((dx/dt)^{-1})$. Failure timing can therefore be predicted by extrapolation to the point where $\Lambda \approx 0$, where the slope deformation velocity approaches infinity.

The approach has been applied retrospectively in a number of studies with varying degrees of success (for example, Zvelebill, 1985; Suwa *et al.*, 1991; Hungr and Kent, 1995; Rose and Hungr, 2007). Figure 2.5 illustrates the variability in pre-failure deformation for a range of published failures. The significant deviation away from linearity in Λ-t space, including asymptotic trends, restricts the application of this technique and indicates both brittle and ductile failure. The exponential increases in strain-rate associated with ductile failures prevents

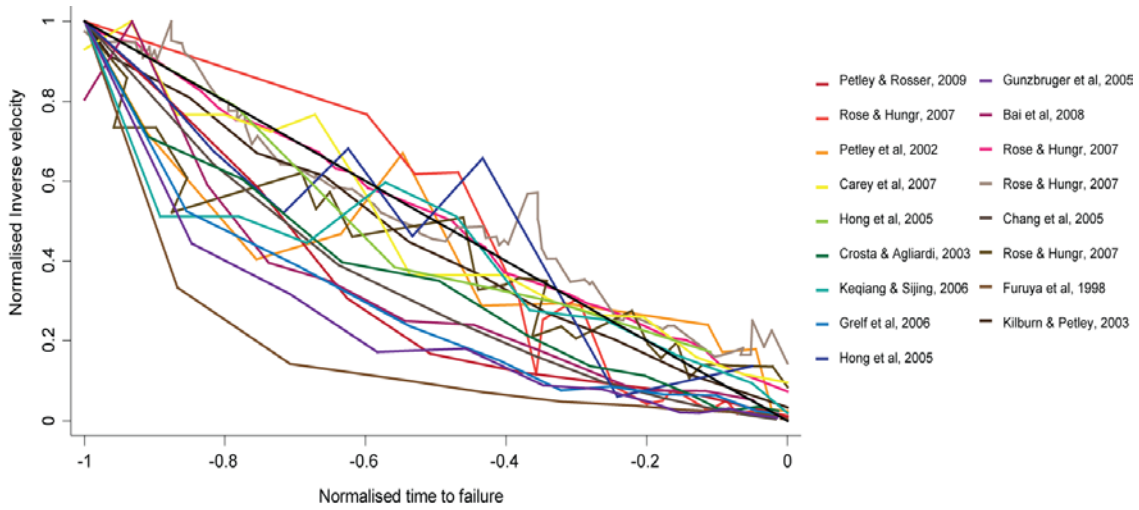

Figure 2.5: *Comparison of published pre-failure deformation data. Normalised time and inverse-velocity values allow direct comparison between sites. The solid black line represents a perfectly linear trend in Λ-t, expected in first-time brittle failures. Asymptotic trends characterise ductile failure, or failure along existing sliding surfaces. Source: Froude (2011:121).*

them developing into catastrophic failures; hence they are unlikely to develop very high rates of deformation as compared to brittle failures.

2.3.2 Pre-failure rockfall activity

Terzaghi (1950) proposed that the amount of downslope movement prior to failure is determined by the thickness of the basal shear zone, defined as the zone where the ratio of shearing resistance to shear strength decreases. Thin shear zones are therefore likely to yield millimetre scale movements, whereas thicker zones, in clay for example, may experience movements of the order of several metres or more. However, laboratory analysis has shown that pre-failure strains in brittle rock masses may reach *ca.* 3% of the rupture surface length (Petley *et al.*, 2008). For example, a 1 m long shear surface mass may creep by up to 0.03 m. Assuming that a slope comprises a rigid body of geologic material, it follows that deformation resulting from the developing failure may propagate through it to define deformation patterns at the surface, providing an opportunity to monitor derivatives of strain accumulation beyond displacement alone.

Voight (1989) suggested that seismic energy release could be measured to determine subsurface failure mechanisms. Amitrano *et al.* (2005) used a power-law to characterise the acceleration of seismic energy release prior to failure of the Mesnil-Val chalk cliffs, Normandy, a phenomena widely observed in laboratory testing. Though seismic monitoring of rock mass degradation has been applied to a number of failing cliffs (e.g. Helmstetter and Garambois, 2010), studies are limited by the ability to install, maintain and interpolate within adequately dense seismic networks. Such networks also do not provide information of rockfall volume or geometry. However, Burjánek *et al.* (2012) deployed a network of 12 three-component velocity sensors and nine digital seismic systems to record ambient vibrations of a potentially unstable rock slope in the Swiss Alps. The resulting amplification data showed a significant orientation orthogonal to open tension cracks at the surface, highlighting the potential to characterise the response of slopes to multidirectional loading during earthquakes.

Many observations and videos of rock slope collapse (see, for example, https://www.youtube.com/watch?v=ZVjr4mii3cE), especially within open-pit mines (e.g. Hoek and Bray, 1981; Suwa *et al.*, 2008; Doyle and Reese, 2011), show crumbling prior to slope collapse, yet the quantification or predictive interpretation of this phenomenon has remained difficult until recently (Harries *et al.*, 2009). Zvelebill and Moser (2001) examined three large individual failures and showed that time-dependent models of tension crack widening could be used to predict rockfall timing over a range of timescales. Using monthly TLS comparisons, Rosser *et al.* (2007a) found accelerated rockfall activity, defined as a combination of failure size and frequency, within the footprint of an incipient sandstone failure. The reciprocal of this

acceleration showed significant resemblance to inverse velocity plots applied to hillslope failures. Royán *et al.* (2015) also observed that spatially contiguous failures occurred at the periphery of a large toppling failure from a cliff. Again the reciprocal of rockfall activity was plotted, here yielding an approximation of failure time to within a matter of days. This approach has also been used to infer the stabilisation of rock slopes by observing a decrease in precursory events in the monitoring area (Pedrazzini *et al.*, 2010). In this study, monitoring is applied to examine the presence and nature of pre-failure deformation but also, for a heavily fragmented rock mass, for the potential to observe precursors in the form of small rockfall

2.3.3 Complexity in deformation rate measurement

Approaches to the prediction of failure timing using observed linearity in log time-log strain rate relationships remain limited in a number of respects. In terms of the extrapolation of observed trends, there is significant ambiguity in the choice of regression used. Petley *et al.* (2002), for example, found that the brittle fracturing used by Fukuzono in a linear interpolation through log time-log strain rate space can only be applied to failures that occur through shear plane development in previously unsheared material. The choice of the time interval over which deformation rates are examined is also significant. Daily deformation rates may provide less variability between successive estimates than hourly deformation rates, owing to an increased signal-to-noise ratio. However, large time intervals are also less suited to capturing short-term variability in deformation rates characteristic of rapid accelerations towards failure, and are hence less likely to provide a precise estimate for the time of failure (Crosta and Agliardi, 2003; Royán *et al.*, 2015). The area over which measurements are taken also remains ambiguous. Dick *et al.* (2014) showed that averaging deformation measurements over a larger area presented a smoother trend to failure, which proved more useful for analysing the underlying failure mechanisms than the use of single pixels (e.g. Harries *et al.*, 2009).

The transition between the use of the inverse velocity for slope failure prediction and the prediction of precursory rockfall activity is also one that, at present, has little underlying mechanical rationale. Both Suwa *et al.* (1991) and Rosser *et al.* (2007a) have shown that a positive relationship exists between precursory activity and the size of final failure. When considering the movement of large volumes of material, final failure can be considered as full failure of the slope. However, for rockfall this deformation is more ambiguous, and defining the type or size of failure that constitutes a final or largest possible failure is subjective. Furthermore, variability in patterns of precursory acceleration based upon the size of final failure remains unclear. Rosser *et al.* (2007a;b) showed that the amount of precursory rockfall activity was proportional to final failure size. For fragmented rockfall of the order of 1 m^3, the existence of this activity was difficult to identify. By implication, even smaller rockfall may be of

insufficient size to exhibit precursory activity. Several mechanical theories can be proposed to explain this: very small rockfall may be of insufficient volume to fragment prior to failure, possible as the failure size approaches that of coherent uniform blocks; a minimum block weight and hence stress may be required to exceed the intact strength of the rock mass; or, if the scale of final failure is approximately equal to the scale of persistence/jointing, then precursors to failure may not be permissible beneath the scale of individual discontinuities. From a methodological perspective, this pattern may also represent the scale at which precursory deformation is comparable with the study's monitoring precision (10^{-3}-10^{-2} m), and hence highlights the importance of accurate and precise measurement of deformation.

Inverse velocity approaches reduce a multitude of surface displacements and controls into a single log time-log deformation plot (Federico *et al.*, 2012). In general, examinations of creep and the use of inverse velocity during the tertiary phase rarely attribute observed patterns to external environmental conditions. Rosser *et al.* (2007a) captured a dataset that allowed the relationship between environmental conditions and rockfall timing to be assessed; however, no relationships between environmental conditions and patterns of increased rockfall activity prior to failure were examined. Increases in rockfall activity were noted within the footprints of the majority of failures analysed. For failures $<$ *ca.* 100 m^3 this pattern was not observed. Furthermore, while failures $>$ *ca.* 100 m^3 showed an increase in rockfall activity, no distinguishable transition from secondary to tertiary creep was evident. This suggests that a hyperbolic acceleration may have occurred at a sub-monthly timescale and retains the possibility that smaller failures undergo accelerations in precursory activity over a similar timescale. This therefore highlights the importance of monitoring intervals below those conventionally used, typically no less than one month.

This section has described current understanding of the temporal progression of a failing slope. In relation to this study, the rate-dependency of movement within the tertiary creep phase allows failure-time prediction via the Saito method and similar approaches. In rigid slope bodies, measurements of surface displacement and rockfall are assumed to reflect movement patterns at the shear surface, induced by microcrack growth, which have exhibited linearity and predictability in a laboratory setting (Petley *et al.*, 2005). As is discussed in the following section, linear relationships between rockfall timing and environmental conditions have been developed in a number of previous studies outside of the laboratory. In part as a function of data acquisition, however, these regressions consider rockfall as a static occurrence, and have rarely characterised the time-dependent failure development with respect to external conditions. The collection of rockfall data over short return intervals therefore holds implications for characterising the presence and nature of pre-failure activity, as well as its relationship with environmental conditions.

2.4 External controls on failure evolution

Analysing the relationship between rockfall occurrence and drivers that are external to the rock face requires a distinction to be made between factors that prepare the slope for failure, and factors that trigger failure. The former can be considered to exert a slow, cumulative effect on the rock mass, whereas the latter constitutes a near-instantaneous influence (Gischig, 2011). In Figure 2.6, progressive failure occurs when the resistance of the rock mass is exceeded by the driving forces. Gunzburger *et al.* (2005) note that this scenario can occur uniquely due to: weathering (point 1) over 10^4 – 10^6 a; over-steepening of the slope due to erosion over 10^2 – 10^4 a (point 2); or through sudden seismic or rainfall events (points 3 and 4), which may act to either reduce the resistance of the slope to failure, or increase the magnitude of driving forces. Long- to medium-term effects can be considered as preparatory factors. While the individual impacts of such factors may be infinitesimally small, their cumulative effect can result in progressive deformation of the rock mass. Below, the occurrence of a rockfall is examined as the culmination of a complex interplay between numerous interrelated preparatory stresses and, in some cases, triggers. This review emphasises that rockfall can therefore never be considered purely as a function of a single trigger (Gunzburger *et al.*, 2005; Krautblatter and Dikau, 2007).

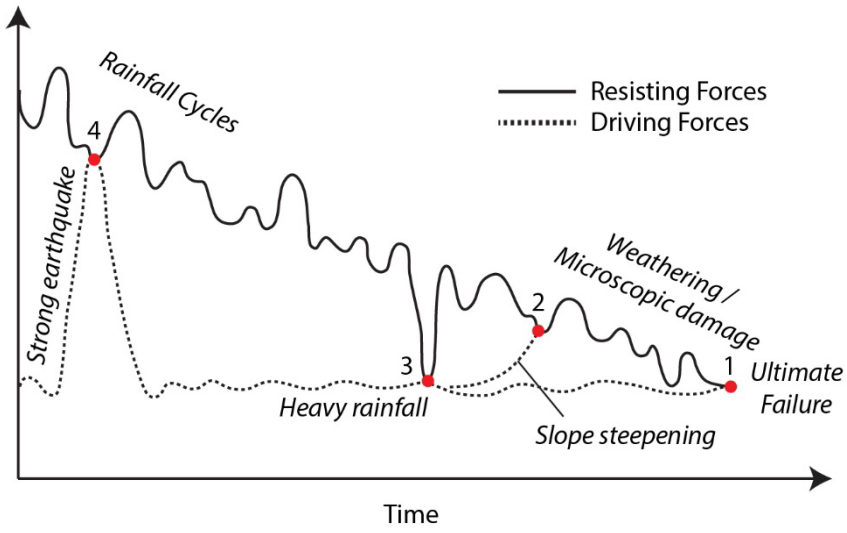

Figure 2.6: *Conceptual figure showing the timescales and roles played by preparatory and triggering factors in landslide evolution. Red dots indicate when progressive failure can occur due to the equalisation of driving and resisting forces. Modified from Gunzburger et al. (2005, Figure 2) and Gischig (2011, Figure 1.1).*

2.4.1 Preparatory factors that accumulate rock mass damage

Weathering of the rock mass acts over a wide range of temporal and spatial scales, and is responsible for the production of disintegrated, rockfall-prone material that has mostly been

detached by the breaking of cohesive rock bridges. The effects of this disintegration are superimposed upon lithological and topographic controls exerted by the rock slope, which hold considerable influence over the rate of erosion (Krautblatter and Dikau, 2007; Viles and Goudie, 2003). A comprehensive examination of the role of weathering is provided by Viles (2013), comprising biological, chemical, and mechanical, all of which can act to lower both the cohesion and frictional resistance of the slope. Chemical weathering, for example, has previously been examined as a preparatory factor with respect to the Randa rockslide (Sartori *et al.*, 2003; Jaboyedoff *et al.*, 2004). Jaboyedoff *et al.* (2004) proposed that chemical weathering of granite-gneisses, and subsequent formation of smectite, resulted from precipitation. This degraded shear resistance along joints and induced accelerations of movement by progressive failure of rock bridges without the development of pore water pressure.

Table 2.2: *Meteorological factors and triggering mechanisms, created using information from Gunzburger et al. (2005:333) and d'Amato et al. (2016:720).*

	Predisposition factors	**Preparatory factors**	**External Event**	**Processes proposed for rockfall triggering**
Mechanical	Steep sided valley Well-developed fracture network Neotectonic stresses Cold environments, e.g. Alpine, permafrost and glaciated	Rise in slope steepness due to valley incision Regular seismicity Damage accumulation Frost shattering	Freezing and thawing of water in fractures High-magnitude earthquake	Increasing pressure in joints due to ice formation (confined dilatation) and sealing of cracks leading to water pressure Ice thermal wedging due to confined thermal dilation
Hydrological and Meteorological	Climate with a high precipitation rate	Regular rainfall regime	Rainfall (intense or prolonged) Rapid snow and ice melt	Clay swelling in rock joint Loss of cohesion Increased water pressure in rock joint
Thermal	Climate with sharp temperature contrast	Thermal stresses that propagate cracks	Daily and seasonal surface temperature oscillations	Permanent deformation of sheeting joints through fracture tip propagation induced at depths < 1 m
Geochemical	Mineralogical content of the rocks prone to weathering	Progressive weathering	Rainfall	

Weathering of material can act to both prepare and trigger rockfall under certain conditions (Viles, 2013). For example, weakening of the rock mass by weathering can trigger rockfall if a cavernous feature is developed that exceeds the material strength. Even once a weathered rock particle is detached from the rock mass through rock bridge failure, it may reside on the slope, and therefore not constitute a rockfall. However. this preparation for failure can constitute a trigger if there is no toe support for the dissected rock mass, such as at an overhang or in steeply dipping joint networks, depending on particle geometry and joint roughness (Krautblatter and Dikau, 2007).

Frost action is the most important cause of rock mass disintegration in permafrost and glaciated environments, and is considered as a form of mechanical weathering. A detailed review of the surrounding literature is provided by Matsuoka and Murton (2008). Freeze-thaw action, often referred to as frost action, can occur due to the *ca.* 9% volumetric expansion that occurs during water-to-ice transition. In a fully saturated sandstone block, this can exert pressures up to two orders of magnitude greater than the tensile strength, assuming that all pores and voids are fully saturated and become frozen (Hallet *et al.*, 1996). Volumetric expansion can also result in weathering by hydrofracture of pores and microcracks, and the breakup of individual mineral particles within microcracks (Hallet, 2006). Growing evidence suggests that ice segregation, rather than expansion, is critical a critical process in the mechanical weathering of moist, porous rocks. This occurs when water travels through a rock mass by temperature-gradient induced suction, towards freezing areas of the mass. Ice lenses subsequently form, which increase tensile stresses at the boundary between frozen and unfrozen conditions. This process has been replicated in lab experiments of sandstone (Hallet *et al.*, 1996) and limestone (Murton *et al.*, 2006), and is widespread in environments with low temperature gradients and where sub-zero temperatures are sustained for significant periods of time. In addition to mechanical weathering of the rock mass, the warming of ice even below freezing also reduces shear strength along discontinuities, thereby predisposing blocks to fail that are constrained by ice-filled joints (Davies *et al.*, 2001).

Phillips *et al.* (2016) examined the Piz Kesch rock slope failure, Swiss Alps, with respect to freeze-thaw conditions and glacial debutressing. Photogrammetry surveys of the failure scar showed that it was likely to have been controlled by fracture propagation and failure of intact rock bridges. Large temperature variation, resulting in above average cumulative freezing and thawing days, was proposed as a mechanism for both. The role of ice wedging in a pre-existing tension crack was also evident, however, the presence of 6 000-year-old organic matter in this crack was drawn upon to infer long-term progressive failure and highlight the importance of phases of loading and unloading due to glacial retreat and advance.

In a non-glaciated and non-permafrost setting, Gunzburger *et al.* (2005) examined the role of diurnal surface temperature fluctuations following a rockfall along a transport corridor in

southern France. Results from a 2D numerical model showed that, if the characterised joint network exhibited perfect elastoplastic behaviour, diurnal surface temperature changes would have been sufficient to expand and induce downward creep of the failed block. Total Station measurements of the remaining unstable mass showed displacements of up to -4×10^{-4} m with slow cooling during the night, and up to 8×10^{-4} m during rapid warming at sunrise. Although this study was undertaken for an individual block, it suggests that failure potential can be enhanced by progressive loosening of material assemblage by differential displacement of blocks and joint openings.

Collins and Stock (2016) monitored the thermally induced displacements of a fracturing granitic exfoliation sheet in Yosemite National Park. Exfoliation occurred when thermally driven stresses resulted in joint creation parallel to the rock surface, allowing sheets or slabs of rock to detach. Over a three-year period, this showed a daily cycle of temperature variation on the exfoliation surface in response to insolation. The crack widened most in the afternoon during the hottest period of the day, though not when the rate of temperature increase was highest (sunrise). During cooling towards the late afternoon and sunset, the crack contracted, with a mean total displacement of the order of ca. 0.008 m d^{-1}. The deformation through multiple daily cycles was shown to result in permanent deformation of the rock mass, with an incremental widening of ca. 0.001 m d^{-1}. Permanent deformation was 0.021 m greater during summer months than winter months suggesting that rockfall may be more likely during summer months when sheet discontinuities are at the maximum outward position from cliffs.

Eppes *et al.* (2016) characterised solar induced thermal stresses that contributed to mechanical weathering of a granite boulder on open ground. This study highlighted that diurnal insolation can introduce elevated tensile stress, which causes rock to become more susceptible to cracking. An 11-month dataset of cracking, measured using acoustic emissions, was combined with measurements of rock temperature and strain. Maximum cracking coincided with maximum insolation driven thermal stresses, and when storms caused perturbations in temperature, suggesting that thermal stress are enough to generate subcritical crack growth that can prepare a slope for failure. The timing of cracking showed significant clustering in the three hours around 13.00 and 18.30, relating to the maximum daily temperature and average timing of the sunset, respectively. Cracking during the middle of the day was the result of tension that developed in the interior of the rock due to volumetric expansion, whereas cracking at sunset related to tension that developed at the near surface due to cooling. Storm events produced thermal stress distributions that were superimposed on background stresses from diurnal insolation. In such instances, tensile stress developments were often a function of dampening of the rock surface, which triggered rapid cooling of the rock surface (Viles *et al.*, 2010). However, no correlation was found between cracking and previously proposed 'thermal shocks' of 2 °C min^{-1} within a single temperature cycle (Hall and Thorn, 2014).

2.4.2 Triggers of rockfall

The main triggering mechanisms of rockfall are meteorological, including rainfall and temperature, and, for marine cliffs, wave action at the cliff base (Duperret *et al.*, 2004). Krautblatter and Dikau (2007) identify two distinct forms of triggering mechanism: (1) external causes, which can produce an increase in shear stress on unaltered shear resistance; or (2) internal causes, which decrease the resistance to shear. Increasing shear stress can arise by steepening of the sliding plane, including through erosion of the rockface, as well as by an increase in stress due to increased overburden, mechanical impact, or water pressure. The shearing resistance can be lowered by physical and chemical weathering of asperities, or a temporary loss of resistance to frictional sliding such as by ice or water (Krautblatter and Dikau, 2007).

Ice melting is a commonly described rockfall trigger that lowers the cohesion of joints. Strunden *et al.* (2015) correlated temperature, precipitation and seismicity with the monthly occurrence of rockfall on deglaciated calcareous cliffs in the Lauterbrunnen Valley, Switzerland. Over the 18-month monitoring period, only a weak coefficient of determination ($r^2 < 0.2$) was found between peaks in rainfall and rockfall occurrence. However, an r^2 value of 0.6 was found between the onset of freeze-thaw conditions and rockfall that occurred after a two-month lag, suggesting that many rockfall are triggered during thawing and snowmelt. This relationship was strongest for events up to 1 m^3, and can be explained by the larger temperature variations at the rock surface that prevent frost wedging of fractures deeper into the rock mass.

For a limestone cliff, D'Amato *et al.* (2016) monitored rockfall through a combination of ten-minute photo collection using a wide angle lens (> 0.1 m^3 rockfall observed), monthly photo collection using a telephoto lens (> 0.01 m^3 rockfall observed), and annual TLS surveys. Monitoring at this high frequency allowed a distinction to be observed between the warming and cooling phases that constitute freeze-thaw conditions. Rockfall occurred more frequently during warming and thawing than during cooling. Rockfall frequency in this study was also found to be up to seven times greater during freeze-thaw conditions than the mean background rate, and 26 times greater when mean rainfall intensity exceeded 5 mm h^{-1}.

For landslides and debris-flows, which often occur as the combined effect of intense rainfall and wet antecedent conditions, empirical models of precursory rainfall characteristics have been developed (Caine, 1980). Rainfall can be defined as antecedent in the days preceding a landslide event, or critical at the time of failure (Rahardjo *et al.*, 2001). The true impact of antecedent rainfall on failure susceptibility is difficult to quantify, as much of the soil moisture is routed into river networks through drainage, or is lost from the slope through evapotranspiration. The rate of decrease in regolith moisture is dependent on the catchment shape and size, relief, slope gradient, vegetation and lithology. Debris-flow initiation on slopes

that are covered by coarse colluviums, for example, is less sensitive to antecedent conditions because of the large, highly permeable interparticle voids (Badoux *et al.*, 2008).

Critical rainfall of a higher intensity typically requires a short duration to initiate slope failure, although the opposite is also true. Intensity-duration plots, proposed by Caine (1980), illustrate this relationship with the general form:

$$I = \alpha D^{-\beta} \qquad \text{[Eq. 2.7]}$$

where I is mean rainfall intensity, D is rainfall duration, and α and β are constants. Equation 2.7 provides an empirical threshold, in this case the minimum level of intensity and duration required for failure (Reichenbach *et al.*, cited in Aleotti, 2004), with the straight-line form:

$$\log I = \log \alpha - \beta \log D \qquad \text{[Eq. 2.8]}$$

where β represents the exponent, or gradient in *log I-log D* space. Empirical thresholds such as this are based on back analysis of landslide-inducing rainfall events (e.g. Caine, 1980; Guzzetti *et al.*, 2008) and have been defined on local, regional and global scales (Guzzetti *et al.*, 2007). For rockfall, however, this form of analysis, alongside the relative importance of rainfall accumulation versus intensity, has seldom been explored.

2.4.3 Summary of external forcing

Krautblatter and Moser (2006) showed that rainfall intensities up to 9-13 mm h^{-1} yielded none or very small increases in rockfall behaviour, but intensities exceeding this significantly increased the rate of secondary rockfall events. As such, Krautblatter and Dikau (2007) note that defining a trigger event is an example of non-linear behaviour, since small changes in a parameter can induce large changes in the qualitative and quantitative behaviour of a system. Given that non-linarites are an inherent attribute of rockfall triggering, there is arguably no reason to suggest that linear relationships between rockfall timing and environmental conditions exist, despite the fact that such relationships are frequently drawn upon.

It is perhaps unsurprising, therefore, that previous research in the setting of this study has yielded weak relationships between rockfall and environmental conditions (Rosser *et al.*, 2007a, Lim *et al.*, 2010; Rosser *et al.* 2013). However, these studies have emphasised that the timing of a rockfall must be related to its path to failure, which represents damage that is accumulated within the rock mass.

Figure 2.7 is based on observations of rockfall from an actively failing coastal rock slope (Rosser *et al.*, 2007a). The model satisfies several observations that highlight the role of spalling of material from a rock slope undergoing progressive failure, and the relationship of this activity with environmental conditions. First, failure triggers are often absent or are not coincident with the failure itself. This implies that a slope may reside close to a critical state, and may only require an infinitesimally small increases in stress to enter the final failure period. Second, some slopes may not collapse despite experiencing a large stress. Many studies have sought to characterise landslide patterns after earthquakes (e.g. Harp *et al.*, 1996; Meunier *et al.*, 2008; Owen *et al.*, 2008; Collins and Jibson, 2015) and rainstorms (e.g. Dai *et al.,* 2001; Guzzetti *et al.*, 2008; Kirschbaum *et al.*, 2011), but often in such events many slopes remain intact despite experiencing an apparently identical stress state to those which do collapse. By implication those slopes which do not fail may accumulate damage, yet may not collapse. This implies that rock masses must accrue a sufficient or critical amount of damage, often before the trigger

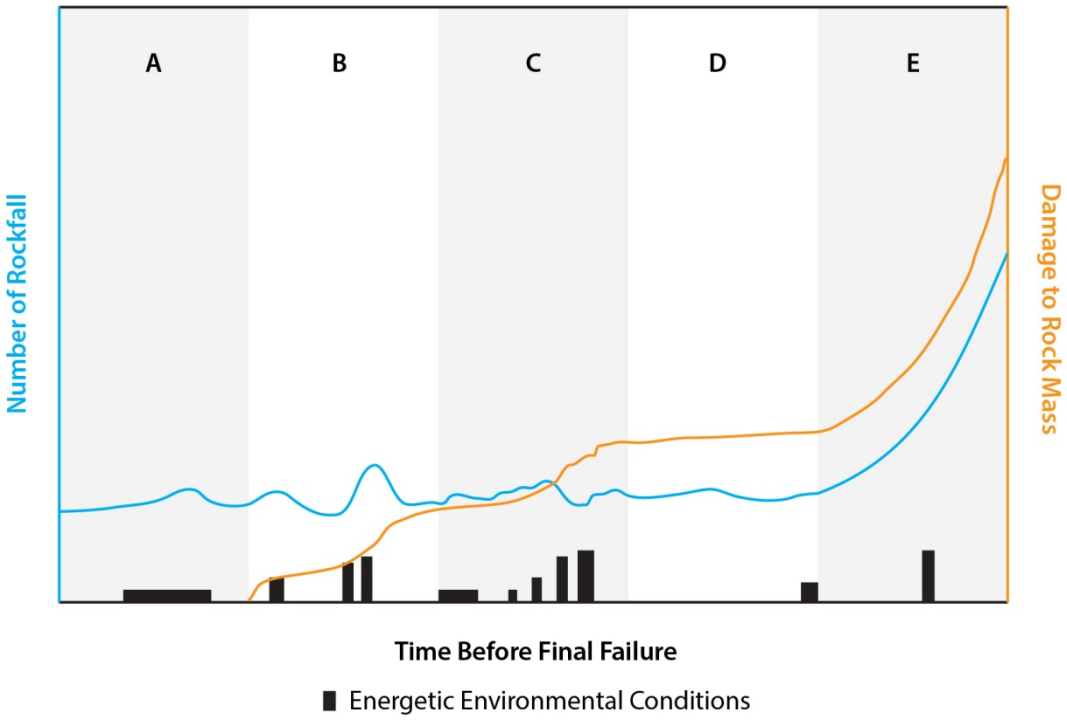

Figure 2.7: *Schematic model of the development of a large slope failure. Slopes accrue damage through shedding of surface material by rockfall. Note the hyperbolic acceleration towards final failure and the variable response to environmental forcing. A: slope undergoes background rate of detachment due to weathering. B: Irreversible damage accumulation begins due to storm occurrence, which accelerates the rate of small rockfall. C: Periods of external forcing that vary in intensity and duration act to increase damage accumulation within the rock mass towards a critical strain. D: At this stage, the slope can remain in a state close to failure, where only an infinitesimally small trigger may be required to initiate the onset of final failure. E: The control on deformation shifts from external forcing to internal drivers, resulting in a hyperbolic increase in strain rate towards failure. Reproduced from Figure 8 in Rosser et al. (2007a).*

event, to instigate final collapse. Third, event-driven landsliding has been observed to adhere to a power-law magnitude-frequency distribution in which the many *small* events may be precursors to *larger* subsequent, but yet to fail events. Fourth, a hyperbolic increase in rockfall activity, if detectable and distinguishable from background noise before collapse, may be conducive to failure prediction.

The model draws upon empirical relationships between the timing of energetic environmental conditions and rockfall occurrence at a monthly resolution. As a result, the temporal correspondence between energetic storm events and failure timing requires validation. Furthermore, while equal intervals are depicted between phases A-E, in reality, the acceleration towards final failure in the tertiary phase is likely to be much shorter, particularly if the final failure size is small. Since laboratory investigations tend only to monitor the deformation of materials under simulated stress conditions, the disparity between the durations of these stages also requires validation. It is therefore clear that a database of accelerations at a high frequency, and one that is supplemented by environmental and lithological datasets, would be ideally suited.

2.4.4 Summary of methods to assess the relationship between external forcing and rockfall occurrence

At present, while weather variables can now be recorded at very high frequency (1 min – 1 h), at low-cost, and with relatively little difficulty, the same does not apply to rockfall monitoring. Due primarily to the logistics involved in monitoring, campaigns typically comprise monthly surveys and environmental conditions must be downsampled to monthly average statistics for comparison. Relationships between the timing of rockfall and the onset of short-term (e.g. hourly) environmental perturbations are therefore impossible to identify.

Laboratory tests provide a means of damage accumulation measurement at a frequency that corresponds to the rate of simulated environmental forcing (e.g. Lajtai *et al.*, 1987; Hallet *et al.*, 1991; Murton *et al.*, 2006). In the field, however, monitoring damage accumulation within the rock mass, manifest as weathering or material detachment, is typically undertaken over time intervals that are orders of magnitude greater than those of climate data measurement. *In situ* monitoring apparatus have provided highly accurate measurements of rock mass response at frequencies that are comparable to the durations of environmental forcing (Collins and Stock, 2016; Eppes *et al.*, 2016). However, the degree to which these analyses can be extrapolated beyond the local scale conditions (individual boulders, or individual unstable blocks) in question remains unclear. Although rockfall can be measured at high spatial resolutions, monthly or weekly monitoring of rock masses requires weather conditions that are averaged over timescales often far greater than the variability of environmental controls. This requires the ability to

attribute small material detachments, which may be superimposed by or coalesce into larger failures over the month, to individual climatic events that fall below the monitoring interval. Improved monitoring capabilities have enabled measurement of the response of entire rock slopes (e.g. Rosser *et al.*, 2007a; Lim *et al.*, 2010; Delonca *et al.*, 2014), as well multiple rock slopes within an induvial valley or coastline (e.g. Strunden *et al.*, 2015; Vann Jones *et al.*, 2015). In order to bridge these deficits, a system is required that records change to the entire slope, at a time interval comparable to that of the timescales of exogenic forcing.

2.5 Magnitude-frequency distribution of rockfall

The interplay between preparatory and triggering factors emphasises the need to consider the path to failure that may occur prior to a rockfall. As described in Figure 2.7, preparatory factors may act to induce damage to the rock mass through the occurrence of smaller rockfall within the footprint of larger, yet-to-fail events. In order to interpret this mechanism, the size distribution of rockfall events that occur must be quantified.

Characterising the size distribution of landslide inventories has been undertaken for a range of purposes, including susceptibility, hazard and risk estimation (Hungr *et al.*, 1999; Crozier, 2005; Guzzetti *et al.*, 2005*;* Fell *et al.*, 2008; Guzzetti *et al.*, 2008; Van Westen *et al.*, 2008) and the development of empirical models of landscape evolution (Hovius *et al.,* 1997; Densmore *et al.*, 1998; Hovius *et al.*, 2000; Dussauge-Peisser *et al.*, 2002; Turcotte *et al.*, 2002; Dussauge *et al.*, 2003; Turcotte and Malamud, 2004; Korup, 2005; Guthrie and Evans, 2007; Parker *et al.*, 2011; Barlow *et al.*, 2012; Li *et al.*, 2016). A variety of failure types induced by specific triggers are often characterised, including fatal landslide events within global disaster inventories (Petley *et al.*, 2007; Petley, 2012), submarine landslides (Issler *et al.*, 2005; Ten Brink *et al.*, 2006; Chaytor *et al.*, 2009), rainfall induced landslides and debris-flows (Fuyii, 1969; Pelletier *et al.*, 1997; Dai and Lee, 2001; Brardinoni and Church 2004; Hungr *et al.*, 2008; Guzzetti *et al.*, 2009), co-seismic landslides (Keefer, 2000; Dai *et al.*, 2011; Gorum *et al.*, 2011; Li *et al.*, 2014; Xu *et al.*, 2014; 2015; Bucci *et al.*, 2016; Robinson *et al.*, 2016), and rockfall (Hungr *et al.*, 1999; Matusoka and Sakai, 1999; Dussauge-Peisser *et al.*, 2002; Rosser *et al.*, 2007a; Marques, 2008; Lim *et al.*, 2010; Barlow *et al.*, 2012; Vallianatos, 2013; Valagussa *et al.*, 2014; Strunden *et al.*, 2015).

Conventional approaches to landslide inventory compilation have drawn upon failures mapped using aerial and satellite imagery, whereby failures are assumed to be triggered by a single large event, or are accumulated over an extensive period of time. In order to estimate erosion rates from this data, where volume cannot be measured directly, the volume of material is estimated using area-volume scaling relationships (Larsen *et al.*, 2010). For rockfall, however, estimating change in this way is only possible if the rockfall yields deposits that are large

enough, and have a long enough residence time, to be observed from above. The use of airborne or terrestrial LiDAR enables 3D measurement of rockfall volumes, therefore avoiding uncertainties in applying area-volume relationships to the entire range of measured rockfall shapes. Young *et al.* (2011) measured rockfall events in a coastal setting using airborne LiDAR, however, the reduced coverage of the cliff face that is possible and the limited frequency of flights increases the likelihood that deposits will be moved, or rockfall scars will be superimposed by larger contiguous failures (Abellán *et al.*, 2014).

Once the magnitude of landslides has been estimated, a relationship between the magnitude and frequency of failures can be defined. Magnitude-frequency curves stem from the observed power-law relationship between the size and frequency of earthquakes (Gutenberg and Richter, 1954). Wolman and Miller (1960) proposed that the frequency distribution of geomorphic events is log-normally distributed, and that the geomorphic effectiveness of events (the product of magnitude and frequency) is greatest for frequent (though not the most frequent), moderately sized events. Sandpile models have been used to explain this relationship with the concept of self-organised criticality (Bak *et al.*, 1987), reflecting the scale-invariant response of hillslopes to failure and yielding a linear relationship between magnitude and frequency in log-log space. Fundamentally, this fractal response suggests that for every large landslide event there are more medium sized events. For every medium sized event there are many more small events, and for every small event there are even more very small events. The ratio between these frequencies of different event sizes remains constant.

Hergarten (2003) noted that this ratio, the exponent of a power-law relationship β, is similar for earthquakes as it is for gravity-driven landslides. However, the exponents for rockfall data were lower than for landslide data, suggesting that smaller rockfall contribute less to the total volumetric loss. In practice, this is likely to relate to the fact that smaller rockfall are hard to measure and, in general, are considerably smaller than landslides. The use of self-organised-criticality models was shown to overestimate these large events. The consideration of a time-dependent weakening of materials, such as the coalescence of microcracks described in *Section 2.2.2*, has been proposed to improve such models by providing a means to generate the observed frequencies of the smallest events (Rosser *et al.*, 2007a).

2.5.1 Magnitude-frequency analysis undertaken on the North Yorkshire coastline

A developed understanding of the magnitude-frequency characteristics of rockfall has arisen from previous research in the setting of the rock slope examined in this study. Lim *et al.* (2010) observed that the magnitude-frequency distribution of rockfall, from a site 12 km north of this study, resembled that of non-marine rock slopes, where 75% of recorded events were

< 0.001 m^3. The exponential nature of this distribution, in which the log of frequency distribution decreases linearly with the log of rockfall volume, supported a hypothesis that rockfall evolve as a continuum of small-scale fragmentation of the rock mass whereby large individual rockfall are in fact the sum of smaller, more frequent detachments. Both Lim *et al.* and Rosser *et al.* (2007a) found that the lithology of the rock face had a considerable influence over the exponent of the magnitude frequency distribution and hence estimated erosion rates for each ($\beta = 1.43 - 1.91$). The intact strength and depth of bedding also showed significant correlations with the permissible dimensions of failure. Mudstones, for example, yielded higher than average exponents, which represented a high proportion of small rockfall events, due to the relatively low material competence and closely jointed structure.

Many landslide distributions are characterised by a decrease in the frequency distribution of the smallest failure events, leading to a rollover in log magnitude–log frequency space. Explanations for this effect for landslides have been physical, for example, where minimum landslide sizes are controlled by the scale at which well-defined channel networks develop, or the possible transition from cohesion controlled failures to failures controlled by basal friction (Guzzetti *et al.*, 2002). More often, these rollovers reflect the level of completeness of the inventory, which is limited by the spatial resolution of monitoring. Relatively little research has been undertaken into the effects of the temporal resolution of monitoring, as this requires data collected at regular intervals over a long duration, usually encompassing the effects of seasonal variations in rockfall occurrence. Using a three-year dataset of change for North Yorkshire coastline, Barlow *et al.* (2012) showed that the tail of rockfall magnitude-frequency distributions is sensitive to the return interval of monitoring. Inventories acquired beneath the timescale of seasonal variations in rockfall activity produced unstable estimates of the frequency density of large events. However, inventories recorded with larger sampling intervals underestimated the frequency distribution of small rockfall events that were superimposed by, or coalesced into, larger, contiguous rockfall. Monthly monitoring inventories were proposed to provide magnitude-frequency relationships that corresponded with observed cliff retreat. For months that contained high magnitude events, however, seasonal inventories were more appropriate. Rosser *et al.* (2007a) noted that the duration of monitoring may be small in comparison to the return period of all possible event magnitudes. While resulting inventories may only capture a limited range of failure sizes, an individual rock face may comprise areas that each reside at a single position on a continuum of stability, which could be considered at different stages of progressive failure. A representative distribution of failure sizes may therefore be captured below the maximum return period of failure sizes.

Abellán *et al.* (2014) suggest that the spatial resolution of monitoring should be sufficient to discretise the smallest rockfall events in a magnitude-frequency distribution, and that the recording frequency should fall below the timescale of superimposition and coalescence.

In practice, defining the timescales over which failures coalesce is complex and requires the ability to monitor the rockface over a sustained period in (near) real-time. *A priori*, therefore, defining the optimum monitoring design is challenging. In order to do so, this study requires a dataset that records rockfall over short time intervals, but over a duration that includes several seasons.

2.6 The spatial development of rockfall

High-resolution monitoring of progressive rock slope failure has provided substantial insights into the spatial patterns of rockfall. Stock *et al.* (2011) observed that precursory rockfall sequences from the Rhombus Wall, Yosemite National Park, propagated upward and laterally along near vertical sheeting joints. Stresses that drive the propagation of such joints are tensile, perpendicular to the cliff face and located primarily at the surface, whereas compressive stresses are dominant at greater depths depending on slope concavity (Martel, 2011). Since rocks are generally weaker in tension than compression (Selby, 2005), sustained tension near to the surface may enhance joint propagation and hence failure along it. Stock *et al.* (2011) also highlighted the role of existing discontinuities and slope convexity in governing the spatial pattern of failure. Failed slabs were bounded by pre-existing discontinuities. At these intersections, including alcoves, sharp topographic corners tend to form with high stress concentrations, promoting the development of new joints and failures. More recent studies by Rohmer and Dewez (2015) and Royán *et al.* (2015) have shown that rockfall between 10^{-3} – 10^{-2} m^3 occur at the peripheries of larger, incipient failures that later develop.

In coastal settings, Styles *et al.* (2011) used a numerical simulation constrained by limit equilibrium models to back-analyse a landslide that occurred at Joss Bay chalk cliff, Kent, UK. This event occurred after the removal of a wave-cut notch initiated progressive failure upslope. At a critical depth, strain concentrations and compressive stresses at the wave-cut notch resulted in the upward migration of shear strain, causing tensile failure and crack growth at the cliff top. As a cluster of failure events progresses across the cliff surface tangential to the subsurface deformation, stress concentrations associated with existing failures tend to spread, predisposing the slope to further failure.

For predominantly sandstone cliffs along the North Yorkshire coastline (the setting of this study), Rosser *et al.* (2013) found a redistribution of marine erosion driven stress up the cliff face through sequencing of contiguous material detachments. Lim *et al.* (2011) and Vann Jones *et al.* (2015) examined the relationship between environmental drivers and erosion of the coastline, drawing upon datasets from terrestrial laser scanning, weather stations, accelerometers, and more recently seismometers continuously recording cliff microseismic movements. Lim *et al.* (2011) found that statistically significant relationships were obtained

between rockfall occurrence and shaking detected using accelerometers. This relationship was strongest between concurrent energetic marine conditions and high fetch winds, and rockfall from across the cliff face. Vann Jones *et al.* (2015) found that similar relationships appeared stronger for rockfall from the entire cliff than for rockfall sourced only from the inundated zone at the cliff base. This is despite the zone being inundated by water at high-tide, and the integration of variable inundation durations and tide heights into the analysis. This supports the observed linkage between failures that initiate at the base of the cliff and propagate upward (Rosser *et al.*, 2013), and suggests that microseismic shaking of the cliff has an impact upon the spatial distribution of rockfall (Lim *et al.*, 2011; Vann Jones *et al.*, 2015). However, the role of seismicity in this setting has been shown to be insufficient as a stand-alone driver of failure (Brain *et al.*, 2014). With regard to *Section 2.4*, therefore, this suggests that microseismicity can be regarded as a proxy variable for environmental forcing of the cliff. While the above studies represent significant advancements in our knowledge of progressive rock slope failure, we lack sufficient data to describe this process in general or more widely applicable terms.

This section has highlighted the importance of monitoring deformation across the entire rock face in order to elucidate rockfall propagation across it. The progression can take the form of spatially contiguous rockfall, or rockfall at varying elevations that are connected in time by the upward migration of shear strain from the base of marine cliffs to the cliff top. Combined with the previous sections, this highlights the importance of monitoring across wide areas at high spatial and temporal resolutions. These characteristics are summarised below, alongside descriptions of potential monitoring apparatus.

2.7 Rockfall monitoring requirements in this study

Based on the nature and controls upon time-dependent failure reviewed above, uncertainty persists regarding the detailed mechanisms of slope failure development and their manifestation as surface deformation. The reasons behind this are reviewed from a monitoring perspective in depth within *Chapter 4*, but are described in brief below:

(1) The scale of small rockfall, which may constitute precursors to larger, yet-to-fail events, is often below or beyond the spatial resolution of monitoring. The power-law distribution of rockfall discussed in *Section 2.5* suggests that failure in some settings could be the result of fragmentation of the rock mass during, or as a result of, wider failure. Hence, monitoring is required at a high spatial resolution that is beneath the scale of structural discontinuities, in order to explore this idea. For large-scale slope deformation, the spatial resolution is arguably less important than the precision of depth estimates. For rockfall, however, the spatial resolution is critical as it determines

the minimum aerial extent that can be defined. For LiDAR applications, this spatial resolution is in part determined by the point spacing of acquisition. Depending on the adopted processing approach, the point spacing further determines the cell size that results from interpolation of the point cloud into a fixed grid.

(2) As discussed in *Section 2.3.1*, critical levels of pre-failure strain believed to be necessary to enable final catastrophic failure, have been shown to be only *ca.* 3% of the final shear surface length (Petley *et al.*, 2008). These can be accommodated along the entire rupture, generating low localised strains and deformation on the surface. Repeated surveying of unchanged, nadir surfaces using LiDAR produces a Gaussian distribution of range estimates. The width of this distribution defines the monitoring precision, such that a narrower distribution implies that range estimates are more consistent. This is an inherent characteristic of LiDAR monitoring that determines the minimum detectable deformation. Precision is often quoted by manufacturers for tests in controlled conditions, typically *ca.* 10^{-3} m, but is often larger and more complex to define over natural topography. The complexity is increased by cyclical changes, such as wetting/drying of the slope and temperature/pressure variations that act between the instrument and the rockface. These can invoke false decimetre scale movements between surveys. Ultimately, monitoring should have the lowest possible precision. For rockfall, this determines the minimum resolvable rockfall depth.

(3) The temporal resolution of monitoring should be sufficient to capture non-linear movement patterns coupled with rapid accelerations during tertiary creep. By definition, most movement also occurs during the final phases of failure, and so may fall below the frequency of monitoring. The timescales over which small rockfall coalesce into, and can be superimposed by, larger rockfall scars remain broadly unconstrained. Monitoring at low temporal resolutions may therefore underrepresent the frequency density of small events, possibly discernible as a rollover in magnitude-frequency distributions (*Section 2.5*). Equally as important, the temporal resolution also has considerable implications for the understanding rockfall occurrence in relation to exogenic forcing (*Section 2.4*). Rockfall data should be acquired at a rate and duration that is as close as possible to those factors that may control rockfall occurrence, such as environmental and marine conditions.

(4) The surface geometry relative to the direction of monitoring is important, in particular if data projection angles are normal to the direction of movement. Rosser *et al.* (2008) showed that, for a point cloud of a deforming slope inclined at 23°, measured

deformation increased by nearly an order of magnitude for every 5° of deviation from viewing angles normal to the face. Deformation that is orthogonal to the view direction of remote monitoring is therefore difficult to capture. This is more significant for monitoring pre-failure deformation than for monitoring pre-failure detachments of material. For the purposes of this study, it highlights the importance of scanning as close to nadir as possible.

Automated monitoring systems hold significant potential for minimising the impact of these factors on the measurement of movement and resulting failure inventories. By characterising change precisely and at high spatial- and temporal-resolutions, rockfall can be examined that occur across a range of sizes and frequencies, with some related to trends in overall progressive damage accumulation and others to localised stress-triggering mechanisms. At present, the deployment of such methods has been restricted to partially stable open-pit mine high-walls, supported by significant associated investment (Abellán *et al.*, 2014). The key attributes of widely applied techniques to monitor surface deformation remotely are outlined below, with state-of-the-art appraisals provided by Petley (2012), Jaboyedoff *et al.* (2012) and Abellán *et al.* (2014).

2.7.1 Electronic distance measurement

Electronic Distance Measurement (EDM) using total stations provides remote displacement measurements for prisms that are installed on the slope. Prisms offer very high, sub-millimetre precision and can be distributed throughout the slope. The results are 3D measurements of the movement of a known point on the slope, providing a significant advantage over one-dimensional instruments, such as extensometers. However, *in situ* apparatus installation is hazardous and can incur high costs (Eberhardt, 2012). In many cases prisms are destroyed by the movements that they are trying to monitor. In the Bingham Canyon mine, Utah, for instance, 200 of 201 installed prisms were damaged beyond repair over a 13-month period (Doyle and Reese, 2011). In general, while accurate, total station measurements necessitate a degree of interpolation within the displacement field, thereby adding uncertainty to estimates of overall slope degradation emphasised in progressive failure literature.

2.7.2 Ground-based radar

Ground-based radar sensors record the phase of both the transmitted and received signals in a radar image. The use of microwaves enables cloud penetration and the ability to operate during the day and night without the need for prisms (Froese *et al.*, 2012). Relative to

satellite-based radar, ground-based platforms also eradicate issues of low revisiting periods (minimum of four days with the COSMO-SkyMed satellite constellation) and geometric distortion due to near vertical line-of-sight (Farina *et al.*, 2011). In pulse radar systems, range measurement, ρ, is based on the time-of-flight, Δt, of the radio wave to travel to and reflect from the surface object:

$$\rho = c \cdot \Delta t/2 \qquad \text{[Eq. 2.9]}$$

where c is the speed of travel. This can be rearranged to show that the total travel time, t_{total}, is:

$$t_{total} = 2\rho/c \qquad \text{[Eq. 2.10]}$$

In practice, emitted pulses are separated by a time T_{PRF} (s), which determines the obtainable temporal resolution of the time-of-flight. Because many radar systems transmit a series of pulses, however, emitted signals are not returned until after the subsequent pulse is transmitted. In essence, an ambiguity is created as there is no way of associating the first received pulse with the first transmitted pulse. An ambiguous range for pulse-systems, R_{amb}, is therefore:

$$R_{amb} = c \cdot T_{PRF}/2 \qquad \text{[Eq. 2.11]}$$

Continuous wave radar transmits a continuous signal, requiring emission and detection antennas. A phase difference ϕ_d can be determined from a predetermined phase of the transmitted signal and the measured phase of the received signal. With wavelength λ_m of the signal, a corresponding range can be calculated by:

$$r = \lambda_m \cdot \Phi_d/4\pi \qquad \text{[Eq. 2.12]}$$

Ambiguity of the range measurement will therefore occur at ranges below $\lambda_m/2$ (Wehr, 2009).

Interferometric Synthetic Aperture Radar (InSAR) uses radar imagery to map surface deformation over time, and is mainly dedicated to the detection and quantification of small displacements over entire slopes (Jaboyedoff *et al.*, 2012). Differential interferometry compares two radar images taken at different times from the same position. Satellite-based techniques compare the phase component of each image, acquired as either repeat pass (two acquisitions from the same antenna) or single pass (one acquisition from two antennas). Ground-based techniques feature two antennas that slide horizontally to form a synthetic aperture, detecting phase change along the line-of-sight. The IBIS-M radar sensor, used for example by Farina *et al.* (2011), detects range variations along the line-of-sight at $1 \times 10^{-4} - 2 \times 10^{-4}$ m precision within

0.5 m × 4.3 m cells at ranges of 1 km. This high resolution, in addition to a wide coverage capacity, allows bench-scale instability detection with several pixels of measurement.

There are, however, some critical limitations to the use of InSAR. Most importantly, measurements are spatially averaged across large footprints despite high deformation measurement accuracy. This often results in rockfall volumes $> 1\ m^3$, in comparison to terrestrial LiDAR datasets that can provide volumes as small as $1 \times 10^{-6}\ m^3$. While small magnitude changes that occur across large areas can be accurately characterised, detecting the spatial progression of rockfall activity and its relationship to the surrounding rock mass structure is therefore compromised. Furthermore, deformation monitored by this technique is along the line-of-sight. This severely limits the ability to characterise deformation that is orthogonal to the line-of-sight. Relative to terrestrial LiDAR, and other 3D techniques such as total stations and GPS monitoring, this represents a significant limitation in interpreting the mechanisms and kinematics of failure (Monserrat *et al.*, 2014). In addition, ambiguity in interferometric phases can induce bias into deformation estimates and is unsuited to the detection of very large, rapid detachments of material (Crosetto *et al.*, 2014). A further limitation of such systems is their cost, which significantly exceeds any other form of deformation monitoring technology.

2.7.3 Terrestrial laser scanning

This section highlights they key characteristics of TLS that make it suited to characterising rockfall volumes. TLS is adopted in this study, and a detailed review of techniques to process Terrestrial Laser Scanning (TLS) data is provided in *Chapter 4*.

TLS is an evolution of the EDM that has seen growing usage in applied geomorphological studies. Instruments can be classified according to the way in which they measure both the range of an object and the associated angle in vertical and horizontal planes (Petrie and Toth, 2008). The primary distinction is the means of range measurement, which, similar to radar, comprises either *Time-of-Flight* (ToF) or *phase difference*. The latter enables rapid collection of highly accurate measurements but at limited distances of tens of metres due to the range ambiguity related to wavelength, outlined in the context of radar above.

ToF operates at slower but nonetheless rapid rates of up to *ca.* 500 000 points per second for ranges up to 6 km. These systems operate with much lower beam divergences than ground-based InSAR, providing a higher spatial resolution and increasing their suitability to the characterisation of rockfall size distributions. Operating in the near-visible spectrum, however, increases their sensitivity to fog, rain, and changes in day/night conditions that are common in many mountain environments (Froese *et al.*, 2012). TLS is also subjected to shadowing or occlusion in rugged topography (Jaboyedoff *et al.*, 2012), which can only be overcome by

scanning from multiple oblique fixed positions. The resulting datasets are 3D point clouds, provided in either Polar or Cartesian coordinate systems with spacing between points typically no more than 0.1 m. For rock slope analysis, these point clouds are generally manipulated to characterise the rock mass structure, and to detect and measure deformation. A comprehensive review of both is provided by Abellán *et al.* (2014; Table 2).

2.7.4 Structure from Motion

Point cloud generation for slope monitoring has been supplemented in recent years by the development of new photogrammetric techniques, in particular Structure from Motion (SfM; Niethammer *et al.*, 2011; Lucieer *et al.*, 2013; Turner *et al.*, 2015; Carrivick *et al.*, 2016). This relies on overlapping images of the surveyed slope captured from different viewpoints in order to reconstruct the point cloud. Image features are detected, described and aligned between different photographs using feature recognition algorithms. These are then drawn upon to identify the 3D position and orientation of the camera and the *xyz* position of the feature, in what is known as a bundle block adjustment (Snavely *et al.*, 2008). Imagery is increasingly acquired from Unmanned Aerial Vehicles (UAVs). In such instances, SfM has the advantage of being available at far lower costs than TLS, minimising areas of occlusion that occur from ground-level monitoring, and providing highly dense point clouds due to the potentially small distances between the UAV and the slope. The need for near-real time constant monitoring, however, necessitates the use of TLS over SfM for a number of reasons. First, SfM relies on photographs using visible light, and cannot therefore operate in dark or low-light conditions. No published studies exist that assess the suitability of SfM for monitoring, particularly under variability lighting conditions and with the presence of shadows across the monitored surface. Second, while new packages enable automated flight path generation, photo acquisition, and auto-piloting, no existing are deployable (and rechargeable) at high frequency, without some form of user intervention.

The rapid acquisition rate of TLS enables accurate, high-resolution datasets to be acquired with sub-hourly return intervals. As such, the permanent deployment of these systems offers a unique opportunity to characterise the spatial and size distribution of rockfall, the relationship between failure timing and environmental forcing, and the evolution of failure. For rockfall characterisation, the systems are uniquely suited relative to the alternative monitoring systems discussed above. While radar systems provide precisions that are an order-of-magnitude higher, their spatial resolution and precision is better suited to the monitoring of larger-scale deformation than it is to delineating small rockfall. Owing to the fractal nature of rockfall, such events constitute a significant proportion of observed failures.

2.8 Summary

First-time landslides and rockfall in brittle slopes have been presented as the culmination of three discrete phases of movement (transient, steady-state and tertiary), rather than instantaneous event that occur in response to discrete triggering conditions. This concept of progressive failure forms the basis for this study, and underpins the research questions outlined in *Section 1.3*.

The occurrence and nature of rockfall may be partially dictated by damage accumulation within the slope, which occurs through microcrack growth or sheeting joint propagation, and is manifest as a series of detachments that may propagate into larger contiguous failures. Consequently, while stress redistribution plays a significant role in predisposing a slope to failure, the process of damage accumulation is viewed here primarily as a function of damage, or strain. Viewing these detachments as part of the progressive failure of slopes underlines the significance of accurate high-resolution deformation monitoring, in particular during the final phase of acceleration. During this phase, assuming that surficial deformation rates represent movements at the shear surface, the rate dependency of failure has lent itself to prediction of failure timing in a number of examples. In both the laboratory and partially stable open-pit slopes, generic strain-rate behaviour that is applicable without being tailored to specific slope characteristics has been used to successfully predict the time of failure. This application remains understudied for catastrophic rockfall events, and has previously only been attempted using irregularly spaced monitoring data collected at intervals that may fall below the timescale of rockfall acceleration.

If microcrack growth is assumed to drive rock slope instability, the relationship between rockfall and energetic environmental conditions becomes arguably more complex to discern (Vann Jones *et al.*, 2015), to the point that attributing a rockfall to a specific trigger may actually be impossible. A number of studies have characterised the relationship between rockfall and environmental conditions, with a considerable focus on rock slopes in glaciated and permafrost landscapes. These have highlighted the importance of temperature, in particular when freeze-thaw conditions are introduced. *In situ* monitoring of non-glaciated or permafrost slopes have expanded this understanding by measuring thermally induced tensile stresses within the slope. However, the validity of these findings cannot yet be extrapolated to other slopes using current monitoring datasets, the return intervals of which often falls below the timescales of variability in the driving conditions under investigation. At present, therefore, the relatively weak correlations in all but glaciated and permafrost environments suggest that brittle rock slopes respond to complex interactions between preparatory factors and triggers, or that current monitoring data is of insufficient resolution to capture this behaviour (Vann Jones *et al.*, 2015).

Capturing sequences of material spalling prior to failure provides insights into the

mechanisms of progressive failure, and highlights the importance of characterising the size distribution of detachments. If different areas of a slope are assumed to reside at varying points along a continuum of progressive failure, an accurate appraisal of the magnitude-frequency distribution can be generated. The accelerations in microcrack growth described in *Section 2.2.2*, and the accelerations in rockfall activity prior to failure described in *Section 2.3.2*, suggest that the power-law magnitude-frequency distribution may be a product of fragmentation of the rock mass. The degree to which this process is defined by pre-existing structural discontinuities requires a combination of high resolution of monitoring and accurate rock mass characterisation. Many studies that have characterised monthly rockfall activity have also highlighted an underrepresentation of the smallest rockfall, exhibited as a rollover in the frequency distribution of smallest events. This has been attributed to superimposition by larger, more recent contiguous rockfall; however, the sensitivity of the overall magnitude-frequency distribution to variability in the return interval of monitoring remains unclear. Analysing the magnitude-frequency distributions of rockfall over different return intervals may be an effective tool for constraining the timescales over which failures occur. The development of a near real-time monitoring system that is designed to address the uncertainties identified this chapter is presented in *Chapter 3*.

Chapter 3

Development of a 4D Rockfall Monitoring System

3.1 Introduction

In *Chapter 2*, our current understanding of the nature and controls of rockfall evolution was presented in the context of existing slope monitoring techniques. It was argued that if rockfall are considered as time-dependent evolving phenomena, rather than as instantaneous events, then it is necessary to implement monitoring that is capable of capturing precursors to failure. Three primary attributes of the proposed methodology have been identified. First, the spatial resolution, or point spacing for LiDAR instruments, should be dense enough to capture a range of rockfall volumes. These include small-scale detachments of the order of $0.001 - 0.1$ m^3, which translate to edge lengths of a cube no more than $0.1 - 0.2$ m. Such events occur most frequently according the fractal distribution of rockfall sizes, may or may not relate to exogenic conditions, and may represent ongoing deformation that precedes larger yet-to-fail rockfall. Second, the precision of range estimates, and hence the accuracy of change detections, should be as high as possible. While the point spacing determines the aerial extent of detectable rockfall on the rock face, the precision of range estimates determines the accuracy of depth and change in depth measurements. This should be no more than several centimetres in order to characterise both creep of the rock mass and small detachments that may precede a larger rockfall. Third, the time interval between surveys should be low enough to detect and distinguish short-term, sub-hourly movements that have previously been observed before catastrophic brittle failure using radar (for example, Dick, 2013). This frequency should also be comparable to the timescales of changes in environmental forcing, and therefore sufficient for monitoring cumulative and instantaneous responses of the rock slope to drivers. Finally, the monitoring should be constant through time to ensure that all events are captured, many of which are episodic and remain uncertain. These events are required to develop a thorough appraisal of the path to failure, and to detect deviation from background conditions.

The focus of this chapter is the development of a near-constant slope monitoring system, defined here as repeated surveying without movement of the instrument or interruption of a pre-defined scan schedule. The system is installed to detect rockfall from a coastal rock slope at Whitby, North Yorkshire, UK. Scans have been acquired since March 2015 at sub-

hourly intervals, providing a terrestrial LiDAR dataset unprecedented in both consistency and resolution. This thesis reports results up to the end of 2015, a period of 10 months. The chapter begins with a description of the site where this system has been developed, before outlining previous research undertaken on rockfall in the area in addition to the research described in *Chapter 2*. This identifies the site as an ideal location for a study into rockfall mechanisms. A detailed specification of the system is then presented, which also includes an overview of the environmental data collection and highlights the significance of considering the spatial resolution of constant monitoring relative its temporal resolution. The data analysis approach used to process the resulting LiDAR surveys is presented in *Chapter 4*.

3.2 Site description

In this study, constant monitoring has been undertaken at East Cliff, an actively

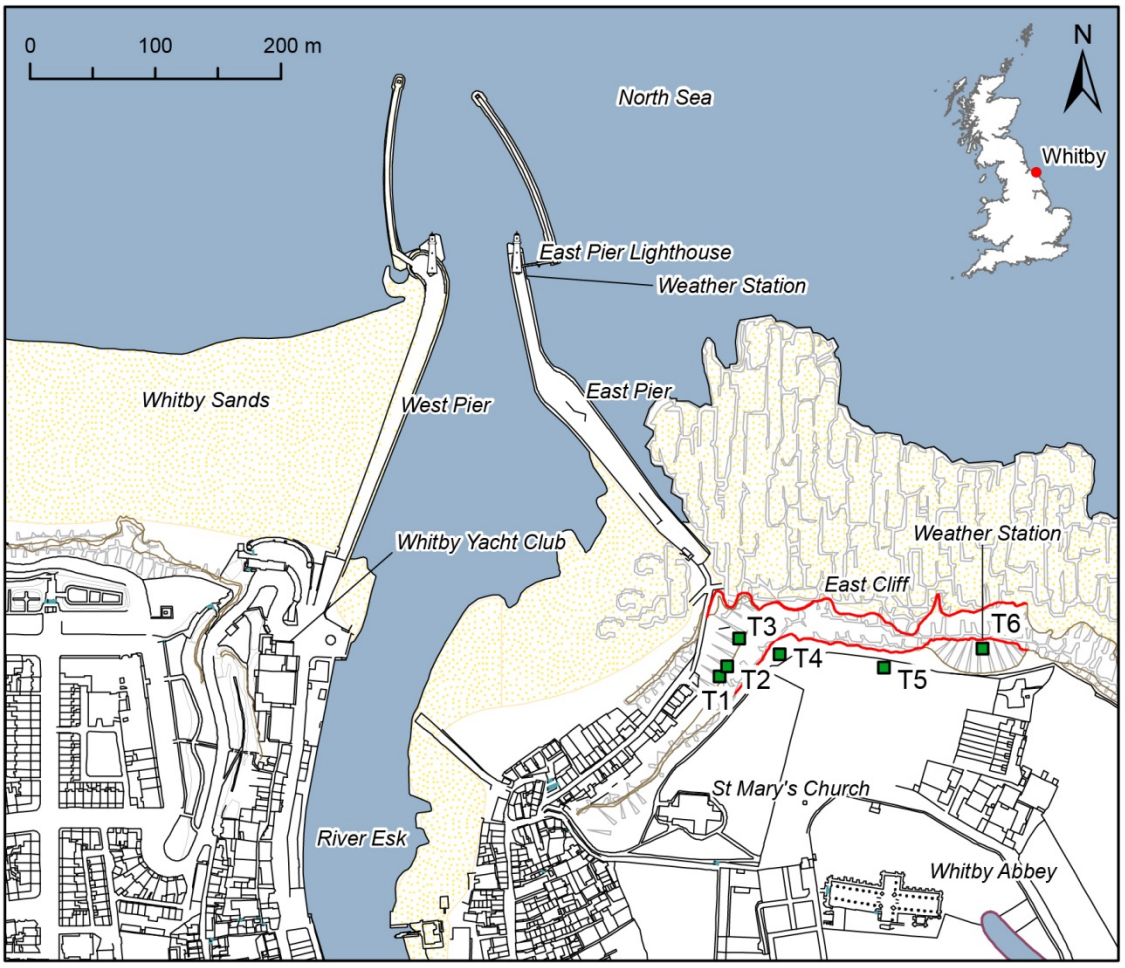

Figure 3.1: *Map of Whitby with the area scanned delineated with red lines. The Riegl VZ-1000 scanner used in this study is installed within East Pier Lighthouse, located at the end of East Pier. The targets installed for the SiteMonitor4D system, in addition to the weather stations, are illustrated (T1 – T6). Whitby Abbey lies 180 m from the cliff top. Map produced using shapefiles from Ordnance Survey © Crown Copyright and Database Right 2016. Ordnance Survey (Digimap Licence).*

eroding coastal cliff that is located east of the town of Whitby, North Yorkshire, UK (Figures 3.1 and 3.2). The near-vertical cliff face reaches up to 60 m high and forms part of the Whitby to Saltwick Site of Special Scientific Interest, designated as such due its geological significance. In front of the cliff, a near-planar, low angle ($< 2°$) wave-cut platform extends *ca.* 150 – 200 m seaward. While exposed at low tide, the platform can be covered by high tides up to 6 m in height (Vann Jones *et al.*, 2015) with significant nearshore wave heights (the mean of the highest one-third of waves from trough to crest) up to *ca.* 3 m. These waves often strike the cliff base. The western 300 m of the monitored site is fronted by rock armour, which acts to limit marine erosion.

Small fragments of the cliff face can be regularly observed and are heard falling almost continually. While the cliff is actively eroding, in previous work and in this study, complete removal of failed material is assumed given the near vertical profile of the cliff and its reworking by marine action (Lim *et al.,* 2010). Retreat of the cliff has been studied intensively in recent years, in part due to the cultural significance of Whitby Abbey, which stands 180 m from the

Figure 3.2: *Infoterra aerial imagery of Whitby (2009), acquired from Google Earth within the same area as Figure 3.1. Here, the foreshore platform in front of East Cliff is partially inundated. Previous LiDAR surveys of the cliff have been undertaken from this platform. The scale here is the same as that applied in Figure 3.1.*

present cliff top location. Although this is not acutely at risk from cliff top recession, a considerable number of artefacts are buried within the headland and its vicinity as a result of prolonged human settlement. As noted by Miller (2007), following a substantial slope failure in October 2000, a salvage excavation was undertaken near the cliff-top to prevent the loss of such artefacts. In 2006, a television mast measuring approximately the same height as the cliff itself, *ca.* 60 m, was dismantled and moved further inland due to the risk of erosion, having previously been positioned 12 m from the cliff edge. Initial monitoring by Rosser *et al.* (2005) was commissioned to inform the decision-making process for its relocation (see *Section 3.4*).

As a result of prolonged wet weather during late 2012 and early 2013, a landslip on 26th November 2012 caused irreparable damage to a row of five cottages on the same cliff escarpment further inland up the Esk Valley, *ca.* 300 m south of the sea cliff face (Whitby Gazette, 2012). In January 2013, failures across the rock slope beneath St Mary's Church (see Figure 3.1) threatened cottages below and also resulted in the exhumation of human remains from the churchyard (BBC, 2013). A rockfall protection barrier currently exists beneath this portion of cliff, and extends up to the seaward section of cliff monitored in this study, which is delineated in red in Figure 3.1.

3.3 Geology

East Cliff lies on the footwall of the Whitby Fault, a normal fault with a north-south trend and downthrow of *ca.* 12 m to the west (Hemingway *et al.*, 1968; Alexander and Gawthorpe, 1993). The rock cliff exhibits near-horizontally bedded strata (Figure 3.3), with the upper 30 m near-vertical and the lower 25 m forming a buttress that fronts the majority of the rock face (Figure 3.4). In 2000, a 4 m high granite rock armour revetment, designed to reduce the impact of marine erosion of the cliff-toe, was placed in front of the cliff. From East Pier, this extends east along the base of the cliff for 300 m. The cliff toe itself comprises grey, fissile shales of the Whitby Mudstone Formation (Upper Lias), which are overlain by yellow-brown siderite sandstone and phosphatic pebbles of the Dogger Formation, outcropping *ca.* 13 m up the cliff (Powell *et al.*, 2010; Barron *et al.*, 2012). The buttress is sparsely vegetated and collects material from rockfall further up the cliff. While the buttress itself comprises intact rock, rockfall deposits from above are lodged on its surface close to a critical angle of repose, such that new material may either continue to build or runout further onto the foreshore. Much of this zone is also covered with a drape of silt derived from fragmented deposits that have fallen from the interbedded siltstones and carbonaceous mudstones above. As a result, neither the structure of the intact geology beneath nor change in this region is easily discernible by observation alone.

At elevations of *ca.* 14 – 50 m in Figure 3.4, non-marine fine-grained Middle Jurassic sandstones are interbedded with clays and siltstone known as the Saltwick Formation (Barron *et*

al., 2012). Within this formation, layers of bedded sandstone protrude beyond the weaker interbedded sandstone and siltstone between them, as represented in the stratigraphic log (Figure 3.4). The fine-grained, sub-horizontally bedded sandstones vary considerably in structure from the alluvial sandstone apparent in West Cliff, on the opposite side of the Esk River. At the top of the rock cliff, there is a band of widely jointed marine sandstone of the Ellerbeck Formation. This is capped with a soft variable thickness Late Devensian glacial till, *ca.* 5 m in depth, from which downslope results in a slight orange staining of the sandstone and cliff face below.

Figure 3.3: *Image of the cliff taken 1 h before high tide on 25h November 2015. The cliff extent photographed here matches that in planform in Figure 3.1, delineated by the red lines. Horizontally bedded strata are evident, with upper beds stained orange from downslope wash from glacial till of variable depth. The lower buttress comprises shales and some sandstone, while the near-vertical upper portion of the cliff comprises outcropping sandstone, and sandstone interbedded with carbonaceous muds.*

A range of rock types and rock strengths has resulted in the cliff's non-vertical profile (Figure 3.4). Failure styles include small-scale wedges, failure along joints, and rock bridge breakage, which can be inferred from exposed fresh fracture surfaces observed after failure. Rockfall from the cliff leave a range of scar geometries, which have shown variability according to rock type and joint structure of each bed. The mudstones, shales and siltstone that comprise the buttress and lower half of the cliff are fissile laminated deposits. These deposits characteristically abrade, releasing small rockfall in which the width is approximately equal to the height, and hence appears to reflect the dense joint network from which it originates. Joint width generally increases with increasing elevation up the cliff. At the cliff top, more widely jointed sandstone has previously produced more elongated failures, reflecting the relatively shallow bed depths and wider joint spacing (Rosser *et al.*, 2005). The rockfall height therefore tends to be more variable than width, suggesting that bed depth (the height of each bed) may

act to constrain the permissible dimensions of released material. For all areas of the rock face, previous monitoring has suggested that rockfall are shallower than they are wide and high.

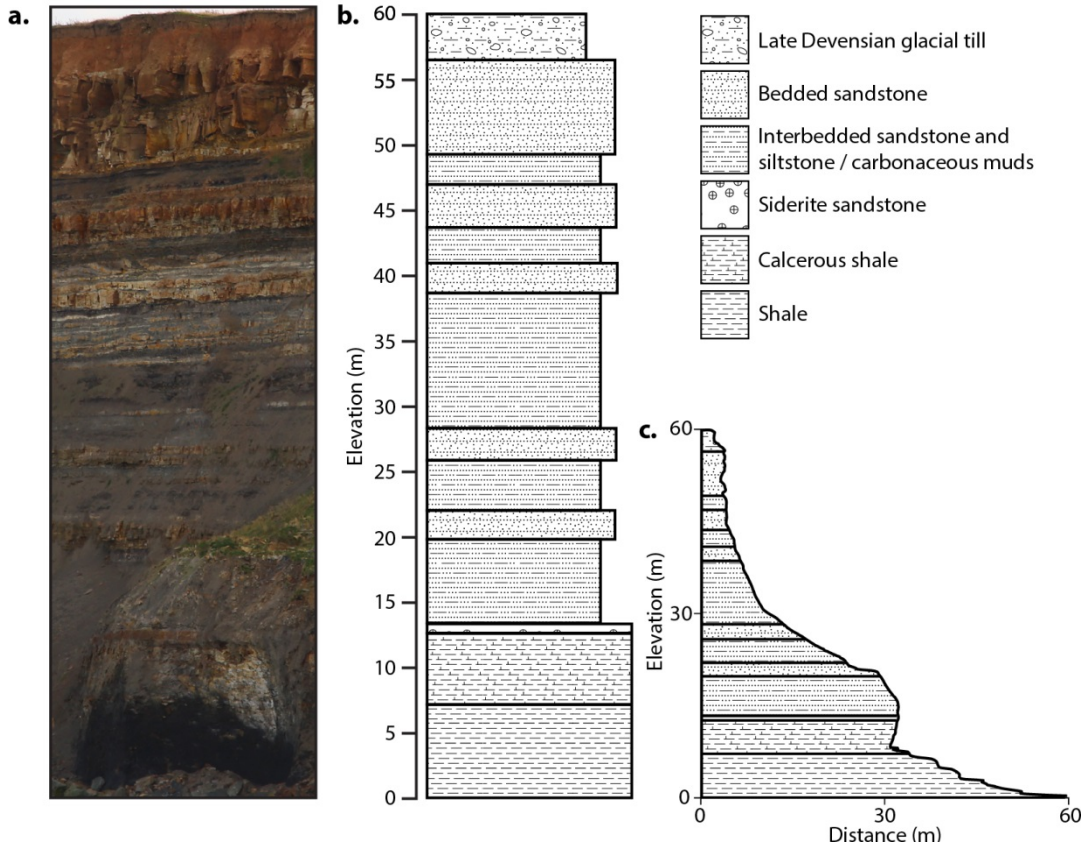

Figure 3.4: *(a) Photo illustrates the near horizontal bedding of sandstone and sandstone interbedded with siltstone. The cliffs are capped with glacial till, ca. 2 m - 3 m in height. (b) Stratigraphic log of the Early to Middle Jurassic sequence at East Cliff. (c) TLS-derived cliff profile taken through (a). The stratigraphic units have been extrapolated inland based on the absence of visible dip in the bedding. A transition from a concave to convex slope profile occurs at the buttress, ca. 20 m elevation, with rock armouring evident at the very base of the cliff. Log modified from Figure 3 in Rosser et al. (2005:365).*

3.4 Rates of erosion and previous research

Monitoring at East Cliff builds upon a large body of ongoing research into the nature of hard rock erosion along the North Yorkshire coast (including, but not limited to, Rosser *et al.*, 2005; 2007a;b; Lim *et al.*, 2010; 2011; Barlow *et al.*, 2012; Rosser *et al.*, 2013; Brain *et al.*, 2014; Vann Jones *et al.*, 2015). Having conventionally received less attention than more visibly eroding soft cliffs, the ongoing research has monitored numerous hard rock cliff sections at monthly intervals since 2002, over a 25 km stretch of coastline. In order to monitor change over this scale and at this frequency, both airborne and terrestrial LiDAR have been employed extensively, generating a large, long-term dataset of varying failure types. These are outlined by Rosser *et al.* (2013) and include slumps, rockfall, and spalling of material. A key finding of this research has been the notable absence of cliff notch development and subsequent cantilever

failure, despite being a well-documented mechanism of cliff line retreat (see, for example, Trenhaile, 1987; Bird, 2011).

The recession of East Cliff was first examined by Agar (1960), who noted that the upper slopes underwent greater sub-aerial erosion compared to wave action at the cliff toe, with an overall erosion rate of 0.19 m a^{-1}. Miller (2007) used the cliff as site upon which to test a robust least squares surface matching algorithm, designed to enable change detection between multi-temporal, multi-sensor datasets. Archive aerial photography and airborne LiDAR were used to create Digital Elevation Models (DEMs) that, once aligned, were subtracted to derive DEMs of Difference (DoDs). Between March 1994 and May 2006, a net loss of 59 326 m^3 was recorded (Miller, 2007). This study underlined a significant contrast between erosion rates on the upper and lower parts of the cliff, at 0.50 m a^{-1} and 0.15 m a^{-1} respectively, with 0.216 m a^{-1} for the cliff face as a whole. Using DoDs derived from monthly terrestrial LiDAR surveys, Rosser *et al.* (2005) recorded an inventory totalling 810 rockfall events between September 2003 and December 2004. Retreat across the cliff during this period ranged from 0.00 – 57.70 m with a mean retreat rate of 0.18 m a^{-1} for the entire cliff face. This study also characterised the dependence of rockfall size and spatial distribution upon the geology and structure of East Cliff. The lowest rates of detachment were found in the widely jointed sandstone band at the cliff top, typically no more than 0.06 m over the 16-month survey period. In contrast, removal of *ca.* 1.5 m of material was identified in the interbedded sandstone and siltstone bands of the Saltwick formation, between 38 – 48 m elevation. In this zone, rockfall clusters were observed along the horizontal bedding and were constrained by bed-depth. The largest failure captured during the period of monitoring was a *ca.* 200 m^3 slump, initiating on the buttress and depositing material on the rock armour below.

These observations support the hypothesis that spatial linkages exist between failures, beginning with erosion of the cliff toe through wave action and propagating upwards by means of small failures along bedding planes, which in turn predispose blocks above to failure. At several sites further north along the same stretch of coastline, upward propagation of instability moderated by intact rock strength and time-dependent rock fracture has been measured from over a decade of monitoring. Rosser *et al.* (2013) observed only one instance in which retreat of the cliff top occurred due to undercutting at the cliff toe. In most other instances, cliff line retreat was only observed when rockfall propagated up the cliff, where kinematically feasible, and extended towards the crest. In settings subject to intense sub-aerial processes, such as rainfall and wind, Rosser *et al.* (2013) suggested that marine driven erosion may be subsumed by quasi-continuous spalling of the rock mass. The incremental removal of material in turn reduces the probability of larger-scale cantilever failure.

The research undertaken along this coastline has highlighted the sensitivity of magnitude frequency distributions to the timescale of monitoring (Barlow *et al.*, 2012), the

evolution of rockfall through time-dependent rock fracture and subsequent propagation of small detachments that is independent of marine action (Rosser *et al.*, 2007a; 2013; Vann Jones *et al.*, 2015), and varying strengths of relationship between the timing of environmental variables and rockfall (Lim *et al.*, 2011; Vann Jones *et al.*, 2015). However, similar to other studies that adopt TLS, the datasets drawn upon in previous research have been acquired at monthly intervals. Amongst other outputs, constant monitoring at sub-hourly intervals has the potential to further examine many of these relationships. The knowledge base that currently exists surrounding failures in this setting makes this site an ideal setting to test the ability of 4D monitoring to help develop our understanding of the nature and evolution of rockfall.

3.5 Environmental conditions during the monitoring period

In this section, the environmental conditions that occurred during the 10-month monitoring period are examined, based on data recorded by weather stations installed at East Cliff. This serves as a general assessment of the external drivers that may act on the cliff face, with the acquisition of data outlined in more detail in *Section 3.9.2* and its analysis in *Chapter 6*. While previous research has shown that rockfall geometry is strongly dependent upon geology, the relationship between failure timing and energetic environmental conditions is poorly constrained for hard rock cliffs in both marine and non-marine environments (Rosser *et al.*, 2007a; Lim *et al.*, 2010).

Tide heights were recorded using the Whitby tide gauge, operated by the British Oceanographic Data Centre (BODC; Figure 3.5). Spring high tides monitored by the gauge, which occur twice a month, ranged from 5.40 – 6.30 m (Ordnance Datum). The mean high tide during the same period was 5.29 m. Wave climate data was acquired from the Channel Coastal Observatory (CCO) wave buoy, with a maximum recorded significant wave height of 14.36 m (representing the mean height of the highest third of waves from trough to crest). These measurements are recorded 1 600 m offshore and hence their height and energy will change on reaching the cliff. Despite this, offshore data serves as a useful proxy for marine forcing since most waves will impact on the cliff base during a high tide, notwithstanding attenuation and shoaling across the foreshore platform (Vann Jones *et al.*, 2015).

The aspect of East Cliff exposes it to easterly and northerly storm surges while protecting it from the prevailing south-westerly winds. Based on weather data recorded by the weather stations used in this study (*Section 3.9.2*), winds were onshore for 43% of the monitoring period, with a median speed of 2.7 km h^{-1} and maximum recorded speed of 114.84 km h^{-1} delivered to the rock face. Three significant storms occurred during the monitoring period, all of which occurred in quick succession during a single month and were named by the Met Office as they had the potential to cause substantial impacts:

(1) Storm Desmond, 5th – 6th December 2015, resulted in widespread flooding in Cumbria, where the UK's highest 24 h rainfall was recorded (341.4 mm; Met Office, 2015). The North East of England also experienced significant rainfall and strong gusts, with 151 mm rainfall recorded by the weather station installed at East Cliff, and 75.6 km h^{-1} wind speeds.

(2) Storm Eva, 24th December 2015, resulted in strong gusts in the UK, with onshore wind speeds reaching 95.8 km h^{-1} at East Cliff.

(3) Storm Frank, 29th – 30th December 2015, resulted in extensive flooding across the UK. 31.2 mm of rainfall was recorded at East Cliff with the year's highest onshore wind speed, 114.8 km h^{-1} recorded on the final day of monitoring reported here, 30th December.

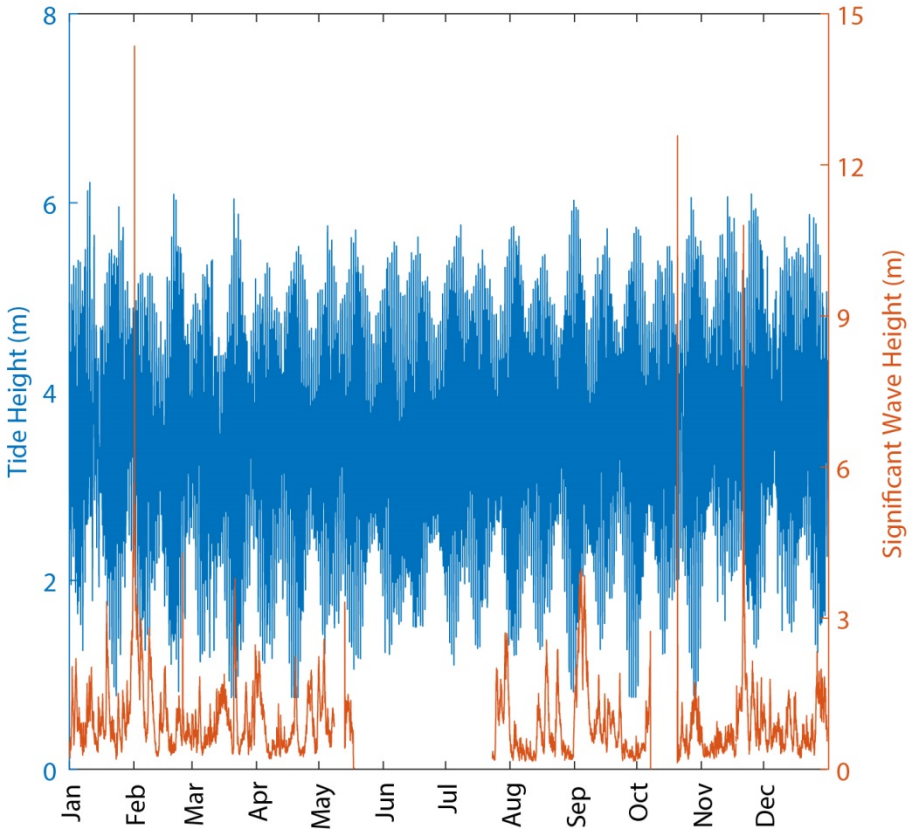

Figure 3.5: *Tide height data from British Oceanographic Data Centre (BODC) and significant wave height data from Channel Coastal Observatory (CCO) during 2015. A gap in wave climate data lasted approximately two months and ended as the six-week gap in scanning from July to August began.*

Minimum air temperatures, recorded by the Met Office at Whitby since 1962, are moderated by Whitby's coastal setting and the relatively warm seawater temperatures. The

coldest air temperatures occur in January and February, where mean monthly air temperatures are 1.6 °C. The highest average monthly temperatures are recorded in July and August, at 18.6 °C. Within this study's monitoring campaign, the maximum air temperature was 25.1 °C, recorded on 4th July, and the minimum recorded air temperature was -0.6 °C, measured on 22nd November. Based on longer term records, minimum air temperatures occur in January, with daily temperatures of -2.0 °C sustained for multiple days. In this study, however, temperatures below freezing were not sustained beyond an hour, minimising the potential for frost action. In historic records acquired from the Met Office and presented in Figure 3.6b, March is the driest month with a mean rainfall of 38.7 mm, while November and December are the wettest with 61.7 mm.

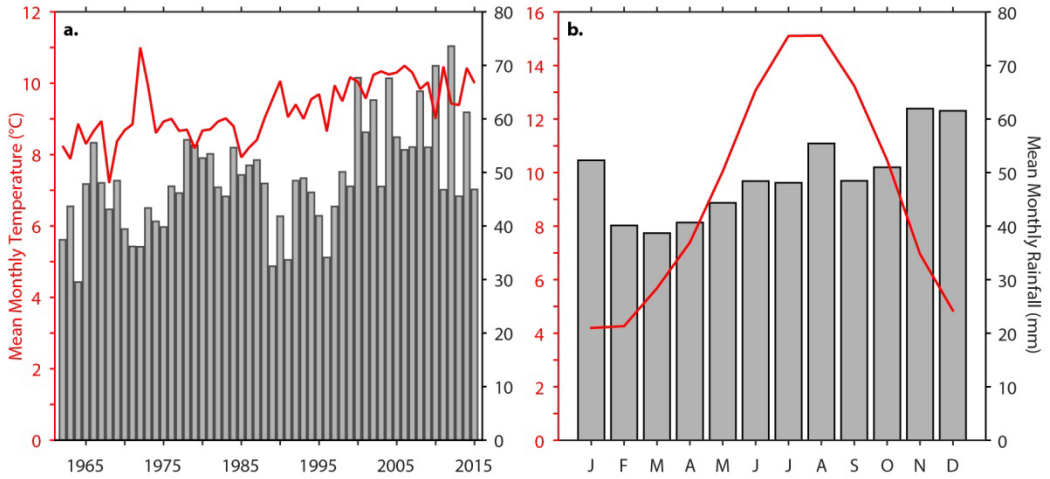

Figure 3.6: *(a) Mean monthly rainfall and temperature for Whitby, presented as annual averages from 1962-2015. The overall rise in both rainfall and temperature are indicative of increased storminess and climate extremes in this area (b) Mean monthly rainfall and temperature, presented as monthly averages over the same period. Source: Whitby meteorological station data published by the Met Office, available from data.gov.uk.*

3.6 Design of constant slope monitoring system

Installation of the slope monitoring system began in December 2014 and was completed in February 2015 (Figure 3.7). The main system is housed inside the former lantern room at the top of East Pier lighthouse (Figure 3.8a) and was powered by two batteries charged by methanol fuel cells (Figure 3.8d). These fuel cells have since been replaced with mains power supplied to the lighthouse, minimising the risk of low battery voltages that interrupt scanning and removing the need for return visits to replace the fuel. The terrestrial laser scanner used is a Riegl VZ-1000, with a measurement range of 2.5 – 1 400 m, an accuracy of 0.008 m, and an 0.005 m precision (Riegl, 2015). This precision is quoted as the standard deviation of repeated range estimates at 100 m, onto an idealised target surface under test conditions. The TLS

survey schedule is managed using *SiteMonitor4D*, a software package provided by 3D Laser Mapping Ltd. Originally designed for use in open-pit high-wall monitoring, the *SiteMonitor4D* data acquisition module enables scheduled scanning of a user-defined area and the ability to switch the scanner on and off between scans to preserve power.

The scanner was secured to a steel base plate within a custom-built metal housing, fixed to a custom-built hardwood doorframe, facing south back towards the rock face. A small pane of laser permissible glass was installed within the door, through which the laser can pass without distortion. The steel base plate was adjusted to ensure that the scanner orientation was never more than 0.005° in either tilt or yaw. Despite this, small movements of the scanner were recorded through each day as a result of temperature variations. Combined with variable

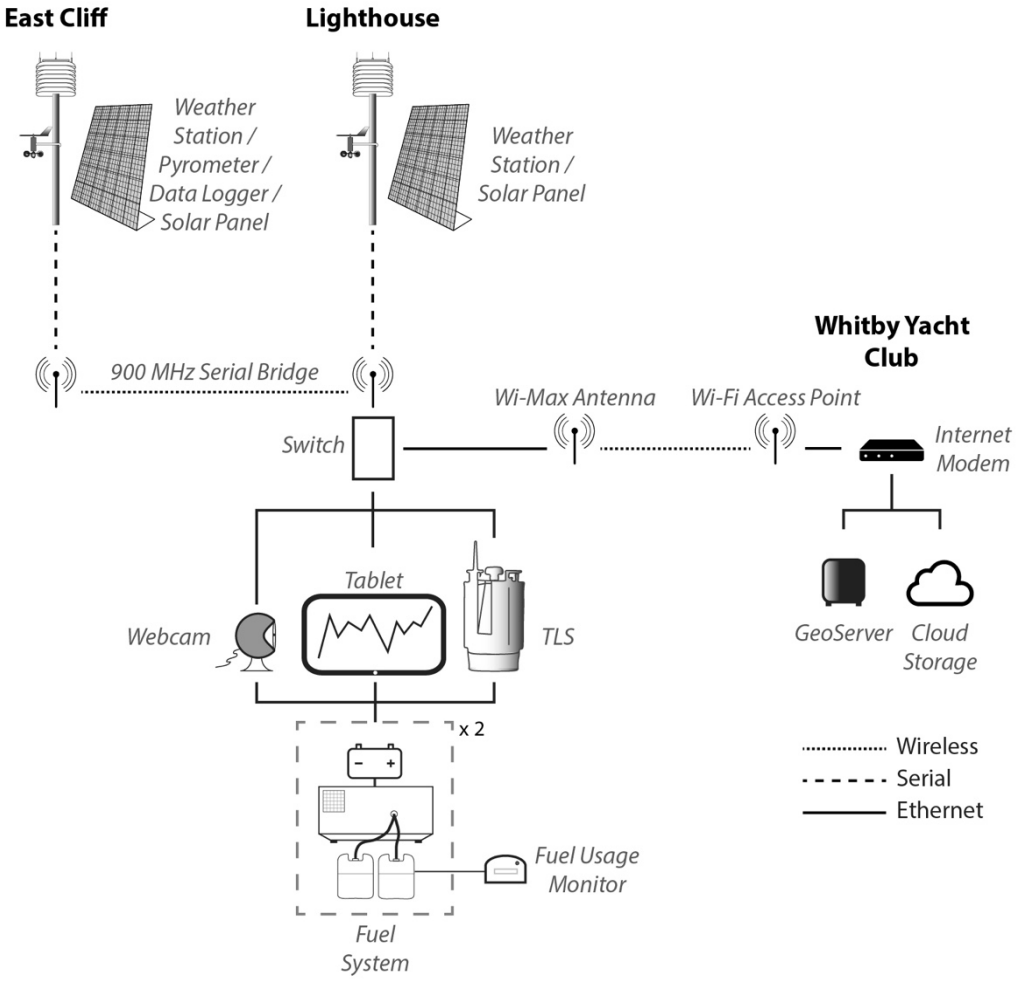

Figure 3.7: *System diagram of the constant monitoring setup. Weather stations, powered using the solar panels, are located on East Cliff and the lighthouse. The fuel cells were used to power the webcam, tablet and scanner and Wi-Max connection; however, this is now powered by mains supply. The tablet runs SiteMonitor (3D Laser Mapping Ltd.), and saves the scan data to a Dropbox™ folder for upload through the yacht-club broadband. Summary statistics of the scanning schedule along with the weather station data are uploaded to GeoServer using the broadband connection, where it can be accessed through GeoExplorer (NavStar Geomatics). Diagram modified from an original concept design created alongside NavStar Geomatics.*

atmospheric and lighting conditions between scans, this resulted in millimetre offsets between successive point clouds. In order to correct for this, *SiteMonitor4D* also provides a range correction factor (RCF) to compensate for drift between sequential point clouds and an affine rigid-body rotation matrix to compensate for tilt and yaw variation. Six stable targets (high reflectivity, blank 0.6 × 0.4 m street signs) were mounted along the periphery of the monitoring area and scanned at 3 h intervals between scans of the cliff (Figure 3.1), enabling RCF estimation and its application to each point in the point cloud. RCF values used in repositioning each scan dataset were typically 1×10^{-5}, equating to *ca.* 0.0034 m at the closest point to the scanner on the monitored cliff (342 m). As such, the data was not subject to atmospheric distortion effects and is considered consistent and rigid through time.

Data collected from the scanner is transferred via a long-range Wi-Max antenna link between the lighthouse and the local yacht club, alongside the weather station and webcam data described in *Section 3.9.2*, where it is subsequently uploaded to a Durham University server through a broadband connection via Dropbox™. The process of converting the uploaded data into change detections is described in *Chapter 4*. The weather station data and webcam imagery (*Section 3.9*), and up to date information on the scanning schedule (including target scans) were recorded and accessible within *GeoExplorer*. This is a software package created by NavStar Geomatics (NavStar, 2015) that compiles, analyses and graphs live datasets from a wide range of slope monitoring instruments that record simultaneously.

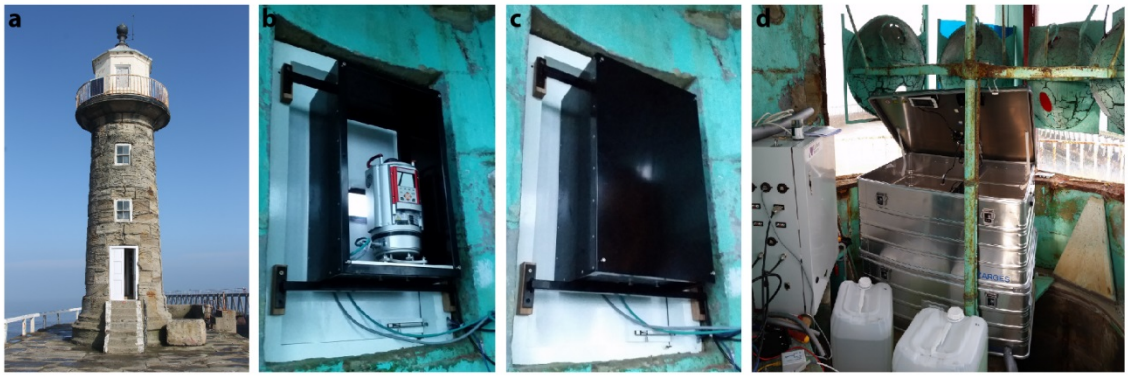

Figure 3.8: *(a) Image of East Pier Lighthouse at the end of East Pier before the installation took place. This side of the lighthouse faces towards the cliff, (b-c) A Riegl VZ-1000 is mounted within an aluminium frame with a secure removable panel at the back. The scanner measures the cliff through a glass panel suited to allowing the laser to pass through with minimal interference, and (d) Two batteries are used to power the system, charged by methanol fuel cells.*

3.7 Scan schedule and point spacing

The size and type of movement that can be detected is a function of the spatial resolution of scanning, its precision, and the time interval between scans. Scans with higher

spatial resolutions provide small point spacings and hence are able to delineate smaller detachments through measurement of scars. The precision of monitoring, here referring to the offset in range estimates between scans, determines the depth of detachments that can be accurately resolved. As a result, this also determines the ability to resolve deformation of the rock mass that occurs without material detachment. These attributes hold implications for the analysis of failure size distribution, the response of the slope to changes in environmental conditions at hourly and sub-hourly timescales, and patterns of precursory deformation.

In conventional monitoring campaigns, the temporal resolution, which is determined by the frequency of scanning, is limited by the feasibility, cost and logistics associated with scan data acquisition (Abellán *et al.*, 2014). Monitoring in coastal settings, for example, is normally only possible during the lowest tides of each month when the foreshore is accessible (Lim *et al.*, 2005). Even in semi-permanent installations in open-pit environments, scanning is restricted during blasting, and instruments are often moved between survey positions to monitor multiple slopes. Given that high-frequency scanning is not a primary objective of most studies, the time taken to acquire each scan is not limited by the time interval between scans. Hence, users can take advantage of the significant improvements to the angular resolution and ranging accuracy of instruments by collecting point spacings on the rock surface between 0.02 – 0.10 m, within a reasonable timeframe (sub-hour). Using a Riegl VZ-1000, for example, it is possible to capture 1 × 10^6 points from across a cliff face at *ca.* 100 m range, within 20 minutes.

The spatial resolution of TLS has a limit imposed by a combination of target geometry relative to the sensor, namely range and incidence angle (Soudarissanane *et al.*, 2011), and the sensor's vertical and horizontal angular step-width. An increase in any of these properties increases the minimum possible point spacing that can be attained on the rock face, increasing the minimum detectable rockfall size. The actual resolution of each scan, where each point gives a unique measurement of the surface at a specific location, is determined by the laser spot diameter on the surface and point spacing, both of which will be discussed in detail in *Section 4.2*. The laser spot diameter increases as a function of beam divergence with range as TLS lasers are not perfectly collinear. Pesci *et al.* (2011) showed that, for controlled tests on a planar board, topographic features smaller than one third of the beam divergence could not be identified. In practice, however, users of modern scanners impose lower bounds on the point spacing, with the aim of reducing the number of points collected to ease data handling while maintaining a point density sufficient to create a high enough resolution topographic surface. Lichti and Jamthsho (2006) suggested that the optimum point spacing is 0.859 times the beam width; if the point spacing is much below this width, fine details become blurred (Jaboyedoff *et al.*, 2012). This ratio enables the characterisation of the rock surface and the detection of small scale movements without the generation of impractically large datasets. Consideration of the appropriate point spacing becomes increasingly important if scans are required from multiple

positions, which considerably increases the number of points to store and post-process.

A system that is able to scan both frequently and permanently introduces a number of additional variables into this decision-making process, ultimately resulting in a trade-off between the spatial resolution of the point clouds and the frequency at which they are acquired. Providing the point spacing is lower than the size of the rockfall to be detected, the emphasis should shift towards the duration of scans and their time interval. Scanning at a very low point spacing, for example 0.02 – 0.03 m at ranges of > 100 m, will increase the scan duration proportional to target range and the area to be scanned. While the scanning frequency should also be consistent with the timescales of movements being detected, a higher scan frequency results in more time spent scanning. Both of these factors use power, which can be problematic where a mains supply is not available. Ensuring that the scanner is able to complete each scan and switch off prior to the next scan will also increase the life of the instrument, many of which have service intervals more suited to conventional surveying rather than constant monitoring. Some of the results in this study are used to help define the significance of a small point spacing relative to the frequency of scanning for monitoring change to a rock slope.

In this study, the point spacing and frequency of scanning is determined by:

(1) The spatial scales of rockfall. Large rockfall up to 200 m^3 have been recorded at East Cliff in the past. However, the magnitude-frequency distribution of rockfall volumes along this coastline, recorded at comparable spatial resolutions to the monitoring system here, have shown that rockfall smaller than 0.01 m^3 (*ca.* 0.2 m in length) account for > 97% of observed events (Rosser *et al.*, 2007a; Benjamin *et al.*, 2016). The exponential increase in rockfall frequency with decreasing volume underpins the need to capture the surface with low point spacings, in this case no more than 0.2 m, if a representative distribution of rockfall sizes is to be observed. In order to assess the spatial variability of failure controls, the point spacing should also fall below the spacing of discontinuities. On East Cliff, joints are spaced predominantly at the decametric scale. The point spacing of scans is set below this to prevent aliasing artefacts within the point cloud, where the scan line spacing is insufficient to resolve local surface relief.

(2) The spatial and temporal scales of precursors. Video footage of rockfall often shows that precursors to failure increase in size and frequency in the period immediately prior to (minutes and seconds) final failure. As discussed in *Section 2.3.2*, Rosser *et al.* (2007a) showed an acceleration in monthly rockfall activity prior to failure. However, no hyperbolic increase was observed, which was suggested to be a function of limited survey frequency in the immediate run-up to each rockfall. Assuming that

rockfall activity accelerates to the point of failure, in accordance with strain accumulation in other brittle landslide masses, this suggests that a more representative quantification of precursory activity can be gained through much more frequent, sub-monthly monitoring. Royán *et al.* (2015) presented data that showed an acceleration of rockfall activity mass in the weeks prior to a 1 012 m^3 rockfall; however, the degree to which interpolation between these change measurements accurately represents failure evolution can only be ascertained through sub-daily, or ideally more frequent, monitoring. Using TLS data acquired at weekly intervals, Kromer *et al.* (2015a) observed deformation in the seven months prior to a 2 600 m^3 rockslide at White Canyon, British Columbia. This monitoring frequency also enabled the detection of a hyperbolic acceleration in pre-failure deformation during the final 28 days before failure, which included rockfall. More recent work by Kromer *et al.* (2017) has identified accelerated deformation prior to an 80 m^3 rockfall from the Séchilienne landslide, France, using TLS data acquired at 30 minute intervals. This work has been undertaken concurrently with the research presented within this study, and emphasises the importance of high frequency surface monitoring in order to describe pre-failure mechanisms.

(3) The timing and duration of potential drivers of rockfall triggering and the controls on rock slope failure, which present an upper-limit on the scan interval. Environmental drivers, such as storms, heavy rainfall and fluctuations in temperature, operate over timescales from minutes to hours to days. Storm events typically last for hours, with variable conditions within these periods. In order to define the triggers of rockfall and relate this specifically to the environmental conditions at the time of failure, the frequency of monitoring must be as close to an hourly rate of monitoring as possible or practical.

(4) The longevity of the monitoring system. As discussed above, a combination of the scan duration and scan interval determines the amount of time that the scanner is powered off, and hence not using power. This is critical for management of the power supply and to ensure that the scanner does not fail as a result of burning out due to continuous operation. A balance is required between frequent scanning for the purpose of failure evolution monitoring and significant periods where the scanner is idle.

Point clouds of *ca.* 1.9 million points were collected (Figure 3.9), starting at intervals between 20 minutes and 30 minutes, depending on power availability from the fuel cells. The

duration of each scan was eight minutes, allowing the scanner to remain switched off for approximately ten minutes between scans. Eight minute scans provide a minimum point spacing of *ca.* 0.05 m at the minimum instrument-target range (342 m), and *ca.* 0.14 m at the distal portion of the monitored cliff (533 m). Calculations in *Section 4.3* show that the beam width is *ca.* 0.10 - 0.17 m as it strikes the surface of East Cliff; hence, the point spacings acquired meet the point spacing to beam width ratio of 0.859, recommended by Lichti and Jamthsho (2006).

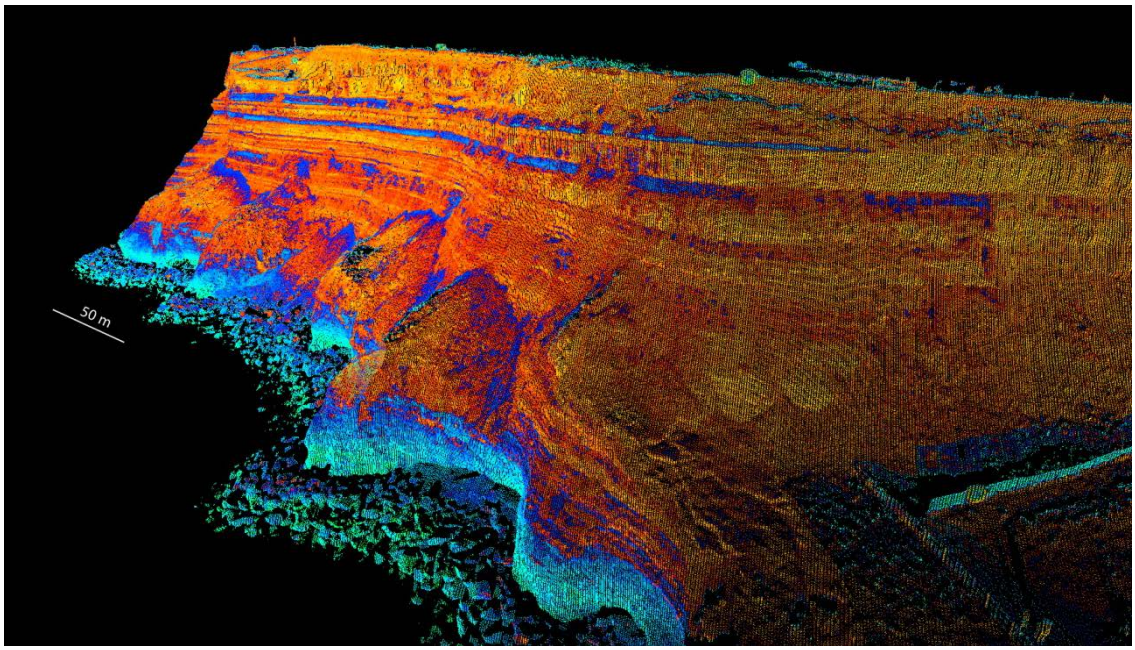

Figure 3.9: *Point cloud of East Cliff acquired from the lighthouse, and coloured by the reflectance of the returned measurements. Cool colours indicate the lowest reflectance values, whereas warm temperatures indicate the highest reflectance. These colours are cycled multiple times to aid visual interpretation of disparity across the surface. Structural features, such as individual blocks and protrusions, are readily identifiable alongside the sub-horizontal bedding of varying lithologies. At the base of the cliff, the 4 m high rock armour revetment is visible. Rotation of the point cloud to view the cliff face-on exposes areas of occlusion across the cliff face (see Figure 3.11).*

3.8 Area of interest and scan geometry

The Area of Interest (AOI) was defined as the seaward cliff, which has little or no vegetation (Figure 3.10). While the AOI originally covered the entire cliff face down to the rock armour, the lowest 10 m of cliff face was eliminated from scans from early December. This was due to low reflectivity measurements, which often accompany a reduced range precision, and inconsistency in data capture between successive scans within each tide window due to wetting of the cliff, which resulted in changing reflectivity. This provided the additional benefits of reduced point spacing on the vertical slopes further up the cliff and an increase in scanning frequency to 20 minutes during the winter storm period.

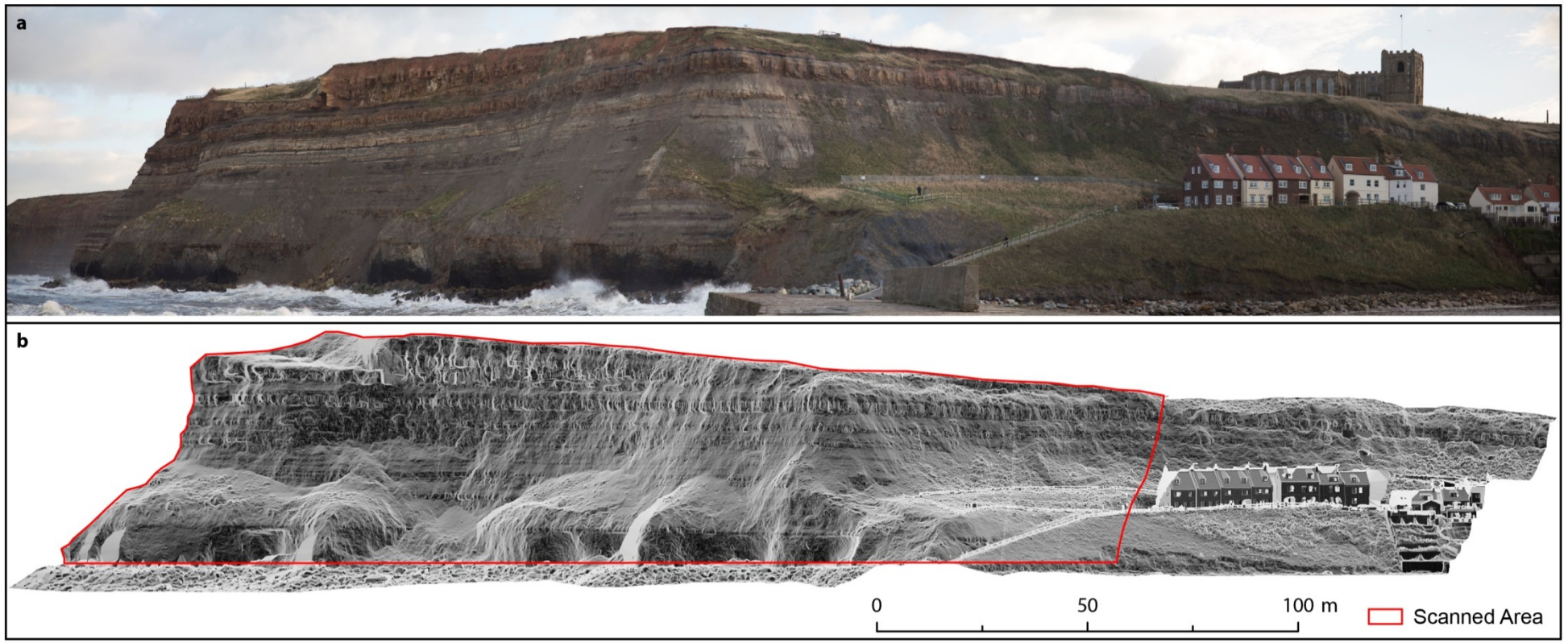

Figure 3.10: *(a) Panorama photo taken at high tide, 5.7 m. East Cliff is left-of-centre, with targets positioned along the rockfall protection barrier right-of-centre. St. Mary's Church is also visible. (b) 0.10 m slope model acquired from the lighthouse in February 2015. Red line denotes scanned area during monitoring campaign.*

A considerable drawback associated with automated monitoring from a permanent installation is the inability to monitor surfaces from multiple positions. The variable relief and orientation of rough surfaces relative to the scanner produce patterns of occlusion in the resulting point cloud (Girardeau-Montaut *et al.*, 2005). The bedded and interbedded sandstones at East Cliff present a significant obstacle to measurement from a single position due to protrusion of sections of the rock, and the resulting shadowing of areas behind. During previous monitoring of the cliff face, the scanner was operated from multiple positions on the foreshore platform, commonly from a more truly nadir position, which were subsequently aligned to fill areas of occlusion. In this study, however, areas of occlusion were unable to be scanned from a different viewing point. As a result, only 8 561 m^2 was measured during repeat scans of the 9 592 m^2 cliff face defined by the AOI (*ca.* 89%). As the surface changes, the occluded areas will also change, with new areas becoming visible and previously visible areas becoming shadowed.

Figure 3.11 represents a slope model of the cliff face acquired from multiple scan positions on the foreshore platform. The area of returned measurements from scans conducted only from the lighthouse is shaded red, with areas of occlusion visible around the small 'bights' and buttress at the base of the cliff. The proportion of the surface that is occluded increases with incidence angle relative to the scanner (Lichti, 2007). As such, the loss of surface measurement due to the inability to move the scanner is exacerbated by the high incidence angle of parts of East Cliff relative to the lighthouse, as can be seen in Figures 3.1 and 3.2. The closest point on the cliff is 342 m from the scanner, at the right (west) of the surface model in

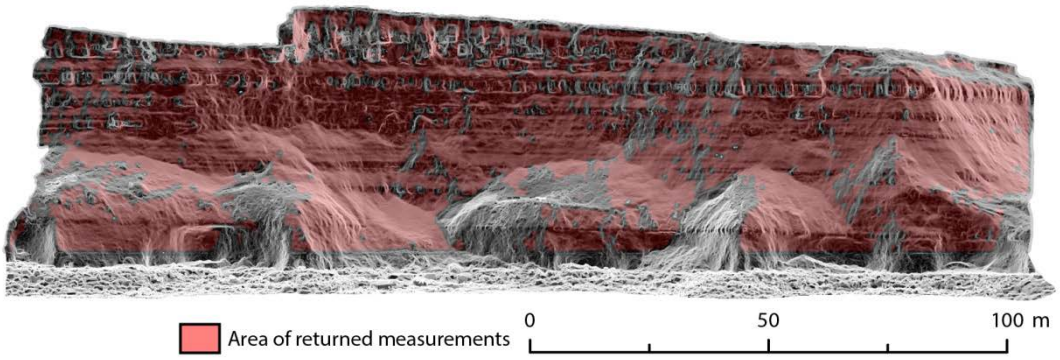

Figure 3.11: *Area scanned by the permanent monitoring system used in this study (red) draped over a complete slope model of the entire cliff captured from multiple positions along the foreshore. The total area measured is 8 561 m^2, 89% of the cliff face total (9 592 m^2).*

Figure 3.11, with an incidence angle of *ca.* 25°. The furthest point is 533 m from the scanner, to the far left (east) of Figure 3.11, with an incidence angle of *ca.* 42°. In previous monitoring campaigns, incidence angles and occlusion levels at these magnitudes would be apportioned to poorly planned survey setups (Sturzenegger *et al.*, 2007; Stock *et al.*, 2011), the importance of which is discussed in several studies (Bonnaffe *et al.*, 2007; Kemeny and Turner, 2008; Lim *et*

al., 2010; Abellán *et al.*, 2014). The implications of this are discussed in *Section 4.10.2* in relation to the method of change detection, and *Section 5.3* in relation to failure volume statistics.

3.9 Acquired datasets

3.9.1 TLS data

In total, 8 987 scans were collected during the period 5th March 2015 – 30th December 2015 (Figure 3.12). Almost all scans were acquired with intervals of 20 minutes or 30 minutes, although maintenance and failure of the system extended a number of these intervals over days or weeks. The largest data gap occurred between 14th July and 2nd September due to a technical fault with the scanner. Between the end of November and beginning of December, the failure of one of the two fuel cells increased the time required to recharge the batteries to a sufficient voltage for scanning (Table 3.1). This is reflected in the lower and less consistent rate of scan acquisition from 18th November to 15th December.

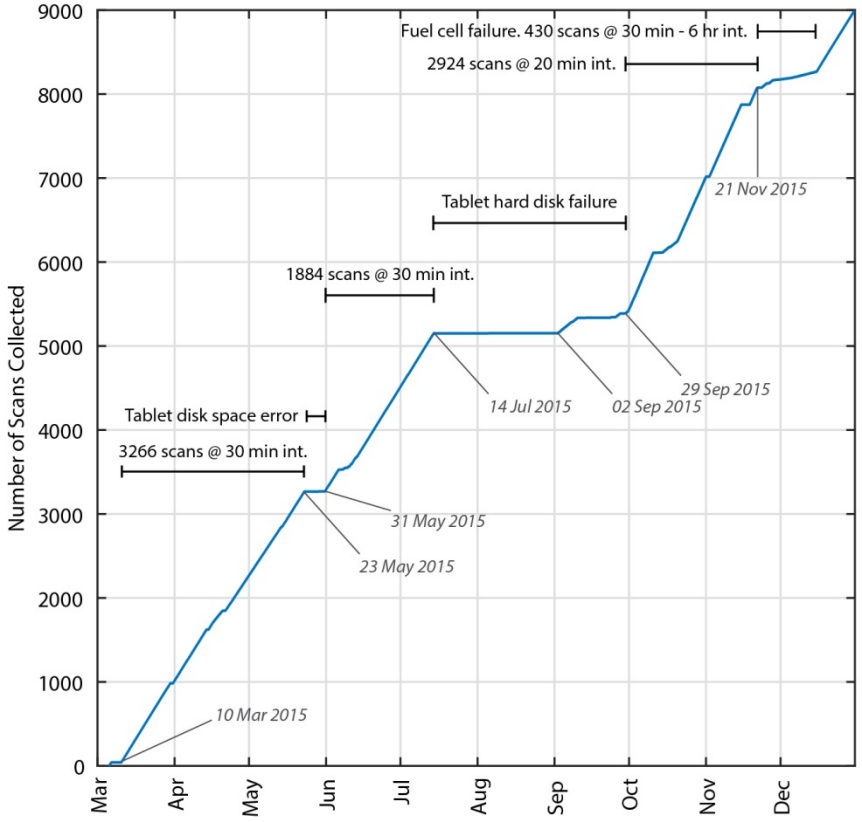

Figure 3.12: *Cumulative number of scans collected between 5th March 2015 and 30th December 2015. The gradient of the line reflects the acquisition rate, either 20 minutes or 30 minutes. Breaks in the gradient reflect system maintenance difficulties discussed in Section 3.10.*

3.9.2 Environmental data

Deterministic approaches that examine rockfall occurrence in relation to environmental conditions rely on accurate weather data alongside a reliable rockfall inventory. Inventories that span large areas often draw on individual weather stations to represent the conditions at any given time across the examined area. Previous research on this coastline (for example, Rosser *et al.*, 2007a; Rosser *et al.*, 2013; Vann Jones *et al.*, 2015) has proposed that smaller rockfall (< 0.1 m^3) show dependence on environmental drivers, whereas larger events do not; however, these studies have used weather data from stations *ca.* 3 km from the monitored rock face. In contrast, the monitoring system at Whitby draws on data from two weather stations; one installed on the cliff top and one installed alongside the VZ-1000 at the top of the lighthouse (Figure 3.1). The frequencies of data collection are outlined in Table 3.1. Each weather station recorded information on the air temperature, humidity, air pressure, wind speed, wind direction, rainfall accumulation and rainfall intensity at one minute intervals. The weather station on the rock face also hosted a pyrometer that was directed at an exposed area of bare rock in order to measure the temperature of the rock face itself. On analysis of the rockfall dataset with respect to environmental conditions, a fault was identified in the measurement procedure for both rain gauges. As an alternative, rainfall data was acquired from a privately-owned weather station 2 km from East Cliff. This was recorded at five minute intervals and provided as total rainfall and mean and maximum intensity at 30 minute intervals, equivalent to the rate of scanning.

Table 3.1: *Summary of the scan data collected during the monitoring period.*

Monitoring period	Number of scans: 8 987 Start date: 05-Mar-2015 16:48:51 End date: 30-Dec-2015 15:27:39	
Scan interval hh:mm:ss	Mode: 00:20:00 Minimum: 00:11:19. Maximum: 43 days 0.25 quantile: 00:21:41 0.50 quantile: 00:30:00 0.75 quantile: 00:30:26	
Measured points	Minimum: 106 285 Mean: 1 896 386 Maximum: 1 939 853	
Data gaps (start/end)	06/03/2015 13:00 23/05/2015 07:00 14/07/2015 11:00 09/09/2015 14:00 27/09/2015 11:00 10/10/2015 20:00 15/11/2015 05:00 21/11/2015 16:00	10/03/2015 12:00 31/05/2015 12:00 02/09/2015 10:00 23/09/2015 11:00 29/09/2015 14:00 14/10/2015 11:00 18/11/2015 15:00 23/11/2015 22:00

In addition to the weather stations, a webcam facing towards the cliff was installed at the top of the lighthouse. The webcam recorded images at 1 h intervals and provided a live-feed that was accessible online. The webcam imagery proved to be a useful supplement to assess the marine and weather conditions during hours of daylight. At times, waves can be observed overtopping East Pier itself and subsequently striking the buttress up to 5 m in Figure 3.4. The imagery also helped to identify periods of data loss due to adverse weather conditions, in which the acquired point cloud was either incomplete or contained artefacts in the range estimates. The consequences of this data loss are examined in *Section 4.12*. The coastal setting of Whitby can promote high atmospheric moisture, particularly between April and September when warm air from inland intersects cool and moist air above the North Sea. The resulting fog, referred to locally as Haar, may last up to several days. The Riegl VZ-1000 operates in the near-infrared (NIR; $\lambda = 1\,604$ nm) and is therefore scattered by atmospheric moisture, rendering the scanner ineffective during foggy conditions. The webcam helps to explain such artefacts in the point clouds that cannot be elucidated using the weather station data alone.

In addition to the datasets collected by the monitoring system above, subsidiary data were acquired for tide height, wave climate and hours of sunlight. For tide height, 15-minute quality-checked surface elevation data from the Whitby tide gauge have been obtained (BODC; Figure 3.5). A linear interpolation has been applied in order to present tide-heights at one-minute intervals, comparable with the weather station variables. Wave climate data was acquired from the CCO wave buoy. The buoy came adrift three times in 2015, resulting in a large gap in measurements between 17th May and 23rd July (Figure 3.5); however, data was acquired at 30-minute intervals for 217 of the 302 days of monitoring reported here. This data includes the significant wave height, maximum wave height, peak wave period (the time separating successive wave crests), average wave period (the time taken for the buoy to undergo a full cycle of movement above and below zero amplitude), and the peak direction of swell.

A database containing all of the environmental variables recorded in 2015 was compiled at one-minute intervals. This enabled resampling in which the environmental data were attributed to each of the corresponding 8 987 laser scans. This combination of rockfall from the scans and environmental data is as close to contemporaneous and continuous monitoring as is currently possible using the equipment in Table 3.2. Although the conditions at the time of scanning are important for analysing the conditions that coincide with the triggering of rockfall, changes in these conditions between scans in the run-up to failure are equally significant. Here, the timestamp for each scan is recorded as the time that the scan was initiated. For every scan, the time interval to the next scan was recorded (this includes time spent scanning and time spent idle) and used to provide a time window over which to provide average statistics for the environmental variables. Derivatives were therefore created; including the mean, standard deviation, minimum and maximum of each of the weather and marine variables during the scan

Table 3.2: *Primary datasets collected by the permanent monitoring system. Methanol fuel cells were used to power the scanner, weather station and webcam at the lighthouse and a solar panel was used to power the weather station on east cliff. The weather station on East Cliff also included a pyrometer directed towards the rockface used to measure rock temperature.*

Location	Instrument	Make / Model	Outputs	Frequency
East Cliff	Weather station	Vaisala WXT520	Temperature Relative humidity Rainfall Wind speed / direction	1 min
Lighthouse	Weather station	Vaisala WXT520	Temperature Relative humidity Rainfall Wind speed / direction	1 min
	Webcam	Mobotix M25	Image of Cliff	Live feed JPEG @ 1 h
	TLS	Riegl VZ-1000	XYZ Reflectance Deviation	20 – 30 mins

window, and the shift in mean conditions (rates of change) since the time of the previous scan. Binary values were also created to ascertain whether certain conditions had been met, including whether the temperature had fallen below freezing, whether the scan was collected during hours of daylight and whether winds were onshore at the time of failure. In total 98 different metrics of environmental conditions at failure were produced for each of the 8 987 scans (Table 3.3).

Table 3.3: *Summary of the environmental variables compiled and resampled to be attributed to each of the 8 987 TLS scans.*

Variable	Location	Attributes	Derivatives	Binaries
Scan ID				
Date and Time				
Weather	Rock face and Lighthouse	Temp Pressure Humidity Wind Direction Wind Speed Rain Intensity Rain Accumulation	Mean Standard Deviation Min. Max. Δ Mean Since Last Scan Epoch	Below Freezing Onshore Wind
	Whitby	Hours of Sunlight		Daylight
Tide Data	Whitby Harbour	Tide Height		
Wave Climate	Offshore Buoy	Significant Wave Height Max. Wave Height Peak Time Period Average Wave Period Direction		

3.10 Practicalities of constant monitoring

Continuous running of the system presented a number of challenges. First, there was no mains power supply to the lighthouse. For the majority of the project, this did not affect the frequency of scanning; however, scans had to be restricted to between 1 h and 6 h during late November and early December due to the failure of one of the two fuel cells. This had implications for the analysis of precursory movement prior to some of the largest failures. At its peak rate of scanning, the system required a full fuel refill approximately every four weeks. While fuel level telemetry (fuel/no fuel) were accessible online, maintaining enough fuel for the system to operate required numerous visits through the monitoring period.

The *SiteMontor4D* software used to schedule the scanning operates on a tablet computer. This tablet also served to transfer the data to an online cloud storage. The approximately six-week hiatus in scan acquisition during July and August was a result of complete failure of the tablet hard disk, which meant that the scanner could not acquire data autonomously. A solid state hard drive is recommended for such applications where near-constant read and write of data to and from the hard drive is required.

3.11 Summary

A permanent monitoring system has been developed and used to collect a large number of scans at a spatial and temporal resolution sufficient to provide a unique insight into the nature of rockfall. Both the number of scans and the scan frequency are approximately two-orders of magnitude higher than previously used to generate TLS-derived rockfall inventories. Analysis of these previous rockfall inventories based on less rich scan data has had limited success in deriving significant relationships between external environmental drivers and the onset of rockfall. It follows that in brittle materials, final failures of this type occur either independently of environmental forcing, as the culmination of a lagged response to damage accumulation, or at finer timescales as a result of variations in environmental conditions below the monitoring resolution (Vann Jones *et al.*, 2015). Recent studies have captured accelerations in rockfall activity prior to final failure; however, these rely on trends that interpolate between intervals of 24 hours up to one month. The frequency of rockfall monitoring here, which captures deformation of the whole slope, is matched only by Interferometric Synthetic Aperture Radar (InSAR) systems, deployed mainly within open-pit mines. However, as discussed in *Chapter 2*, the spatial resolution of these systems falls short in comparison with the range precision (Farina *et al.*, 2011), and as compared to TLS.

The acquisition of a 4D dataset of this nature requires an automated means of rockfall detection and inventory extraction, given the volumes of data generated. The system described

above generates *ca.* 1 GB of raw compressed point cloud data per day, totalling *ca.* 96 million points. Significant technological advances in the acquisition of TLS data have enhanced our ability to capture larger datasets in less time. Until recently, these advances have outstripped developments in the efficiency of processing, such that it is far easier to collect scan data than it is to process it. Datasets that take minutes to acquire may require hours of manual processing in order to filter redundant information, align them with previous scans, isolate regions of interest, quantify their geometry and to perform change detection. Rockfall inventories are now increasingly acquired using techniques that take advantage of the true-3D nature of the original point clouds, rather than 2.5D analysis of change between successive DEMs (Lague *et al.*, 2013). Although a number of commercial and open-source packages exist for point cloud processing and visualisation, these are only able to provide semi-automated data processing at best. An automated approach to change detection has therefore been developed and is presented in *Chapter 4* as a means of extracting an accurate rockfall inventory from such a large dataset.

Chapter 4

4D Analysis of Rockfall using Continuous TLS Data

4.1 Introduction

In *Chapter 3*, the development of a near-real time slope monitoring system was presented. The spatial and temporal resolution of data acquisition was selected to address the knowledge gaps identified in *Chapter 2*; in particular, the degree to which rockfall can be defined as instantaneous, and the spatial-temporal relation between the onset of failure and environmental drivers, joint characteristics, and pre-failure deformation of the rock mass. This chapter outlines the methods applied to this dataset in order to compile a rockfall inventory that included the size and shape of each rockfall alongside the environmental conditions at the time of failure.

The minimum detectable movement obtained using TLS is a function of the absolute accuracy of measured topography within a survey and the precision of range measurements between surveys. Analysis of scan pairs can propagate and amplify uncertainties in the absolute position of a surface, as well as introducing relative uncertainties between each scan. These relative uncertainties arise because of systematic errors in range precision and the fact that the exact same point on a surface can never be rescanned. Comparison of scans is critically not comparing like with like. Reducing the measurement error between scans is required to lower the number of small-scale rockfall detachments, or small scales of surface deformation, that are censored. This therefore has implications for analysing magnitude-frequency distributions, and the precursors to and drivers of the onset of final rockfall failure.

The data processing workflow described in this chapter aims to minimise the impact of epistemic error upon the size of rockfall reported in the final inventory by first optimising the raw point clouds prior to change detection. This pre-processing step filters points with low range precision, such as those located along topographic edges, before 3D cloud-to-cloud change detection is undertaken using an adaptation of the M3C2 algorithm (Lague *et al.*, 2013). The resulting change is rasterised and individual failures are extracted and compiled into an inventory. It is shown that, while the geometry of the surface relative to the scanner raises some uncertainty in the relative position of multiple point clouds, the method of change detection adopted yields a level of detection of 0.03 m at *ca.* 300 m – 500 m, which is considerably lower than that produced using methods such as DEMs of Difference and M3C2.

4.2 Sources of error within individual surveys

Terrestrial laser scanning of rock slopes comprises individual surveys, which can be used to characterise discontinuities for input into stress-based modelling of slope failure (Slob *et al.*, 2002; Sturzenegger and Stead, 2009a; Sturzenegger and Stead, 2009b; Lato *et al.*, 2010; Gigli and Casagli, 2011; Lato and Vöge, 2012; Vöge *et al.*, 2013; Assali *et al.*, 2014), and repeat surveys for monitoring change (Rosser *et al.*, 2007a; 2007b; Teza *et al.,* 2007; Oppikofer *et al.*, 2008; 2009; Abellán *et al.*, 2009; Lim *et al.*, 2010; Viero *et al.*, 2010; Rosser *et al.*, 2013; Royán *et al.*, 2015; Vann Jones *et al.*, 2015). For any one survey, the accuracy of the scan data is limited by instrument errors, point spacing, target geometry, atmospheric conditions and surface characteristics. When measuring deformation between two surfaces, assuming that those surfaces may have moved rather than a block having been detached, the scale of movement that can be detected is determined by measurement accuracy within each individual survey and the amplification and propagation of these inaccuracies between surveys. For a rockfall, while the precision of depth estimate is critical in estimating its depth and size, its aerial extent is determined by the locational accuracy of the point measurement on the surface. When generating a large volume of scans, there is a need to understand both the individual scan error and the error between scan pairs in order to minimise the overall error in the resulting rockfall inventory. These errors are summarised in Table 4.1.

4.2.1 Instrument error

Systematic errors in TLS measurement exist because of imperfections in instrument hardware, combined with the beam width divergence and angular resolution of the scanner (Soudarissanane *et al.*, 2011). Similar to theodolites, the vertical axis (around which the scanner rotates), the trunnion axis (which moves with the instrument and pivots up and down) and the collimation axis (the line of sight) of scanners are assumed to be orthogonal to one another and to intersect a common point (Lichti and Skaloud, 2010). However, this is rarely the case and therefore produces uncertainty in the horizontal and vertical angular position of the scanner at any given moment during scanning. Corrective adjustments can be applied to range estimates (Rüeger, 2003; Kersten *et al.*, 2005; Lichti and Franke, 2005; Lichti, 2007; Lichti and Lampard, 2008; Salo *et al.*, 2008; Schneider and Schwalber, 2008) but the direct impact upon resulting point positions in 3D remains difficult to quantify. Rotating mirror systems, such as the Riegl VZ-1000, result in additional uncertainties in the direction of scanning due to the positional offset of each mirror facet from the rotation axis of the scanner. Accounting for these uncertainties, the estimated angular resolution E_A of the Riegl VZ-1000 is approximately 0.0005 ° (Riegl, 2015). The position offset of the centre line of each laser beam E_P can therefore

Table 4.1: *Sources of epistemic error between successive surveys, including the magnitude of their influence upon the level of detection. Pre-processing approaches applied to the point clouds to minimise the resulting change errors are detailed on the right-hand side in red. Here, filtering is applied. An approach to 4D smoothing was not, but is detailed in both Section 8.2 and Appendix F.*

Error Source	Magnitude	Description	
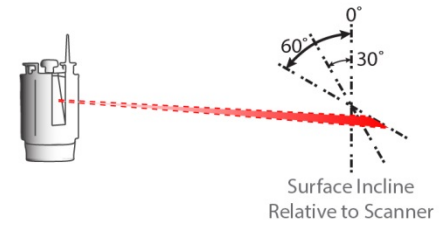	mm - cm	If the laser strikes a surface with a non-zero incidence angle, the resulting footprint is elongated, spreading the energy distribution over a greater target surface area. The Signal-to-Noise ratio of a return beam detriorates with the cosine of incidence angle (Soudarissanane *et al.*, 2011).	Filtering
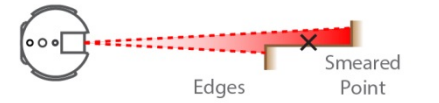	cm - m	Beam diameter @ 450 m ≈ 0.14 m. Points within ca. 0.14 m of an edge thus return echoes from multiple surfaces, dependent on surface geometry and range. 'Smearing' occurs when the average range of multiple returns is used.	
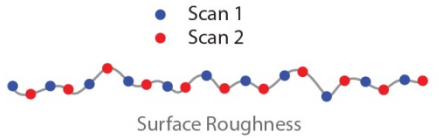	mm	Surface roughness relative to point spacing determines the proximity of a point to its closest measurement in subsequent scans. At finer-scales, for light at 785 nm, the incident surface can be considered rough with surface variations ca. 1 x 10^{-7} m. Roughness values greater than this increase scatter and reduce the intensity of the signal returned to the scanner (Pfeifer *et al.*, 2008; Kaasalainen *et al.*, 2009; Soudarissanane *et al.*, 2009).	4D Smoothing
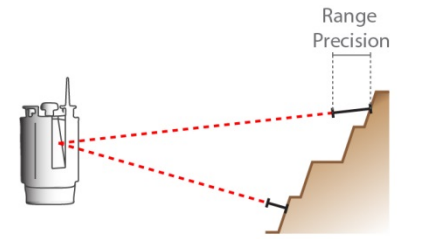	mm - cm	Attenuation of the laser energy and hence the Signal-to-Noise ratio increase with the square of range. Greater object distances produce larger footprint sizes; thus, weakening the returned signal.	
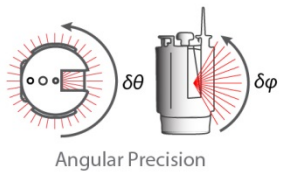	mm - cm	The angular resolution of the horizontal and vertical step-width determines the accuracy of the measurement's 3D position, where: Positional offset = range x sin(angular resolution). For a Riegl VZ-1000 with an increment resolution of 0.0005° and target distance of 550 m (equal to the maximum range of East Cliff), the positional offset may be 4 x 10^{-3} m both vertically and horizontally.	
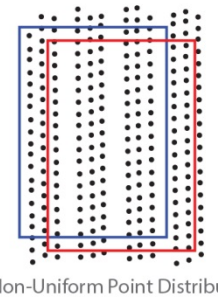	cm	Scanner mechanism directly affects the distribution of points in the point cloud. The Riegl VZ-1000 uses a three-faceted mirror, producing triple-stripes interspersed with areas of no data. This reduces the comparability of subsequent scans, whereby different areas of the rockface may or may not be measured.	
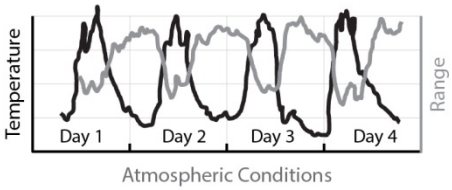	cm	Energy attenuation varies according to the degree of water vapour in the atmosphere and its particle size, where scattering is more significant than absorption for Near-Infrared light (Kim *et al.*, 2001). Bright sunlight also reduces the sensitivity of the detection unit to low-energy returns.	

be estimated by:

$$E_P = R \cdot \sin E_A \quad \text{[Eq. 4.1]}$$

where R is the range. At the closest point on East Cliff, 342 m, this translates to a 0.003 m uncertainty in the location of the centre point of the beam, and a 0.0047 m uncertainty at the distal portion of the cliff, at 533 m range. The above factors have a direct impact on the uncertainty of the position of each point in 3D space. For rockfall monitoring, this is important, as the minimum detectable size of the rockfall is reliant upon the accuracy to which its aerial extent is resolved. The magnitude and spatial variability of this uncertainty are impossible to determine for surfaces of varying complexity surveyed under varying atmospheric conditions, and the inability to quantify this uncertainty is therefore compounded between surveys. The magnitude of this error (millimetre scale), however, is small in comparison with the dimensions of the rockfall that are sought to be detected here, which are in the region of 0.15 m in length at the smallest.

4.2.2 Atmospheric conditions

Atmospheric conditions have an effect upon the total number, precision and signal-to-noise ratio (SNR) of the returned measurements. Fluctuations in temperature, humidity and pressure determine the air density through which the laser travels, thereby affecting the speed of light. For the target ranges at East Cliff, this has no significant impact upon the accuracy and precision of range estimates (Boehler *et al.*, 2003). Rises in atmospheric temperature, however, can exacerbate already high temperatures within the instrument itself, resulting in the expansion of components and increased deviations in range estimates. Direct sunlight onto the scanner can also increase the uncertainty in range estimates and therefore the SNR of measurements if the ambient light energy is comparable to that of the returned signal (Voisin *et al.*, 2007). At East Cliff, the scanner faces the sun; however, any shifts in the position of the point cloud were unnoticeable. This can be attributed to the range correction factor that is acquired through target scanning, the positioning of the scanner behind a white-painted wooden door to prevent direct insolation of the instrument, and the absence of noticeable temperature variations within the lighthouse. Published empirical relations between atmospheric conditions and range estimates do not currently exist, primarily due to the inherent difficulties in isolating and varying a single aspect of the climate in controlled tests. As such, quantitative estimation of the influence of atmospheric variables on the point clouds is not undertaken here. The importance of weather conditions, including rainfall and fog, is discussed in *Section 4.11.*

4.2.3 Target properties

The anisotropy of light reflected by an object, which is determined by its reflectivity and microscale roughness relative to the scanner wavelength, can affect the accuracy of the returned measurements (Baltsavias, 1999; Pesci *et al.*, 2008; Soudarissanane *et al.*, 2011; 2016). Moisture delivered by the tide resulted in data loss at the cliff toe even after the tide had retreated. For this reason, the lowest 2 m of cliff face above the rock armour revetment was removed from the study. Variations in the colour of reflected surfaces are also likely to affect the accuracy of range estimation across the cliff face, since darker surfaces produce lower energy returns (Clark and Robson, 2004), particularly for beds of shale and siltstone. Conversely, surfaces with high reflectivity can result in saturation of the detector, in particular for metal objects or prisms that may be present on the monitored slope. For the VZ series of Riegl scanners, this can result in a loss of data within scan lines where highly reflective objects are present. Neither of these effects occurred within this study.

4.2.4 Scan geometry and point distribution

The scanning geometry (the position of the scanner relative to the monitored surface) affects both the accuracy of individual scans, by directly influencing the size of the laser footprint on the monitored surface, and comparisons between scans, by determining the point spacing and thus the likelihood that the same location on the surface will be rescanned in successive surveys. The geometry comprises target range and incidence angle relative to the scanner, with an increase in either attribute causing an increase in the footprint of the beam as it strikes the surface due to the beam divergence (Bae *et al.*, 2005; Křemen *et al.*, 2006; Lichti, 2007; Soudarissanane *et al.*, 2009; 2011).

On leaving the scanner, the laser beam diverges to create a circular footprint on a perfect nadir, planar surface and an elliptical footprint on an oblique planar surface, the width of which is referred to as the *spot dimension* (Petrie and Toth, 2008). If the beam hits the surface perfectly nadir, the footprint will be circular and the distribution of energy within this footprint is Gaussian (Lichti *et al.*, 2002; Alda, 2003). As the footprint spreads with range, the uncertainty in the location of the recorded measurement increases and the returned signal is weaker. The influence of target range on spot dimension can be defined as:

$$SD = \sqrt{\left(d_a{}^2 + R^2\theta^2\right)} \qquad \text{[Eq. 4.2]}$$

where SD is the spot diameter (m), d_a is the initial diameter or beam aperture (m), R is the

instrument-object range (m) and ϑ is the beam divergence (rad). Beam divergence is typically specified by the manufacturer; for example, the Riegl VZ-1000 has an aperture width of 0.008 m and a divergence of 0.3 mrad, corresponding to a beam-widening of 0.030 m per 100 m of flight assuming a circular beam (Riegl, 2015). At East Cliff, the spot diameter ranges from 0.1029 m at the closest point on the cliff (342 m) to 0.1601 m at the furthest (533 m) assuming a surface that is orthogonal to the incident beam.

If the laser beam strikes the surface with a non-zero incidence angle, the resulting footprint is elliptical, spreading the energy distribution over a greater target surface area. The angle of incidence α is defined as the angle between the laser beam and the vector normal to the surface and may change with deformation of the rock slope. It can be related to spot dimension by:

$$SD = R \cdot \tan \alpha + d_a \qquad \text{[Eq. 4.3]}$$

where α is the angle of incidence. Greater range and incidence angles have been shown to decrease the SNR of resulting point clouds as less intense signals are less likely to be detected. Soudarissanane *et al.* (2011) undertook controlled experiments and determined that the SNR of a laser return deteriorates with the cosine of the incidence angle. Moreover, SNR deterioration is inversely proportional to the square of range.

While object geometries in most published studies are generally planar and produce low target incidence angles (Schürch *et al.*, 2011; Brodu and Lague, 2012), the incidence angle of the surface strike of East Cliff relative to the scanner is between 25° and 42° (Section 3.7). Combined with a moderate target range, this results in spot dimensions of *ca.* 0.10 – 0.17 m in diameter assuming the surface to be planar at scales comparable to the spot size (Equation 4.2). Despite divergences < 1 mrad, multiple adjacent surfaces belonging to protruding, widely jointed sandstone blocks may be intersected within a single line of sight, creating a smearing effect sometimes referred to as mixed pixels. Here the estimated range is a function of the distance between the scanner and each reflection returned from any surface in the laser footprint which might be at different ranges, observed from a single laser pulse. In instances where the beam intersects a single surface and the footprint is close to the edge of this surface, the position of the point may be attributed to the centre of the beam when in fact the range measurement corresponds to the edge of the surface, or a surface beyond. As such, the object may appear larger in the point cloud than in reality (Lichti *et al.*, 2005; Hodge *et al.*, 2009).

4.3 Sources of epistemic error between surveys

The sources of error in surface comparison can be divided into errors associated with individual component scans, alignment error between successive scans (discussed in detail in *Section 4.7*) and uncertainties in the method of change detection (Teza *et al.*, 2007).

4.3.1 Target geometry and error amplification

The scan geometry determines the heterogeneity of point spacing across each scan and therefore the consistency of point distributions captured in multiple scans. A single position on a surface cannot be rescanned with certainty, and the likelihood of being able to scan the exact same point twice decreases with increased point spacing and variations in point spacing across each scan. In the scanner's Polar coordinate system, points are acquired and stored at fixed vertical, ϑ, and horizontal, φ, intervals alongside the range between the scanner and the object R (Vosselman *et al.*, 2004; Girardeau-Montaut *et al.*, 2005; Durrieu *et al.*, 2008). Translation of the resulting φ, ϑ, R coordinates into an x, y, z Cartesian system imposes a spatial-variation in point density throughout the 3D point cloud (Belton and Lichti, 2006). These variations increase given unfavourable target geometry, whereby fewer points are collected on surfaces according to the inverse of the square of range and the cosine of the incidence angle (Pesci *et al.*, 2008; Soudarissanane *et al.*, 2011). The angle of incidence in this study and the presence of sharp edges on the cliff face mean that it is impossible to acquire a truly uniform point density that is consistent between scans. For a complex debris-flow channel, Schürch *et al.* (2011) found that the overall quality of 3D point clouds was determined by difficulties in the registration of multiple scan stations, rather than the intersection of multiple surfaces within a single line-of-sight. While Schürch *et al.* (2011) highlighted the impact of heterogeneous point distributions on scan registration within a single time epoch, it follows that the alignment of successive scan surveys also suffers given that the same point can never be scanned twice.

4.3.2 Change detection methods

Three types of change detection technique are commonly applied in geomorphological research, each of which introduces methodological uncertainties into measured surface change. To date, the most common of these is the gridding and interpolation of point clouds to create Digital Elevation Models (DEMs) that are subsequently subtracted on a pixel-by-pixel basis to provide a DEM of Difference (DoD). This technique has been used to monitor debris flows (Scheidl *et al.*, 2008; McCoy *et al.*, 2010; Blasone *et al.*, 2014); rock avalanches (Kasperski *et al.*, 2010); rock glaciers (Avian *et al.*, 2009); diffuse erosion (Schürch *et al.*, 2011) and precursors to

slope failure (Rosser *et al.*, 2007; Abellán *et al.*, 2009). This approach is advantageous in many respects, particularly when dealing with near-planar horizontal or vertical surfaces. This approach also negates computationally intensive processing of point cloud data, and can easily be used to produce topographic or hydrologic derivatives. However, the production of DoDs can amplify errors associated with the creation of the original DEM surface. In particular, the interpolation of 3D point cloud data into a pseudo-3D (2.5D) surface results in a loss of true 3D detail and measures change exclusively along a user-defined depth axis. Loss of detail increases with slope (Vosselman *et al.*, 2004), introducing a bias in change detection towards planar surfaces. Features such as overhangs and surface inflections, which are often of vital mechanical importance on a rock face, often remain poorly resolved (Martel, 2006; 2011; Stock *et al.*, 2011). The determination of a fixed grid spacing also limits the resolution of rough surfaces (Hodge, 2010) and fine-scaled features within regions of high point density (Lague *et al.*, 2013).

A number of approaches quantify error in DEMs and apply this as a threshold when interpreting DoDs. The minimum Level of Detection (LoD) can be estimated from the root sum square of errors associated with each of the component DEMs. Wheaton *et al.* (2010) found that aerial and volumetric estimates of change are highly sensitive to the chosen LoD, with a loss of real change occurring below this threshold. Other studies thus apply a confidence error based on the error distribution across the entire surface, typically 1.96 times the standard deviation (Brasington *et al.* 2003; Lane and Chandler, 2003). However, these assume that there is a normal distribution of errors across the surface, and that the errors in successive DEMs are similarly distributed. Other approaches incorporate the spatial variability in uncertainty across the component DEMs (Wheaton *et al.*, 2010; Milan *et al.*, 2011; Bangen *et al.*, 2016). Wheaton *et al.* (2010) applied a fuzzy inference that incorporates different topographic attributes associated with error. Using local slope, point density, and GPS error, each DEM cell is ultimately assigned a weighted error value that can be incorporated into DoDs to define an acceptable LoD on a pixel-by-pixel basis. This approach succeeded in retaining greater volumes of erosion and deposition compared to the use of a single LoD across the entire surface. However, its application is tailored to monitoring large areas in which DEM cells are unlikely to contain more than one point. Schürch *et al.* (2011) highlighted the importance of incorporating a large number of range measurements within each cell in order to accurately constrain range uncertainty.

A second common approach to change detection is the calculation of surface change as the distance between a point cloud and a reference surface (Lague *et al.,* 2013). The reference surface used can be derived by meshing or view-dependent triangulation (Monserrat and Crosetto, 2008; Abellán *et al.*, 2009; Olsen *et al.*, 2010) and is well-suited to smooth structures such as dams (e.g. Alba *et al.*, 2006). For rough surfaces, however, surface construction is more computationally intensive and necessitates a large amount of smoothing (Kromer *et al.*, 2015b).

More recently, a number of studies have directly compared successive point clouds without the need to grid or mesh either of the surfaces; this technique is also known as cloud-to-cloud comparison (Teza *et al.*, 2007; Monserrat and Crosetto, 2008; Oppikofer *et al.*, 2009; Viero *et al.*, 2010; Lague *et al.*, 2013; Kromer *et al.*, 2015a;b; Stumpf *et al.*, 2015). In its simplest form, change between two point clouds S and S' can be computed as the Hausdorff distance d, which is the distance between each point p in cloud S and its closest neighbour in cloud S':

$$d(p, S') = \min_{p' \in S'} \|p - p'\|_2 \qquad \text{[Eq. 4.4]}$$

This method has several drawbacks. First, as it operates over all points in the point cloud, the approach can be time consuming if the point cloud is not organised to allow rapid neighbourhood searches; for example, within an Octree or K-D tree structure (Girardeau-Montaut *et al.*, 2005). Second, the change estimates that are produced are highly dependent upon point density. In areas of low point density, Hausdorff distances are inevitably larger than in areas of high point density (Girardeau-Montaut *et al.*, 2005), and are therefore more accurately estimated as a point to surface distance. Third, a point will always have a closest neighbour in the next scan. As the same location of a surface will never be rescanned, a change value will be recorded regardless of whether or not movement has occurred in reality. Fourth, the distances produced are unsigned; without detailed *a priori* knowledge of the movement style, this technique is therefore unsuited to landslide masses in that they exhibit both forward and backward movements relative to the scanner. For analysing rockfall detachments over monthly survey periods, this may not be a significant drawback. In this study, however, signed distances are crucial for the examination of precursory movements, which can be both forwards and backwards, as well as for quantifying the size of the final detachment. Accumulation of material on the buttress at the toe of the slope at East Cliff, combined with the potential for slumping, further necessitates an approach that generates signed distances.

An extension of the Hausdorff approach is the creation of distance vectors by manual matching of particular point pairs. Oppikofer *et al.* (2008) examined the collapse of the eastern Eiger flank in the Swiss Alps, noting that the front failing block underwent toppling with higher velocities at its top relative to its toe. Point pairs were defined using topographic features distinguishable in both clouds, such as spurs and the summits of blocks. For each point i of the point cloud, a shortest-distance algorithm was used to search for its nearest neighbour j and compute the shortest distance vector v_i:

$$v_i = \begin{pmatrix} \Delta X_i \\ \Delta Y_i \\ \Delta Z_i \end{pmatrix} = \begin{pmatrix} X_{i.ref} \\ Y_{i.ref} \\ Z_{i.ref} \end{pmatrix} - \begin{pmatrix} X_{i.data} \\ Y_{i.data} \\ Z_{i.data} \end{pmatrix} \qquad \text{[Eq. 4.5]}$$

where positive values indicate that the points are moving towards the scanner and away from the reference cloud, representing advancement of the mass. Conversely, negative values tend to indicate removal of mass through rockfall. In addition to the Euclidian distance $|v_i|$, this method also yielded the 3D orientation of the movement vector, indicating vertical, horizontal, and oblique differences. Similar to the Hausdorff distance, however, the point distribution had a significant effect on the accuracy of this technique by determining the minimum physical proximity between selected point pairs. This resulted in movement errors of 0.05 – 0.20 m.

A more automated approach is to isolate and triangulate points belonging to a single discontinuity or object of interest and register them to the same surface in the next scan (Monserrat and Crosetto, 2008; Oppikofer *et al.*, 2009; Viero *et al.*, 2010). As discussed by Teza *et al.* (2007), the registration uses an affine rigid-body transformation, and hence assumes no deformation of the moving mass, that expresses the translation of the centre point from its initial to final state, followed by a sequence of three rotations about three axes (non-commutative). Typically, a 3-2-1 combination is used such that the overall rotation R and translation (the column [0;0;0;1]) is represented by:

$$R = R_x(\phi)R_y(\theta)R_z(\psi) \qquad \text{[Eq. 4.6]}$$

$$\begin{bmatrix} cos\theta cos\psi & cos\theta sin\psi & -sin\theta & 0 \\ -cos\phi sin\psi + sin\phi sin\theta cos\psi & cos\phi cos\psi + sin\phi sin\theta sin\psi & sin\phi cos\theta & 0 \\ sin\phi sin\psi + cos\phi sin\theta cos\psi & -sin\phi cos\psi + cos\phi sin\theta sin\psi & cos\phi cos\theta & 0 \\ 0 & 0 & 0 & 1 \end{bmatrix} \qquad \text{[Eq. 4.7]}$$

This technique relies on the presence of corresponding elements and structures between sequential point clouds for accurate registration. Prior to this the point clouds must be accurately aligned using stable surfaces present within the scene. This cannot be guaranteed for geomorphic surfaces that are frequently subject to the erosion and removal of material, for example river or debris-flow channels and hard rock cliffs.

A more recent approach for cloud-to-cloud comparison is the M3C2 algorithm (Lague *et al.*, 2013; Earlie *et al.*, 2013; Stumpf *et al.*, 2015), which is a freely avaialble function in CloudCompare. A normal vector is defined for each core point in the cloud by fitting a plane through a neighbourhood within a radius *D/2* from the core point. *D* is the normal scale and is related to local roughness of the cloud, represented by the standard deviation of distances between the neighbourhood points and the plane. Once the normal is computed, it is used to create a cylinder of radius *d*/2 that runs through the core point. The projection scale, *d*, determines the size of the neighbourhood that is enclosed within the cylinder for each point cloud. The distance between the two point clouds is defined as the distance between the centres

of each neighbourhood, along the normal vector. This method operates in 3D and is robust to fluctuations in point density and noise across the point cloud, and returns a signed measure of change.

4.4 Processing structure

In the remainder of this chapter, a series of codes created and applied to acquire an accurate rockfall inventory is outlined. This analysis has been undertaken in MATLAB, in order to take advantage of its parallel computing capacity, which allows multiple scan pairs to be examined simultaneously (Mathworks, 2017). In addition, it permits handling of three-dimensional datasets, interpolation into two dimensional rasters and statistical analysis of resulting rockfall inventories, all without the need to import and export data between separate software packages. The workflow is the result of multiple iterations using subsets of the scan data as well as the entire dataset (Figure 4.1). It generates a rockfall inventory containing the size, shape and environmental conditions at the time of failure. For a number of largest rockfall, plots and videos of the pre- and-post-failure movement within the event scar are also created.

4.5 Rotation

An example of the raw point cloud data was provided in *Section 3.7*. Depth, the distance between the lighthouse and the cliff, runs approximately along the *y-axis* of the raw point cloud. The *x-axis* runs across the slope, and the *z-axis* represents the vertical axis. Due to the high surface incline of the cliff relative to the scanner, the cliff itself is not planar within the *x-z* plane. In addition to East Cliff, the point cloud includes returns from the pier, foreshore platform, St Mary's Church and Whitby Abbey, such that East Cliff accounts for 82% of returned measurements (*ca.* 1.9 million of a total *ca.* 2.3 million collected). In order to minimise the effects of the above upon change detection between scan pairs, rotation and filtering of the point cloud were undertaken.

DEM creation requires a point cloud to be rotated prior to rasterisation. This rotation ensures the most planar surface possible, meaning that the depth or elevation of each point is measured along a new arbitrary axis normal to the dominant strike of the surface, rather than along the original line of sight or a global coordinate system (e.g. OSGB'02). Given that the subtraction of successive DEMs yields change along this depth axis only, the rotation of the point cloud is therefore critical for determining the degree to which changes measured using DoDs represents true 3D deformation of the slope (Rosser *et al.*, 2008; Benjamin *et al.*, 2016). For example, Rosser *et al.* (2008) showed that the observed deformation of a synthetic slope increased by nearly an order of magnitude for every 5° deviation from viewing angles normal to

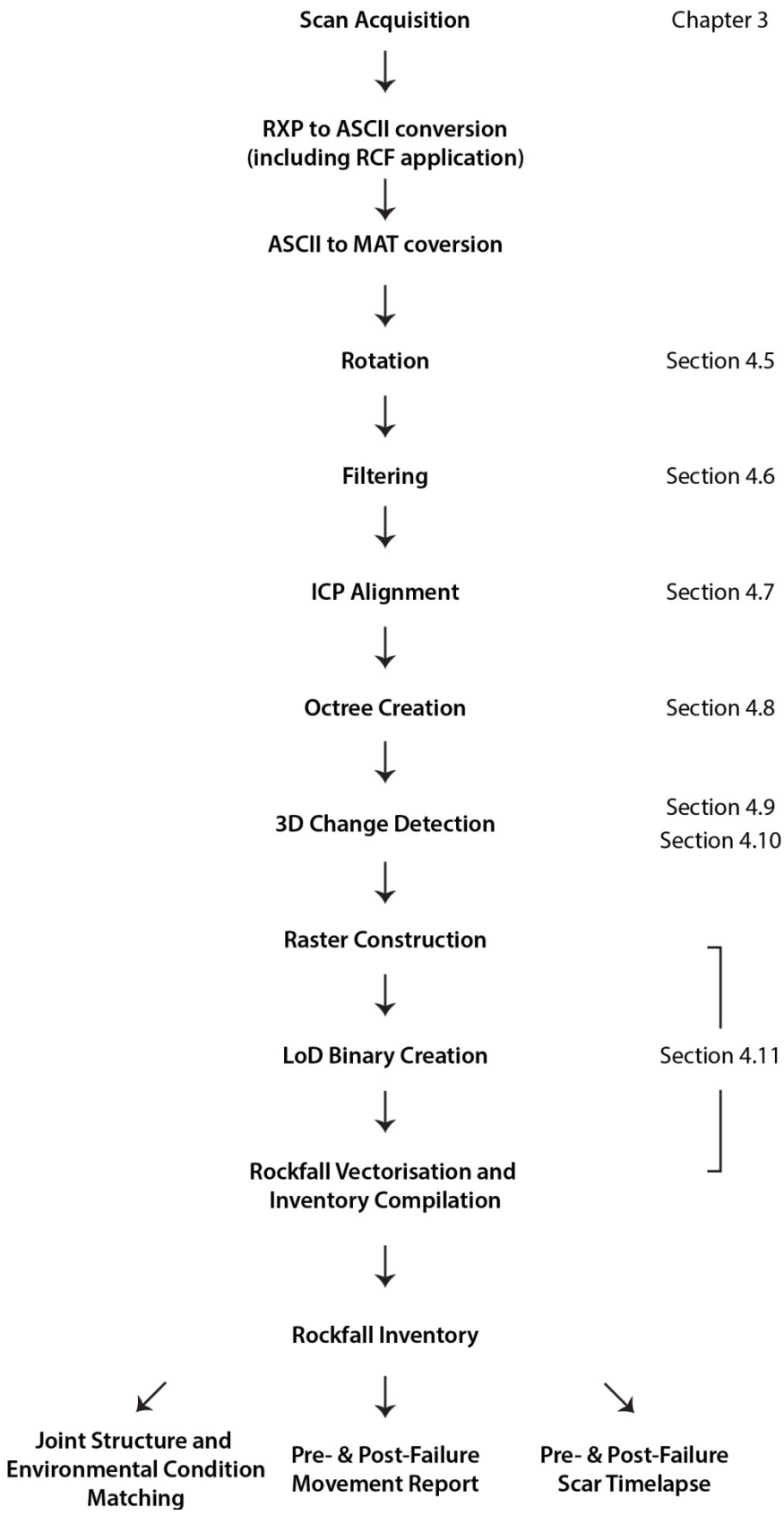

Figure 4.1: *Flow diagram representing each phase of the rockfall inventory compilation. All stages following ASCII to MAT conversion were written in MATLAB. ICP alignment used the pcregrigid function, and rockfall vectorisation used the bwboundaries function.*

the rock face. Cloud-to-cloud techniques overcome this bias by maintaining the 3D nature of the raw point clouds, measuring change along adaptive surface normals, rather than a single axis. Here, point clouds were rotated prior to change detection for the following reasons:

(1) Filtering of the point clouds required an automated approach (*Section 4.6*). As an initial step, a fixed clockwise rotation of 220° was applied to each point cloud until it became approximately planar across the *x*-*z* plane. The rotation was undertaken around the central point of the cliff, defined using the first collected point cloud. This rotation allowed the creation of a tight bounding box around the cliff that was used to filter extraneous measurements, such as birds or dust captured close to the lighthouse scanner.

(2) The estimation of surface normal vectors at each point is fundamental to the change detection process as it determines the positions on the original and new surface between which a length is calculated. However, the direction of each vector exhibits a sign ambiguity whereby the fitted plane has a normal in each direction (Mitra and Nguyen, 2003; Ioannou *et al.*, 2012). When calculating change along the normal, the direction of the normal vector was used to determine whether the monitored movement was forward or backward relative to the rotated coordinate system. This can typically be resolved using the position of the query point q relative to the sensor position s, as follows:

$$\hat{s} = [X_s, Y_s, Z_s] - [X_q, Y_q, Z_q] \quad \text{[Eq.4.8]}$$

$$\text{In } \mathbb{R}^3: \alpha = \arctan(\|\hat{s} \times \hat{n}\|_2) \quad \text{[Eq.4.9]}$$

where × denotes the vector cross product and ‖ denotes the Euclidean norm of the cross product. ∝ denotes the angle between the unit normal vector $\hat{n}$ at q and the vector between q and s, $\hat{s}$. If $\alpha > \frac{\pi}{2}$ or $\alpha < -\frac{\pi}{2}$, i.e. if the angle between the direction of the normal vector and the vector between the surface and the sensor is not within ± 0.5π rad, the normal direction $\hat{n}$ is reversed:

$$\hat{n}_{rev}\langle u, v, w\rangle = \hat{n}\langle -u, -v, -w\rangle \quad \text{[Eq. 4.10]}$$

Here, once the point clouds were rotated, the axis orthogonal to the surface was introduced as a string of either 'X' or 'Y'. With this information, the relevant component of the unit vector was used to determine whether the vector should be reversed in order to minimise the computation time required in Equations 4.8 and 4.9.

For example, range in the rotated cloud was measured along the y-axis; if $\hat{n} = \langle -u, +v, -w \rangle$. This meant that the vector $\hat{n}$ pointed into the surface and should be reversed using equation 4.10. For each normal, this provided a *ca.* 50% reduction in the time taken for sign correction.

(3) While deformation estimates were calculated in 3D, and are therefore unaffected by rotation of the point cloud, the point clouds of change were rasterised to delineate individual failures and calculate their area and volume. Maximising the planarity of the surface through rotation ensured that changes belonging to different points were not assigned to the same pixel in the resulting raster.

4.6 Filtering

Scan data collected outside of the monitoring area can provide useful information for scan-to-scan registration, especially if it is stable, covers a wider geographical and more three-dimensional area, and if the monitored slope is moving. To avoid false change estimates, however, this area must be removed alongside any objects that are temporarily introduced into the scene, such as birds, vehicles or people (Kemeny and Turner, 2008). For datasets containing a small number of scans (< 20), the data is often cleaned by manually delineating and erasing these points. In order to automate this procedure for the 8 987 scans used here, a rectangular bounding box was initially used to mask each rotated point cloud, allowing removal of extraneous points. This removed parts of the pier, structures on the cliff top, exposed areas of the foreshore platform and spurious measurements returned from birds, fog and heavy rain. Applying this mask reduced the raw point cloud sizes from *ca.* 1.9 million points to *ca.* 1.1 million points, thereby increasing the speed of subsequent filtering algorithms.

Extraneous points within the area of interest can include those belonging to vegetation, or those that are scattered around the true value of the surface due to measurement noise (Kemeny *et al.*, 2011; Abellán *et al.*, 2014). Two filters were applied to eliminate points with high range uncertainties, with the ultimate aim of enhancing the accuracy of point cloud used in the change detection. As the change detection used in *Section 4.10* draws on a point and its surrounding neighbours, the measurement quality of all points is critical for correctly determining the direction of the normal vector and the distance between neighbourhoods within successive point clouds. As a consequence, rather than filtering erroneous change measurements after the change detection, points with uncertain range estimates were removed first to prevent them from influencing the change detection of the surrounding points. Two filters were therefore applied to eliminate points with high range uncertainties, with the aim of enhancing the accuracy of the later change detection. These were an edge and hole filter (*Section 4.6.1*) and a

filter based on the radiometric return of the signal (*Section 4.6.2*).

4.6.1 Edge and hole filter

Edges present unique uncertainties for laser measurement that are exacerbated by high target ranges and steep incidence angles, such as those at East Cliff. These uncertainties arise from the averaging, or smearing, of multiple returns within the same beam footprint, alteration of the size of the discontinuity owing to uncertainty in the lateral position of the point of measurement within the footprint (Lichti *et al.*, 2005; Hodge *et al.*, 2009), and the tendency for scan lines to include or omit edges between scans when the scan-line spacing exceeds the scale of surface relief (aliasing). A code to detect the presence of edges and holes in the point cloud was developed and applied to each point cloud.

For each point, its neighbours within a fixed radius were identified and the *CoG*, the central location within the neighbourhood, was calculated as follows:

$$CoG = \left(\frac{\sum_{i=1}^{n} x}{n}, \frac{\sum_{i=1}^{n} y}{n}, \frac{\sum_{i=1}^{n} z}{n}, \right) \quad \text{[Eq. 4.11]}$$

where n is the number of neighbouring points. The 3D Euclidean distance, *ED*, between the query point, q, and the *CoG* was then calculated:

$$ED = \sqrt{(X_q - X_{CoG})^2 + (Y_q - Y_{CoG})^2 + (Z_q - Z_{CoG})^2} \quad \text{[Eq. 4.12]}$$

For a point on the edge of a surface, the distribution of its neighbours is skewed towards the interior of the surface and the resulting *CoG* is further away from the query point. The distance *ED* is larger than that of a query point that does not belong to an edge. Before using *ED* as a threshold to remove points, the distance between the query point and the *CoG* must account for the varying point density across the cloud. In regions of low point density, *ED* will always be larger than regions of high point density regardless of the point's positon relative to an edge. In order to compensate for this, the value *EH* assigned to each point is reported as a ratio of the distance *ED* to the number of points in a spherical domain centred on each point:

$$EH = \frac{ED}{n} \quad \text{[Eq. 4.13]}$$

Incorporating the point density ensures that this filter removes points that are surrounded by very few neighbours, such as single returns from birds or partial reflections from atmospheric

moisture. Points belonging to surfaces with only very low point densities are also removed; such surfaces have the potential to produce unrealistically high values of change as points are significantly less likely to be measured in similar physical locations between successive scans. Change detection in these locations is therefore unreliable.

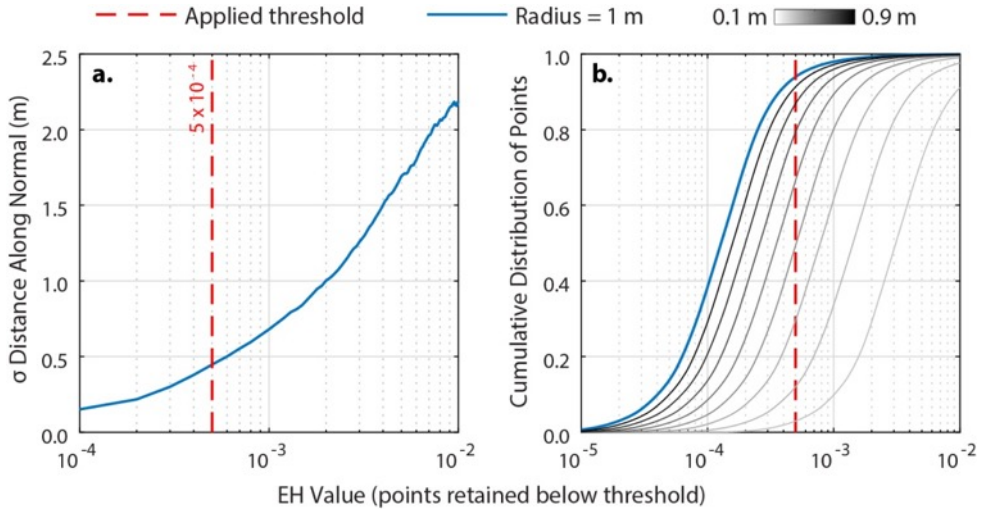

Figure 4.2: *(a) A change detection is undertaken between two point clouds where no observable movement occurred. The standard deviation for a single point cloud therefore indicates the level of noise between the two. This value is estimated by first including only points with the lowest edge/hole values (EH 10^{-4}), and then including points with increasingly large edge/hole values (up to EH 10^{-2}). When high EH values are retained, the total error, defined by the standard deviation of change, increases. Edge and hole values for the point cloud are retained below the position of the threshold (red dashed line). (b) The cumulative proportion of EH values within an entire point cloud. Each line represents a different neighbourhood radius search. For the same points, EH values are lower using a larger search radius because more neighbouring points (n in Equation 4.13) are found. An inflection in the number of points retained is used to define the threshold at 95%. This ensures that artefacts such as holes are not introduced into the point cloud by removing too many points.*

Figure 4.2a demonstrates the role played by points attached to high *EH* values in increasing the error in change detection between scan pairs. Two successive unfiltered point clouds were compared using the 3D distance estimation in *Section 4.10*. No observable changes occurred between these two point clouds and, therefore, 3D distance estimation serves as an indicator of the level of measurement noise between them. *EH* values were then calculated for all points in the first point cloud. If the *EH* threshold (*x*-axis in Figure 4.2) is set high, a greater proportion of edges and holes are retained within the point cloud. The standard deviation of change that is preserved is also higher, owing to the uncertainty attached to high *EH* points (discussed in more detail in *Section 4.10.3*). The red line indicates the threshold that is applied in this study; while the standard deviation of change increases with points of higher *EH*, this metric does not provide a clear value of *EH* to apply as a threshold. In Figure 4.2b, the

distribution of *EH* values within the point cloud is presented. Using a search radius of 1 m (blue line) the threshold of 5×10^{-4} retains 95% of the points within the point cloud while removing the 5% of points that are attributed to errors > 0.5 m in Figure 4.2a. The grayscale distributions illustrate the influence of varying the search radius at each query point. While the *EH* values change, their distribution across the point cloud remains the same due to the normalisation by point density. A 1 m radius was chosen to ensure that a minimum of four points, the minimum needed to estimate the *CoG* in addition to the query point, would always be found.

Figure 4.3b shows an example point cloud coloured by the point density, defined as the number of points within a 1 m radius. The 95th percentile, 80, is shaded red. In Figure 4.3a, the point cloud is coloured by *EH* with filtered points $> 5 \times 10^{-4}$ shaded in red. This metric comprises the zones of red in Figure 4.3b but also accurately delineates zones of occlusion, or 'holes', along with edges across the cliff face.

4.6.2 Deviation filter

A major drawback of TLS systems is the inability to identify unreliable point measurements, as each does not have a measured reliability. The introduction of new systems, which record the energy characteristics of reflected returns, offers a means of estimating the quality of recorded measurements. In this section, the use of such measures in removing unreliable data prior to change detection is examined. Here, characteristics of the returned signal are used to filter out regions of vegetation and edges in order to reduce noise in point cloud comparisons. This is undertaken with respect to a recorded average of the energy return, referred to in Riegl systems as the deviation.

The Riegl VZ-1000 records the intensity of each returned signal in addition to the time-of-flight. Here, point clouds were filtered based on comparisons between the measured reflection intensity of each point and an associated 3D change value between scan pairs. Previous studies have used intensity measurements for surface characterisation alone. Akca (2007) used the common intensity of reflected surfaces in industrial settings to provide a weighting to least squares alignment of sequential point clouds, such as pipes and walls. Pesci *et al.* (2008) characterised the stratigraphy and deposits within the Vesuvius crater using the intensity of the returned signal combined with RGB values derived from imagery. Kurz *et al.* (2011; 2013) combined hyperspectral imagery with TLS data to classify outcrops of limestone and dolomite, including the presence of fractures within the rock mass.

In conventional TLS systems, range is estimated using the time at which an undisclosed feature of the reflected waveform, which may vary between manufacturers, is detected; this can be a threshold of the reflected energy or the maximum amplitude returned. Recently introduced

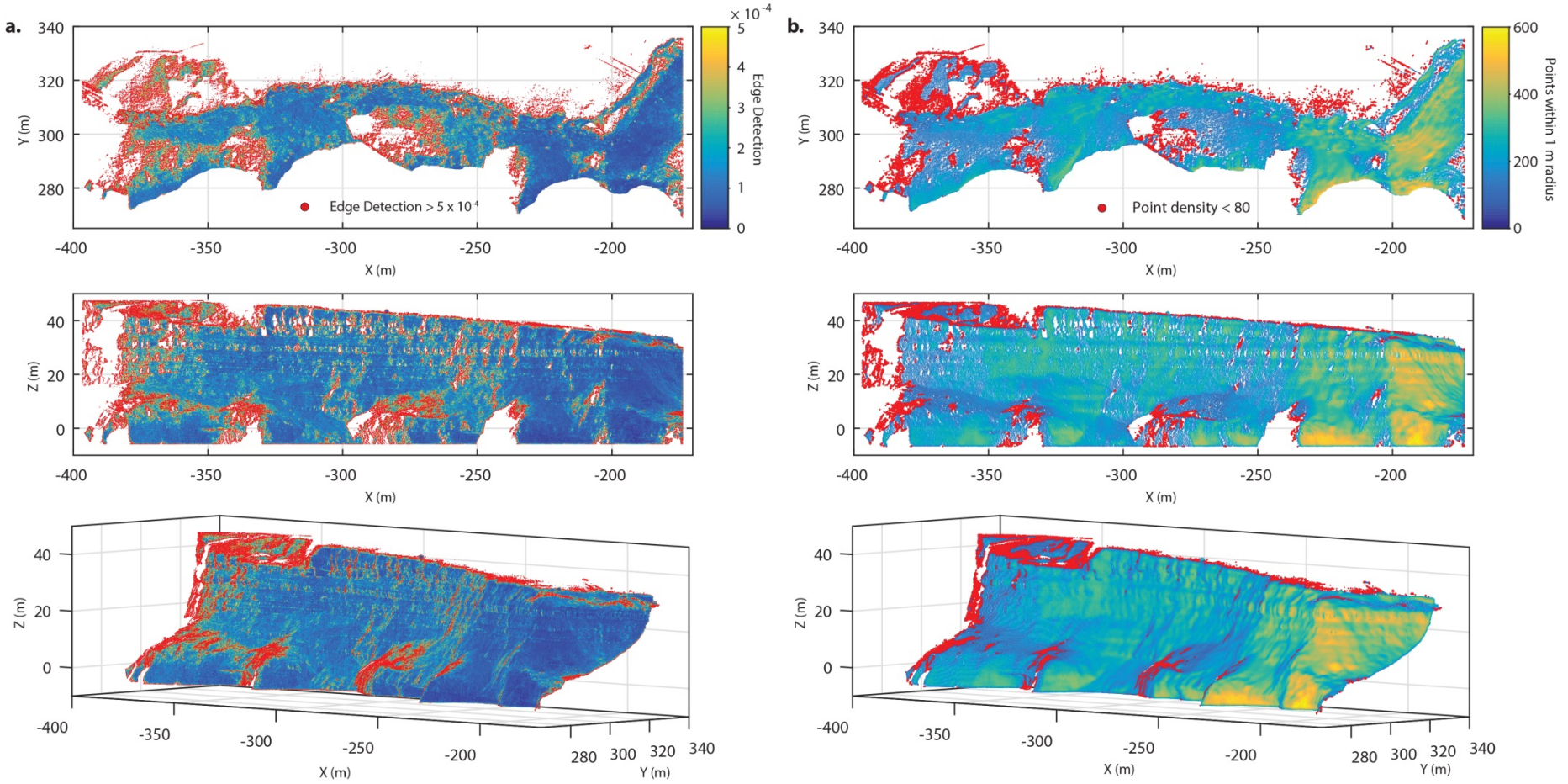

Figure 4.3: *(a) Edge/hole values across the cliff face shown from an aerial (top), x-z plane (middle), and rotated perspective similar to the scanner look angle (bottom). Edge detections above the applied threshold are coloured in red and occur predominantly around holes but also along sandstone protrusions 30 m up the scanned cliff. (b) Point density across the cliff face from the same perspectives. This metric is more sensitive to low density areas, including areas with numerous holes, than it is to edges.*

systems have been equipped with the ability to capture and digitise the full structure (energy-time distribution) of the waveform of the reflected laser pulse, providing measures of change in the laser reflection beyond the range alone. A Riegl VZ-1000 with 'full-waveform' capacity records the energy of the received waveform at 2.01005 ns intervals, providing 15-70 amplitude measurements per pulse. The energy of the received laser pulse structure depends on the spatial energy distribution of the emitted beam, and the geometric and reflectance properties of the surface (Stilla and Jutzi, 2008). Since pulses may encounter multiple objects during flight, the full-waveform of the backscattered pulse in airborne LiDAR systems has enabled filtering of vegetation based on first, intermediate and last pulses (Fowler *et al.*, 2011; Jaboyedoff *et al.*, 2012). Though a number of studies have successfully characterised the waveform in airborne LiDAR systems, use in terrestrial platforms has remained limited. Williams *et al.* (2013) observed that shifts in the geometry of a series of boards, analogous to deformation of a rock slope surface, could be measured using observations of change to the received waveform's total and maximum energy. In reality, observing these changes to derive movement of natural slopes requires the effect of variable atmospheric conditions, surface roughness and surface moisture to be normalised (Kaasalainen *et al.*, 2010). Since the same point on a surface can never be rescanned, this method also relies on the assumption that local variations in reflectance properties across the surface have less impact on the waveform than geometric surface change. This is exacerbated on complex surfaces that yield non-uniform point distributions between scans. The use of full-waveform technology for slope monitoring thus remains in its early stages.

Riegl instruments, including those without full-waveform capacity, provide simple metrics that describe the received waveform structure including the maximum amplitude and deviation. The deviation, δ, of the waveform describes the change in shape of the received waveform relative to a reference Gaussian waveform (Figure 4.4) according to:

$$\delta = \sum_{i=1}^{N} |s_i - p_i| \qquad \text{[Eq. 4.14]}$$

where N is the number of energy-time values s_i matched to the reference values p_i. A value of 0, for example, indicates that the received waveform is identical in shape to the reference waveform, as would be expected in a single return from a perfectly nadir planar specular reflector.

Experiments have shown that the deviation value is far less sensitive to target range than incidence angle, as is apparent in the deviation distribution across East Cliff (Figure 4.5). To test this, a 1.5 m × 1.5 m target was positioned indoors, with controlled atmospheric and lighting conditions, at a fixed distance from the scanner (20 m). The board was rotated in 5° increments from an incidence angle of 0° (orthogonal to the direction of scanning) to 60°, and

was scanned three times at each position. Figure 4.6 shows the distribution of deviation values returned from the board, illustrating that the proportion of high deviation values increases with incidence angle, as the board is rotated off-nadir. This is attributed to the spreading of the beam cross-section as it intersects the surface, reducing the returned energy and increasing the period of time over which the backscattered pulse is returned.

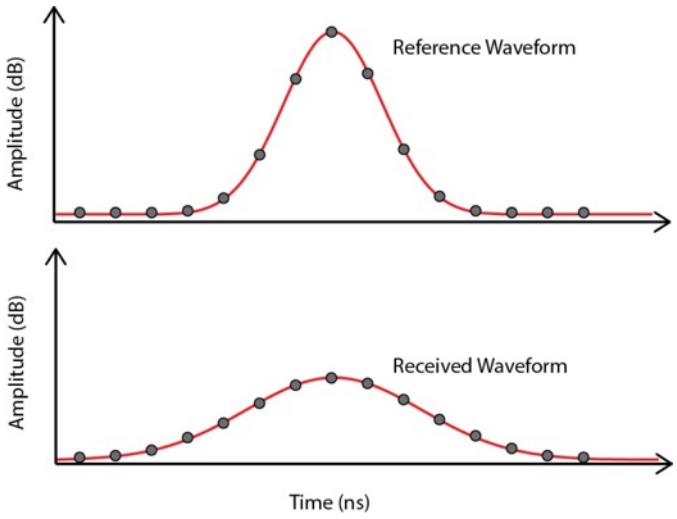

Figure 4.4: *Comparison of the reference waveform structure to the received waveform, with each measurement separated by ca. 2 ns. High target incidence angles relative to the beam incidence angle can spread and skew the distribution of the received waveform. Increased target range also attenuates the returned signal. If multiple discontinuities are intersected within a single line-of-sight, multiple peaks are created. Deviations of zero indicate identical waveform structures.*

Figure 4.5 shows the variation of deviation values across the cliff face. The deviation value is capable of identifying differences in surface topography attributed to different rock layers, edges, and multi-returns from vegetation.

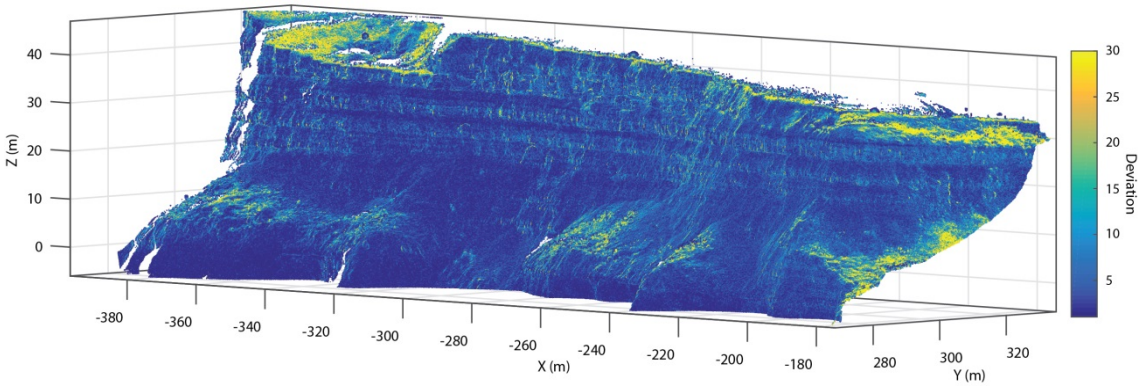

Figure 4.5: *Distribution of deviation values across the cliff face. The highest values coincide with the presence of multiple surfaces within a single line of sight, in particular at the near-horizontally bedded sandstone protrusions and vegetation. While deviation increases with target range, this effect is small relative to the incidence angle.*

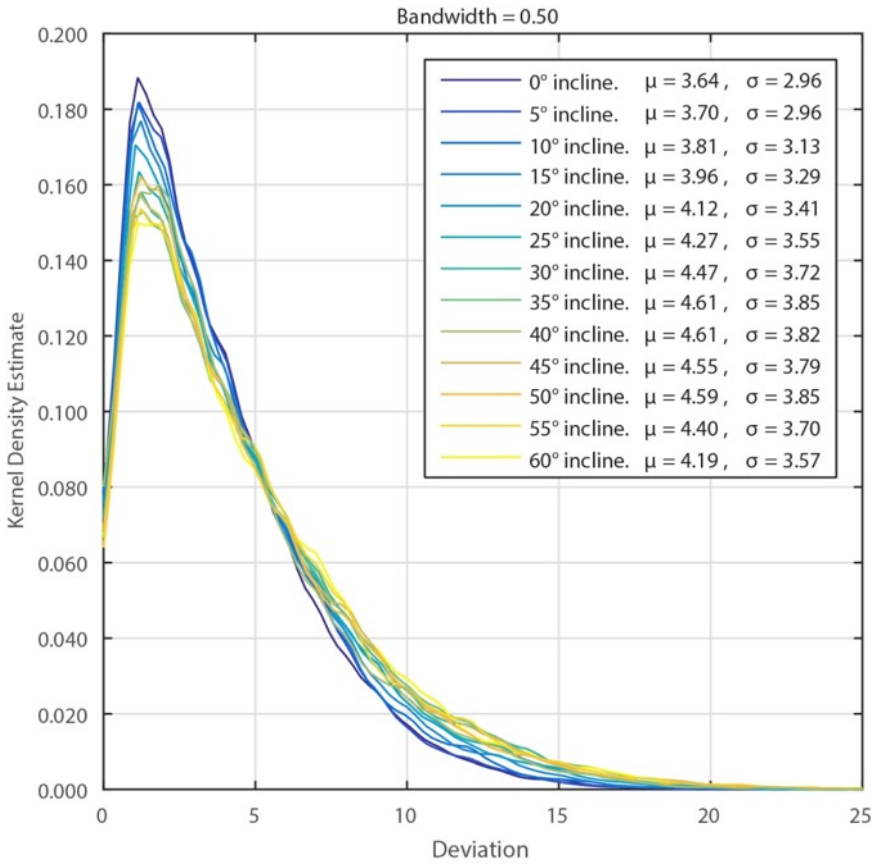

Figure 4.6: *Kernel density estimate of the returned deviations for a board rotated between 0° and 60°. Small deviations values (< 5) account for a higher proportion of reflected returns when the board is facing the scanner. A higher proportion of deviations > 5 is found when the board is inclined. This is shown by both the mean (μ) and standard deviation (σ) of deviation values, which increase with surface incline. This highlights the sensitivity of the deviation value to the spreading of the laser footprint when the surface is increasingly inclined with respect to the scanner.*

As with Figure 4.2a in the previous section, Figure 4.7a represents data from a change detection between non-filtered clouds. Again, no observable change occurred between these point clouds, and so the difference between them is representative of the offset between them. Here, the mean absolute change is presented for points belonging to each deviation class, recorded as integer values. The mean estimated change rises from *ca.* 0.02 – 0.03 m for points with deviation values ≤ 25. Points with deviation > *ca.* 25 exhibit significant scatter that often corresponds to change estimates two to three times the level of noise presented elsewhere in the cloud. There is therefore a need to remove these points in order to provide more reliable change detection. The position of the applied threshold indicates the deviation value above which points are removed. Using a threshold of 25 for data collected at this site, Figure 4.7b shows that 98% of points in the dataset are retained, which accounted for a standard deviation of error between point clouds of 0.18 m. As with the edge and hole filter, removing only those points associated with high levels of uncertainty removes artefacts that are often on the periphery of the point cloud but if

not removed hold a significant influence on the overall reliability of the change detection. Figure 4.8 illustrates the distribution of deviation value across the cliff face.

The filters described in this section were applied with the aim of removing points with inherent uncertainty attached. Both filters remove many of the same points and, typically, no more than 15% of points were removed from a point cloud. When combined, the filters reduce the standard deviation of change measurements between two stable scans from 0.078 m to 0.055 m, thereby lowering the LoD that can be applied during rockfall or deformation identification by 30%. Once filtering has occurred, the remaining points are aligned between successive point clouds. By filtering the points before this process, measurements that are spatially unreliable and have the potential to move between scans, such as edges and vegetation, are not used during the alignment process.

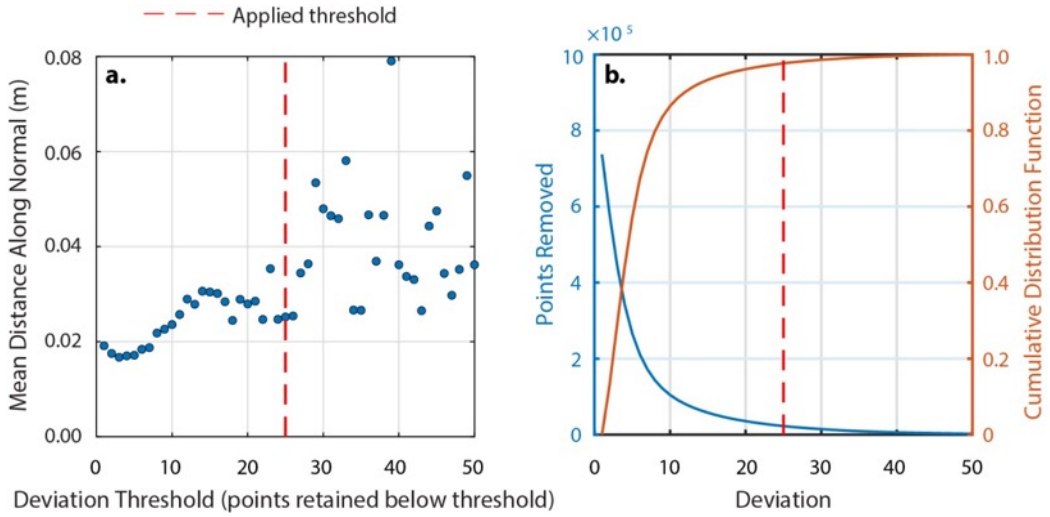

Figure 4.7: *(a) Mean absolute distance between two point clouds with no observable change. Similar to Figure 4.2, this indicates the comparison uncertainty between both scans. The mean distance is calculated for change estimates attributed to points with each deviation, from 1 – 50. Error increases from ca. 0.03 – 0.06 m at values > 25. The variability in error also increases such that the selection of an appropriate threshold > 25 is not possible. (b) The number of points removed (blue) alongside the cumulative distribution of deviation values. A threshold of 25 ensures that only 2% o points are removed.*

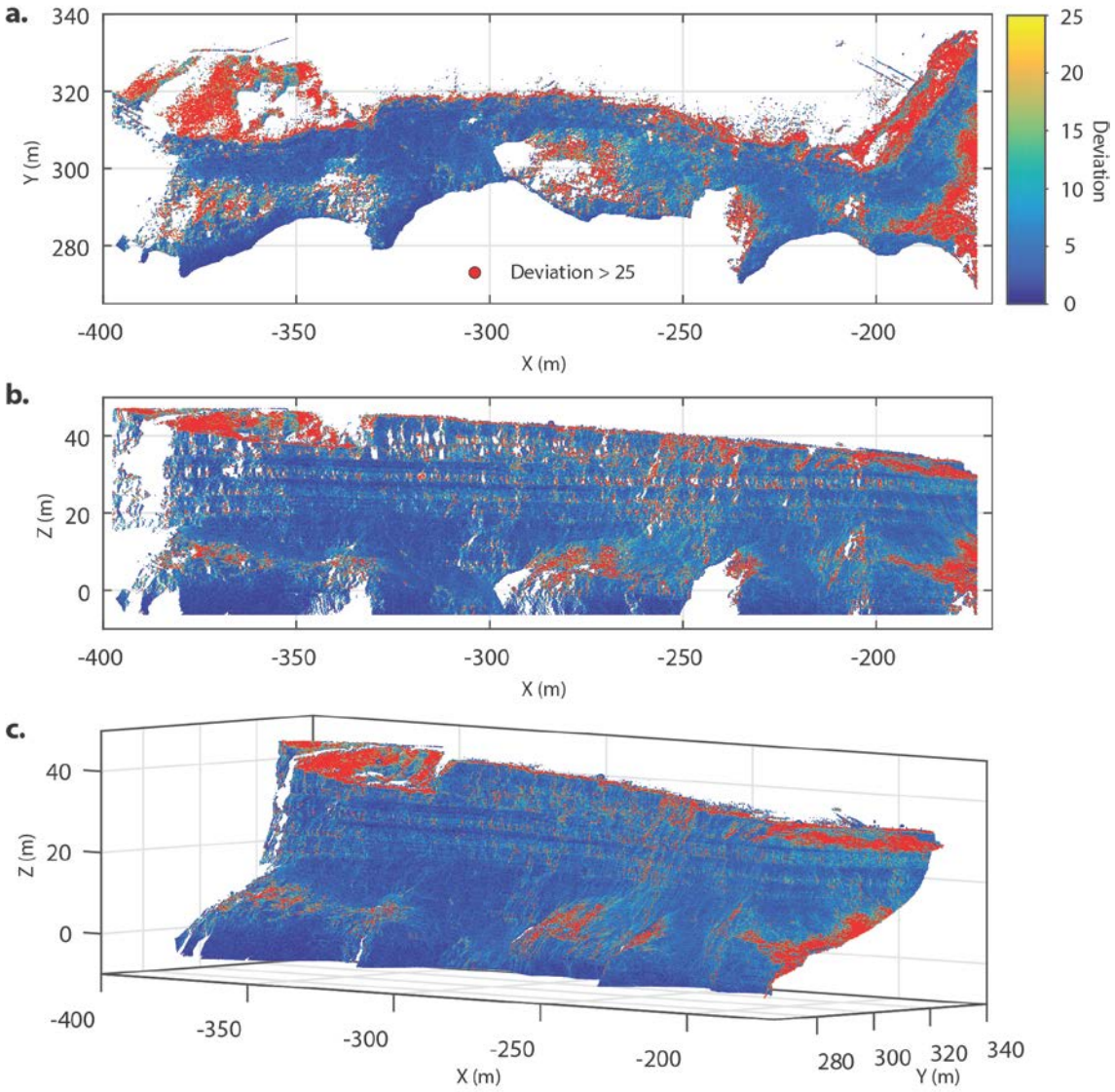

Figure 4.8: *Deviation across the cliff with values > 25 coloured red and removed from each point cloud prior to change detection. (a) Aerial perspective showing the sensitivity of vegetation at the cliff top and on top of the buttress to deviation. (b) x-z plane directly viewing the cliff. Holes in the point cloud are now apparent, with their edges delineated in red. (c) View from the angle of scanning.*

4.7 Alignment

While range correction factors derived from target scanning were applied to each point cloud, the position of each cloud has the potential to drift due to variable atmospheric conditions and small shifts in the position of the scanner. On two occasions, the scanner was also removed from the lighthouse for servicing, and was therefore not replaced in its exact original position. As such, a method was required to align successive scans based on the positions of points that were collected. Point cloud alignment, or registration, refers to the co-registration of two point clouds. This is most often expressed as a rigid Euclidean

transformation that combines a 3D rotation and a translation of a single point to a fixed reference. Registration is used for a number of purposes, including the creation of a single surface from multiple scan positions, registration of the dataset to a reference coordinate system, and the alignment of sequential scans. As discussed by Abellán *et al.* (2014), this process can align scans using common targets that are fine-scanned and then modelled, and measured in global coordinates (Teza *et al.*, 2007; Olsen *et al.*, 2010); feature based registration based on the planarity and curvature of surfaces (e.g. Besl and Jain, 1988; Belton and Lichti, 2006; Rabbani *et al.*, 2006); and point-to-point and point-to-surface methods, that use iterative closest point (ICP) alignment to progressively reduce the distance between two clouds (Besl and McKay, 1992; Chen and Medioni, 1992; Zhang, 1994).

Alignment using targets would have enabled projection of the datasets into a global coordinate system, such as OSGB '36. However, by preserving *x,y,z* coordinates in a local project coordinate system defined after rotation, file sizes were halved due to the shortening of multi-digit coordinates. The scale of the point cloud here ($<$ 1 000 m), means coordinates in each axis are seven digits maximum, as opposed to 12 digits in OSGB '36. In this study, ICP registration was undertaken using MATLAB's *pcregrigid* function. This method searches for the closest point in the reference scan, p, for each point in the moving scan, q, and estimates the combination of rigid rotation and translation, α, that best aligns them (Mitra *et al.*, 2004). This process is applied iteratively until a user-defined convergence distance is reached. This is typically the mean squared distance, ε, between the two closest points:

$$\varepsilon(\alpha) = \sum_{i=1}^{N} d^2(\alpha(q_i), p_i) \qquad \text{[Eq. 4.15]}$$

where d is either the point-to-point distance (Besl and McKay, 1992) or the point-to-plane distance (Chen and Medioni, 2004). For the point-to-plane metric, the error can be defined as:

$$\varepsilon = \sum_{i=1}^{N} ((Rp_i + t - q_i) \cdot \hat{n}_i)^2 \qquad \text{[Eq. 4.16]}$$

where R is the rotation, t is the translation vector and $\hat{n}$ is the normal direction. Pottman and Hofer (2003) showed that for point clouds that are approximately aligned, as in this study, minimising the point-to-plane distance provided the best estimate of convergence. Point-to-point distances are better suited to point clouds that are further apart but, unlike point-to-plane minimisation, they are susceptible to local minima due to noise in the point cloud (Gelfand *et*

al., 2003). The rate of convergence of ICP methods is determined by the choice of distance function and the number of points, with point-to-point distance typically the slower of the two metrics. Reducing the number of points to match can be achieved by downsampling the point cloud. Downsampling also benefits the accuracy of the alignment, since the influence of point density variations and outliers can be reduced and the point distribution becomes more consistent between scans if fixed interval downsampling is applied.

In order to validate the relative benefits of point-to-plane matching and point-to-point matching, both were tested on two point clouds between which no large rockfall events had occurred. The influence of the downsampling into a regular fixed grid was also examined. The two point clouds were registered using Riegl's RiSCAN PRO, providing a benchmark alignment error of 0.005 m, defined as the mean absolute distance between the resulting datasets. Registration using RiSCAN PRO, which is referred to as Multi Station Adjustment (MSA), downsamples the point clouds by determining a least-squares plane for each neighbourhood of points. Here, the neighbourhood is subdivided if the distance between the points and the fitted plane is beyond a user-defined error. Point pairs are then aligned using least squares fitting. For each alignment, the distance between the two point clouds was estimated, with a theoretical distance approaching zero being most desirable.

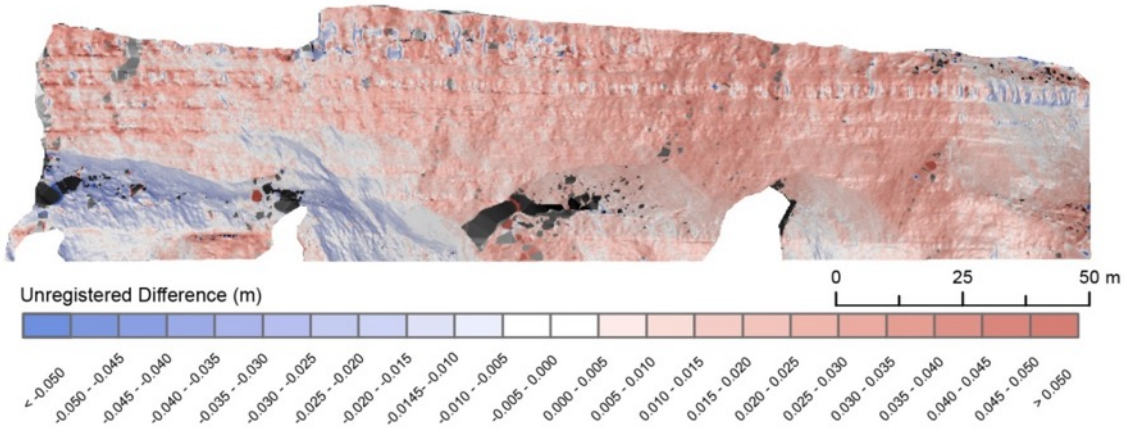

Figure 4.9: *Change between two stable scans that are unregistered. While the scanner is securely installed, small variations in its orientation propagate the offset in measured point positions at targets distances from 350 m – 550 m. Regions of positive and negative change can be observed on surfaces that are inclined towards and away from the scanner position, indicating that a small rotation of the scanner may have occurred.*

Figure 4.9 illustrates change between two point clouds that are unregistered. Despite the scanner being securely installed in the lighthouse, small shifts in its angular position produce offsets at distance of 350 m – 550 m away from the scanner that are equivalent to 0.004 m at maximum range (assuming a single 0.0005° angular shift in the scanner rotation). The negative

change can be attributed to surfaces oriented towards the scanner, while the positive change occurs on areas facing away; this is symptomatic of small shifts around the scanner's vertical axis. The results of the point-to-point matching of two non-downsampled scans are shown as a DoD in Figure 4.10, with the alignment process exacerbating error in the unregistered dataset. Figure 4.11 shows that this performance occurs because point-to-point methods are susceptible to outliers and require similarity in the point distributions between scans, which can be attained by downsampling each point cloud. While high levels of downsampling bring the distribution of change closer to the results of MSA, the mean change is still an order of magnitude greater at *ca.* 0.07 m when downsampled to 1.25 m.

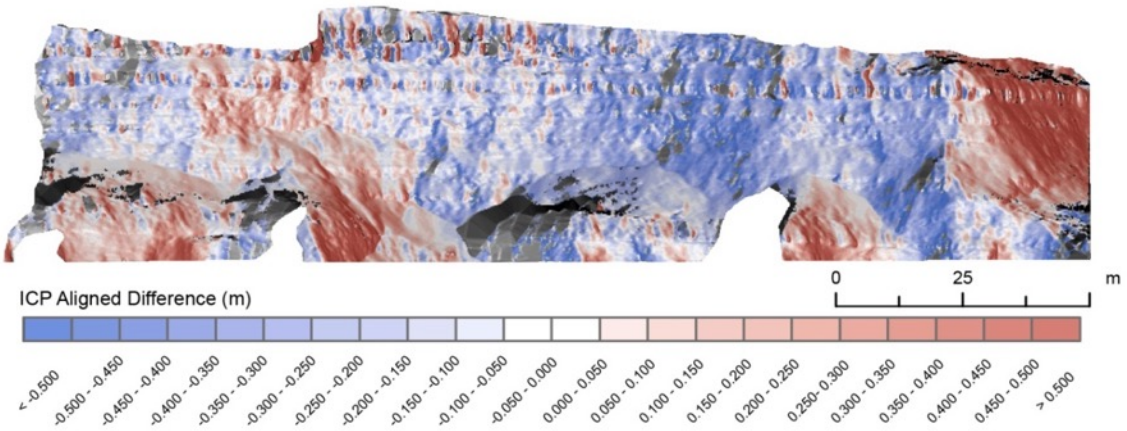

Figure 4.10: *Change between two stable scans that are registered using ICP to minimise the point-to-point distance. Here, no downsampling is applied to either point cloud. As such, inconsistences in the point distribution between scans compromise the accuracy of the alignment procedure. The colour scheme here is the same as that applied in Figure 4.9; point-to-point ICP therefore exacerbates the small offset in the position of the scans around the vertical axis.*

The results of point-to-plane alignment are far closer to the performance of MSA (Figure 4.13). As can be seen in Figure 4.12, excessive downsampling of the point cloud had the effect of increasing the error in change detection. However, when the point cloud was reduced into a 0.25 m fixed grid, the mean error was within 0.001 m of the MSA, at 0.0052 m.

Figure 4.14 compares the change error between scans aligned using non-downsampled point-to-plane ICP (red), 0.25 m downsampled point-to-plane ICP (blue) and MSA (black). The absolute value of the mean obtained using MATLAB (*ca.* 0.0053 m) is almost identical to that obtained using RiSCAN PRO (*ca.* 0.0052 m). For both MATLAB and RiSCAN PRO, the mean values in Figure 4.14 also equate to a standard deviation of change of 0.055 m. Having undertaken a sensitivity analysis on point cloud alignment through MATLAB, this process could be automated for all of the 8 987 filtered scans.

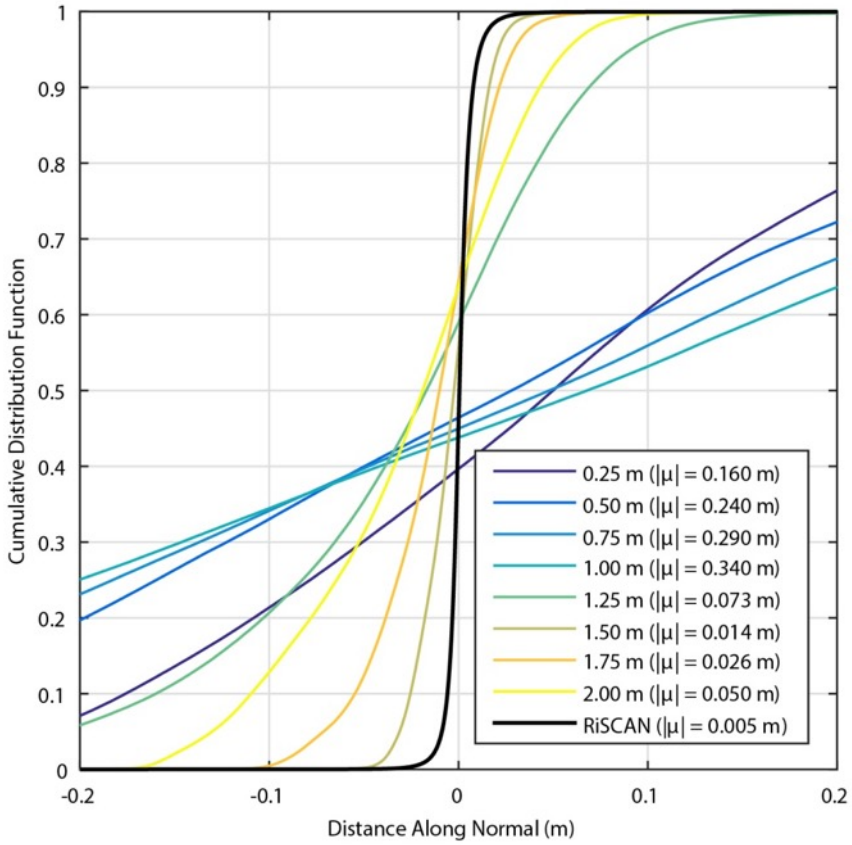

Figure 4.11: *Cumulative distribution of the change for each point between two scans aligned using ICP (point-to-point). Since no observable change occurred between the scans, the distribution should approach zero across the point cloud. MSA using RiSCAN PRO (black) produces a mean absolute distance (μ) of 0.005 m, significantly lower than point-to-point ICP. An increase in the spacing of the downsampled point clouds benefits the alignment.*

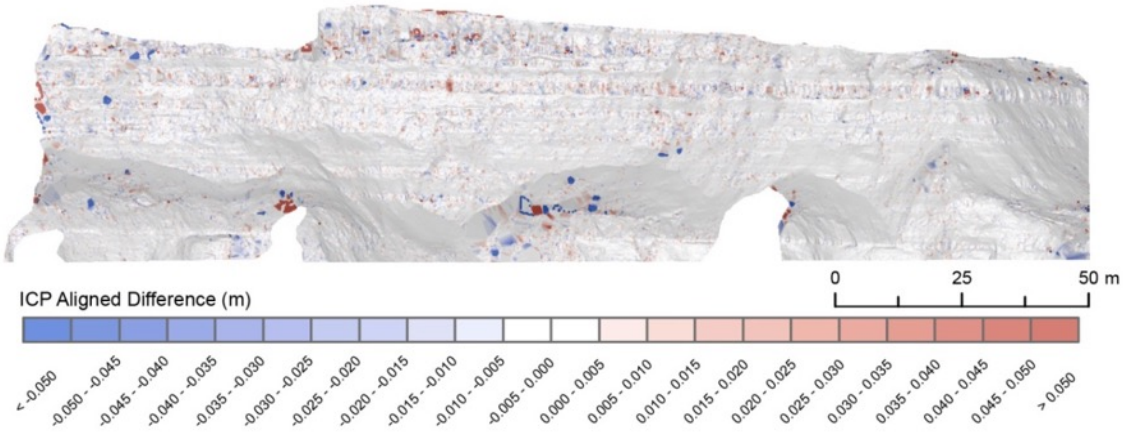

Figure 4.12: *Change between two stable scans that are registered using ICP to minimise the point-to-plane distance. Here, 0.25 m downsampling was applied. The dependence of alignment accuracy on surface orientation exhibited in Figure 4.10 and Figure 4.11 is removed. The colour scale here is the same as that applied in Figure 4.10.*

An important consideration for registering time-series of scans is the designation of the reference, or 'fixed', model. At present, there is no established protocol for this decision, which determines whether scans are aligned to the first scan of the entire dataset or the first scan of each scan pair, or treated all previous scans as the reference. Schürch *et al.* (2011) aligned scans to the previous scan, rather than the first of the monitoring campaign, in order to gain more precise change estimates between surveys. As such, the absolute accuracy of the fit to a carefully projected initial point cloud was lower than the relative accuracy between scans. This procedure is advantageous as it ensures that the shape of a rapidly deforming mass can be matched to the previous survey, rather than one captured days, weeks, or months earlier. However, the scans in this study were matched to the first survey for a number of reasons. First, this type of alignment minimised the point-to-plane distance of point clouds that were downsampled, such that individual rockfall events over time did not have an effect on the quality of the alignment. Second, even with low alignment errors between scan pairs, the potential of the point clouds to drift over time increases with the number of scans collected. While Schürch *et al.* (2011) only assessed pairwise change, the rich temporal resolution of the dataset used here allows for change detection at multiple timescales, such as daily, weekly and monthly. It is therefore critical to ensure that all scans are consistently aligned. Third, automated interpolation of the point clouds

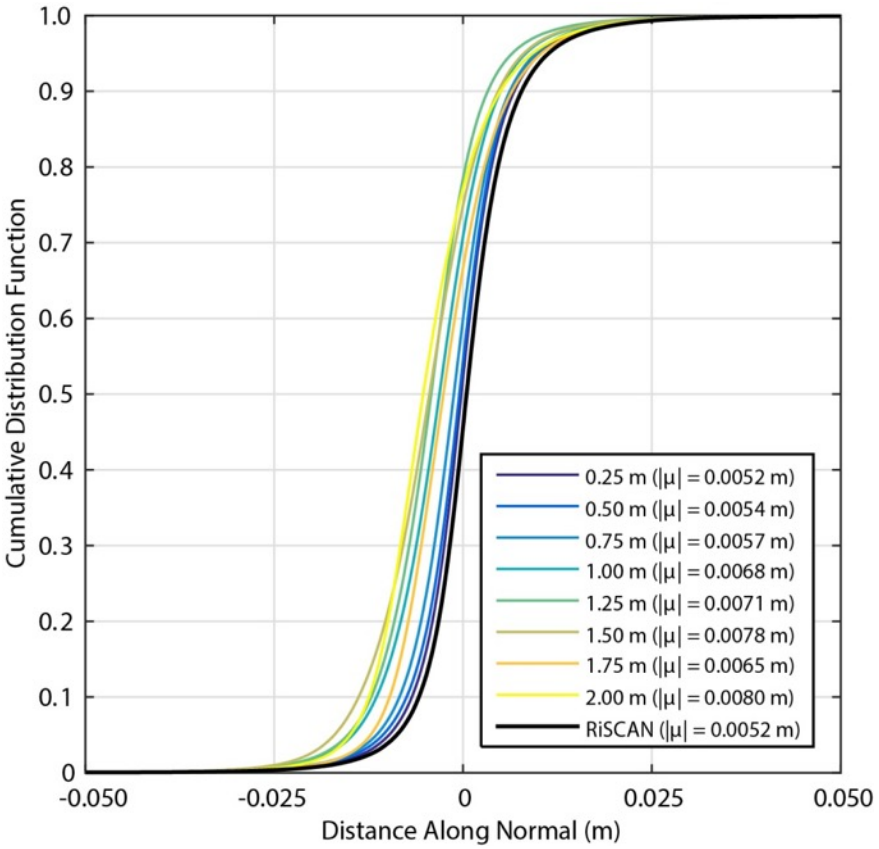

Figure 4.13: *Cumulative distribution of the change for every point between two scans aligned using ICP (point-to-plane). Each coloured line represents a different scale of downsampling. A downsampling of 0.25 m produces the same mean absolute error (μ) value 0.005 m as MSA through RiSCAN PRO.*

of change was simplified when points occupied similar positions in *x*-*z* space. Finally, since the point clouds were segmented by octrees (*Section 4.8.1*), it was possible to create only one octree structure using the reference scan and rapidly assign subsequent clouds to this structure. No differences in the quality of the alignment were observed when scans were aligned to the first scan of the series, even after nine months. However, the occurrence of a single large event, such as a 200 m^3 failure observed by Rosser *et al.* (2005) at this site, or the continued spalling of material over time, would considerably alter the surface topography. In order to maintain the accuracy of alignment, a new more representative point cloud would be required as a reference for subsequent alignment, and a new octree structure (described in the next section) would have to be generated.

The accuracy of alignment is one of the key sources of error when detecting change between two point clouds (Teza *et al.*, 2007). The results above suggest that the scans have been aligned in accordance with what is capable with current leading software that relies upon user intervention to optimise the alignment. It is noted, however, that the values of error provided by RiSCAN PRO's MSA were significantly lower than the standard deviation of 3D change measured between point clouds in this section. For the scans used in Figure 4.15, for example, the reported alignment was 0.0028 m, which is an order of magnitude below the 0.055

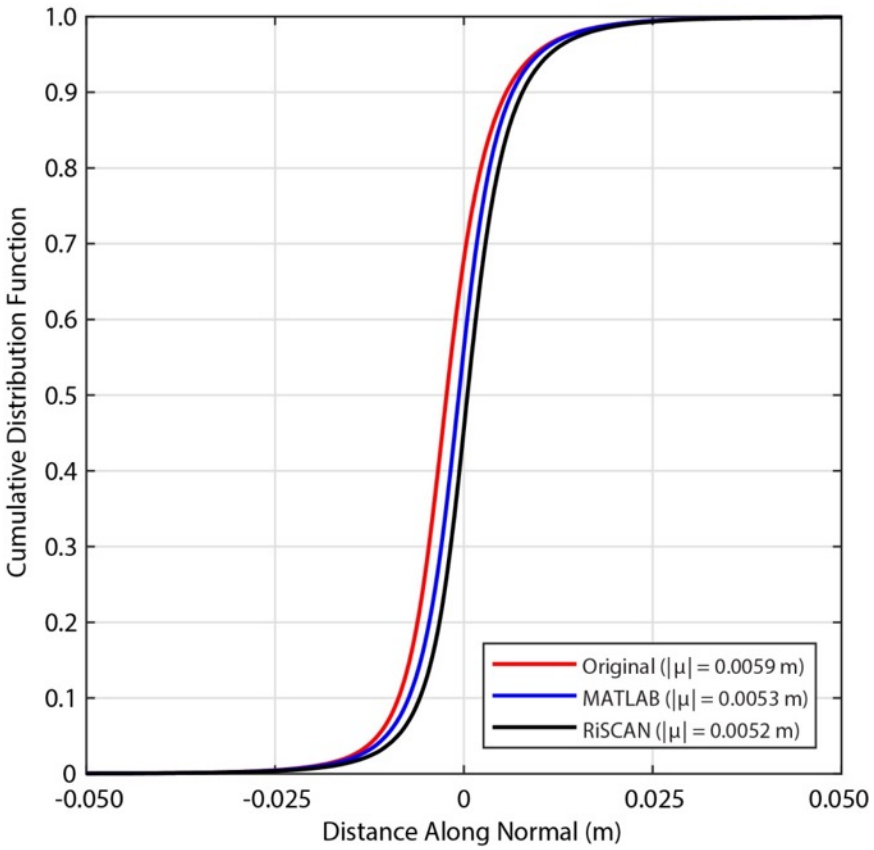

Figure 4.14: *Cumulative distribution of the change for the unregistered point clouds, MATLAB aligned and RiSCAN PRO MSA aligned. While the mean offset in the unregistered point cloud data is 0.0059 m, this is reduced to similar levels using with ICP using both MATLAB and RiSCAN PRO.*

m standard deviation calculated here. This difference can be explained by the fact that the MSA reports error as a Hausdorff distance (and therefore the minimum distance) between pairs of downsampled points used in the registration. For a typical cliff scan in this setting, this constitutes *ca.* 1 000 – 5 000 point pairs.

4.8 Segmentation and structuring of point clouds

Segmentation refers to the labelling of each measurement in a point cloud such that points belonging to the same surface will be given the same label (Hoover *et al.,* 1996). More generally, the process partitions a point cloud into meaningful regions or features of similar geometry (Woo *et al.*, 2002) and, in rock slope analysis, segmentation plays an important role in 3D classification and efficient processing. In geomorphology, this has previously focussed on vegetation modelling for fluid dynamics (Tymkow *et al.*, 2010; Rutzinger *et al.*, 2011; Boothroyd *et al.*, 2016), the classification of geomorphic elements (Brodu and Lague, 2012); and rock slope discontinuity characterisation (Slob *et al.*, 2004; Jaboyedoff *et al.*, 2007; Sturzenegger and Stead, 2009a; Sturzenegger and Stead 2009b; Lato *et al.*, 2010; Gigli and Casagli, 2011; Sturzenegger *et al.*, 2011a; Assali *et al.*, 2014; Riquelme *et al.*, 2014).

Discontinuities are planes within a rock mass. They exhibit lower tensile strengths adjacent to, and shear strengths along, the discontinuity relative to surrounding material (Assali *et al.*, 2014). Since most large rockslides creep and/or fail along such structures, (Varnes, 1978; Agliardi *et al.,* 2001; Jaboyedoff *et al.,* 2009) the identification and description of discontinuity sets is a crucial first phase in risk assessment and hazard-mitigation. These datasets can be used as accurate inputs for stress-based failure models; however, they are seldom used to characterise shifts in strike and dip in repeat monitoring of the rock mass. In this study, an initial approach was to segment the rockface into a series of cubes, with each cube containing a set of points that fall on a planar surface, with a minimum length of 1.4 m to ensure that at least 10 points could be used for Principal Component Analysis. This segmentation was initially designed both to increase the efficiency of subsequent point cloud processing, and to enable change in the dip and strike of points within each cube to be monitored. As is described below, however, this technique was ultimately used only for the former.

4.8.1 Voxels and octrees

The division of a point cloud into cubes can be done using a voxel structure or an octree structure. A voxel is a small cube that partitions a point cloud domain, equivalent to a three-dimensional pixel in a raster image (Roth-Tabak and Jain, 1989). A voxel space is constructed by adding voxels in a constant horizontal and vertical spacing in a Cartesian coordinate system

(Bienert *et al.*, 2010). Voxels have a fixed length scale, d, similar to the cell size in a raster, that determines the resolution of the voxel space. Empty voxels may occur if d is too small, creating holes in the resulting domain. Conversely, if the scale is too coarse, too few voxels will be created and they will therefore be indistinguishable (Gorte and Pfeifer, 2004). The number of divisions that occur along all three dimensions is determined by d, and so a major drawback for processing using this segmentation is that the number of voxels increases as d reduces (Hornung *et al.*, 2013). For example, $d/2$ results in eight (2^3) more voxels and a proportional increase in the computation times of operations within the voxel domain. Using a fixed voxel resolution of d also assumes a degree of homogeneity of the point cloud structure across the surface. For the purpose of rock mass characterisation, Gigli and Casagli (2011) divided a point cloud of a rock cut slope into voxels and fitted a plane to each point cluster. Once the strike and dip were plotted onto a stereonet, clusters of similarly oriented surfaces were defined in order to identify individual discontinuities.

An alternative approach to voxel creation is hierarchical clustering through octrees (Pauly *et al.*, 2002; Woo *et al.*, 2002; Bienert *et al.*, 2013; Hornung *et al.*, 2013), which describes the recursive division of 3D space without the use of a fixed grid spacing (Figure 4.15). During this process, the point cloud is divided into a series of cuboids, typically cubes, if the neighbourhood size, N, is greater than a user-defined maximum. The process results in a tree-like data structure that can be used to index data, known as an octree. As a data structure, octrees have been used as a memory efficient means of rendering in computer graphics (Laine and Karras, 2011) as well as in photogrammetry and LiDAR to store and address large point clouds (Frisken and Perry, 2002; Girardeau-Montaut *et al.,* 2005; Elsberg *et al.* 2011; 2013;

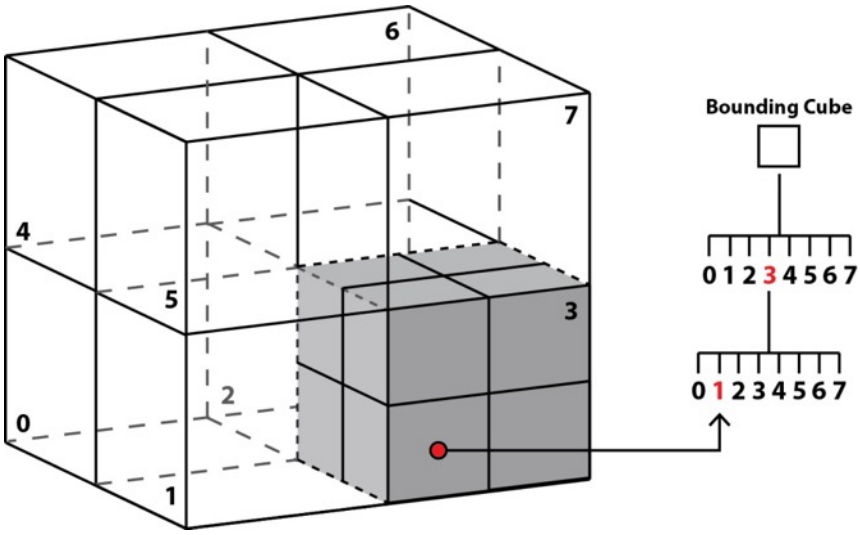

Figure 4.15: *Principle of octree subdivision, where the location of a point within the cloud (red) is identified by an m× 8-bit code, where m is the number of subdivisions. Here, there are two subdivisions, which generate a 2× 8 identifier for the point. Adapted from Figure 2 in Girardeau-Montaut (2005).*

Hornung *et al.*, 2013), including within CloudCompare and the topographic analysis software Coltop-3D (Jaboyedoff *et al.*, 2007; 2009).

Subdivision begins with a bounding cuboid that contains the entire point cloud and is recursively split into eight sub-cuboids. The subdivision stops when no more points lie within a cube, a minimum threshold of points is reached, or a maximum depth (the number of subdivisions a cube has undergone) is reached. In this study, division is halted if the number of points within the cubes falls below 15, a threshold identified by Riquelme *et al.* (2014) as the minimum number required for accurate estimation of normal vectors. In order to maintain the planarity of the surfaces being analysed, subdivision is also stopped when the surface curvature exceeds threshold of 20%, defined in detail for normal vector estimation in *Section 4.9.1* (Equation 4.21). The resulting octree structure applied in this study contained 3 421 cubes (Figure 4.16). Every point is assigned a $3\times n$ bit code, where n is the maximum number of subdivisions that occurred. The combination of 0 and 1's that arises from the three bits represents an integer between 0 and 7, giving a code that is unique to the cube to which each point belongs (Figure 4.15). This enables rapid searching of points and identification of point neighbourhoods. Since all point clouds are aligned to the first point cloud of the series, each cloud can be assigned to a pre-defined octree structure to increase the speed of change detection.

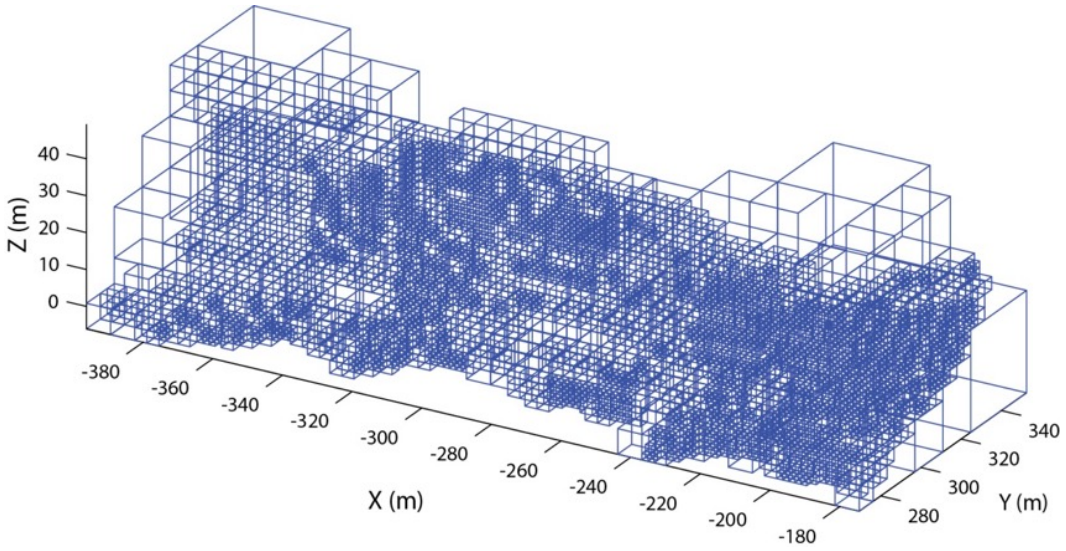

Figure 4.16: *Octree structure created for the first scan of East Cliff. This structure is a reference to which subsequent point clouds are assigned. Unlike voxels, this approach to segmentation is robust to variations in point density across the cliff face. Since no major alteration to the topographic structure of the rock face occurred, all points in subsequent point clouds were assigned to this same structure.*

4.8.2 Change detection by octree

Although octree structures have been used in surface segmentation and, by extension, the extraction of discontinuities, their use in change detection between surfaces has remained

limited. Girardeau-Montaut *et al.* (2005) suggested that when two point clouds are assigned to the same octree structure, change can be measured on a cube-by-cube basis as the mean distance between the points in each cloud. Although this technique is robust to noise and variations in point density, and illustrative of change to groups of planar surfaces, this metric provides a coarse 'patchwork' change detection at far lower spatial resolution than the original point cloud. This is shown in Figure 4.17 for an open-pit high-wall, where distance is measured along the normal vector of each surface. This method has proved useful for monitoring creep of an entire slope by providing precise estimates of change to each surface; however, it inhibits the detection of smaller scale failures, such as small rockfall.

Teza *et al.* (2007) used a regular voxel grid in order to segment point clouds for change detection. Two point clouds were initially aligned using stable structures within the scene. 3D movement vectors were subsequently generated by calculating the ICP transformation that aligned the moving point cloud to the reference point cloud on a cube-by-cube basis. In order to test this approach, scans of East Cliff were aligned through ICP using only the positions of the pier and the control targets. An area of the buttress was then isolated and a forward movement of 0.10 m, simulating a slump, was applied (Figure 4.18). The movement vector for each cube did not accurately depict the simulated movement. On closer inspection, as depicted in the aerial perspective (centre panel), movement vectors are dominated by a bias orthogonal to the scan line spacing and direction of scanner view. This is attributed to the scale of movement, which falls below the scan line spacing, and the orientation of movement, which is not oriented towards the direction of scanning. As the point spacing at East Cliff cannot be decreased without compromising the temporal resolution of scanning, this technique is thus limited in its ability to detect fine-scale movements. Due to the complexity and loss of spatial resolution attributed to scan comparison within octree structures, the use of the octree structure was limited in this analysis to efficient point cloud handling alone. Change was therefore estimated on a point-by-point basis, rather than cube-by-cube.

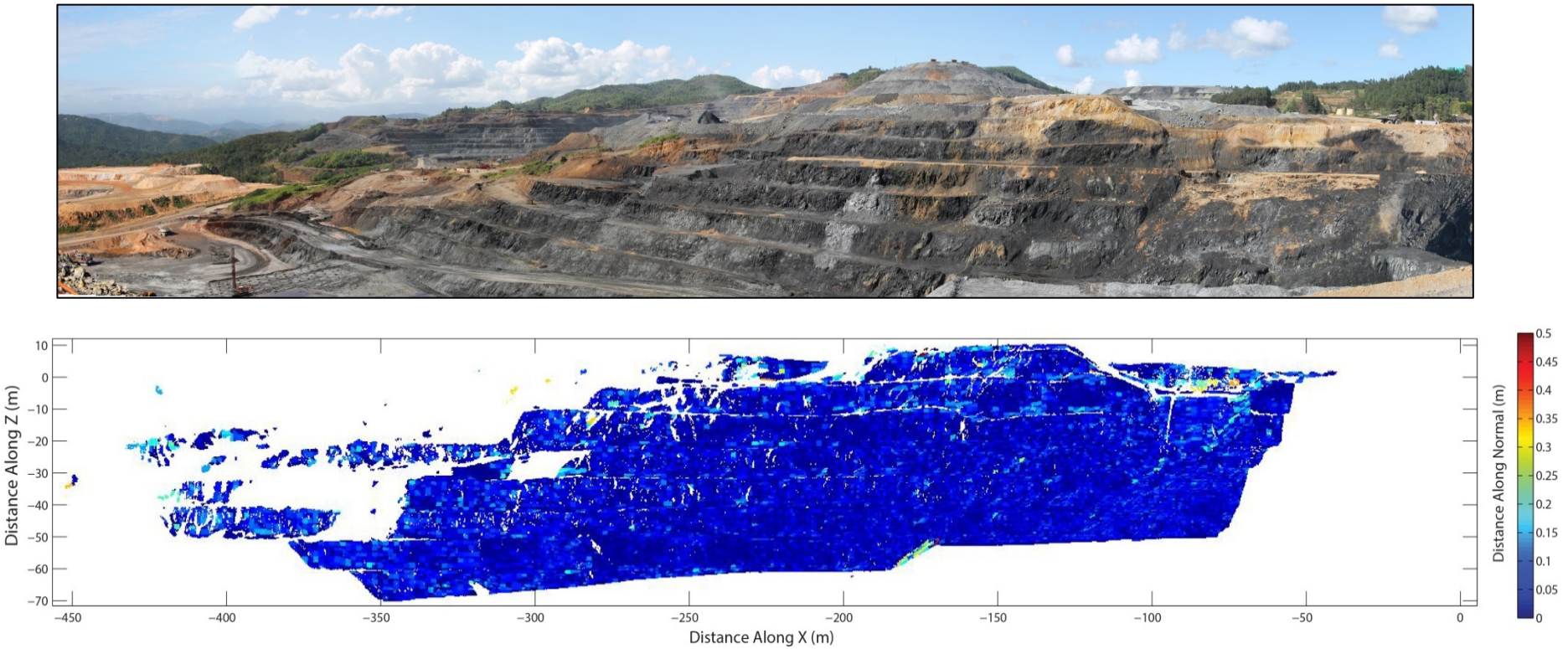

Figure 4.17: *Top: Image of open-pit slope. Bottom: An example of cube-by-cube change detection of the high wall. Here, each cube represents the average distance along the normal for all the points that it contains. A patchwork effect occurs because of the coarse subdivision of octrees. Due to the averaging of change within each cube, the overall accuracy of change is higher than for individual points. For monitoring deformation over a large surface, this is desirable; however, for the purpose of rockfall identification, the spatial resolution is insufficient.*

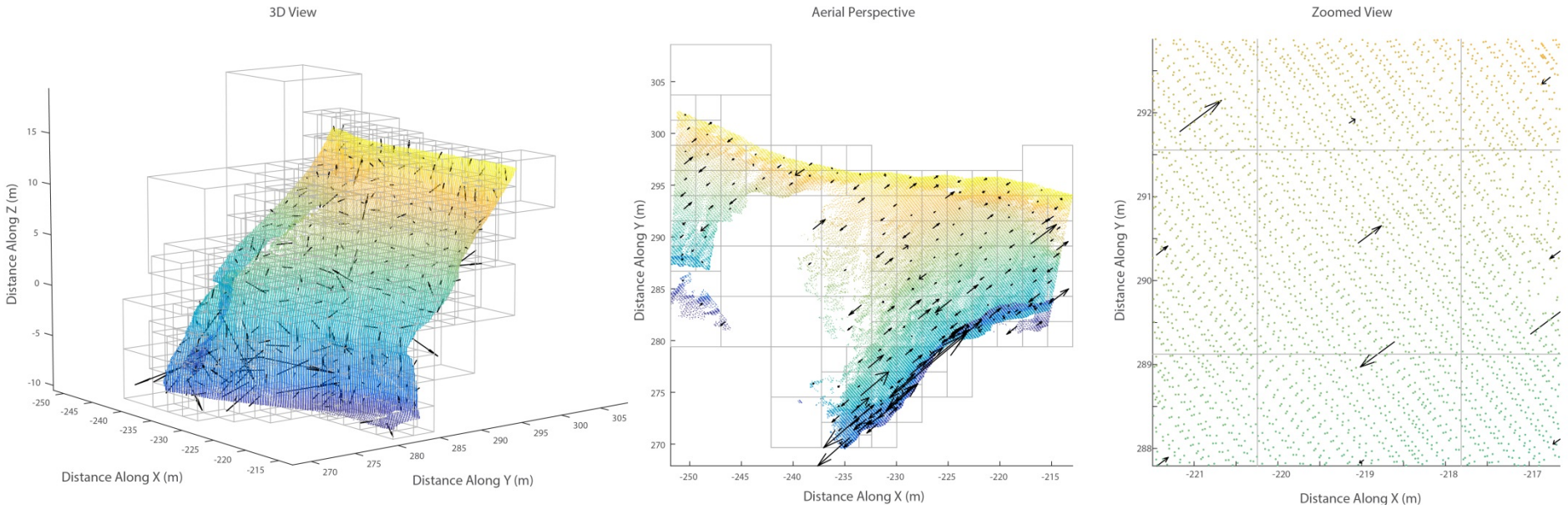

Figure 4.18: *An isolated area of the buttress, viewed from the scanner position (left), above (middle), and from above in greater detail (right). A forward simulated movement of 0.10 m is introduced along the along the y-axis. Each arrow represents the affine 3D transformation that best aligns the two point clouds within each octree cube (estimated using least-squares). The length of the arrow represents the magnitude of the translation. Since the surface is not completely planar, uniformly aligned arrows of 0.1 m would not be expected. However, on close observation, a bias in direction of arrows is found orthogonal to the scan lines. With both point-to-point and point-to-plane matching, a best-fit was produced when alignment corrected for this offset.*

4.9 Normal estimation

For this dataset, the distance between successive clouds is measured along the normal vector of each point in a similar approach to the M3C2 algorithm discussed in *Section 4.3.2*. Accurate estimation of each normal vector is therefore critical in determining the magnitude and direction of movement. A normal vector cannot be derived from a single point alone, but only from an appropriately sized cluster of neighbouring points that adds topological context to each point. Normal directions can be estimated by triangulating point clouds and calculating the normal direction for each face (Slob *et al.*, 2002; Woo *et al.*, 2002). Woo *et al.* (2002) adapted the triangulation fitting to operate between scan lines; thus for a point P the normal value N can be estimated by averaging the normal direction, $\hat{n}_i$, of the surrounding six edge pairs.

$$\widehat{N}_{P_{i,j}} = \frac{\sum_{i=1}^{K} \hat{n}_i}{6} \qquad \text{[Eq. 4.17]}$$

where K is the number of edge-pairs. Although the vector for each point is the mean of the vectors of the surrounding 6 triangles (Figure 4.19), these individual vectors are derived from single edge pairs that are created using only three points, and are therefore susceptible to noise in range estimates. The creation of a Delaunay Triangulation is also time-consuming and unsuited to the point clouds of East Cliff, which contain regions of occlusion.

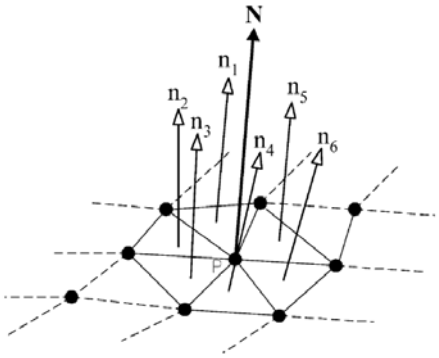

Figure 4.19: *Normal estimation by averaging the normal directions of six triangles that surround the query point (centre). This method is optimised for scans with very low point spacing and uniform scan line spacing.*

A more common approach is to estimate the surface normal of a plane that is constructed through a neighbourhood of points surrounding the query point (e.g. Jaboyedoff *et al.,* 2009; Lague *et al.*, 2013; Riquelme *et al.*, 2014). This neighbourhood can be selected using either the Fixed Distance Neighbours (FDN) or *k* Nearest Neighbours (KNN; Rabbani *et al.*, 2006). The FDN approach selects all points within a user-defined Euclidean distance from the

query point. This is unsuited to scans acquired using fixed resolution angle scanners that produce an uneven distribution of points and spatial variations in point density. In regions of low point density, for example, few points may constitute neighbours and the estimation of surface normals is more susceptible to noise (Lato *et al.*, 2010). KNN provides a more robust means of defining neighbourhoods. For each query point, the k most proximal neighbours are selected. By fixing the number of points, this method adapts the volume of the neighbourhood according to local point density, such that fewer points result in a larger volume. Consequently, a consistent degree of accuracy in normal estimation can be maintained across the point cloud.

4.9.1 Neighbourhood size in normal estimation

The neighbourhood size strongly determines the direction of surface normals (Mitra and Nguyen, 2003; Lalonde *et al.*, 2005; Bae *et al.*, 2009; Lague *et al.*, 2013). If the size of the neighbourhood is below the scale of surface roughness, the resulting normals will fluctuate in direction across the surface and are less likely to be consistent between scans. In certain cases, the difference in normals at multiple scales can be used to classify structures within a point cloud (Ioannou *et al.,* 2012). For this study, however, incorrect estimation of normals has the potential to overestimate change between point clouds.

Riquelme *et al.* (2014) have shown that the number of points, k, determines the curvature of the neighbourhood. Values of $k < 15$ result in much greater variability in the strike and dip of a single discontinuity as a consequence of high curvature, whereas values of $k > 30$ over-smoothed adjacent surfaces; $15 < k < 30$ was therefore recommended. In a similar approach, Lague *et al.* (2013) selected the scale at which the neighbourhood of points could best be approximated by a plane.

A covariance matrix can be used to describe the statistical properties of the point distribution in a neighbourhood, and is the first step required to test the planarity of a surface. More specifically, covariance measures the extent to which the dimensions of a dataset vary from the mean with respect to one another, in this case by summing the squared distances of points to the neighbourhood centroid (Pauly *et al.*, 2002). Since covariance is measured between two dimensions, for a series of *x,y,z* Cartesian coordinates the covariance should be measured between the x and y dimensions, x and z dimensions, and the y and z dimensions, with the covariance between each dimension and itself representing the variance. This can be represented in the matrix, C (Pauly *et al.*, 2002; Belton and Lichti, 2006):

$$C = COV(X) = \begin{bmatrix} \sigma_{xx} & \sigma_{yx} & \sigma_{xz} \\ \sigma_{xy} & \sigma_{yy} & \sigma_{yz} \\ \sigma_{xz} & \sigma_{yz} & \sigma_{zz} \end{bmatrix} \quad \text{[Eq. 4.18]}$$

where σ is the variance (e.g. of *x* and *x*) and the covariance (e.g. of *x* and *y*). The entries for a neighbourhood containing *k* points are defined as:

$$\begin{aligned} \sigma_{xx} &= var(x) \\ \sigma_{xx} &= E(x^2) - E(x)^2 \\ \sigma_{xx} &= \frac{1}{k}\sum_{i=1}^{k}(x_i - \bar{x})^2 \end{aligned} \quad \text{[Eq. 4.19]}$$

$$\begin{aligned} \sigma_{xy} &= cov(x, y) \\ \sigma_{xy} &= E(xy) - E(x)E(y) \\ \sigma_{xy} &= \frac{1}{k}\sum_{j=1}^{k}(x_i - \bar{x})(y_i - \bar{y}) \end{aligned} \quad \text{[Eq. 4.20]}$$

Since *C* is square (Pauly *et al.*, 2002), covariance analysis is followed by calculating the eigenvalues λ and eigenvectors v using Principal Component Analysis (PCA). Three eigenvectors exist for a 3 × 3 matrix, each of which is orthogonal to the other and is presented as a unit vector. The eigenvectors (v_1, v_2, v_3) represent the principal components, or directions, of the neighbourhood, while the eigenvalues $(\lambda_1, \lambda_2, \lambda_3)$ indicate the variance (Equation 4.20) of the corresponding eigenvector (Riquelme *et al.*, 2014).

When all three eigenvalues are equal, the points cloud is perfectly 3D, and any line or plane passing through the centroid shares the same dimensionality. In contrast, assuming that $\lambda_1 \geq \lambda_2 \geq \lambda_3 \geq 0$, the first two components form a basis for a plane as they explain the majority of the variability in the first two dimensions. In this case, the planarity can be defined as:

$$\frac{\lambda_3}{\lambda_1 + \lambda_2 + \lambda_3} \quad \text{[Eq. 4.21]}$$

If the third eigenvalue represents more than 20% of the variance, the surface is no longer planar, and instead approaches a 3D point distribution.

4.9.2 Plane and normal vector estimation: overview

In order to calculate the normal direction of each neighbourhood, a tangent plane must be fitted to every point and its neighbours, with each being considered as a potential plane subset. A total least squares adjustment may be fitted as follows (Nurunnabi *et al.*, 2012; Riquelme *et al.*, 2014):

$$Ax + By + Cz + D = 0 \quad \text{[Eq. 4.22]}$$

where A, B, and C are the three components of the unit normal vector to the plane and D gives the perpendicular distance from the origin to the plane.

In the total least squares approach, the sum of square distances is orthogonal between each point and plane, since the plane passes through the centroid $\bar{p}$. In ordinary least squares methods, data points are expressed as $(x, y\, f(x, y) \approx z)$ where z is considered a function of x and y such that error is only measured in the z-direction. The method thus minimises the sum of square residuals r as follows:

$$\sum_{i=1}^{k} r_i{}^2 = min \sum_{i=1}^{k} (z_i - \bar{z}_i)^2 \quad \text{[Eq. 4.23]}$$

where r is the distance between points and the plane considered only in the z-direction (Nurunnabi *et al.*, 2012).

Using the eigenvectors calculated by PCA, the eigenvector v_3 with the smallest associated eigenvalue is orthogonal to the plane, and therefore defines the normal (Hoppe *et al.*, 1992). It so follows that the plane minimises the sum of squared distances to the neighbours of query point, p:

$$(p_i - \bar{p}) \cdot v_3 = 0 \quad \text{[Eq. 4.24]}$$

and passes through the centroid, $\bar{p}$:

$$\bar{p} = \frac{\sum_{i=1}^{k} p_i}{k} \quad \text{[Eq. 4.25]}$$

where k is the number of neighbours in the neighbourhood, and p_i represents the Cartesian coordinates of each point within the neighbourhood (Pauly *et al.*, 2002). The identification of a local surface normal using the third eigenvector is the equivalent to forming a total least squares fitting plane. However, in a total least squares fitting the entities in the covariance matrix are not divided by k, and the smallest eigenvalue is equal to the sum of the residuals, squared (Pauly *et al.*, 2002; Belton and Lichti, 2006).

4.9.3 Application of normal estimation

The above review of normal estimation highlights the effectiveness of using PCA for normal estimation and suggests that the use of raw point cloud data, rather than a triangulated surface, produces the most accurate results. In particular, the neighbourhood should be allowed to vary in size to accommodate non-uniform point distributions and variations in point density, producing a planar surface from which to estimate the normal. These techniques are applied in this study, producing normal vectors such as those displayed in Figure 4.20.

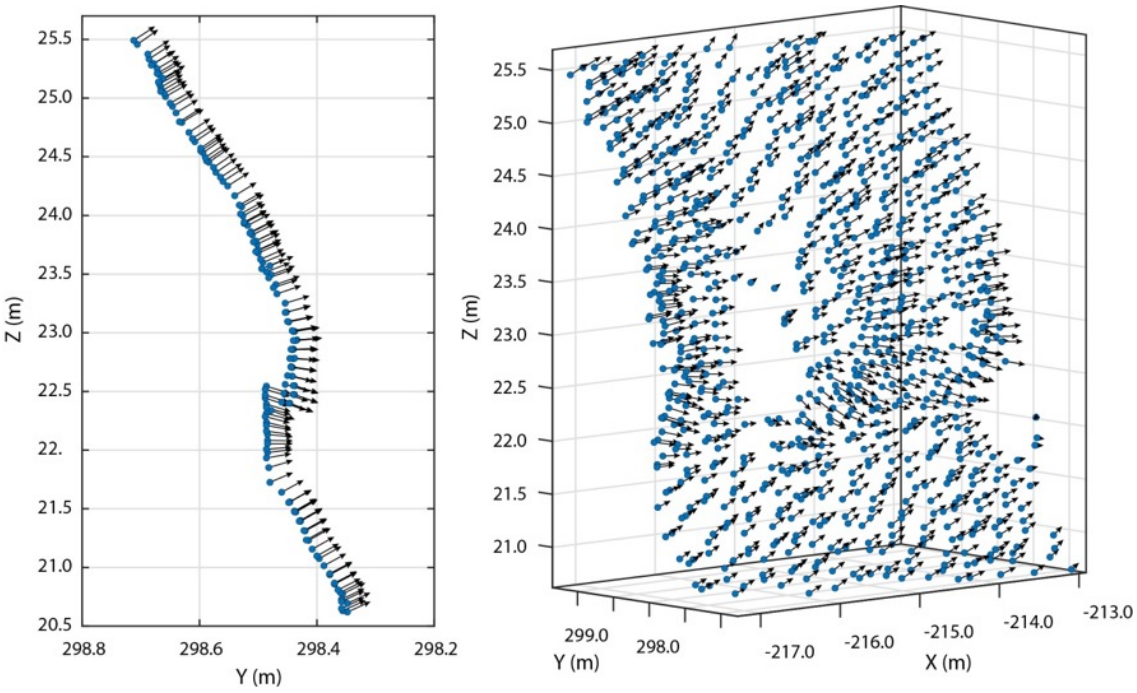

Figure 4.20: *An example of the normal vectors estimated for at an interbedded sandstone protrusion 20 m up the cliff face. Normal estimation is robust to variations in the density and distribution of points within this area.*

By varying the size of the neighbourhood radius for each point between 0.1 m and 2.5 m, the radius that produced the most planar surface was identified and mapped. This is shown in Figure 4.21a, with Figure 4.21b illustrating the planarity across the rock face. This figure shows clear similarities with the distribution of point density shown in Figure 4.3b, such that the search radius is increased in regions of low point density. The mean search radius used here was *ca.* 1 m. The computational cost of identifying the optimum neighbourhood radius made it unfeasible to apply this procedure to all change detections. As a compromise, the neighbourhood radius of each point was determined by the value of its closest point in the reference cloud in Figure 4.21a. This is only applicable in scenarios where the scanner position and point spacing have not changed, and so an alternative method is used here (Figure 4.22).

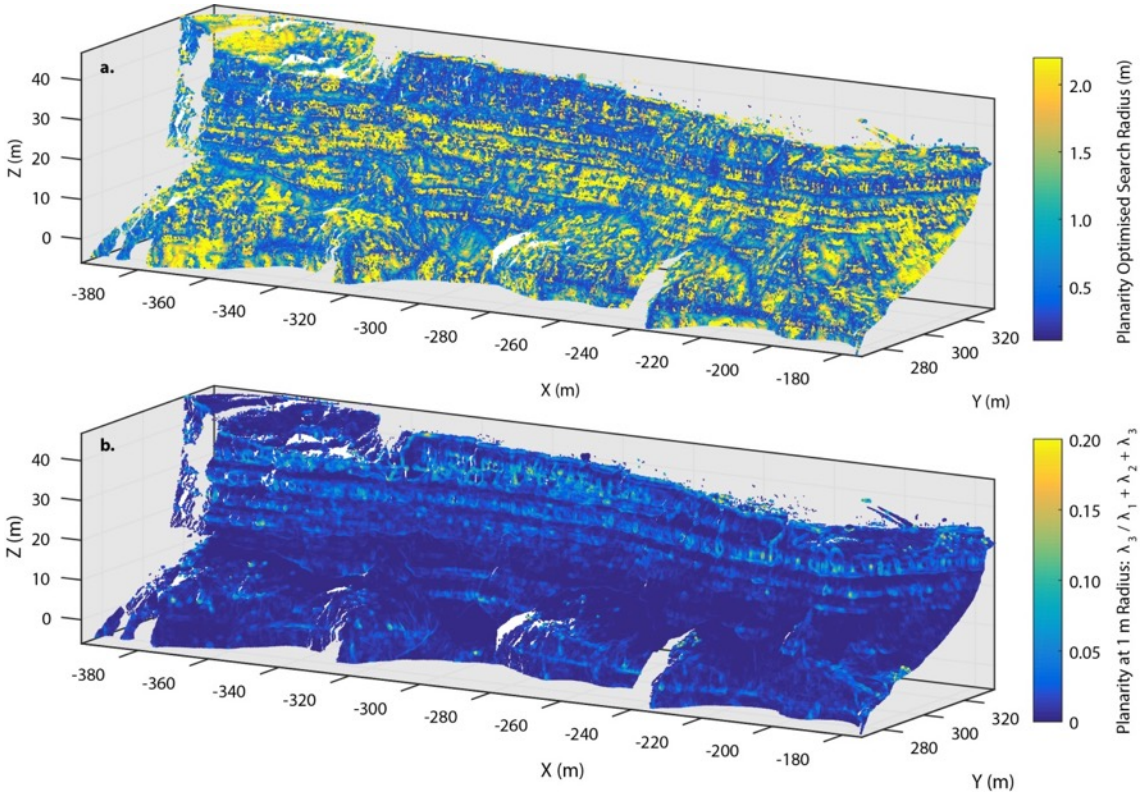

Figure 4.21: *(a) The radius for each point on the cliff at which the point clouds is most planar, with a mean value of 1.1 m, used to estimate the normal vector prior to change detection. This point cloud was used as a reference model, such that the normal radius of points in subsequent scans was assigned based on the radius of closest point in this scan, (b) Surface planarity at a radius of 1 m, where higher values indicate a more 3D neighbourhood. These occur at inflections in slope profile and in areas of high local relief, such as the sandstone beds near the cliff-top.*

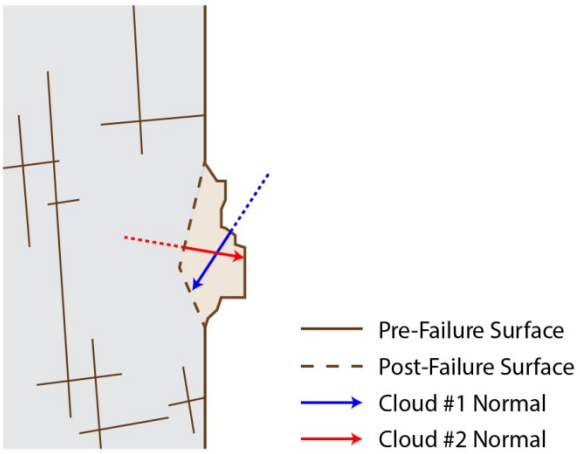

Figure 4.22: *The normal direction estimated using a planar, post-failure surface (cloud #2) more accurately represents the direction of change than the post-failure surface vector (cloud #1), due to the complexity of the pre-failure surface. The difference in vector lengths also illustrates the sensitivity of the 3D change measurements to the normal estimation. Dashed lines indicate that normal directions are subject to sign ambiguity. The cylinders used in the change detection (next section) are represented by the solid arrow.*

The normal for each point estimated here uses the second point cloud, such that change is accurately measured along the normal of a planar, post-failure surface, rather than a more complex yet-to-fail surface (Figure 4.22). The sign ambiguity of each vector is also corrected as outlined in *Section 4.5*. It is important to note that the boundaries of any neighbourhood search calculations should not be restricted to a single cube in the octree structure. For operations such as normal vector estimation, points from each individual cube as well as the surrounding 26 cubes are drawn upon to avoid errors along the cube boundaries. The subdivision level at which normal estimation and change detection is performed influences only the computation time, and not the result (Girardeau-Montaut *et al.*, 2005).

4.10 Distance calculation

The distance calculation used here is based upon the M3C2 approach, developed by Lague *et al.* (2013) and made freely available within CloudCompare. Some variations have been incorporated in order to improve the overall accuracy of the change detections and to streamline the workflow for large time series datasets. In Figure 4.23, the change detection process is summarised for a 1 m wide transect of points taken through East Cliff following a rockfall event. Once the normal vector is estimated, a bounding cylinder with a user-defined radius is created along the normal running through the query point (see *Section 4.10.1*). In order to enforce the boundaries of this cylinder, the orthogonal distance between every point within the 27 octree cubes and the normal vector was estimated as follows:

$$\hat{d} = [X_n, Y_n, Z_n] - [X_p, Y_p, Z_p] \quad \text{[Eq. 4.26]}$$

where $\hat{d}$ is a vector that connects each neighbour point, p, to a point on the normal vector $\hat{n}$, such as the query point, q. The projection of each point onto the normal, P, is therefore:

$$P = q \times \hat{d}, \text{ or}$$
$$P = q + \left(\frac{\hat{d} \cdot \hat{n}}{\hat{n} \cdot \hat{n}}\right) \times \hat{n} \quad \text{[Eq. 4.27]}$$

and the orthogonal distance is:

$$d_{orth} = \sqrt{(X_n - X_P)^2 + (Y_n - Y_P)^2 + (Z_n - Z_n)^2} \quad \text{[Eq. 4.28]}$$

Given that the position of each neighbouring point and its orthogonal distance to the normal

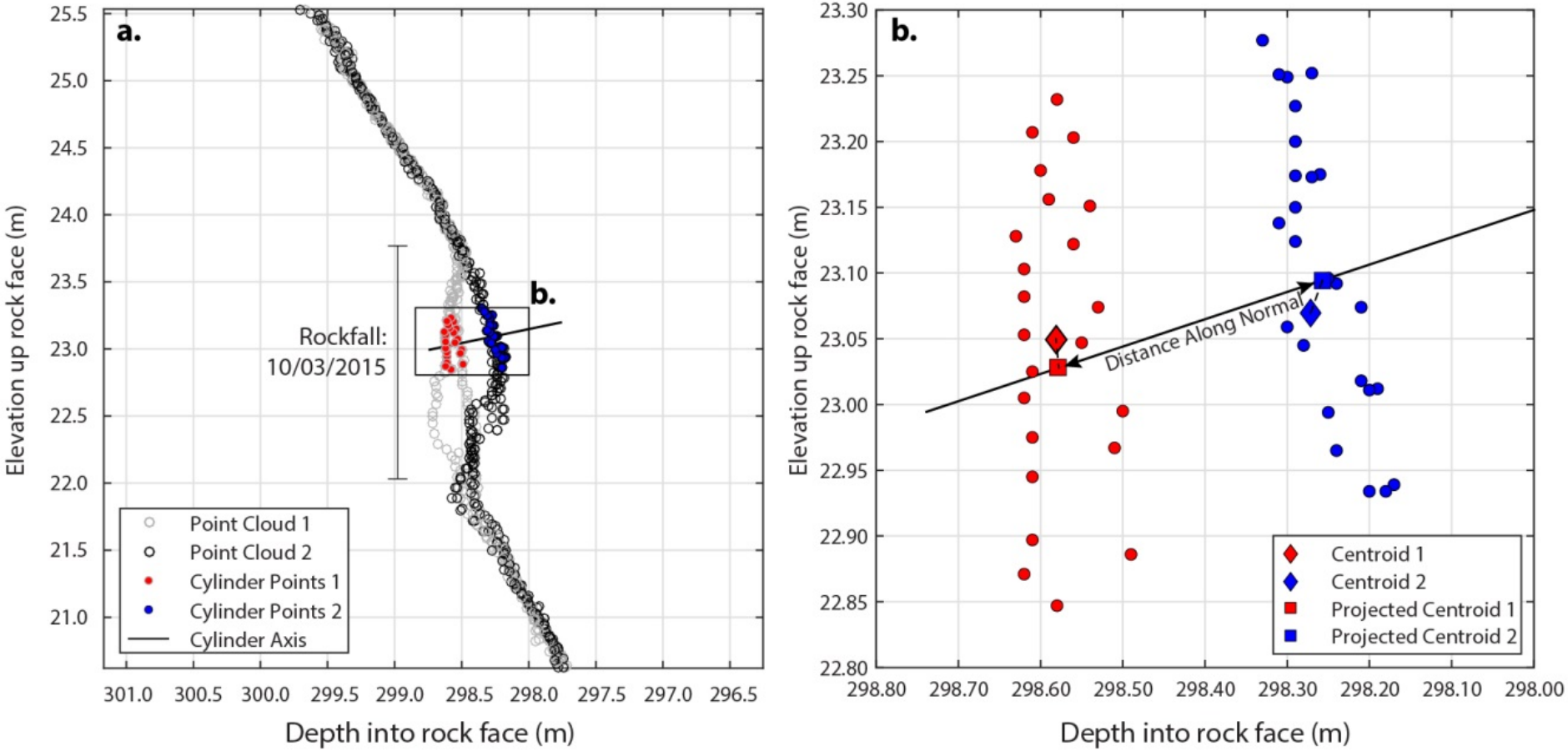

***Figure 4.23**: (a) A 2 m wide transect taken mid-way up East Cliff. The black points are taken from Cloud 1 and the grey from Cloud 2, with a 1.75 m high rockfall clearly shown. Points within the cylinder radius, which intersects the two clouds, are shown as red and blue. The cylinder axis, which travels through the query point, is also shown, (b) Area of intersect selected from (a) the centroids of each point cloud are determined and their orthogonal projection onto the normal vector (cylinder axis) is estimated (dashed lines). The distance measured in this study is between these projections, along the normal.*

vector are known, the cylinder boundaries can be enforced using the user-defined cylinder radius r, retaining only points where $d_{orth} \leq r$. Once the points n in the cylinder are isolated for both point clouds, the mean point CP is estimated as follows:

$$CP = \left(\frac{\sum_{i=1}^{n} x}{n}, \frac{\sum_{i=1}^{n} y}{n}, \frac{\sum_{i=1}^{n} z}{n}, \right) \quad \text{[Eq. 4.29]}$$

and projected onto the normal vector using Equation 4.26 and 4.27. The mean points of each sub-cloud are subtracted to give a distance vector, $\hat{v}$:

$$\hat{v} = CP_2 - CP_1 \quad \text{[Eq. 4.30]}$$

If the vector of change is along the direction of the normal vector (forward movement), the dot product of both vectors is > 0. If it is against the normal direction (backward movement), the dot product is < 0 and the vector is inverted.

Although the M3C2 algorithm has been rigorously tested in a gravel-bed river setting (Lague *et al.*, 2013), other works that have applied this technique to rockfall analysis have tended to overlook the influence of both the cylinder radius and length on the change detected (for example, Earlie, 2015). The discussion below illustrates the importance of these parameters for governing the change measured using distance along the normal methods of change detection.

4.10.1 Cylinder radius

The cylinder radius determines the degree of spatial averaging over change measurements and, as such, should be informed by the movements being monitored. In theory, the smaller the radius, the finer the spatial detail that can be established. However, this comes with a compromise in that the increase in accuracy by accounting for neighbouring points is reduced, the likelihood of intersecting points in the second point cloud is reduced, and the statistical significance of calculations is reduced by only drawing on a small number of points. Lague *et al.* (2013) suggest a minimum of 20 points should be included within the cylinder for each point cloud.

In Figure 4.24, the distribution of change along the normal is estimated for two scans in which no apparent change has occurred. In theory, the distribution should be as close to zero as possible, although the background noise between scans makes this impossible (*Section 4.2*). As the cylinder radius increases, the deviation of the distribution reduces. The noise in the

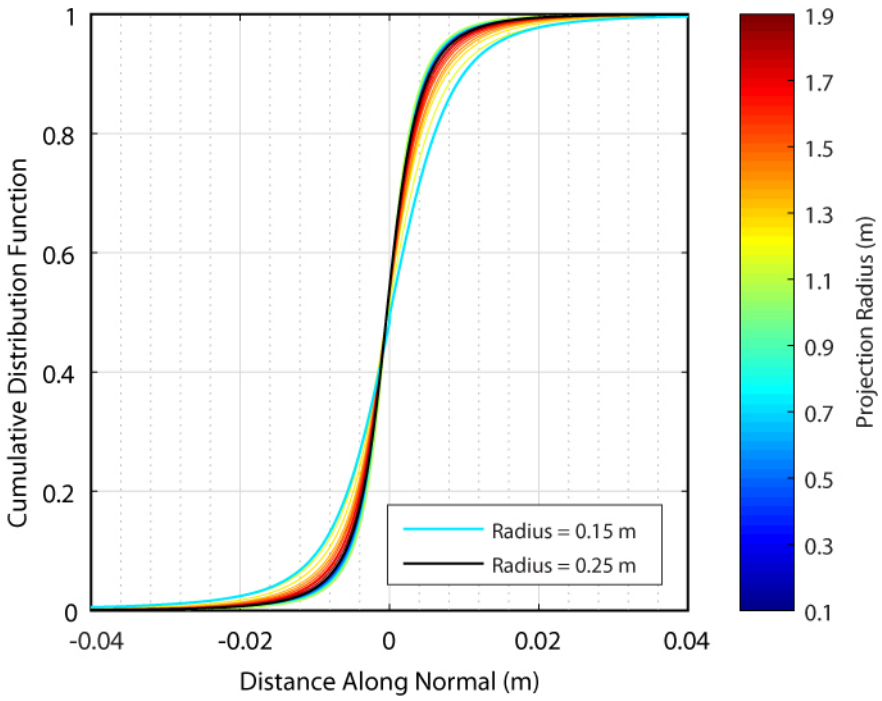

Figure 4.24: *Cumulative distribution function of change between two point clouds, between which no observable change occurred. As such, the distribution of points should be as close to 0 m change as possible. Each line represents a different cylinder radius that is used. 0.15 m exhibits the highest deviation away from change values close to zero.*

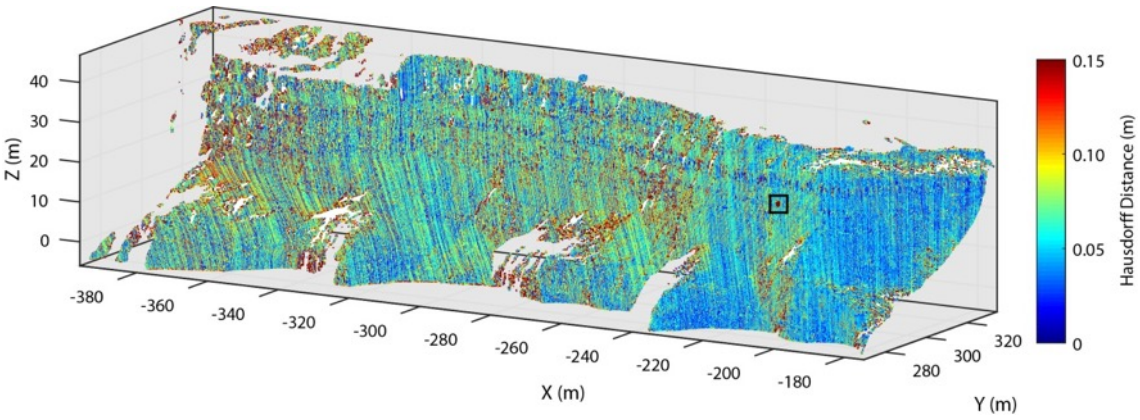

Figure 4.25: *Hausdorff distance estimation between two point clouds where a rockfall occurred. This metric yields change between scan lines, highlighted by the striping effect, and change that is sensitive to point density, highlighted by the distance decay from left (distal) to right (proximal). However, this provides an accurate measure of the scar shape that is useful for refining the parameters used in the change detection in this research.*

measured change is greatest at a radius of 0.15 m, as this value approaches the point spacing in some regions of the cliff. At 0.25 m, the error is similar to the largest projection radii; indicating an optimum balance where enough points are included to yield accurate change measurements but not enough to introduce false change incorporated from wider areas of the cliff.

While noise reduction is critical for determining the scale of movement that can be detected, increasing the cylinder radius has the potential to inhibit accurate delineation of a rockfall scar as spatial resolution is lost. In order to estimate the most appropriate cylinder size, the shape of a rockfall obtained using this technique was compared with that of the same rockfall obtained using a Hausdorff comparison. In Figure 4.25, a Hausdorff distance was calculated for two scans taken on 10 March 2015. The small black box marks a rockfall event that occurred and is presented in Figure 4.25 above. The Hausdorff distance measure itself is influenced considerably by the scan line spacing and the local point density but, for this purpose, it provides a good indication of rockfall geometry.

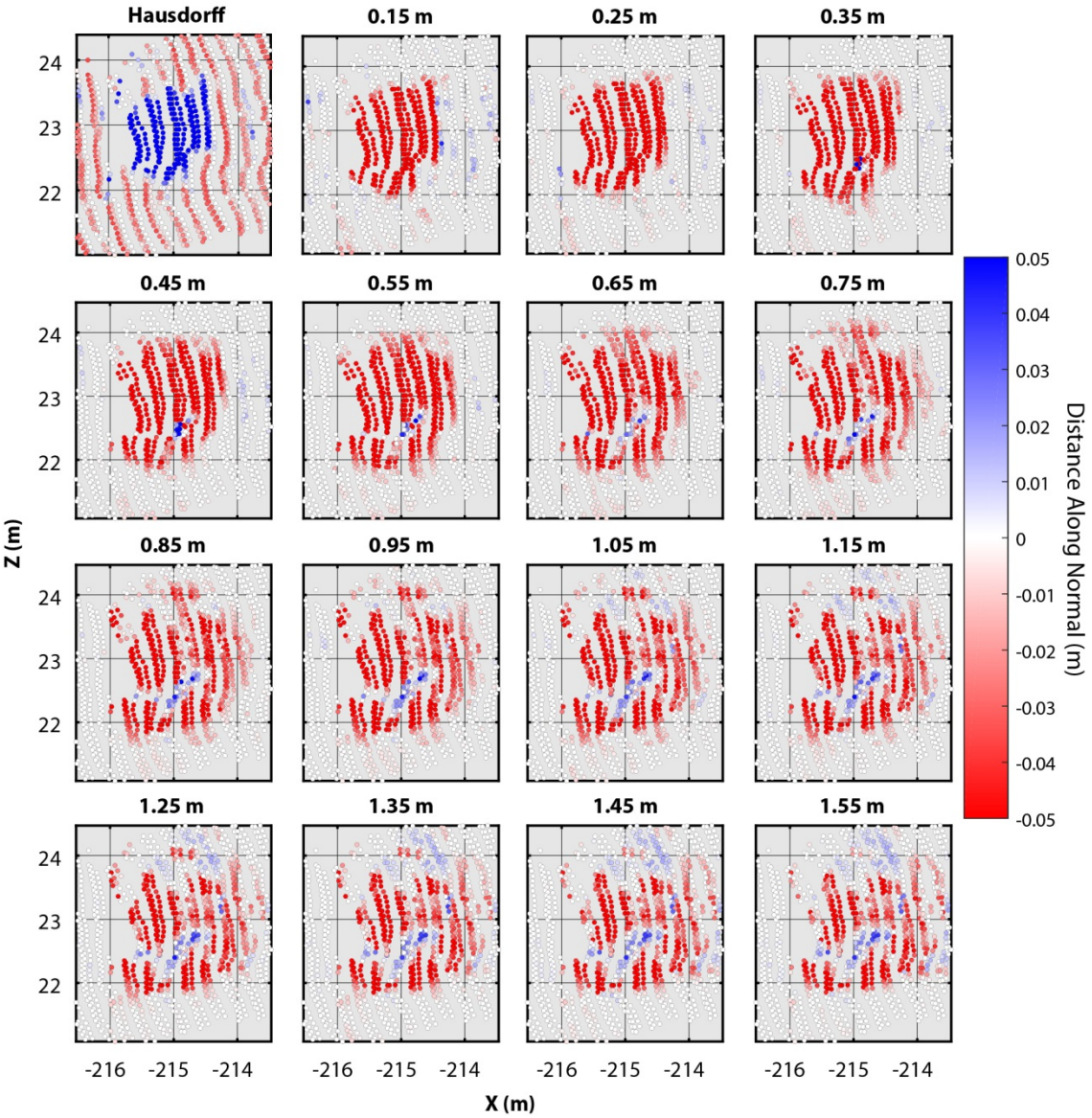

Figure 4.26: *Distance along the normal approximated using a variety of cylinder radii from 0.15 – 1.55 m. These are compared to an unsigned Hausdorff distance in the top-left. As the cylinder radius increases, the rockfall scar expands by averaging change across a wider area. This also has the effect of introducing forward movement (blue) into the rockfall scar.*

In Figure 4.26, the Hausdorff distance is compared with the distance along the normal, calculated using a range of search radiuses. The colours for the Hausdorff distance differ compared to subsequent tiles as the Hausdorff distance is unsigned. As the projection radius increases, the difference in shape relative to the Hausdorff approximation also increases. Above a radius of 0.25 m, negative change is incorporated into the rockfall as the neighbourhood begins to incorporate points from outside of the failure scar. While a radius of 0.15 m best approximates the size and shape of the rockfall, this value is too close to the scan line spacing at the distal portion of the cliff face. A search radius of 0.25 m was therefore selected.

4.10.2 Cylinder length

The M3C2 algorithm imposes a maximum cylinder length in order to decrease processing times (Lague *et al.*, 2013). It is shown here that the cylinder length is critically important for determining the accuracy of change estimation at edges in the point cloud. Edges are far more prominent in the point clouds of East Cliff than in most published surveys, due to the absence of multiple scan positions, high incidence angles and protruding section of rock on the cliff face. However, given their complex morphology, edges are a ubiquitous feature of rock slopes as they remain difficult to scan entirely, even from multiple viewing angles. A method to reduce the effect of edge uncertainty in the change detection processing is therefore required.

As an example, Figure 4.27 shows a typical change detection using the planarity optimised normal radius and 0.25 m cylinder radius outlined above. Change occurs predominantly along the edges of the point cloud. Although uncertain range estimates were removed during filtering, the absence of scans from alternative viewing angles requires a change detection approach that overcomes the difference in point distributions between scans.

Figure 4.28 is a subset of the point cloud shown as the black box in Figure 4.27. The point cloud is coloured according to the normal vector ($\hat{n}\langle u, v, w\rangle = \langle Red, Blue, Greeen\rangle$) of each

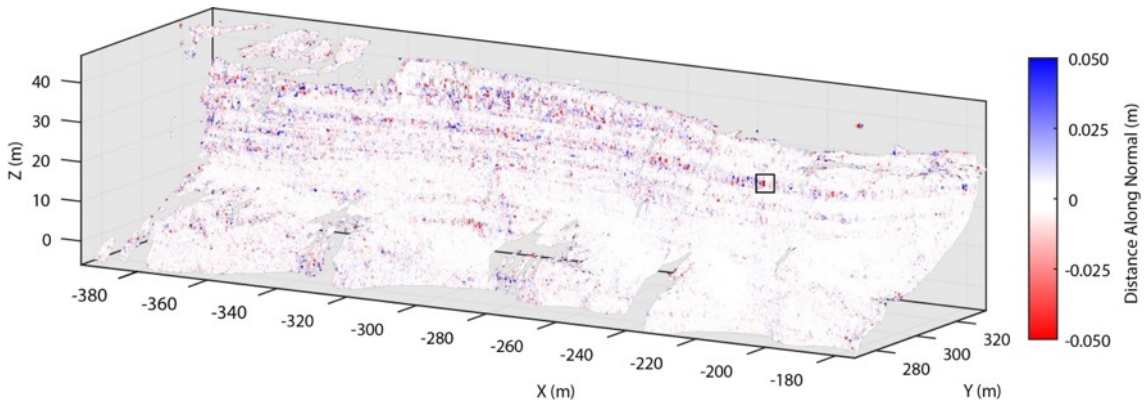

Figure 4.27: *Distance along the normal between two scans. Edges present a significant uncertainty even after the filtering process. The black box indicates the example area used in subsequent figures.*

point, which highlights three planar surfaces in red. The right-hand plot is viewed orthogonal to the surfaces, highlighting a scattered point distribution between scan lines that is inconsistent between scans. As a result, the range estimates for these points appear smeared.

In Figure 4.29, the influence of the cylinder length is illustrated with respect to these surfaces. The plots take a zoomed view of Figure 4.28 and illustrate variation in measured change for a single point belonging to the largest surface in this region. When the cylinder extends 0.25 m in both directions, only points from this surface are included in the cylinder; as such, the centroid positions of each point cloud are both fitted onto that surface. The measured distance for this point, the distance between the two centroids is +0.0011 m. With a cylinder extending ± 0.50 m, points that lie between surfaces are included in the change detection. Since the distribution of points between surfaces is rarely consistent between scans, the position of the centroids of each neighbourhood differs considerably from the centroids estimated using a shorter cylinder and the resulting change estimate is -0.1460 m. At a length of ±10 m, the cylinder intersects multiple surfaces and the centroid positions are between these surfaces. The inclusion of a greater number of points over a wider area increases the similarity of the mean position in both point clouds, but the resulting vector of change is +0.0938 m; a difference of 0.24 m from the 0.50 m cylinder length and significantly higher than the true change estimate.

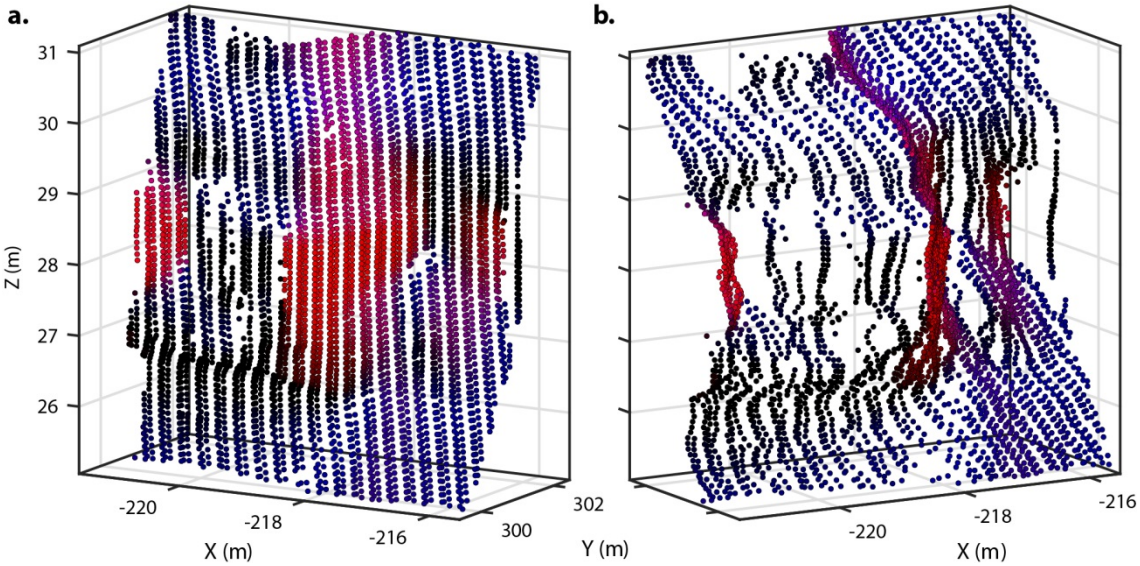

Figure 4.28: *(a) Subset of bedded sandstone, coloured by the surface normal. Red points define planes orthogonal to the scanning direction. (b) When rotated away from the scanning direction, points that are incoherent within and between scans, and averaged between surfaces, become evident.*

To address this problem, a variable length cylinder was introduced for each point, referred to below as DAN VCL, beginning with a cylinder that extends ± 0.10 m. If fewer than four points are found, the minimum number to accurately estimate a centroid, the cylinder extends. This process is recursive and accepts a user-defined array of possible cylinder lengths. By using this method, the standard deviation and error in change measurements drops significantly across the point cloud, as illustrated in the following section.

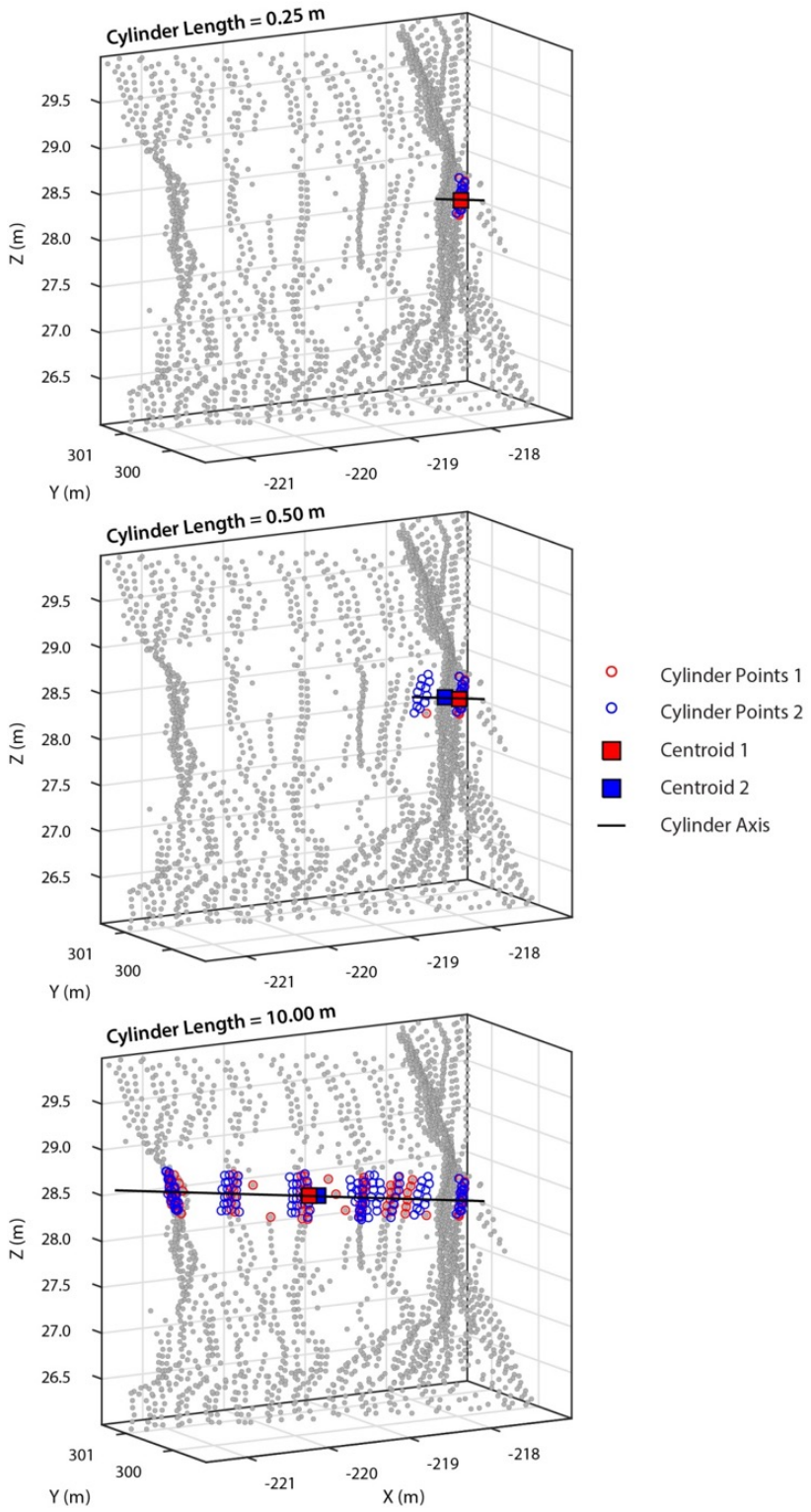

Figure 4.29: *Inputs used for distance estimation with varying cylinder lengths. No appreciable change occurred between these two scans. Here, the same subset of points as in Figure 4.28 is used. As the cylinder length increases (from 0.25 m to 0.50 m to 10 m), the number of surfaces that the cylinder intersects increases (direction equal to the normal vector). All points within a 0.25 m radius would be included as cylinder points (circles), and the distance between their mean positions (squares) calculated. From top to bottom, this distance is 0.0011 m to -0.1460 m to 0.0938 m. Longer cylinders intersect multiple surfaces and therefore measure the distance between projected centroids that do not accurately represent the surface to which the query point belongs.*

4.10.3 Distance along the normal

To complete a single change detection between two point clouds of *ca.* 1×10^6 points, a machine with 32 GB RAM and a 2.40 GHz processor took approximately ten minutes running in MATLAB. The code was written to allow multiple change detections to be executed in parallel. On a machine with 12 CPU's, 12 change detections could be undertaken within this time.

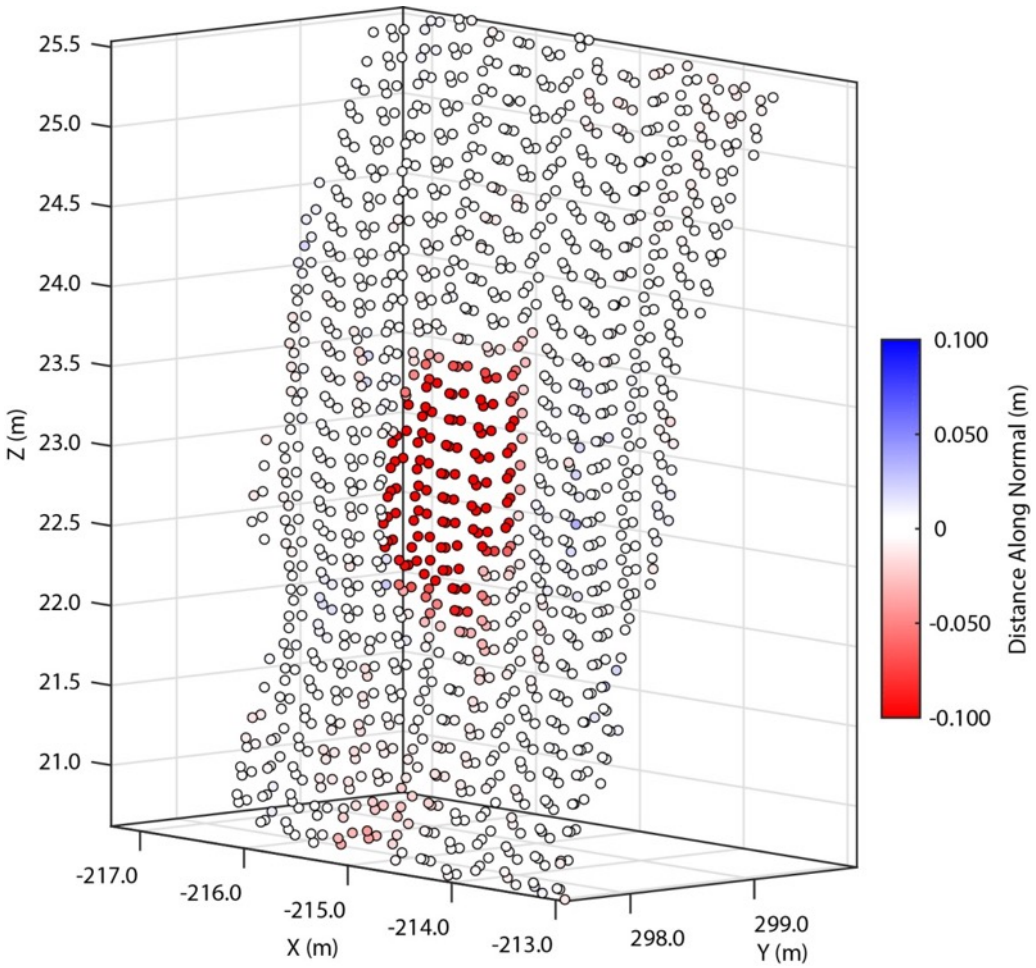

Figure 4.30: *An example of a rockfall calculated using the distance along the normal.*

The resulting rockfall appear in the point cloud as depicted by the subset shown in Figure 4.30. For each scan, the LoD can be determined as 1.96 times the standard deviation of the change estimates. This represents the 95th percentile of data (Abellán *et al.*, 2009) assuming that no physical change occurred. With this in mind, the standard deviation was acquired for a series of stable scan pairs in which no detectable rockfall were observed. By combining the distance along the normal for each of these scan pairs, the standard deviation used to calculate the LoD is 0.015 m and the LoD is 0.03 m. As shown in Figure 4.31, this is considerably lower than the same pairs of scans that were rasterised at 0.25 m, such that each pixel contained > 1

point, and subtracted to create DoDs. They are also significantly lower than the M3C2 algorithm. This ultimately yields a six-fold improvement in the final LoD value, from 0.18 m to 0.03 m, and, by extension, a six-fold decrease in the depth of rockfall that can be identified.

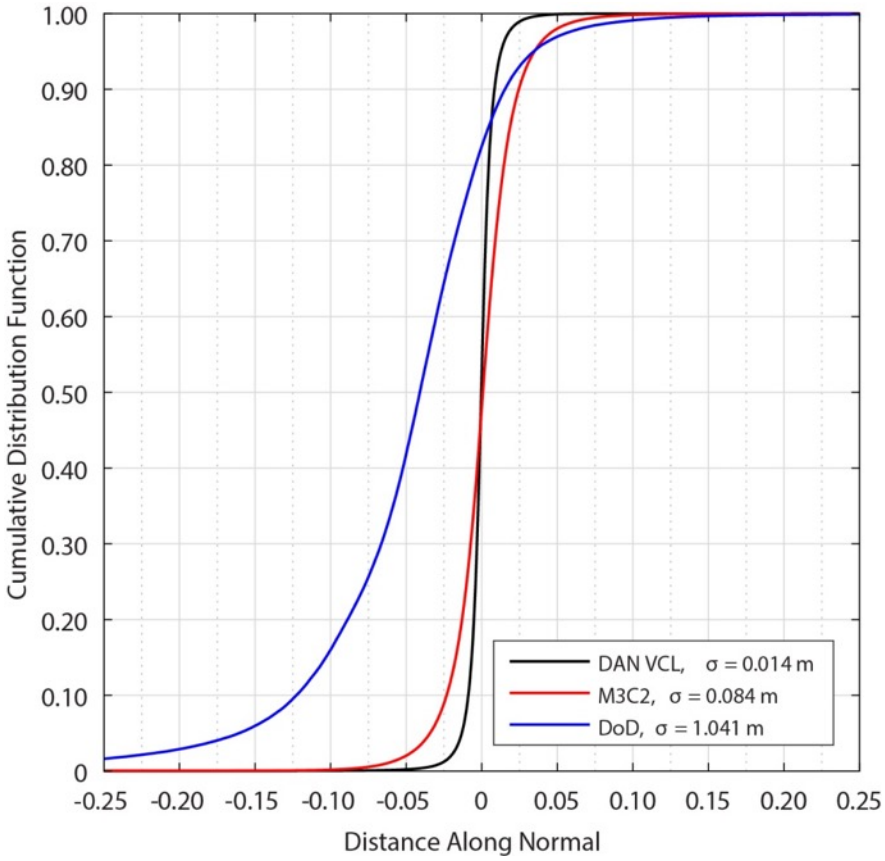

Figure 4.31: *Cumulative distribution function for the change detections of multiple pairs of stable scans, such that the theoretical distribution of distance along normal values should be zero. The methods used are DEMs of Difference (DOD; blue line), M3C2 (red line) and Distance Along the Normal, Variable Cylinder Length (DAN VCL; black line).*

4.11 Failure extraction

In recent years, the development of visualisation and 3D change detection techniques has not been matched by their translation into usable products. Analysis of 3D change is often limited to the observation of movement patterns across the point cloud or by rasterising the dataset, with the exception of more recent research that clusters change estimates into individual 3D rockfall (Carrea *et al.*, 2012; Benjamin *et al.*, 2016). At present, the algorithms presented in this body of research are computationally intensive and hence unsuited to repeated application over a high number of multiple scans. In this study, therefore, 3D change estimates were rasterised and the rockfall then delineated using the LoD.

Rasterising point clouds of change differs to DEM generation in that multiple points are not required for each pixel. In DEM creation, cell sizes should typically include at least two

points (Hengl, 2006) to minimise the impact of local minima or maxima on the resulting raster. Here, points were gridded at 0.15 m intervals. This approaches the maximum point spacing and maintains the spatial resolution of the dataset. Although some cells are left empty, these can be identified and masked. By stacking the resulting change images, pixels that exhibit forward and backwards movement between scans over sustained intervals can also be removed, typically along the sharp edges created by the widely jointed sandstone at the cliff top.

In order to delineate rockfall, a binary image of erosional values was first created and a threshold applied based on the measurement precision. A threshold of 1.96σ of change along the normal was selected, thereby defining a rockfall as any cluster of cells > 0.03 m using MATLAB's `bwboundaries`. In many instances, the boundaries created using the LoD binary over-constrained the failure extent when compared with an unthresholded change image. In Figure 4.32, the largest rockfall volume identified using this technique is illustrated in red. The true area of failure on the cliff face (blue) was identified by vectorising changes greater than the quoted instrument precision (0.005 m) illustrating that in some areas of the cliff the localised accuracy of the change detection was < 0.03 m.

To account for this, binaries were created using the 0.03 m LoD alongside binaries created using the 0.005 m instrument precision (IP). For each rockfall detected in the LoD mask, a ratio R was created to describe its pixel count N_{LoD} (defined by the polygon in Figure 4.32a), relative to the pixel count of the extended area in the IP binary (the difference between the polygons in Figure 4.32a and Figure 4.32b):

$$R = \frac{N_{LoD}}{N_{IP} - N_{LoD}} \qquad \text{[Eq. 4.31]}$$

where N_{IP} is the pixel count for the same rockfall in the IP binary and $N_{IP} > N_{LoD}$. If $R > 0.5$, the LoD rockfall is more than twice the size of its extension in the IP binary. In this instance, the pixels of the instrument precision binary are incorporated. This enabled the automatic delineation of the rockfall in Figure 4.32. Conversely, when $R < 0.5$, the adjacent IP rockfall is more than twice the size of the LoD failure. When $N_{LoD} = 1$ and $R < 0.5$, LoD failures were extensions along the periphery of holes in the change raster and were removed.

Wheaton *et al.* (2010) proposed that uncertainty in the change value of a cell can be partially determined by the spatial coherence of erosion and deposition surrounding the cell. A single cell of deposition surrounded by cells of erosion, for example, is deemed unlikely to represent true-erosion of the surface. On a rockface, however, the presence of erosion cells surrounded by forward movement could represent a number of processes operating at fine spatial scales; for example, the loss of small amounts of material from the surface of a larger forward moving wedge. This approach was not used in order to preserve this detail.

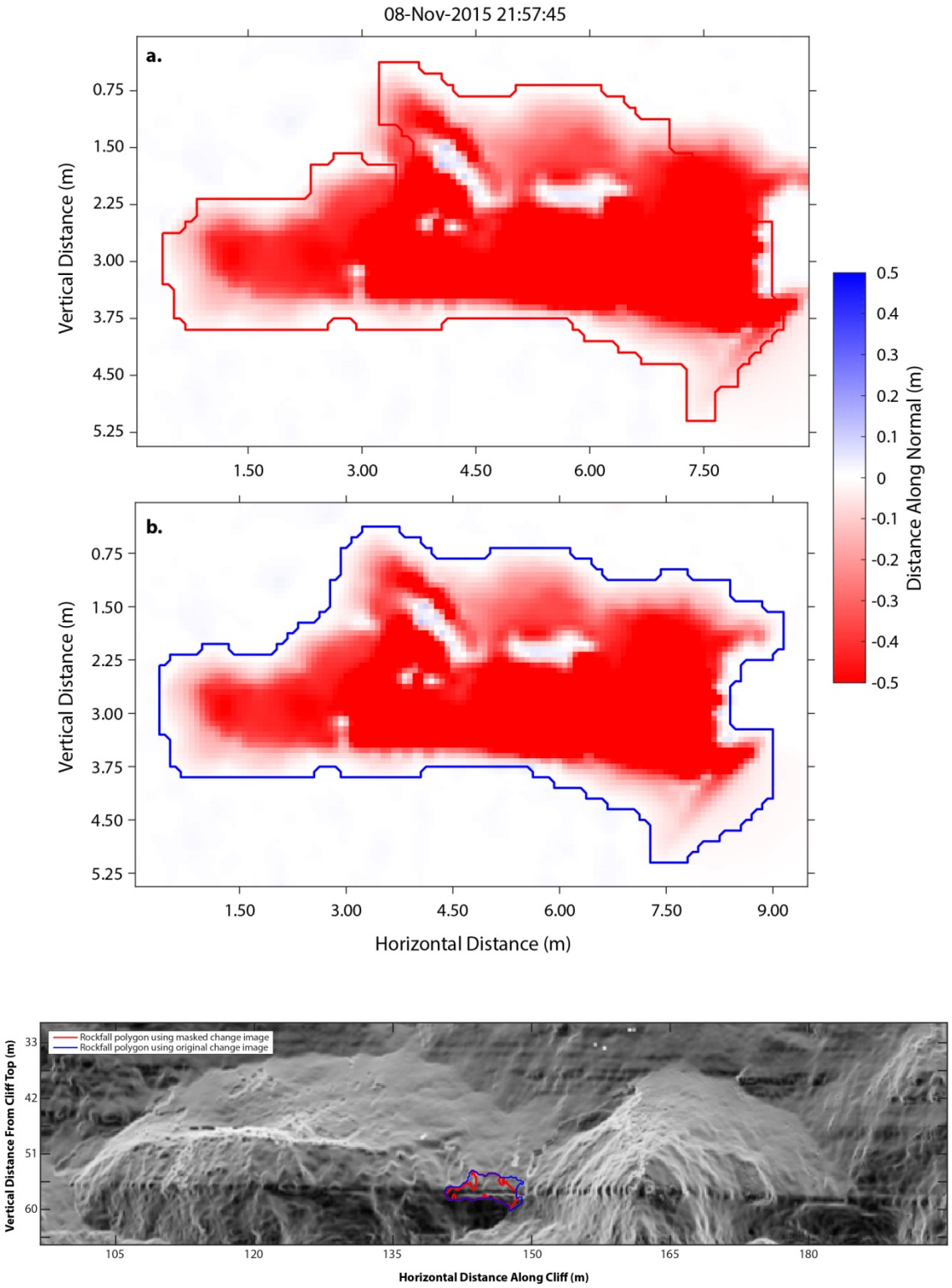

Figure 4.32: *A section of the cliff buttress, with the largest failure in the study superimposed. The red polygon is shown in detail in (a) and the blue polygon in (b). (a) A still taken from the video of pre- and post-failure movement that is automatically created for each failure. Here, the polygon (red) is created using the LoD, and significantly underestimates the failure size relative to the unthresholded change map beneath it, (b) Rockfall polygon (blue) created using by extending the polygon to include change above the instrument precision, using the criterion in Equation 4.31.*

4.11.1 Systematic error in segmentation and rockfall volume estimation

Using the resulting change images, the rockfall volume V_{RF} is calculated as:

$$V_{RF} = \sum_{i=1}^{N} d_i \times A_c \qquad \text{[Eq. 4.32]}$$

where N is the number of cells within the estimated failure scar, d_i is the depth of cell i and A_C is the area of each cell. Error estimation is rarely undertaken with regard to this equation, with most studies ignoring any cells with a depth change below the instrument precision and accepting that failures with an aerial extent less than A_C will not be detected (e.g. Rosser *et al.*, 2005; Abellán *et al.,* 2006). Rockfall with areas less than A_c are acknowledged when examining the presence of rollovers in magnitude-frequency distributions (e.g. Dussauge *et al.*, 2003), however, uncertainty in volume estimates derived using Equation 4.32 are seldom quantified for rockfall with areas greater than A_C. Assessing the volume error associated with rockfall identification requires basic assumptions about how the uncertainty in its aerial extent propagates into volumetric uncertainty, in particular for failures of varying shapes and sizes. This is of critical importance considering the low spatial resolution of raster cells relative to the accuracy of the raw measurements recorded by TLS.

In this study, for example, the spatial resolution of change images is determined by the point spacing of the point cloud. Since the change images are rasterised from point clouds of change, the point spacing and pixel size are more closely related than for conventional DoDs. In these comparisons, the construction of representative cell depths in each DEM requires a cell size large enough to draw on multiple points, which is not the case in this study. Cell sizes of 0.15 m across a 200 m wide cliff thus yield an accuracy of approximately 1 in 1 000. Conversely, the scanner's range estimation, combined with the pre-processing and change detection procedures outlined above, provides change depths accurate to a minimum of 0.03 m over 500 m and in some cases as small as 0.005 m. This translates to an accuracy of 1 in 10 000 or 1 in 100 000 at best, an order-of-magnitude higher than the spatial accuracy of the DoD.

Assuming any cell that lies on the boundary of the rockfall contains any fraction of the true rockfall scar, the maximum area of the rockfall A_{RF_max} approaches:

$$A_{RF\_max} = A_C \times N \qquad \text{[Eq. 4.33]}$$

In reality, however, this equation represents the largest possible area because the likelihood that border cells are entirely covered by the true rockfall scar is small. Conversely, the theoretical

minimum area A_{RF_min} approaches:

$$A_{RF\_min} = A_C(N - N_b) \quad \text{[Eq. 4.34]}$$

where N_b is the number of boundary cells. The maximum error associated with the area estimate of the rockfall scar is then:

$$A_{maxerror} = A_{RF\_max} - A_{RF\_min} \quad \text{[Eq. 4.35]}$$

This value can be applied as a threshold to the rockfall inventory, such that failure areas below $A_{maxerror}$ are removed. Using $A_{maxerror}$ as a threshold reduces the number of failures in the inventory from 1 885 482 to 135 186. This threshold, however, represents the maximum possible error associated with the rockfall area.

Jahne (2000) defined the variance ${\sigma_x}^2$ of the position of a single point in an image, introduced by the pixel length d_x, as:

$${\sigma_x}^2 = \frac{1}{\Delta x}\int_{x_n-\Delta x/2}^{x_n+\Delta x/2}(x - x_n)^2 dx = \frac{(\Delta x)^2}{12} \quad \text{[Eq. 4.36]}$$

assuming a constant probability density function within the length of a pixel, i.e. all positions within the cell are equally probable. The standard deviation σ_x is approximately $\frac{1}{\sqrt{12}} \approx 0.3$ times the cell size. Therefore, to accommodate for uncertainty in the position of the rockfall scar within each boundary cell as a function of cell size, 2σ can be used as a threshold as follows:

$$\begin{aligned} A_{RF\_max} &= A_C\left(N + \frac{1}{\sqrt{12}}N_b\right) \\ A_{RF\_min} &= A_C\left(N - \frac{1}{\sqrt{12}}N_b\right) \\ A_{error} &= A_{RF\_max} - A_{RF\_min} \end{aligned} \quad \text{[Eq. 4.37]}$$

The volumetric error is thus:

$$V_{error} = \sum_{i=1}^{N_b} d_i \times \frac{2}{\sqrt{12}}A_c \quad \text{[Eq. 4.38]}$$

The number of border cells relative to the total number of cells is critical in determining the estimated area error relative to the total area of the rockfall cluster, whereby a higher ratio of border cells to total number of cells will result in a greater error. A simple descriptor of this is

the eccentricity of the cluster (Figure 4.33), where 0 is a square and 1 is an infinite line, resembled by an elongated rectangle. By extension, the volumes of square shaped rockfall are therefore more precisely defined than elongated shapes. The relation between eccentricity and the number of boundary pixels of rockfall clusters in this rockfall inventory is illustrated below.

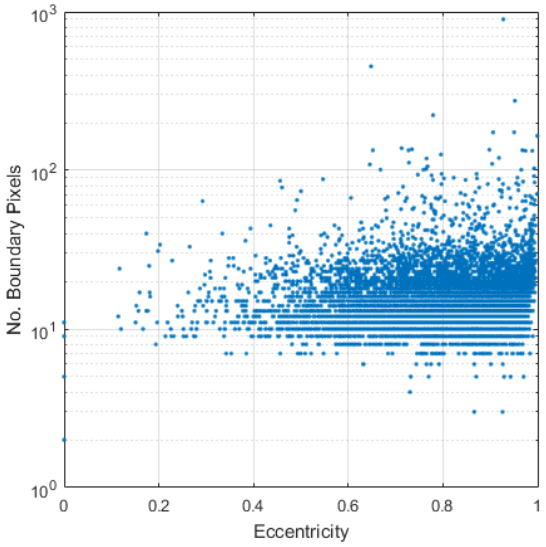

Figure 4.33: *Eccentricity of failures measured against the number of boundary pixels. A higher ratio of boundary cells relative to the total number of cells in the failure (eccentricity) results in a greater volumetric uncertainty.*

At the edges of a rockfall scar, the depth of change is lowest and bears the greatest degree of uncertainty as the laser footprint averages both the edge of the original surface and the failure surface itself. While this influence upon depth change estimates is small, it is increased by an order of magnitude when converted to volume using A_C further highlighting the influence of the shape's perimeter relative to its area. In the next chapter, the implications of the number of edges of a rockfall scar, relative to its area is described in relation to the overall volume estimates yielded in this study.

4.12 Inclusion of partial scans

As discussed in *Chapter 3*, inclement weather conditions can prevent scanning of the cliff. If the number of points fell below 500 000, which is approximately half of the number of points in an unimpeded scan of East Cliff, the scan was removed from the inventory and pairwise detection was instead undertaken between the previous scan and the subsequent scan. As a result of this process, 8 596 change detections out of a possible 8 986 were completed, equating to a loss of 380 (4%).

Figure 4.34 and Figure 4.35 show the distribution of rockfall events from the cliff during storms from 24th December – 26th December. In Figure 4.34a, rockfall are derived from 120 pairwise change detections during the three day period. In Figure 4.34b, rockfall are derived from daily change detections between midnight on each of the three days. In *Section 7.3*, the influence of the time interval between surveys is examined with respect to the ability detect and monitor precursory rockfall activity. Small, precursory events are less easily discerned when the monitoring interval is increased, due in part to their superimposition by larger, subsequent events. However, over the same period of monitoring, the shape of the rockfall scar should be identical, irrespective of the time interval of monitoring. On close examination of Figure 4.34, however, there are significant discrepancies in the spatial pattern of failures between the two epochs, in particular within the failure cluster delimited by the square box. Here, a 4.9979 m^3 rockfall that is observed with Figure 4.34b is not observed within Figure 4.34a. By analysing the pairwise change detections individually, this discrepancy was attributed to the inclusion of partially complete scans. Due to the frequency of scanning and duration of each scan, inclement weather conditions often interrupted the beginning or ending of the eight minute scan period. As such, a number of scans contained more than the 500 000 point threshold but with some areas of the point cloud left empty.

Figure 4.36 describes a scenario in which a rockfall occurs between 12.00 and 12.30 during adverse weather, which partially obscures the impending scan at 12.30. While some areas of this scan allow accurate change detection of the surface, if the rockfall occurs in an obscured area, it is missed from the inventory entirely. However, if surfaces are compared between 12.00 and the following scan at 13.00, with both captured during fair conditions, the rockfall will be observed and included in the inventory. At present, no automated means of detecting partial scans has been developed. The point distribution was therefore manually examined by creating a video of every point cloud prior to reanalysis of the dataset. While the maximum possible number of change detections was 8 986, these were reduced to 8 596 as a result of poor weather conditions and finally to 8 270 as a result of partial scan removal. The reduction in the number of scans has a direct impact on the time interval between scans and hence deformation analysis prior to failures that occur during bad weather. However, as illustrated in Figure 4.35, the rockfall that occurred within the square box are now closer to the size and shape of those collected by the scan-by-scan detection. Of particular note is the fact that this rockfall, while identified as a single event in the daily change detections, appears to comprise multiple failures that occurred at different times before the 4.9979 m^3 event, though this is beyond the scope of this chapter.

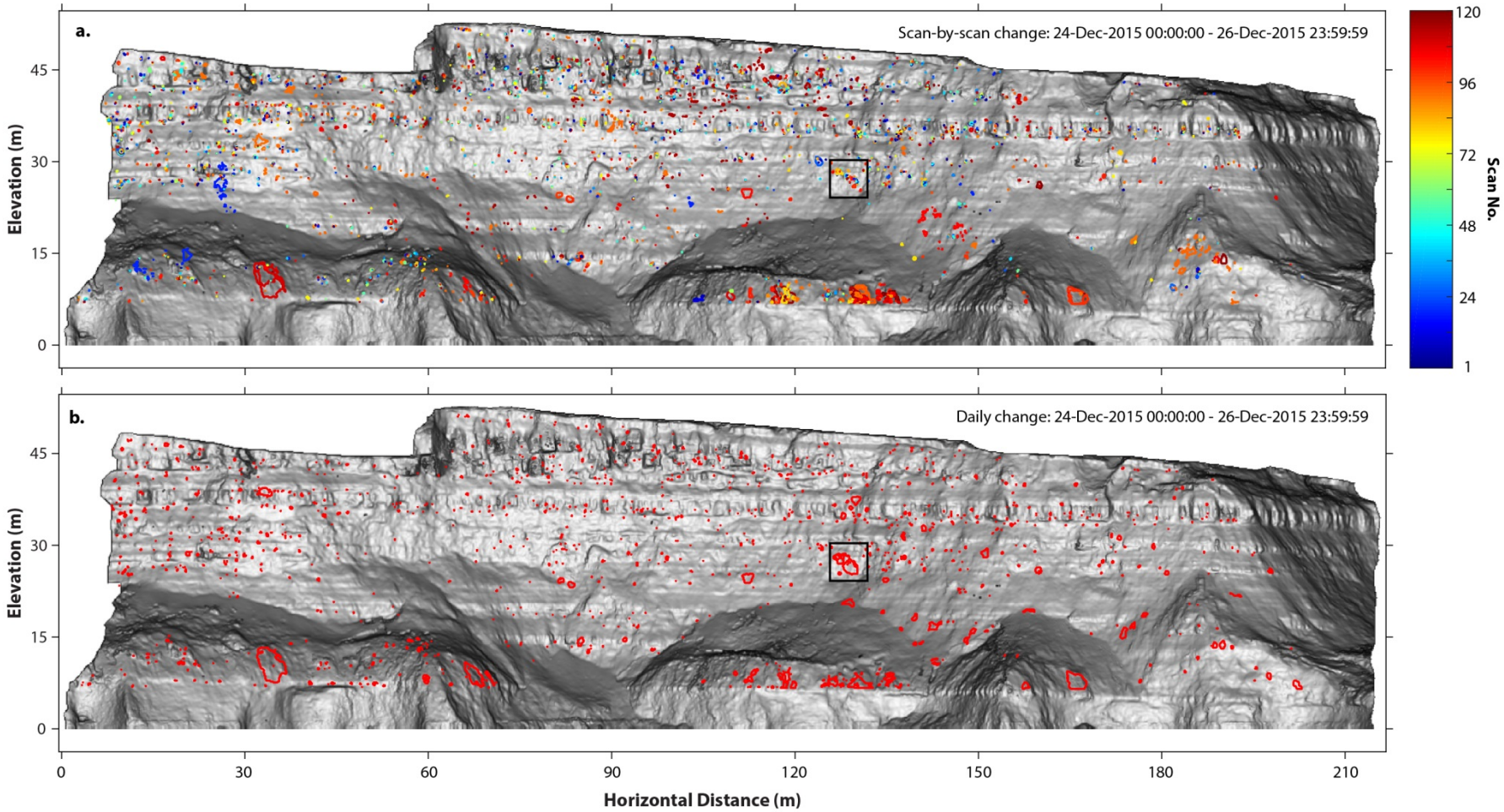

***Figure 4.34**: (a) Rockfall derived from pairwise change detection of 120 scans. This fails to detect many of the individual rockfall events that occurred within the square box, including a 4.9979 m^3 event. This is caused by the omission of this area of cliff within partial-scans due to rainfall. (b) Rockfall derived from daily change detections over the same storm period.*

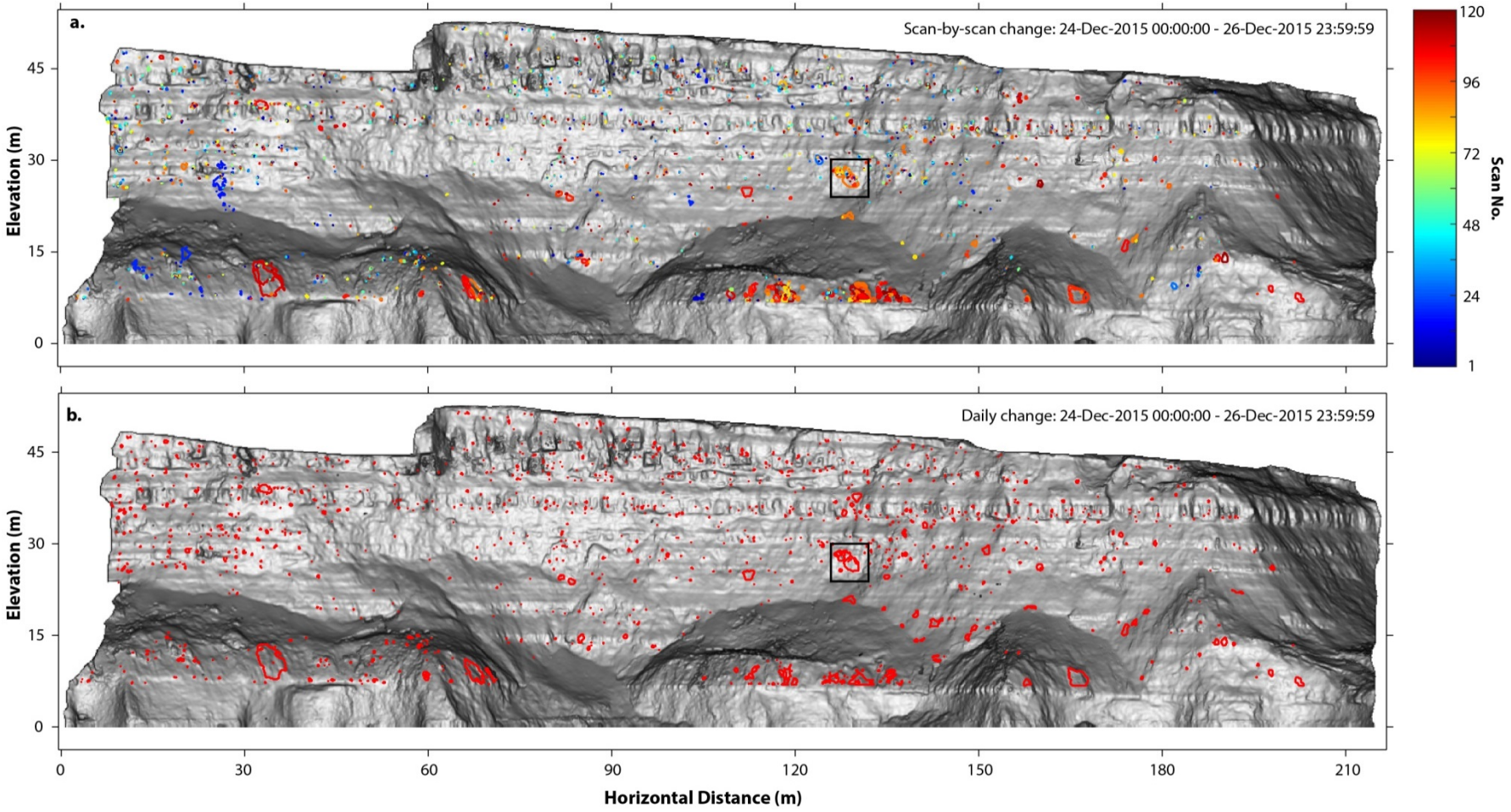

Figure 4.35: *(a) Rockfall derived from pairwise change detection of a scan database that includes only point clouds with entire cliff coverage. This includes numerous small rockfall within the square box that are depicted as a single event in the daily change images. (b) Rockfall derived from daily change detections over the same storm period.*

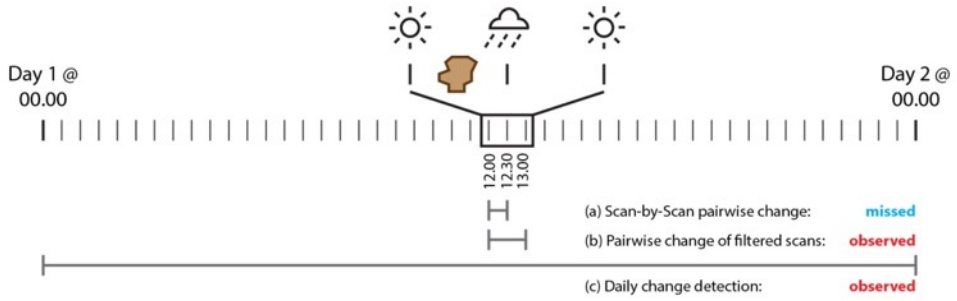

Figure 4.36: *Conceptual illustration of the significance of removing partial scans. While parts of these scans provide accurate estimates of surface change, if a rockfall occurs in an area of no data, the failure will be missed using pairwise change. These scans must therefore be removed prior to change detection of the scan database.*

4.13 Summary

The collection of thousands of point clouds requires a novel, automated approach to change detection that is capable of minimising the epistemic error between scans, such that the derived time-series of rockfall activity do not reflect the aggregation of multiple false change estimates. Regions of epistemic error between stable scans coincide with edges and holes, areas of low point density, and areas in which the returned radiometric signal deviates significantly from a reference waveform. Here, a range of filtering techniques has been applied to reduce the effects of these uncertainties from *ca.* 0.07 – 0.05 m. Following alignment of the scan data, the method of change detection used is critical for determining the scale of movements that can be detected. 3D change detection methods retain the raw point cloud data and are therefore robust to variations in point density. They also have the potential to both reduce the Level of Detection (LoD) between scans and provide distances that are consistent with the direction of failure. The method of change detection developed and presented here shows a significant reduction in the LoD to 0.03 m at *ca.* 300 m – 500 m. This more than halves the LoD available using the M3C2 algorithm. Although these estimates are then reduced to 2.5D rasters, the combined accuracy of change estimates and techniques to extract rockfall in 2D produces a rockfall inventory that contains > 180 000 rockfall events. A simple method for extending the rockfall polygons into regions below the defined LoD when appropriate is also presented. A description of the frequency distribution of failure sizes and the distribution of failures in time and space is presented in the following chapter.

Chapter 5

Spatial and Size Distributions of Rockfall from Near Real-Time Constant Monitoring

5.1 Introduction

In *Chapter 4*, the development of a methodology to process constant near-real time TLS data was outlined. As error is accumulative and proportional to the number of scans used to derive an inventory, the collection of 8 987 scans required a methodology capable of enhancing the accuracy of cloud-to-cloud comparison, and subsequent rasterising and delineation of rockfall. The rockfall inventory that is drawn upon in this chapter comprises 183 363 detachments, and is described in terms of their spatial and size distribution.

The size distribution of rockfall and landslides has often been quantified using magnitude-frequency analysis, which in turn can be used to estimate and predict erosion rates at a range of spatial and temporal scales (Guzzetti, 2005). The use of such models requires an understanding of the scaling behaviours of mass wasting, and has been drawn upon in instances where failure volumes could not be measured directly (Larsen *et al.*, 2010). The resulting size distributions have been used to infer underlying failure mechanisms and the efficacy of large-scale perturbations, such as large ($M_W > 7.0$) earthquakes and extreme rainfall events, in removing sediment from orogens (for example, Hovius *et al.*, 1997). One characteristic of most distributions is the presence of a rollover (reduction) in the frequency of the smallest failures. Explanations for this effect for landslides have been physical, for example, where minimum landslide sizes are controlled by the scale at which well-defined channel networks develop (Brardinoni and Church, 2004), or the possible transition from cohesion controlled failures to failures controlled by basal friction (Pelletier *et al.*, 1997; Guzzetti *et al.*, 2002). Furthermore, in some cases these rollovers reflect the level of completeness of the failure inventory, which has been limited by the spatial and temporal resolution of monitoring. Relatively little research has been undertaken into the effects of the temporal resolution of monitoring. This requires monitoring at frequent intervals over a sufficient duration to capture a sample size that is representative of the global behaviour of the rock slope in question. This usually encompasses the effects of seasonal variations in event occurrence or longer term responses to perturbations.

Barlow *et al.* (2012) used a three-year dataset of rockfall to establish an appropriate monitoring window for estimating rockfall-driven erosion from coastal cliffs over decadal timescales. Superimposition of rockfall events, whereby single rockfall may actually be the sum of multiple smaller, more frequently occurring rockfall, has the effect of reducing the frequency of the smallest rockfall. The average rockfall return period is thereby increased if the sampling resolution if insufficient to minimise this effect (Rosser *et al.*, 2007a; Lim *et al.,* 2010; Barlow *et al.*, 2012).

In this chapter, the magnitude-frequency distribution of rockfall is examined over a range of sampling intervals, referred to herein as T_{int}, from < 1 h to 90 d (the monitoring epoch, and temporal resolution), by conducting pairwise comparisons between surveys to generate increasingly low temporal-resolution inventories. This analysis shows that the frequency of small rockfall in the inventory is inversely proportional to the monitoring epoch length. With increasingly high frequency monitoring (short epochs ≈ 1 h to 1 week), the proportion of small rockfall events increases, while the frequency of the medium and largest volume rockfall reduces. By implication, a portion of rockfall events captured at anything greater than the finest monitoring frequency may be the sum of multiple smaller events. Put simply, the more often you survey the surface, the more rockfall you record.

This relationship has some further complexity. While the data show a marked alteration in the size distribution of rockfall captured when monitoring more frequently than every 4 d to 7 d, over longer monitoring epochs the frequency distribution is insensitive to monitoring epoch length. This is reflected in both the dependence of the exponent of a power law fitted to the non-cumulative magnitude-frequency distribution, and the least squares fit of the data to this power law. This is also reflected by shifts in the intensity or severity of the rollover for smaller rockfall volumes, where fewer rockfall are captured than would be expected if the inventory were to adhere to a power law. This suggests that rockfall in this location are highly fragmented, and result in the production of small detachments over periods of 4 d to 7 d, until the unstable, incipient scar has fully developed. The size distribution of rockfall is similar for all return intervals > 7 d. This suggests that 'single' rockfall fail over a period < 7 d, and that increasing the scanning frequency in this setting could reveal further characteristics of rockfall fragmentation during a period of detachment.

A comparison of rockfall sizes with the dimensions of planar exposed joints (facets) that together constitute the cliff face, suggests that rockfall dimensions are both smaller than those of individual facets, and are limited in size by these structural discontinuities. Geometric analysis of the shape of rockfall shows that they are primarily surface parallel slabs, and therefore have a geometry that is largely independent of the overall structure of the rock mass.

This chapter considers the use of magnitude-frequency distributions collected over a variety of timescales as a means of constraining the processes by which rockfall evolve. The

chapter begins with an error assessment that highlights the importance of rockfall size in determining the accuracy of its estimated volume. As higher frequency monitoring yields an increase in the proportion of small rockfall in an inventory, the total volumetric uncertainty is also higher. This has implications for the accurate use of high frequency monitoring for quantifying long-term erosion and rockslope evolution.

5.2 Inventory Description

Multiple rockfall inventories were compiled using pairwise change detection between point clouds separated by 11 monitoring epochs: < 1 h, 3 h, 6 h, 12 h, 24 h, 96 h, 7 d, 14 d, 21 d, 30 d and 90 d. The first inventory, sub-hourly, draws on the entire dataset of scans, in which return intervals were typically between 20 min and 30 min. This dataset has formed the basis of the analyses presented in this chapter, along with *Chapter 6* and *Chapter 7*. However, for comparisons between inventories of different T_{int}, any rockfall identified between scans separated by more than 1 h (for example, due to bad weather) were removed. For each rockfall, the parameters detailed in Table 5.1 were recorded, including the timing of the first scan of the change detection pair, properties of the rock mass from which it failed, and failure geometry.

Table 5.1: *Summary of the geometric and lithological properties recorded for each rockfall. Geometric properties were extracted by connecting contiguous pixels within binary images of detectable change (<= -0.03 m LoD) and accumulation and undetectable change (> -0.03 m LoD). Structural properties, described in Section 5.9, were extracted using the CloudCompare Facets plug-in, combined with a high-resolution (0.03 m) slope model and image of the cliff in ArcMap.*

Date and time properties	Geometric properties
Date and time	Area (m^2)
Scan ID	Volume (m^3)
Time since last scan (hh:mm:ss)	Volumetric error (m^3)
	Perimeter (m)
Structural properties	Depth (m)
Bed number (Figure 5.29)	Centroid (m / Pixel ID)
Horizontal joint spacing (m)	Minor axis length (m)
Vertical joint spacing (m)	Major axis length (m)
	Pixel ID list
	Boundary pixels

Table 5.2 shows the total recorded rockfall volumes for the period 5th March to 30th November, comparable between each T_{int} database, alongside average statistics for the rockfall volumes. The non-bracketed volumes are curtailed at 30th November. This limit was applied to account for the fact that only three 90 d change detections (between four scans) could be applied within the 10-month period of monitoring. The last of these was measured between scans captured on 2nd September 2015 and 30th November 2015. As such, in analyses that

compare datasets from different T_{int}, only rockfall up to this end date are used. The more often the cliff is monitored, the higher the number of rockfall observed. Interestingly, the size of detachments is proportional to T_{int}, such that small rockfall volumes on average are recorded at more frequent sampling intervals. The implications for failure evolution that can be drawn from this are discussed in *Section 5.8*, in the context of variations in the magnitude-frequency distribution of rockfall.

Table 5.2: *Summary statistics of rockfall inventories, acquired using change detections with different T_{int}. T_{int} < 1 h comprises T_{int} of ca. 20 mins – 30 mins, with some removed due to inclement weather conditions. The number of recorded rockfall is greater when the cliff is monitored more frequently. Values reflect the number of rockfall up to 29th November, as the month of December is not included by the last 90 d change detection. Bracketed values show the total recorded up to 30th December.*

T_{int}	Recorded Rockfall	Mean Volume (m^3)	Median Volume (m^3)	σ Volume (m^3)
< 1 h	170 965 (183 363)	0.0169	0.0054	0.1060
3 h	46 689 (52 235)	0.0169	0.0055	0.1291
6 h	26 064 (28 857)	0.0152	0.0041	0.1263
12 h	13 674 (15 392)	0.0210	0.0046	0.1663
24 h	8 027 (9 197)	0.0280	0.0052	0.1946
96 h	4 403 (4 898)	0.0407	0.0067	0.2590
7 d	3 288 (3 635)	0.0446	0.0075	0.2734
14 d	2 939 (3 043)	0.0391	0.0078	0.2442
21 d	2 679 (3 145)	0.0409	0.0078	0.2570
30 d	2 346 (2 855)	0.0344	0.0085	0.1704
90 d	1 796 (1 796)	0.0438	0.0100	0.1993

5.3 Volumetric Error

Techniques developed to reduce uncertainty in 3D change estimation were presented in *Chapter 4*. The data collected were converted into raster form though linear interpolation prior to rockfall delineation. This requires an error assessment of the resulting change images in order to determine the applicability of the chosen Level of Detection (LoD). Analysis of the first inventory compiled showed that many reported rockfall occurred in the same locations on the cliff face, resulting in an inventory of > 700 000 discrete events. Inspection of the rasters of change showed that pixels adjacent to holes in the original scan data exhibited forward and backward movements, greater than the 0.03 m LoD (*Section 4.10.2*). To overcome this, for the first 100 change images of the dataset, the standard deviation of change for each pixel was calculated (Figure 5.1). Pixels with a 99.87th percentile deviation (3σ), > 0.02 m in Figure 5.1, were identified and used to create a binary mask that prevented these pixels from being identified as rockfall in the subsequent inventory. This threshold percentile was selected to prevent pixels that appeared to be rockfall, identified visually, from being included in the mask.

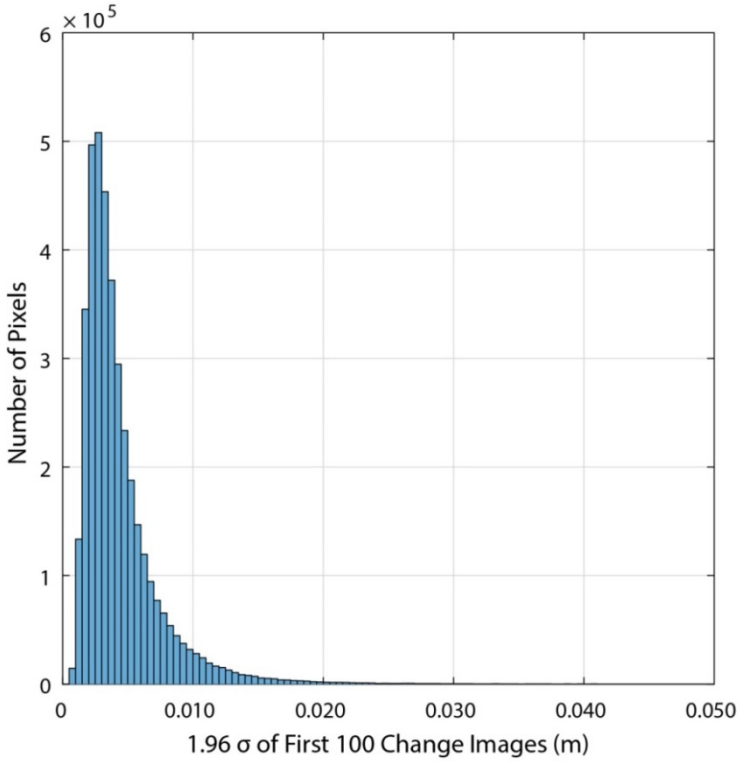

Figure 5.1: *1.96 σ of the first 100 change rasters (0.0005 m bin widths). These values fall below the 0.03 m LoD used to mask rockfall. This shows that the accuracy of the 3D change detection techniques, developed in Chapter 4, is not reduced though interpolation.*

The distances attributed to each pixel in this subset of images, ignoring the masked pixels described above, are shown in Figure 5.2. The distances follow a Gaussian distribution, which is characteristic of errors in measured point cloud data, and those presented in *Chapter 4* for this dataset. This shows that, although change is measured in 3D, its interpolation into 2D does not impact upon the accuracy of rockfall identification. Only 0.34% of pixels fell outside of the ±0.03 m LoD. These pixels were not masked as they did not fall close to holes or edges in the dataset and themselves appeared to resemble rockfall.

Tests conducted in *Section 4.7* (Figure 4.14) showed an average registration error of 0.005 m between successive point clouds (n to $n+1$), and that this error was independent of whether the scan (n_i) was registered to the first of the database (n_i *to* n_1), or to the previous scan (n_i *to* n_{i-1}). To ensure that no increase in registration or epistemic error occurred though the monitoring period, the LoD was calculated for every scan and plotted in Figure 5.3. This value lies consistently between 0.01 m – 0.03 m, representing the 95% confidence level of each point cloud. Residuals are attributed to scans in which significant rockfall events occurred, or when significant numbers of rockfall occurred. The latter scenario represents change detections taken during inclement weather conditions, or change detections that span a longer than average period where the system was not scanning, periods delineated by the grey dashed lines. A small but appreciable increase in the LoD estimates can be observed during December. This is attributed to the heightened rockfall activity during this month, which is discussed in *Chapter 6*.

However, the consistency in error distribution shows that patterns of rockfall occurrence though time, discussed in *Chapter 6*, are not influenced by methodological errors. Moreover, the 0.03 m LoD can be applied to each point cloud, in order to prevent erroneous pixels from being recorded in the resulting rockfall inventory.

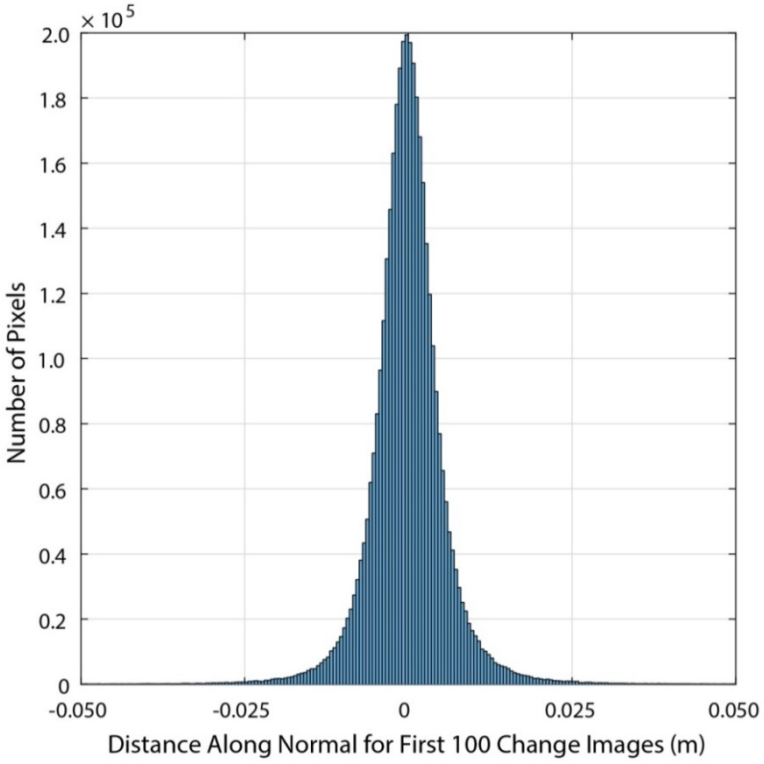

Figure 5.2: *The distances along the normal direction in resulting change rasters form a Gaussian distribution, as described in published examples of error assessment from LiDAR.*

In this section and in *Section 5.8*, patterns of rockfall occurrence are examined across the different T_{int} inventories. Figure 5.4 shows the LoD estimates for every change detection of the 11 different T_{int}. For change detections $<$ 7 d, the average LoD distribution is broadly consistent with that of the sub-hourly scans in Figure 5.3, suggesting that a 0.03 m LoD is again applicable for rockfall delineation. For larger T_{int}, however, the standard deviation of change estimates increases beyond a 0.03 m LoD. This increase in measured rockfall is most apparent during the autumn and winter months of September to December. No changes to the point cloud registration were implemented for change detections at different T_{int}. This pattern appears to reflect a positive relationship between T_{int} and measured rockfall activity, as well as an increase in the rate of rockfall activity though the monitoring period. To ensure that none of the change detections exhibited noise, for example due to rainfall, a 2 h long video of every change detection was compiled and manually examined.

Rockfall occurred throughout the monitoring period, with a minimum of one rockfall measured in a $<$ 1 h change detection, a maximum of 32 rockfall, a mean of 9.9, and a mode of 15 rockfall per scan. In Figure 5.5, all individual rockfall volumes are plotted though the

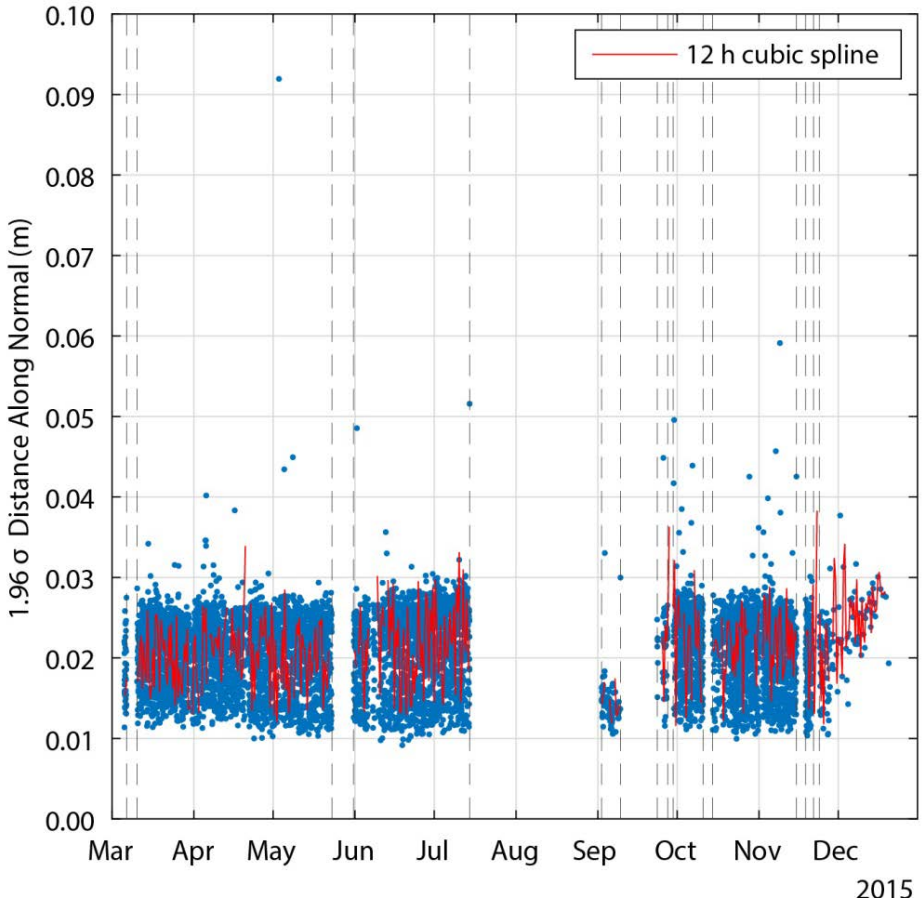

Figure 5.3: *LoD for individual change detections though time, measured at sub-hourly intervals. A background level of noise of 0.01 m – 0.03 m is apparent. Values above this correspond to increased measurement of rockfall. This is sometimes caused by change detections over longer time periods, caused by gaps in scanning (vertical dashed lines).*

monitoring period. The minimum recorded rockfall volume was twice that of the minimum detectable volume, V_{min}:

$$V_{min} = LoD \cdot A_C \qquad \text{[Eq. 5.1]}$$

where LoD is 0.03 m, and A_C is the cell size (0.0225 m^2). Volumes therefore range from 1.3×10^{-3} m^3 to a maximum of 7.2536 m^3. The individual rockfall volumes show an increase in activity though the calendar year as represented by the LoD estimates in Figure 5.4. This is discussed further in *Chapter 6*. In relation to the size of events, all 18 rockfall > 1 m^3 that occurred during the monitoring period did so from September onwards.

Cumulative rockfall volumes though time are represented in Figure 5.6. In this chapter, discrepancies in these volumes are compared between different T_{int} values for the purpose of error quantification. The nature of the increased rockfall activity though time is discussed in *Chapter 6* in relation to environmental conditions. Cumulative rockfall volumes show significant discrepancy between T_{int}, such that more frequent monitoring produces higher accumulated

volume estimates. There are two possible explanations for this, both of which relate to the increased proportion (97.7%) of small detachments of the order of 0.001 – 0.010 m^3, which are recorded at lower T_{int} (Table 5.2). First, a 0.15 m cell size has the potential to exceed the scale of small fragmentation of the rock mass though spalling. Since 0.15 m is equivalent to the maximum point spacing, detachments smaller than this may be recorded in regions of higher point density across the cliff face. In such instances, while the depth of the detachment is maintained during rasterization, the aerial extent and therefore volume is overestimated. Second, the error attributed to volume estimation is proportional to the size of the measured detachment, as is discussed below. Their more frequent occurrence within the low T_{int} dataset, possibly because of superimposition within high T_{int} datasets, therefore increases the overall uncertainty in total volume estimates.

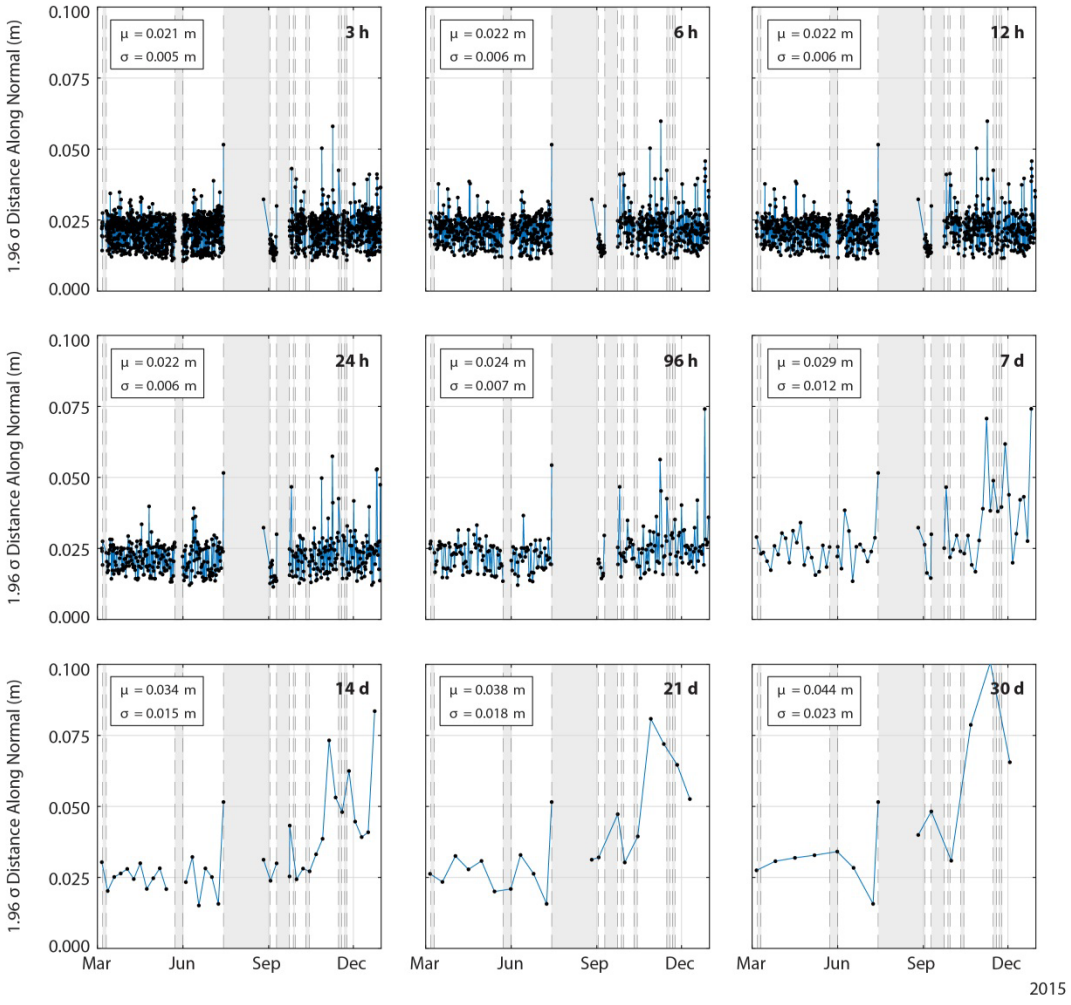

Figure 5.4: *LoD for change detections at different T_{int} though time. As the scan interval increases, the standard deviation (σ) of change measurements also increases though time. This reflects an increase in measured rockfall owing to the larger time between scans of the cliff. For scan intervals below and including 7 d, the mean background rate (μ) is below the LoD used to identify rockfall from the change rasters. As with Figure 5.3, dashed lines indicate monitoring gaps.*

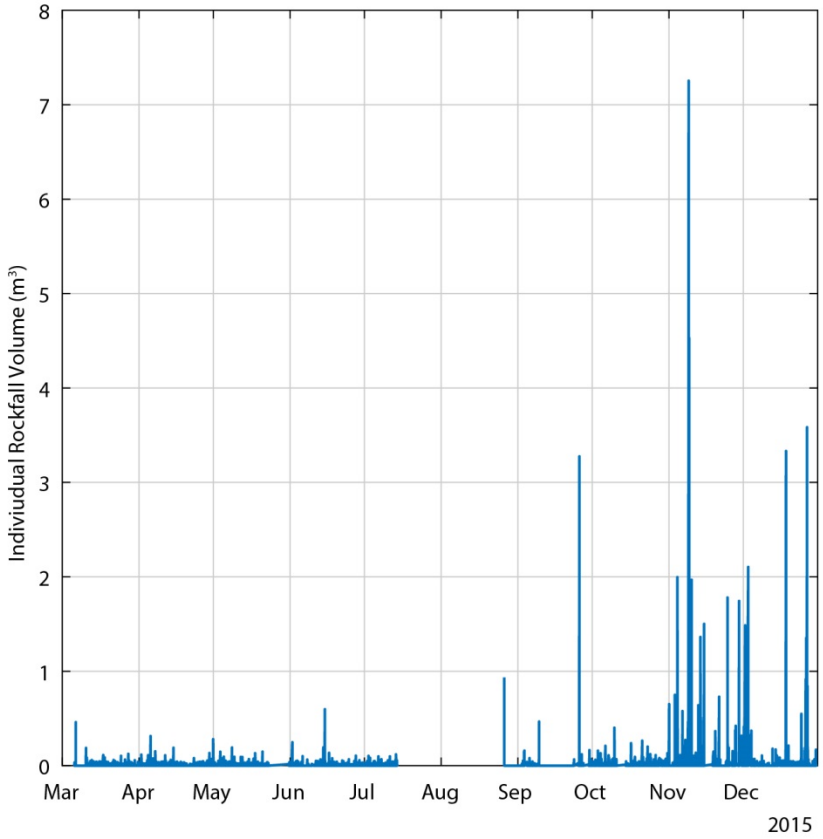

Figure 5.5: *Individual rockfall volumes accumulated for each change detection measured though the monitoring period. Rockfall events > 0.1 m³ occur throughout the monitoring period, increasing in frequency towards the Autumn and Winter months. An appraisal of the temporal patterns of rockfall occurrence is provided in Section 6.2. Within this chapter, rockfall though the monitoring period are presented in the context of error estimation.*

In order to model the errors that are present in this dataset, the error estimation procedure outlined in *Section 4.11.1* was applied to a synthetic dataset of rockfall volumes (Figure 5.7). The mean rockfall shape for this study, described in *Section 5.7*, is a hypothetical slab with a depth of 0.156 times the horizontal and vertical extents (m), or 0.201 times the cross-sectional area (m^2). The synthetic rockfall volumes are created by varying the horizontal and vertical dimensions at 0.15 m intervals, in order to replicate a cell-by-cell increase in volume while maintaining the mean rockfall shape. This synthetic dataset assumes that all rockfall are slabs with four edges. As the rockfall area, and hence volume, increases, so too does the number of edge pixels. These edge pixels represent the highest source of volumetric error of each rockfall since, as discussed in *Section 4.11.1*, they may have up to 50% error in their aerial extent. In this study, this error is added to error of pixels within the rockfall that do not belong to an edge, referred to as 'internal' pixels:

$$V_{InternalError} = \sum_{i=1}^{N} LoD \cdot A_C \qquad \text{[Eq. 5.2]}$$

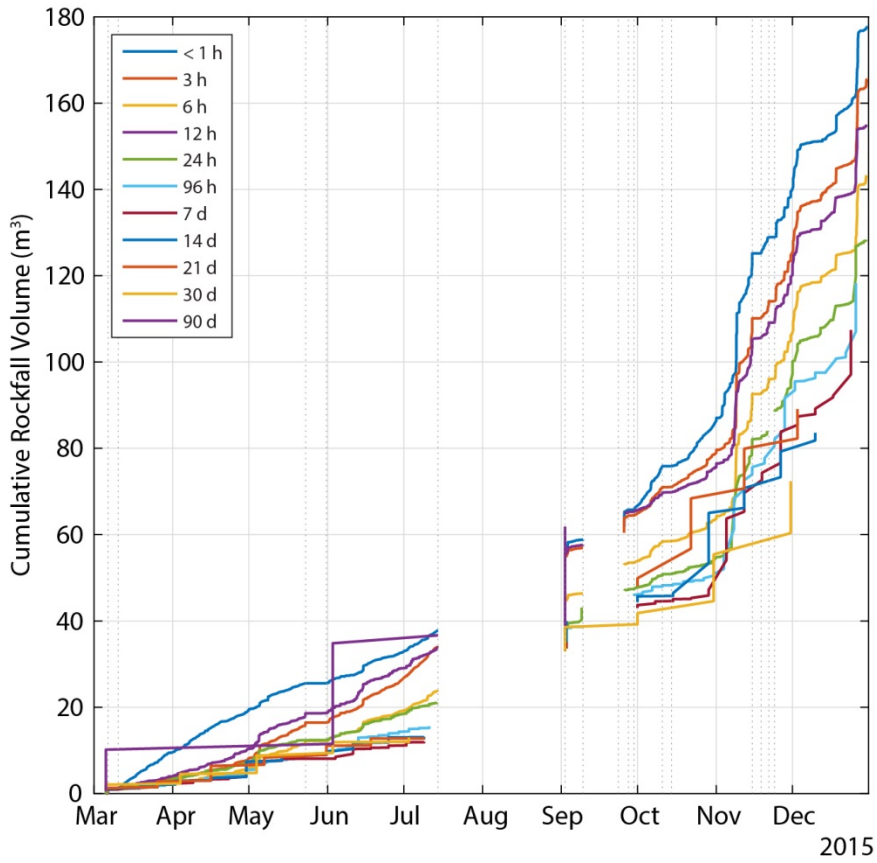

Figure 5.6 *Cumulative rockfall volumes measured though the monitoring period, using data from all 11 monitoring intervals. The results show that far higher volumes of material, up to twice those recorded by 90 d monitoring, are measured at sub-daily intervals. The times of pairwise change detections are recorded as the date of the first scan, rather than the second. As a result, although all scan intervals record a significantly increased rate of rockfall activity during November; this appears earlier on the plot for longer scan intervals. The total estimated volumes are not included for comparison as change detections cannot be recorded up to the final day of monitoring for longer time intervals (30th December).*

where N is the number of internal pixels. While the number of edge pixels increases with the synthetic rockfall volume, the proportion relative to the total number of rockfall pixels decreases. As a result, smaller rockfall have a higher volumetric error as a proportion of the total estimated volume. The highest theoretical error is for rockfall of a single pixel. In such instances, the volume error is calculated as four times the error of a single edge pixel. This concept is outlined in Figure 5.7, which illustrates the smallest and largest theoretical areas that a rockfall may occupy in relation to its size in a rasterised image of change.

For all of the rockfall in the sub-hourly inventory, this pattern was replicated using the estimated volume of each rockfall, combined with the total number of edge pixels and the number of internal pixels, modelled using the mean rockfall geometry (Figure 5.9). Larger rockfall volumes exhibit a smaller percentage volume error; however, for the majority of rockfall volumes that lie between 0.001 m^3 (a minimum of two pixels) and 0.01 m^3 (a minimum of 14

pixels), the error is between 80% and 160% of the estimated volume. This error value is slightly lower than the aerial uncertainty reported in Figure 5.7, because the depth of each rockfall here is assumed to be exact for the purpose of the modelling the above figure. Magnitude-frequency analysis of the size distribution of rockfall events (*Section 5.8*) indicates that more frequent scanning detects a greater proportion of smaller rockfall events. Consequently, more frequent scanning also presents increased uncertainty in cumulative volume, and given that the size distribution adheres to a power-law, cumulatively this error can be significant relative to the total volume lost though the monitoring period.

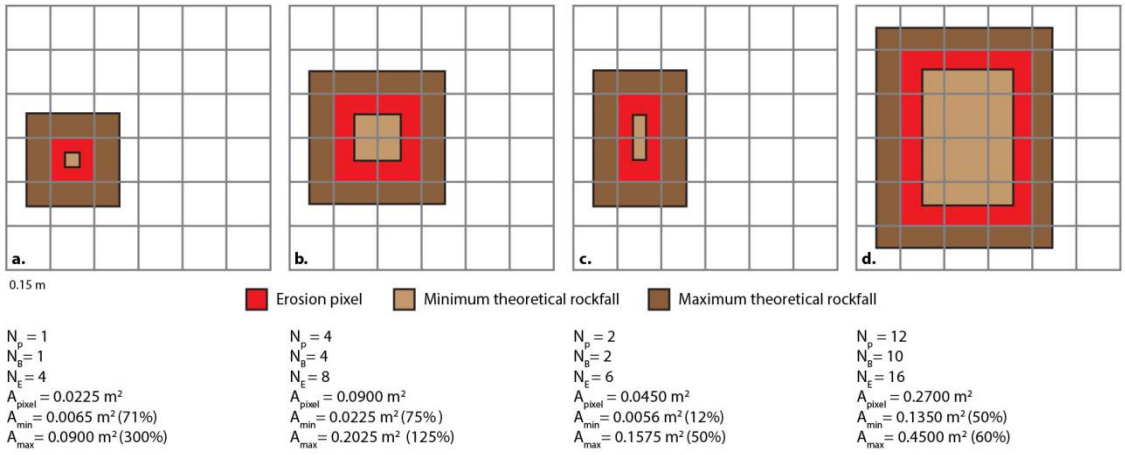

Figure 5.7: *(a) A theoretical grid of pixels, with a single erosion pixel (red). The minimum theoretical rockfall area is illustrated, with edge lengths ca. 30% (1/√12) of the erosion pixel edge lengths. A theoretical maximum rockfall size is also drawn, using the same principle. N_P represents the number of erosion pixels, N_B represents the number of boundary pixels, and N_E represents the number of edges. The area of the pixel (A_{pixel}), the area of the minimum theoretical rockfall (A_{min}), and the area of the maximum theoretical rockfall (A_{max}) are calculated. Uncertainties of each rockfall area, relative to the size of the pixel, are provided as a percentage. The single pixel results in the highest uncertainty due to the large number of edges relative to its size. (b) As the size of the pixel increases, the percentage uncertainty decreases. (c) As the number of edges relative to the number of pixels decreases, so too does the uncertainty. (d) A larger rockfall, but with fewer boundary pixels relative to its size, results in lower uncertainties than in (b).*

In addition to the error estimates in Figure 5.8, error estimates were produced for the separate T_{int} inventories. This enabled the creation of an uncertainty envelope for each of the total cumulative failure volumes (Figures 5.10 and 5.11). Unlike Figure 5.6, the cumulative volumes are curtailed at 30th November to enable comparison between different T_{int}.

The resulting error margins show that the uncertainty in volume estimates is greatest for the datasets captured at the highest frequencies (Table 5.3). For the sub-hourly dataset, the total estimated volume is 110.87 +/- 52.44 m^3, while the total estimated volume for the 30 d dataset is 72.37 +/- 27.50 m^3. As this is primarily a consequence of the higher proportion of

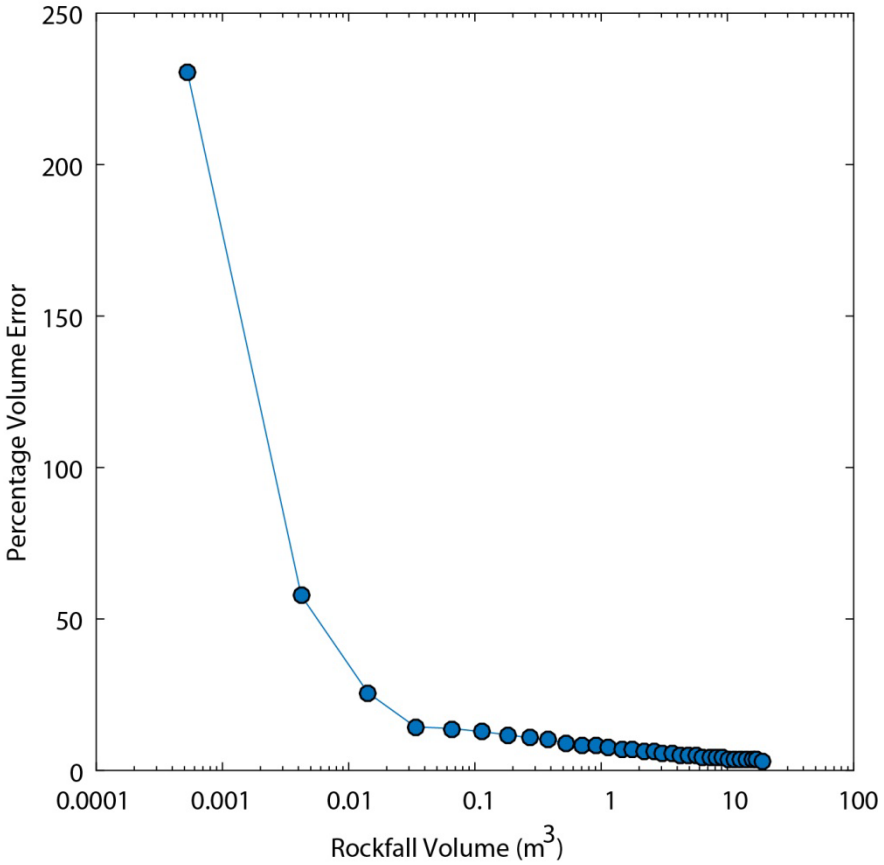

Figure 5.8: *Rockfall volume uncertainty estimated for a range of synthetic rockfall. Rockfall volumes are simulated by varying the cross-sectional area and depths of the failure, while maintaining the mean rockfall shape measured in the total inventory. The mean rockfall shape is discussed in Section 5.6 and has approximately similar horizontal and vertical dimensions with a depth 0.15 times these lengths.*

small rockfall events, one means of reducing this error is to reduce the cell size. A reduction in cell size has the effect of increasing the number of internal pixels relative to the number of edge pixels, as well as reducing the uncertainty in edge pixel volumes, related to the cell area A_C by $depth \times \frac{1}{\sqrt{12}} A_C$. As discussed in *Chapter 4*, however, pixel sizes cannot be decreased below 0.15 m as this approaches the maximum point spacing. While methods of identifying rockfall volumes using true-3D techniques overcome certain limitations attributed to the cell size (Lague *et al.*, 2013), the accuracy of these techniques is still limited by the point spacing of the original point clouds relative to the size of the rockfall. Accurate 3D estimation of rockfall shape and volume requires a minimum of four points (Besl and McKay, 1992), which is significantly higher than the number of points required for linear interpolation into a single cell.

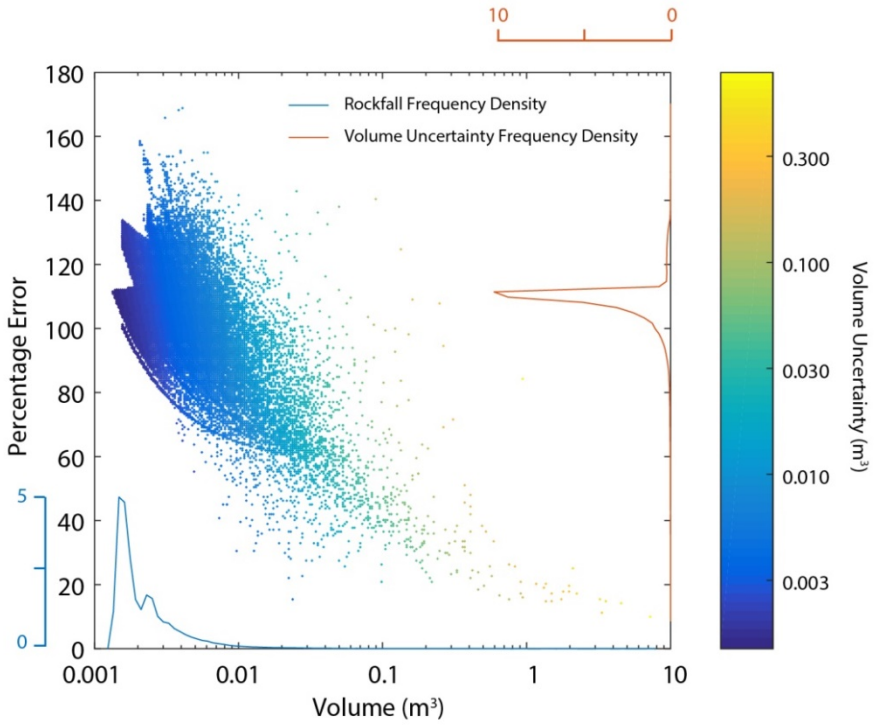

Figure 5.9: *Rockfall volumes from < 1 h rockfall inventory. Percentage volume error is estimated using the LoD, number of internal pixels and number of edge pixels. Frequency densities (kernel density estimates) are appended to each axis, showing that rockfall volumes < 0.01 m^3 account for the greatest proportion of measured rockfall (modal volume = 0.0081 m^3). As a result, errors range from ca. 60% to ca. 140% for most rockfall (modal error percentage = 109%). Cumulative volume estimations using rockfall of this size may vary by at least the actual volume.*

Table 5.3: *Rockfall volumes estimated by monitoring the cliff face at different frequencies from 5th March to 30th November 2015, plotted in Figure 5.10.*

T_{int}	Minimum Total Volume (m^3)	Estimated Total Volume (m^3)	Maximum Total Volume (m^3)
< 1 h	58.43	110.87	163.32
3 h	50.99	100.41	149.82
6 h	48.13	90.94	133.75
12 h	45.79	83.9	122.01
24 h	45.86	73.92	101.99
96 h	40.04	71.29	102.55
7 d	43.11	75.44	107.76
14 d	39.67	71.59	103.51
21 d	35.77	73.01	110.24
30 d	44.86	72.37	99.88

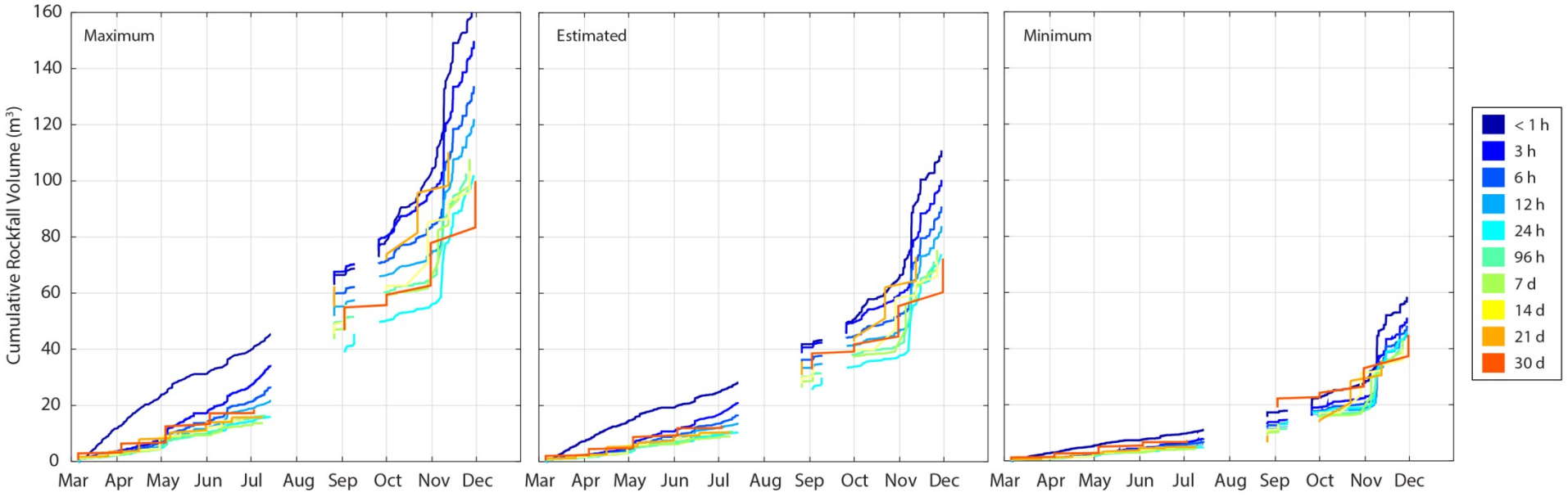

Figure 5.10: *Rockfall volumes from < 1 h rockfall inventory, showing the maximum, estimated and minimum totals. Totals curtail at 30th November for comparability, reflecting the fact that change detection at 90 d intervals could not include data from December. The shape of these lines is approximately similar throughout the monitoring period. However, during the summer months of May, June and July, the maximum estimated volume for the sub-hourly inventory deviates more from the estimated cumulative volume. This reflects the high frequency and proportion of small rockfall events during these months, which provide a higher volumetric uncertainty.*

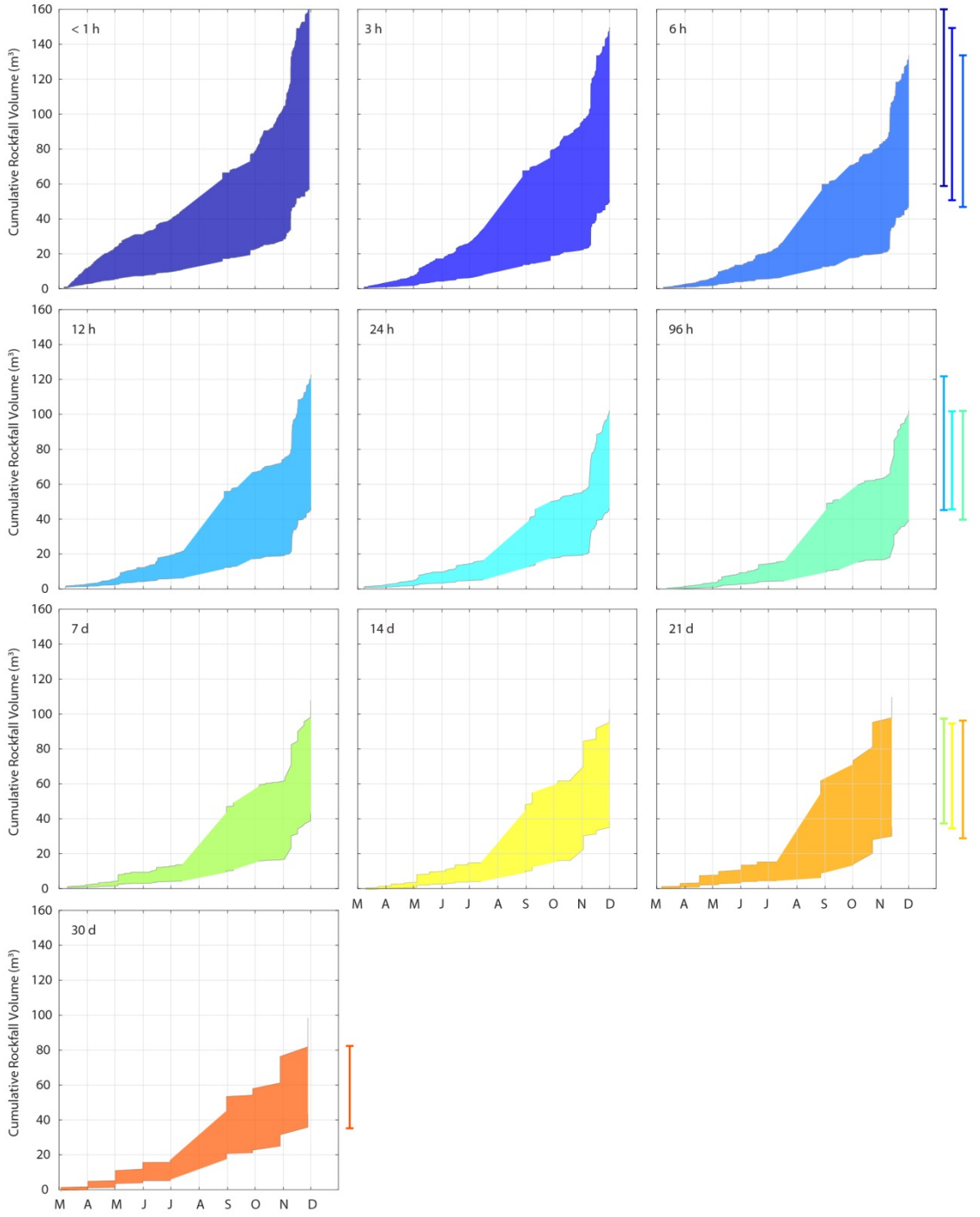

Figure 5.11: *Envelopes of estimated rockfall volumes for the period 5th March 2015 – 30th November 2015. The envelopes increase in width with decreased T_{int} as the proportion of the rockfall inventory containing small events increases. Bars at the side of each plot represent the final upper and lower volume estimates, and generally decrease in size with T_{int}.*

By estimating the theoretical maximum volume error, I have shown in this section that uncertainty in rockfall volume can range from 20% - 160% of the estimated volume. This uncertainty is greatest for the smallest rockfall, in particular those with a high proportion of edge pixels, for example shapes that tend away from cubic forms. This suggests that monitoring at lower frequencies may provide more accurate estimates of predicted retreat rates over longer

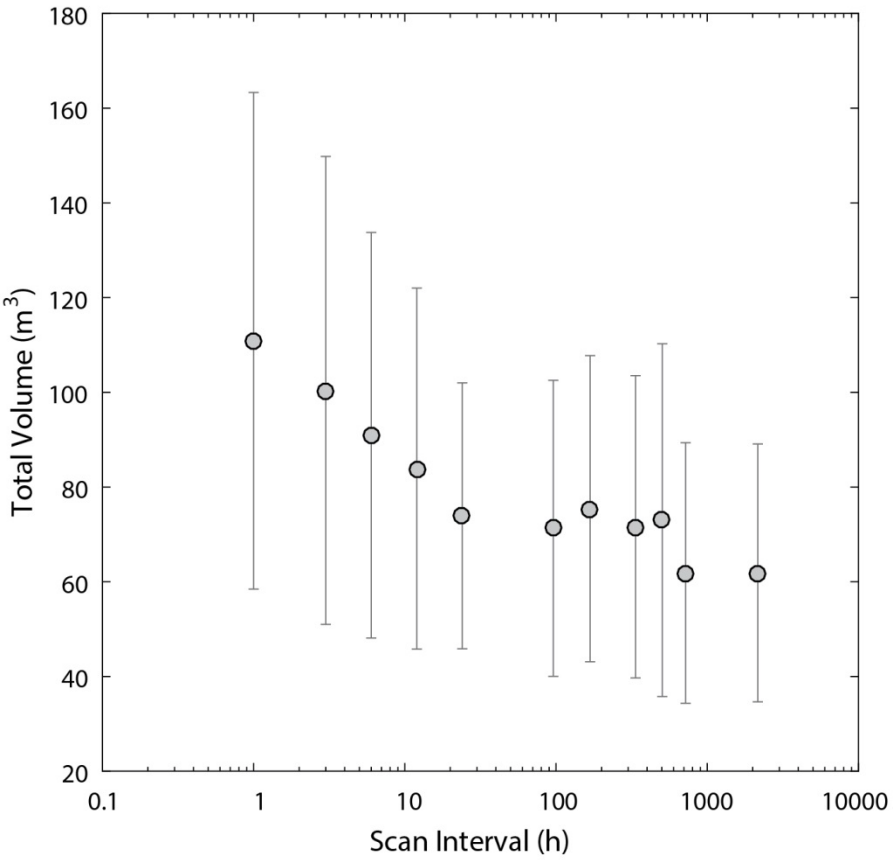

Figure 5.12: *Estimated cumulative rockfall volumes (circles) accompanied by percentage volumetric error bars. A linear decrease in the total estimated volume in apparent between 1 h and 96 h, possibly signifying that increasingly high proportions of small rockfall are recorded when monitoring frequency is increased beyond 96 h. This is reflected in the size of the error bars, which decrease with scan interval. These error bars converge at volumes between 60 m^3 and 90 m^3.*

time periods where precision is needed. This is not purely because longer time-averaged conditions are captured, but also because longer intervals reduce the measurement error relative to the change detected, particularly when change is accrued by many small, discrete events. Although the net errors in volume estimates can be high using this method, high frequency monitoring is critical for enhancing our process understanding of rockfall, such as the cause-effect relationships between rockfall and triggers, as well as precursory activity. These are discussed in *Chapter 6* and *Chapter 7*. However, it is notable that the net errors in volume estimates can be high.

When using any change detection technique, the constituent surface models will have a degree of uncertainty in surface topography (elevation). When comparing the datasets used here, the resulting uncertainty, E_{DoD}, can therefore be defined as the root sum square of errors in each:

$$E_{DoD} = \sqrt{{E_{Z1}}^2 + {E_{Z2}}^2} \qquad \text{[Eq. 5.3]}$$

If analysis of cumulative datasets is required, the error will increase in proportion to the number of change detections undertaken. At present, there is no established method to overcome this increase in error, even with the application of 4D smoothing techniques discussed in *Chapter 8*. The size distribution of rockfall adheres to a power law, presented in *Section 5.8*, which presents a considerable obstacle to cumulative change analysis. Rather than the occurrence of individual large events, which present a limited volumetric error in only one scan, the power law behaviour of rockfall is such that small failures, with high percentage volume errors, occur frequently. As a result, high frequency monitoring in this setting is ill suited to examining the net volume that is displaced by large numbers of small events. Conversely, rockfall analysis is undertaken here using the results of pairwise change detections. As such, it is uniquely applicable for discerning the spatial, temporal and size distributions of rockfall events at high frequencies ($<$ 1 h).

5.4 Spatial Distribution of Rockfall

The spatial distribution of rockfall events over the 10 months of the monitoring period is shown in Figure 5.13. The general pattern shows that scars are distributed across the entire rock face. No rockfall were recorded on the upper slopes of the buttress, which runs across the cliff face at *ca.* 17 m elevation. This area of cliff comprises loose surficial material built up from rockfall deposits from the near-vertical rock face above. Residence times of material on the buttress are variable, with areas of low gradient that are in direct contact with the upper cliff face retaining much of the intercepted debris. For this analysis, all areas of the buttress that comprise loose material were removed, allowing a focus on the near-vertical rock face only. By far the largest events in both area and volume occur along the top of the seaward snout of the buttress. From the snout of the buttress, rockfall occur at a slightly higher frequency than elsewhere up the rock face. Rockfall often take place along exposed beds of specific lithologies. Small, horizontally aligned clusters of rockfall occur at structural discontinuities, in particular at the boundaries between sandstone and interbedded sandstone and siltstone beds. Small rockfall also occur at the edges of protruding blocks, despite filtering of edge points from the original data, the application of the variable cylinder length 3D change detection, and the filtering of empty pixels that occur next to areas of occlusion in the resulting change image. This suggests that these small events are not artefacts of the data collection and processing.

Over the 10-month period, no net change in the cliff profile occurred. The profile offset between the near-vertical slopes of the upper cliff and the face of the buttress prevents any direct connectivity between failures in these areas. However, failures that occurred towards the end of the monitoring period, which are shown in blue, appear to have propagated upwards.

Many rockfall are contiguous, with smaller failures preceding larger events. Figure 5.14 presents an example of contiguous failure that developed over a three-day period. This pattern

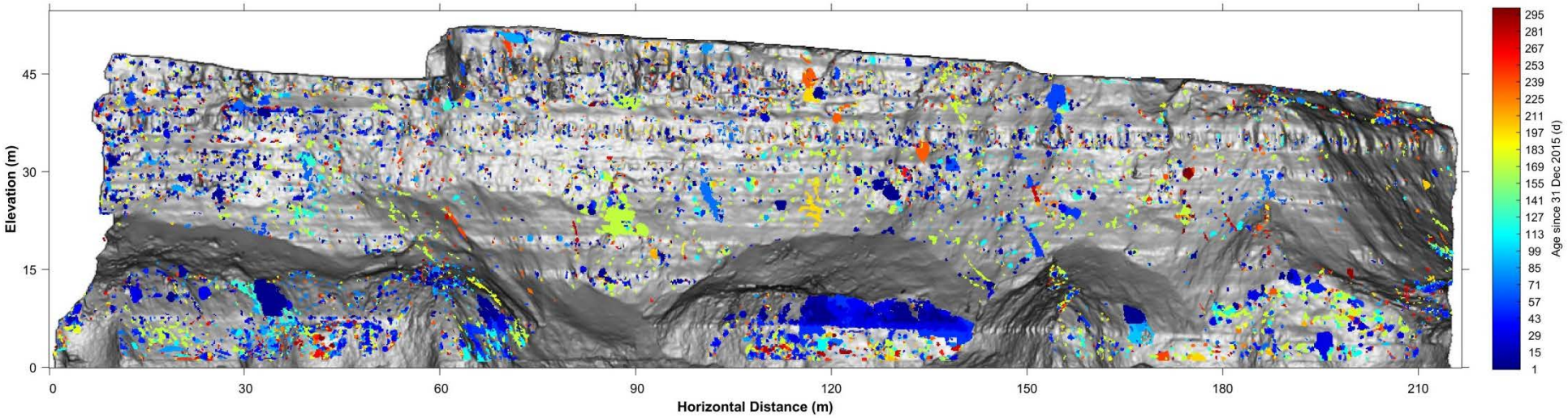

Figure 5.13: *Distribution of rockfall across East Cliff monitored at sub-hourly intervals between 5th March 2015 and 30th December 2015. Rockfall are distributed across the entire cliff face, in particular in areas of exposed bedrock. Although the high water mark is below the portion of cliff shown in this figure, the largest and most frequent rockfall occur at the base of the cliff. Accumulation and loss of material in the areas of non-exposed bedrock on the cliff buttresses, which runs across the cliff face at ca. 17 m elevation in the above figure, were removed. Colours represent the age since 31st December, where red represents the oldest rockfall.*

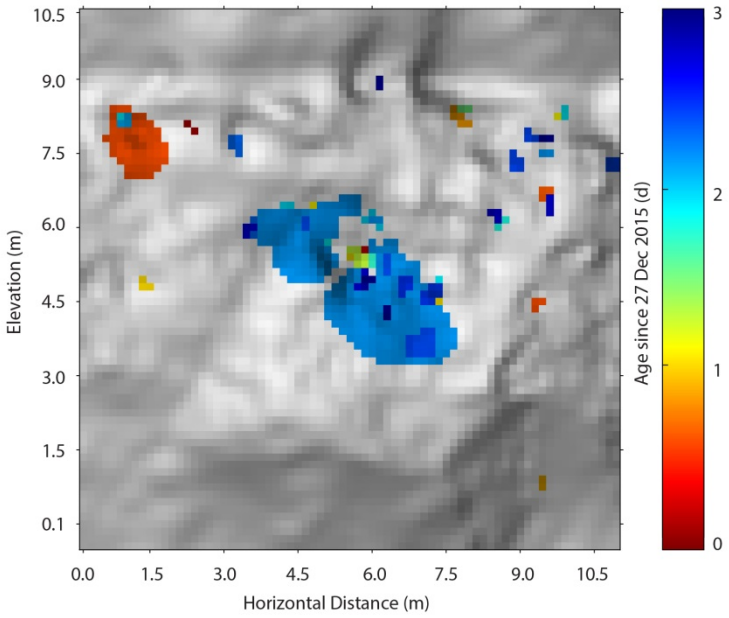

Figure 5.14: *An example of contiguous rockfall over a three-day period. Here, small rockfall occur before and after the large rockfall in the centre. Close inspection of many of the largest rockfall showed similar patterns, in particular of the accumulation of small rockfall events prior to failure.*

of rockfall growth has been observed in previous studies along this coastline (Rosser *et al.*, 2007a; Lim *et al.*, 2010); however, the presence of this process at far shorter T_{int} suggests that the timescales over which failures occur have not yet been fully characterised.

Figure 5.15 shows the erosion rate over the 10-month monitoring period, measured across discrete lithological exposures up the cliff face. Erosion rates are extrapolated from the 10-month period to annual retreat rates by multiplying by a factor 1.217, which is the reciprocal of the ratio of the number of days monitored (300) to the total number of days in the year. The areas of each bed, used to divide the total failed volume, did not include any of the cliff face that went unmonitored due to occlusion. The different T_{int} show a clear discrepancy in retreat estimates, as these draw upon cumulative total volume estimates. This discrepancy continues up the cliff face. The widely jointed sandstone beds at the cliff top and vertical walls of the buttress present the highest rates of retreat, identified as 0.046 m a^{-1} and 0.047 m a^{-1} respectively when measured over 30 d. This is lower than the 0.18 m a^{-1} estimated from longer-term monthly monitoring undertaken by Rosser *et al.* (2005), which may be attributed to either previously lower precision monitoring, or the lack of large rockfall (100 m^3) occurring during this monitoring period.

When estimated erosion rates include the 90 d dataset, data up to 30th November is used. Here, the conversion factor (the ratio between the 270 days of monitoring and the number of days in a year) is 1.352. For most units, the erosion rates are approximately similar, however, erosion rates on the buttress are considerably lower (0.074 m a^{-1} compared to 0.098 m a^{-1} for the

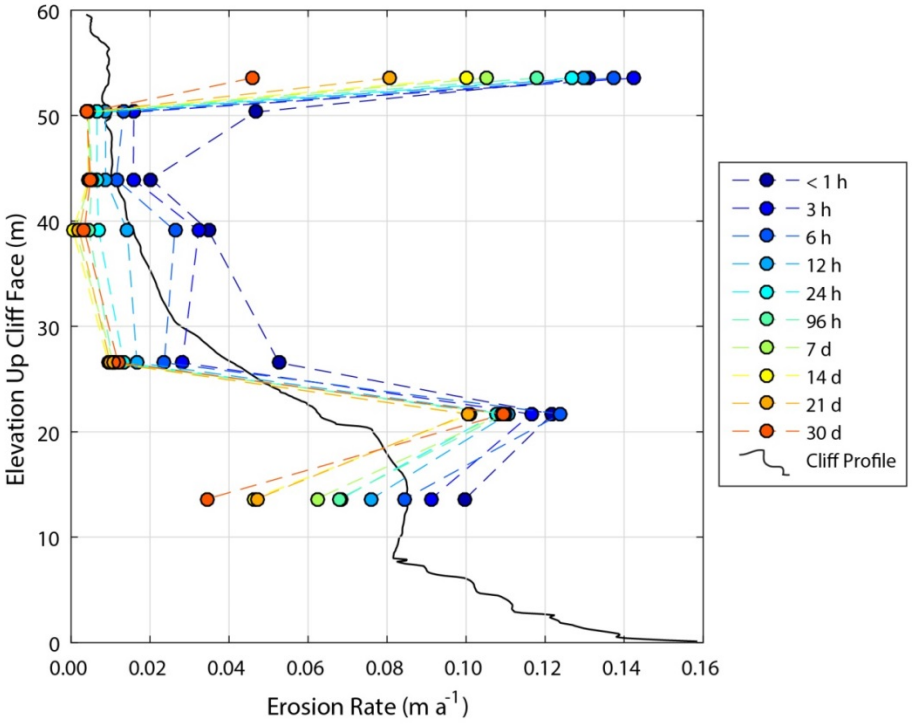

Figure 5.15: *Erosion rate estimations in m a^{-1} measured from 5th March 2015 – 30th December 2015 for discrete lithological exposures. As such, rockfall measured using the 90 d scan interval are not included. The widely jointed sandstone at the cliff top provides the highest erosion rates, up to 14 cm per year. At the base of the cliff, similarly high values of erosion are estimated. A similar pattern to Figure 5.9 is evident, whereby lower scan intervals provide the highest estimates of erosion.*

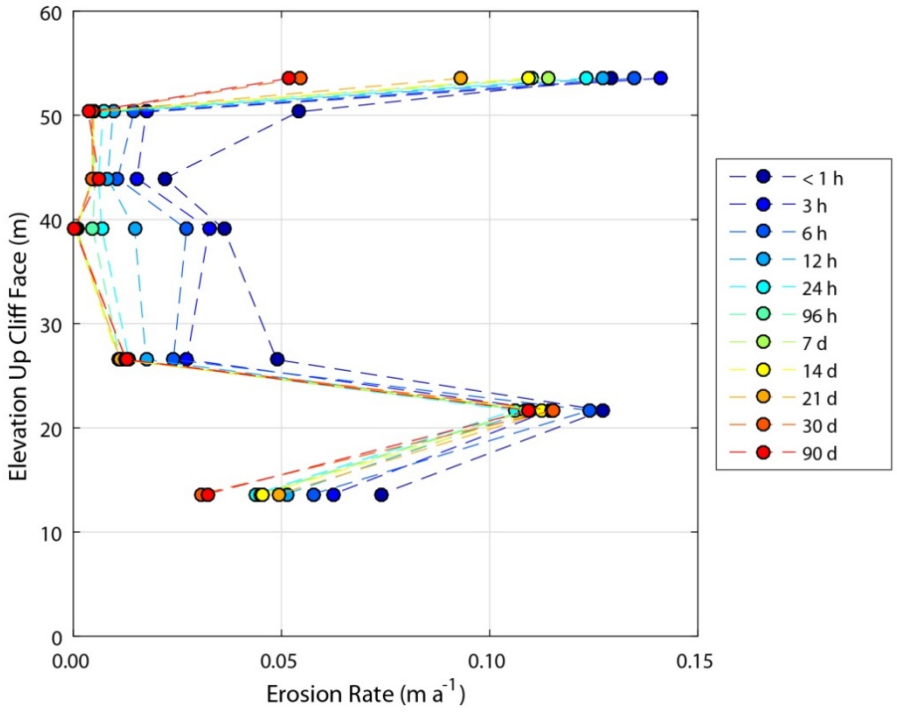

Figure 5.16: *Erosion rates measured between 5th March 2015 and 30th November 2015, allowing the inclusion of the 90 d dataset. Erosion rates are lower in this figure than in Figure 5.13, reflecting the increase in rockfall activity during December 2015.*

sub-hourly dataset). This reflects the increased activity in this area of the cliff face during December, and highlights the complexity in estimating erosion rates using monitoring data that does not encompass multiple cycles of seasonal variability in rockfall occurrence.

In Figure 5.17, the depth of measured change is presented up the cliff face. The positions of exposed lithological beds, drawn upon in *Section 5.9*, are marked in red. While the estimated rates of retreat for the widely jointed sandstone are high in Figure 5.15 and Figure 5.16, the mean depth of change (solid black line) is similar at this elevation to the rest of the cliff face. This suggests that, while large events occur on this portion of the cliff face, a high proportion of small failure events, with depths < 0.06 m (below the scale of structural discontinuities described in *Section 5.9*), account for a significant proportion of total estimated erosion. While retreat rates appear broadly consistent within each lithology, this cannot be ascertained with certainty as 10% of the cliff face area is occluded during scanning (*Section 3.8*).

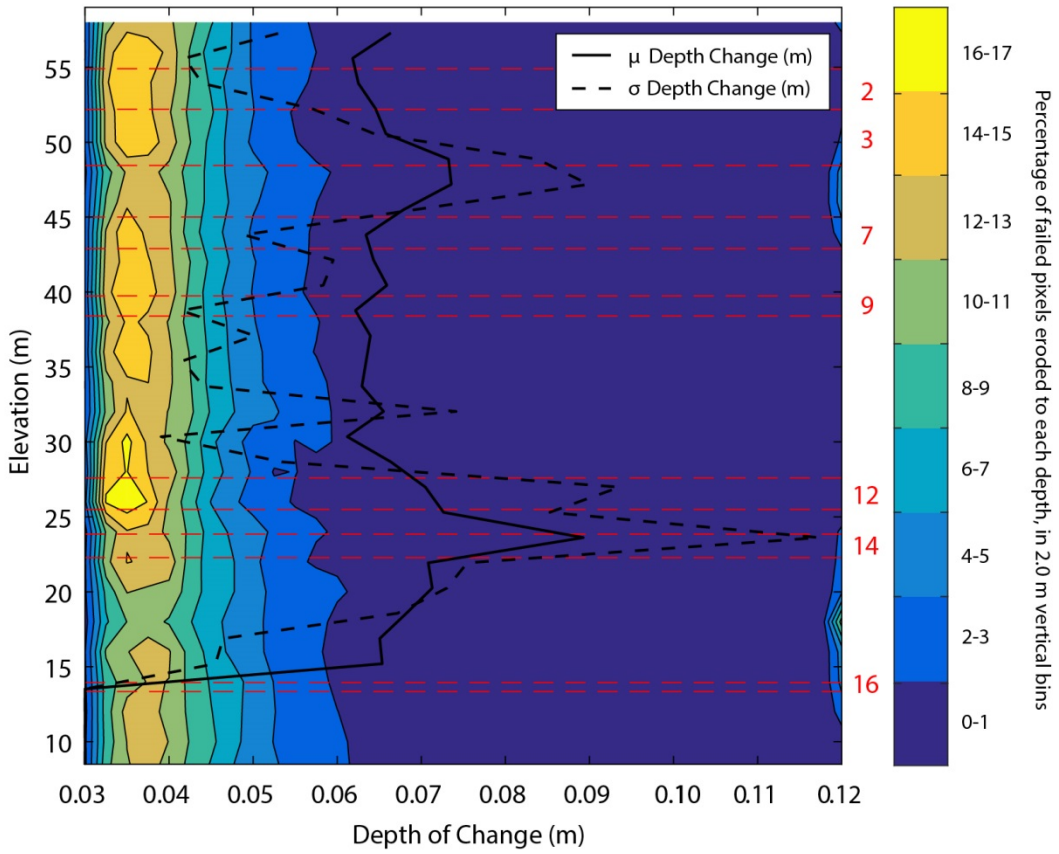

Figure 5.17: *Depth of measured change up the cliff (2 m vertical bins), with mean (μ) and standard deviation (σ) also added. Colours represent the percentage of the cliff face at each vertical bin that failed to each depth. Red lines show the elevation of exposed units examined in Sections 5.6 and 5.8.*

Although differential rates of erosion have been observed during the 10-month monitoring period, these rates must equalise over time in order to permit profile parallel retreat of the rock mass. Miller (2007) observed a reduction in overall slope between June 1994 and

May 2006, from a consistent angle of *ca.* 64° across the slope to the creation of differing angular units of the upper and lower cliff face. The elevated erosion rates monitored here at the cliff base indicate an overall steepening of the cliff profile, possibly towards an angle of repose, from 55.9° to 56.7°.

5.5 Rockfall Trajectories and Impacts

A noticeable feature of the change map in Figure 5.13 is the presence of clusters of rockfall extending up the cliff, occurring simultaneously across the upper-vertical slope. This is particularly evident for detachments that occurred from the bedded sandstone at the cliff top. Figure 5.18 illustrates this for the rockfall polygons in the sub-hourly inventory. For rockfall that occurred on 6th March (top) and 15th June (bottom), the original 3D change detections are presented, where red colours represent loss of material and blue colours represent accumulation of material. The insets show the resulting rockfall polygons as they appear in Figure 5.13. These are interpreted as rockfall paths and impact marks, reflecting the transport of material from the cliff top to the cliff toe and buttress via the concave near-vertical portion of slope. Importantly, this is not a vertical, structurally controlled feature being exploited by rockfall.

For the 6th March event, the rockfall cascades down the slope until it makes contact with the buttress. From here, much of the debris appears to have left the cliff along the edge of the buttress approximately parallel to the cliff face. The rockfall depth was 0.601 m with a volume of 0.4616 m^3. This is larger than the trajectory scars, which measured between 0.037 – 0.081 m in depth and 0.0053 – 0.0151 m^3 in volume. For the 15th June event, the rockfall also detaches material from the cliff face below on impact, culminating in the accumulation of material on top of the buttress where a transition in profile from concave to convex occurs. The rockfall depth was 1.160 m with a volume of 0.5979 m^3, whereas the trajectory scars measured between 0.033 – 0.132 m in depth and 0.0029 – 0.2659 m^3 in volume. The small scar volumes relative to the original failure volume suggest that these detachments have a negligible influence on the overall magnitude-frequency statistics in the inventory presented here.

Capturing rockfall trajectories highlights a potential use for high frequency scanning that is beyond the scope of this research. Matching trajectory scars to the original rockfall is complex when scanning an actively failing rockslope over timescales longer than a few hours. Using high frequency scanning, the scars can be matched to their original failure, providing a useful data source for empirical models of rockfall runout and rebound. Within this study, it is likely that this process has an effect on the estimation of rock face resurfacing though time, presented in *Chapter 6*, and on the area-volume relationship for measured rockfall. Prior to both analyses, therefore, these scars were manually identified and removed from the dataset.

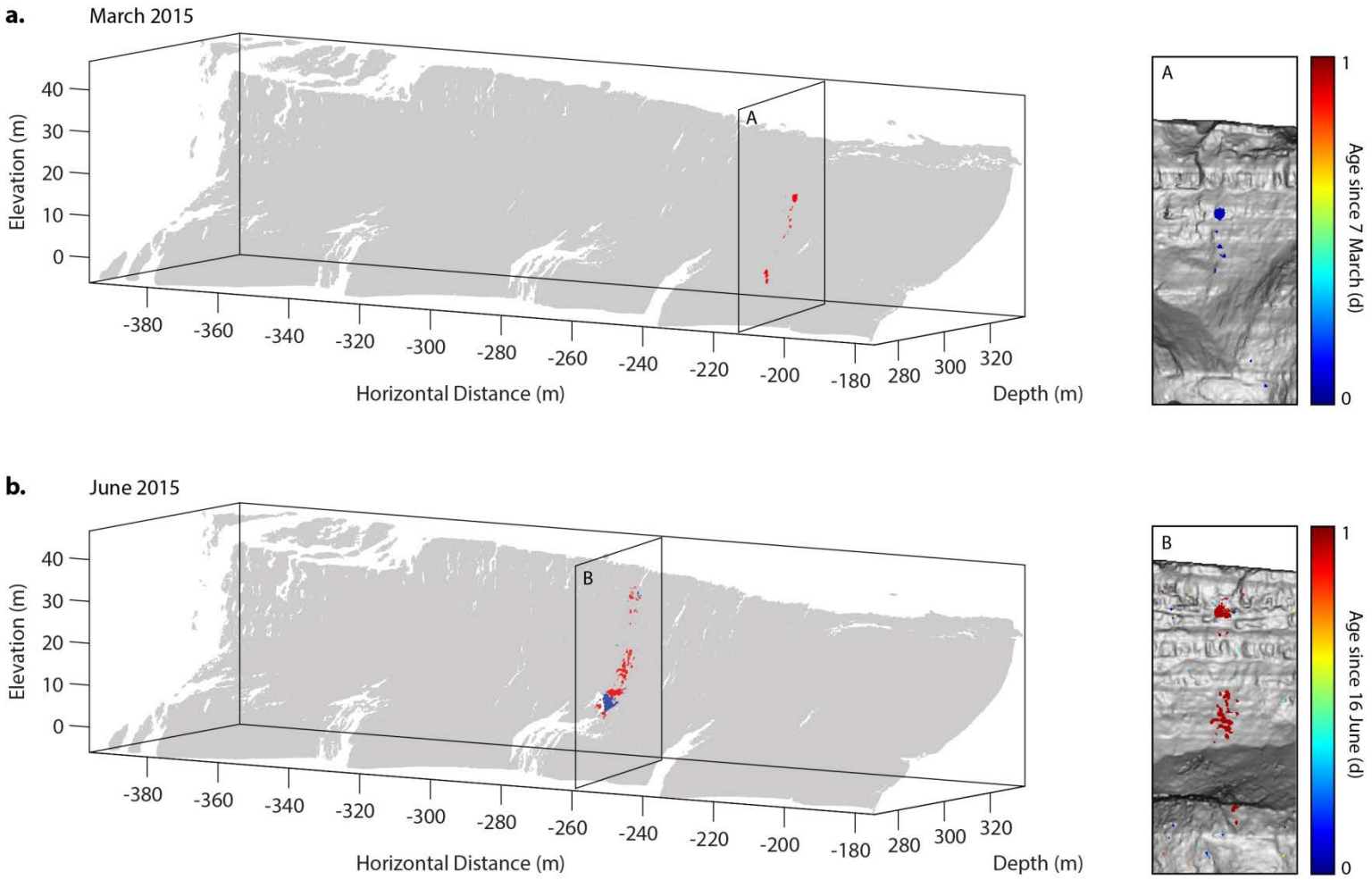

Figure 5.18 *(a) Point cloud of change showing rockfall on 6th March 2015. Inset shows the resulting polygons. (b) Point cloud of change showing rockfall on 15th June 2015. For both, the trajectory of the rockfall is identifiable as it detaches material from the concave profile below.*

5.6 Area-Volume Relationship

Empirical scaling relationships that predict the volume V of a measured landslide area A have been applied to inventories containing thousands of landslides derived from airborne or satellite imagery (Hovius *et al.*, 1997; Guzzetti *et al.*, 2009; Larsen *et al.*, 2010; Yanites *et al.*, 2010; Parker *et al.*, 2011; Li *et al.*, 2014, 2016). Such inventories are useful for quantifying the efficacy of landsliding as a means of transporting soil, rock, and associated biogeochemical constituents, such as particulate organic carbon, from and within orogens. However, these inventories are two-dimensional in nature and therefore provide no quantification of landslide depth. In order to extrapolate ground-truthed depth measurements from individual landslides to an entire inventory, scaling factors α and k are estimated from a power law between A and V that can be used to calculate total mobilised failure volume. Here, the three-dimensional change detection procedure yields measurements of both A and V that can be related using the same power-law (Equation 5.3):

$$V = kA^{\alpha} \qquad \text{[Eq. 5.3]}$$

where α is 1.152 and k is -1.265. The resulting coefficient of determination (r^2) is 0.76.

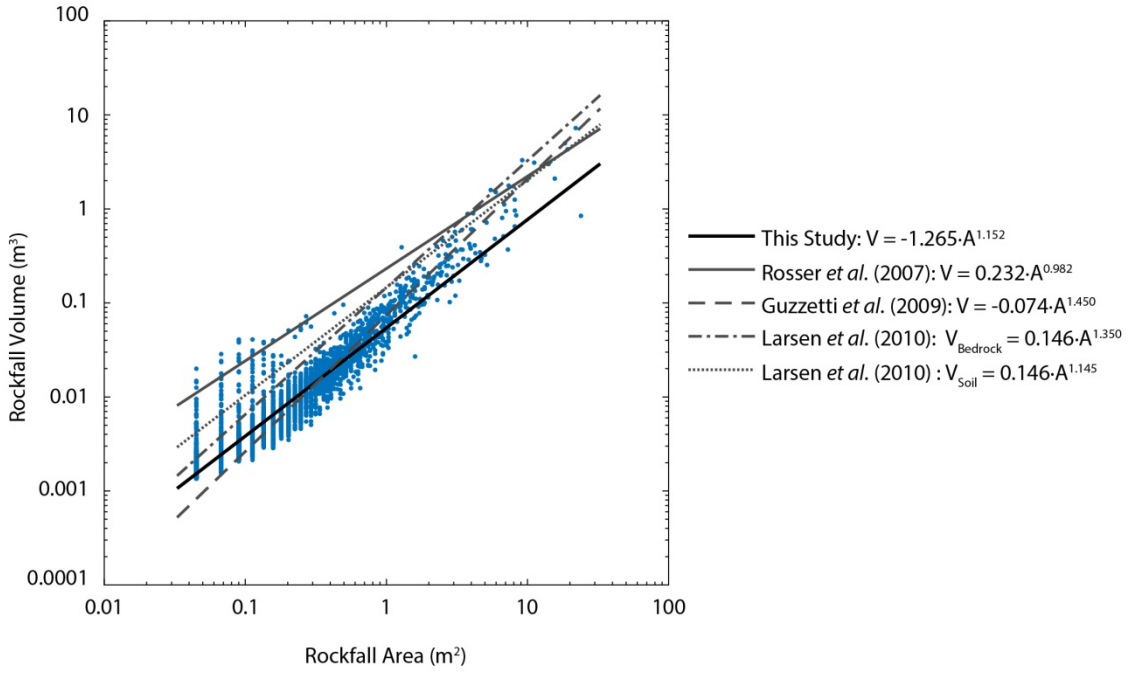

Figure 5.19: *Rockfall area-volume relationship. Vertical stripes at the lower end of the distribution reflect the 0.15 m cell size intervals.*

Equation 5.3 shows that the log of rockfall volume is *ca.* 1.152 times the log of rockfall area. This is comparable to another rockfall exponent quantified by Rosser *et al.* (2007a; Figure 5.19).

The higher exponent found here suggests that rockfall are in general deeper relative to their overall area; however, since the range of rockfall volumes used here is smaller than that used by Rosser *et al.* (2007a), it is likely that the approximate rockfall geometry is comparable. The exponent is lower than those estimated by Guzzetti *et al.* (2010) and Larsen *et al.* (2010) for landslides mapped using 2D imagery. This suggests that the underlying mechanisms of failure here are likely to relate to near-surface tensile stresses in comparison with shear stress development along deeper shear planes found in landslides. In the following section, a more thorough appraisal of rockfall shape is presented with respect to *in situ* controls on failure.

5.7 Rockfall Shape

In this section, the shape of rockfall scars is examined in order to partially constrain the influence of structural discontinuities. The shape of rockfall scars indicates the permissible kinematics of failure and also influences the likely runout of detached material. While the shape of large-scale instabilities is often characterised from LiDAR datasets (Oppikofer *et al.*, 2009; Viero *et al.*, 2010), the shape of rockfall scars is rarely quantified following visual interpretation. Shape comprises four main characteristics that include the form, roundness, irregularity and sphericity. Detailed descriptions of these measures are provided by Blott and Pye (2008). In this study, the rockfall shape is described as a tri-dimensional characteristic that comprises ratios of three orthogonal axes, interpreted as the length, breadth, and thickness of each rockfall, where length >> breadth >> thickness (Sneed and Folk, 1958; Benn and Ballatyne, 1993; Graham and Midgley, 2000; Lukas *et al.*, 2013). While rockfall geometry is considered independent of the cliff face orientation, typically although not always, depth is normal to the rock face, length is horizontal, and breadth is vertical. This method of representing the rockfall shape has traditionally been applied to the analysis of clasts shaped by glacial erosion, transportation or deposition (Barrett, 1980; Illenberger, 1991; Benn and Ballatyne, 1993, Larsen and Piotrowski, 2005). However, this method has also been used to characterise clast exposure in arid environments (Higgitt and Allison, 1999) and fluvial environments (Verrecchia *et al.*, 1997; Allan *et al.*, 2006), block geometry in rock masses (Kalenchuk *et al.*, 2006), and the reconstruction of mass-movement deposits (Šilhán and Pánek, 2010). Benn and Ballatyne (1993) used a ternary plot originally presented by Sneed and Folk (1958), and presented here in Figure 5.20 (adapted from Blott and Pye, 2008, Figure 3A). In Figure 5.20, ratios of the three axes vary linearly, resulting in a continuum of clast shapes. The ratios are as follows:

$$Left = \frac{C}{A} \qquad \text{[Eq. 5.4]}$$

$$Bottom = \frac{A - B}{A - C} \quad \text{[Eq. 5.5]}$$

$$Right = \frac{B}{A} \quad \text{[Eq. 5.6]}$$

where A, B, and C refer to the length, breadth and depth of the rockfall in size order. As shown in Figure 5.20, shapes vary between: (1) prolate spheroids with one long and two short axes, referred to here as 'rods', (2) oblate spheroids with two long axes and one short axis, referred to here as 'slabs', and (3) spheres with three equal axes, referred to here as 'cubes'.

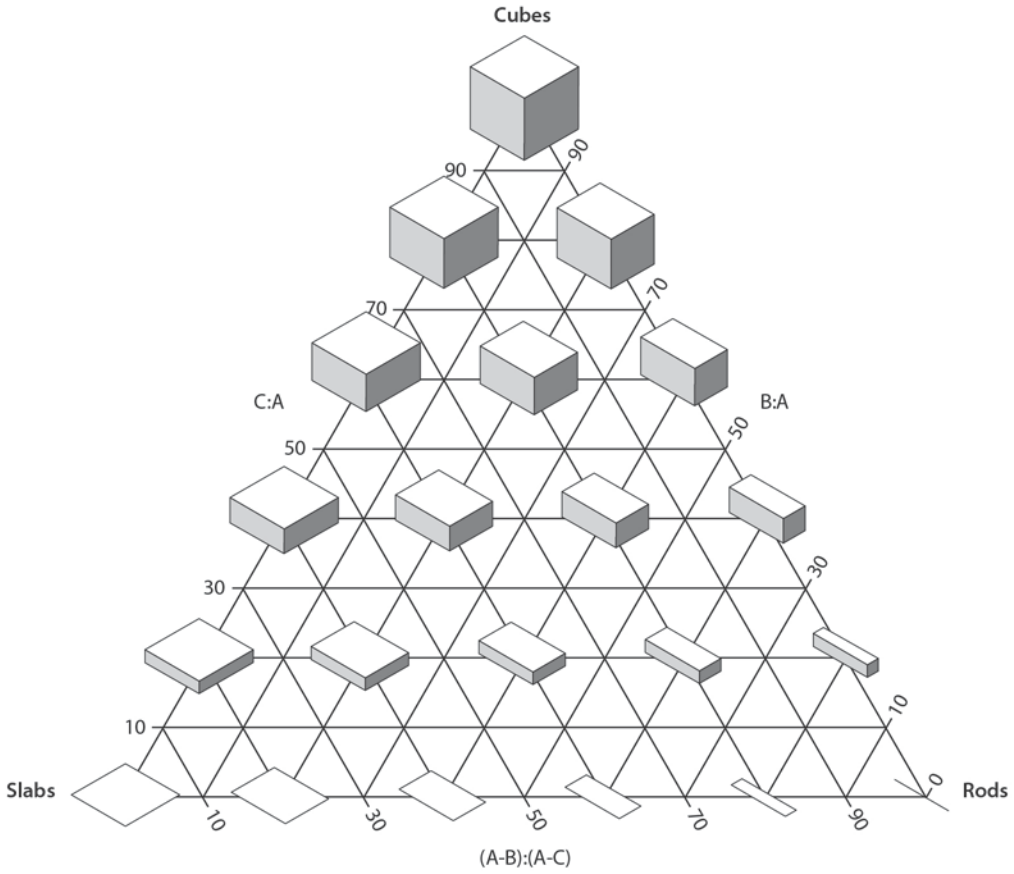

Figure 5.20: *The Sneed and Folk (1958) ternary plot, adapted and modified from Figure 3 in Blott and Pye (2008). Cubes represent shapes where all three axes lengths are similar, often determined by the joint structure. Slabs represent shapes with two long axes and one short axis. These shapes can be controlled by joint structures within the rock mass, but can also represent small failures that occur on fragmented, heavily weathered rock masses. Rods represent shapes with one long axis and two short axes. These shapes may occur along topographic edges, which may also represent inaccurate distance estimation if measured using LiDAR, or along boundaries between lithological units.*

Available packages for the creation of ternary plots draw all three axes in a consistent clockwise or anticlockwise direction. The Sneed and Folk (1958) diagram, however, arranges the left and right axes in ascending order towards the crown of the plot. Graham and Midgley (2000) presented a freely available Microsoft Excel spreadsheet that can be used to generate

these diagrams for larger datasets, avoiding the need to hand draw plots. In this study, however, over 180 000 rockfall shapes required plotting. In order to group rockfall by a specified attribute, a method was also required to provide each point on the ternary plot with a unique classified colour. A MATLAB code was therefore developed for the purpose of this research. The code modifies an existing anticlockwise function available from the MATLAB File Exchange (Sandrock, 2008). It accepts a variable used to assign individual point colours and plots the divisions in shape outlined by Sneed and Folk (1958).

In Figure 5.21, synthetic rockfall shapes are plotted to provide a general indication of the axis length ratios as they appear in the ternary plot. The ratios are provided in percentages. Axis lengths are displayed for the *A*, *B*, and *C* axes respectively and are measured in 0.15 m increments according to the cell size used in this study. As rockfall move towards the left of the plot, the *A* and *B* axes (typically the lateral and vertical extents of the rockfall) become increasingly similar. As rockfall approach the bottom-left slab zone, the *C* axis (typically scar depth into the rock face) decreases in thickness. Conversely, as the *C* axis length approaches the *A* and *B* axes, rockfall are closer to the crown of the plot and a more likely to be cubic in form.

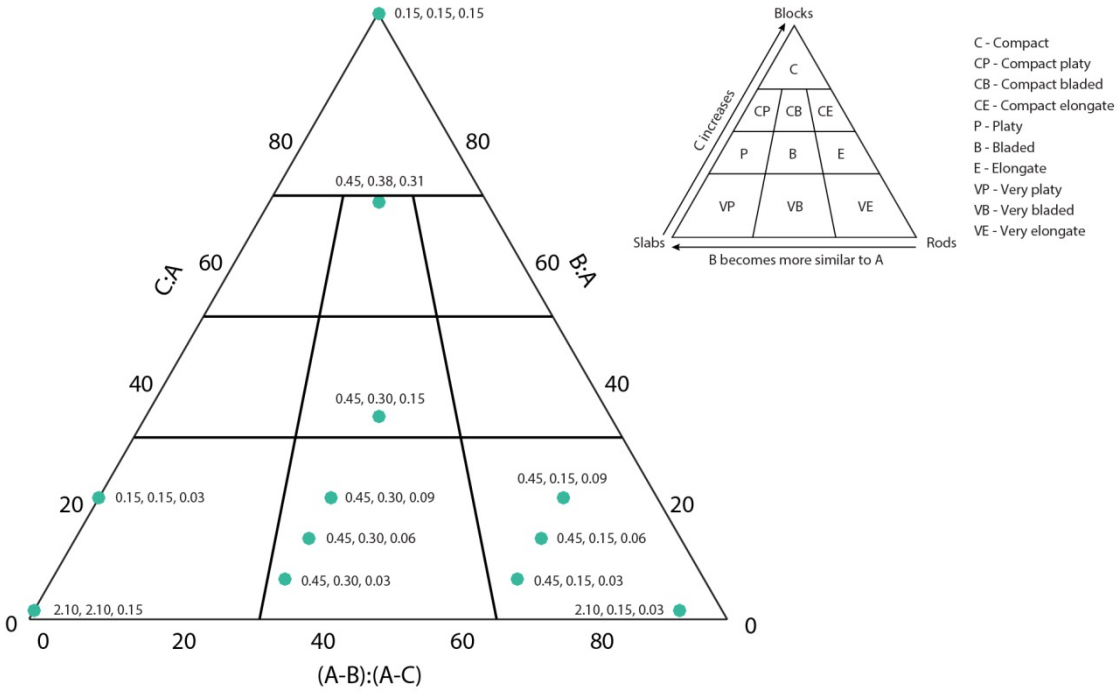

Figure 5.21: *Synthetic rockfall axes lengths plotted at 0.15 m cell size increments (A and B). Increases in C that occur with the same A:B ratio result in diagonal stripes.*

Figure 5.22 shows the rockfall shapes for the entire inventory. While rockfall shapes are distributed across the ternary plot, three distinct patterns are evident. First, there is a distinct pattern of diagonal striping across the ternary plot. These stripes reflect the resolution of the data, which is a function of pixel size and multiples thereof. It is notable that the stripes cover the entire range of values of the *C:A* ratio. From a methodological perspective, this distribution

is perhaps unsurprising. The depth estimation of rockfall, calculated in true-3D with a LoD of 0.03 m, is of a higher distance resolution than the aerial estimations that are constrained by the 0.15 m pixel size. Assuming a slab-like particle shape in which the two long axes (A and B) constitute length and breadth, and the short axis (C) is depth, this supports the hypothesis that the depth estimates can yield a full range of values at a higher precision than the major and minor axes, which are rounded to 0.15 m intervals.

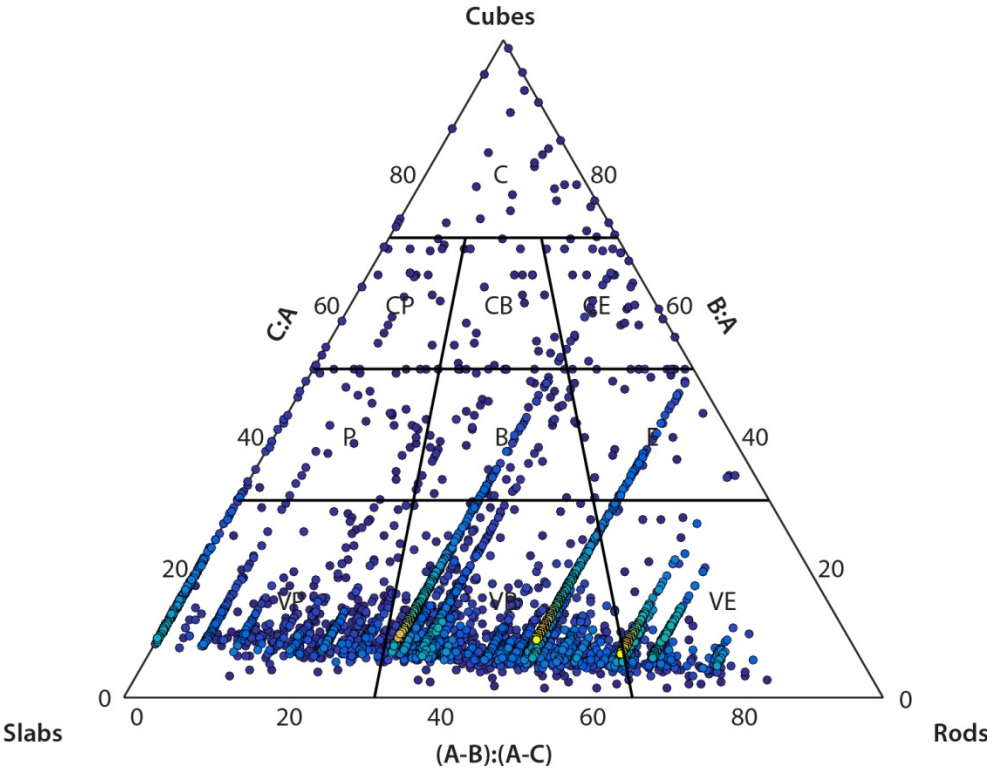

Figure 5.22: *Distribution of rockfall shapes. Rockfall are predominantly very platy and very bladed slabs. The depth of these slabs compared to the length and breadth is not small enough to distribute the shapes along the lower axis of the plot. However, some rockfall are distributed along the left axis, indicating that the length and breadth are equal. Diagonal stripes of consistent B:A ratios (but varying depths) indicate the limited variation in horizontal and vertical dimensions compared with depth.*

Second, there is a paucity of very rod-like features. From a methodological perspective, this nullifies the hypothesis that the edges of protruding blocks, which yield inconsistent range estimates and point distributions, produce vertical point clusters < -0.03 m that are incorrectly recorded as rockfall. From a kinematic perspective, confining stresses that exceed the material strength of sandstone are unlikely to permit rockfall that are deeper than they are wide and high (assuming a rod-like shape protruding into the cliff). Furthermore, assuming that a rod-like shape occurred laterally across the cliff face, this suggests that small rockfall are unlikely to occur across multiple discontinuities. Third, there is a considerable concentration of rockfall towards the base of the plot, indicating that the majority of shapes were slabs that are highly blade- or plate-like. Failures are generally wider than they are deep, with the mean shape equating to a ratio of depth to width/height of 0.156.

Figure 5.23: *Images of the cliff from top (left) to bottom (right), highlighting the units of exposed bedrock that are used to categorise rockfall shape in this section, and again in joint structure analysis in Section 5.9.*

In Figure 5.24, the rockfall shape is plotted by different beds, presented in Figure 5.22. The structure of these beds and the control that they exert upon rockfall size is presented in *Section 5.9*, below. In order to assign a mean shape for each bed, the lengths of each rockfall axis were normalised against the maximum axis length. This provided A, B and C measurements between zero and one, with A always assigned a value of one. The B and C measurements therefore represented a proportion of the maximum length that could be averaged. These averages were taken for the largest 10 rockfall from each bed (diamonds) and for all of the rockfall from each bed (circles).

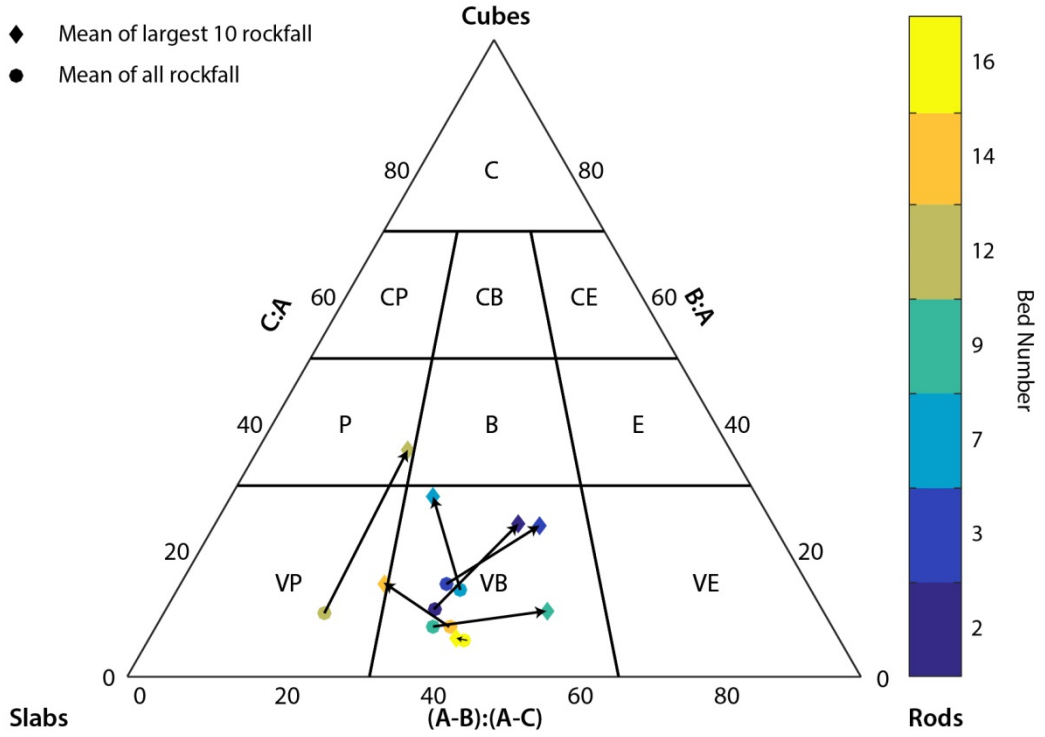

Figure 5.24: *Rockfall shape grouped by bed number and plotted as the shape of the 10 largest rockfall (diamonds), and the shape of all rockfall (circles) that occurred within each bed. For each bed, the larger the rockfall fraction, the more block-like the rockfall shapes.*

The distribution of these mean shapes mirrors the overall distribution of rockfall shapes in Figure 5.22. The very bladed form illustrates that the A axis is approximately 1.5 times the size of the B axis. This corresponds to a tendency for rockfall to be oriented horizontally across the cliff, rather than vertically, which may reflect a constraint in failure size by the depth of each bed. This is highlighted by the direction of the arrows, which shows that larger rockfall (diamonds) tend to be positioned closer to rod-like forms than the mean of all rockfall (circles). These arrows also show that, for each bed, the mean of the largest 10 rockfall is always closer to a cube-like form than the mean of all rockfall: larger rockfall are therefore always more cube-like than smaller rockfall. If the C axis is assumed to correspond to rockfall depth, this suggests that larger rockfall are deeper in proportion to their volume than smaller rockfall from the same bed.

Figure 5.25 shows the distribution of rockfall shapes for the largest 100 rockfall during the monitoring period. While there is no distinct pattern based on event size, the largest events are again clustered towards slab-like (very bladed and very platy form), with very few rockfall of any type of compact form. Figure 5.26 shows the shape of rockfall in bins between the minimum and maximum of rockfall volume. There appears to be little change in shape with the volume of rockfall. However, while the smallest rockfall, < 0.50 m^3, exhibit the greatest spread of shapes, there appears to be a gradual increase towards cube-like forms with increased volume.

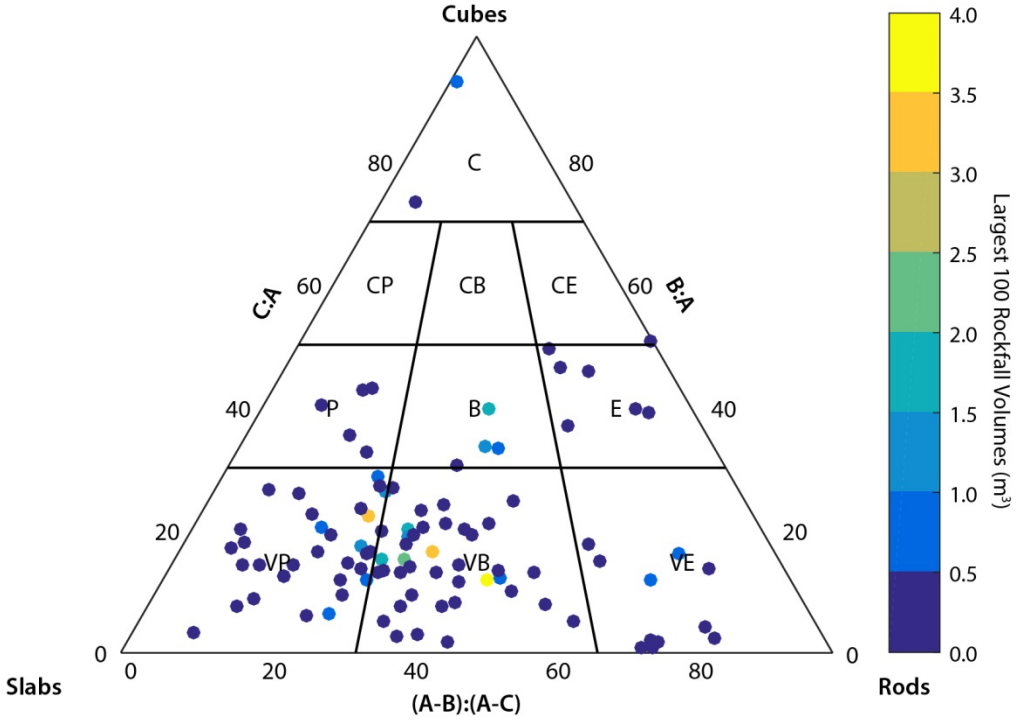

Figure 5.25: *Rockfall shapes for the largest 100 rockfall, by volume.*

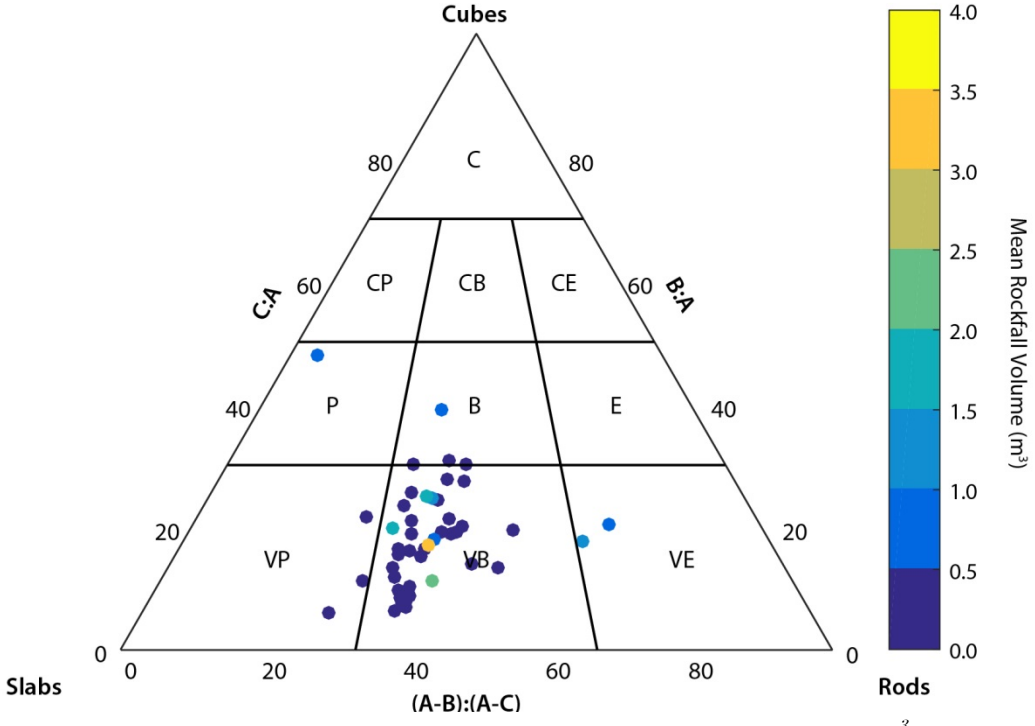

Figure 5.26: *Rockfall shape displayed as linearly spaced bins from 0.001 – 10 m^3.*

5.8 Magnitude-Frequency Distribution of Rockfall Events

To characterise the distribution of rockfall sizes sourced from the cliff face, relationships between the magnitude of events and the frequency of their occurrence within the 10-month period have been produced. A range of attributes has been used to describe the magnitude of rockfall, including the length, area, volume and, where appropriate, the number of fatalities or losses (reviewed in *Section 2.5*). Here, magnitude is described in terms of the measured rockfall volume. This removes uncertainties that propagate from modelling the volume of landslides using area-volume scaling (Li *et al.*, 2016) because the surface is measured in 3D. Unlike area, the use of volume enables a more accurate estimation of erosion rates and a better understanding of the forces required to mobilise rockfall of varying size.

The magnitude-frequency relationship can be reported using either cumulative or non-cumulative probability density functions that are derived by plotting data as histograms with log volume bin widths. Non-cumulative distributions of logarithmic volumes allow a linear trend to be observed (Lim *et al.*, 2010). Published examples of such distributions tend to report the frequency of rockfall events in a variety of ways, with no single metric identified as being more, or less, useful. In this study, therefore, frequency is reported in three different ways, in order to provide a comprehensive analysis that is comparable to published examples. These are: (1) normalised rockfall frequency, (2) rockfall frequency, and (3) probability density. Based on the findings of Malamud *et al.* (2004), rockfall volumes were divided into logarithmically spaced bins, and the number of rockfall was computed for each. In order to examine the timescales over which rockfall size distributions vary, magnitude-frequency analysis was undertaken using the 11 inventories derived for increasingly large survey epochs. To enable comparison, the logarithmically spaced bins were consistent between each T_{int} dataset. The normalised rockfall frequency $f(V_R)$ for each bin was calculated as:

$$f(V_R) = \frac{\delta N_R}{\max \delta N_R} \quad \text{[Eq. 5.7]}$$

where δN_R is the number of rockfall with volumes that fall within each bin and max δN_R is the maximum frequency recorded across all bins. By normalising the frequency values, the offset between distributions on the magnitude-frequency plot is reduced, but the differences between the exponents derived for each inventory (see Equation 5.10) are preserved. The second method draws upon the actual frequency of rockfall that fall in each bin, whereby:

$$f(V_R) = \delta N_R \quad \text{[Eq. 5.8]}$$

The final method calculates frequency density in accordance with Malamud *et al.* (2004):

$$f(V_R) = \frac{\delta N_R}{\delta V_R} \quad \text{[Eq. 5.9]}$$

where δV_R is the bin width, measured in m^3. For all three descriptors of frequency, the distribution of rockfall volume frequency is typically modelled using least-squares regression on logarithmically transformed frequency density and magnitude data. As discussed by Barlow *et al.* (2012), least squares regression may be inaccurate at the tails of power law distributed data due to this log-log transformation, which results in uneven error distribution within the tails. However, least-squares regression yields identical models to the alternative maximum likelihood estimator method, provided points from the mid-range of the data are included (Goldstein *et al.* (2004). As with the rockfall inventory presented by Barlow *et al.* (2012), the data presented here is considered complete though the mid-range and adheres to negative power-law scaling that is modelled by:

$$f(V_R) = sV_R^{-\beta} \quad \text{[Eq. 5.10]}$$

where V_R is the rockfall magnitude, s is the intercept and β is the exponent (Brunetti *et al.*, 2009). β indicates the relative frequency of different rockfall volumes, analogous to the ratio of small to medium to large rockfall. By plotting this distribution on a plot of log-volume against log-frequency, Equation 5.11 represents the straight-line form of Equation 5.10:

$$\log f(V_R) = \log s - \beta \log V_R \quad \text{[Eq. 5.11]}$$

The production of these plots yields a number of important attributes. The exponents β reflects the overall size distribution of events. For rockfall within the same volume ranges, such as in this study, higher exponents (manifest as steeper gradients in log-log space) reflect an increase in the proportion of small events relative to large events. Conversely, a lower exponent indicates that large rockfall account for a higher proportion of material loss. The total volume of eroded material for each inventory can be found by integrating the observed power law, such that the area under each curve represents the total volume lost. Many distributions are characterised by a 'rollover' in the frequency density of the smallest events, where a deviation below the predicted trend is apparent (reviewed in *Section 2.5*). Explanations for this have been both physical and methodological. However, since the minimum detected rockfall size here is above a measured level of detection, under-representation of the smallest events due to methodological error is considered unlikely.

Figure 5.27a shows a negative power law-scaling distribution that is characteristic of published magnitude-frequency relationships. The volume data are above an imposed size threshold, between the minimum detected volume, 0.0014 m^3, which is larger than the minimum detectable volume of a single cell (6×10^{-4} m^3), and the maximum detected volume, 7.2536 m^3. While the smallest failure volumes are consistent with previous studies undertaken in this setting, the maximum rockfall volume is lower than, for example, 12.73 m^3 (Vann Jones *et al.*, 2015), 200.4 m^3 (Rosser *et al.*, 2005), and 2 614.88 m^3 (Lim *et al.*, 2010; Barlow *et al.*, 2012; Rosser *et al.*, 2013), as a function of the events that occurred during the period of monitoring.

As the T_{int} decreases from 90 d to < 1 h, the exponent increases from 0.663 to 1.311 (see Appendix A). This indicates that small rockfall represent a greater proportion of the inventory when monitored at low T_{int}, contributing more towards the overall volume of detached material. Uncertainty in volume estimates is highest for small rockfall events (*Section 5.3*); Figure 5.27a therefore explains the large uncertainty resulting from a predominance of small rockfall in the cumulative volume estimates acquired using low T_{int} monitoring.

The different distributions are also characterised by rollovers of varying intensity and direction. For the 90 d dataset, a rollover begins to develop at *ca.* 0.010 m^3 and results in a decreased proportion of measured rockfall events below this volume relative to power-law behaviour (straight line, no rollover). As T_{int} increases, the rollover becomes less defined as a parabolic shape and the volume at which it becomes discernible from power law behaviour (i.e. the point at which it deviates from a straight line) reduces (*ca.* 0.005 m^3 for 7 d – 30 d). For high frequency monitoring datasets, this rollover appears to invert into an anti-rollover form, indicating an increased proportion of small events at these scan intervals as compared to what would be expected for power law behaviour (for example, T_{int} = 3 and 6 h). The manner in which the form of these curves change with T_{int} is, however, more complex (Figure 5.27b).

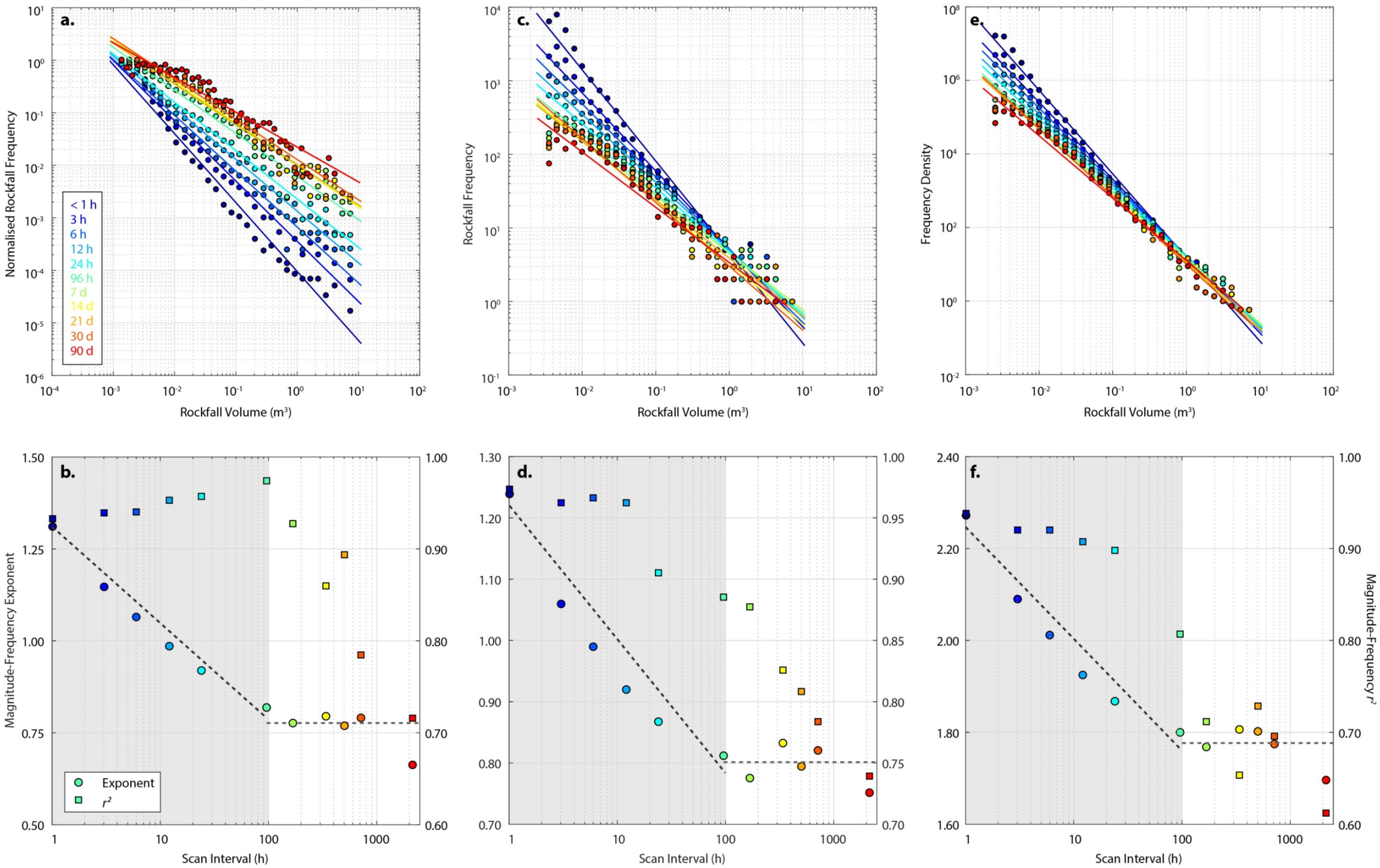

Figure 5.27: *(a) Magnitude-frequency distribution by scan interval, where frequency is measured as the number of rockfall in each volumetric bin, normalised by the maximum-recorded frequency for that scan interval. A steeper exponent for high frequency monitoring < 7 d indicates that a higher proportion of small rockfall are detected, which are not captured over larger scan intervals. A shift from a rollover distribution over long scan intervals (signifying the underrepresentation of small rockfall due to superimposition) to an anti-rollover distribution (signifying an increasingly high proportion of smaller and smaller events) is evident. (b) The overall r^2 values of each distribution are high, but these decrease with scan intervals > 96 h as more large rockfall are detected. Below 4 – 7 d, more frequent scanning increases the magnitude frequency exponent, i.e. the proportion of small rockfall. This pattern does not continue for scan intervals > 7 d. (c) Magnitude-frequency distribution by scan interval, using the frequency of rockfall in each volumetric bin. A similar pattern to (a) is shown. (d) A decrease in magnitude exponent is again evident between 1 h and 4 d – 7 d. (e) Magnitude-frequency distribution by scan interval, using the frequency density of rockfall in each volumetric bin. (f) Again, an increase in scan frequency yields a higher proportion of small rockfall events, for intervals below 4 d – 7 d.*

Figure 5.27b shows the decrease in the absolute exponent with an increase in T_{int}, as well as the overall decrease in the coefficient of determination of the regression. While a linear decrease in the power law exponent is observed for (log) T_{int} between $<$ 1 h and approximately 96 h (4 d) to 168 h (7 d), this decrease levels off between 7 d and 90 d. This suggests that below approximately 4 – 7 d, more frequent monitoring captures a higher proportion of small rockfall adhering to the premise that *the more you look the more you see*, but for larger values of T_{int} ($>$ 4 – 7 d), here measured at T_{int} = 14 d, 21 d, 30 d, and 90 d, all T_{int} capture an effectively identical rockfall size distribution. Three interesting observations arise: first, while an increasingly short value of T_{int} shows more and more smaller rockfall are detected, there must be a physical limit on the number of smaller fragments that can make up a 'single large rockfall'; rockfall deposits are not composed of just fines. As such, it would be expected that with hour to minute to second resolution monitoring, the relationship between the increasing proportion of small rockfall and T_{int} would reduce and perhaps plateau, thereby matching these findings with field observations of rockfall collapsing as large discrete blocks as seen in various videos of rock slope collapse, which are now available online. Second, the change in behaviour at 4 to 7 d is indicative of the degree to which this rock mass fragments during periods of instability, and we would expect in some instances, perhaps in massive rock masses that do not undergo fragmentation during collapse, such as in Yosemite National Park (Stock *et al.*, 2011), not to exhibit such behaviour. This inflexion may occur at different values of T_{int} in different settings, and could be a valuable comparative measure to indicate the manner in which rockfall fail and evolve. The results are reassuring in that the size distribution of rockfall detected over 90 d intervals are broadly identical to those captured at 4 d to 7 d intervals, and as such longer survey epochs give a good estimation of rockfall magnitude-frequency relations at a wide range of time scales. Such results may be useful for capturing erosion rates or seasonal fluctuations in rates of activity, but are however not suited to capturing the mechanics of how rockfall fail, or how rockfall distributions reflect shorter term forcing, such as single storm events. Finally, the change in behaviour may also reflect two different process domains experienced during rockfall development. First, the internal deformation experienced during progressive failure, whereby the failing mass is collapsing and fragmenting under its own weight. Second, the externally driven loss of material from the rock face that exploits previously destabilised rock blocks (for example, by energetic weather and seismic conditions), whereby forcing magnitude is essentially independent of the resulting rockfall volume.

Figure 5.27c represents the magnitude-frequency distribution for each monitoring interval, with rockfall frequency measured for each volume bin. Here, the frequency of each bin is no longer normalised. The integral of each line therefore represents the total amount of eroded material. The height of each line in Figure 5.27c reflects the disparity in total estimated volumes of each T_{int} inventory, such that lower T_{int} results in a higher estimated volume. Once more,

Figure 5.27d shows that a decrease in T_{int} below 4 – 7 d results in a higher proportion of small rockfall events. This pattern does not continue beyond 7 d, and the frequency distribution of rockfall sizes remains the same.

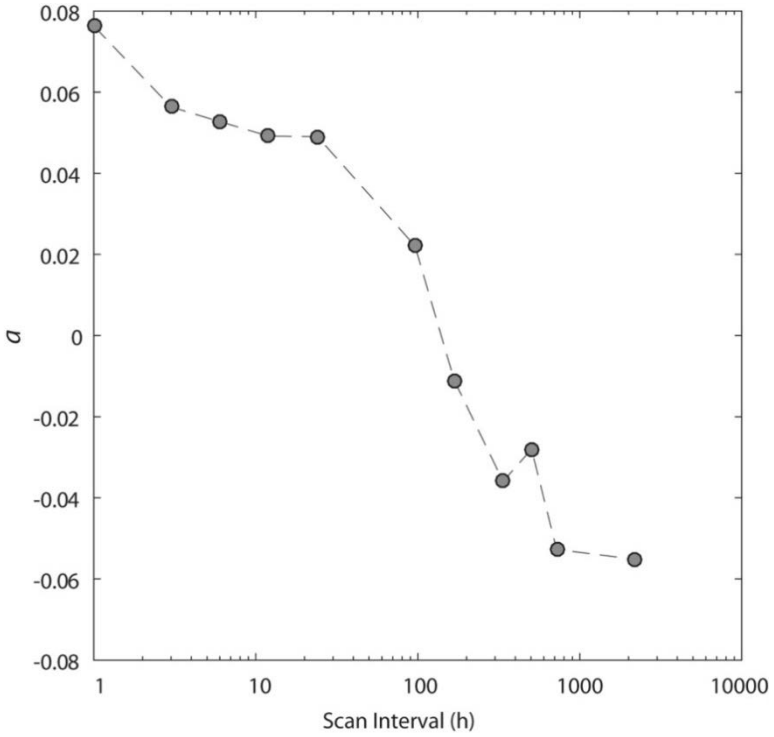

Figure 5.28: *The intensity and direction of the rollover in Figure 5.27, plotted against scan interval. An anti-rollover is indicated by $a > 0$, whereas $a < 0$ indicates a rollover. As scan interval (T_{int}) increases, the distribution of small rockfall volumes shifts from an anti-rollover to a rollover effect. The value of T_{int} that marks the boundary between anti-rollover and rollover, i.e. $a = 0$, is 106 h.*

The final magnitude-frequency relationship (Figure 5.27e) draws on the frequency density plots used by Malamud *et al.* (2004; Equation 5.9). In this plot, the rollovers are less observable than for the original frequency data in Figure 5.27a. This is because the total number of measured rockfall δN_R is normalised by the bin width δV_R. High frequencies attributed to small rockfall volumes are normalised using small bin widths, therefore appearing as a higher frequency density relative to larger rockfall. However, the exponents created using this procedure fall within the range of exponents in published non-cumulative distributions, from *ca.* 1.0 to *ca.* 2.0 (Figure 5.27f).

A number of methods exist to characterise the rollover observed in non-cumulative magnitude-frequency distributions. Malamud *et al.* (2004) fitted an inverse Gamma distribution to landslide area data that, unlike two-parameter Gamma distributions, includes a third parameter to control the exponential decay of small event magnitudes. Here, for each distribution, the volume below which the measured frequencies fall consistently below the fitted power law (for a rollover), or above the power law (for an anti-rollover) was identified. As a

simple measure of the power law, a 2nd order polynomial of the form $f(x) = ax^2 + bx + c$ was fitted to the logarithm of these volumes. Here, the magnitude of the leading coefficient a controls the curvature of the rollover. The sign determines the direction of the rollover, such that positive values indicate an upward trend on the magnitude-frequency plot (anti-rollover), whereas negative values indicate a downward trend (rollover). The value of a is plotted against the T_{int} of monitoring in Figure 5.28. For T_{int} less than 96 h (four days), positive a values reflect an anti-rollover that decreases in intensity with increasing T_{int}. For $T_{int} > 7$ d, negative a values reflect the presence of a rollover that increases in intensity at longer T_{int}. The T_{int} that intercepts $a = 0$, marking the transition from rollover to anti-rollover, is 106 h.

5.9 Structural Controls on Rockfall Occurrence

The previous section has indicated that the role of fragmentation of the failing mass is vital in defining the magnitude and frequency distribution of rockfall over short timescales. Wider literature has suggested the critical role of rock mass structure, and notably pre-existing joint structures, in defining both block geometry and size, and failure mode. In this section, emphasis is placed upon deriving a detailed quantitative appraisal of the geometry of cliff face planar surfaces (for example, the character of the cliff face source material). This is based upon the hypothesis that the exposed jointing on the rock face defines what has or what could fall from the cliff, and is broadly representative of the wider global rock mass structure for each lithological band. Given that the previous analysis implies fragmentation, the similarity between rockfall geometry and the structure of the source material will therefore be assessed, both in terms of absolute length scale but also in terms of visible persistence of discontinuities and rockfall distributions, to explain the degree to which joints relative to fragmentation of intact rock may define rockfall size.

Discontinuities are joints and planes defined by physical interruptions within a rock mass. They exhibit lower tensile strengths adjacent to, and shear strengths along, the discontinuity relative to surrounding intact material (Assali *et al.*, 2014). Since most large rockslides can creep and/or fail along such structures (Varnes, 1978; Agliardi *et al.*, 2001; Jaboyedoff *et al.*, 2009), and the intersection of discontinuities defines both (rockfall) block sizes and possible failure kinematics, the identification and description of discontinuity sets is a crucial first phase in assessing rock slope stability. Although discontinuities can be measured by hand in the field, TLS can provide more representative samples of the rock face that are not restricted to the accessible base of the slope, and so provide more accurate samples for orientation measurements (Slob *et al.*, 2004; Assali *et al.*, 2014). Sturzenegger and Stead (2009b) found good agreement between field measurements and TLS-derived dip and dip directions. Residuals of 4° and 8° respectively also illustrated that higher residuals stemmed from inherent

differences in the scale over which TLS and compass clinometers operate, especially when measuring wavy or curved yet persistent discontinuities. One challenge remains with both approaches, however, as they can only measure the persistent exposed surfaces of joints, which may either be weathered, altered by surface processes, or by chance may not represent the full set of jointing that conditions a rock mass for failure.

In order to extract the dip and dip directions of discontinuities, Slob *et al.* (2002) computed the Delaunay triangulation of the point cloud and calculated the cross product of two edges for each triangle in the mesh. The corresponding poles of the triangles were plotted on a stereonet and a kernel density estimated to distinguish sets of discontinuities. A similar approach was adopted by Gigli and Casagli (2011) and Riquelme *et al.* (2014), which instead used the raw point cloud data to reduce the potential for small features to be neglected and for distorted polygonal surfaces to arise from complex surfaces (Gigli and Casagli, 2011). In order to analyse the impact of point spacing on the interpretation of discontinuities, Assali *et al.* (2014) plotted the orientation of discontinuities using six different resolutions, between 0.01 m and 0.50 m point spacing. Smaller clusters of plane orientations were missed at 0.50 m resolution; nevertheless, despite some variation, 0.01 m, 0.02 m, 0.05 m and 0.10 m point spacings produced similar stereoplots. Downsampling strategies, such as the reduction of a point cloud from 2 cm to 5 cm point spacing, still produced comparable results while reducing the dataset to almost a sixth of its original size.

In order to assess the influence of structural controls on the size distribution of rockfall in this study, the open source CloudCompare plug-in *Facets* was used to derive the horizontal and vertical width of visually persistent exposed planar discontinuity surfaces ('facets') across the rock surface (Dewez *et al.*, 2016). The term 'facets' is used herein to describe the extracted discontinuities, while acknowledging that the joints that separate contiguous discontinuities may be too subtle for identification by point cloud data alone. This plug-in performs planar 'facet' extraction using a Fast Marching algorithm to sub-divide the point cloud. Based on a co-planarity criterion, defined as the maximum tolerable point-to-plane distance, adjacent voxels are merged and a set of planar facets is produced, with each defined by a centroid, normal vector, estimated precision and contour. As discussed in *Section 3.3*, East Cliff comprises a number of sub-horizontal sandstone beds, with varying siltstone interbedding. As a result, no single co-planarity criterion could be used to extract facets across the entire cliff face. An initial approach was to divide the cliff face, in raster form, into exposures of separate lithologies (Figure 5.29). This division was prepared by collecting a series of images from the foreshore (using a 30.4 MP Canon 5D Mark IV with a 300 mm f/2.8L telephoto lens) and merging these images into a single transect image up the cliff while correcting for geometric distortion. To orthorectify the imagery, a high resolution TLS point cloud was acquired from the foreshore to minimise small scale occlusions on the rockface due to view angle. The resulting point cloud

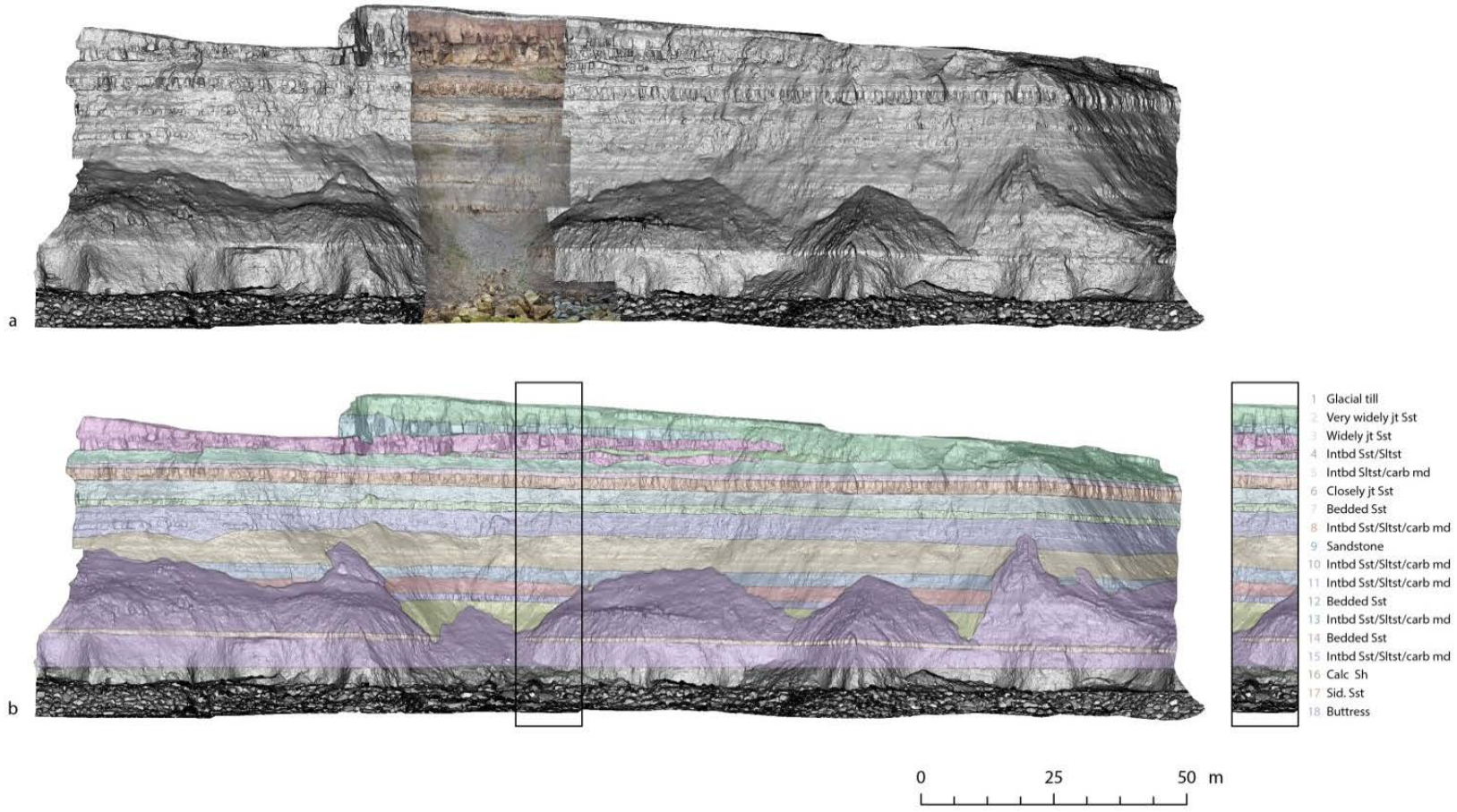

Figure 5.29: *(a) 0.03 m slope model of East Cliff and 0.006 m RGB image used to identify the lithological units.. (b) Lithological units identified across the rock face. These are numbered from 01 at the top of the cliff (glacial till) to the buttress at the base of the cliff. The properties of these units are described in Table 5.8.*

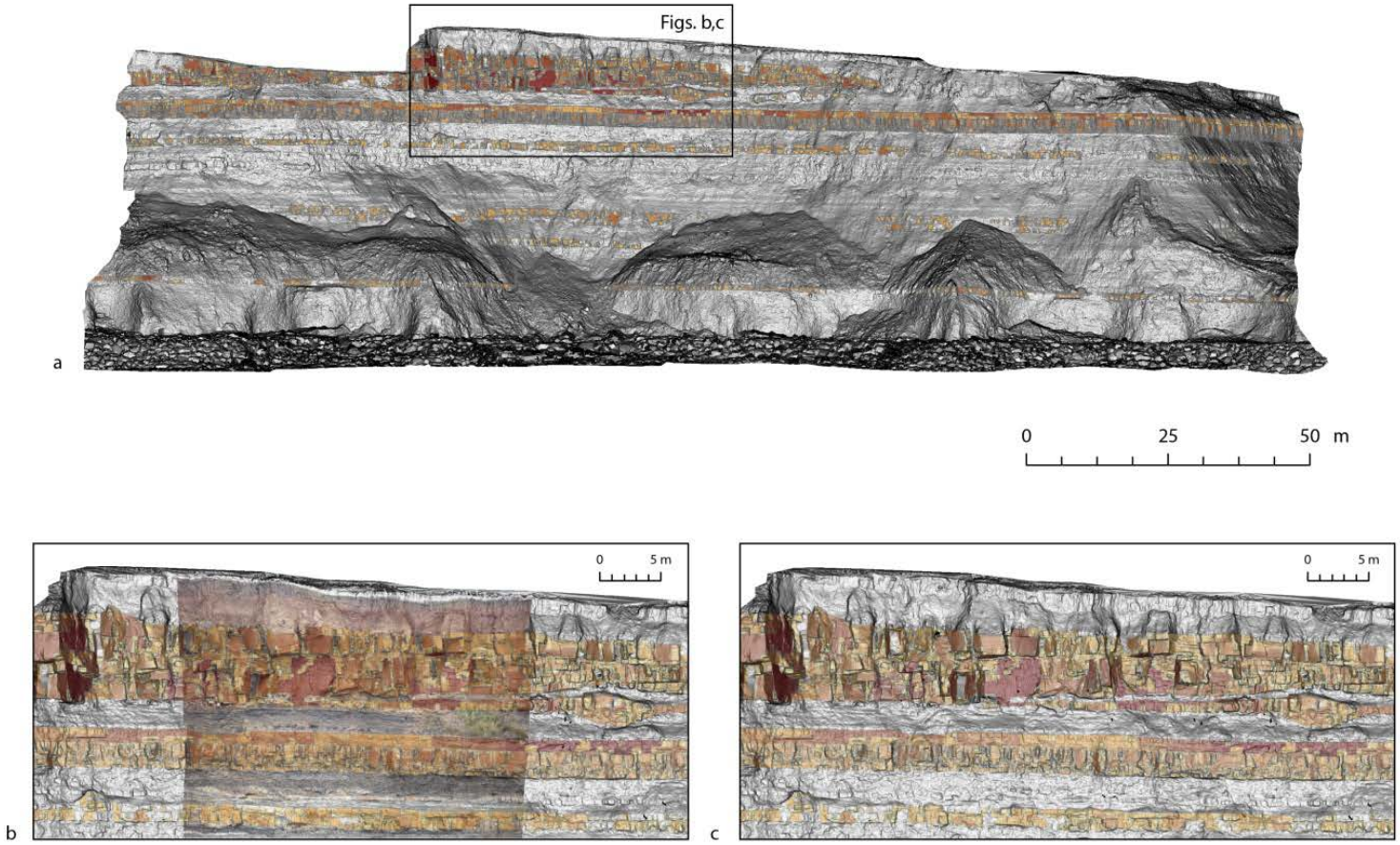

Figure 5.30: *(a) Facets for the 7 exposed beds, coloured by facet width (darker colours = greater width). After exporting from CloudCompare, these facets were compared against the slope model and image in Figure 5.33a. (b) Zoomed view of facets at the cliff top draped over the slope model and RGB image,.(c) Zoomed view of facets at the cliff top draped over the slope model.*

was resampled to a point spacing of 0.025 m, within the range of points spacings described by Assali *et al.* (2014), and used to create an 0.030 m slope model. The resulting image was manually orthorectified in ArcMap, providing a pixel resolution of *ca.* 0.006 m across the cliff.

Using a combination of the transect image and slope model, the different lithologies in Figure 5.29 were mapped. Seven sandstone and interbedded sandstone beds in which rock structure was visible were delineated, and these were used to crop the 0.025 m point cloud data as .dxf polygons in RiSCAN PRO. The 'Facets' plug-in was applied to the nine separate point clouds and the facet polygons exported as .shp files. These were subsequently validated against the slope model and transect image in ArcMap (Figure 5.30). Initially, the imported facets appeared to have merged across multiple planes on the surface. In these instances, the parameters in facets were refined to improve the surface discrimination, which tended to include a reduced point-to-plane threshold. Figure 5.31 shows an example of the facet polygons, extracted for the widely jointed sandstone of bed 2 at the top of the cliff.

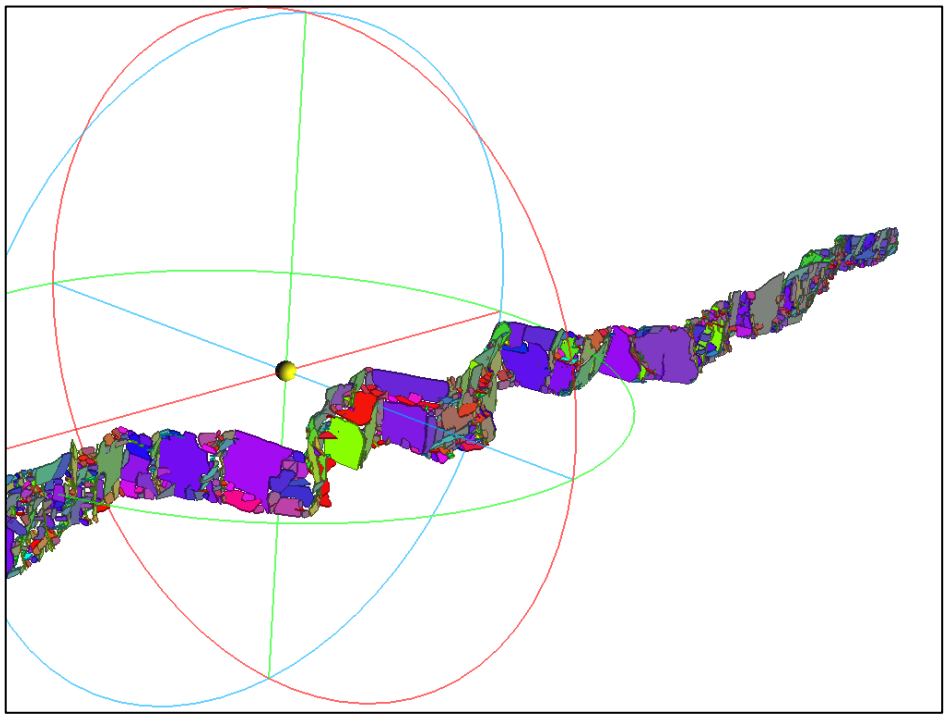

Figure 5.31: *Example of 3D facets in CloudCompare. These are shown for bed 2 at the cliff top, which is also shown in 2D form in Figure 5.34, across 35 m of the cliff face.*

Each lithology was assigned a bed number from 1-18 running from the top of the cliff to the bottom. Figure 5.32 shows the distribution of bed depths and the facet density, measured as the number of facets per square metre. Facet statistics reflect the characteristics of individual beds, rather than position of the bed or order of stacking of the beds within the rockface. Bed depths were measured using ten evenly spaced transects across the cliff face. The mean, median and standard deviation of facet width and height is recorded for each bed. The widely jointed sandstone beds at the cliff top yielded both the largest facet width and the largest facet height, reaffirming the success of this approach in quantifying the planarity of the cliff surface.

Table 5.4: *Geometric properties of each lithology and its facets. Bed depth is presented as the mean of ten vertical profiles drawn at fixed intervals across each bed. The area of each bed is estimated without the areas of occlusion of the lighthouse scans, outlined in Chapter 3. The average statistics of facet width and facet height, both of which are measured in 3D, show that the largest facets occur in the widely jointed sandstone beds (2 and 3) at the top of the cliff. The smallest are found in bed 7. These are contrasted against rockfall dimensions in order to examine the relationship between structural properties of the rock mass and its failure patterns.*

Lithology	Bed Number	Bed Depth (m)	Area (m^2)	Facet Width (m)			Facet Height (m)			Facet Density (m^{-2})
				Mean	Median	σ	Mean	Median	σ	
GlacialTill	1	4.357	684.664							
Very widely jt Sst	**2**	2.173	164.853	0.534	0.377	0.475	0.515	0.369	0.500	3.82
Widely jt Sst	**3**	3.033	491.510	0.527	0.373	0.475	0.496	0.377	0.436	3.80
Intbd Sst/Sltst	4	0.756	64.714							
Intbd Sst/Sltst	5	2.257	437.038							
Closely jt Sst	6	1.013	226.737							
Closely jt Sst	**7**	2.310	477.830	0.202	0.134	0.236	0.191	0.134	0.210	5.13
Intbd Sst/Sltst/CarbMud	8	3.231	659.308							
Closely jt Sst	**9**	1.198	277.192	0.290	0.200	0.248	0.277	0.203	0.231	3.68
Intbd Sst/Sltst/CarbMud	10	4.770	984.195							
Intbd Sst/Sltst/CarbMud	11	5.918	1.131							
Closely jt Sst	**12**	2.622	319.005	0.299	0.203	0.272	0.300	0.210	0.276	1.53
Intbd Sst/Sltst/CarbMud	13	2.730	205.831							
Closely jt Sst	**14**	1.201	69.501	0.399	0.309	0.261	0.391	0.310	0.235	1.59
Intbd Sst/Sltst/CarbMud	15	3.946	143.814							
Sid Sst	**16**	0.970	197.751	0.380	0.272	0.338	0.366	0.256	0.315	3.01
Calc Sh	17	4.460	0.438							
Buttress	18	Variable	3.057							

The resulting facet dimensions are listed in Table 5.4. The cumulative distributions of facet widths are shown in Figure 5.33a, and the cumulative distributions of facet heights in Figure 5.33b. Here, the blue lines represent beds 2 and 3 at the top of the cliff, which comprise the largest facets, whereas bed number 7 (turquoise) has the smallest facets.

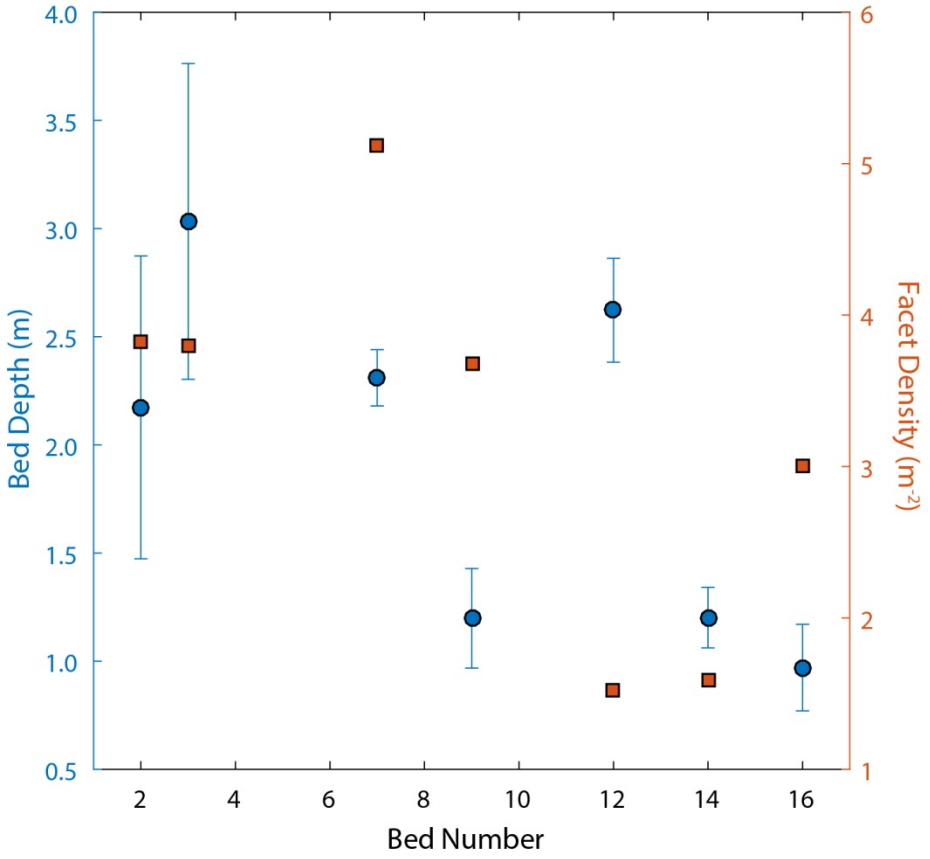

Figure 5.32: *Depth and facet density of each bed. Blue circles represent mean depth, and error bars represent the standard deviation of 10 measurements for each bed. Orange squares represent facet density, the number of facets per square metre. This is highest for the highly fragmented rock mass of bed 7.*

The relationship between average statistics of the facet dimensions and average statistics of rockfall sizes was also assessed. Rockfall were located according to the bed in which they occurred. Initially, rockfall sizes were examined using the major axis length, defined as the longest axis running though the centroid of the rasterised rockfall, and the minor axis length. The rockfall size distribution appears smaller than the facet size, pointing towards a process of rockfall occurring in fragmented or failing masses, in which jointing of the rock mass determines an upper limit of rockfall size. Images of the cliff in Figure 5.34 show that the size of rockfall is generally less than that of the joint spacing. This is presented for each of the lithological units identified in *Section 5.7*. The smallest yellow boxes indicate the minimum-recorded rockfall area in these beds, with the square root taken to estimate the edge length assuming a square shape. The suggestion from this simple visual analysis is that the largest events from a single lithological exposure reflect the dominant joint spacing, but the smaller events reflect fragmenting rockfall scars, damaged rock, or rockfall that are progressively shedding (smaller)

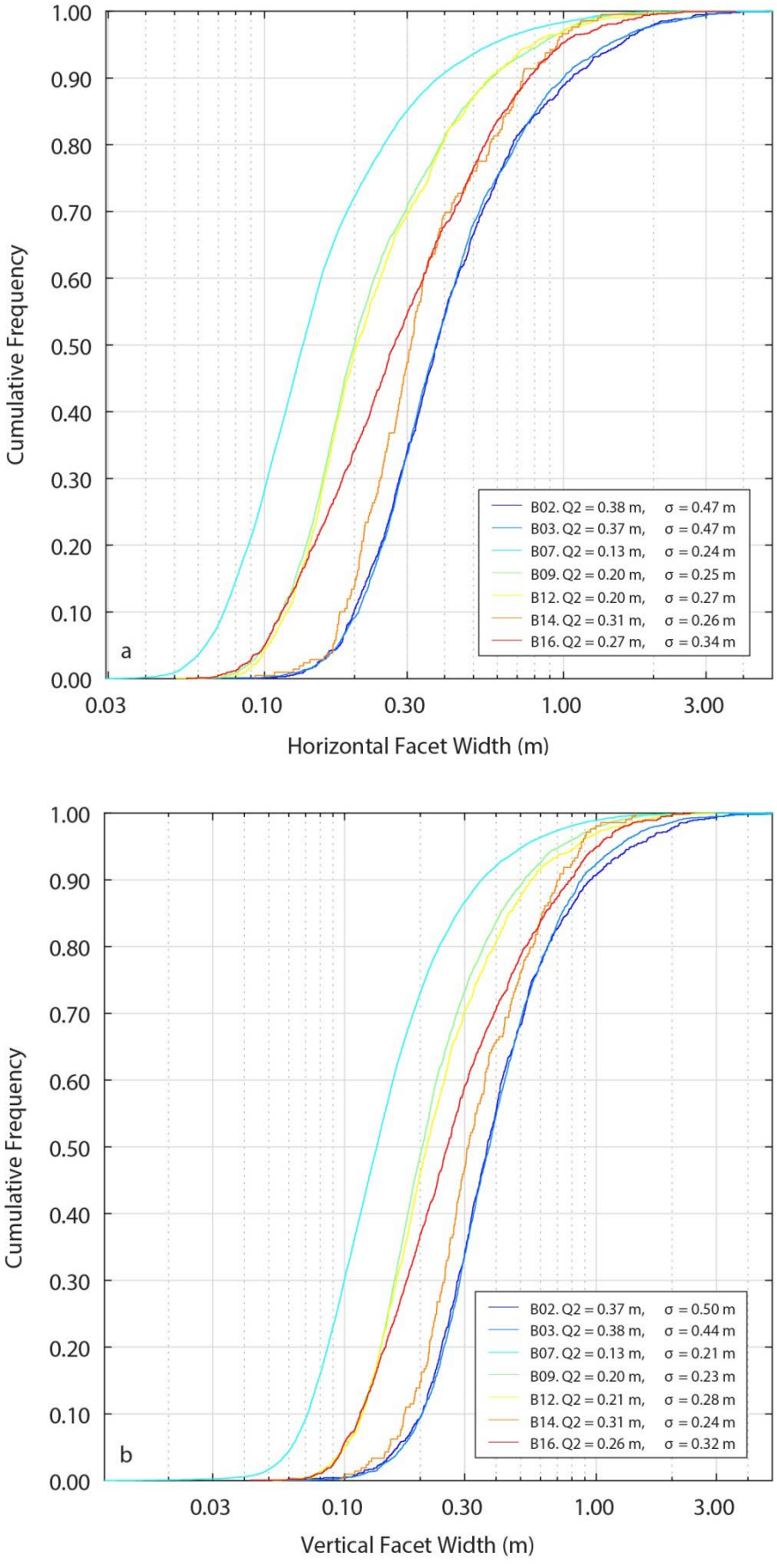

Figure 5.33: *Cumulative distribution plots for the horizontal and vertical facet lengths. Beds 2 and 3 have the largest dimensions and bed 7 the smallest.*

material though time. The mean and maximum recorded rockfall areas are also displayed. The rockfall lengths are provided in Table 5.5, along with the percentile of rockfall areas that the smallest boxes (0.2121 m edge length) represent. It is shown that the smallest rockfall areas contribute between 50% and 60% of the total recorded rockfall, supporting the hypothesis that rockfall size is generally constrained by the scale of discontinuities and that the shape may therefore be independent of discontinuity geometry, occurring as surficial slab-like detachments of damaged rock.

Table 5.5: *Rockfall edge lengths for each bed. The percentile of rockfall equal to the minimum edge length shows that between 50% and 60% of the rockfall that occur in each bed have the minimum cross-sectional area.*

Bed Number	Minimum Edge Length (m)	Mean Edge Length (m)	Maximum Edge Length (m)	Percentile of Rockfall Equal To Min. Edge Length
2	0.2121	0.3013	3.0557	57
3	0.2121	0.2696	3.0112	54
7	0.2121	0.2786	2.0730	53
9	0.2121	0.2573	1.0712	59
12	0.2121	0.2914	2.0622	58
14	0.2121	0.3068	2.8421	57
16	0.2121	0.2765	1.2639	51

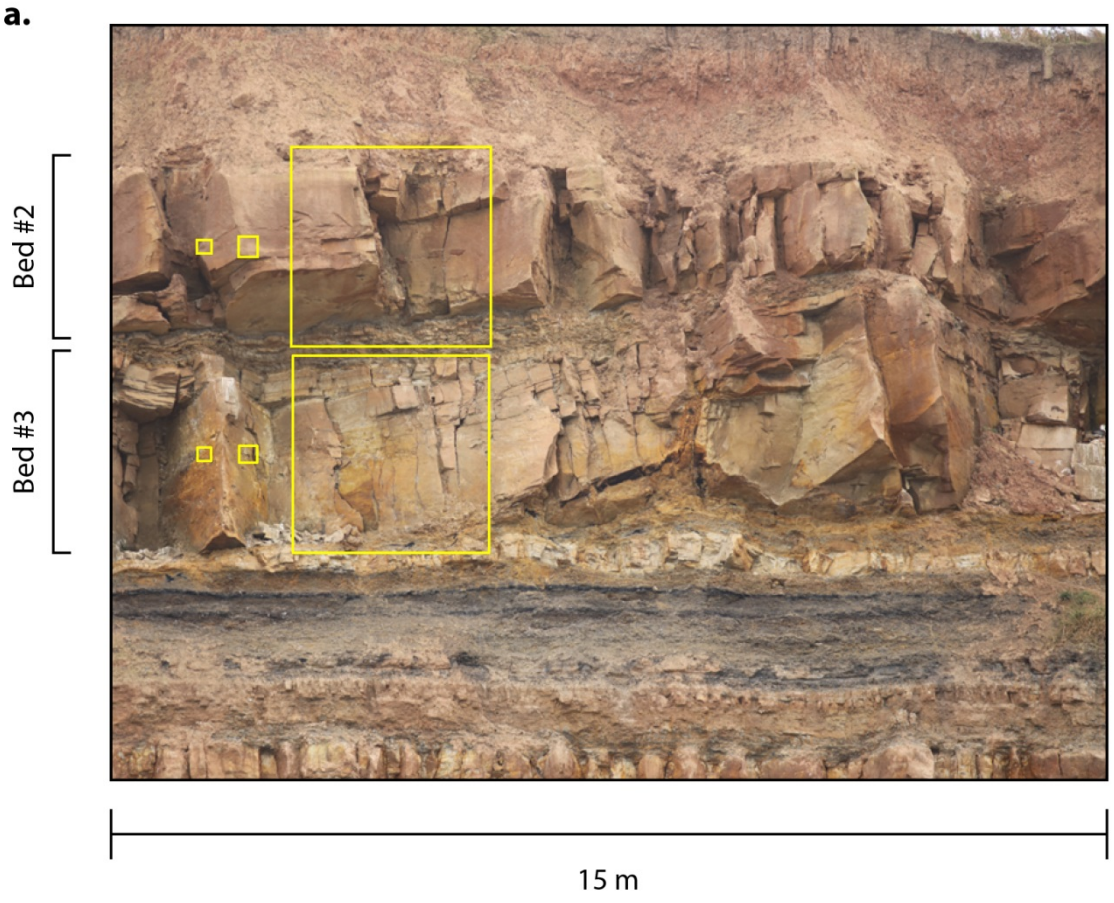

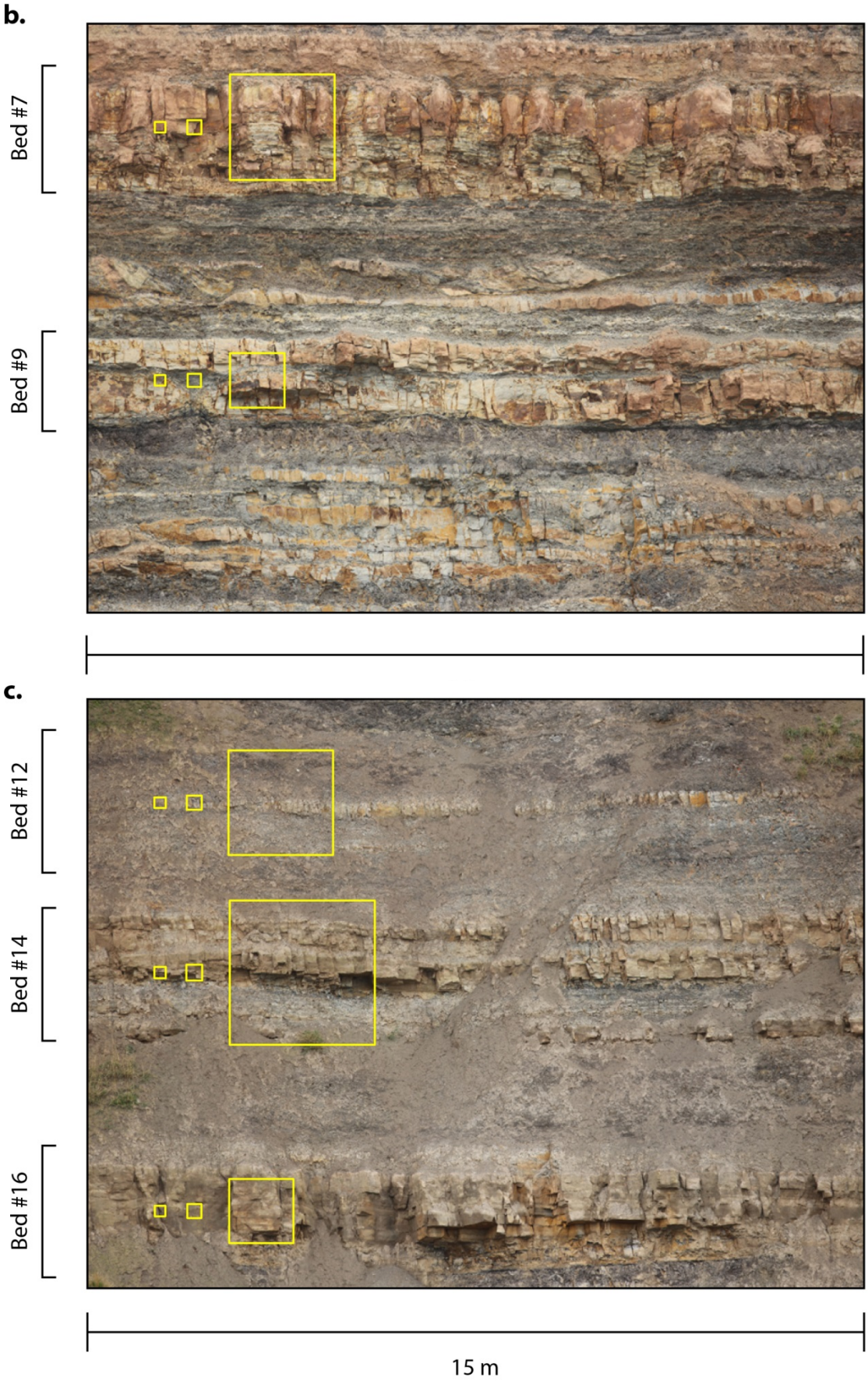

Figure 5.34: *Images of the cliff from the cliff top (a) to base (c), highlighting the unit of exposed bedrock. Squares of the minimum, mean and maximum areas are superimposed for comparison with facet size, indicating that the smallest rockfall are likely to be contained within individual facets.*

In Figure 5.35, the relations between the mean, median and standard deviation of rockfall and facets are plotted. The colour scheme used in Figure 5.33 is also applied here, with blue representing the upper sandstone beds. A line of unity is added to each plot. If, for example, the mean length of rockfall major axes was directly related to the mean horizontal facet width, points would lie on this line of unity. If, however, the mean length of rockfall major axes is below the line of unity, then events are smaller than the facet dimension in the source rock.

From plots of the mean and median distribution of rockfall and facet dimensions, the rockfall data exhibits little variability in axis length. This suggests that, for the majority of rockfall events, there is little variation in horizontal and vertical dimensions, possibly due to the fixed 0.15 m increments of cell size. For all plots, the positioning of rockfall in beds 2 and 3 (widely jointed sandstone) is furthest from the line of unity. This shows that rockfall in these beds are smallest relative to the facet size in the source rock. Notably, for each bed, the minor axis of the rockfall lies further from the line of unity than its major axis. This suggests that the minor axis of the rockfall is less dominated by joint spacing than its major axis. Assuming that the major axis represents the height of the rockfall, this assumes that the width of the rockfall is more constrained by the joint spacing than height. This implies that width may more readily relate to the ease with which a block can be kinematically released, whereas the height of the rockfall may be more related to the tensile strength of the material. However, there is a negligible increase in the mean and median rockfall axes as bed facet size increases. This is represented in Table 5.7 as the slope of an ordinary least squares regression, which is approximately zero. The lack of variation in mean and median rockfall dimensions between the different beds necessitates an alternative measure of the relation between rockfall dimensions and facet dimensions.

Table 5.6: *r^2 values of the least-squares regressions shown in Figure 5.35.*

	Mean		**Median**		**σ**		**M-F Exponent**	
	H	V	H	V	H	V	H	V
Rockfall minor axis r^2	0.891	0.924	0.926	0.829	0.950	0.904	0.413	0.429
Rockfall major axis r^2	0.842	0.000	0.048	0.261	0.059	0.111	0.326	0.373

Table 5.7: *Slope values of the least-squares regressions in Figure 5.35. While the r^2 values are high, slope values tend towards 0. This highlights the lack of variability in the facet size that is represented using these averages.*

	Mean		**Median**		**σ**		**M-F Exponent**	
	H	V	H	V	H	V	H	V
Rockfall minor axis gradient	0.00	0.03	0.00	0.00	0.00	0.00	1.57	1.09
Rockfall major axis gradient	-0.03	0.00	0.00	0.00	0.00	-0.02	1.91	1.39

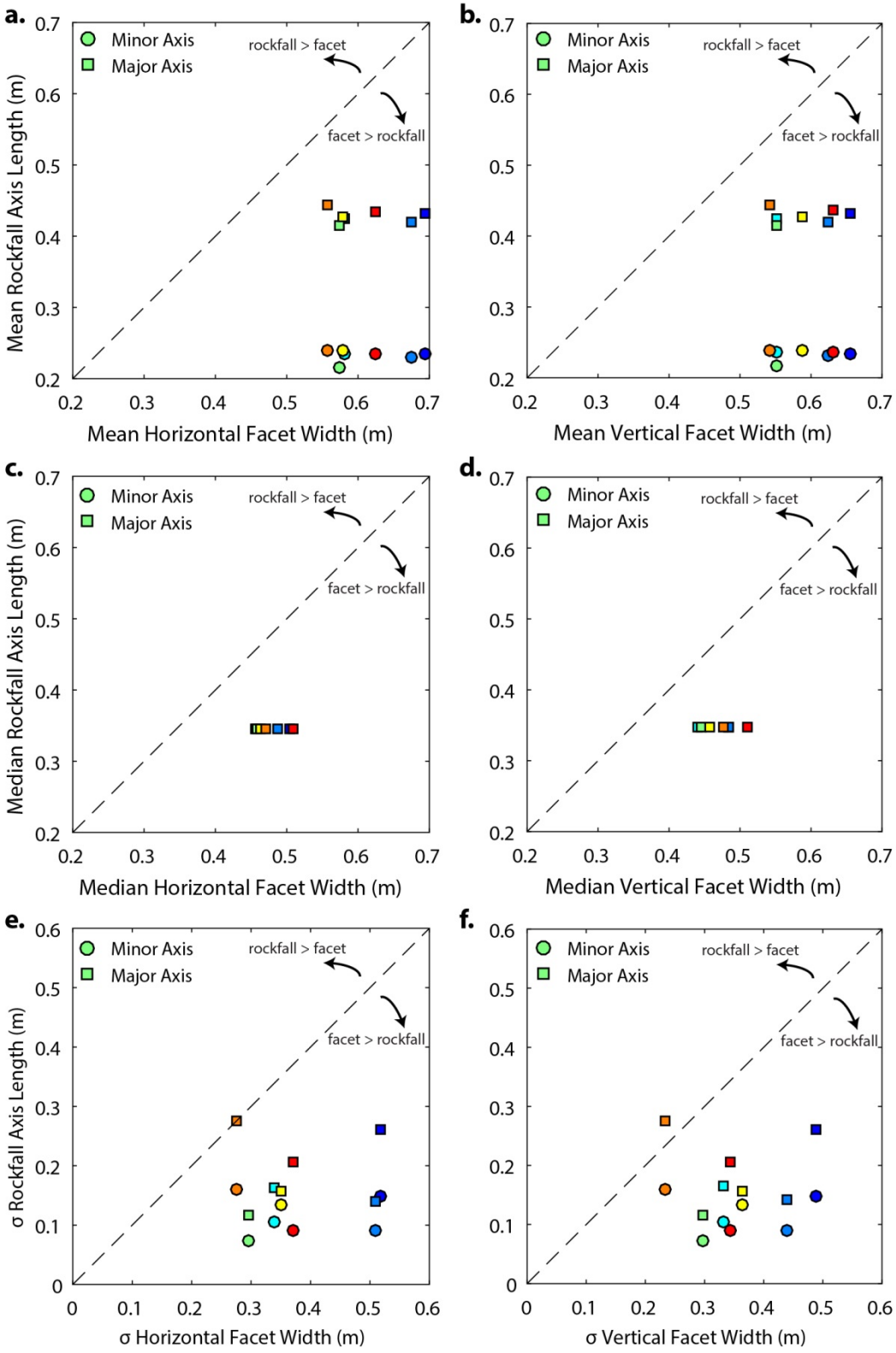

Figure 5.35: *Comparisons of mean (a-b), median (c-d), and standard deviation (e-f) of facet sizes with rockfall sizes for each bed. Horizontal facet dimensions are compared with the major and minor axis lengths of rockfall in a, c, and e. Vertical facet dimensions are compared with the rockfall in b, d, and f. Colours are the same used in Figure 5.33. The positions of these points, which fall below the line of unity, suggest that rockfall dimensions are beneath the measured dimensions of the facets.*

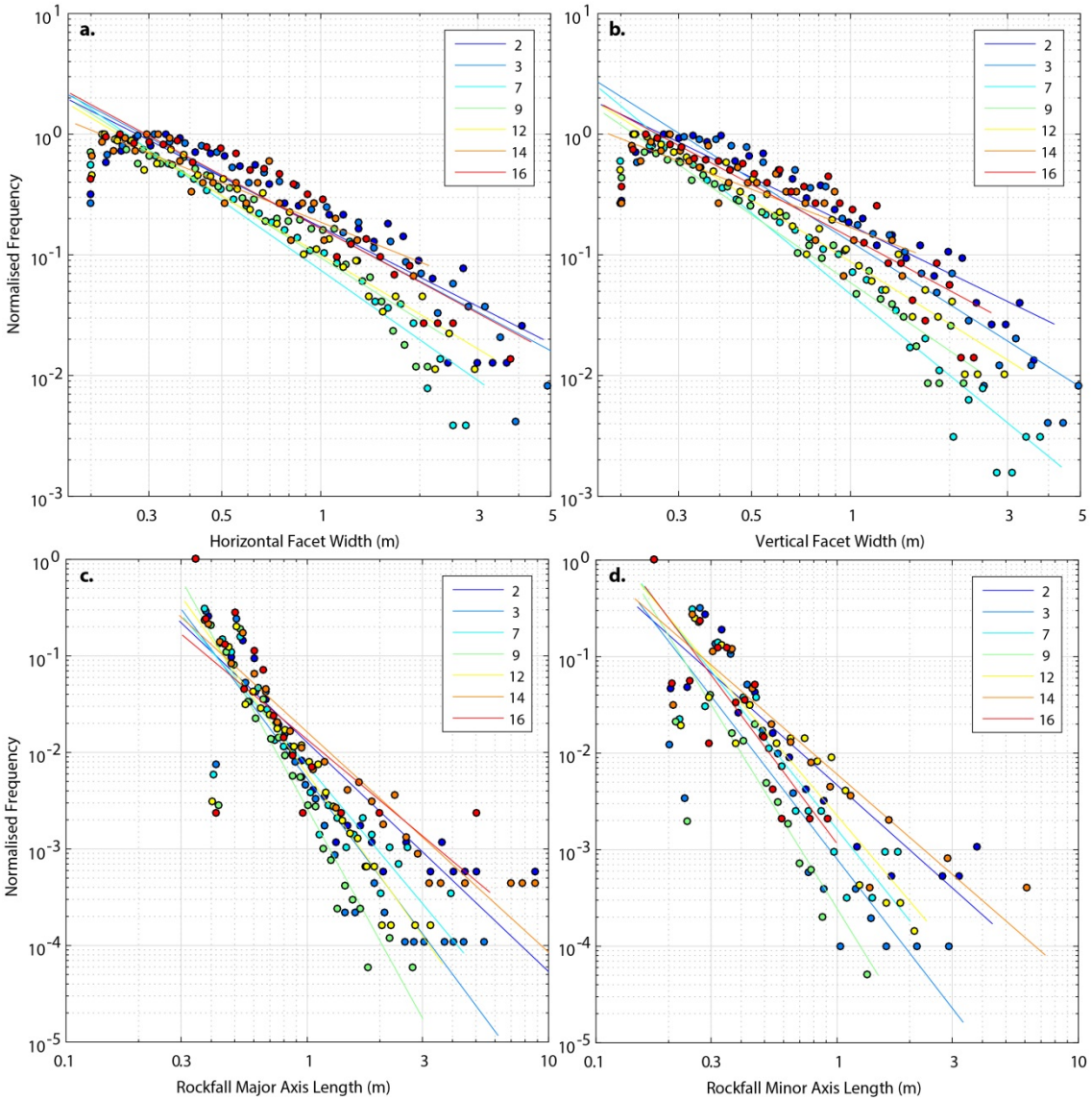

Figure 5.36: *(a-b): Magnitude-frequency plots show that the horizontal and vertical facet sizes follow a negative power-law scaling distribution. A rollover is evident for facet dimensions in each bed, below 0.2 m. A similar pattern is evident to the cumulative distribution plots in Figure 5.33. The exponent of this distribution offers a more representative description of this distribution than the mean, median and standard deviation. (c-d): Magnitude-frequency plots for the rockfall that occurred in each bed, separated by the major axis length (c) and minor axis length (d). Note that all four plots use the normalised frequency. This enables comparison between the distributions, despite more rockfall being recorded than facets, by normalising against the maximum-recorded frequency for each distribution.*

Figures 5.36a-b show that the frequency distribution of facets widths and heights for each bed adhere to a power law. Normalised frequencies are plotted in order to account for the fact that the number of rockfall in each bed differs from the number of facets, thereby enabling direct comparison between the two. Figures 5.36c-d show the magnitude-frequency distributions of rockfall for each bed, measured again as the major and minor axis lengths. The exponent is smallest for the sandstone beds at the top of the cliff, indicating that larger facets constitute a

greater proportion of the size distribution for those beds. Bed number 7 has the largest exponent, indicating a higher proportion of small facets. To some extent, this matches the distribution of rockfall sizes within each bed, whereby bed number 7 also has the highest exponent, indicating that smaller facet dimensions may limit the size of rockfall. When exponents are plotted in Figure 5.37, while not a statistically significant relationship, as facet width exponent increases, rockfall length exponent increases. There is also more deviation away from a 1:1 relationship for higher exponent values (for example, compare facet width exponents of 1 – 1.5 as compared to 1.5 to 1.75, to 1.75 to 2.0), therefore, for higher exponents (the most fragmented rock layers), the effect on rockfall width exponent is greater. This means that an increasingly fragmented rock layer disproportionally generates an even more fragmented rockfall distribution. This may be indicative of a cascading process, whereby a rock that is fragmented recursively generates rockfall that are even more fragmented.

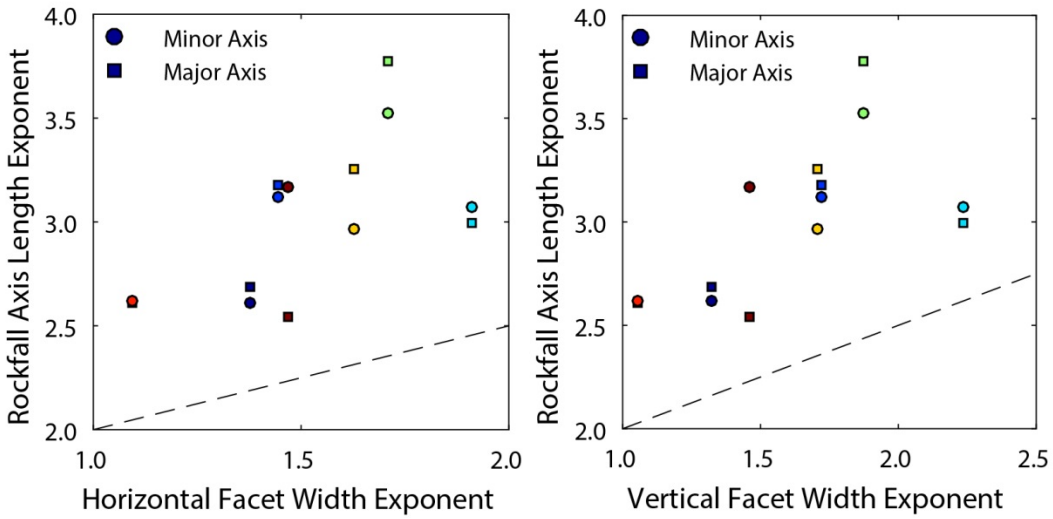

Figure 5.37: *Comparison of the exponents of rockfall axis lengths against facet lengths. All beds lie above the line of unity. This suggests that the distribution of rockfall sizes tends towards smaller length than the distribution of facet sizes.*

Rockfall depths were then compared with the dimensions of the measured facets on the rock face. Depth measurements are measured to a higher degree of accuracy (LoD = 0.03 m) than the aerial extent of the rasterised rockfall (0.15 m cell size). Since the facets were acquired from a 3D point cloud, and their horizontal and vertical dimensions measured in 3D space, the depth of rockfall are more suitable for comparison between layers than the aerial extents. In Figure 5.38, the exponents of rockfall in each bed reflect the exponents of facet dimensions for each source rock. This suggests that facet dimensions may exert an upper limit on the size of rockfall in these beds, as described conceptually in Figure 5.39. The exponents are plotted in Figure 5.40, in the space axis of 5.37, and are provided in Table 5.8. Here, if the facet exponent value falls below the line of unity, the exponent of rockfall depths is smaller than the exponent

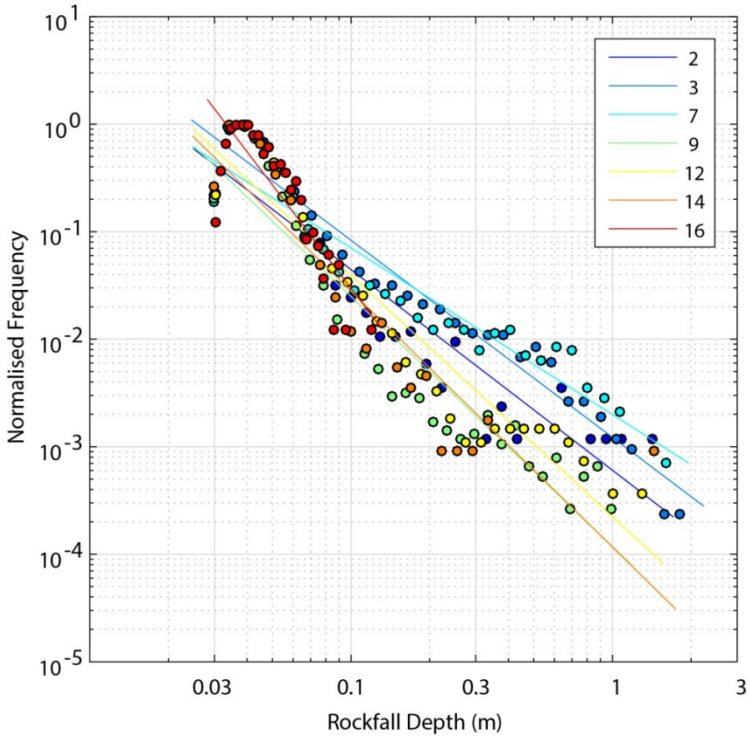

Figure 5.38: *Magnitude-frequency plot of the rockfall depths. Like the facet dimensions, these are measured in true-3D and provide a greater range of values.*

of the size distribution of facets. This suggests that there is a greater proportion of large rockfall, compared with the proportion of large facets. The fact that almost all beds fall above this line suggests that rockfall are always smaller in size than the facets, so rockfall dimensions are not defined by the joint structure that is exposed at the surface, but rather the fragmentation of the rock mass. For bed number 7, however, the exponent is greater for rockfall depth than for the facet size and this bed falls below the line of unity. This suggests that in this bed, which exhibits the smallest facet dimensions anywhere on the cliff, facets do not introduce an upper limit on rockfall size, and so rockfall are rather multiples of the facet size.

Table 5.8: *Facet depth exponents and rockfall depth exponents estimated in Figure 5.36 and Figure 5.38, respectively, and plotted in Figure 5.40.*

Bed Number	Horizontal Facet Exponent	Vertical Facet Exponent	Rockfall Depth Exponent
2	-1.378	-1.320	-1.865
3	-1.446	-1.722	-1.833
7	-1.916	-2.232	-1.548
9	-1.711	-1.870	-2.326
12	-1.628	-1.706	-2.244
14	-1.093	-1.054	-2.379
16	-1.470	-1.458	-3.193

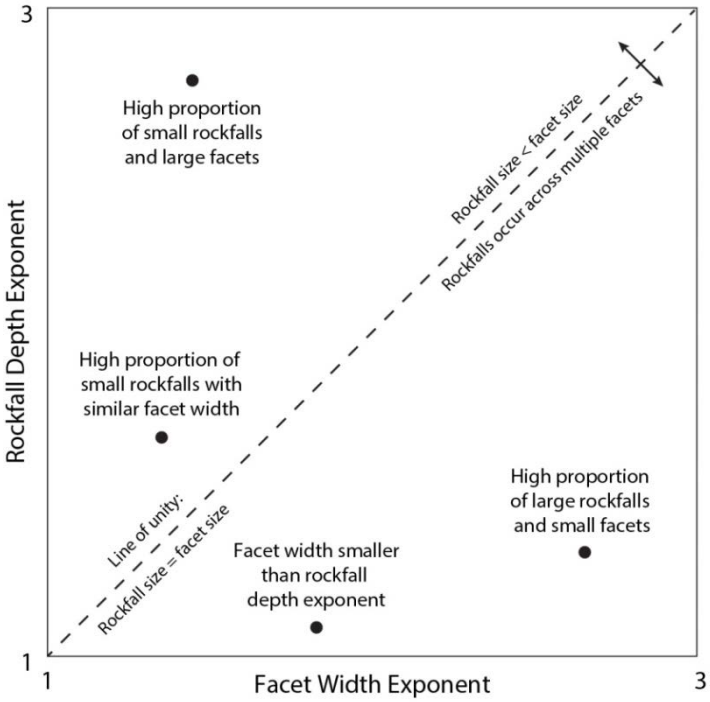

Figure 5.39: *Conceptual plot of the relationship between facet width exponent and rockfall depth exponent. The higher the rockfall depth exponent, the greater the proportion of small rockfall relative to larger events. Similarly, the higher the facet width exponent, the greater the proportion of small facets relative to larger facets. Points above the line of unity therefore indicate that the size distribution of rockfall tends towards a higher proportion of small depths than the proportion of small facet sizes. By maintaining the same length bins, these exponents also provide a comparison of the true size of facets and rockfall, rather than simply the distribution.*

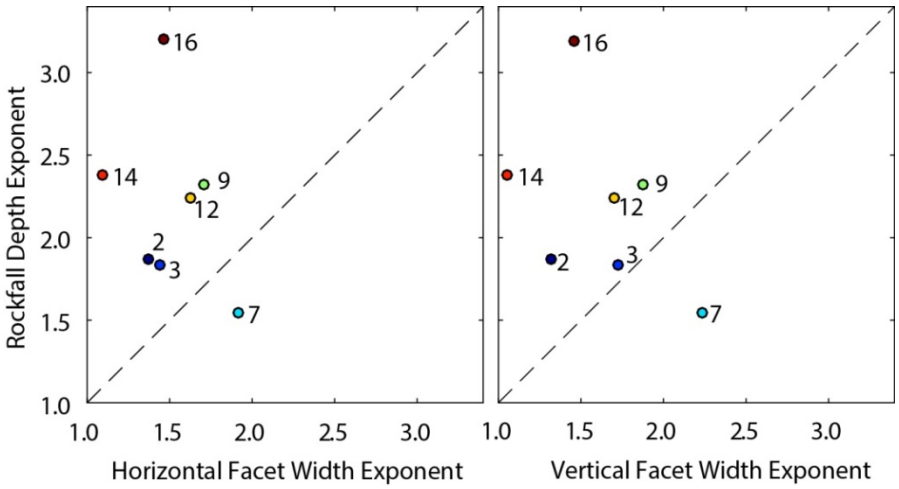

Figure 5.40: *Rockfall depth exponents relative to facet size exponents. Most beds lie above the line of unity (dashed) suggesting that rockfall are likely to be contained within individual planar facets, rather than spreading across multiple facets. For bed number 7, however, rockfall appear to have a lower exponent than the facet length. As length bins were consistent between facet lengths and rockfall depths, and the frequency is normalised to account for discrepancy in the total number of measured features, this suggests that rockfall occur across multiple facets in this bed.*

5.10 Summary

In this chapter, an examination of rockfall shape has indicated that rockfall are predominantly slab-like in form. Much of the exposed bedding on this cliff is protruding relative to the overall cliff profile, with intervening layers of shale with a less well-defined surface joint structure, which is not considered here. Here, the confining stresses are lower than those deeper within the cliff, and the rock mass is in general far more weathered. This points towards a process of rockfall evolution though fragmentation of surficial material, as opposed to the occurrence of large, instantaneous rockfall that exceed the scale of the overall joint structure.

The errors attributed to high frequency scanning have also been discussed. Monitoring at high frequencies, in particular below 4 d – 7 d, results in the detection of more rockfall as the superimposition of contiguous events in close spatial and temporal proximity is resolved. As has been shown in *Section 5.8*, the size distribution of these rockfall adheres to a power law, such that the increase in observed rockfall with shorter values of T_{int} comprises many smaller events. As discussed in *Section 5.3*, these smaller events have a higher proportional volumetric uncertainty, as a function of the increased number of boundary pixels relative to the number of interior pixels used to derive their volume. While this limits the use of high frequency datasets in cumulative analysis of rockfall volumes and direct derivatives such as erosion, this study identifies small scale rockfall using pairwise change detections to enable insights into the timescales over which single rockfall evolve. This holds significant implications for our understanding of rockfall, the mechanisms that promote destabilisation and triggering, and the relative role of internal versus external forcing. For example, slope stability models of rockfall do not simulate the fragmentary nature of the evolution of rockfall scars depicted here, whereby smaller events – which invariably require a smaller perturbation to initiate failure - may be indicative or may be direct drivers of the larger failures into which they are later subsumed. The stress or force needed to drive rockfall therefore needs to be considered in reference to a mechanism that evolves though time. The analysis of magnitude-frequency distributions at different timescales shows that, for high frequency monitoring datasets, the exponent of the distribution changes with the frequency of monitoring, so the more frequently you measure, the more rockfall you will capture.

The gradient of the straight-line form of the log-log magnitude-frequency distribution is represented by the parameter β. For each large event, there are more medium sized events, many more small events and even more very small events; the ratio between these frequencies, β, is constant. The rollover in the distribution that is evident for longer return intervals indicates that relatively few small rockfall (< 0.01 m^3) are observed with less frequent monitoring. Since the bounds of the magnitude-frequency distribution are between 0.00135 m^3, above the minimum detectable volume (6×10^{-4} m^3), and 7.2536 m^3, the largest detected

volume, this does not represent a limitation in the spatial accuracy of the rockfall measurement. Instead, this process appears to reflect the superimposition of small failures by larger, contiguous events. By monitoring at very high temporal resolution, it is apparent that this rollover begins to reverse over timescales < 106 h, illustrating an increase in the proportion of smallest events. This is accompanied by an overall increase in the exponent of the distribution across all volumes. Below approximately 4 d to 7 d, there is a clear increase in the exponent with T_{int}; however, at longer timescales (> 7 d) no significant change in the size distribution of rockfall events is observed. This suggests that rockfall may evolve as a process of fragmentation over timescales up to 4 d to 7 d, rather than as instantaneous events. The effects of perturbations, such as storms triggering rockfall, may therefore not just be instantaneous, but there may be a period of time where the cliff face settles or returns to background levels, here indicated to be a period of 4 d – 7 d. In this setting, therefore, decreasing the T_{Int} of monitoring is unlikely to enhance our understanding of net rockfall characteristics and failure evolution unless the T_{Int} falls below 4 d – 7 d.

In this chapter, magnitude-frequency distributions have been characterised over varying timescales to constrain the process of rockfall evolution. This has been accompanied by a geometric analysis of the size of rockfall in comparison with the facet dimensions of each source rock. By estimating the magnitude-frequency exponents of facet and rockfall sizes (using fixed length bins and normalised frequency data), the size distribution and actual sizes of rockfall and facets could be compared. The distribution of rockfall sizes appears to be constrained by the joint structure, such that most rockfall are smaller than the facet size. This is the case when rockfall are measured in terms of the length, breadth and depth but is not the case for the highly fragmented bed number 7. This bed exhibits the highest proportion of small facets of any bed. Most rockfall occurring in this bed therefore appear to release material across at least one (and often more than one) facet.

The limited control that the visible persistence of discontinuities appears to exert upon the size and shape of rockfall necessitates an examination of the influence of external forcing. In *Chapter 6*, the duration of energetic environmental conditions, as well as the length of time between them and the onset of failure, is examined. Since the magnitude-frequency analysis above has highlighted the significance of small rockfall in material removal from the slope, relationships between environmental drivers and the timing of rockfall are categorised by the size of individual failures. Furthermore, following the considerable shift in magnitude-frequency distributions of observed rockfall beyond *ca.* 100 h, in *Chapter 7* the evolution of failures from the cliff is examined with respect to both precursory rockfall and precursory creep of the mass.

Chapter 6

The Relationship between Rockfall Timing and Triggers

6.1 Introduction

In *Chapter 5*, an analysis of the size distribution of rockfall activity showed that rockfall of the order of 0.001 – 0.010 m^3 accounted for 97.7% of the total number of measured events, manifest as an 'anti-rollover' when plotted in log volume-log frequency density space. A comparison of the aerial extent of these rockfall relative to the visible persistence of discontinuities in the rock mass showed that they are smaller than the scale of the observable joint network, suggesting that rockfall are the result of fragmentation. The geometry of detachments showed a tendency towards cliff face parallel slabs, with rockfall depths considerably smaller than their respective height and width. Hence, while the joint network appears to determine the maximum permissible rockfall size, the size and shape of by far the majority of rockfall appears to be determined by rock mass fragmentation. The shallow depth of these fragments suggests that rockfall may arise as the result of the interplay between preparatory exogenic forces, which progressively reduce the resistance of the rock mass to failure, as well as a trigger, which may in itself be either exogenic or purely the result of *in-situ* fragmentation. An appraisal of exogenic controls is therefore required.

In this chapter, the nature and timing of rockfall activity is examined with respect to external drivers. The rate of rockfall activity and frequency as categorised by volume and shape are compared to both weather and marine conditions. These include temperature, rainfall, wind speed, tide height, and significant wave height. As discussed in *Chapter 2*, previous research into rockfall triggering by environmental conditions has shown that the timing of rockfall follows the timing of environmental conditions that exceed specified thresholds, mostly defined as temperatures that are conducive to freeze-thaw action on the rock mass or storm conditions that exceed specific rainfall intensity-duration conditions. *In-situ* apparatus, such as crack gauges and acoustic emission nodes, can provide higher frequency, higher precision strain measurements than those in this study, and have previously been compared to environmental records of similar frequencies (Vlcko *et al.*, 2009; Collins and Stock; 2016; Eppes *et al.*, 2016). However, these instruments are often localised, rarely monitor deformation across an entire slope, and are unsuited to rockfall detection as discussed in *Chapter 2*.

If rockfall are considered as a manifestation of ongoing deformation and deterioration that occur across a slope, capturing their occurrence over an entire slope at a frequency consistent with the variability in environmental conditions presents the opportunity to examine slope response to external perturbations, over a range of timescales. The review of literature in *Chapter 2* highlights that final failure cannot be considered as the result of a single trigger, and that a slope may reside at varying levels of damage, such that the same two exogenic events may or may not trigger failure. The response of a slope to external drivers may, therefore, exist beyond cause-effect relationships that are the often cited from datasets of monthly monitoring, and related using liner regression (Strunden *et al.*, 2015). Here, the tidal, temperature and rainfall conditions that relate to failure are assessed in a number of ways. A first-order assessment of the significance of particular environmental conditions at particular timescales is first undertaken using a traditional least-squares approach, which draws upon the high-frequency rockfall and environmental data that are binned by time and summarised by time-averaged statistics. In addition to time averaging, the high-frequency nature of scanning allows the rockfall data to be recentred in order to assess rates of activity by the timing relative to each tide cycle, the hour of day, and the proximity to large temperature gradients at sunset. Cross-correlation of environmental conditions and rockfall time-series is also used to explore the strength of relationships when varying lag times are considered.

The chapter begins by outlining the environmental and sea surface conditions that occurred during the monitoring period, alongside the pattern of rockfall activity and geometry of rockfall. Ordinary least square regressions are presented, with the environmental and rockfall variables having been averaged across $<$ 1 h, 1 h, 24 h, 7 d, and 30 d intervals. This is followed by an analysis of rainfall events that immediately precede rockfall, which shows that a significant relationship exists between rockfall activity and rainfall intensity and accumulation. The chapter concludes with an assessment of the influence of tidal cycles and fluctuations in diurnal temperature. This highlights that, while cause-effect relationships between threshold exceedance events and above normal rockfall activity are applicable for some variables, this form of analysis is complex for high frequency datasets and does not account for all observed trends in rockfall activity through the monitoring period.

6.2 Temporal patterns of rockfall occurrence

Rockfall activity, presented as both the cumulative volume and the total volume measured between each scan pair, is displayed alongside the distributions of weather and tide conditions in Figure 6.1. The volume estimates derived from scan-by-scan monitoring contain a considerable level of uncertainty because small rockfall, which account for the highest proportion of detachments, comprise a greater number of edges relative to the number of pixels that they

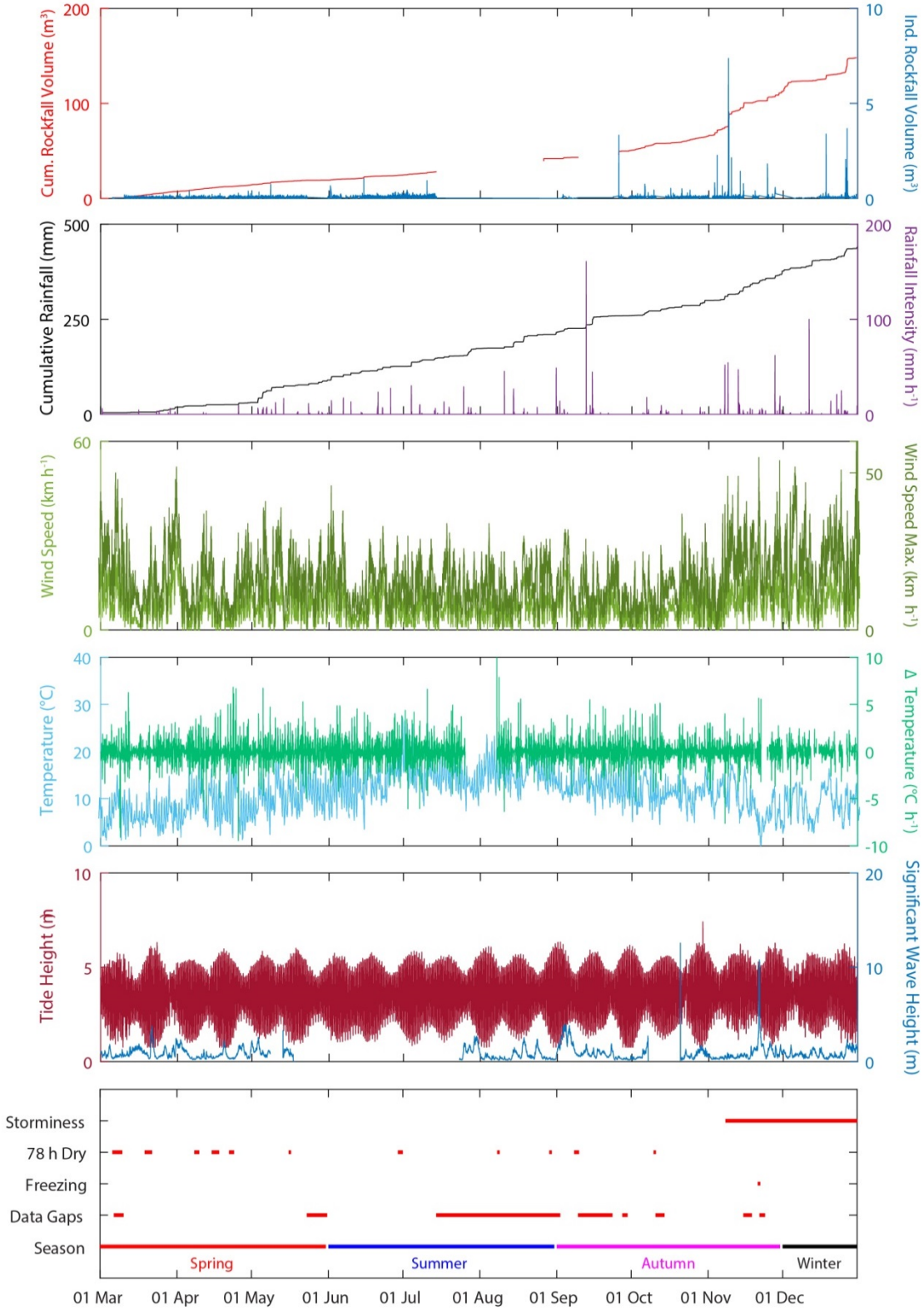

Figure 6.1: *Distribution of rockfall activity, rainfall intensity and cumulative accumulation, mean wind speed and maximum wind speed, temperature, tide height and significant wave height. Gaps in cumulative volume reflect the data gaps shown in Chapter 3. From visual observation it is clear that no single variable has an appreciable impact on rockfall activity, therefore questioning the applicability of least squares approaches. However, an increase in both wind speed and rainfall suggests that an onset of stormy conditions may be attributed to the increase in rockfall activity towards the end of the year.*

occupy (see *Section 5.2*). Despite this, the overall pattern of rockfall occurrence through time is consistent even with the addition of the minimum and maximum uncertainty envelopes, and is hence a representative metric of failures against which to compare environmental data. The data gaps that occurred between July and September result in some uncertainty with regard to this pattern. However, as the cumulative rockfall activity after each gap continues at the rate previously recorded, this uncertainty may be limited to superimposition of small rockfall events rather than seasonal variations in activity. Between March and October, the rate of rockfall activity is broadly consistent, *ca.* 0.17 m^3 d^{-1}. Five events > 1 m^3 occurred, resulting in small steps in the cumulative rockfall activity; however, it is clear that smaller, frequent rockfall across the slope account for the majority of activity recorded. The rate of rockfall activity begins to accelerate from October onwards, with the most pronounced increase occurring from 8th November until the end of the monitoring period on 30th December. Loss of material during this period accounted for 54.3% of the total recorded rockfall volume. Abrupt increases in the rate of activity during this period coincide with individual large rockfall events, with eight timestamps recording > 1 m^3 during this period alone. Alongside this, there is an appreciable increase in the total rockfall volume recorded between each scan pair made up of small rockfall events, *ca.* 0.59 m^3, more than three times the previous rate.

The distribution of rockfall during the monitoring period is broadly coincident with rainfall. Three phases of higher levels of rainfall can be distinguished, which are 5th March – 7th May, 7th May – 8th November, and 8th November – 30th December. During the latter, rainfall intensities are higher than at any other time during the year, and the time-averaged intensity of recorded rainfall events also increases from 1.32 mm d^{-1} to 2.37 mm d^{-1}. The single largest rainfall event coincided with a gap in rockfall acquisition during September. While January and February are not included within the monitoring period, the highest mean monthly rainfall occurs during November followed by July, June, August and December respectively (mean calculated using available Met Office rainfall data from Loftus, 1961-2010, 20 km away). Dry periods, classified here as a running three-day window without recorded precipitation, seldom occur and decrease in frequency throughout the monitoring period. Wind speeds are analysed for only those gusts that coincide with a direction of 0° - 180°, and are hence towards the cliff face. Both the mean and maximum recorded wind speeds are lowest during the summer and early autumn months; however, higher wind speeds (maximum > 25 km h^{-1}) occur most frequently during November and December. Temperature records, provided from the weather station on the rock face, show that freezing conditions (< 0°C) were only maintained for 1.5 h during the monitoring period. While longer periods of sub-zero temperatures were recorded during January and February, these fell outside of the rockfall monitoring period.

It is clear that at this site no single environmental variable has an appreciable impact upon the temporal pattern of rockfall activity. The absence of sustained air temperatures below

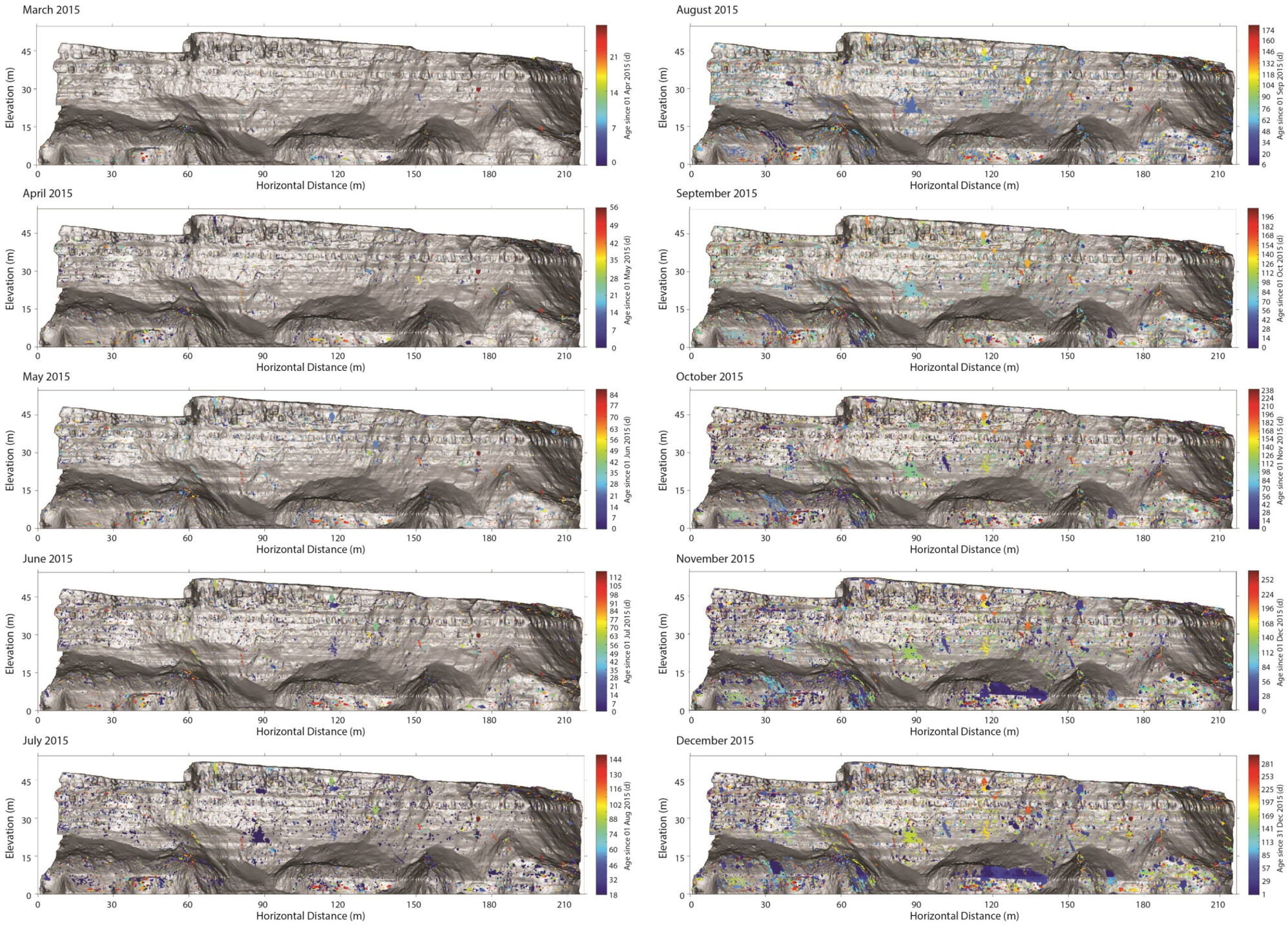

Figure 6.2: Rockfall growth throughout the monitoring period, measured on a scan-by-scan basis and aggregated by calendar month. The final image therefore shows the total rockfall distribution within the monitoring period. The overall distribution of rockfall across the upper near-vertical portion of the slope is similar throughout the monitoring period, though the overall size of rockfall increases. An increase in rockfall and slumps is evident across the base of the cliff, with substantial slumping during November and December.

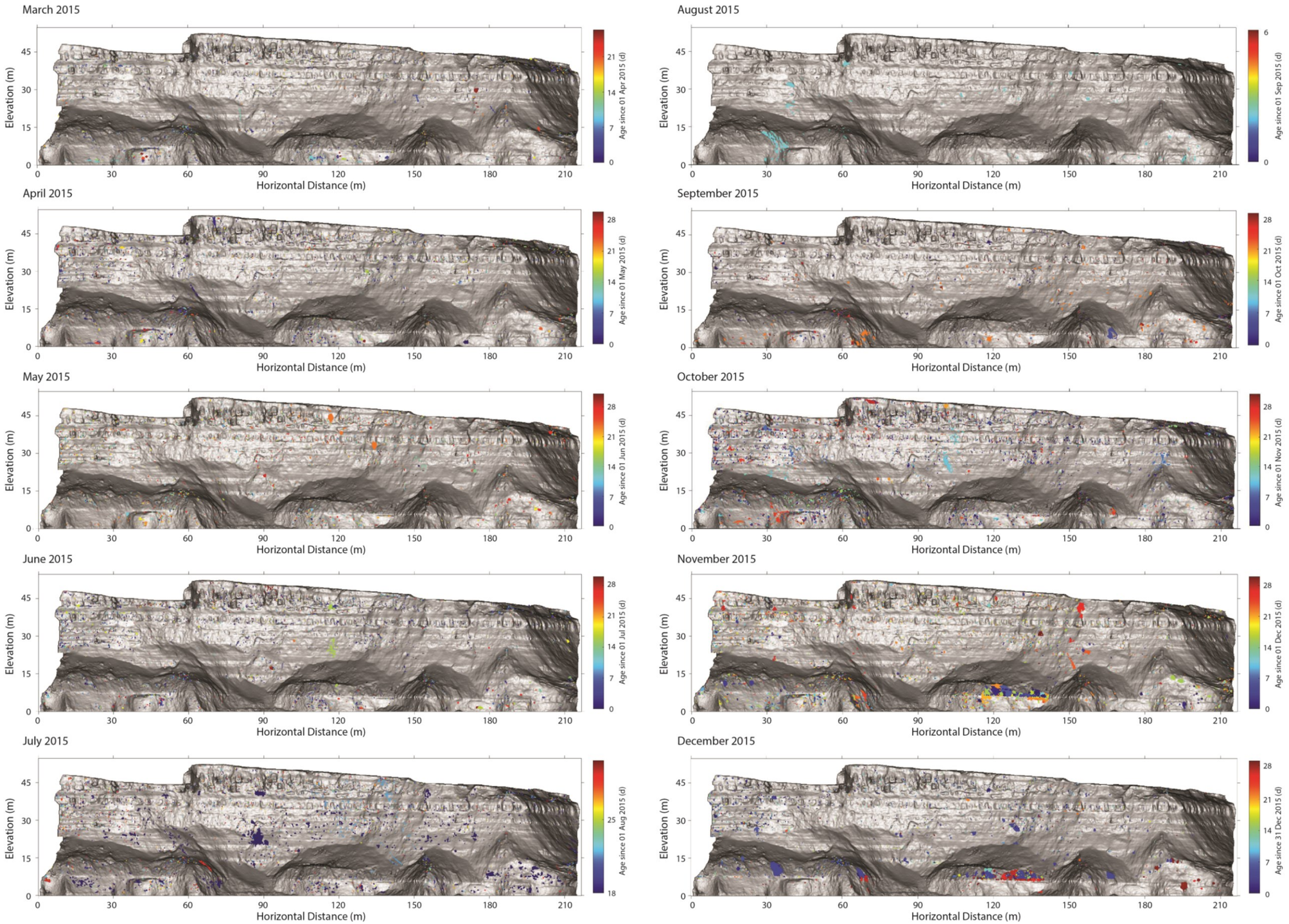

Figure 6.3: Rockfall growth throughout the monitoring period, measured on a scan-by-scan basis and presented as rockfall that occurred within individual months.

freezing also shows that no rockfall were triggered or predisposed by freeze-thaw conditions. A combination of high wind speeds and increased rainfall between 8th November and 30th December can be considered a proxy for increased stormy conditions during this phase of monitoring. While this term is loosely defined here, this period included several named storm events such as Desmond, Eva and Frank (see *Chapter 3*). This period coincides with increased rockfall activity and indicates that the relationship between rainfall and rockfall may be of a simple cause-effect nature, whereby a threshold of groundwater pressures may be exceeded, rainfall may trigger surface flow down the cliff, or that rockfall are sensitive to particular combinations of environmental conditions that include rainfall.

The pattern of increased rockfall activity across the cliff is shown on a monthly basis in Figure 6.2 (cumulative rockfall) and Figure 6.3 (individual rockfall). Appendix B shows in video format the same data that is recorded in Figures 6.2 and 6.3, but accumulated on a daily basis. The spatial distribution of all rockfall, indicated in Figure 6.2 by the month of December, has been discussed in *Section 5.4*. Within each month, the rockfall are distributed almost ubiquitously across the upper near-vertical portion of the cliff. While the rate of rockfall occurrence in this zone shows a small increase through the year, the overall spatial distribution remains consistent. An increase in the size of the largest rockfall per month also occurs, though the background rate remains dominated by the smallest events. Although small (a 0.001 m^3 cube has lengths 0.1 m), these events still present a significant hazard.

During November and December, several rockfall occurred that were contiguous with previously recorded failures. As will be explored in *Chapter 7*, these rockfall were preceded by smaller rockfall events. The reason that such patterns are observed in November and December is likely to be because (a) only rockfall occurring during these months are large enough to have observable precursory events within them due to instrument precision; (b) a critical rockfall volume exists, below which a rockfall will not creep due to its mass relative to the rock strength; or (c) precursory spalling of material is driven by environmental forcing of the rock mass, which becomes increasingly energetic during the winter months.

The volumes of material lost, presented in Figures 6.2 and 6.3, are detailed in Table 6.1. Based on calendar month, 55.6% of material that was eroded during the 10-month monitoring period was lost between 1st November and 31st December 2015. The impact of this upon resurfacing of the rock face, or the damage that it accumulated, was examined by computing a ratio for each month of the area of rock face that failed compared to the total area of rock face. This Figure 6.4 shows a conceptual diagram of the evolution of this ratio. If the rate of rockfall activity is constant, the cumulative percentage of the area of the rock face that is damaged will yield a linear trend through time. While this trend may approach 100% (i.e. the entire cliff is damaged), this is unlikely in realty unless an instantaneous failure of the whole rock face, or significant proportion, occurs. Deviations from this trend can reflect one of two scenarios.

First, a gradient below the line of unity may reflect superimposition of rockfall. In such instances, the rate of rockfall activity may remain constant, or even increase, but areas of the rock face that have already failed undergo further failure, possibly as part of a sequence of increased rockfall activity within developing incipient failure scars. Between the months of November and December, this pattern is evident (Figure 6.5a) and corresponds to the observed increase in contiguous failures across the rock face during this period. In Figure 6.5b, rockfall that occur within individual months exceed the sum of the cumulative percentage area in Figure 6.5a. This suggests that multiple rockfall below the size of a pixel occur within a 0.15 m area, that rockfall occur within the same area of the cliff surface as yet-to-fail events, or a combination of the two.

Second, an increase in gradient, manifest as a deviation above the line of unity, suggests an acceleration of rockfall activity across the rock face, which is likely to reflect seasonal perturbations in environmental drivers. Such an instance occurs between October and November but also between June and July, suggesting that this seasonal variation does not solely represent change in the accumulated rainfall. This could also reflect the removal of a thin layer of rock close to the surface, which had accrued damage between January and February prior to the monitoring campaign. Overall, the total area of rock face that was resurfaced is 1 602 m^2, which constitutes 18.9% of the total monitored rock slope area.

Table 6.1: *Scan-by-scan rockfall estimates presented in Figures 6.2 and 6.3, aggregated into calendar months. Both November and December recorded increases > 2·σ that are considerably larger volumes than elsewhere during the monitoring period and account for 55.6% of material loss recorded during the 10 months. Due to the high proportion of small rockfall that approach the size of a single pixel, the volume uncertainty increases in proportion to the monthly-recorded rockfall volume.*

	Volume Loss (m^3)	**Cumulative Volume Loss (m^3)**	**Volumetric Uncertainty (m^3)**	**Cumulative Volumetric Uncertainty (m^3)**
March	7.2869	7.2869	4.5300	4.5300
April	7.3621	14.649	4.3469	8.8769
May	4.6802	19.3292	3.0824	11.9593
June	5.4514	24.7806	2.9504	14.9097
July	3.4006	28.1812	2.2420	17.1517
August	13.6761	41.8573	7.4487	24.6004
September	8.8993	50.7566	3.5229	28.1233
October	14.9971	65.7537	9.7716	37.8949
November	45.1163	110.8777	15.6001	53.4949
December	37.2825	148.1602	4.3469	65.7554

Figure 6.6 shows the distribution of rockfall shapes categorised by the day of the year in which they occurred. A trend through the monitoring period from cube-like shapes to more slab-like shapes is apparent. An initial hypothesis is that temperature or weather variations

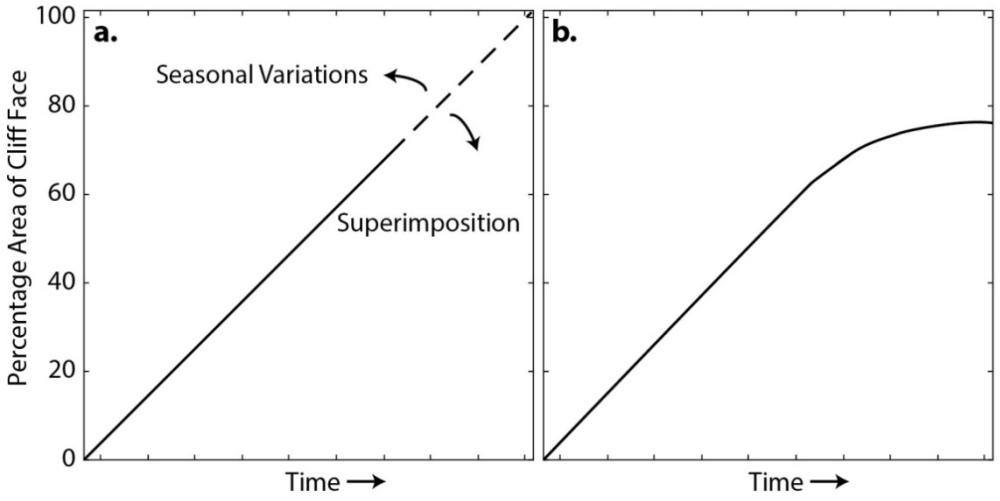

Figure 6.4: *Conceptual plots of the increased rock face resurfacing through time. (a) A constant rate of rockfall activity results in a straight line through eroded area-time space. In reality, this line is unlikely to remain straight due to superimposition, whereby rockfall occupy the same aerial location on the surface (often as precursors to incipient rockfall scars), resulting in a decreased below the line of unity. Seasonal variations, in particular the onset of sustained stormy conditions, may increase the rate of material removal from the rock face, raising the resurfacing rate above unity. (b) Not all areas of a slope may erode. As a result, the erosion trajectory is likely to plateau before reaching 100% resurfacing.*

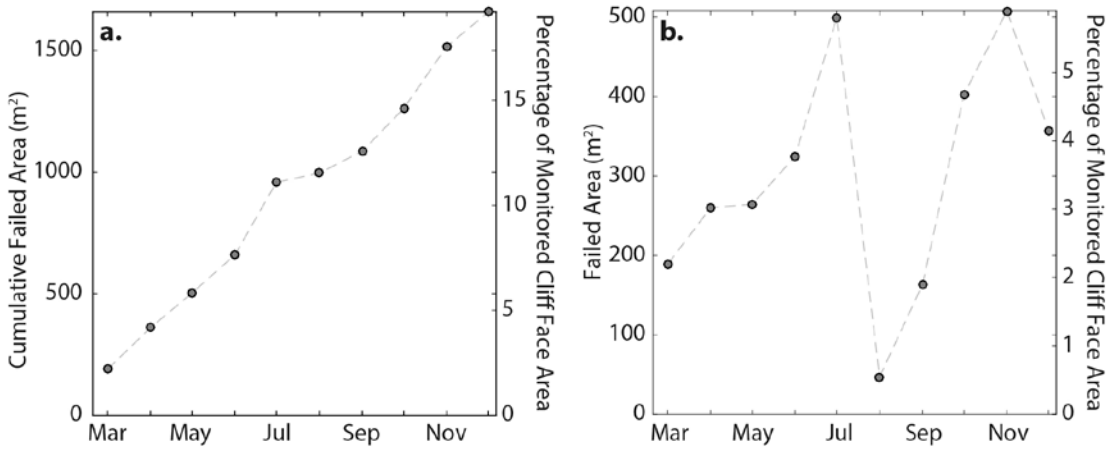

Figure 6.5: *(a) Cumulative failed area, represented in m^2 (left-hand axis), and as the percentage of the cliff face that has failed after each consecutive month (right-hand axis). Here a pixel that failed is only counted once. Increases above a uniform gradient occur during November and July, possibly as a result of increased rainfall. In total, 18.9% of the rock face underwent some form of failure. (b) Failed area calculated for individual months. The sum of failed area is greater here than for the left-hand plot suggesting that rockfall occur below the pixel size and/or that rockfall occur in yet-to-fail areas of the rock face.*

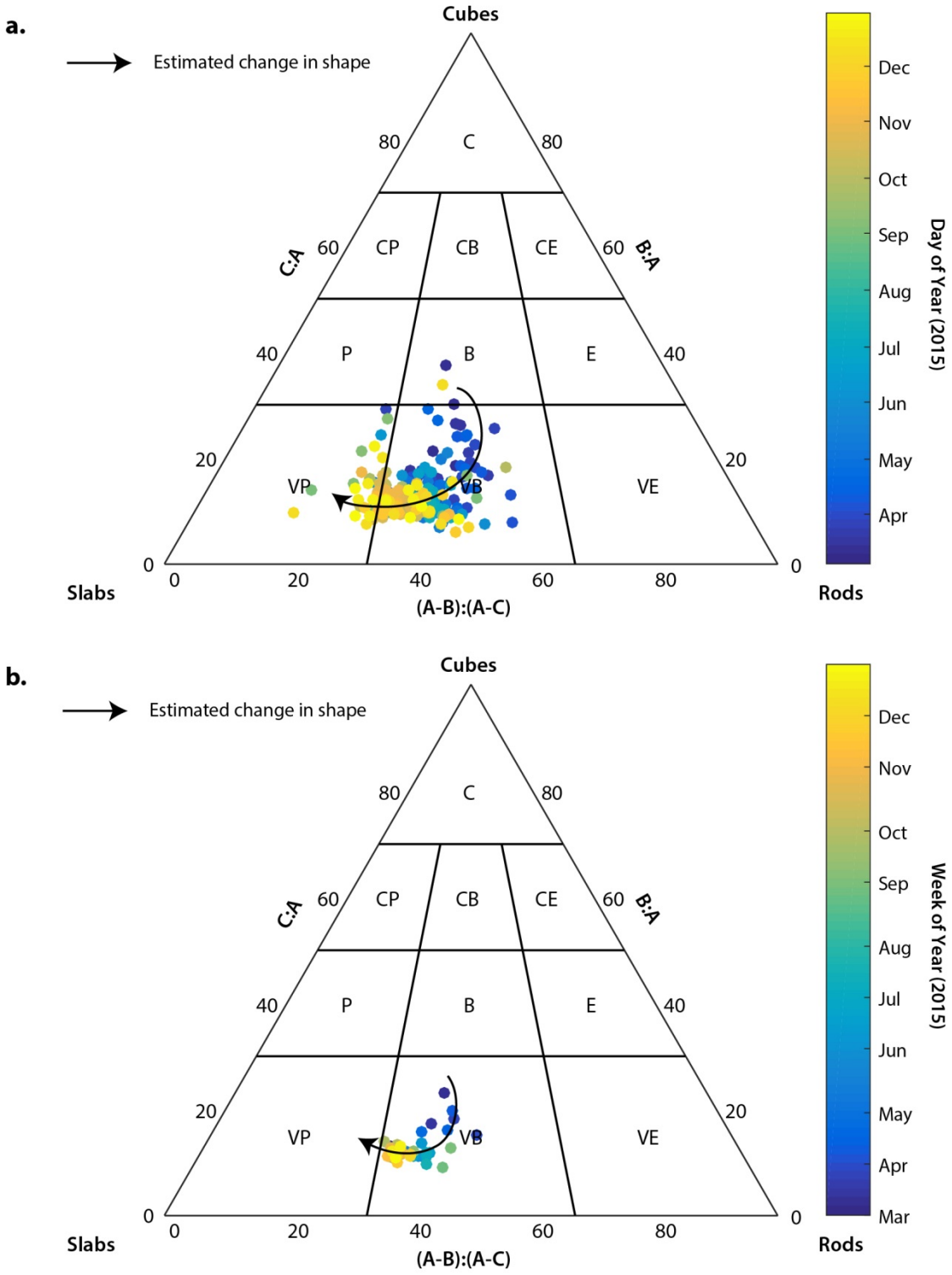

Figure 6.6: *(a) Mean rockfall shape by day of year shows an increase towards slab forms through the monitoring period. A manual approximation of this trend is applied (black arrow). This plot draws uniquely on rockfall collected at T_{int} less than or equal to 24 h, to ensure that no bias in shape due to superimposition or coalescence occurs. (b) Mean rockfall shape by week of year, with a similar approximated trend. This plot draws uniquely on rockfall collected at T_{int} less than or equal to one week, again to ensure that no bias in shape due to superimposition or coalescence occurs.*

determine the mechanism of failure. For example, increased near-surface tensile stresses may produce more slab-like rockfall during hot weather. However, such a pattern does not appear in during the monitoring period. Increased rainfall and wind speeds may have resulted in the loss of surficial, loose material from the rock face or predisposed the rock face to smaller fragmenting rockfall. This shift in the mean shape may purely reflect the increase in rockfall size through the monitoring period, since it is kinematically more difficult for larger rockfall to fail as cubes, as opposed to slabs, from this rock mass. However, it also emphasises the importance of damage that is accumulated in a shallow depth zone of the rock mass, or 'damage skin', that may extend across the cliff face. Periods of higher seasonal damage, such as during the summer and winter months, may be manifest as the development and removal of this 'damage skin' from the rock face, for example, through progressive exfoliation.

6.3 Regression analysis

6.3.1 Data selection and averaging

In this section, a least squares regression analysis is undertaken to establish if statistically significant relationships exist between environmental variables and both the occurrence and size of rockfall. In line with previous studies reviewed in *Chapter 2*, an initial approach was to bin the high-frequency weather data to provide time-averaged statistics for comparison with the rockfall data. While this averaging is normally undertaken to align weather data to weekly, monthly, or seasonal scans, both the environmental data and the rockfall data were therefore downsampled by varying degrees in order to align with one another. The averaging process yields numerous metrics of rockfall activity and environmental conditions, with each averaged across hourly, daily, weekly, and monthly timescales. Scan-by-scan patterns were also derived such that the fidelity of data on the timing of rockfall data was preserved, but the weather data was averaged within each scan interval.

For each timescale, rockfall activity was summarised as the rockfall volume rate (the total volume that occurred), the total number of rockfall, and the number of rockfall as categorised by discrete volume fractions ($0.001 - 0.01$ m^3, $0.01 - 0.1$ m^3, and > 0.1 m^3). Environmental conditions comprising accumulated rainfall, rainfall intensity, temperature, temperature gradient, wind speed, significant wave height, tide height, were also summarised using the metrics justified below.

The total rain accumulation within each period was used to represent the combined intensity and duration of rainfall events, alongside the peak rainfall intensity. Relatively little research has been undertaken into the sensitivity of rockfall to patterns of rainfall delivery. Due to the 0.2 mm resolution and fixed recording interval, the rain gauge used often recorded similar

values of intensity during the monitoring period. As such, the peak rainfall intensity was used to represent intense rainfall conditions that would have otherwise been lost using the mean intensity. The peak rainfall is therefore used to indicate the occurrence of storm events.

The mean, peak and minimum temperatures were all used in the regression analysis. While temperatures below freezing were not sustained in this monitoring campaign, maximum temperatures have been related to the dislocation of blocks relative to joint openings through disparate expansion (Gunzburger *et al.*, 2005). Temperature gradient was also recorded for the scan-by-scan, hourly and daily data as the change in degree Celsius, over *ca.* 30 minutes, one hour, and the peak scan-by-scan temperature gradient over the course of a day. All of these variables are recorded in °C h^{-1}. The relationship between temperature gradient and very small rockfall, in particular those that are interpreted here as constituents of rockfall evolution through fragmentation, remains poorly understood. However, as reviewed in *Chapter 2*, temperature gradients above freezing have been related to progressive damage accumulation within intact rock and joint openings.

Both significant wave height and tide height produce mean values that are far from their maximum values. The semi-diurnal sinuosity of tide levels is the prime reason for this. The minimum value of each gives little information about the rate of energy delivery to the rock face and, as such, the maximum tide height and maximum significant wave height were selected for analysis.

6.3.2 Gaussian transformations

Linear regression requires that both the dependent and independent variables, or more specifically the residuals of each, are normally distributed. While coefficients of determination, such as the r^2, do not strictly require a normal distribution, this is required for tests of statistical significance (UCLA Statistics Consulting Group, 2016). Transformations were therefore applied to improve the strength of the correlation between environmental and rockfall variables by making each more normally distributed. A range of simple transformations exist and, in order to select the most appropriate, a chi-squared goodness-of-fit test was used to determine whether the transformed data originated from a Gaussian distribution (Equation 6.1). Data was grouped into bins of observed and expected counts:

$$\chi^2 = \sum_{i=1}^{N} (O_i - E_i)^2 / E_i \qquad \text{[Eq. 6.1]}$$

where O_i are the observed data and E_i are the predicted data based on a Gaussian distribution (Balakrishnan *et al.*, 2013). Retuned values indicated whether the hypothesis of a normal

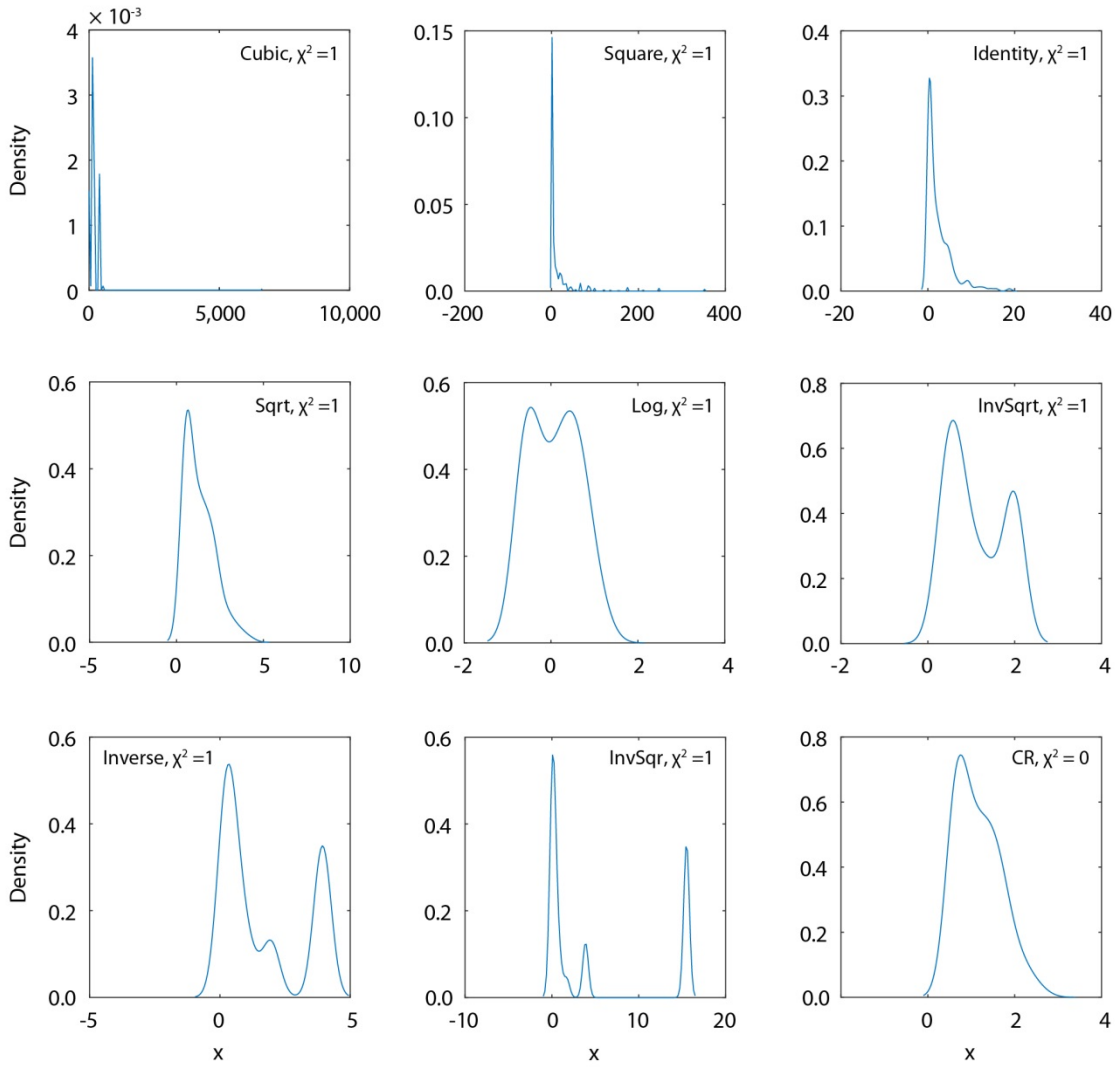

Figure 6.7: *Kernel density estimates of for the daily rainfall accumulation data after nine different transformations were applied. Chi-squared goodness of fit results are displayed, with the bottom-left (cube root) accepting the hypothesis that the data fits a Gaussian distribution. The identity transformation describes the data in its original form.*

distribution was accepted (zero) or rejected (one) at the 5% significance level. Several transformations were tested, including the square (x^2), cubic (x^3), identity (x), square root ($x^{1/2}$), cube root ($x^{1/3}$), logarithm ($\log_{10}x$), the inverse-square root ($1/x^{1/2}$), the inverse ($1/x$), and the inverse square ($1/x^2$).

Figure 6.7 shows an example of the relationships taken for the daily-accumulated rainfall. Of the transformed distributions presented, only the cube root results in a chi goodness of fit of 0. While for some variables, other transformations also yielded a value of 0, the cube root was selected as a transformation that consistently yielded $X^2 = 0$. The cube root, while weaker than a log transformation, has a substantial impact on distribution. Unlike logarithms, it has the advantage of being used for both positive and negative values, and in this sense has an advantage over the square root for certain applications (Cox, 1999).

Normal quantile plots graph the quantiles of a variable against the quantiles of a Gaussian distribution. In particular, these plots are sensitive to non-normality at the tails, which is characterised as a deviation from the diagnostic line, which represents a perfectly normal distribution. In Figure 6.8, while no transformation is aligned throughout the distribution, the cube root (CR) is approximately so above the lower tail.

An example comparison between the raw data and cube root transformed data is provided for the daily datasets in Figure 6.9 and Figure 6.10. For each sub-plot, 200 data points are graphed representing each day of monitoring. In general, transforming the data using the cube root results in higher r^2 values, though *p-values* from student's t-test are marginal for both, *ca.* 0.05 (Table 6.2).

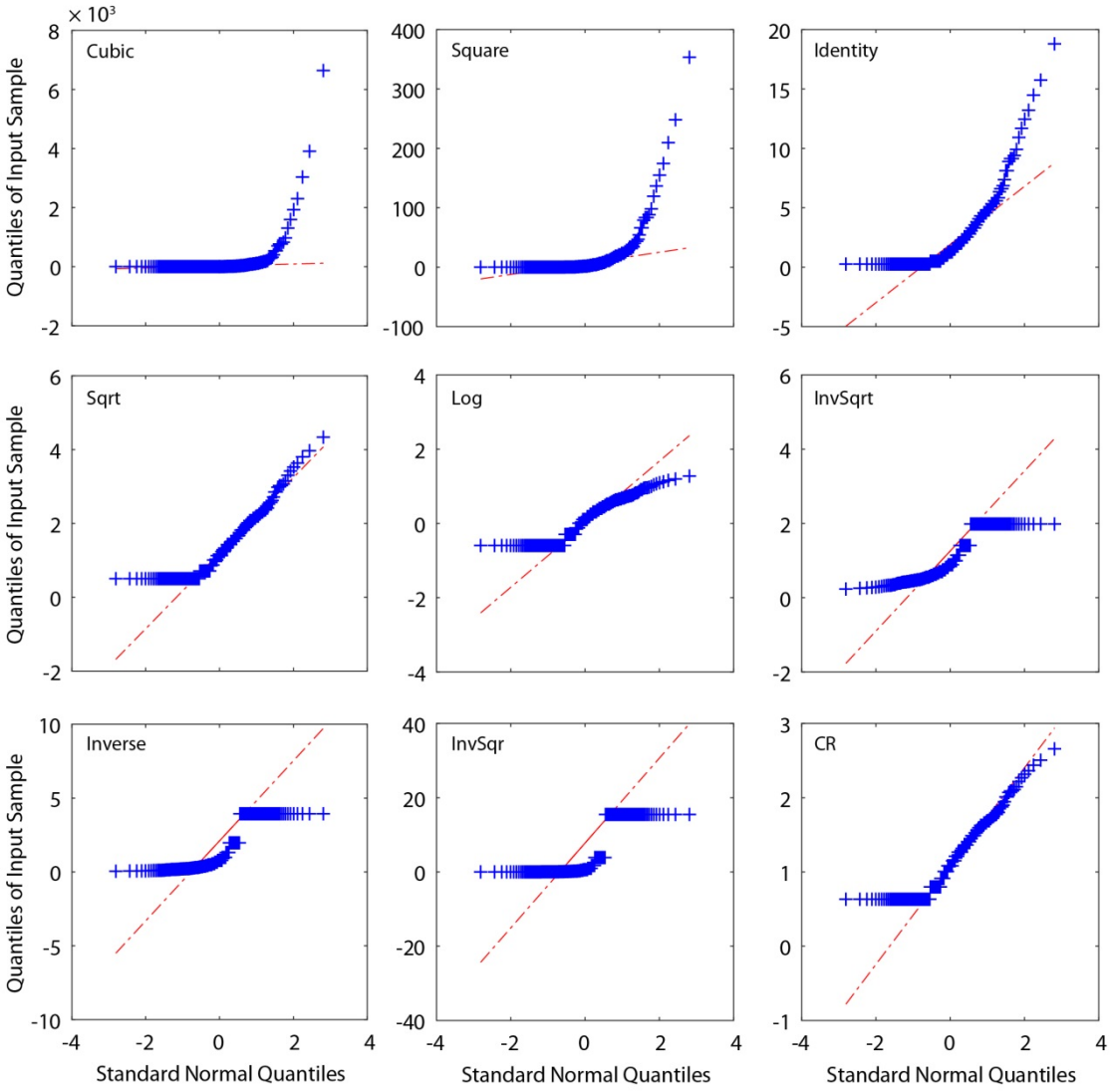

Figure 6.8: *Normal quantile plots for the daily rainfall accumulation data after nine different transformations were applied. While tails in the distributions never perfectly align to a Gaussian distribution, the best overall fit was observed by the cube root (CR).*

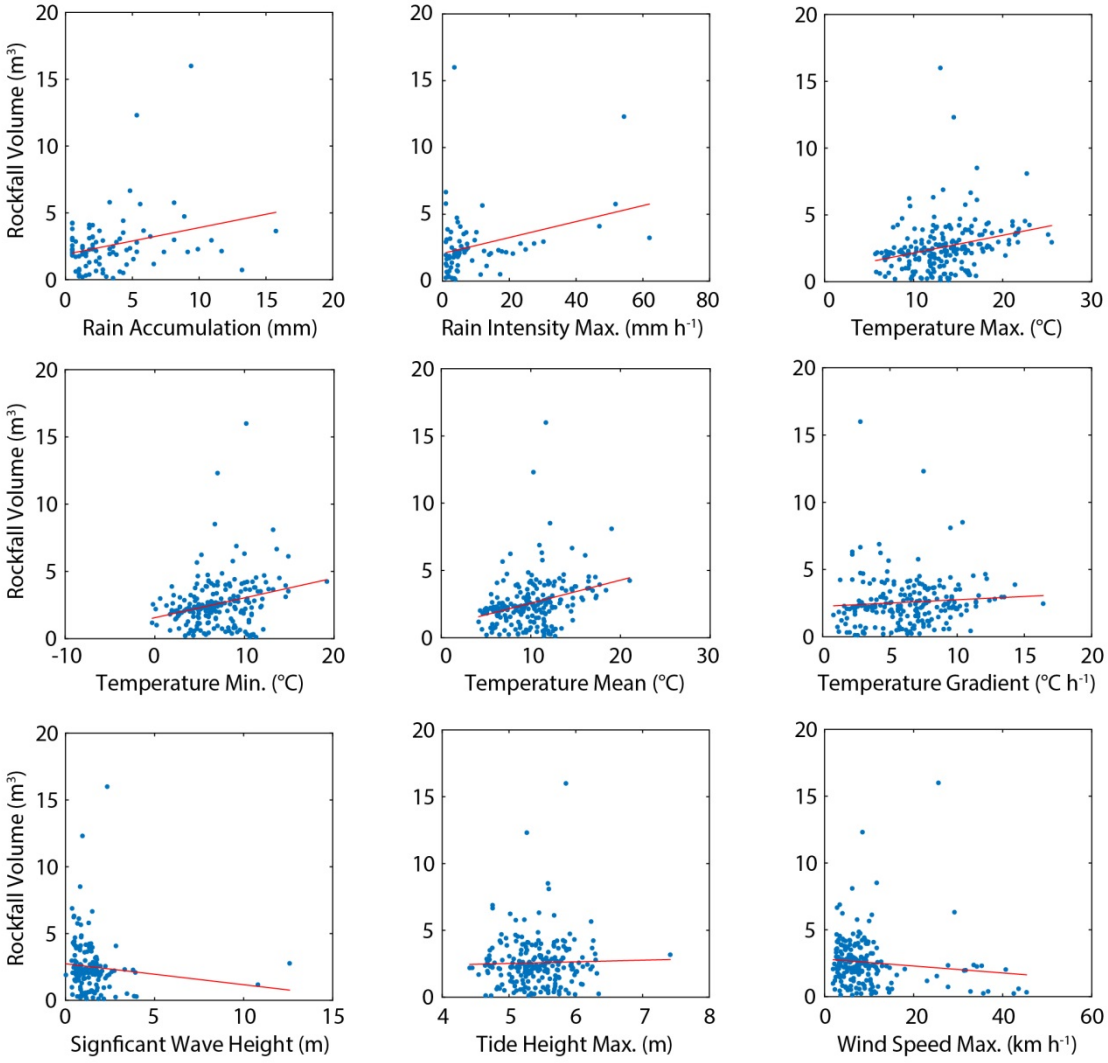

Figure 6.9: *Scatter plots of the raw rockfall volumes against the raw environmental variables, averaged over a 24 h period.*

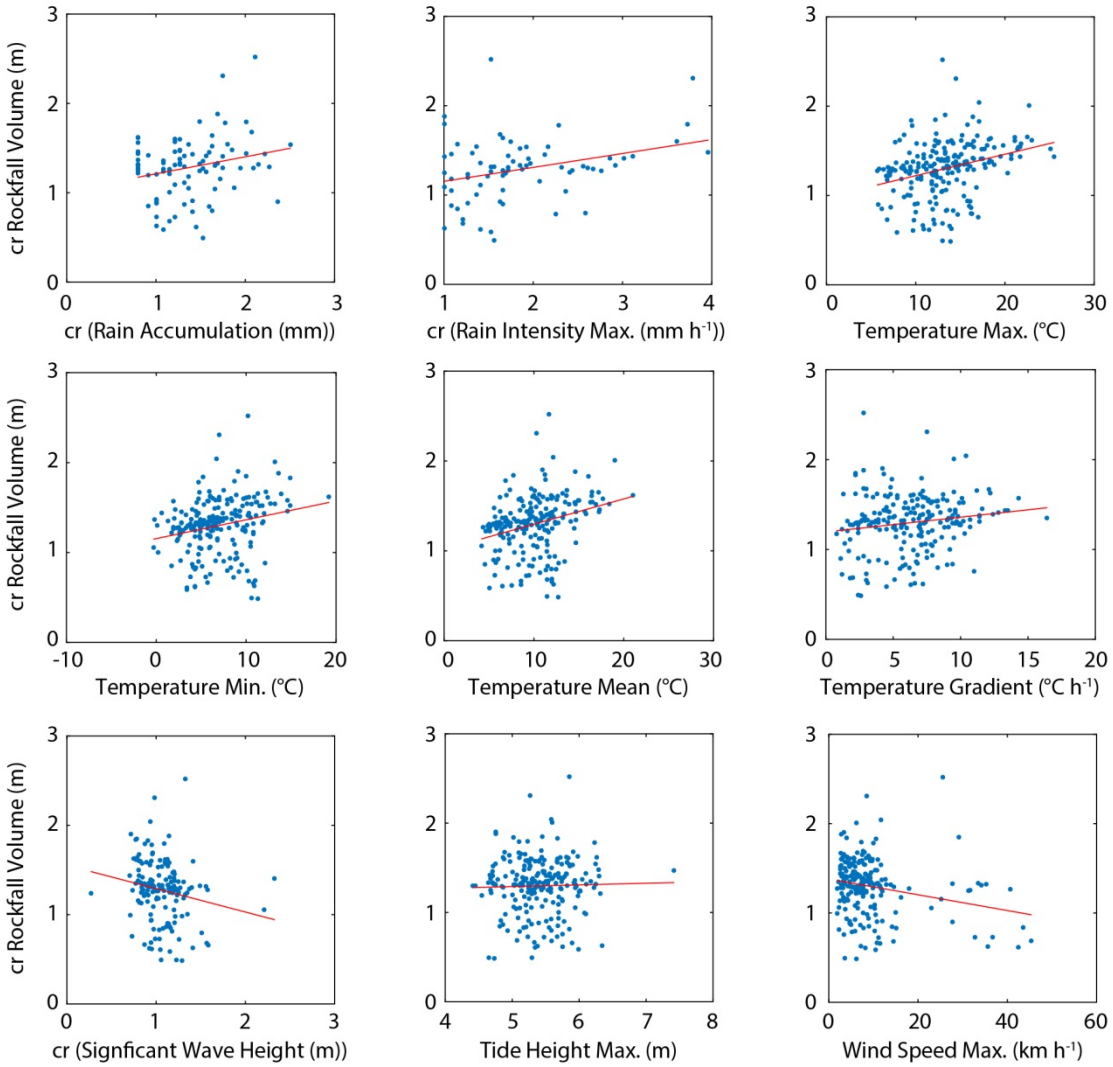

Figure 6.10: *Scatter plots of the cube root transformed rockfall volumes against the cube root environmental variables, averaged over a 24 h period. As in Figure 6.10, marginal t-test results are produced but an overall increase in the gradient and r^2 of each plot is observed.*

Table 6.2: *A comparison of raw and cube root transformed relationships for daily data, including the slope r^2 and p-value derived from the Student's t-test. A small but overall increase in all three elements of the least squares regression is observable.*

	Raw			**Cube Root**		
	gradient	***r^2***	***p-value***	***gradient***	***r^2***	***p-value***
Rain Accumulation	0.20	0.04	0.04	0.19	0.04	0.04
Rain Intensity Max.	0.06	0.09	0.09	0.16	0.09	0.08
Temperature Max.	0.13	0.08	0.10	0.02	0.09	0.07
Temperature Min.	0.15	0.02	0.11	0.02	0.05	0.06
Temperature Mean	0.17	0.06	0.11	0.03	0.08	0.05
Temperature Gradient	0.05	0.01	0.08	0.02	0.02	0.05
Significant Wave Height	-0.16	0.01	0.05	-0.26	0.03	0.10
Tide Height Max	0.12	0.00	0.20	0.02	0.00	0.10
Wind Speed Max	-0.03	0.01	0.13	-0.01	0.05	0.04

6.3.3 Results of regression analysis

Insignificant relationships were obtained between almost all environmental variables and rockfall, both for weather and sea surface conditions. Of the 200 regression tests undertaken (Table 6.3), only 19 showed significant results even after transformations to approximately normal distributions (Table 6.4). Significant relationships were obtained predominantly for the number of rockfall 0.1 – 10 m^3. For this rockfall size, significant relationships were found with marine conditions (significant wave height and tide height) using the scan-by-scan, hourly, and month datasets; however, the coefficient of determination for these relationships was minimal ($r^2 < 5\%$). *Rainfall accumulation* and *intensity* both showed significant relationships for the rockfall volume rate (weekly and monthly) and the number of large rockfall (scan-by-scan, hourly, daily, monthly). For these, the significance of the relationship was greater for the *accumulation* than for the *intensity*. Both marine conditions and rainfall are explored in greater depth later in this chapter. Below, each of the five plots in Figure 6.11 are described.

The *rockfall volume rate* produces r^2 that are almost exclusively below 10%. The scan-by-scan and hourly weather correlations produced the least significant relationships, with the highest correlation strength recorded between the minimum recorded temperature and the monthly rockfall volume rate. This can be explained by the fact that the coolest temperatures of the monitoring period were recorded in November and December, in which the highest rate of rockfall activity was also recorded. Regression strengths were highest for daily averaged statistics of *maximum temperature, mean temperature, temperature gradient, maximum rainfall intensity,* and *maximum significant wave height*.

The *number of rockfall* that occurred yields higher r^2 than the *total rockfall volume*, and again shows that the overall strength produced by daily averaged datasets is highest, albeit it insignificant. The *number of rockfall* recorded between each scan and at hourly intervals both show stronger relationships than for the *rockfall volume rate* when related to temperature variables. This strength is also apparent when temperature data is averaged at the daily interval. In relation to sea surface conditions, both weekly and monthly monitoring yields the highest strength relationships with the *number of rockfall*. Similar strengths are observed between *wind speed* and the *number of rockfall* for daily, weekly and monthly monitoring. These relationships are comparatively weak for scan-by-scan and hourly data.

The *number of rockfall of the order of 0.001 m^3 – 0.01 m^3* produces similar relationships to those of the *total number of rockfall* owing to the high proportion of rockfall within this volume range. This suggests that small rockfall are likely to show the strongest response to temperature. For medium sized rockfall, here defined as the *0.01 m^3 to 0.1 m^3* range, the overall strength of relationships is considerably weaker. An increase in the sensitivity of monthly rockfall patterns to temperature variables may be a result of the data gap that occurred during

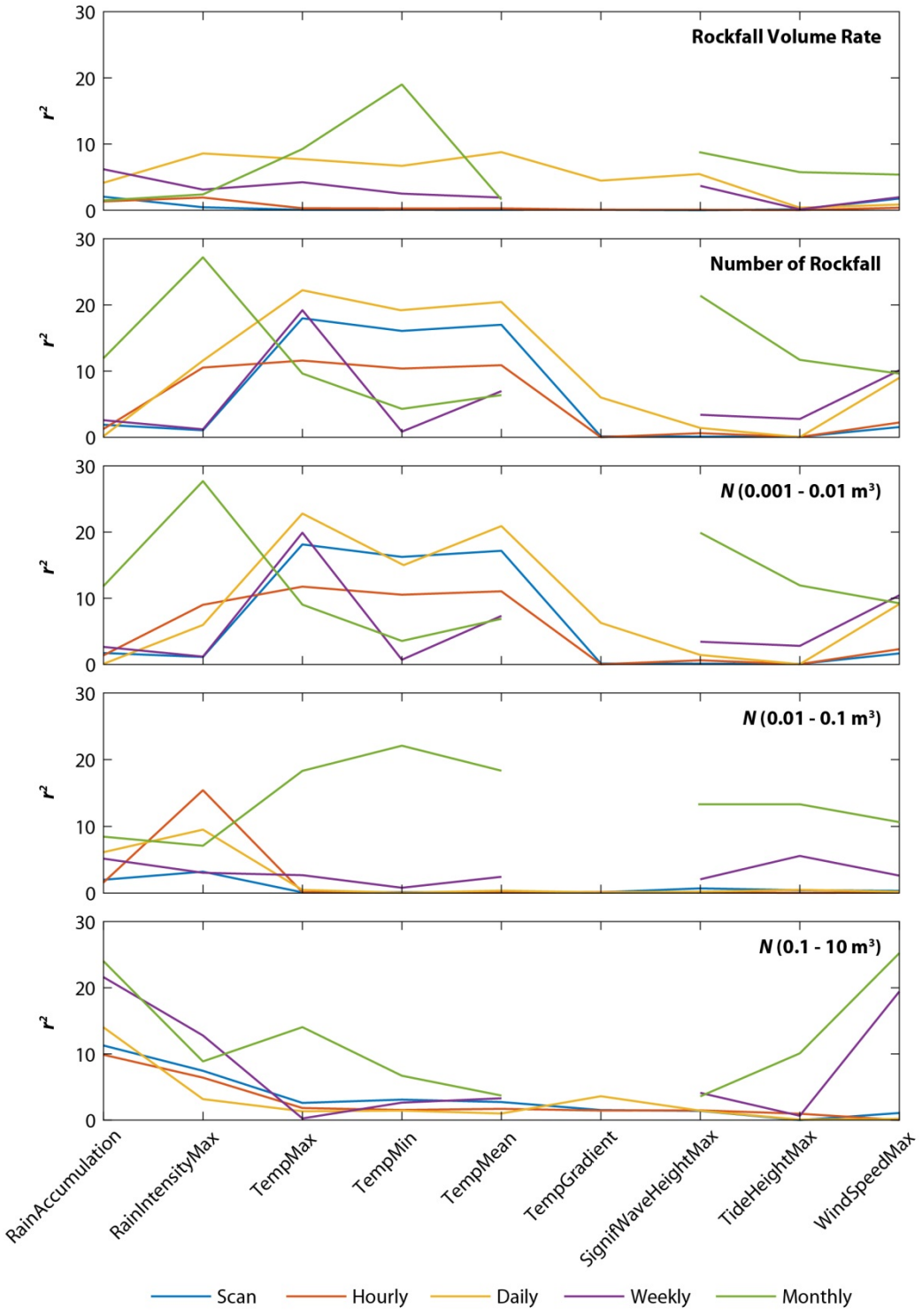

Figure 6.11: *The strength of ordinary least squares regressions, following normal transformation, between five different metrics of rockfall activity (each individual plot) and nine different environmental variables. Each line on the plot represents data averaged over a variety of timescales. For each rockfall metric, daily averaged data appears to show the highest correlation strengths, though these are insignificant.*

Table 6.3: r^2 *values for relationships between rockfall occurrence and environmental conditions, recorded as percentage values between 0 and 100. Rockfall occurrence is described as the rockfall volume rate (the total volume of rockfall within each time interval), the number of rockfall, and the number of rockfall in three discrete size fractions. Environmental variables are detailed in the first column. For each combination of rockfall and environmental metric, regression is undertaken for scan-by-scan (S), hourly (H), daily (D), weekly (W) and monthly (M) average statistics.*

	Rockfall Volume Rate					**Number of Rockfall**					***N* (0.001 – 0.01 m^3)**					***N* (0.01 – 0.1 m^3)**					***N* (0.1 – 10 m^3)**				
	S	H	D	W	M	S	H	D	W	M	S	H	D	W	M	S	H	D	W	M	S	H	D	W	M
Rain Accumulation	1.4	0.1	2.6	11.8	2.0	1.6	6.1	5.2	8.4	11.3	9.9	1.0	21.6	47.0	1.4	0.1	2.6	11.8	2.0	1.6	6.1	5.2	8.4	11.3	9.9
Peak Rain Intensity	9.0	6.0	1.2	27.7	3.2	15.4	9.5	3.0	7.1	7.5	6.4	3.2	12.8	8.9	9.0	6.0	1.2	27.7	3.2	15.4	9.5	3.0	7.1	7.5	6.4
Max. Temperature	11.8	22.8	19.9	9.0	0.1	0.1	0.5	2.7	18.3	2.6	1.8	1.3	0.3	14.0	11.8	22.8	19.9	9.0	0.1	0.1	0.5	2.7	18.3	2.6	1.8
Min. Temperature	10.5	11.2	0.7	3.5	0.1	0.1	0.0	0.8	22.1	3.1	1.5	1.4	2.6	6.7	10.5	11.2	0.7	3.5	0.1	0.1	0.0	0.8	22.1	3.1	1.5
Mean Temperature	11.0	20.9	7.3	6.9	0.1	0.1	0.4	2.4	18.3	2.7	1.7	1.0	3.3	3.7	11.0	20.9	7.3	6.9	0.1	0.1	0.4	2.4	18.3	2.7	1.7
Temperature Gradient	0.0	6.3	-	-	0.1	0.2	0.1	-	-	1.5	1.4	3.6	-	-	0.0	6.3	-	-	0.1	0.2	0.1	-	-	1.5	1.4
Significant Wave Height	0.6	1.4	3.4	19.9	0.7	0.1	0.2	2.1	63.6	1.4	1.5	1.4	4.1	3.6	0.6	1.4	3.4	19.9	0.7	0.1	0.2	2.1	63.6	1.4	1.5
Max. Tide Height	0.0	0.0	2.8	11.9	0.4	0.0	0.5	5.6	28.6	0.0	1.0	0.1	0.7	10.1	0.0	0.0	2.8	11.9	0.4	0.0	0.5	5.6	28.6	0.0	1.0
Max. Wind Speed	2.3	9.1	10.4	9.2	0.3	0.1	0.2	2.6	4.9	1.1	0.0	0.2	19.4	57.4	2.3	9.1	10.4	9.2	0.3	0.1	0.2	2.6	4.9	1.1	0.0

Table 6.4: *p values for significant relationships at the 5% significance level between rockfall occurrence and environmental conditions. Rockfall occurrence is described as the rockfall volume rate (the total volume of rockfall within each time interval), the number of rockfall, and the number of rockfall in three discrete size fractions. Environmental variables are detailed in the first column. For each combination of rockfall and environmental metric, regression is undertaken for scan-by-scan (S), hourly (H), daily (D), weekly (W) and monthly (M) average statistics.*

	Rockfall Volume Rate					**Number of Rockfall**					***N* (0.001 – 0.01 m^3)**					***N* (0.01 – 0.1 m^3)**					***N* (0.1 m^3 – 10 m^3)**				
	S	H	D	W	M	S	H	D	W	M	S	H	D	W	M	S	H	D	W	M	S	H	D	W	M
Rain Accumulation	-	-	-	-	0.47	-	-	-	-	-	-	-	-	-	-	-	-	-	-	-	0.88	0.29	-	-	-
Peak Rain Intensity	-	-	-	0.38	0.28	-	-	-	-	-	-	-	-	-	-	-	-	-	-	-	-	0.27	0.16	-	0.28
Max. Temperature	-	-	-	0.48	-	-	-	-	-	-	-	-	-	-	-	-	-	-	-	-	-	-	-	-	-
Min. Temperature	-	-	-	-	-	-	-	-	-	-	-	-	-	-	-	-	-	-	-	-	-	-	-	0.59	0.31
Mean Temperature	-	-	-	-	-	-	-	-	-	-	-	-	-	-	-	-	-	-	-	-	-	-	-	-	0.16
Temperature Gradient	-	-	-	-	-	-	-	-	-	-	-	-	-	-	-	-	-	-	-	-	-	-	-	-	-
Significant Wave Height	-	-	-	-	-	-	-	-	-	-	-	-	-	-	-	-	-	-	-	-	0.75	0.76	-	-	0.92
Max. Tide Height	-	-	-	-	-	-	-	-	-	-	-	-	-	-	-	-	-	-	-	-	-	-	-	0.28	0.72
Max. Wind Speed	-	-	-	-	-	-	-	-	-	-	-	-	-	-	-	-	-	-	-	-	-	-	-	0.51	0.13

July to September, of which the monthly timescale is the only dataset to include. Superimposition of rockfall events during this period, where the longer scan intervals result in multiple events considered as one, may have increased the proportion of intermediate sized rockfall, thereby yielding increased regression strengths for both the peak and mean temperatures.

For the largest rockfall group, *0.1 m^3 – 10 m^3*, temperature appears to have a far less appreciable influence on the probability of failure. For all survey intervals, a more significant regression is apparent between the rain accumulation, rainfall intensity, significant wave height, maximum tide height and maximum wind speed. This may reflect an increase in these event occurrences during the period of increased storminess between November and December.

6.3.4 Summary of time-averaged regression approach

A number of insights can be gained by creating time-averaged regressions between environmental variables and rockfall, and categorising these regressions by both varying timescales and rockfall volumes. Although almost all relationships are statistically insignificant, they are strongest when temperature variables are compared against the smallest rockfall. This is evident using both the total number of rockfall, and the number of rockfall with volumes between 0.001 - 0.01 m^3. Although drawing a cause-effect relationship from this requires a considerable degree of caution, this may imply that failures that occur through fragmentation of the rock mass may be predisposed by variations in temperature. The *peak wind speed*, *rainfall intensity* and *rainfall accumulation* are most strongly related to intermediate and larger rockfall volume classes. As discussed above, this is likely to reflect the occurrence of these events predominantly during the tail-end of the monitoring period, when stormy conditions were most prevalent.

When comparing all rockfall metrics, *peak wind speed* yields an above average correlation strength (mean r^2 for all maximum wind speed relationships is 0.07). This relationship is stronger for daily, weekly, and monthly average statistics than it is for scan-by-scan and hourly timescales. This can perhaps be explained by considering the effect that averaging has on *peak wind speeds*, where they become more indicative of the passage of storm events when averaged over longer timescales. The timescales over which environmental perturbations are effective in inducing damage to the rock mass is also likely to play a significant role in the strength of the relationships above. The insignificance of the relationship between peak wind speed and hourly and scan-by-scan rockfall metrics may suggest that storm events are either not represented by such short intervals, or are effective over longer timescales.

The over-arching finding of this section is that an insignificant relationship between rockfall and environmental conditions exists when the two are time-averaged and related

through linear regression. This has been observed in a number of previous studies (e.g. Rosser *et al.*, 2007a), with a number of possible explanations. First, this method of assessment assumes that environmental conditions are triggers of rockfall. This is contrary to theories described in *Chapter 2*, which suggest that rockfall occur as the result of a complex interplay between preparatory factors and triggers. As a result, the same two environmental conditions may or may not trigger failure, depending on the history of the rock mass with respect to damage accumulation by preparatory factors and the incremental reduction of resistance to failure. Second, the time-averaging process does not account for lags in the response of the rock mass to exogenic forcing. This pattern of behaviour has been observed in laboratory experiments, in which increases in pore water pressure are required to initiate crack growth, but the timing of final failure is determined purely as a functional of internal deformation and hyperbolic increases in microcrack interactions (Petley *et al.*, 2005). Third, the relationship between environmental conditions and rockfall may occur only when specific thresholds of environmental forcing are exceeded (Krautblatter and Moser, 2006). In reality, therefore, the analysis presented here is a first order approach to understanding the sensitivity of rockfall to environmental variables, which provides limited understanding of the nature of the response of rockfall. By plotting more than 8 000 measurements (the number of scans used), unless a strong correlation exists, patterns are very difficult to decipher where multiple controls may be active. A more tailored approach that makes better use of the high-frequency data is therefore required. Below, the influence of rainfall, marine conditions, and temperature are explored using alternative approaches.

6.4 Influence of rainfall events

The dataset presented enables the analysis of rockfall events in relation to discrete rainfall events, which remains unreported in the literature to date. Relationships between rainfall and slope failure are often focused upon large-scale ($> 1\ 000\ m^3$) catastrophic events (Hong *et al.*, 2006; Dahal and Hasegawa, 2008). Even in the context of rapid brittle rock slope failures in open-pits, published monitoring results have focused upon movement across comparatively large radar footprints relative to those of LiDAR, which are able to delineate smaller rockfall. While ordinary least square regressions are commonly used to relate rockfall occurrence and rainfall, these have been closer to the monthly scale of monitoring and, as in this study, have only yielded weak relationships (Rosser *et al.*, 2007a; Strunden *et al.*, 2015; Vann Jones *et al.*, 2015; d'Amato *et al.*, 2016).

Below, the passage of individual rainfall events is examined with respect to the largest 1 000 rockfall in the inventory. These rockfall were selected according to their size, as the regression between rainfall and rockfall activity was strongest for larger events, as shown above. For each rockfall, a search was conducted to identify the closest occurrence of a rainfall event.

The time of rainfall with respect to the rockfall was recorded alongside its duration. Duration was measured as the number of continuous 30 minute intervals in which any amount of rainfall above 0 mm was measured. Had minute resolution rainfall data been used, an on/off criterion for defining a single rainfall event is likely to have been overly sensitive to short bursts of rainfall. For each rainfall event, the intensity was recorded as the total rainfall accumulation divided by the duration of the whole storm. The maximum rainfall intensity measured within each rainfall event, represented in 30 minute intervals, was also recorded. The same analysis was undertaken for slumps at the top of the buttress.

Of the 1 000 rockfall, 60% were preceded by rainfall within 24 h of failure, and 78% were preceded by rainfall within 48 h (Figure 6.12). For slumps, this value is similar, with 62% preceded by rockfall within 24 h and 80% preceded by rainfall within 48 h. It is noted that if rainfall occurred during the scan within which a failure occurred, this scan was removed due to the influence of rain on the scan data consistency and the rockfall was only detected by a change detection between the two nearest scans during which no rainfall occurred. It is possible, therefore, that many of the rainfall events that occurred within a few hours before failure may actually have occurred during failure. The result is a potential increase in the proportion of events that occurred during rainfall. In this study, 11.4% of rockfall occurred during rainfall.

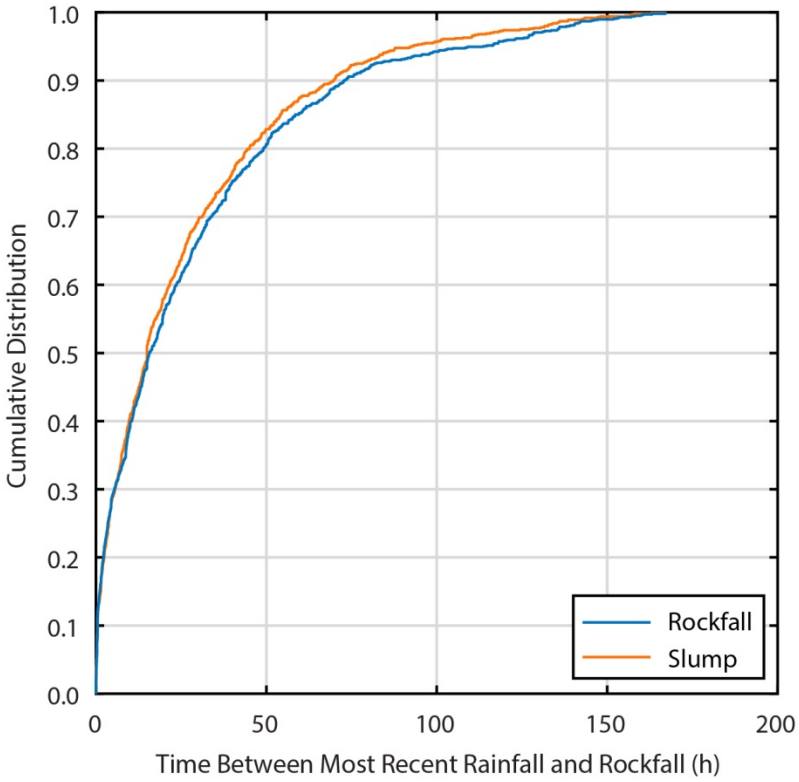

Figure 6.12: *Cumulative distribution of the time between the top 1 000 rockfall and the closest rainfall events. 60% of rockfall were preceded by rainfall within 24 h, and ca. 80% within 48 h. While this does not confirm a cause-effect relation, it affirms the need to examine rainfall prior to rockfall activity. Blue line = rockfall. Orange line = slumps.*

Assuming that only a limited number of scans were removed due to coincidence with rainfall, and based on the fact that the longest recorded rainfall duration was 7.5 h, it is possible that due to scan removal the true proportion of rockfall that occurred during rainfall could be 33.0% (if all rainfall within this duration is assumed to have occurred at the time of failure). Based on the mean rainfall duration (2.5 h), however, a likely upper proportion of rockfall that occurred during rainfall is 21.6%. The fact that an increase in intermediate and large rockfall activity occurred within the final two months of the monitoring period, which also recorded the greatest rainfall, suggests that wetting of the rock face may predispose it to failure.

Rainfall intensity-duration plots were created for both the estimated and maximum rainfall intensities that occurred before each rockfall. This pattern conforms to that of previously published datasets for landslides (Caine, 1980; Guzzetti *et al.*, 2008; Kirschbaum *et al.*, 2012), in which both short intense bursts of rainfall (*ca.* 0.5 – 2 h), and longer less intense rainfall (*ca.* 5 - 10 h) occur before failure. Given that 40% of the largest rockfall are not preceded by rainfall within 24 h, these are removed from the intensity-duration plots below. For the rockfall observed at East Cliff, the intensity-duration relationship is:

$$I = 2.57 \cdot D^{-0.25} \qquad \text{[Eq. 6.2]}$$

where I is intensity (mm h^{-1}) and D is duration (h). Hence, an increase in the log of rainfall duration must be met by an 0.25-fold rise in the log of intensity in order to initiate failure. Figure 6.13, which is perhaps the highest temporal and spatial resolution analysis of rainfall intensity duration to date, reveals a vertical clustering of events at each increment of duration. Guzzetti *et al.* (2008) identified a similar bias at 3 h, which was attributed to a predefined measuring interval (3 h) that exceeded the timescale over which many storms occurred. In this study, the 30-minute resolution of rainfall data is responsible for the pattern of vertical striping that exists in Figure 6.13, though no appreciable increase in clustering is evident at this duration, suggesting that rockfall triggering rainfall events occur at timescales greater than this monitoring interval.

The thresholds in Figure 6.13 are positioned below 95% of rockfall-triggering rainfall events using a 5% quantile regression. This reflects the minimum rainfall conditions necessary for instability, while also eliminating sporadic and therefore unrepresentative data points. Though intensity-duration thresholds are well used in the literature, no generic method exists for their construction (Aleotti, 2004). Figure 6.14 illustrates variation in threshold position and incline based on the quantile used.

As expected, the maximum-recorded rainfall intensity for each storm increases the value of many of the data points up the intensity-duration plot in comparison with the mean-recorded rainfall intensity-duration plot. Given that the 5th percentile of rainfall measurements was

unaffected by this, however, the actual I-D power law remains the same. For slumps, the same patterns are observable as with the rockfall. This may be relate to the precision of the rain gauge used in this study and the fixed interval over which it records, which is insufficient to create subtle differences between the two.

Intensity-duration exponents typically vary between -2.00 and -0.19 (Cepeda *et al.*, 2010), and the exponents in this study therefore sit at the lower end of this range. This is

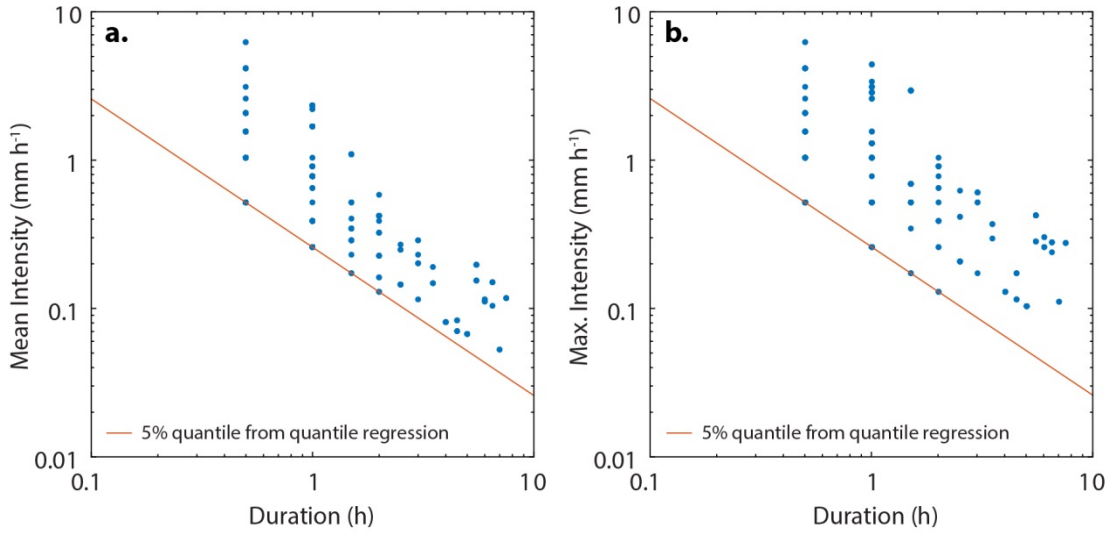

Figure 6.13: *Intensity-Duration plots. (a) Rainfall that preceded rockfall using the mean estimated intensity. (b) Maximum recorded intensity. Both are sourced from rainfall events that occurred within 24 h of failure. As the log of intensity decreases, the log of duration must increase to predispose failure, assuming that the relationship between rainfall and rockfall is cause-effect.*

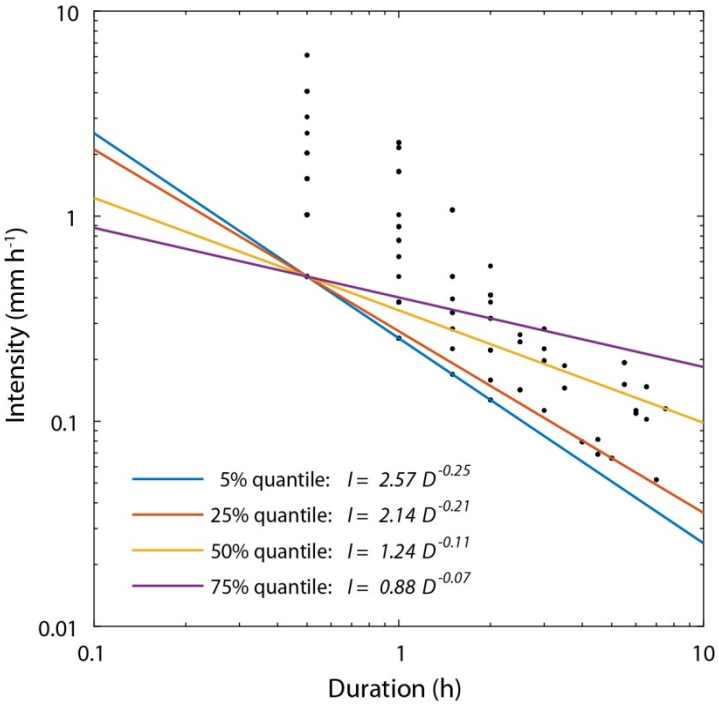

Figure 6.14: *Intensity-Duration relationship for the mean estimated intensity of each storm, with thresholds for varying quantile regressions.*

depicted by a lower gradient in Figure 6.15, which also yields a lower than usual intensity intercept, suggesting that less intense rainfall is required for failure. Guzzetti *et al.* (2007) noted that exponents may be influenced by variability in rainfall conditions within the region, geological or geomorphological differences in setting, or incompleteness in the failure inventory. A lower exponent and intercept indicate that, for durations below *ca.* 10 h, less intense rainfall is required to induce rockfall at East Cliff. Comparing these datasets requires caution; while some comprise landslides within brittle material, the failure mechanism examined here differs considerably in its sensitivity to rainfall. Furthermore, one possible explanation for the relatively small y-intercept is that the delineation of rainfall events and the timing of rockfall are both accurate to within 30 minutes. As such, they do not suffer from over-averaging of conditions through time as in previously published datasets.

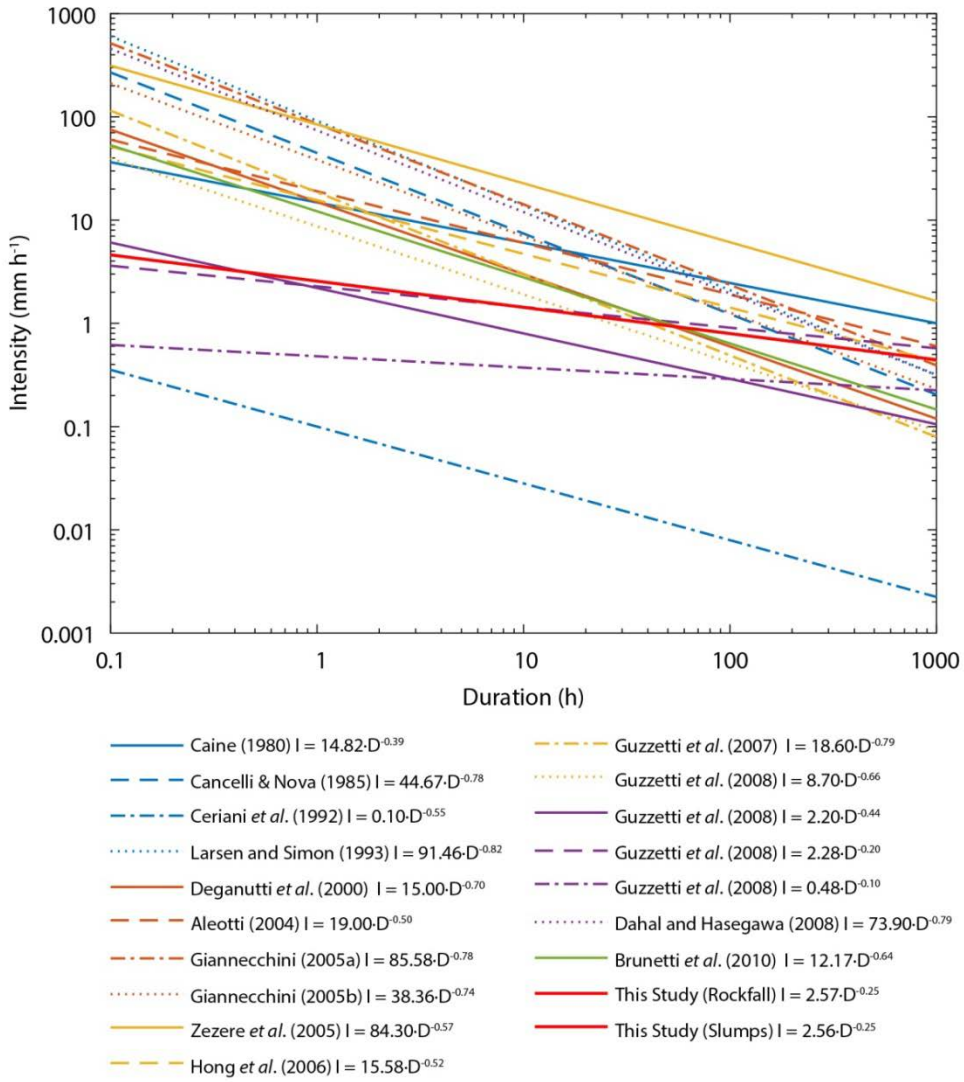

Figure 6.15: *Intensity-Duration plots compiled from an analysis of published literature. Those in this study exhibit a lower exponent value, suggesting that, for durations below ca. 10 h, less intense rainfall is required to induce rockfall at East Cliff The line also sits below the majority of other thresholds, constructed for landslide volumes several orders of magnitude larger, indicative of the relatively low rainfall totals in this region and/or an apparent sensitivity of rockfall to small rainfall events.*

In order to assess whether the response of rockfall to rainfall intensity and accumulation is significant when lagged, cross-correlations were undertaken between rainfall intensity-rockfall rate and rainfall accumulation-rockfall rate, with lags introduced between 1 h and 24 h prior to failure. This method of analysis was also applied by Delonca *et al.* (2014) and requires a time series of data with a number of measurements that is sufficient for lags to be applied. For consistency, and in light of the fact that 60% of rockfall occurred within 24 h of failure, this comparison was undertaken for the hourly-averaged rainfall data and hourly-averaged rockfall volume rates (Figure 6.16). Confidence bounds of 95% are added, representing two standard deviations for the sample cross correlation estimation error, assuming that the two inputs are uncorrelated. For both the rainfall intensity and rainfall accumulation, the correlation strength increases as the lag decreases. Statistical significance only occurs when the lags are below 5 h, suggesting that rockfall are most sensitive to rainfall that occurs within this period. The most statistically significant correlation is observed 1 h and 0 h before failure, where the peak for rain intensity is 0.0476 and the peak for rain accumulation is 0.0629. This supports the relationship significance obtained by linear regression in *Section 6.3* (Table 6.4). This disparity in correlation strengths, where cross correlation values are higher for rainfall accumulation than they are for rainfall intensity, suggests that the rock face may be more responsive to rainfall accumulation than rainfall intensity. This is perhaps unsurprising, given that a high proportion of rockfall occurred during the storms of November and December. The high permeability and dense fracturing of the sandstone therefore points towards a decrease in frictional resistance along discontinuities, which increases with rainfall accumulation. Alternatively, it may suggest that a 'damage skin' zone at the surface is developed through weathering and exploitation of microcracks below the scale of rockfall volumes.

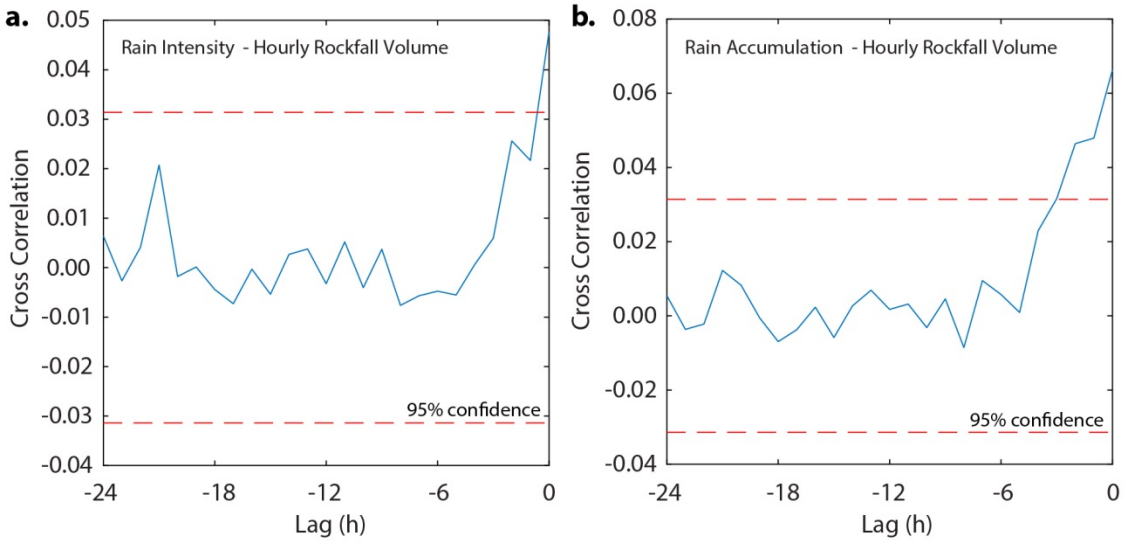

Figure 6.16: *(a) Cross-correlation for rainfall intensity and rockfall, and (b) rainfall accumulation and rockfall. Both show significant positive correlations between 1 h and 0 h before failure, where significance is determined as two standard deviations of the sample cross correlation estimation error.*

6.5 Influence of tidal conditions

In order to examine the influence of the tide, all rockfall recorded in the scan-by-scan inventory were recentred based on their position relative to the tide cycle. The timing of the closest two low tides was identified for each rockfall, with the oldest of the two low tides representing the first low tide and the second representing the most recent low tide. Each low tide is separated by a *ca.* 12 h window; as such, it was possible to identify the timing of each rockfall within this 12 h tide period. 0 h therefore represents a rockfall that occurred at exactly low tide, 6 h represents a rockfall that occurred at high tide, and 12 h represents a rockfall that occurred at the following low tide. Rockfall measured between scan pair intervals greater than 2 h were removed from this analysis. The cumulative distribution of rockfall, categorised by volume fraction, is displayed in Figure 6.17.

For rockfall volumes in the order of 0.001 – 0.01 m^3, the pattern of rockfall shows no sensitivity to the tide height, which supports the regression analysis shown in Figure 6.7. Variation from a linear pattern increases with the rockfall volume fraction. For the largest rockfall events, a shift towards a Gaussian distribution (represented by an *s*-shaped curve in a cumulative distribution plot) is evident. While only 17 events > 1 m^3 occurred, this suggests that larger rockfall may be more sensitive to the tide height and that there is an increased likelihood of rockfall in this fraction during high tide. Given the low numbers of rockfall within this size faction, this distribution is more likely to be a coincidence than the distribution generated for events < 1 m^3.

In recentring the data according to a 12 h tide window, the chronology of the dataset is lost as its timing becomes essentially circular. Kernel density estimates were used to depict the probability distribution of rockfall occurrence by volume fraction during the tide window. Rockfall that occur during 0 h are as proximal to those that occur at 12 h, as they are to those that occur at 1 h. As such, a circular kernel density function was used that accounts for 24 h data (Atanasiu, 2014). Figure 6.17b shows that, as the rockfall volume fraction increases, it becomes increasingly normally distributed. For rockfall > 1 m^3, therefore, the probability of a rockfall occurring during high tide ($P = 0.128$) is more than 2.5 times that of a rockfall at low tide ($P = 0.049$). While the sample size in this study is insufficient to suggest that these processes are physically driven by, for example, microseismic activity due to cliff shaking at high tide (Norman *et al.*, 2013; Brain *et al.*, 2014), the sample size for the smallest rockfall events is sufficient to suggest that tide has no bearing on the detachment of very small fragments of rock from the rock face. This could indicate, therefore, that the evolution of rockfall through fragmentation of the rock mass is independent of this rock slope's coastal setting.

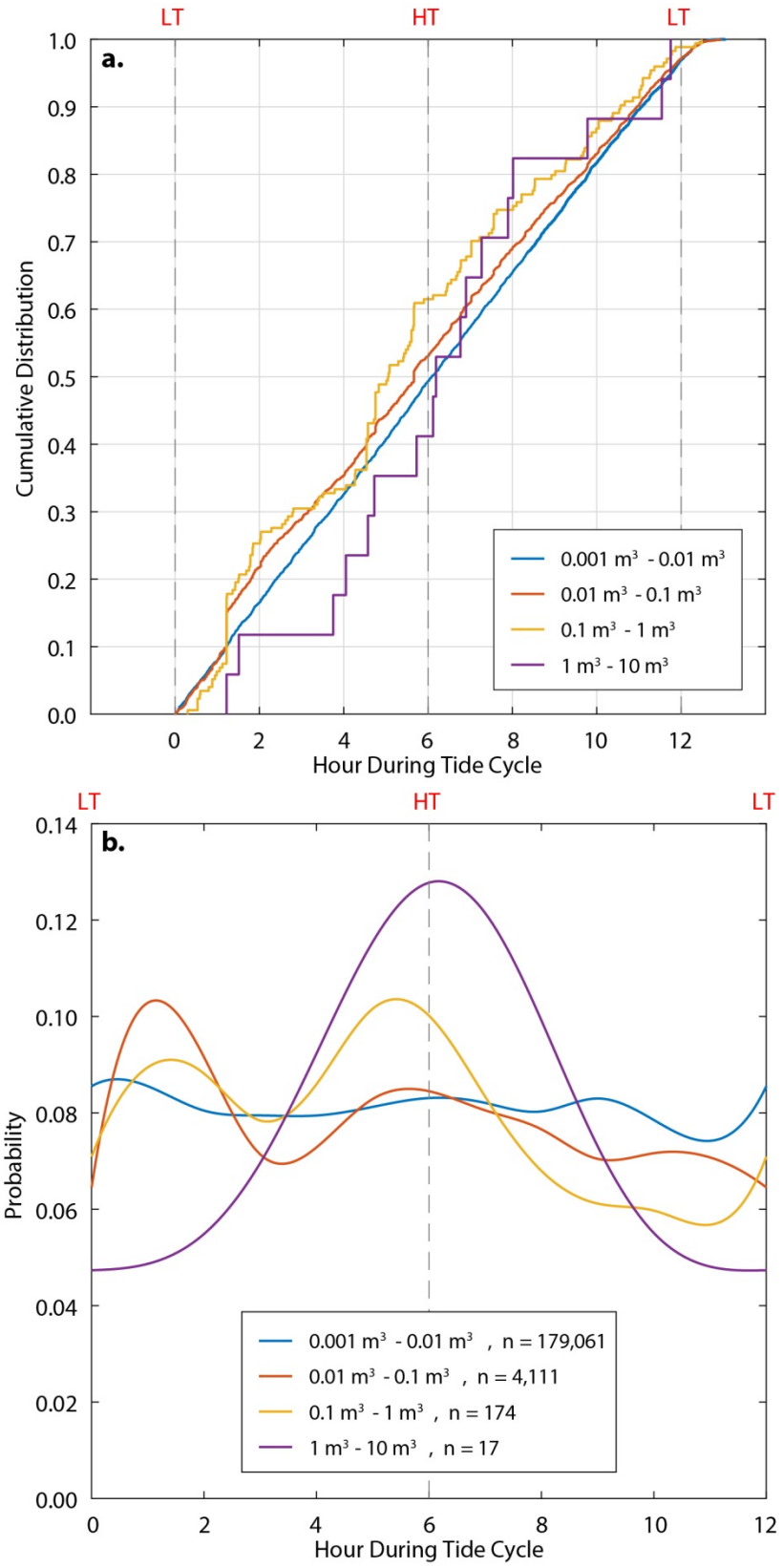

Figure 6.17: *(a) Cumulative distribution of rockfall that are distributed according to the position with a ca. 12 h tide window, from one low tide to the next. For the small and intermediate size fractions, no dominant position is evident. However, for larger rockfall, a skew towards high tide is evident. (b) Probability distributions for the same datasets, derived using a circular kernel density estimate. For large rockfall, a peak in probability of occurrence at high tide suggests that a rockfall of this size fraction is more than twice as likely to occur as one at low tide.*

6.6 Influence of variations in temperature

6.6.1 Rockfall frequency

As discussed in *Chapter 2*, a number of studies have sought to characterise damage accumulation within a rock mass as a result of solar-induced thermal stresses (Vlcko *et al.*, 2009; Collins and Stock; 2016; Eppes *et al.*, 2016). The collection here of rockfall data at such a high frequency presents a unique opportunity to examine this process, and is well placed to draw upon material detachment as a direct proxy for rock mass damage, progressive failure, and the removal of a 'damage skin' of microcracked and weathered intact rock. If final failure is defined as failure that is preceded by an acceleration in precursory rockfall events (presented in the following chapter), then the significant relationships defined here between temperature and the smallest rockfall may suggests that these reflect preparatory stresses within the rock mass.

To conduct this analysis, timing of rockfall data was recentred, initially by identifying the hour of day within which each rockfall occurred. Rockfall were categorised again by size, but with rockfall > 1 m^3 appended to the 0.1 m^3 – 1 m^3 data, given that there were now fewer rockfall (17) than the number of hours in a day. The probability of rockfall occurrence averaged by all days monitored is presented in Figure 6.18, categorised by the volume fraction. For the largest rockfall, the pattern of rockfall shows significant variability, with no appreciable pattern in occurrence during the day. For intermediate sized rockfall (0.01 – 0.1 m^3), however, an increase in rockfall activity occurs through the hours of daylight, with the highest probability, 0.065, between 17.00 and 18.00. The smallest rockfall (0.001 – 0.01 m^3) also show an increase through the middle of the day. Peak activity is observed between 05.00 and 06.00, and again between 17.00 and 18.00. There is significant variation in sunrise and sunset times throughout the monitoring period. The range of observed timings is therefore added (Figure 6.18).

The peak rockfall activity for all three size fractions occurs during the hours of sunset, with increased rates of small and intermediate rockfall activity observed during this period. In both the small and intermediate size ranges, despite small peaks in rockfall activity during sunrise, an overall increase can be observed through the day towards sunset (Figure 6.18). While this does not necessarily reflect temperature or solar-induced thermal stresses, this dataset comprises all rockfall in the 183 363 event dataset with a scan interval < 2 h. As such, no bias is introduced by change detections that include large numbers of rockfall that occurred over a longer period of time. The level of instrument noise can be attributed to the temperature of the air mass through which the laser passes. Point clouds acquired using LiDAR can therefore vary in distance from the scanner with varying temperatures. In this study, however, this effect was removed by applying a range correction factor to each point cloud, as noted in *Section 3.6*. This,

combined with the fact that all change detections fell below the 0.03 m applied LoD, negates the possibility that diurnal patterns of rockfall are a result of a methodological error.

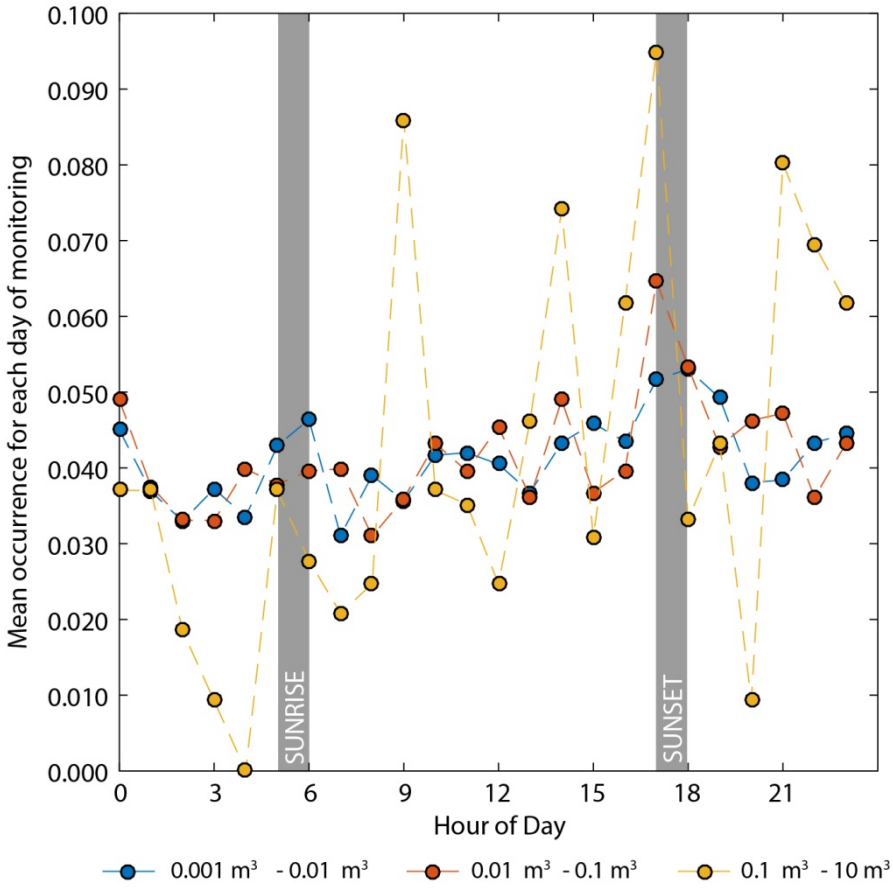

Figure 6.18: *The occurrence of rockfall, accumulated by the hour of the day within which each rockfall occurred. Average positions of sunrise and sunset are shown, highlighting the correspondence with peaks in rockfall activity for the small and intermediate size fractions. Overall increases in rockfall activity are observed within both of these categories, with the most significant peak corresponding to cooling temperatures at sunset.*

In order to assess the sensitivity of the rock mass to changes in air temperature throughout the day, a time series of both air temperature (measured from the rock face weather station) and rock face temperature (measured by the pyrometer) were cross-correlated. While these measurements do not exactly match the 10 month rockfall monitoring period, they provide an overall indication of the response of the rock mass to changes in air temperature. The pattern of rock face temperatures matches that of the air temperature (Figure 6.19). During the summer months, the disparity in temperature between the air and rock mass is greatest, between ca. 5°C – 15°C during the daytime, but the overall patterns of rock face temperature match that of the air temperature. Diurnal temperature variations within the rock mass are of the order of 1°C – 3°C, with the greatest variation for both occurring during the summer months.

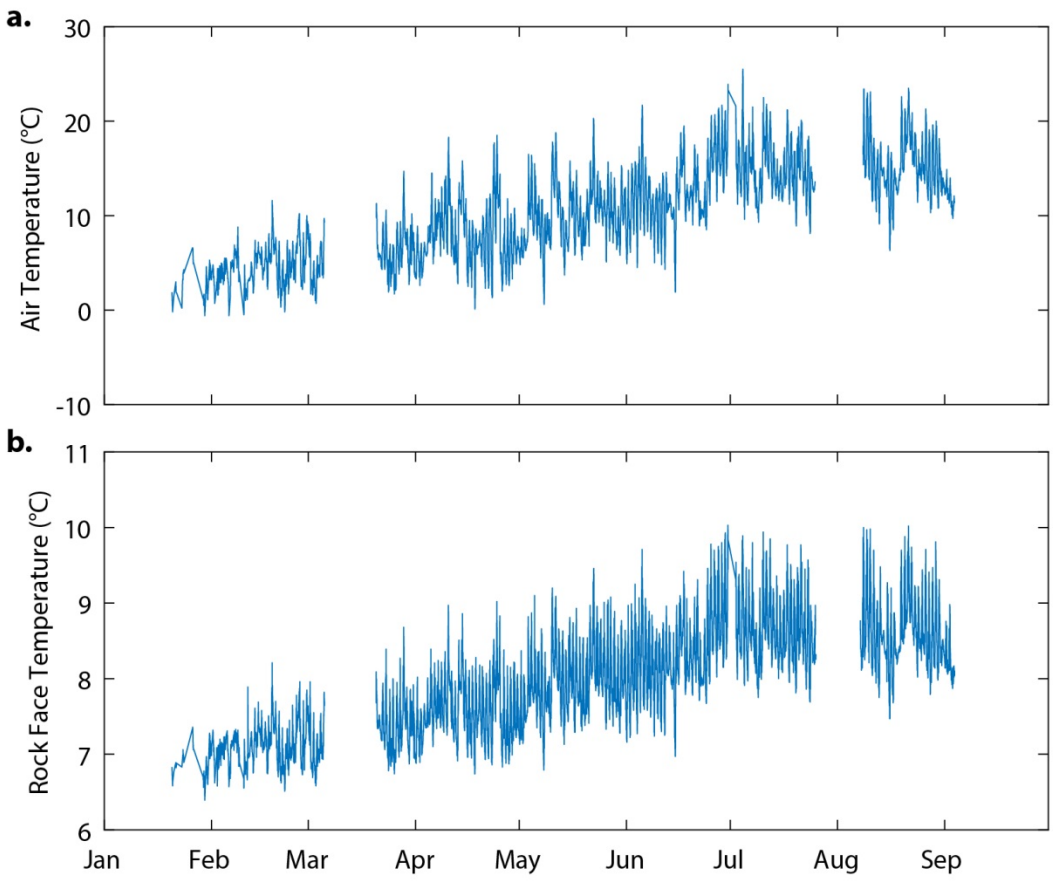

Figure 6.19: *(a) Air temperature and (b) rock face temperature signals used for the cross-correlation in Figure 6.20. Weather data began recording on 20th Jan, while the pyrometer ceased to record data for a sustained period on 12th September. While these do not correspond exactly to the rockfall monitoring period, their relationship to one another is assumed to remain constant.*

A least squares regression between air temperature and rock face temperature yields a direct relationship that includes air temperatures below freezing. A gradient of 0.13 indicates that a 10°C air temperature rise is met with an approximately 1°C temperature rise of the rock face (Figure 6.20a). At an air temperature of 0°C, the rock face temperature is 6.56°C. While this does not account for any moisture that resides within pores and voids within the rock mass, this suggests that much lower air temperatures would be required to induce freeze-thaw conditions. The strength of the relationship ($r^2 = 0.94$) suggests that changes in air temperature directly affect the rock face temperature, and may therefore be used in assessing the influence of temperature upon rockfall occurrence. Deviations from a perfectly linear relationship may arise due to direct insolation of the rock mass. A cross-correlation analysis between the two variables shows that a peak in correlation strength occurs when the time series are offset by 1 h 27 min, such that the response of the rock face temperature to air temperature change is lagged. When the same approach is used to relate air temperature gradient to hourly resampled rockfall throughout the monitoring period, the cross correlation strength is greatest, and becomes significant above 2σ, at one hour prior to failure. In addition to the fact that the peak in rockfall

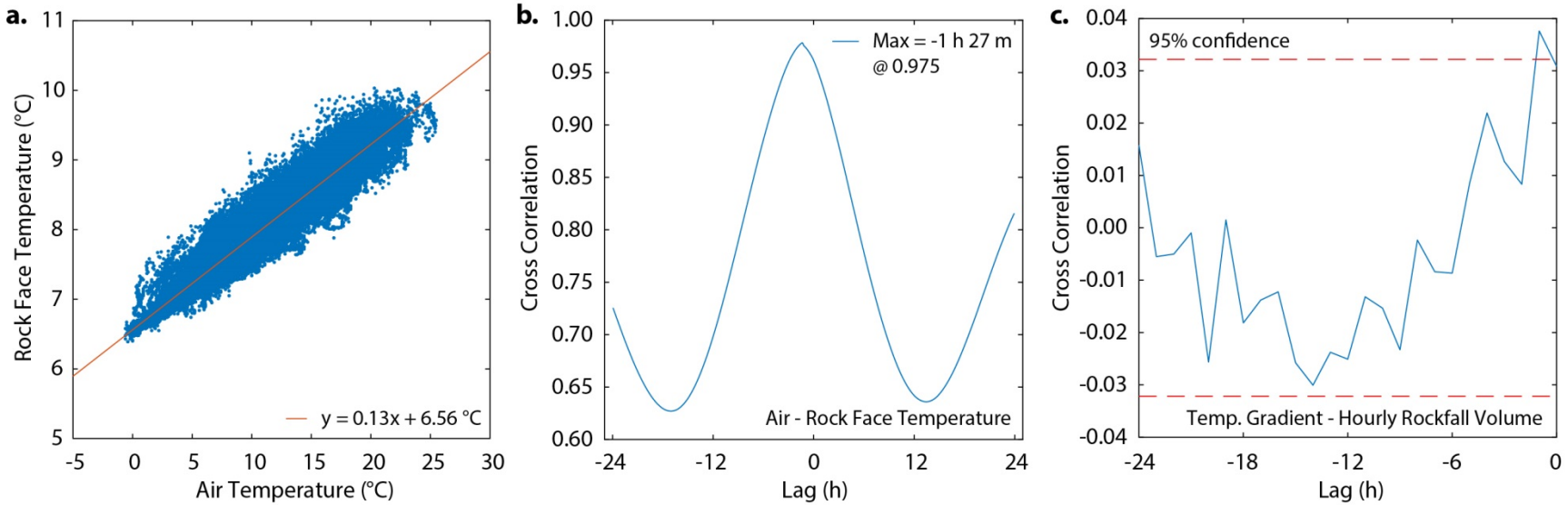

Figure 6.20: *(a) Ordinary least squares regression between air temperature measured by the cliff-top weather station, and rock face temperature, measured by the pyrometer. While freezing temperatures are recorded (outside the rockfall monitoring period), the rock face temperature remains above 6.56°C. (b) Cross correlation between air temperature and rock face temperature, showing a peak in correlation at 1 h 27 min lag. (c) The cross correlation between air temperature and rockfall activity also becomes significant between 2 h and 1 h before failure (hourly resampled data). Moreover, this correlation is negative, indicating that cooling temperatures are responsible for significant rockfall activity.*

occurrence matches the timing of the rockfall response to air temperature change, the negative correlation indicates that the relationship between the occurrence of rockfall is most sensitive to negative temperature gradients, i.e. cooling, as opposed to heating. While this correlation cannot be directly assigned as a cause of rockfall, the relationship between the time series of temperatures and rockfall affirms the diurnal variability in rockfall probability that has been shown. In these results, cooling air temperatures, and thereby lagged rock face temperatures, correspond to an increase in the probability of rockfall occurrence.

The timing of rockfall were further recentred to examine their response to cooling rock face temperatures, providing a similar averaging process to the tidal analysis in *Section 6.5*.

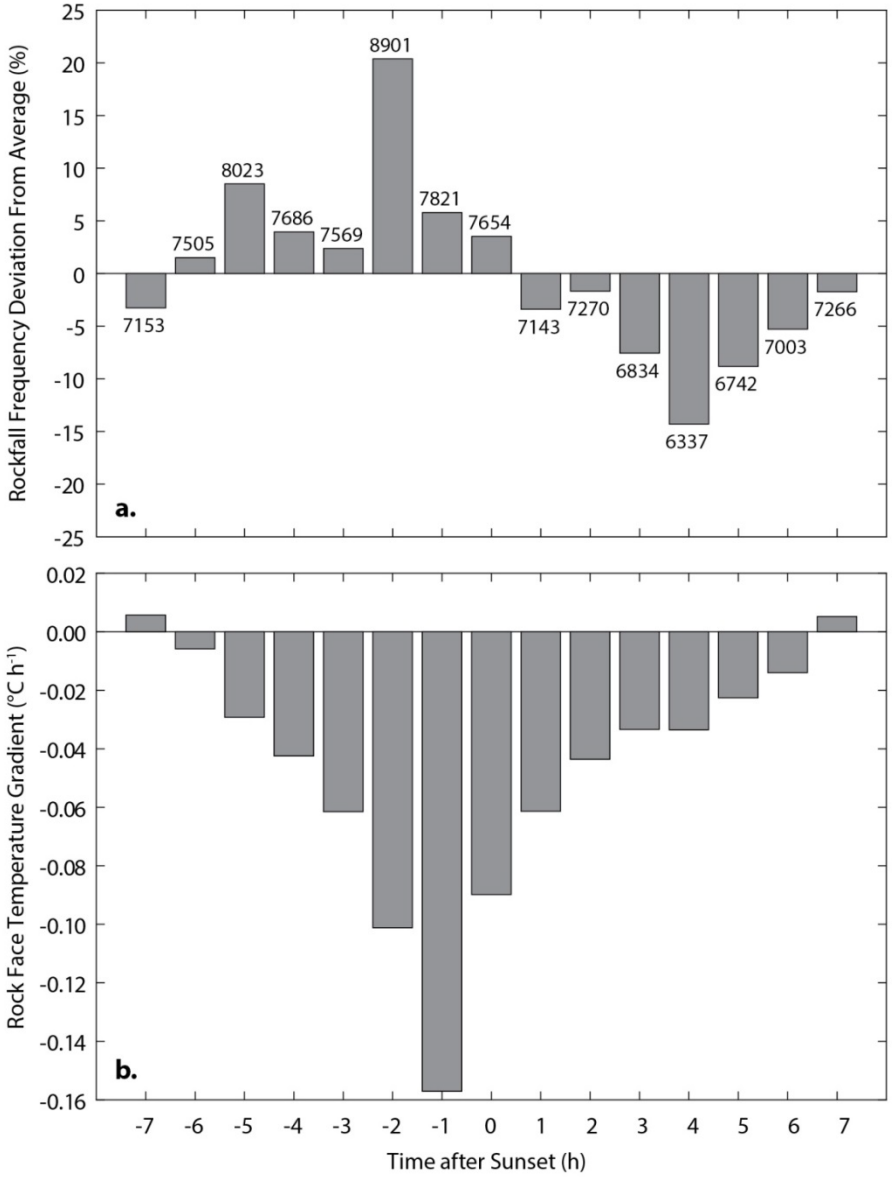

Figure 6.21: *(a) Rockfall frequency binned by its time in hours from the closest sunset. A deviation of 20.8% above the average occurs between 1 h and 2 h before sunset. In general, rockfall frequency before sunset is above the average frequency, while rockfall activity after sunset is below the average. (b) Air temperature cooling is on average greatest one hour before failure. The most pronounced cooling occurs before sunset, which may explain the disparity in rockfall activity rates before and after.*

Here, the time of sunset was recorded for each day of monitoring, and the time between each rockfall and the sunset derived. Rockfall were examined within seven hours before and after sunset, accounting for the minimum hours of daylight recorded during the study period. This prevented bias during winter months, where rockfall could not have occurred more than seven hours before sunset in the days and weeks surrounding the winter solstice. When binned by hour of occurrence from sunset, a peak in the number of rockfall that is significant ($p < 0.05$), and is 20.8% greater than the mean hourly rockfall total, occurs within one and two hours before sunset (Figure 6.21a). When compared with rock face pyrometer distributions recentred using the same approach (Figure 6.21b), this coincides with the second greatest hourly temperature change (cooling) that occurs before sunset. A general transition from rockfall frequencies above the mean to rockfall frequencies below the mean occurs before and after sunset (Figure 6.22). Although temperatures after sunset continue to lower, this cooling effect is less pronounced than immediately before sunset.

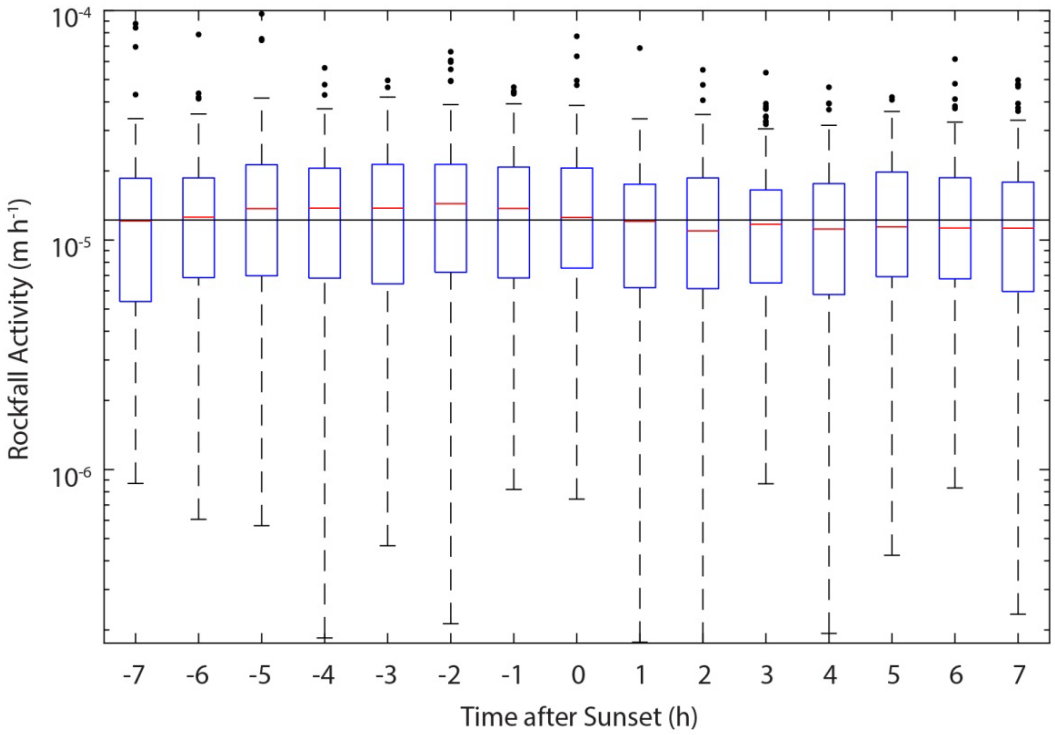

Figure 6.22: *Box plots showing the same distributions as in Figure 6.21. Rockfall activity, accounting for variations in the size of each rockfall that occurred, is presented in addition to the number of rockfall that occurred. The dots above each whisker represent measurements that exceed 1.5 times the interquartile range, and hence greater than the 75th percentile, which may be considered as outliers. The median rockfall activities for each hour, represented by the red lines, show a similar pattern above and below the median for the entire dataset.*

6.6.2 Rockfall size and shape

In addition to the rate of rockfall activity, the size distribution of rockfall through the monitoring period is correlated with temperature. By using the magnitude-frequency exponent derived in *Section 5.8,* the size distribution of rockfall for each week is displayed through the monitoring period alongside a plot of air temperature measured at the rock face (Figure 6.23). An increase in the exponent is evident towards the summer months, during June and July, indicating that a higher proportion of small rockfall events occurred during this time period. This increase in small events appears to follow the increasing temperatures that occur towards summer, and their return to an original background level suggests that, had scanning not been interrupted during August and September, the exponent of the magnitude-frequency distribution would have decreased in accordance with temperatures. By examining changes to the magnitude-frequency distribution using fixed time intervals through time, seasonality in the size distribution of rockfall is evident. This highlights the significance of monitoring across multiple seasons for the determination of accurate coastal retreat estimates, as initially proposed by Barlow *et al.* (2012). In relation to the mechanisms of failure, it also suggests that fragmentation of the rock mass and microcrack growth may be predisposed by thermal induced stresses. The role of temperature gradient has been highlighted above and, since the largest hourly temperature gradients occur during the summer months, this suggests that temperature gradient may be of significant importance in predisposing rock slopes to large rockfall events.

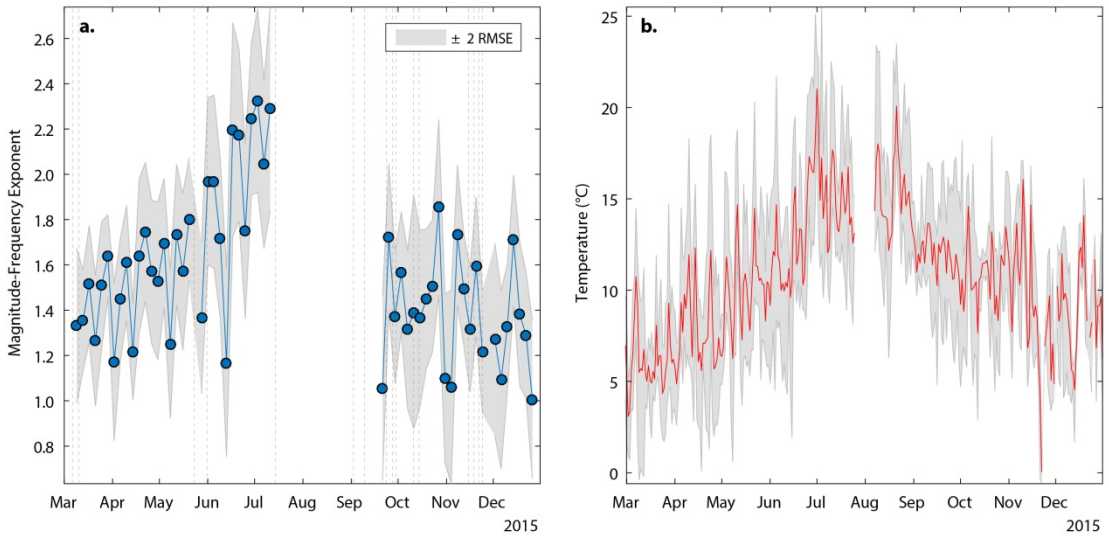

Figure 6.23: *(a) Magnitude-frequency exponent collected using the 7 d change detection dataset and plotted through the monitoring period. (b) Mean temperature distribution (with upper and lower bounds) for each day of the monitoring period. The overall increase in the proportion of small events appears to coincide with warming during the summer months, and returns to a background level that is more variable during the winter months.*

The shape of rockfall was used as a further metric of rockfall sensitivity to temperature variation, categorised in Figure 6.24 by the hour of the day within which the rockfall occurred. The mean rockfall shape for each hour shows little variation; however, at night (dark blue and yellow), the mean shapes tend towards a slab-like form within the Sneed and Folk (1982) plot (this difference cannot be tested for significance). Despite this, the two data points that are most slab-like in form, having exhibited a more slab-like form, occur at 18.00 and 19.00 and hence are proximal to the average timing of sunset. This may support the idea that near-surface tensile stresses are generated by thermal induced forcing.

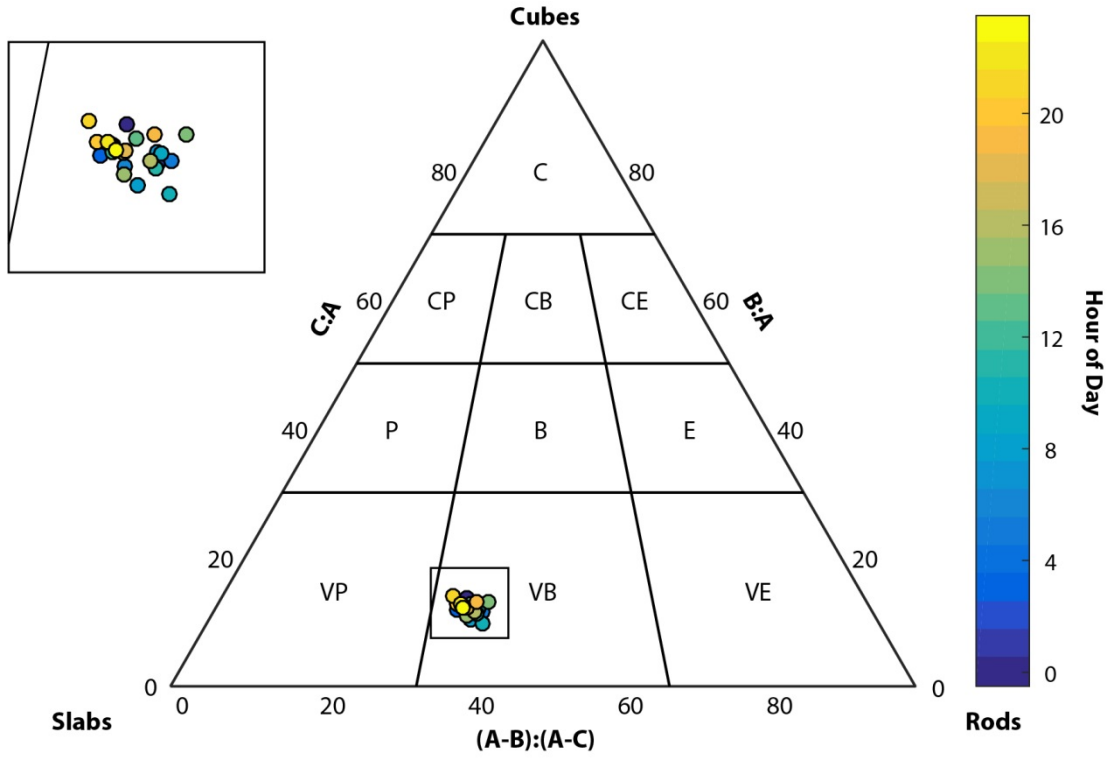

Figure 6.24: *Sneed and Folk (1958) ternary plot. No clear trend in rockfall shape can be observed by hour of day; however, more slab-like forms occur between 18.00 and 19.00.*

In summary, the collection of high frequency rockfall data has enabled it to be binned according to the hour of the day for the first time. An increase in the total number of rockfall from the average sunrise to the average time of sunset shows that rockfall activity increases throughout the day, with a significant peak that occurs during the hours of sunset. A cross-correlation of rock face and air temperature shows that rock face temperatures are most sensitive to air temperature change within approximately 1.5 h. When the air temperature is related to rockfall, cooling air temperatures showed a significant correlation with rockfall activity. When the timing of rockfall is considered in relation to the timing of each sunset, both the number of rockfall and the rockfall activity is higher before sunset than after sunset, with a considerable increase in rockfall activity between one and two hours beforehand. This decrease

relates to the period of greatest cooling. While previous studies have monitored damage accumulation by acoustic emission (Eppes *et al.*, 2016) and joint widening (Collins and Stock, 2016), this analysis represent a similar process over the entire rock slope face, if the detachments here are viewed as components of larger, developing failures.

6.7 Summary

The analysis in this chapter supports many relationships that have only previously been hypothesised, but equally raises many additional questions and ideas about the controls on rockfall, both as preparatory factors and as triggers. A relationship between onset of more frequent storms and an increased rate of rockfall activity is apparent in the months of November and December. During individual storm events, up to 10% of the total erosion can occur within the space of several hours. This suggests a direct link between rainfall and rockfall occurrence; however, linear relationships between the two yielded only marginally significant relationships. Given the emphasis placed on the interaction between preparatory factors and triggers of failure presented in *Chapter 2*, this is perhaps unsurprising. More significant relationships were obtained when the signal of rainfall accumulation and rockfall activity were compared, than when the signal of rainfall intensity was used. This suggests that some saturation of the sandstone is required to trigger the detachment of material from the rock face, through both elevated pressures and a reduction in frictional resistance along discontinuities. Both rockfall and slumps of loose material appeared to fail after similar thresholds of rainfall intensity and duration were exceeded. While this may reflect the characteristics of rainfall events in this setting, it also implies that the response of the rock face to rainfall is non-linear and inherently complex.

In Figure 6.25, the complexity of the response of the rock face to rainfall is evident. Here, the rockfall volume recorded in each scan, alongside the number of rockfall is recorded alongside rainfall and other exogenic conditions for the period 16th December- 31st December. Peaks in rockfall activity can be observed in (a) periods in which no rainfall or apparent 'trigger' occur, (b) times that occur shortly after (hours – days) rainfall events, and (c) rockfall that coincide with storm events. The most rockfall activity occurs during 25th – 27th December, during rainfall that was less intense than previous events but accumulated *ca.* 20 mm. This reinforces the suggestion that the rock face is more sensitive to accumulation than intensity, which may reflect the high porosity of the sandstone beds and the importance of ground water flow at depth, but also highlights the complexity in constraining the influence of rainfall.

The collection of data at sub-hourly time intervals has allowed rockfall to be examined with respect to their position within each tidal cycle. For rockfall < 1 m^3, the probability of failure showed no variation through the tide cycle. This suggests that the influence of marine

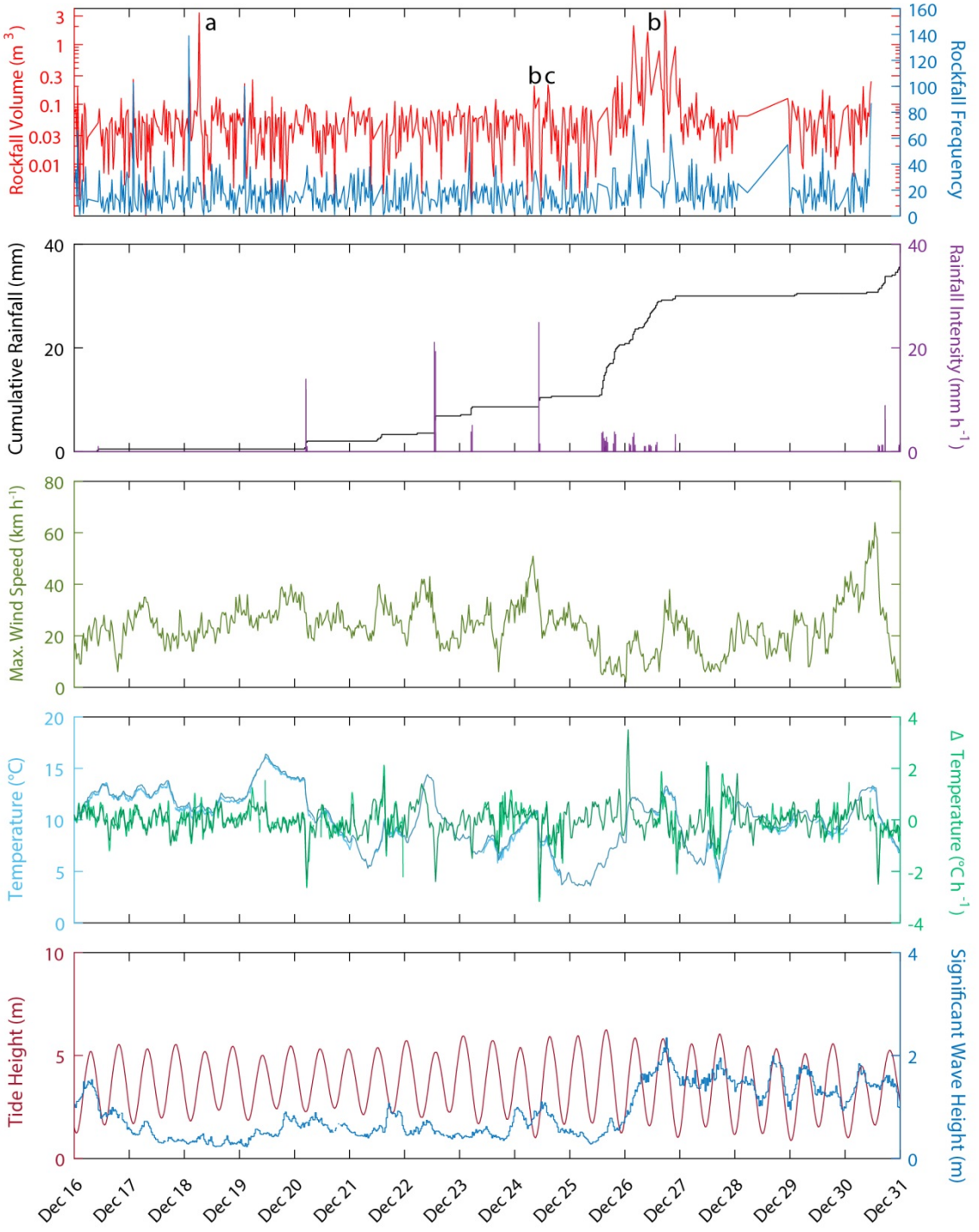

Figure 6.25: *Rockfall can occur during (a) periods in which no rainfall or apparent 'trigger' occur, (b) times that occur shortly after (hours – days) rainfall events, and (c) rockfall that coincide with storm events. Peaks in rockfall events across the cliff face adhere to all three of these timings with respect to rainfall. The largest increase in rockfall activity occurs during sustained rainfall that accumulates ca. 20 mm within 24 h, suggesting that in this setting, the porosity of sandstone is such that rainfall accumulation is of greater importance than its intensity.*

conditions does not necessarily prepare the slope for failure by damage accumulation of the rock mass through small rockfall. However, while only 17 rockfall > 1 m^3 were recorded, these events showed a probability at high tide that was twice that at low tide. Furthermore, linear regressions between the maximum tide height and significant wave height, and the occurrence of rockfall > 1 m^3, constituted some of the few significant relationships obtained. This may be partially explained by the fact that some of the largest rockfall occurred at the base of the cliff.

The collection of high frequency data has also enabled an examination of rockfall activity with respect to the time of the day and, by implication, temperature gradient. While similar studies have examined damage that is accumulated through thermomechanically induced microcracking (Eppes *et al.*, 2016) and joint widening (Collins and Stock, 2016), this chapter has for the first time provided insights into the temporal distribution of rockfall across a cliff face with respect to temperature change. This showed a considerable increase in rockfall activity ($> 20\%$ above the mean hourly rate) during maximum daily cooling between one and two hours before sunset. This corresponds to peaks in damage accumulated in both of the aforementioned studies. Moreover, Eppes *et al.* (2016) observed that the high levels of microcracking during falling air temperatures occurred at the near-surface. This corresponds to the shallow depth of rockfall identified in *Chapter 5*. Given that slab-like shapes have been found to be most predominant for small detachments, near-surface microcracking during cooling may also explain why the sunset peak in rockfall timing is apparent for all volume fractions, but is most pronounced for rockfall < 0.1 m^3.

The creation of magnitude frequency relationships through time represents the first use of such an approach, and supports the suggestion that small rockfall are predisposed by temperature variation to a greater extent than large rockfall. The analysis here has shown that that the proportion of small rockfall events within the inventory increases towards the summer months, and decreases to a background rate during autumn and winter. During June and July, the diurnal temperature ranges are higher than during any other month of the year, implying that small rockfall are predisposed by above average cooling of the air and rock mass. In *Chapter 7*, the occurrence of small rockfall in the footprints of future, larger events is examined. If small rockfall are shown to precede larger failures, then the analysis in this chapter implies that thermomechanical forcing of the rock mass predisposes failure by material detachment. This may represent fragmentation of the rock mass, including the failure of intact rock bridges.

Chapter 7

Patterns of Pre-Failure Deformation and Rockfall

7.1 Introduction

Chapter 2 presented existing research into rock slope failure forecasting that draws on pre-failure displacements, with particular emphasis on the Fukuzono method and 'Saito' linearity (Saito, 1965; Fukuzono, 1985; Federico *et al.*, 2012). In addition to pre-failure displacements, other expressions of strain accumulation have been documented (Amitrano *et al.*, 2005; Helmstetter and Garambois, 2010; Burjánek *et al.*, 2012). These include precursory rockfall activity, spalling, and micro-seismic activity. Royán *et al.* (2015) observed that both the evolution of rockfall (pre-failure rockfall activity) and the displacement of a rock face (pre-failure deformation) reflected the hyperbolic increase in deformation rates characterised by Saito linearity, prior to a large cliff collapse in Catalonia, Spain. However, this was inferred from surveys separated by an average of 104 days, and therefore requires a developed understanding of the timescales over which accelerating strain rates occur, the cumulative displacements and associated velocities involved, and more generally the controls over this behaviour. Although this study has recorded relatively small rockfall ($\mu = 0.0169$ m^3), the application of sub-hourly scanning presents a unique opportunity to capture patterns of precursory deformation prior to failure at timescales as fine as hourly, daily and weekly. In addition to characterising the tertiary phase of failure, described in *Chapter 2*, measurements of displacement within yet-to-fail rockfall footprints enable a comparison between patterns of precursory deformation and contemporaneous weather conditions. Assuming that failures in this setting conform to Bjerrum's (1967) model of time-dependent strain, this analysis will allow an examination of the causes of, and timescales over which, the transition between secondary and tertiary phases of deformation occur.

In *Chapter 6*, the timing of rockfall occurrence was examined with respect to both marine and weather conditions. Linear regressions using high frequency, time-averaged rockfall and weather data yielded low coefficients of determination, highlighting the complexity of the relationship between the two. This arises due to the importance of preparatory factors, such as thermomechanical stresses, but also because a time lag may exist between the onset of triggers and the timing of final failure. In laboratory testing of samples (for example, Petley *et al.*, 2005) the offset between fluctuations in pore water pressure and the timing of final failure is

punctuated by internal deformation, such as hyperbolic microcrack growth. Prior to rockfall, hyperbolic accelerations in strain rate may manifest at the surface through the widening of joints or fragmentation of the failing mass. However, due to the spatial and temporal resolutions of previous studies, this remains poorly constrained. In this chapter, deformation of the rock mass at a temporal resolution of hours and days prior to failure, which incorporate potential lag durations, is examined.

The chapter begins by addressing the influence of the Level of Detection (LoD) in monitoring precursory displacement (*Section 7.3*), before considering its sensitivity to the length of the monitoring interval. This analysis shows the significant benefits of high precision, high frequency scanning for detecting patterns of accelerating deformation. Based on precursory rockfall activity from a selection of the largest rockfall in the database, high frequency monitoring at time intervals below four to seven days identifies more precursory rockfall activity than monitoring over epochs greater than two weeks. Subsequent analysis on a subset of the largest events shows that each rockfall was preceded by at least one detachment within the footprint of the final failure within *ca.* 100 h of failure. The approach developed to analyse accelerating displacement and inverse velocity is then described, followed by results attributed to two separate failure modes on the cliff; slumps and material detachment through rockfall. The chapter concludes by drawing upon environmental data in *Chapter 6*, in order to assess the relationship between the nature and onset of accelerations toward failure, and the timing of energetic tide and weather conditions.

7.2 The influence of the Level of Detection

In this section, the ability to detect pre-failure deformation is examined with respect to the LoD that has been applied. This LoD censors change beneath ±0.03 m, and therefore has the ability to remove pre-failure deformation within the rockfall scar if it is below this scale. However, since the applied LoD accounts for the 95th percentile of change observed across each surface (> 200 m across), this value is potentially considerably higher than the scale of deformation able to be detected across many areas of the cliff. Previous research into deformation prior to the failure of vertical rock faces has centred upon back analysis of large rockfall events. Rosser *et al.* (2007b) showed that monthly accelerations were evident prior to events of 18.9 - 2 614 m^3 in volume. Royán *et al.* (2015) recorded total displacements of up to 0.40 m for a 1 012 m^3 rockfall. In general, these rockfall are between one and three orders of magnitude larger in volume than the maximum-recorded volume in this study. Critical levels of pre-failure strain in brittle materials have been estimated at *ca.* 3% (Petley *et al.*, 2005); it therefore follows that for smaller events, the magnitude of precursory deformation reduces, and approaches the scale of natural variability in slope movements through dilation and contraction

along joints and or the instrument error. As discussed in *Section 2.3.3*, from a mechanical perspective a minimum rockfall size may also exist, below which a rockfall is unable to generate strain prior to failure. Rosser *et al.* (2007) showed a direct relationship between precursory rockfall activity within incipient rockfall scars, and the volume of the resulting rockfall.

In *Chapter 4*, a methodology was developed to minimise this error and allow the delineation of small rockfall events from binary images. These images distinguished areas of change greater than the LoD (±0.03 m) from areas of noise. However, the application of this single threshold across all of the change detections resulted in the omission of some rockfall pixels (*Section 4.11*). These pixels exhibited displacements below ±0.03 m but were contiguous with pixels above the LoD that were delineated as a rockfall. Visual inspection of many such instances illustrates that while the 0.03 m LoD is necessary for first-order delineation of rockfall; many pixel values below this value also represent change greater than the instrument precision or natural variability.

In order to test the influence of the LoD on the ability to detect precursory deformation, a short video clip was made for the largest 30 failures within the inventory, showing change within the failure scar leading up to failure, without the application of a LoD. For those failures with an observed increase in activity towards failure, an inverse-velocity plot (Rose and Hungr, 2007; Dick, 2013; Royán *et al.*, 2015) was created using change from within the incipient failure scar. This inverse-velocity plot was then created for each failure, but with an increasing LoD applied.

Figure 7.1 shows a series of inverse velocity plots created for the same 6.26 m^3 failure on the cliff, representative of failures with appreciable precursory activity. For all pixels within the incipient failure scar, the mean displacement was recorded at 30-minute intervals over four days. Each plot was created using pixels selected based on a varying LoD, beginning with 0.000 m (no threshold applied) through 0.006 m increments to 0.030 m (the LoD for rockfall delineation). While the nature and physical implications of these inverse velocity plots are discussed in detail in *Section 7.7*, two distinct differences in pattern can be observed. First, as the time to failure decreases, the convergence of inverse velocity estimates is greater when lower change detection thresholds are applied. This convergence reflects an increasing signal-to-noise ratio whereby larger displacements approach and exceed the instrument noise, and is a key indicator of the point at which accelerated deformation becomes detectable. Second, inverse velocity estimates using no LoD exhibit linearity in the final phases of failure that is not replicated when thresholds greater than 0.006 m are applied. This suggests that displacements exceed the true level of measurement noise within at least the final hours before failure but remain below the 0.03 m LoD. For higher LoDs, therefore, gaps in the data occur in which no significant movement is detected.

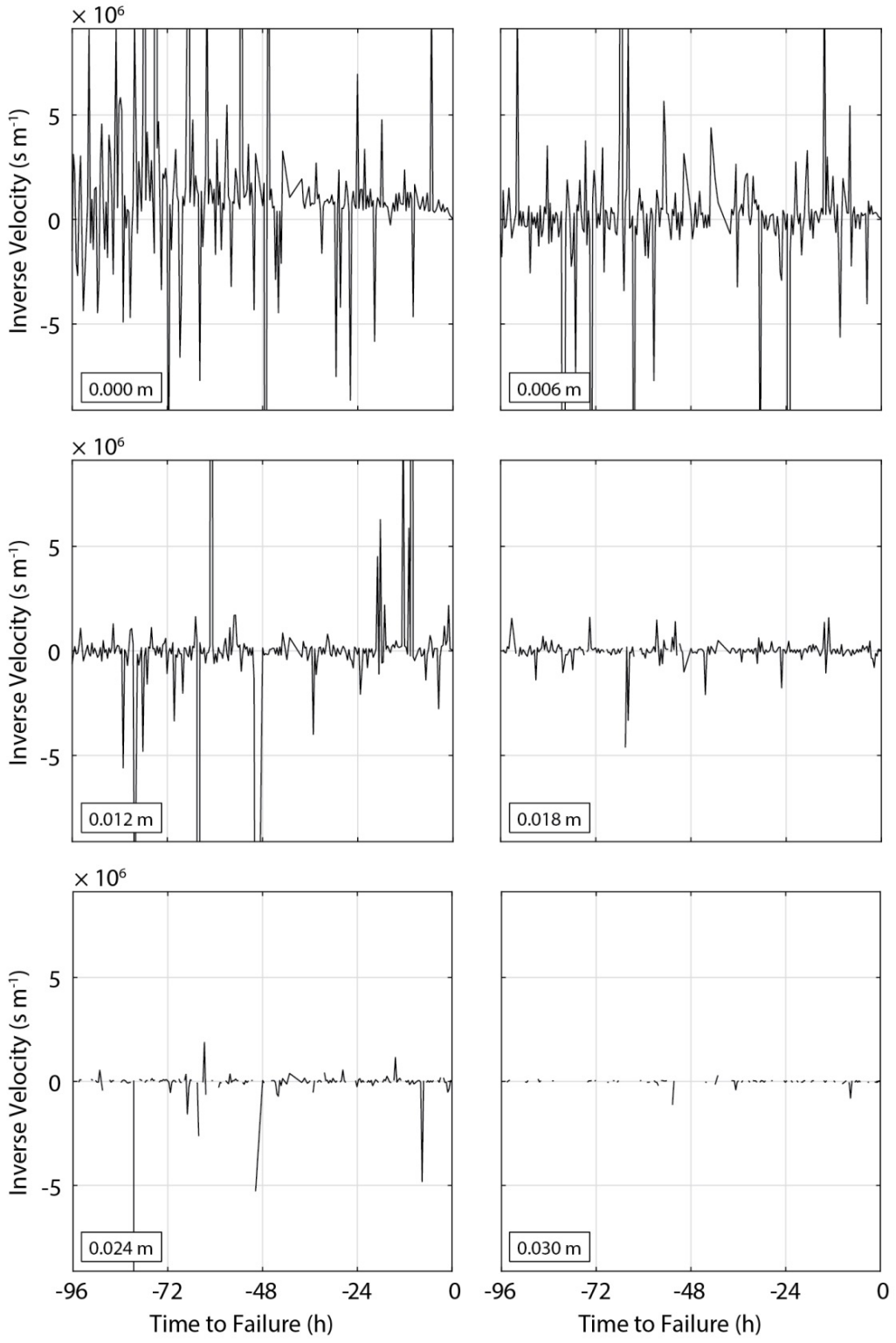

Figure 7.1: *Inverse velocity plots created for a 6.26 m^3 failure, using varying LoD thresholds defined by the values at the bottom-left of each plot. Inverse velocity estimates represent the mean of all pixels within each failure scar. As the LoD increases, an increase in data gaps occurs as displacement measurements fall below the LoD. Convergence and rapid acceleration towards failure is evident when the raw measurements are used. The increase in inverse velocity measurements above the abscissa axis is likely to reflect a systematic bias in the alignment between surveys.*

Where displacements are examined within this chapter, the raw measurement data is used. While this has the effect of preserving noise within the time series, it enables the identification of acceleration patterns in both rockfall and slumps that would otherwise remain undetected. Furthermore, convergence in the inverse velocity behaviour can be detected, allowing the identification of the time at which strain rates accelerate.

7.3 The influence of monitoring interval

In this section, the influence of monitoring interval upon the ability to detect and monitor progressive evolution of rockfall scars is assessed. Rockfall have been examined using change detections derived over different time intervals, T_{int}, drawing on the same change detection data that was used for magnitude-frequency analysis in *Chapter 5*. These intervals are: $<$ 1 h, 3 h, 6 h, 12 h, 24 h, 4 d, 7 d, 14 d, and 21 d. The largest 30 rockfall ($V > 0.2643$ m^3) were selected from the $<$ 1 h inventory, representing data acquired scan-by-scan, and subsequently identified within each database. For each rockfall, a square polygon was established with a minimum length greater than the largest rockfall dimension, which fully enclosed the final failure scar. All rockfall within this square were recorded for every change detection at each T_{int}.

While the same square polygon was used to compare change identified at each T_{int}, defining a consistent duration over which to compare pre-failure rockfall activity was more complex (Figure 7.2). First, isolating change detections of varying T_{int} within a fixed time before

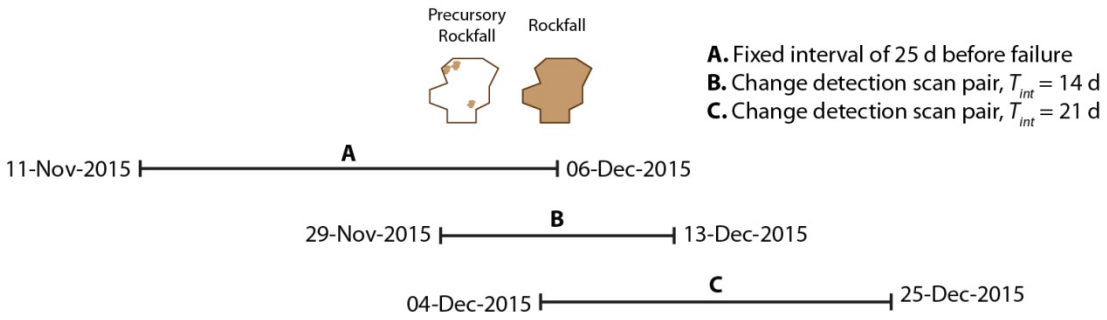

Figure 7.2: *Conceptual diagram of the complexity in comparing pre-failure rockfall activity between inventories of varying T_{int}. A fixed time window of 25 days before failure is selected (A). With the exception of the very first scan pair of the monitoring period (5th March 2015), the scans that constitute the scans pairs of different T_{int} are not synchronised. As a result, a change detection of T_{int} = 14 d (B) may span a different time period to a change detection of T_{int} = 21 d (C), even though they both begin within the 25 d fixed interval. In this instance, pre-failure rockfall activity has been recorded in the T_{int} = 14 d change detection, but not the T_{int} = 21 d. For the 21 d inventory, recording this precursory activity would require a scan pair that falls outside the 25 days before failure (from 9th November to the 4th December).*

the rockfall event does not ensure that each change detection reports rockfall that occur at similar times. For example, considering a rockfall that is identified in the < 1 h dataset on 6th December, a fixed duration of 25 d beforehand (11th November) is guaranteed to include at least one T_{int} = 21 d scan pair. However, the first component scan may have occurred at any point within this 21 d period. For example, the 21 d change detection may begin on 4th December and end 21 days later on 25th December. Conversely, a T_{int} = 14 d change detection may begin on 29th November and span until the 13th December. While both the T_{int} = 14 d and T_{int} = 21 d change detections are found within a fixed number of days before the rockfall event, a direct comparison between the pre-failure rockfall captured within these datasets is complex. As a compromise, a large 50 d duration was applied to ensure that more than one T_{int} = 21 d change detection was included beforehand. As a result, a T_{int} = 21 d change detection beginning the day before the rockfall, and ending 20 days after the rockfall was not the only dataset for comparison. The date of the first 21 d scan of this period was recorded, and only those T_{int} < 21 d change detections that began after this date were used. As such, while this does not eliminate variation in the possible dates over which change detections were made, it minimises the impact to the greatest possible extent.

The second complexity is that many of the largest rockfall occurred in the final weeks of the monitoring campaign, during December 2015. As a result, it was not possible to capture these in the 14 d and 21 d databases. For this reason, neither the 30 d nor 90 d change detections were examined. This differs from the magnitude-frequency analysis in *Chapter 5*, which only included rockfall up to the end of November.

For each measurement interval, rockfall were identified and plotted as shown in Figure 7.3. The total rockfall area was used to compare the rockfall activity identified by each monitoring interval, as this measure accounts for the area of the final failure in addition to small, precursory rockfall that are eventually superimposed. Conversely, the combined volume of the final rockfall and any precursory rockfall that occurred within its detachment scar is equal to the final rockfall volume alone, plus or minus the volumetric uncertainty of each precursor. The total volume, therefore, does not serve as a representative indicator of rockfall activity for comparison of monitoring over different timescales. For each of the 30 rockfall, the area of activity was recorded for the nine monitoring intervals. This was also normalised against the maximum-recorded area, producing a value between 0 and 1. The mean normalised area was then plotted for each scan interval to provide an indication of the level of rockfall activity measured. A sample of the results is described below, with further examples provided in Appendix C.

Figure 7.3 shows precursory detachments measured over different T_{int}. The final failure scar is displayed as the red polygon in the centre of each window. For < 1 h scan interval, many small detachments occur within the same pixels through the monitoring period. As these

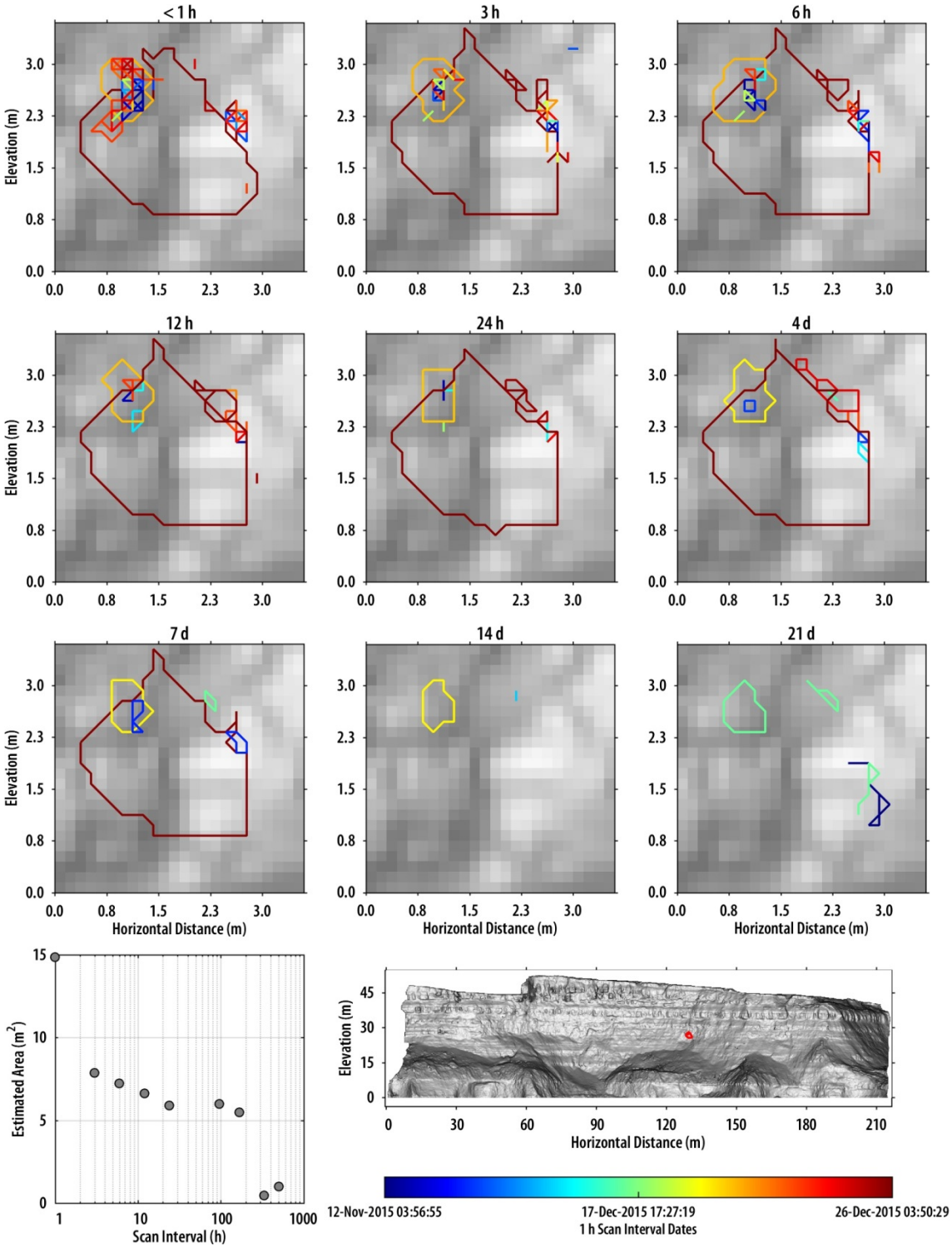

Figure 7.3: *Scar growth for a rockfall. The colour bar is applicable to the < 1 h dataset only, given that change detections at greater intervals are not synchronised. Pre-failure rockfall activity occurs at the upper boundary of the rockfall. This activity is missed for monitoring intervals > 7 d. Successive detachments that occupy the same pixels reflect changes to the rock mass that occur beneath the 0.15 m cell size, suggesting that the dominant control on failure may be fragmentation of the rock mass.*

detachments are derived by rasterising point clouds of change, multiple failures within the same pixel represent spatially contiguous material release over areas of less than 0.15 × 0.15 m, the cell size used to interpolate the point clouds. Many of these detachments occur at the top of the incipient rockfall scar and, as such, they may reflect the presence of higher levels of tension in than the surrounding rock mass. The overall result is that a considerable increase in the number of precursory detachments is recorded using high frequency monitoring. The absence of rockfall polygons for the 14 d and 21 d monitoring intervals reflects the fact that the rockfall occurred four days before the end of the monitoring period. In instances where the final rockfall scar was not detected, data from these monitoring intervals were not considered when estimating normalised estimated areas, and therefore have no influence upon the results presented in Figure 7.6.

In Figure 7.4, a similar pattern to Figure 7.3 can be observed, in which detachments at the top of the rockfall polygons occurred prior to failure. These detachments may indicate a release of strain accumulated within the rock mass prior to toppling, and highlight the role of rear release surfaces in predisposing wedge failures (Brideau and Stead, 2009). In Figure 7.5, precursory basal damage through rockfall (dark red) occurs approximately two weeks before erosion breakout (coloured as blue in < 1 h plot). This is detected by monitoring at all but the 21 d interval, which integrates this rockfall into the scar of the final failure event. 24 hours before the final rockfall, however, a 2.38 m high detachment occurred at its base (red). The pattern of precursory failures here suggests a redistribution of stress up the rock mass, and a progressive loss of support at the base of the failing mass. Due to its occurrence shortly before the time of final failure, this event was not observed using rockfall monitoring > 24 hours.

This section has so far shown the existence of precursory rockfall activity prior to some of the largest rockfall recorded over the monitoring period. As presented in Figure 7.5, when the total failed area is normalised for each rockfall, the activity detected decreases with scan interval. Visual inspection shows that this relationship is derived from precursory spalling of material that superimposes into the resulting failure scar. For 4 d $< T_{int} <$ 7 d, more frequent monitoring results in the detection of a greater amount of rockfall activity, whereas monitoring above this time period yields far less variability in change estimates. This data bears a considerable resemblance to the exponent of the magnitude-frequency relationships derived for the same range of rockfall inventories in *Chapter 5*. In *Chapter 5*, this transition was drawn upon to support the concept that rockfall evolve through a process of fragmentation of the rock mass over the timescales, rather than as instantaneous events. While the magnitude-frequency distributions are representative of the sizes of all rockfall that occurred within the 10-month monitoring period. Figure 7.6 instead represents case studies of individual rockfall events, showing that the pattern of increased rockfall activity when monitored at higher frequencies captures characteristic accelerated rockfall activity prior to failure, only observable at this finer

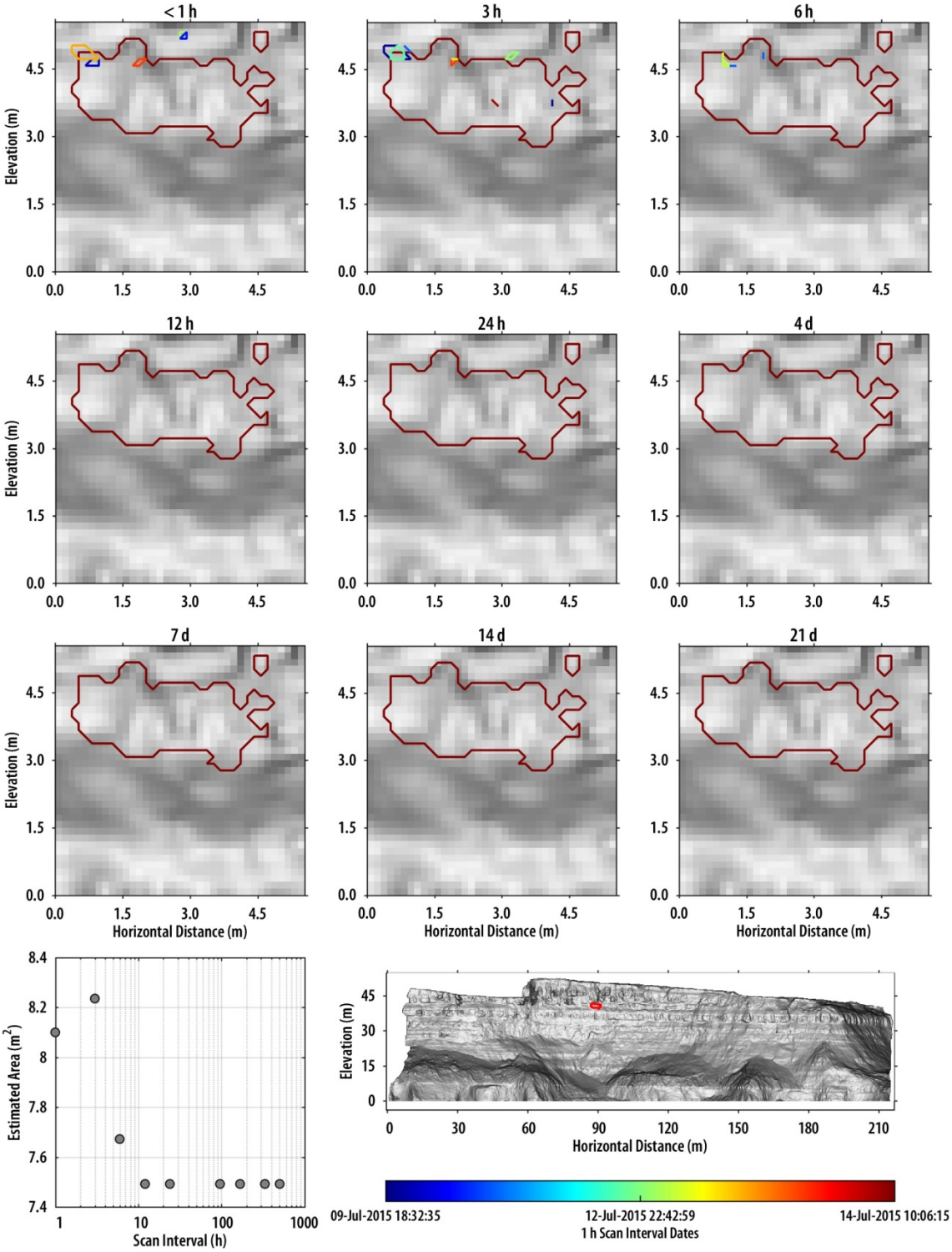

Figure 7.4: *Scar growth using change detections over a 5 d period prior to failure. The estimated area is lager for the < 1 h and 3 h datasets, than for datasets of larger monitoring intervals. As in Figure 7.2, precursory rockfall activity occurs at the periphery of the incipient rockfall but is incorporated into the final failure scar > 3 h.*

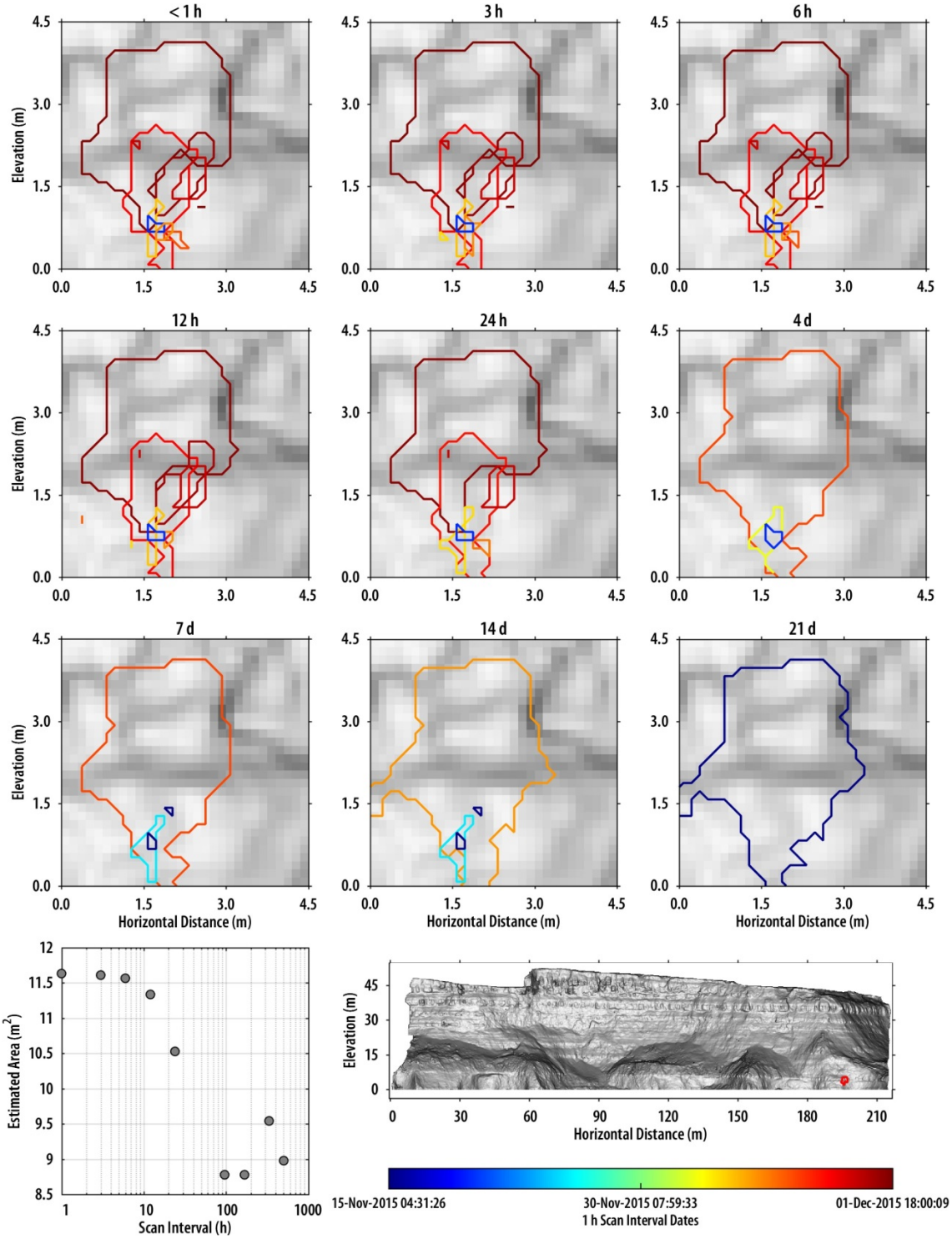

Figure 7.5: *Scar growth for a rockfall over a 16-day period. A similar pattern emerges whereby the estimated area of precursory activity is greatest for more frequent monitoring. A small rockfall at the base of the incipient failure occurred two weeks earlier, and was therefore recorded in all but the 21 d dataset. An upward propagation of rockfall becomes evident for monitoring intervals < 4 d.*

timescale of monitoring. While the spatial progression of rockfall activity has been demonstrated (Rosser *et al.*, 2007a; Abellán *et al.,* 2010; Royán *et al.*, 2015), the above result suggests that in a number of studies at monthly monitoring intervals monitoring over shorter intervals can distinguish pre-failure rockfall activity that is otherwise aggregated as a single failure. The spatial distribution of pre-failure detachments showed a tendency for deformation at the edges of a developing, incipient rockfall. This could indicate the need for rock bridges to be broken to provide release. Using high frequency scanning, movements were recorded within these areas, often within the same pixel, during multiple monitoring epochs. This suggests that many of these detachments are small, below the 0.15 m pixel size, and may represent spalling of material from the rock face. The complex shape of each precursory rockfall and the variability in their size may reflect rock bridge breakage between different scales of fractures, such as microfracturing and jointing), in addition to step-path release mechanisms (Sturzenegger and Stead, 2009b).

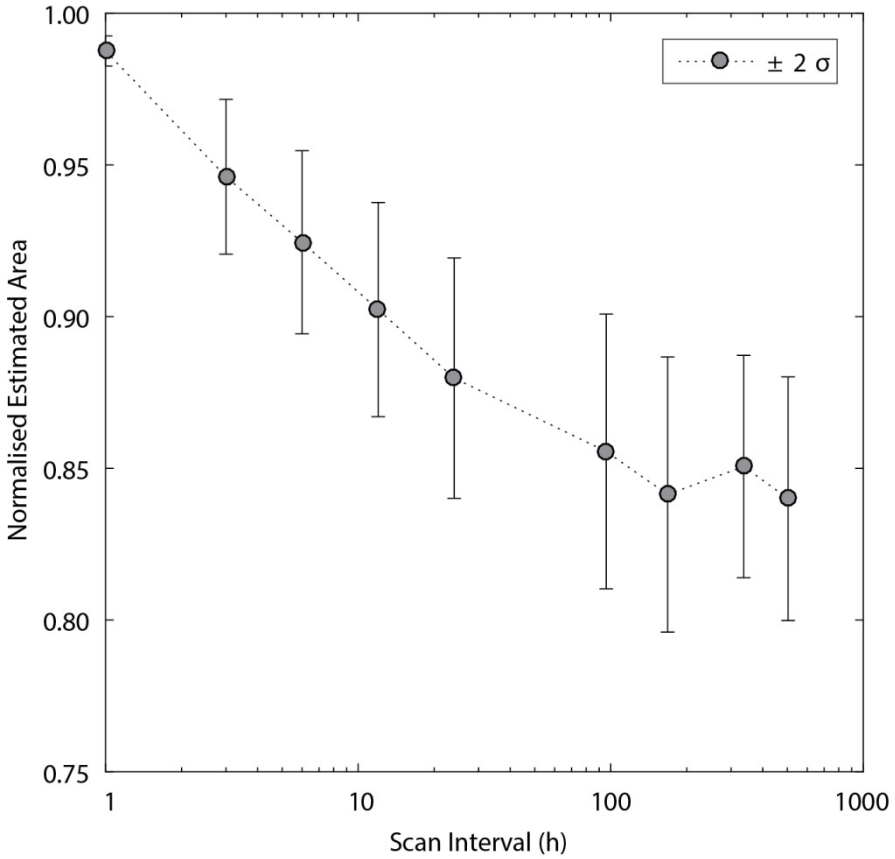

Figure 7.6: *Precursory rockfall activity, measured as the normalised estimated area for each rockfall, plotted against the interval of each change detection (log axis). In instances where the incipient rockfall was not identified (if it occurred within 21 d of the end of the monitoring period), the estimated area was not drawn upon for use in this plot. Below approximately 4 d – 7 d, more frequent scanning yields an increase in observable pre-failure activity, indicating that the 30 individual rockfall events examined fail within this period of time. This mechanism resembles the variation in size distribution of the entire databases, presented in Chapter 5.*

In addition to rockfall, a number of slumps were observed along the convex upper portion of the buttress (Figures 7.7 and 7.8). As with analysis of pre-failure rockfall activity, losses of material from these slumps exemplify relationship between monitoring interval and the

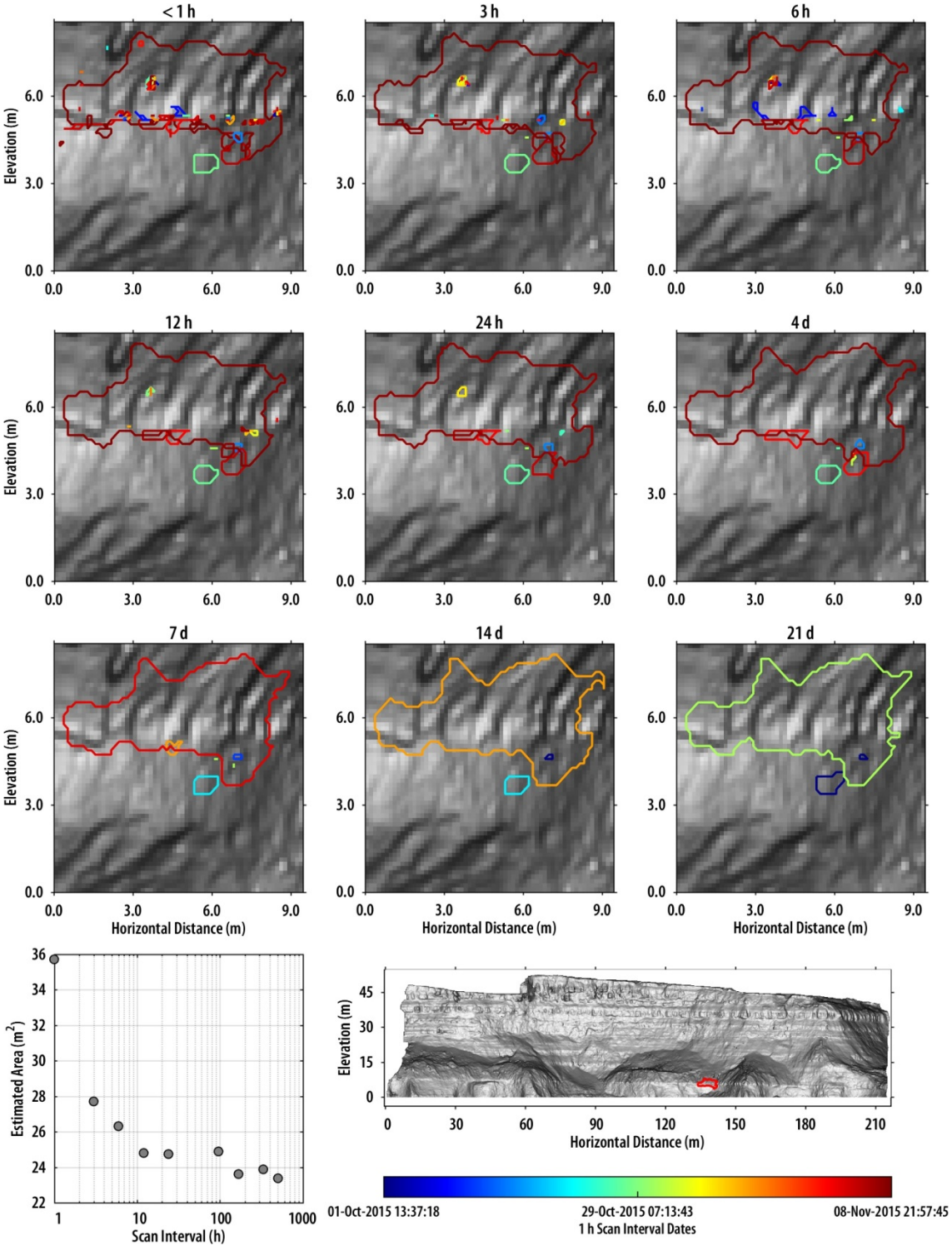

Figure 7.7: *Scar growth for the largest observed slump monitored at varying timescales over a six-week period. Pre-failure activity is again shown to increase when monitored more frequently. Here, precursory detachments appear to occur at the base of the incipient failure (red), suggesting a removal of support and lowering of resistance to failure.*

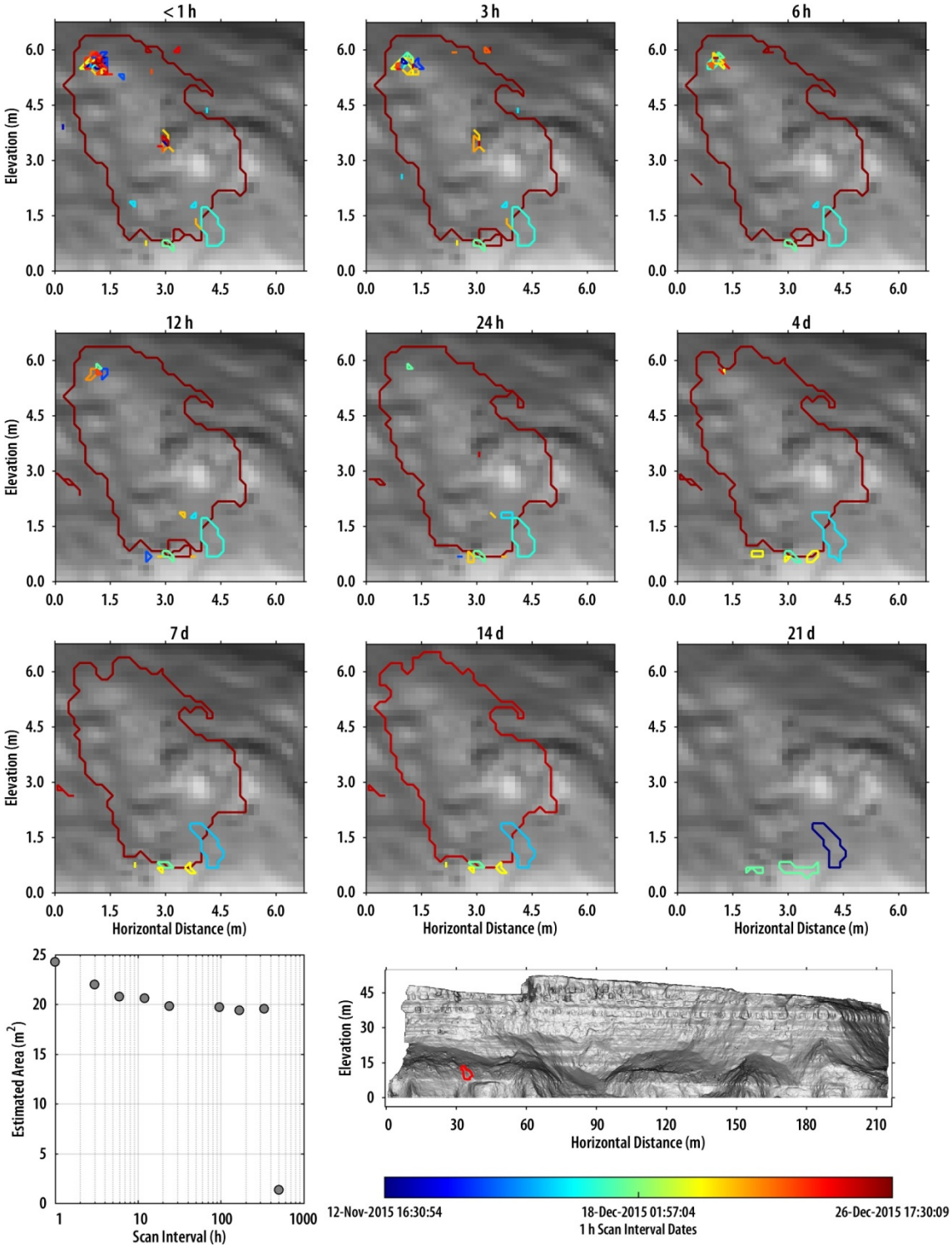

Figure 7.8: *Pre-failure detachments from within the third largest slump, monitored at different intervals over a six-week period. Spatial clustering of pre-failure activity is evident and much of this activity is missed by monitoring at time intervals > 4 d – 7 d.*

detection of precursory displacements. Within the incipient failure scars, precursory activity is less preferentially distributed at the edges of the failure scar than for rockfall. Nevertheless, these precursors form a similar spatial clustering, again suggesting that the aerial extent of some contiguous deformation is below the 0.15 m cell size. The omission of many of the smallest events using longer interval monitoring is also evident.

7.4 Inverse velocity analysis

This section outlines the methods used to analyse precursory displacement patterns for both rockfall and slumps from the rock slope and the lower edge of the buttress. For each failure, the IDs of pixels within its scar were recorded and examined for the previous seven days. Dick *et al.* (2015) proposed a pixel selection criterion, whereby the pixels used for inverse velocity regression were those contiguous with the pixel of maximum displacement, as well as exhibiting deformation greater than 50% of the maximum displacement. This was applied as an alternative to random pixel selection for radar monitoring of bench-scale failures in open-pit slopes, with the advantages of decreasing noise in the dataset and increasing the emphasis of inverse velocity on the zone of maximum failure likelihood. With far less understanding of the timescale and magnitude of displacement that precede smaller rockfall at this site, the 50% deformation technique has the potential to average out or omit patterns of precursory deformation within some areas of the failure scar. Furthermore, unlike radar, the TLS used in this study has enabled far more spatial detail in the delineation of the rockfall scar, here to within ±0.15 m for each boundary pixel, reducing uncertainty in the process of pixel selection. Indeed, in case studies of rapid brittle failures (defined as events in which acceleration only occurred within five hours of failure) inverse velocity analysis using the 50% deformation technique failed to yield clear patterns of Saito linearity (Dick, 2013). In this study, the mean displacement for each change detection was estimated using the values of change in every pixel within the final failure footprint. The mean value was used in order to account for both negative change via rockfall occurrence, and positive change via displacement of the surface through, for example, tension crack expansion.

Plots of cumulative displacement were created for each failure scar for seven days and 24 h before failure, an example of which is shown in Figure 7.9. The time over which successive change detections occurred varied between approximately 20 minutes and 30 minutes, but increased if scans had been removed due to rainfall. These intervals were used to calculate velocity from the non-cumulated displacement data, enabling plots of its reciprocal, inverse velocity, against time. As with the cumulative displacement data, these plots were constructed for both the 7 d before failure and the 24 h before failure.

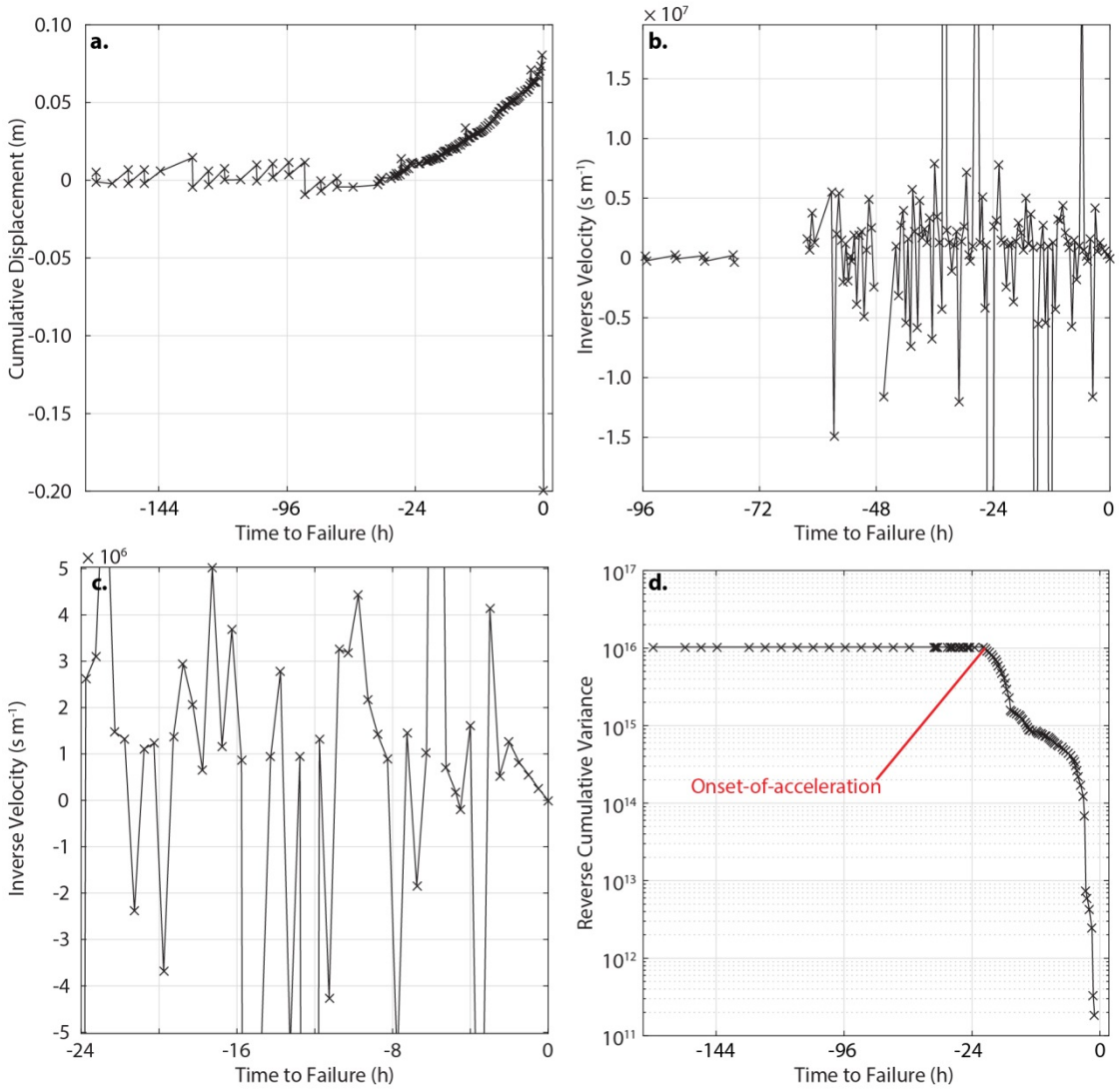

Figure 7.9: *An example of the plots used to describe deformation through creep prior to failure. (a) Cumulative displacement over a seven-day period. By cumulating the displacement, the overall trend in strain accumulation is more easily distinguished and the total precursory creep can easily be estimated as the difference in cumulative displacement between the onset of acceleration and the final measurement before failure. (b-c): Inverse velocity data over a 4 d and 1 d period. (d) Reverse cumulative variance used to identify the onset of acceleration and successive phases of varying displacement rates for Figure 7.9a.*

The onset of acceleration refers to the time step at which accelerated displacements begin (Mazzanti *et al.*, 2015). Using the Fukuzono (1985) method, this is typically manifest as the beginning of a straight line towards failure in inverse velocity-time space. In order to forecast failure timing, this line is extrapolated to the point at which inverse velocity is zero. User-selection of this point is subjective and therefore presents uncertainty in the number of subsequent measurements through which to regress and, hence, the timing of incipient failure. In this study, the onset of acceleration is interpreted as the point of transition from secondary to tertiary phases of creep, beginning at the time step at which inverse velocity estimates converge

towards linearity. As a statistical indicator of this point, the reverse cumulative variance, *RCV*, of inverse velocity measurements was calculated when points were iteratively added working backwards from the time of failure:

$$V = \frac{1}{N-1}\sum_{i=1}^{N}|x_i - \mu|^2 \qquad \text{[Eq. 7.1]}$$

where V is the variance, N is the number of measurements, and μ is the mean of the sample. Figure 7.10 represents synthetic inverse velocity data and the resulting *RCV*, and assumes that the measurement interval between each point is the same. At point *A*, the large increase in *RCV* between three and eight hours before failure reflects the significant variability in velocity estimates relative to the sample mean. Here, the sample mean becomes increasingly unrepresentative of the inverse velocity estimates, which vary rapidly during the final phase of acceleration. Since variance estimation requires a minimum of three points, the variance cannot be calculated for the final two measurement points and, as such, onsets of acceleration that occur within the final two measurements cannot be identified. Phase *B* is characterised by increasing *RCV* of several orders of magnitude. This represents the transition from low strain rates (high inverse velocities) to high strain rates (low inverse velocities) that occurs eight hours before failure. This transition is evident in the *RCV* plot for two reasons. First, the inverse velocity estimate undergoes a sudden significant increase. Second, the mean of the sample at this point is low due to the small inverse velocity measurements close to failure; the deviation from the mean for the 9 h inverse velocity value is therefore high. During phase *C*, the pattern is stable as the mean of the sample approaches consistently high inverse velocity measurements. In the synthetic inverse velocity data, displacements oscillate above and below zero, which is symptomatic of measurements close to the instrument precision. This does not affect the overall cumulative variance pattern because the variance of a sample provides only positive values, and is therefore suited to small displacements that precede rapid brittle failure. However, the small break in gradient is indicative of small increases in velocity (decreased inverse velocity) that are sustained towards failure. As presented in *Section 7.7*, the timing of these small but nonetheless appreciable increases in velocity relate to the occurrence of individual rainfall events and are identifiable using the *RCV*.

7.5 Precursory acceleration in slumps

Precursory movements in slumps observed at the top of the buttress are presented in Figure 7.11. All of these slumps occurred in the months of November and December 2015 and formed resulted in > 1 m^3 of material loss. Since no movement was observed between seven days

and 24 hours prior to failure, the cumulative displacement for the final 24 h is presented in Figure 7.12. In six of the eight events, an increase in total displacement can be observed during the final six hours of failure of the order of 0.002 m – 0.012 m. Each individual displacement falls below the 0.030 m LoD applied for the delineation of rockfall events, highlighting the importance of examining displacements below this threshold.

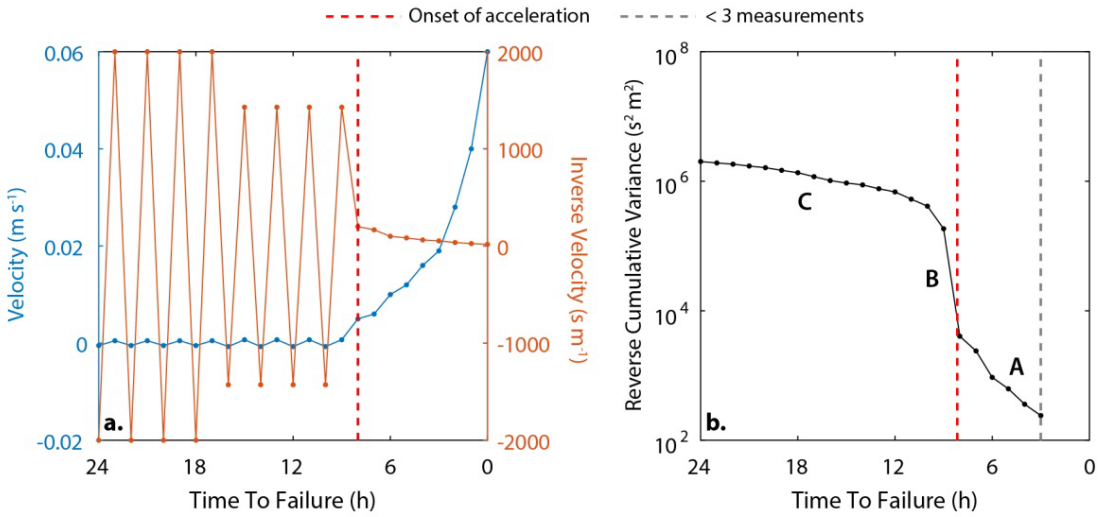

Figure 7.10: *(a) Synthetic inverse velocity data, simulating an acceleration in creep that follows a background rate oscillating above and below zero, simulating variation within the instrument noise and natural variability in slope displacement. Red line indicates onset of acceleration, as velocity increases and inverse velocity converges to linearity. (b) Reverse cumulative variance, RCV, which measures the variance of increasing numbers of measurements, working from right to left. The time at which cumulative variance decreases over several orders of magnitude is presented represents the onset of acceleration. Grey line indicates the cut-off in the number of measurements prior to failure, below which reverse cumulative variance cannot be estimated.*

Inverse velocity data is presented in Figure 7.13 for both the seven day and one day periods. The deformation measurements produce both positive and negative inverse velocities that occur around zero. While larger displacements and higher precision monitoring may have reduced this pattern, it may represent the presence of both backward and forward displacements through creep and subsequent material detachment. While some successive measurements shift from negative to positive inverse velocity, and sometimes approach zero, the smallest inverse velocity values, of the order of 1×10^{3} s m^{-1}, are consistently measured at the time of failure. For all events, the inverse velocity data is most variable further from failure time; however, as the time to failure reduces, the inverse velocity estimates begins to converge.

To provide a more detailed assessment of the nature of these accelerations, Figure 7.14a presents the displacement and inverse velocity data from Slump 2 (defined in Figure 7.11). Linearity in the acceleration pattern begins in the final two hours before failure, while inverse

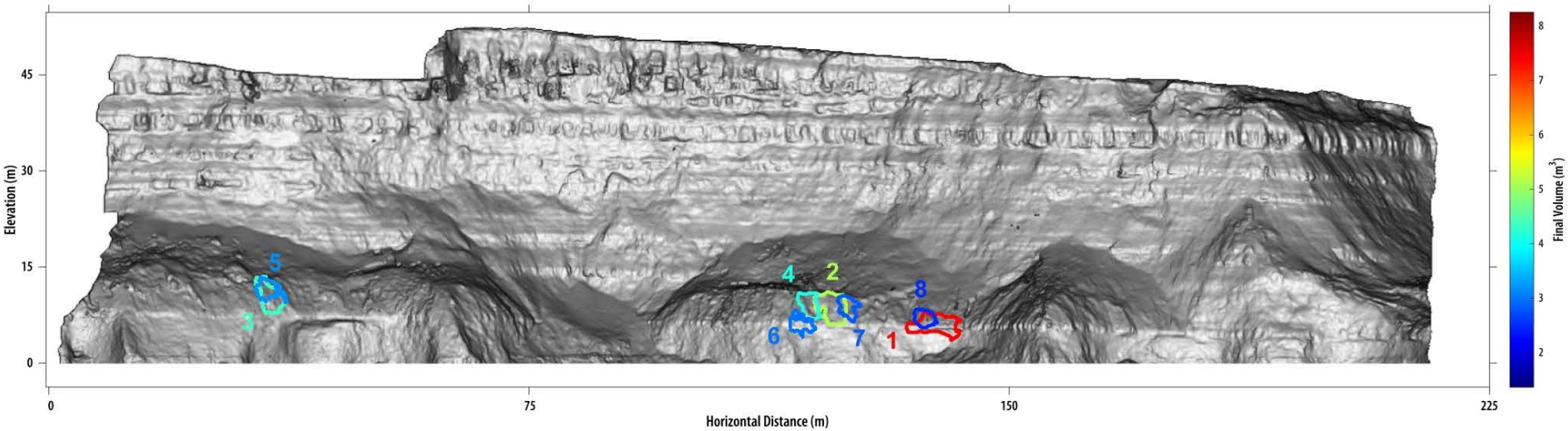

Figure 7.11: *Slumps selected for analysis (> 1 m^3). Colours represent the volume of final failure and are replicated in subsequent plots of cumulative displacement, inverse velocity, and cumulative variance*

velocity patterns begin to converge significantly at around 6 h. This duration corresponds with other previously published research into cumulative deformation trends in open pits (Rose and Hungr, 2007; Dick, 2013).

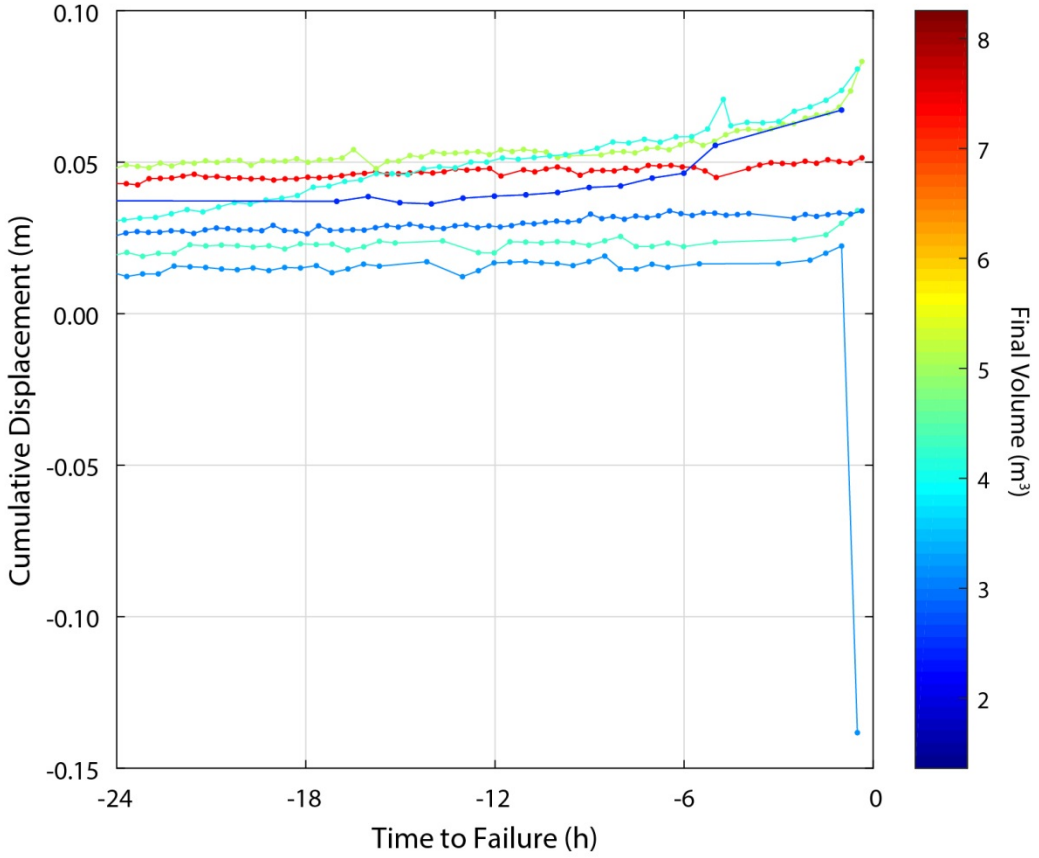

Figure 7.12: *Cumulative displacements for the slumps in Figure 7.11 over a 24 h period Accelerations typically occur within the final 6 h of failure, characteristic of rapid brittle failures observed in open pit environments. Cumulative displacement drops in Failure 5 (see Figure 7.12) as this event occurred in multiple stages, captured over the period of an hour.*

In Figure 7.14b, the convergence of inverse velocity estimates is approximated by the red-dashed line. A number of possible explanations for this convergence exist. First, as displacement rates increase, the magnitude of movement in each epoch approaches and ultimately exceeds the approximate instrument noise and natural background variability in rock face movement. Second, the direction of movement becomes dominant in one particular direction, and the resulting mean velocity, which is directional, begins to align. The transition from negative to positive inverse velocity measurements, for example, may reflect a shift from loosening and removal of material to forward movement of the entire incipient mass prior to failure. This may relate to the removal of rock bridges and subsequent release by sliding.

The *RCV* plotted in Figure 7.16 is stable between seven and two days for seven of the eight events. The onset of failure for each can be identified within the final six hours before

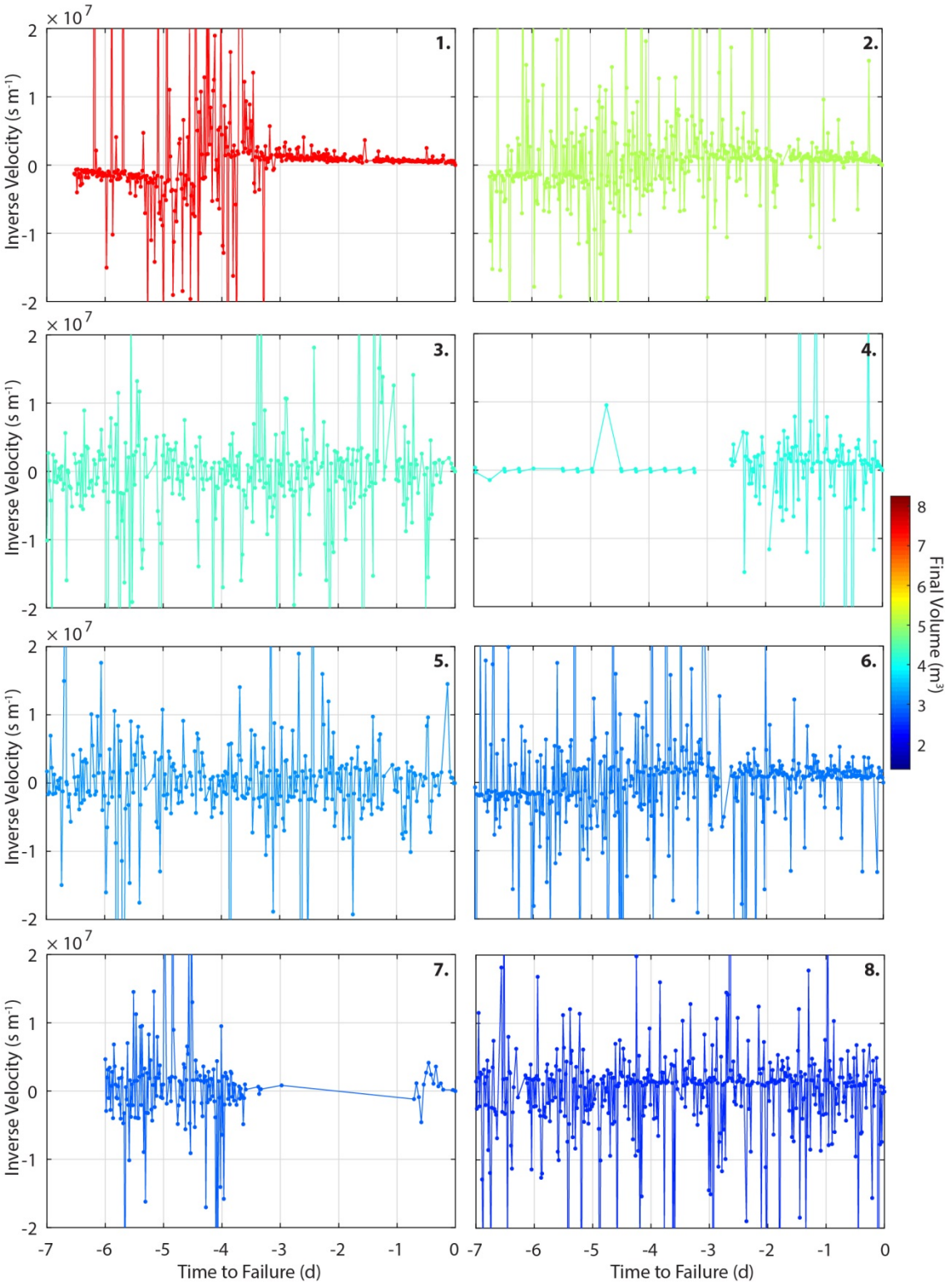

Figure 7.13: *Inverse velocity for material slumps over a seven-day period. While some inverse velocity measurements extend outside of the range of the y-axis, these are points in which almost no change occurred and hence high magnitude inverse velocity estimates were recorded. Consistent shifts between positive and negative inverse velocity values are also indicative of small changes, which may fall beneath the monitoring precision. Convergence of inverse velocity estimates, representing an overall increase in displacements that approach or exceed the instrument precision, occur after ca. 48 h.*

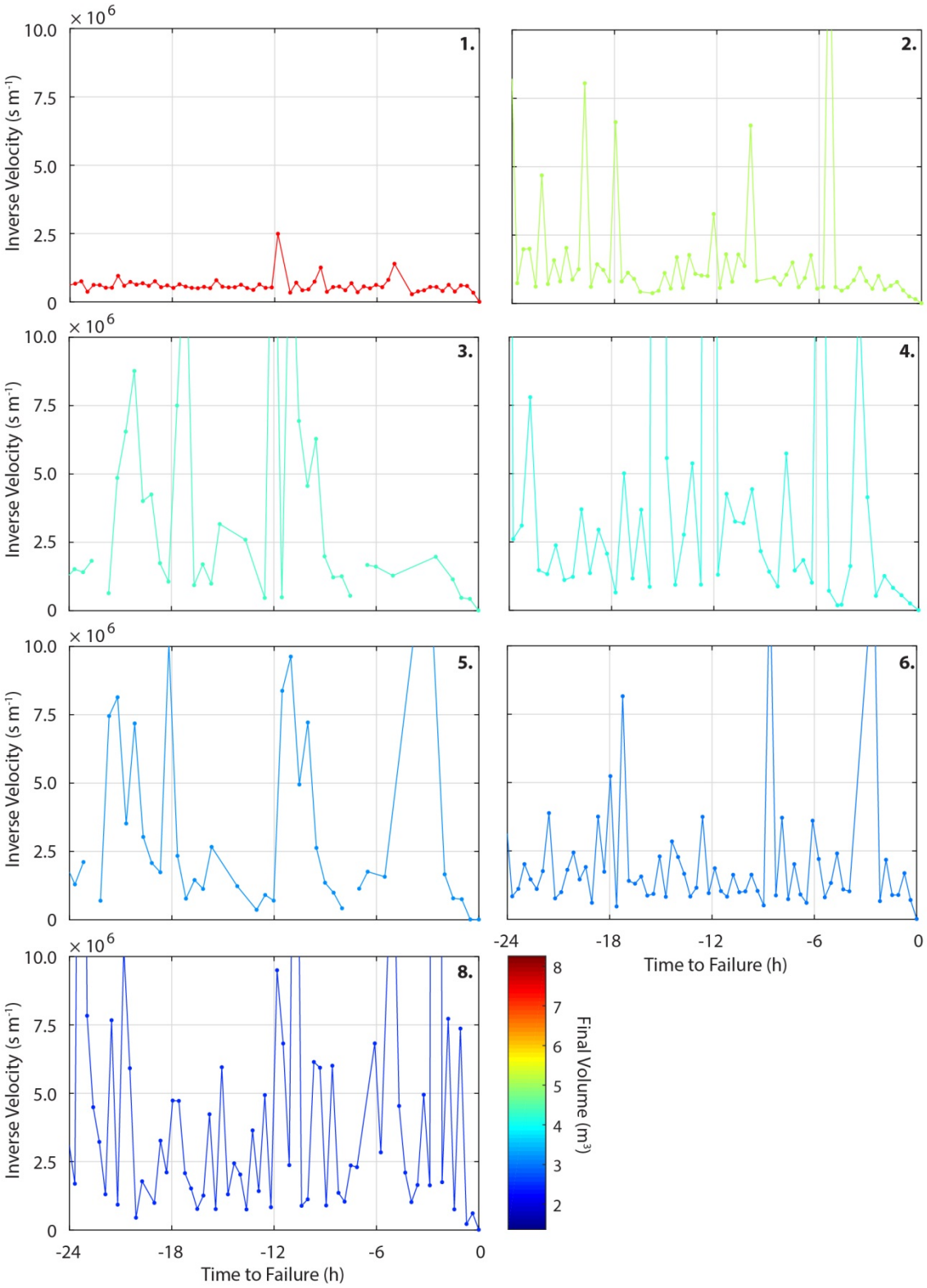

Figure 7.14: *Inverse velocity for material slumps over 24 h. Numbers refer to failure IDs assigned in Figure 7.11.*

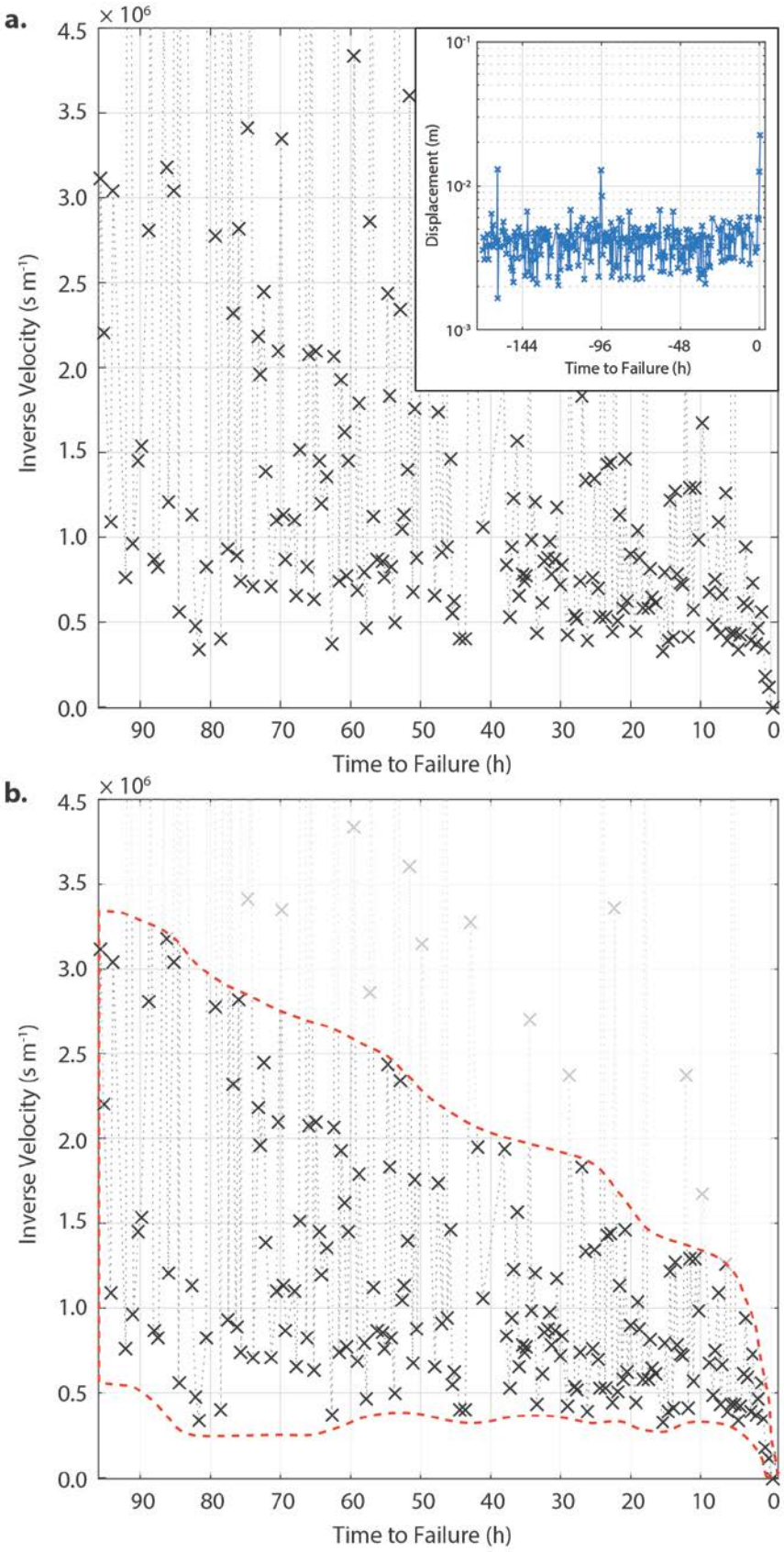

Figure 7.15: *(a) Inverse velocity and cumulative displacement for the second largest slump, examined over the final four days before failure. The final acceleration occurs within 2 h of the failure time. (b) A manually delineated envelope of convergence.*

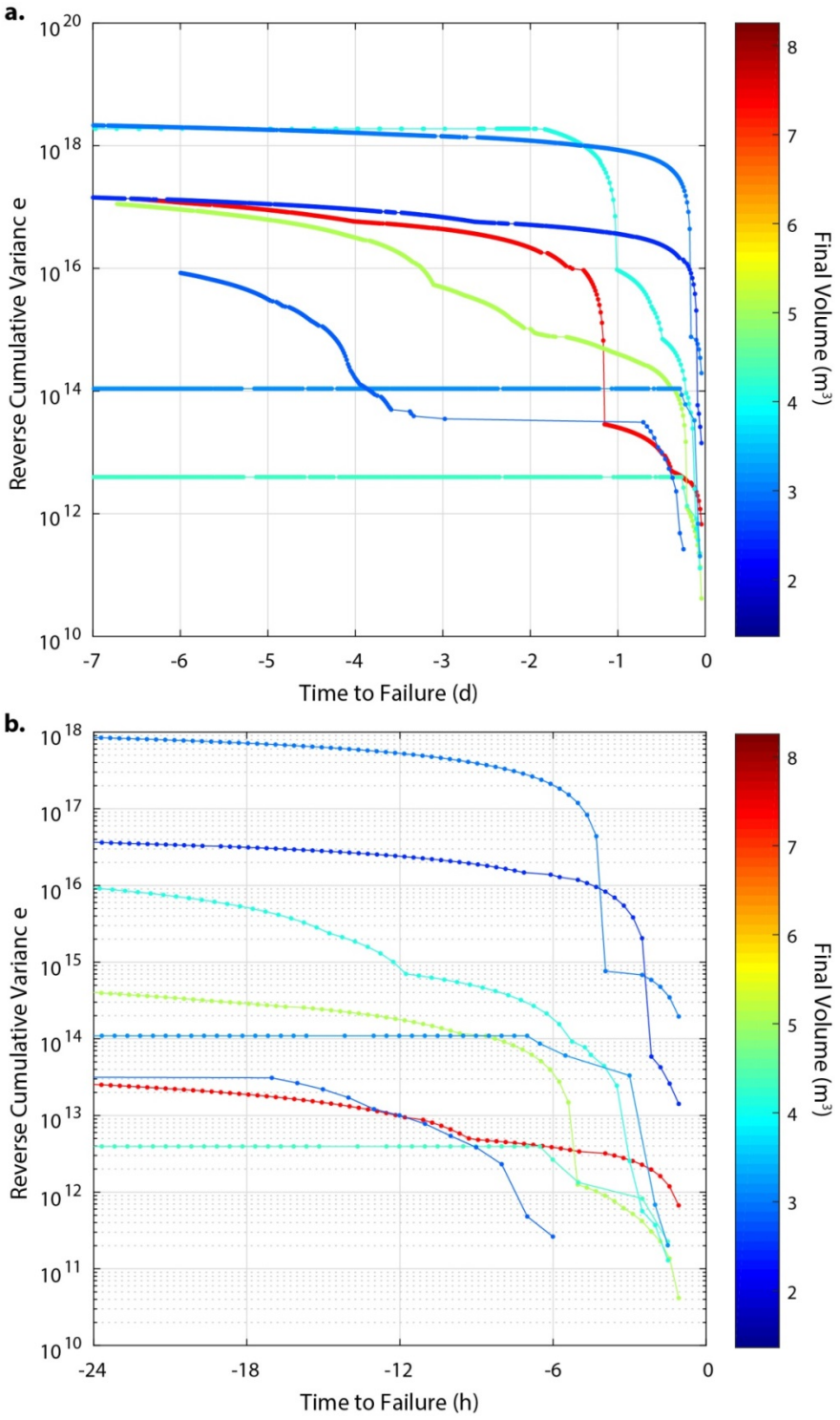

Figure 7.16: *(a) Reverse cumulative variance estimates for the inverse velocity data, measured over 7 days prior to failure. In some instances, this reflects a near-constant background rate of displacement, followed by a sudden decrease in cumulative variance, representative of inverse velocity data that decreases to much lower values, and continues to do so over a period of acceleration typically within 6 h. Some failures undergo sudden displacements that result in multiple phases of creep. (b) Reverse cumulative variance over the final 24 h. The variance shows that the onset of acceleration occurs at a maximum of 5 hours before failure. Note that variance requires a minimum of three points prior to failure. Slump 7 is monitored at reduced frequency, with the result that this minimum of three points fall outside of the window of final acceleration.*

failure, representing a decrease of several orders of magnitude in *RCV*. For many of the failures, in addition to this decrease it is clear that multiple phases of change in *RCV* can be identified in the period prior to failure. This is interpreted as multiple separate phases of pre-failure acceleration, all of which occur within the final 78 h before failure. Since the cumulative variance provides only a positive value, these phases of movement cannot be directly attributed to material detachment or forward creep. However, their presence suggests that a transition from secondary creep to tertiary creep may not be instantaneous; in Slump 2, for example, this transition may occur over a period of two to three days.

7.6 Precursory acceleration of rockfall

Figure 7.17 displays six rockfall that have been examined in the detail and a reported upon in this section. As shown in the cumulative displacement patterns, the overall displacements are smaller than for the slumps above, and are of the order of 0.001 m to 0.038 m (Figure 7.18). These were initially examined by creating videos of pre-failure deformation, such as that provided in Appendix D. However, four of the six rockfall presented show an accelerated pattern of displacement before final failure, bearing some resemblance to the tertiary creep phase. The overall displacements exhibit far less variability within the final 24 hours than for the slumps. While the material that the slumps comprise is brittle, its failure mechanism may be ductile and therefore more likely to exhibit on-going deformation and that does not develop into a catastrophic failure. Based on the acceleration pattern prior to rockfall, inverse velocity patterns are plotted in Figure 7.19 for four of the rockfall in which accelerated displacements are observed.

RCV plots of the inverse velocity data are plotted in Figure 7.20. While inverse velocity plots are useful indicators of displacement prior to failure, the reverse cumulative variance of the inverse velocity allows changes as a result of displacement and rockfall to be observed. Rockfall 3 (defined in Figure 7.17) presents multiple phases of movement in the cumulative displacement data. These multiple phases of movement coincide with events shown in a map of precursory rockfall activity through time in Figure 7.21. Here, multiple initial phases of small movements, dark blue, occur prior to the rockfall, accounting for the multiple phases of decreasing *RCV*, which occur during the final 10 hours before failure. The multiple phases in reverse cumulative variance of creep prior to rockfall suggest that either a smooth transitions between secondary and tertiary creep does not apply for these failures, or that observed hyperbolic accelerations to failure, such as runaway microcrack growth (Petley *et al.*, 2005), actually occur in stages. As has been shown for rockfall 3, this represents the detachment of blocks from the failing mass. Alternatively, it may represent the failure of intact rock bridges within the rock mass, which may in turn induce a shift from its fragmentation to deformation.

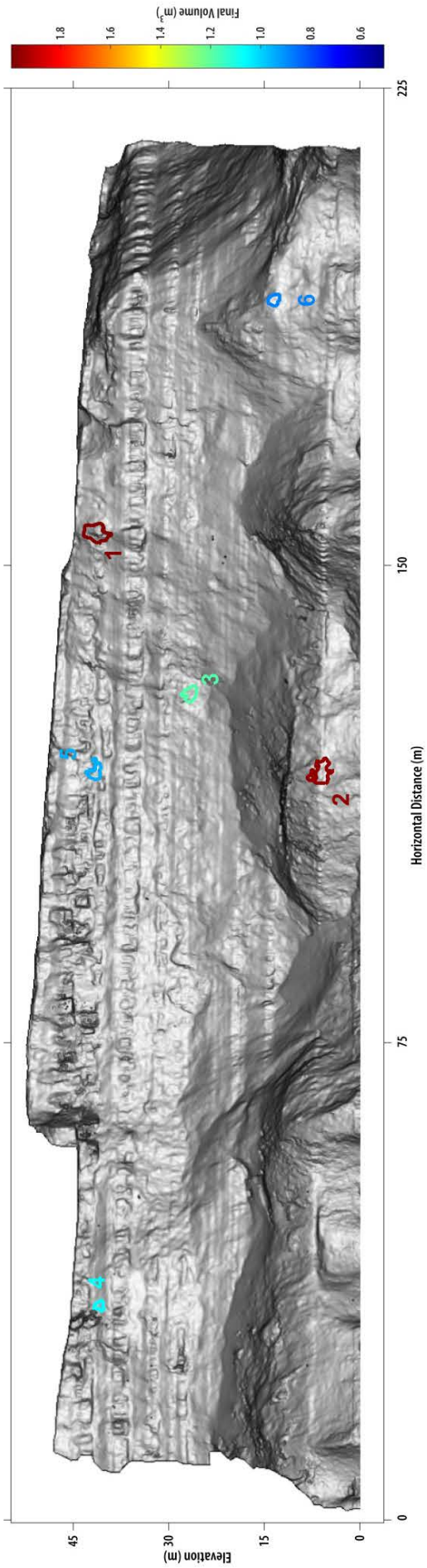

Figure 7.17: *Rockfall selected for analysis, again coloured by failure volume.*

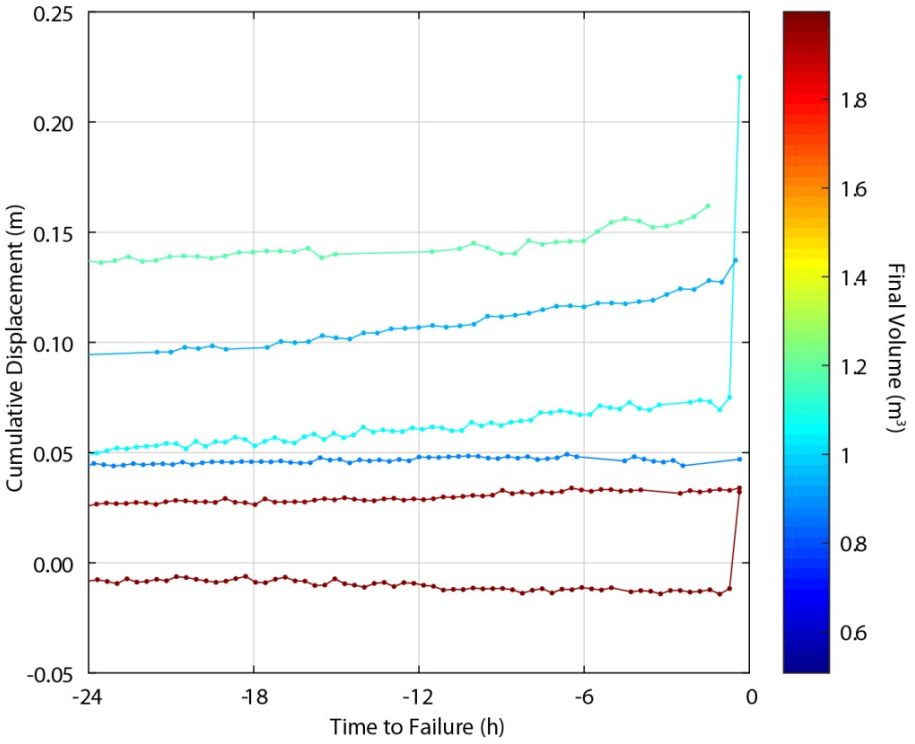

Figure 7.18: *Cumulative displacement plots for the rockfall. Far smaller displacements are observed than for slumps in the same material.*

An increase in precursory displacement for both slumps and rockfall has been shown during the final hours before failure. Figure 7.22 illustrates this observation, showing a positive albeit weak relationship between the final rockfall volume and the total precursory creep. The total precursory creep was estimated by integrating plots of displacement against time, after the onset of acceleration. Hence, larger rockfall appear to be preceded by larger precursory deformations than those preceding small failures. This suggests that precursory deformation is scale-dependent, and that, had larger rockfall occurred during the monitoring campaign, these would have exhibited a greater amount of creep than the events detected here. The intersect of this regression implies that rockfall of all sizes will exhibit creep. In reality, this is unlikely given that very small rockfall may be of insufficient volume to fragment prior to failure; a minimum weight may be required to exceed the tensile strength of the rock mass; or, if the scale of final failure is approximately equal to the scale of persistence, then precursors to failure may not be permissible beneath the scale individual discontinuities.

In Figure 7.23a, precursory rockfall activity, which draws on the scan-by-scan rockfall inventory and does not include creep within the rock mass, is presented for the largest 30 rockfall ($V > 0.2643$ m^3) drawn upon in *Section 7.3*. This size distribution was selected to ensure that rockfall were large enough to encompass precursory rockfall that are detectable with the 0.15 m cell size. Mean rockfall activity, R_A, measured as the volume per unit area per hour

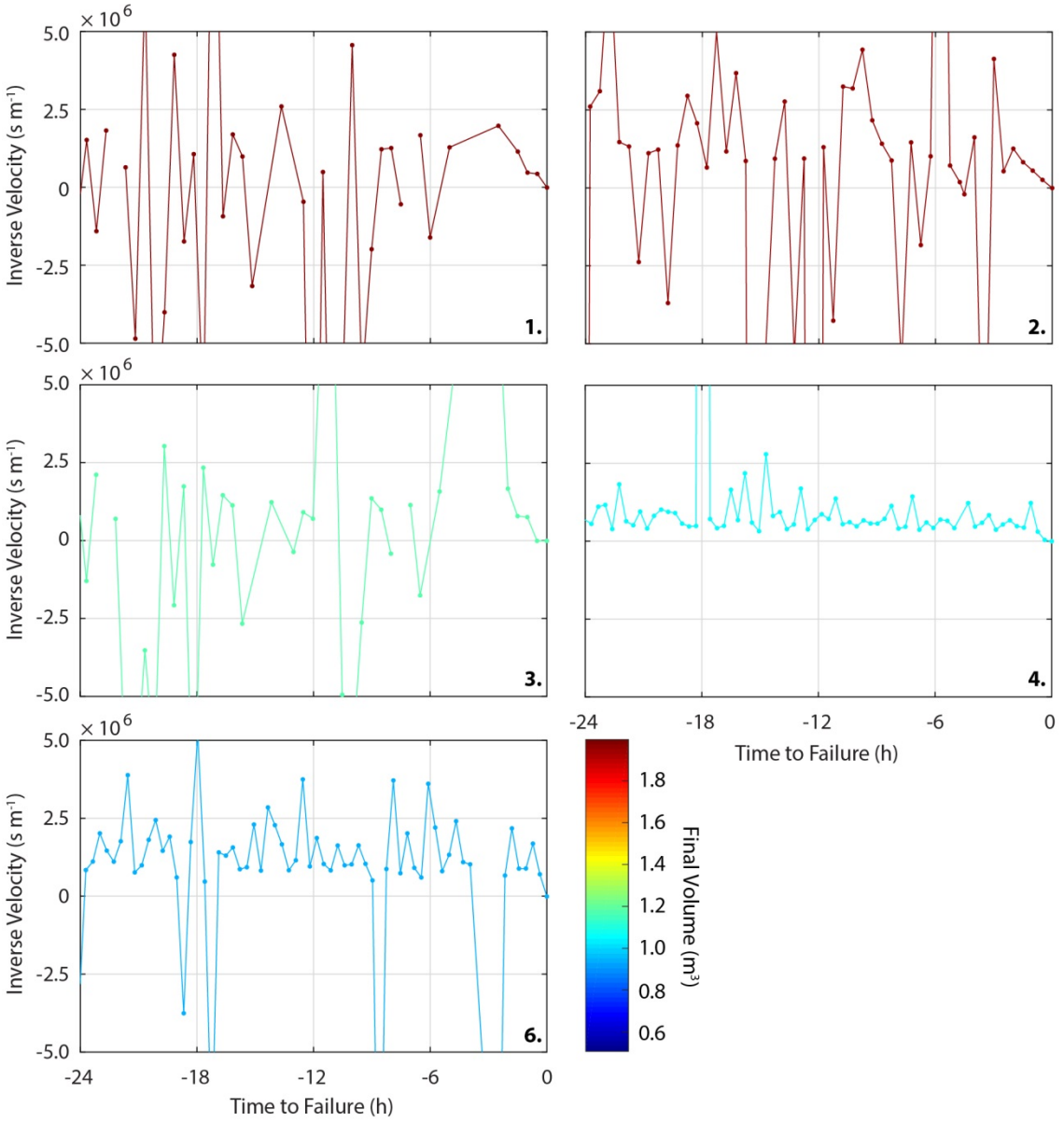

Figure 7.19: *Inverse velocity plots for the rockfall data show that rockfall also adhere to accelerated forward displacement patterns. However, the onset of acceleration occurs only within a maximum of three hours before failure. Numbers indicate rockfall IDs assigned in Figure 7.17.*

(m h^{-1}) is measured for the 28 days prior to each rockfall. Precursory rockfall were defined as detachments that occurred entirely within the incipient rockfall scar, or those that contained at least one shared pixel. R_A was estimated in six-hour bins until failure, reflecting the fact that deformation appears to accelerate within this window before failure, and to enable unbiased comparison between events that were monitored at varying scan intervals.

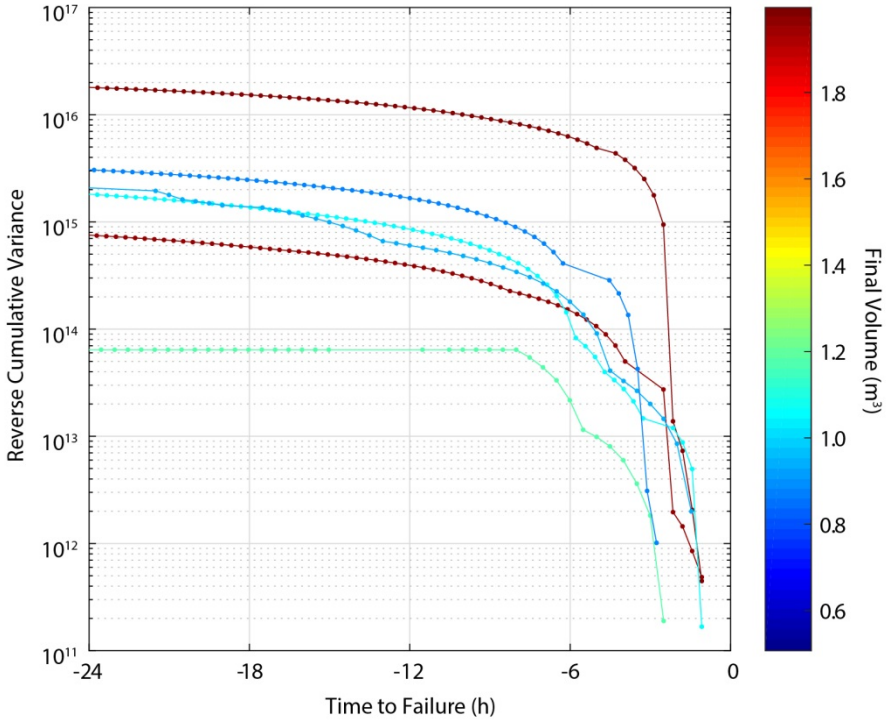

Figure 7.20: *Reverse cumulative variance plots for the selected rockfall, again showing that the onset of acceleration for rockfall occurs within approximately 3 hours from failure. Two phases of pre-failure acceleration are observed for rockfall 3.*

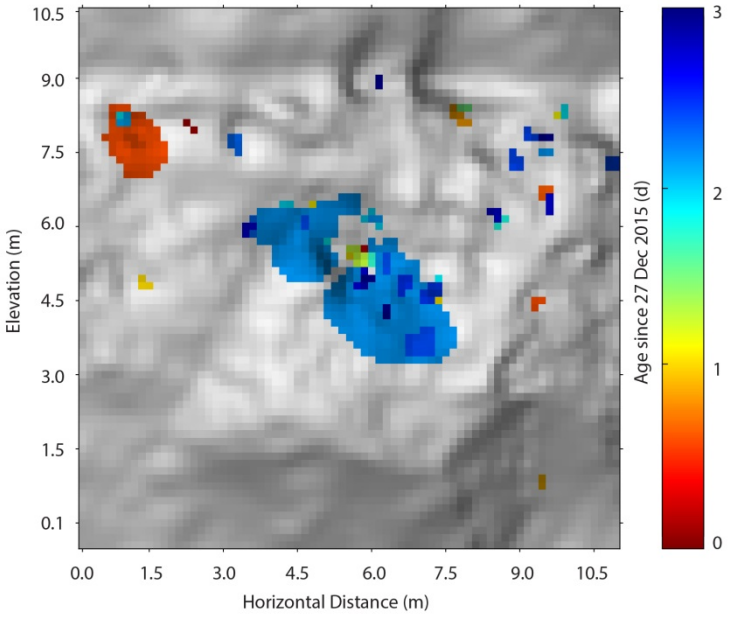

Figure 7.21: *An example of contiguous rockfall over a three-day period for rockfall 3. Here, small rockfall occur before and after the large rockfall in the centre. Close inspection of many of the largest rockfall showed similar patterns, in particular of the accumulation of small rockfall events prior to failure. This distribution may explain the reverse cumulative variance pattern for rockfall 3 in Figure 7.20.*

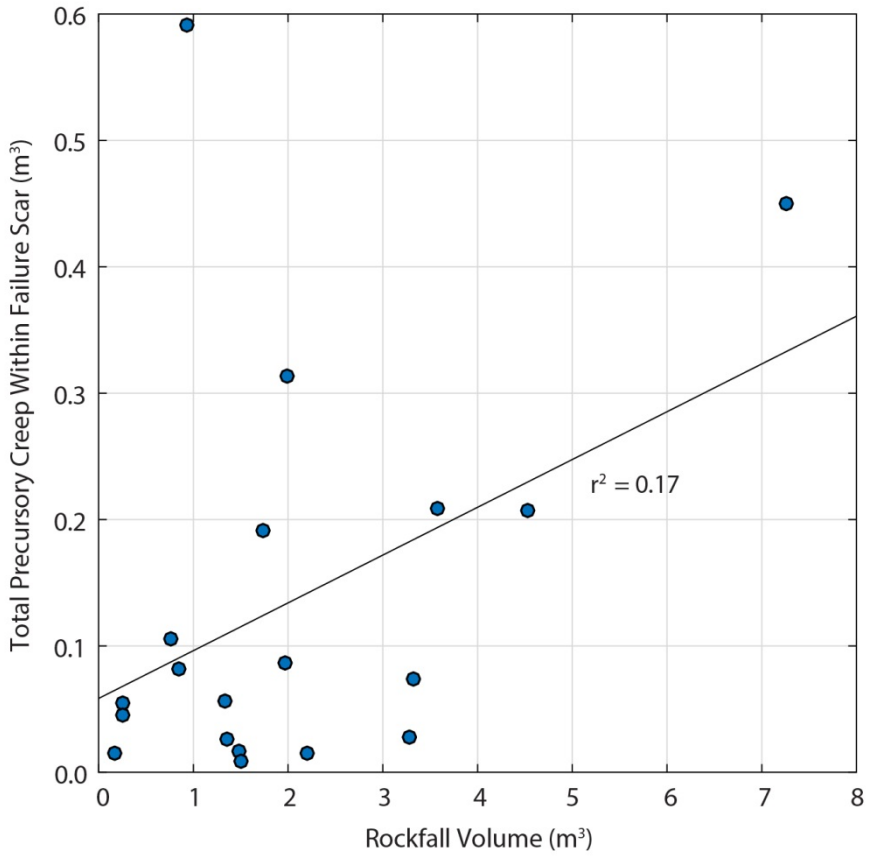

Figure 7.22: *Total precursory creep within the failure scars of rockfall, plotted against the rockfall volume. While the relationship is weak (r^2 = 0.17) a small increase in rockfall creep is observed with volume.*

The rockfall activity is cumulated and normalised by the total activity of each rockfall for comparison:

$$R_{norm} = \frac{R_A}{\sum_{i=1}^{N} R_A} \qquad \text{[Eq. 7.2]}$$

where R_{norm} is the normalised rockfall activity in six hour bins from 0-1, R_A is the rockfall activity within each six hour bin, and N is the total number size hour bins with the 28 day period. Having cumulated the data, the line of unity illustrates the divide between activity rates that slow prior to failure (above the line unity), and those that accelerate towards failure (below the line of unity). Trajectories along the line of unity show a continuous, uniform rate of rockfall activity towards failure. Since not all rockfall exhibited precursory activity during the initial stages of the 28 d window, the line of unity would not be applicable if each trajectory was plotted on a scale of 1-28 days. For example, if rockfall activity began 14 days before failure, the cumulative trajectory would always fall beneath the line of unity. As such, each trajectory

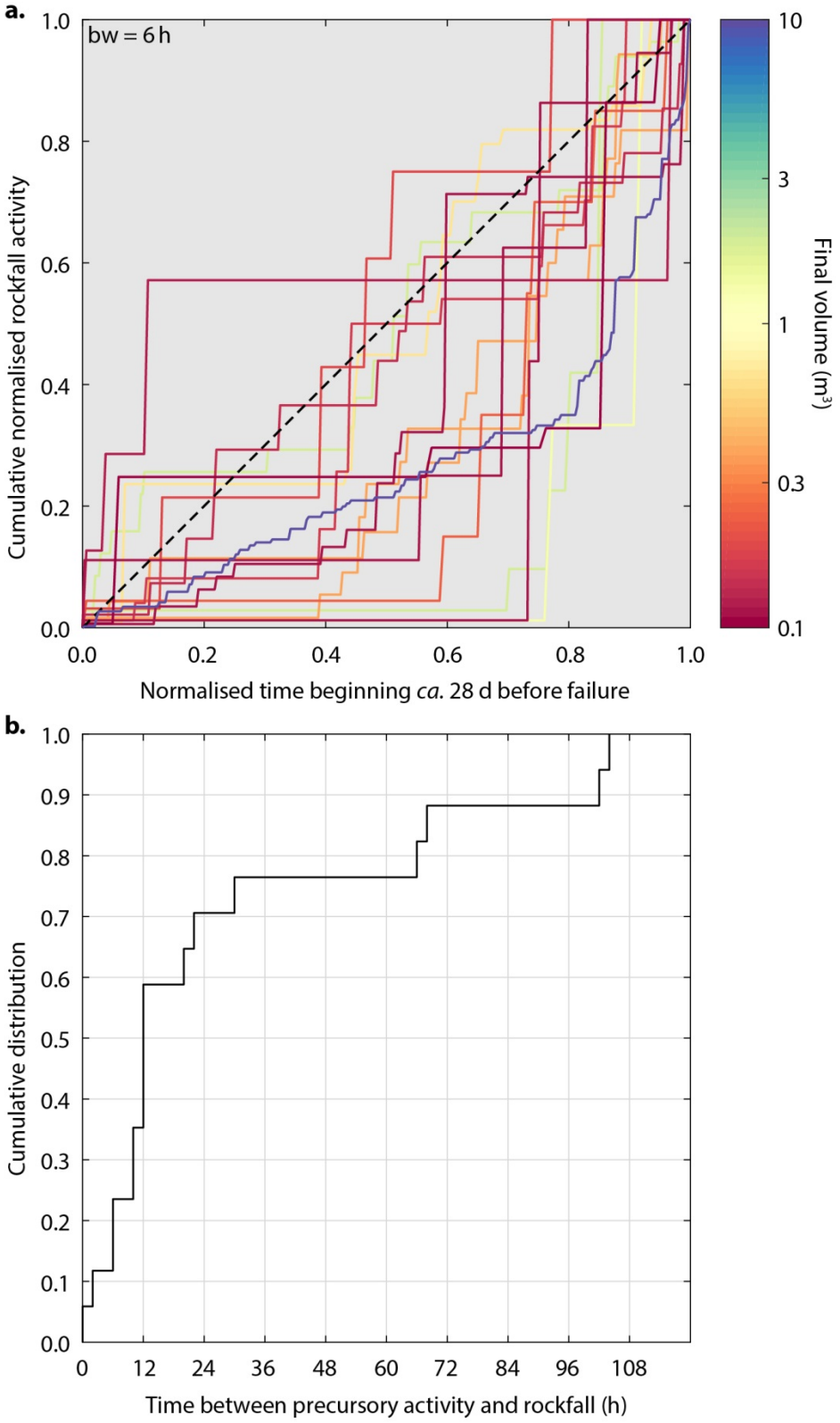

Figure 7.23: *(a) Cumulative rockfall activity, described as the volume per unit area per hour, normalised by the total activity for each event. This is plotted against the normalised time to failure, which represents the time from the first rockfall within a 28 d period. The distribution of trajectories below the line of unity (dashed line) shows that rockfall activity increases prior to failure. (b) Non-normalised time between failure and most recent precursory rockfall. More than 70% of the sample recorded precursory rockfall within 24 h of failure.*

begins from the time of the first precursory rockfall that occurred within the 28 d period, and the value N in Equation 7.2 adjusted accordingly. When normalised, this becomes time 0. Time 1 represents 30 minutes before final failure, to ensure that only precursory rockfall activity is included.

While not all R_{norm} trajectories indicate precursory rockfall activity immediately before failure ($t = 1$), there is always some precursory rockfall activity within the final 20% of the monitoring window. In absolute terms, every rockfall scar experienced some form of precursory detachment within *ca.* 100 h of final failure (Figure 7.23b). Of the subsampled rockfall, 70% underwent some form of precursory failure within 24 h. While this data reflects a subsample of the largest events, this range of time intervals resembles the size distribution analysis undertaken in *Chapter 5*, which highlighted that rockfall may evolve through a process of fragmentation and this process is likely to be apparent only below approximately four to seven days. This is also consistent with *Section 7.2*, where it was shown that there is relatively little benefit in monitoring pre-failure rockfall activity after this same period.

All but five of the R_{norm} trajectories fall below the line of unity, indicating that while rockfall occur within the incipient scars throughout the 28 d period, accelerated rockfall activity generally begins within the final 14 d. The trajectories are not smooth and instead increase incrementally towards failure, with intermittent periods of zero rockfall activity manifest as a zero gradient. Since no monitoring gaps > 6 h occurred within the analysed trajectories (and hence, no precursory rockfall were missed), this suggests that rockfall do not increase in a consistent manner towards failure. Accelerations in pre-failure activity resemble the exponential increase in time-dependent creep during the tertiary phase, shown above and by others (Royán *et al.* (2015). This may reflect a correspondence between damage accumulation through spalling, and strain development prior to failure, which is possible a result of the breaking of intact rock bridges, which results in material loss and more freely enables creep of the rock mass. The pre-failure rockfall activity prior to the largest rockfall (blue) exhibits two important patterns. First, the acceleration in rockfall activity is high, indicated by pronounced steepening towards failure. Second, during this increase, rockfall activity is recorded in almost every time interval. The R_{norm} represents the rate of rockfall activity within the developing rockfall footprint (volume per unit area per hour), not the total volume per hour. As such, this pattern does not occur because of a uniform probability in which larger rockfall footprints are more likely to contain a rockfall. Rather, the sharp increase in activity for the largest rockfall event suggests that final rockfall size is a function of the activity rate of precursory rockfall.

7.7 Environmental conditions at time of failure

In this section, the onset of precursory deformation is examined with respect to weather conditions, combining the results of *Chapter 6*. Using near real-time constant monitoring to examine this relationship allows an appraisal of the timescales over which deformation in the secondary creep phase progresses into accelerated tertiary creep, as well as the timing of this progression relative to inclement weather conditions. In Figure 7.24, the cumulative deformation, the inverse velocity, and the RCV of Slump 2 is plotted alongside rainfall, wind speed, temperature and sea conditions for the week before failure. As described above, as the time to failure approaches zero, the inverse velocity estimates converge due to the increasing displacement throughout the monitoring period that approaches and exceeds the measurement noise. Given that no LoD is again applied to this data, the overall increase in cumulative deformation is likely to reflect some variable displacements that occur beneath the instrument resolution. However, increases in the gradient of this displacement curve, representing velocity, are evident between separate phases of rainfall, delineated by the black vertical lines. These increases, which exclude the initial phase with no rainfall and the final phase of acceleration, translate to discrete periods of movement with velocity changes from 0.55 mm h^{-1} to 0.74 mm h^{-1} to 1.11 mm h^{-1}. Rainfall therefore acts to ratchet up the velocity of the rockfall in the period prior to failure. In all rockfall, a reduction in velocity is never observed. Between the short-duration rainfall events, overall displacement rates do not appear to change, suggesting that damage accumulation within the rock mass may be more sensitive to short-term larger rainfall events as opposed to lower magnitude, sustained rainfall.

During the final hours before failure, the significant increase in displacement rates results in a reduction in inverse velocities that approach zero. In relation to both temperature and temperature gradient, no obvious changes appear to coincide with either the onset of acceleration or final failure. Mean and maximum wind speeds also do not appear to relate to the time of failure but it is noticeable that the highest wind speeds during the seven days coincide with the onset of acceleration. This may, however, be coincident with rainfall and storm conditions. Both the timing of high tide and the timing of peaks in significant wave height correspond to the onset of acceleration and the time of failure, despite the fact that neither are of sufficient height to inundate or strike at this elevation up the cliff, but it has previously demonstrated that wave impacts result in microseismic excitation of the cliff rock mass (Vann Jones *et al.*, 2015).

A noticeable relationship between rainfall and the onset of final failure is apparent. Despite this, no rainfall occurred during failure. While rainfall may have resulted in the onset of failure, this rainfall was neither the greatest intensity, nor the greatest accumulation event observed in the 7 days prior to failure. Two possible explanations may therefore be proposed.

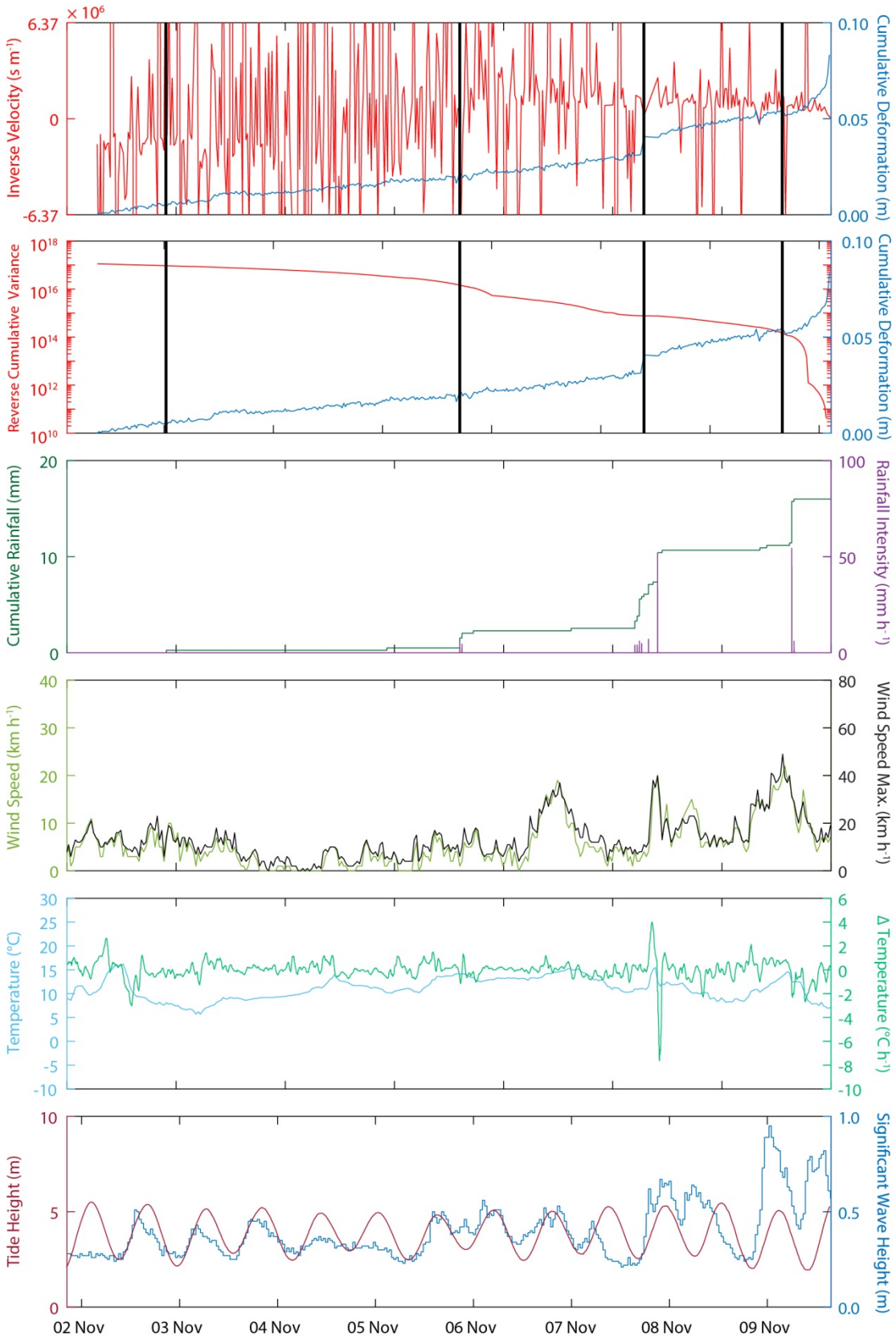

Figure 7.24: *Slump 2. While rainfall coincides with failure, it does not match the timing of final failure. Black dashed lines indicate rainfall events, between which sustained increases in displacement rate occur. Decreases in cumulative variance occur at similar times to rainfall events, but do not perfectly coincide, indicating a lagged response of the rockface to instantaneous perturbations.*

First, the overall increase in velocity throughout the seven days may indicate that, although an event is required to force the rockface into a final stage of acceleration, this event does necessarily need to be highly energetic. Instead, damage may be accumulated by successive rainfall events, and require only a small to induce failure. Second, the rainfall that occurred on 8th November had the largest accumulation; however, it did not coincide with high wind speeds, tide heights and significant wave heights that were as large as those at the onset of failure were on 9th November. One implication of this is that a combination of environmental conditions may be more important for triggering the onset of acceleration than a single high intensity rainfall event. Since high tides occur twice a day, establishing with certainty that a causative relationship exists between marine conditions and the onset of acceleration, which is not simply coincidence, is complex. Furthermore, such combinations are not possible to assess with only a limited number of rockfall of sufficient volume to explore such correlations.

Figure 7.24 also shows the reverse cumulative variance in addition to the inverse velocity. The timing of the onset of acceleration can be related to the significant drop in variance over several orders of magnitude. Throughout the seven days, breaks in the gradient of the cumulative variance are evident in response to rainfall events, highlighting the sensitivity of this metric to small, instantaneous shifts in deformation rates. Noticeably, however, the *RCV* appears to be unrelated to any other the environmental conditions within the final hours of failure. This, combined with the multiple phases of movement, suggests that fragmentation of the rock mass may be accelerated by external forcing; however, the failure of intact rock bridges may promote deformation of the rock mass in phases that are independent of external forcing.

Slump 3 is presented in Figure 7.25 and exhibits final acceleration over a much shorter timescale than slump 2 above. As in Figure 7.24, the cumulative displacement increases through the period and is divided into four windows, each separated by an individual rainfall event. Rainfall appears to have a similar impact to that in the above example, by increasing the overall rate of displacement from 0.20 mm h^{-1} to 0.27 mm h^{-1} to 0.21 mm h^{-1} to 0.30 mm h^{-1}, though a slight decrease in displacement rate during the third phase occurs. Again, while rainfall precedes failure, the final rainfall event coincides with the onset of acceleration, rather than the failure itself. Although no direct relationship appears to exist between wind speed and failure, an increase in tide height and significant wave height is again apparent, but with significant wave heights nearly twice those of slump 2. Rainfall accumulation in the 24 hours prior to failure is 18.8 mm, compared with the 4 mm recorded for slump 2.

For rockfall 2, the pattern of deformation is more variable than that for the slumps (Figure 7.26). Again, the rockfall occurs at high tide, following the pattern of increased probability of rockfall occurrence ($V > 0.1$ m^3) during high tide presented in *Chapter 6*. The rockfall does not coincide with a single rainfall event; however, with each rainfall event there is a clear increase in displacement within the rockfall scar prior to failure. Within the black bars

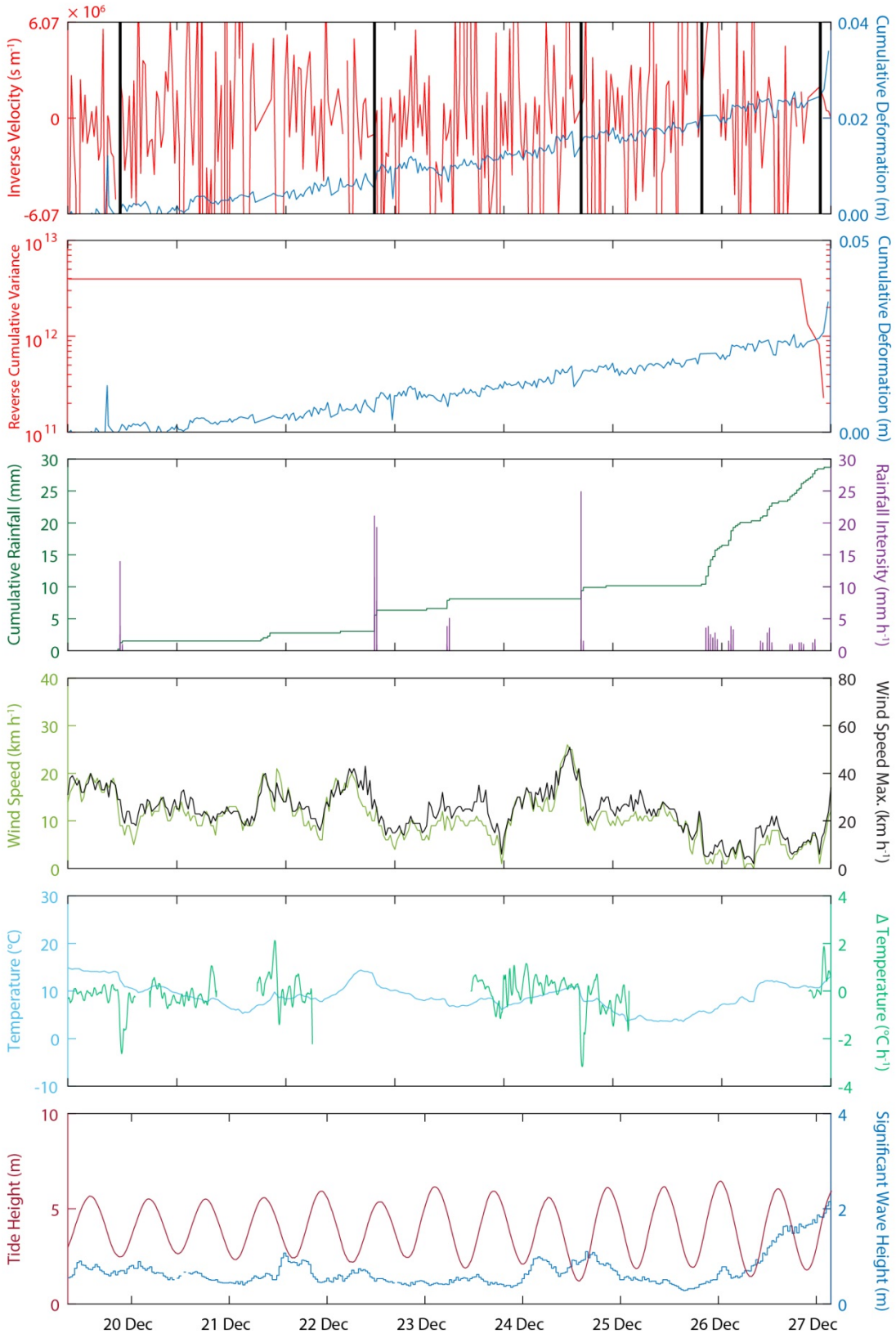

Figure 7.25: *Slump 3. Here the reverse cumulative variance provides a more accurate assessment of the location of the time at which the onset of acceleration occurs, with an order of magnitude decrease. While rainfall occurs closer to the timing of failure, these plots again show that rainfall does not directly correspond to the timing of failure, suggesting that internal deformation of the rock mass is required for final failure. Rainfall does, however, appear to ratchet up the rate of movement, and therefore acts as a preparatory factor that decreases the slope's resistance to failure. In slumps, this is most likely due elevated pore pressures and reduced frictional resistance at the shear plane.*

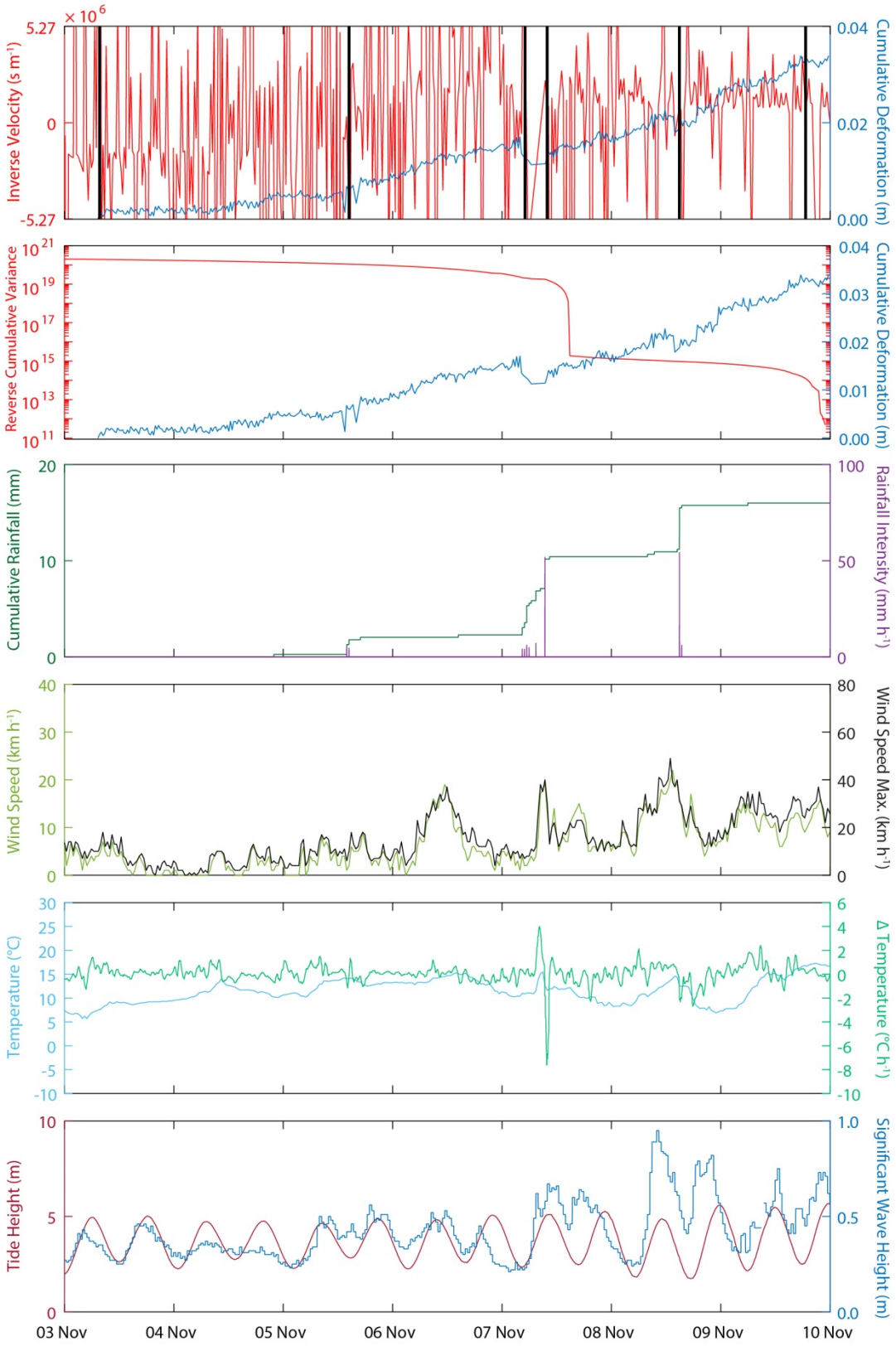

Figure 7.26: *Rockfall 2. Rainfall acts to increase the rate of deformation, suggesting that rainfall can act to prepare the slope for rockfall, although it fails to coincide with the timing of failure. Increased rates of precursory deformation occur from 4th November, six days prior to failure. A precursory rockfall that occurred during rainfall is responsible for the dip in cumulative deformation measurements on 7th November. Failure occurs during high tide, mirroring the distribution of rockfall events > 0.1 m³ at high tide described in Chapter 6. However, since high tide occurs twice a day and the sample size of such events is small, it is difficult to establish whether this correlation reflects a causative effect. The reverse cumulative variance shows several small, discrete phases of failure during the final hours, implying multiple phases of final failure.*

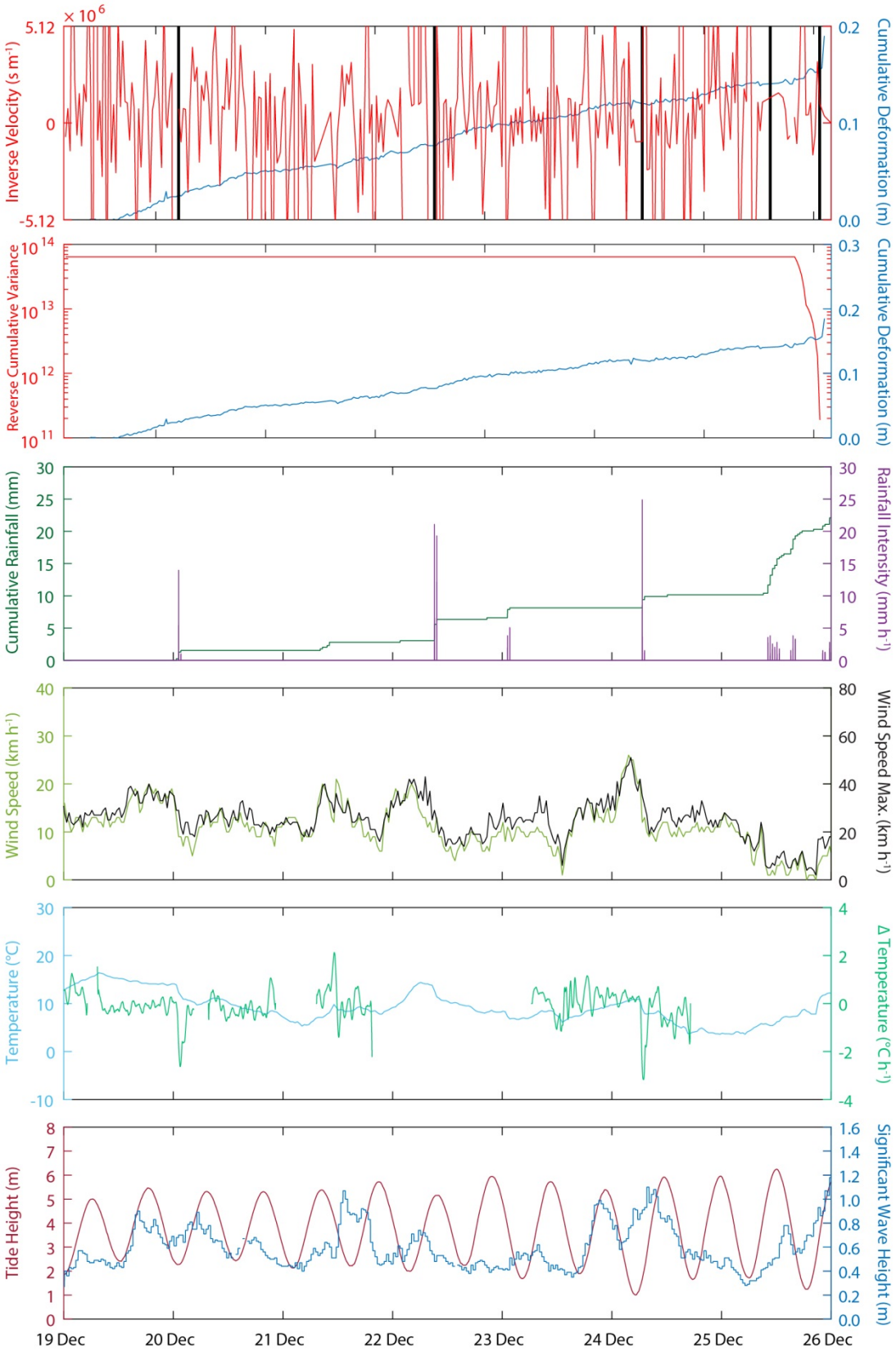

Figure 7.27: *Rockfall 3. Rainfall appears to have little appreciable effect on the cumulative pre-failure deformation. The reverse cumulative variance again shows multiple inflections towards failure, providing a clear estimate of the onset and phases of acceleration that the inverse velocity does not. While subtle, these inflections may represent the breaking of intact rock bridges that trigger failure.*

after the first rainfall event in Figure 7.26, this increase occurs from 0.21 mm h^{-1} to 0.68 mm h^{-1} to 0.72 mm h^{-1} to 1.20 mm h^{-1}. This is particularly evident following the last rainfall event before failure. For rockfall 3 (Figure 7.27), rainfall appears to have a lower impact on the overall pre-failure displacement rate; however, the rockfall occurred during sustained rainfall.

7.8 Summary

In this chapter, several observations have been made that serve to develop our understanding of the nature and controls upon the precursory behaviour of rockfall and slumps:

(1) Rockfall activity < 0.1 m^3 can be observed to cluster spatially within the footprint of larger, yet-to-fail rockfall when monitoring at T_{int} below *ca.* 4 d – 7 d. This clustering often appears at the periphery of the ultimate detachment, suggesting the development of tensile stresses and the removal of support from beneath the unstable mass. The small scale of these precursors suggests that they are shallow depth and hence may occur in response to exogenic forcing. A proposed explanation for this effect is the growth of microcracks at the near-surface as a result of thermomechanical stress development induced during periods of cooling (*Section 6.6*).

(2) The timescale over which precursory rockfall develop mirrors the timescale of fragmentation, inferred from the magnitude-frequency analysis in *Chapter 5*. However, while the magnitude-frequency analysis provides an indication of the distribution of rockfall volumes over a defined time interval across the entire rock face, the analysis presented here has been undertaken using case studies of the 30 largest rockfall events. This further emphasises the importance of monitoring below *ca.* 100 h in order to capture the path to failure of rockfall events. More importantly, it suggests that accelerations to failure that are driven by internal mechanisms occur over this timescale.

(3) The rate of pre-failure rockfall activity is not constant, and instead increases towards failure. This has been quantified using the rockfall activity, R_{norm}. This mirrors previous studies of rockfall at far larger time intervals (monthly by Rosser *et al.*, 2007a;b; and 104 days by Royán *et al.*, 2015).

(4) In addition to pre-failure rockfall activity, pre-failure creep has been observed prior to rockfall. These magnitudes are lower than for slumps, but reflect laboratory simulations of increased microfracture growth in brittle failures (Petley *et al.*, 2005). Deformation prior to rockfall has also been observed by Royán *et al.* (2015), but at far larger scales (0.40 m) than in this study (0.001 - 0.038 m) and over far shorter periods (several hundred days *cf.* two hours). This suggests that hyperbolic increases in the rate of microcrack growth may occur prior to failure, and raises the question of the relative

importance of creep and rockfall as derivatives of strain accumulation prior to failure.

(5) While relatively few events have been recorded that are large enough to fail, the increase in final failure size with the amount of creep that precedes it resembles previous studies containing larger rockfall (Rosser *et al.*, 2007).

(6) While hyperbolic accelerations to failure have been observed in previous studies, these studies have drawn upon surveys separated by much longer timescales. One implication of this is that the nature of the final acceleration towards failure is difficult to resolve. The use of the reverse cumulative variance (*RCV*) has shown that, for both rockfall and slumps, this process is not necessarily a smooth acceleration towards failure. Instead, internal deformations such as the fracture of rock bridges may act to incrementally reduce the resistance of the rock mass to failure. Precursory detachments at the edges of incipient rockfall could indicate the need for rock bridges to be broken to provide release, with the complexity in shape and size of detachments reflect breakage at a range of fracture scales (from microfractures to joints).

(7) The cumulative deformation and *RCV* patterns have been related to environmental and marine conditions. For both rockfall and slumps, these events occur at high tide. This can be explained either in support of the enhanced probability of failure for events > 1 m^3 presented in *Chapter 6* or as coincidence, since two high tides per day occur and only 30 events were examined.

(8) The paths to failure of both rockfall and slumps have also been examined with regard to rainfall. In several respects, this provides for the first time data that supports previous conceptual models of damage accumulation, preparation for failure, and the triggering of failure from datasets of far lower temporal and spatial resolution. The occurrence of rainfall has shown to be related to the onset of final failure. In other cases the onset of final failure occurs days after the most recent rainfall. This suggests that the same two rainfall events may or may not induce failure, and that this is a function of damage accumulation in the rock mass. The rate of deformation of the rock mass appears to undergo a sustained increase after a rainfall event. Therefore, the occurrence of failure cannot be considered purely as a function of a trigger event (Krautblatter and Dikau, 2007). This supports the weak relationships derived by linear regression in *Chapter 6*.

(9) Rainfall often does not appear to trigger failure. Instead, it appears to act only to trigger the onset of failure. This supports laboratory analysis of brittle failure, in which hyperbolic reduction of the shear zone through microcrack growth is irreversible and achieved independently of pore pressures.

(10) While the acceleration to final failure appears to occur in phases, a straight line is formed in inverse velocity-time space. This occurs over a shorter period than for the failure of loose material on the buttress, and indicates that first-time brittle failures in

general accelerate over shorter periods but still conform to a predictable pattern of deformation towards failure.

(11) While the LoD is critical in defining the aerial extent of rockfall (i.e. defining which pixels can and cannot be considered as noise, beneath the instrument precision), the data derived in this chapter appear to show that a signal-to-noise ratio > 1 can be achieved using measurements below the LoD. It is likely that this reflects some variability in precision across the cliff face and within the series of scans acquired, above which the LoD is set.

Chapter 8

Discussion

8.1 Introduction

The aim of this thesis was to use high frequency continuous monitoring to understand the mechanisms and nature of rock slope failure, in conjunction with the role of structural controls and external drivers. This chapter describes advances in 4D slope monitoring and the understanding of rockfall evolution developed during the study. The aim of the chapter is to set the findings of this study within the wider context of (a) the development of 4D monitoring techniques, and (b) current understanding of rockfall occurrence. The chapter begins by presenting insights into the development of 4D monitoring in the context of a state-of-the art review of slope monitoring using TLS (Abellán *et al.*, 2014; 2016), which forms the justification for such a system. The research undertaken in *Chapters 3-4* has provided a reference for future 4D monitoring systems based on acquiring, pre-processing and analysing large volumes of time series point cloud data.

Sections 8.3-8.6 present the contribution of this thesis to the understanding of the spatial and size characteristics of rockfall, in addition to their sensitivity to rock mass structure and environmental conditions. This is followed by an examination of the findings in relation to the timescales over which rockfall occur and evolve, culminating in a new conceptual model of the controls on rockfall development. The findings discussed are used to directly address the research questions outlined in *Chapter 1*, and which are repeated below:

(1) Does the previously observed power-law behaviour of rockfall extend to short timescales?
(2) To what extent does the rock mass structure determine the size of rockfall?
(3) Are environmental conditions significant as triggers of rockfall occurrence and, if so, which conditions promote failure?
(4) Can 4D monitoring detect precursory rockfall or deformation of the rock mass at timescales below those previously observed for rockfall?

8.2 4D monitoring of rock slope failure

In a state-of-the-art review, Abellán *et al.* (2014) highlighted that datasets of high temporal resolution, obtained from frequent surveying, are a necessary area of development for studies using terrestrial laser scanning to monitor rock slope instabilities. The use of TLS has

seen significant advances in range and coverage, capturing wide areas experiencing failure in combination with improvements in the accuracy and efficiency with which rockfall inventories can now be acquired. The latter is in part a function of improvements in scanner hardware, but is also a function of the increased availability of efficient point cloud handling software and an increase in users developing algorithms tailored to rockfall acquisition from their own datasets (Tonini and Abellán, 2014). The development of new processing techniques or the extraction of original insights into rock slope failure are highlighted by Abellán *et al.* (2016) as a significant requirement for future research. The relative ease with which high-quality point clouds can now be acquired reinforces a need to develop novel work flows, data treatment, and the interpretation of results that inform our understanding of slope instability. In this research, the development of a constant near-real time monitoring system, combined with the development of methods to interrogate the data collected, presents a step-forward in data collection and analysis that to date remains undocumented. In conjunction with observations of the nature of rockfall from an actively failing rock slope, this study builds upon and develops the directions for future research described by Abellán *et al.* (2014; 2016).

Terrestrial laser scanning has enabled the derivation of magnitude-frequency distributions of rockfall volume, such that a power-law can be calculated to describe the exponential increase in the numbers of increasingly small detachments (Lim *et al.*, 2010; Barlow *et al.*, 2012). Improving the ability to discretise the smallest detachments is required in order to quantify the net contribution of these events to mass wasting from slopes and to consider how they might relate to larger events. Such an understanding is compromised by the ability to discretise these detachments in the temporal domain, as defined by T_{int} between surveys. Low temporal resolution surveys (greater than two weeks, for example) increase the likelihood of rockfall coalescence between scans, and their superimposition by larger, yet-to-fail detachments (Barlow *et al.*, 2012). The results from this study show that, by reducing the scan interval from one hour to three months, the frequency of the largest events recorded reduces by more than three orders of magnitude. Both of these effects produce seemingly larger failures, where the net volume of material from individual events is actually the sum of many smaller events. This has the effect on underplaying the efficacy of small rockfall in eroding the rock face.

In addition to minimising the effects of coalescence and superimposition, acknowledged by Abellán *et al.* (2014), the need to monitor over short epochs holds several other benefits for understanding the controls and mechanisms of rockfall, which were originally considered.

(1) Given that the frequency (T_{int}) of environmental monitoring and the timescales over which weather variables change is finer than the intervals of normal TLS monitoring campaigns, increasing the scan frequency is vital for accurately determining the relationship between environmental conditions and the occurrence of rockfall. By creating average statistics for both, the rock face's response to

extremes and short-term rates of environmental change, which may logically have the greatest influence on rockfall, becomes difficult to discern with confidence. If scans are acquired closer to the T_{int} of weather station data, which is invariably more aligned to capturing the timescales over which the weather changes, there is a reduced need to time-average datasets and hence overlook potentially important short-term detail.

(2) The use of 4D monitoring allows an examination of the nature of precursory deformation of the failing rock mass. The relatively small magnitudes of strain that occurs in brittle materials ($< 3\%$), shown in both the field and laboratory (Petley *et al.*, 2005; Rose and Hungr, 2007; Oppikofer *et al.*, 2009; Dick, 2013), highlights the importance of not only using precise change data, but also frequent measurements in order to resolve the development of failure. Frequent and precise measurement has the potential to provide an understanding of the kinematics of failure and the role of precursory rockfall, in addition to quantifying accelerations towards failure.

8.2.1 Implications of constant TLS deployment

A frequent observation made from monitoring undertaken at $T_{int} \geq 1$ month is that the resulting insights into rock slope instability could be achieved if more frequent monitoring was possible. However, the findings from this study emphasise the importance of consistency in monitoring through time, as well as frequent monitoring. In practice, with the exception of slopes that present an immediate risk of collapse, installing a terrestrial laser scanner for a prolonged period is costly. However, since rockfall have been shown to be apparently episodic in nature (Lim *et al.*, 2010), permanently installing a scanner ensures that rockfall are recorded and, as shown in this study, that their spatial and temporal distribution can be examined. This allows deviations from a background behaviour to be identified, such as increases in rockfall frequency, increases in rockfall size, or changes to rockfall shape. These deviations in rockfall properties may arise as the result of a triggering factor, but a long duration of monitoring is also necessary in order to quantify the difference between triggers and preparatory factors (Gunzburger *et al.*, 2005). In this study, an increase in the volume frequency scaling exponent β was observed during June and July, indicating that a higher proportion of small rockfall $<$ *ca.* 0.1 m^3 occurred. This was higher than the background exponent recorded for previous months, and appears to return to this level from September onwards (Figure 6.23, *Section 6.6.2*). The hiatus in scanning during late July and August, however, prevented direct observation of this return.

While not an initial reason for installing the system, it is important to consider the implications of creating a system that constantly and frequently monitors a rock face for use in

cliff stability management. It is important to note that precursory detachments may scale in time and space: smaller rockfall have been previously suggested to generate small precursors over a relatively short timeframe, whereas larger events have bigger precursors that are active over a longer time period (Rosser *et al.*, 2007b). As is discussed in more detail below, only a small number of rockfall captured in the inventory presented here were large enough to generate or display any pre-failure deformation or detectable precursory detachments. For reliable forecasting, based upon measurement and interpretation of creep and rockfall rate acceleration trends to failure, a larger database of observed accelerations is required across a larger range of rockfall sizes and settings to assess when and where precursors occur and can be used in forecasting. If smaller rockfall perpetuate larger-scale slope failures by releasing stress and/or removing load that is necessary for a future rockfall to occur, then their identification and monitoring may be informative for potential slope management practices.

Another potential benefit for rockfall management is the ability to map rockfall trajectories by distinguishing a falling block from the material that it detaches when impacting the slope surface below. With less frequent monitoring of actively failing slopes, the ability to associate an individual rockfall with any impact marks becomes more problematic. This information has potential significance for model development in validating predictions of rockfall runout, which may not be possible using data obtained from less frequent monitoring. Here, rockfall impact marks were shown to be several orders of magnitude less deep than the rockfall scar from which the falling block originated, but contemporaneous (*Section 5.5*). While the overall volume loss that these marks represents was small, and therefore will not have affected the tails of the resulting magnitude-frequency power law, identifying trajectory scars in this way allows them to be removed from future analysis. In this data, there is no conclusive evidence that a falling block triggers the release of further blocks from the rock face below. Rockfall from this cliff therefore do not appear to trigger cascades of mass wasting.

8.2.2 Considerations for 4D monitoring

The use of constant monitoring has been fundamental to the research undertaken in this study. However, its use also presents some unique drawbacks that required consideration. Since scanning is frequent and constant, point clouds can only be acquired from a single position. While a future, albeit costly, development could be the combination of two scanner positions to minimise occlusion on a rough or complex rock face, this would present significant logistical difficulty and would require a more sophisticated automated scan alignment procedure. The coastal setting of East Cliff prevents such a system layout. The relatively high surface relief on the cliff face due to protruding beds of sandstone, in combination with the acute angle between the slope and the position of the lighthouse, results in the occlusion of *ca.* 11% of the rock face

in each scan. In a more open setting, the scanner could be positioned closer to a nadir (90°) view of the cliff, thereby minimising occlusion. In this study, it is acknowledged that the rockfall inventory collected may be smaller than would be possible without the relatively high level of occlusion, and that the sizes and shapes of some rockfall close to occluded areas may be misrepresented.

From a single scan position, infinitely small shifts in the scanner zero azimuth angle (rotation about the instrument z-axis) can cause the edge of a discontinuity to be measured in a scan line of one scan, but the discontinuity behind it to be measured by the same scan line in the next scan. At the closest target range observed in this study (342 m), only a 0.0005° shift in azimuth (the step-width precision of a Riegl VZ-1000) produces a 0.06 m shift in point position on the cliff face at nadir. The heterogeneity of point measurement positions between sequential scans can therefore result in unrealistically large change estimates, or the omission of some areas of the slope from the change calculation. In addition to the point distribution, the accuracy of the individual range estimates that relate to specific feature edges is inherently uncertain. This is based upon the fact that the footprint of the diverged laser on the cliff face may intersect multiple surfaces or discontinuities that are separated by a topographic edge within the same line-of-sight. A single laser footprint may therefore encapsulate a large range in distances from the scanner. As a result, the range of a point generated may be the average of two distinct and separate surfaces contained within a single footprint. This averaging of range estimates, or so-called 'smearing' or 'mixed pixels', is more likely to occur for longer-range targets, due to the linear increase in footprint due to beam divergence with range (Lichti *et al.*, 2002; Alda, 2003).

Multiple laser return 'echoes' have been used in airborne and spaceborne LiDAR surveys to resolve canopy heights from the ground surface below (for example, Ni-Mesiter *et al.*, 2001; Lefsky *et al.*, 2005; Simard *et al.*, 2011) and filter low-lying shrubs in order to measure the position of the ground surface. A number of new terrestrial LiDAR systems are able to resolve multiple returns, or 'echoes', using the same approach (Afana *et al.*, 2015). Between pairs of scans, this data may offer a means of adjustment such that the ranges of points at the edge of discontinuities are allocated to the same surface or deleted where uncertain, thereby avoiding 'smearing' and the resulting uncertainty in change detection. Between large numbers of scan pairs, however, a systematic adjustment of this nature is not possible.

In this study, a means of estimating the proximity of points to edges and holes was established. A decrease in the precision of points that are deemed (too) close to edges, inferred by detecting change with a subsequent scan over a period with no appreciable surface change, has also been presented. Further to this, the use of a statistic that summarises a point's radiometric return, known in Riegl measurement systems as the 'deviation' (Riegl, 2015), also helped to identify points within each cloud that produced high estimates of change, most often around semi-occluded surfaces behind edges but also in areas of vegetation. The automatic

removal of these points from successive scans resulted in a 30% lowering of the Level of Detection, from 0.078 m to 0.055 m. This highlights that these methods are of considerable importance in the reduction of error within large scan series, and can be applied automatically to every point cloud in the scan series. In addition to the use of filtering, the presence of holes and edges in the dataset necessitated a new approach to optimising data for change detection. In this study, computation of the distance along the normal was undertaken using a MATLAB code constructed according to the principles of M3C2 (Lague *et al.*, 2013). The abundance of edges and holes within the datasets resulted in the omission of discontinuities oriented away from the scanner, and produced significant offsets between those oriented towards the scanner. The introduction of a variable cylinder length into the distance along the normal calculation (DAN VCL) ensured a *ca.* 400% reduction in the standard deviation of Gaussian-distributed noise between scans, from 0.084 m to 0.014 m.

Another drawback of the use of a single scan position is the inability to perform volume and shape estimation in true 3D, as can be performed from multiple scan positions by Carrea *et al.* (2012), and from data collected from a moving airborne platform by Benjamin *et al.* (2016). While potentially highly valuable for understanding the kinematics of individual failures, these techniques rely on rockfall scars not to be occluded in order to create a closed hull of points.

In addition to the considerations related to scanning from a single position, several complexities introduced by the constant monitoring setup have been addressed in this study. Instability monitoring using LiDAR becomes less reliable in wet atmospheric conditions, here caused by rainfall, sea spray, or fog. In open-pit mines, for instance, periods of heavy rain are also likely to be the periods that require the most frequent monitoring of large, slope-scale instabilities. For monthly rockfall monitoring, however, wet atmospheric conditions are not sustained for more than several hours, far below the monitoring interval. For the constant monitoring in this study, rainfall and fog often persisted for several hours, far longer than the T_{int} of monitoring (20 – 30 minutes). As a result, the scans collected in this study cannot be considered a truly continuous time-series, due to the irregular intervals between them during periods of rainfall. Approaches to time-series and spectral analysis, such as Fast Fourier Transform and Wavelet Analysis, which could provide significant advances in the ability to characterise patterns of rockfall activity at a range of spatial and temporal scales, cannot therefore be applied without using either repeated earlier data or synthetic interim data. This study has highlighted that if a scan is partially obscured due to rainfall, its inclusion as part of the wider scan series introduces the risk of missing rockfall occurrence. This risk arises because change is detected between scan pairs, rather than cumulatively; hence, if part of a surface is missing in a constituent scan, no change will be recorded between it and the previous scan, or it and the next scan (Figure 4.36, *Section 4.12*). It is therefore recommended that a threshold close to the number of expected points under dry atmospheric conditions be used to identify scans

with rainfall for exclusion. Scans that are removed could be retained for use in monitoring the evolution of an unobscured rockfall; however, their inclusion in the wider dataset was avoided in this study. The need to remove scans captured during rainfall adds to the complexity of establishing a cause-effect relationship between rainfall and rockfall occurrence, as attempted in *Chapter 6*, since scans taken during rainfall were often removed, with the next scan used to form the scan pair for comparison.

When considering the alignment of scans using iterative closest point (ICP), Schürch *et al.* (2011) noted that the alignment of one scan to a previous scan of the same survey scene, rather than a fixed baseline scan, reduces the absolute accuracy of their position, but increases the relative accuracy for comparison between them. As discussed in *Section 4.7*, this is advantageous for monitoring a rapidly deforming mass, since the structure of the monitored surface is best represented in the most recent scan, and may not reflect the topography of a scan hours, days or weeks ago, at the start of monitoring. While the spatial distribution of rockfall from East Cliff is almost homogenous in this dataset, the topography of the cliff as a whole remains broadly similar when downsampled to a fixed-point spacing. All scans were therefore aligned to the first scan. This avoided drifts in the absolute position of scans over time and, since the scanner was securely fixed within the lighthouse, did not compromise the relative accuracy of the change detection between scans. The occurrence of a large failure over a significant portion of the cliff face, or full step-back retreat of the coastline would, however, necessitate alignment to a post-failure reference scan. When this becomes necessary is a consideration for further research.

The trade-off between the temporal resolution of scanning and its spatial resolution has been identified as a consideration of significant importance prior to establishing a 4D monitoring system (*Section 3.7*). In this study, a half hour scan interval was selected, with a point spacing of 0.15 m at the maximum range. By examining the timescales over which creep prior to rockfall and slumps were observed to accelerate to failure, a timescale of approximately 6 h during which most accelerations can be observed, with most occurring within the final 2 h prior to failure. From the perspective of failure evolution monitoring, therefore, the 30 minute scan interval could have been reduced to a $T_{int} \approx 1$ h. The fact that many failures occurred within a single pixel, in particular those that occurred at the periphery of developing rockfall, suggests that many of the rockfall that occurred were below the minimum aerial extent of 0.15×0.15 m permitted by the linear interpolation of points used in the data processing here. At present, the system's operating schedule therefore comprises 1 h scans with a maximum point spacing of 0.10 m. This frequency also ensures that the scanner is idle for a greater period, increasing the instrument service interval, which is a function of total scan time. The scan schedule defined in this study is clearly unique to this setting, with the scanner model and its distance from the slope determining the point spacing that is possible to collect within a defined T_{int}. However,

this set-up emphasises the importance of examining the spatial and temporal scales of movement in order to define and refine scan schedules that are optimised for the process of failure being monitored.

8.2.3 Is constant monitoring fit for purpose?

Constant scanning has the potential to generate a considerable number of point clouds (10^3-10^4). Here, the total number of scans drawn upon is two orders of magnitude higher than previous studies (including, for example, Teza *et al.*, 2007; Abellán *et al.*, 2010; Rosser *et al.*, 2013; Kromer *et al.*, 2015a;b; Royán *et al.*, 2015). Their use in this study has shown that rockfall from East Cliff conform to previously published magnitude-frequency distributions for rockfall (Rosser *et al.*, 2005; Lim *et al.*, 2010; Barlow *et al.*, 2012), in which an exponential increase in the number of increasingly small rockfall is observed. In addition to this, the time between scans, T_{int}, is inversely related to the rate of increase in the proportion of small rockfall events, β. As described in *Section 5.3*, the aerial extent of rasterised rockfall events relative to their perimeter determines the uncertainty in area that it is exhibited relative to their true size. Consequently, the power-law behaviour of rockfall when observed at low T_{int} is such that small failures, with high percentage volume errors, account for a significant proportion of the net failed volume estimate. The frequent and repeated collection of scans with low T_{int} therefore has the potential to propagate this volumetric uncertainty into long-term estimates of erosion and cliff retreat. This is in contrast to the measurement of individual large events, with limited proportional volumetric error, between only a single scan pair. While the period between the first and last scan may be the same, measurement at lower T_{int} may result in a lower overall certainty.

By estimating the theoretical maximum volume error, analysis in *Chapter 5* has shown that uncertainty in the net volume of eroded material can range from 20 - 160%. This implies that monitoring at lower frequencies (e.g. monthly) may provide more accurate estimates of predicted retreat rates over longer time periods. This is not purely a function of longer time-averaged conditions drawn upon by Barlow *et al.* (2012), but is also because longer intervals reduce the measurement error relative to the change detected, which in turn over time is more likely to represent coalesced or superimposed rockfall events. While high frequency monitoring is critical to enhance process understanding and to gain a full insight into rockfall magnitude and frequency, the uncertainty in net volumetric loss therefore makes it less suited to longer-term erosion estimates.

Barlow *et al.* (2012) found that the selection of T_{int} has a considerable impact upon the frequency density of large events. Monthly inventories provided representative magnitude-frequency relations for inventories of failure volumes similar to those in this study, assuming

that no significant rockfall occurred. In order to accurately predict long-term rates of erosion, the frequency distribution of inventories that also contain large rockfall, was required; typically with a T_{int} equivalent to the length of an individual season. While Barlow *et al.* (2012) provide an upper limit of T_{int} in order to accurately estimate long-term rates of retreat, the high frequency monitoring here indicates that a T_{int} of *ca.* 100 h can be considered as a lower bound for monitoring for the same purpose. Any lower than this and the data represents a shift towards monitoring the failure process of individual rockfall or clusters of rockfall.

Despite being based upon simplified step-back retreat mechanisms, present models of cliff retreat may derive similar estimates to those derived from face-on, monthly rockfall monitoring. Rosser *et al.* (2013) argued that capturing the timing and scale of episodic events is of considerable importance in future erosion modelling. Without an improvement in our ability to accurately resolve rockfall volumes, however, the research presented here suggests that constant monitoring datasets will remain unsuited to long-term erosion measurement. The recent development of 3D volume estimation from point clouds (Carrea *et al.*, 2012; Benjamin *et al.*, 2016) may play an important role in the development of 4D monitoring. This reduces uncertainty in the aerial extent of rockfall, and enables a comparison between the rockfall shape and the joint structure from which it was released. The uncertainty of these techniques is determined by the precision of the point cloud; as such, they provide a means of reducing uncertainty in the aerial extent of rockfall that arises from linear interpolation into a fixed grid in a 2.5D approach. Due to the reliance of these techniques on a minimum of four points to create a closed hull, fully 3D techniques are limited in their ability to resolve small, single point displacements, but the development of scanners with increasingly small angular step widths and increased rates of point acquisition should decrease the minimum resolvable detachment.

8.2.4 4D smoothing

While the uncertainty of detachment volumes has been discussed, a means of reducing uncertainty in the depth or deformation measurements between scan pairs, and therefore the resulting LoD, is through 4D smoothing, smoothing in both space and time. The collection of a rich time-series of scan data has the potential to reduce the distance between successive point clouds by drawing on the fact that the points they comprise are neither independent in space nor in time. In this study, control targets were scanned at regular 6 h intervals in order to derive a range correction factor and transformation matrix that could be used to reduce the positional offset of successive point clouds. Repeated nadir scanning of planar surfaces is known to produce range estimates that conform to a Gaussian distribution (Abellán *et al.*, 2009; Soudarissanane *et al.*, 2011; Williams *et al.*, 2013). The width of this distribution defines the precision of monitoring, and is an inherent characteristic of repeat scanning of an unchanging

surface. The distribution's width is affected by a combination of the instrument-target range, the incidence angle of scanning, surface roughness, surface reflectance, atmospheric conditions, and the heterogeneity of point spacing that results from surface roughness and alignment error. Fundamentally, however, it is also a function of inherent uncertainty in the accuracy of range estimates from the instrument. Movements of the surface are unable to be distinguished if they are below the noise that is characterised by this distribution. Logically, therefore, if the width of this Gaussian distribution can be reduced, smaller movements are detectable between scans.

The collection of large numbers of scans presents an opportunity to characterise the distribution of range estimates and average out random noise that results from any combination of the factors described above. As noted by Kromer *et al.* (2015b), this averaging can take the form of averaging the 3D position of each point, such as the case of M3C2 (Lague *et al.*, 2013), or the averaging of differences between points (Abellán *et al.*, 2009). Kromer *et al.* (2015b) devised a method of averaging the distance between point clouds, whereby the change between them was assigned based on the median change for a neighbourhood of points along the normal direction. This yielded a reduction in the LoD of between one and two orders of magnitude. In this research, an adaptation of the M3C2 algorithm was developed that calculates the distance along the normal direction, but for surfaces that are averaged through space and time using a Moving Least Squares algorithm. The technique was not employed in the data presented because averaging a surface across the temporal domain has the potential to remove small, apparently instantaneous detachments and so is unsuited to monitoring the types of rockfall observed here. However, since a premise of the permanent monitoring in this study was originally centred upon larger scale creep of open-pit high-walls and on the basis that future research may attempt to explore this further, a brief overview is provided in Appendix E.

While a series of advantages and disadvantages of 4D slope monitoring have been discussed above, the insight into the nature and controls on rockfall evolution in this study would have been impossible to generate without a step-change improvement in the application of terrestrial laser scanning. As presented below, these insights have been made possible by aggregating size distributions that are unaffected by superimposition and coalescence of the rock mass. Equally, collecting rockfall data at a frequency comparable to weather data acquisition, enabling individual cause-effect and aggregated relationships to be derived with external forcing and by monitoring the evolution of individual failure scars has been possible. Eitel *et al.* (2016) noted that, due to the relatively small number of studies that use 4D constant monitoring LiDAR, a standardised approach for processing and analysis does not currently exist. While many of the techniques adopted here have been tailored to the rockface in question and the mechanisms of failure under examination, this section has nonetheless presented some aspects of 4D monitoring that should be considered prior to the development of such a system in the future.

8.3 The nature of rockfall

8.3.1 Joint control on rockfall size

Controls on erosion mechanism and retreat are locally specific (Naylor *et al.*, 2010) and can be attributed to the interaction of rock strength (Collins and Sitar, 2011), structure, and the efficacy of environmental forcing. Rock slopes rarely develop under conditions where tensile strength is the dominant control on resistance to failure (Lockner, 2013). Rather, resistance to failure is determined by the strength of natural discontinuities, which concentrate compressive stresses, control the movement of groundwater, allow weathering to permeate the rock mass and, if closely spaced, may cause the material to behave in a granular manner (Selby, 2005). As such, rock mass strength and the persistence of discontinuities partially determine when and how a rockfall may occur (Stead and Wolter, 2015), with stress redistribution at the sub-metre scale likely to drive small rockfall that precede large, yet-to-fail blocks.

Studies that have analysed the magnitude-frequency distribution of rockfall volumes have done so by categorising resulting exponents according to lithology (Rosser *et al.*, 2007a; Lim *et al.*, 2010; Barlow *et al.*, 2012). While this accounts for a qualitative combination of material tensile strength and the persistence of discontinuities, the magnitude-frequency exponents derived in this study have been directly related to the measured visible persistence of discontinuities in the rock mass, which varies between different beds of similar rock type.

This analysis has shown that rockfall in general are smaller than the scale of blocks in the discrete fracture network from which they originate. This suggests that rockfall size is not necessarily defined by the joint structure that is exposed at the surface, but primarily that the joint structure likely sets a maximum permissible size for rockfall that fail within one rock type. This is in contrast to measured distributions of rockfall in other settings, which have been shown to intersect discontinuities, including joint and fault sets (for example, Pedrazzini *et al.*, 2011). However, it adds weight to the basis for rockfall occurrence on these cliffs through fragmentation or disintegration of the cliff face, and suggests that closely jointed rock masses may more freely produce small-scale rockfall. Between beds, the magnitude-frequency analysis of rockfall produced exponents ranged from 1.48–2.01, with higher exponents found in beds of more closely jointed surfaces. Given that the beds for which exposed joint dimensions could be identified were predominantly in sandstone, this implies that the possible magnitude of rockfall is more likely to be affected by the degree to which the material is fractured than its tensile strength. This is logical and conforms to patterns of rockfall volumes observed by Hungr *et al.* (1999), which were higher for more jointed rock ($\beta = 0.65$–0.70) than for more massive rock ($\beta = 0.40$–0.43), and supports the recommendation made by Barlow *et al.* (2012) that magnitude-frequency estimates should be constrained by rock slope properties, in particular

when used to forecast erosion.

It is notable that the visible persistence of discontinuities was only examined where the resolution of the point clouds allowed individual discontinuities to be extracted. At the base of the cliff, very densely jointed (centimetre scale), weak shales produced some large scale rockfall on the footwall of the buttress. This may relate to the removal of material by wave action (Kogure and Matsukura, 2010), and the formation of concave slope geometry which predispose larger-scale cantilever failure of the rock mass.

8.3.2 Rockfall shape

Rockfall dimensions tend to be a product of the geometry of jointing. The presence of three orthogonal joint sets in bedded sedimentary rocks, for example, predisposes the release of blocks (Wyllie and Mah, 2004). The dominant failure type from East Cliff is shallow depth rockfall, with the ratio of the log of area and the log of volume similar to that established by Rosser *et al.* (2007a) for a nearby site 13 km along the coast. This is lower than for published landslide inventories, suggesting that rockfall here are generally shallower in proportion to their aerial extent than other types of mass-movement, such as landslides. Similarly, the average form of the rockfall observed is a slab, such that the length and breadth of the detachment are considerably larger than its depth. As a result, the driving mechanisms that instigate the majority of failures from the cliff appear to relate to the exposure of the rock mass at the surface, rather than mechanisms at depth that drive deeper failure, which perhaps more relate to rock strength and structure normal to the cliff face. This indicates the potential importance of subaerial weathering of the rock mass or exposure on the rock face or the possible role of face parallel stress relief jointing rather than release along pre-existing (oblique) joints.

Confining pressures that are exerted on rock masses supress the growth of dilatant microcracks, thereby increasing the resistance of the rock mass to failure (Lockner, 2013; Siman-Tov *et al.*, 2017). The tendency for slab-like block forms therefore suggests that confining stresses inhibit the release of blocks that fail to depths in the cliff that are greater than the block width or height. However, when rockfall shape was examined for each bed, the shape of the ten largest rockfall appeared more block like than the shape of the mean rockfall. For these rockfall, the size of failure also approached the scale of the joint network suggesting that, for the largest events, an appraisal of strength degradation along joints is required. The densely jointed nature of the rock face is such that these rockfall occur at the intersection of discontinuities, and therefore can be considered small wedges. It may therefore be the case that the geometry of the larger rockfall is more controlled by rock mass structure, but smaller rockfall, which here dominate the mean statistics, respond to surface processes that primarily act to release a shallow depth of material from across rather than into the cliff face.

8.3.3 Spatial progression of rockfall

Vertical progression of rockfall have been observed on both coastal rock slopes (Rosser *et al.*, 2007a) and inland rock slopes (Abellán *et al.*, 2010, Stock *et al.*, 2011; Royán *et al.*, 2015). Stock *et al.* (2011) found that precursory rockfall sequences from the Rhombus Wall, Yosemite, propagated upward through and laterally along the edges of near vertical sheeting joints, highlighting the role of existing discontinuities and slope surface topographic convexity in governing the spatial location and sequencing of failure. At the intersections of these discontinuities, high stress concentrations promoted the development of new joints and failures. Stresses that drive the propagation of such joints are tensile, perpendicular to the cliff face and located primarily at the surface, whereas compressive stresses tend to be dominant at greater depths depending on slope concavity (Martel, 2011). Given that rocks are generally weaker in tension than in compression (Selby, 2005), sustained tension near to the surface can enhance joint propagation and hence failure in these locations.

Analysis in *Chapter 7* has shown that the displacement of failing blocks prior to collapse is proportional to their size, whereby larger rockfalls experience more displacement. While this data also included some of the slumps that were examined, the relationship holds for rockfall events. This suggests that either: (1) the active stresses and resultant strains as a block fails are also insufficient to generate fragmentation or fracture and, as such, generate pre-failure rockfall; or (2) the spatial and temporal scales over which precursors occur are beneath the precision and resolution of monitoring; or both. Since relatively few large rockfall ($> 1\ m^3$) occurred here, failure clustering in space and time has been less readily observable. For the largest rockfall that occurred, sequencing of smaller failures falling from within incipient rockfall scars was evident, suggesting an incremental failure that is progressive through time. While some precursory rockfall occur within the footprint of a developing failure, the most obvious sequencing of smaller failures occurs predominantly around the perimeter. This suggests that precursors represent a release of accumulated tensile stress at the boundary (i.e. tensile cracking) between the intact and failing section of the cliff. However, as noted by Stock *et al.* (2011), such precursors can also drive stress concentrations by the development of new discontinuities across the rock mass. This raises the question of whether rockfall precursors induce further failure by the redistribution of stress at the intersections of newly created discontinuities, or prevent further larger failure by the incremental release of accumulated stresses and strain (Pedrazzini *et al.*, 2010; Rosser *et al.*, 2013).

Understanding of how rockfall develop spatially is implicitly invoked, or more commonly overlooked, in models widely used to assess slope behaviour and evolution. For example, the near-continuous removal of mass inferred from the magnitude-frequency analysis (*Section 8.4.1*) reduces the likelihood of larger-scale cantilever failure within the same bed because larger

protruding features, of sufficient mass, do not have sufficient chance to develop. In a coastal setting, the geometry and mechanism of step-back of a marine cliff face by wave undercutting of the toe and cantilever failure of the cliff face above is well understood (Krogu and Matsukura, 2010), where rock mass strength and/or structure prohibits deep-seated failure. Styles *et al.* (2011) back analysed a chalk cliff failure in Kent, UK, highlighting the importance of wavecut notch development in predisposing the slope above to failure. At a critical depth of erosion, strain concentrations and compressive stresses at the wave-cut notch resulted in the upward migration of shear strain, causing tensile failure and crack growth at the cliff top. Notch-driven failure models define an episodic process of coastal cliff retreat, primarily because they are mechanically incapable of simulating the small-scale ubiquitous rockfall and the progressive processes that often link them that has been observed here. The majority of cliff stability models do not consider time-dependent failure and rarely retain the resolution to allow surficial rockfall to evolve, exploit inherent structure, and to propagate across the cliff. As noted by Rosser *et al.* (2013) this can be entirely but incorrectly attributed to the fact that analysis of monitoring over a single epoch does not elucidate how failures develop through time.

8.4 The timing of rockfall

8.4.1 Rockfall magnitude-frequency

A total of 183 363 detachments were recorded during the 10 month monitoring period. Of these, 97.7% were of the order of 0.001 – 0.01 m^3 and 2.3% were of the order of 0.01 – 0.1 m^3. Only 17 detachments (0.01% of the total inventory) were larger than 0.1 m^3 and resulted in any appreciable change to the cliff profile. The range of rockfall sizes reflects the progress that face-on slope monitoring techniques, such as photogrammetry and TLS, have yielded. For aerial surveys at similar spatial extents, the precision between surveys could be several orders of magnitude larger than the scale of retreat (Moore, 2000; Lim *et al.*, 2005). Owing to the high cost of surveys, cliff line position has typically been monitored at $T_{int} > 1$ a. This misses the complexity of failure processes on the rock face below, equating retreat with erosion, and implying that retreat originates from single, large rockfall events alone. The high proportion and absolute number of small rockfall found here implies that erosion occurs predominantly through quasi-continuous mass-wasting of the rock face.

The analysis of the magnitude-frequency distribution of rockfall has shown that the size of detachments adheres to a power law, and indicates that the occurrence of the largest events can be estimated by analysing the frequency distribution of those that are smaller, and *vice versa*. This is of considerable importance for estimating future rates of retreat, as shown by Guzzetti *et al.* (2003) for Yosemite National Park and Barlow *et al.* (2012) for the North

Yorkshire coastline. In this study, face-on measurement in true 3D removes error propagation that arises from area-volume scaling (Larsen *et al.*, 2010). While the precise magnitude-frequency exponent reported is specific to East Cliff, the scale-invariant behaviour of rockfall is similar to that observed in other rockfall inventories, albeit across a wider range of magnitudes. At 30-day survey intervals, the exponent of the frequency density, $\beta = 1.78$, is higher than that for rockfall suggested by Hergarten (2003), $\beta = 0.4$-1.0, but is similar to lithology-dependent exponents provided by Rosser *et al.* (2007a), $\beta = 1.43$-1.91, and Barlow *et al.* (2012), $\beta = 1.65$-1.76, derived from monthly monitoring in this setting.

8.4.2 Timescales of failure evolution informed by magnitude-frequency distributions

Previous research has related the magnitude-frequency exponent to both the lithology within which rockfall are sourced and T_{int}, the length of time that separates surveys, previously based on monthly or seasonal inventories. Having performed change detections between scans separated by a wide range of T_{int}, an inverse relationship has been established between T_{int} and the exponent of the magnitude-frequency relationship, β. Two distinct patterns in this relationship are apparent: (1) an increase in the exponent with decreasing $T_{int} <$ *ca.* 106 h; and, (2) a broadly constant exponent at 7 d $> T_{int} >$ 90 d. This suggests that the progression towards final failure may occur over timescales within *ca.* 4 d – 7 d and that perturbations to slope stability, such as storms, may have prolonged effects on the stability of the slope, that outlast the storm itself. This timescales supports observations of the timescales over which precursory rockfall events occur (*Section 7.3*), which suggests that rockfall evolve over a period of *ca.* 4 d – 7 d, rather than instantaneously. This period cannot necessarily be related to a particular environmental condition, but its onset may occur as a result of a particular external trigger. This is discussed in more detail in *Section 8.4.3*.

The timescale of failure implies that monitoring at any interval greater than approximately seven days is unlikely to yield a significantly different magnitude-frequency distribution of rockfall, regardless of changes in T_{int}. This is advantageous in that less frequent monitoring (e.g. 30 to 90 days) can be considered reliable and representative of behaviour observed over shorter timescales (e.g. seven days), and so there is little benefit to the increased cost of higher frequency monitoring. As a consequence, this study provides confidence in data collected with lower frequencies that have the intention of capturing rock face erosion rates. Importantly, this advantage does not extend to studies focussed on rockfall mechanisms and the analysis of triggers, and highlighting that the frequency of monitoring must be tailored to the intended analysis. Within previous studies of rockfall distributions along this coastline, and elsewhere, the importance of monitoring at higher frequencies has been emphasised in order to

more accurately understand the development of failures both within incipient scars and across the cliff face. In turn, higher frequency monitoring minimises the artefacts of rockfall coalescence and superimposition within the resulting failure inventory, enabling a greater understanding of the mechanisms and kinematics of failure as well as more accurate estimates of retreat.

A shift in the nature of the rockfall volume frequency rollover accompanies the change in exponent, below $T_{int} \approx 4$ d – 7 d. Rollovers in the magnitude-frequency distribution of rockfall have been observed in a number of studies, and refer to distributions in which the frequency density of the smallest reported events falls below modelled predictions. Both methodological (Stark and Hovius, 2001; Dussauge-Peisser *et al.*, 2002; Brardinoni and Church, 2004; Malamud *et al.*, 2004; Teixeira, 2006) and physical (Guzzetti *et al.*, 2003) explanations have been provided for this observation. Methodological reasons focus on the decreasing ability to resolve fine-scale changes to a surface, and therefore reflect the level of completeness of the inventory. For landslide distributions created by mapping from airborne imagery, estimating this minimum detectable landslide area is complicated by the fact that each pixel in the image represents a different sized area on the ground, particularly where the topography is of varying steepness, and the sensor is off-nadir. Furthermore, while recent satellite-borne sensors can provide pixel sizes of 0.5 – 10 m, landslides are rarely mapped at this scale and the minimum detectable size is instead determined by the scale of mapping.

For rockfall distributions created from TLS surveys, however, quantifying the minimum detectable rockfall size is less complex than it is from aerial mapping. To do so requires an assessment of both the point spacing, which determines the minimum aerial extent of a rockfall, and the precision of range estimates, which determines the minimum depth of an observable rockfall that can be resolved. Young *et al.* (2011) noted that the ability to resolve small-scale changes should not introduce a rollover, because the smallest reported rockfall should be above the minimum detectable event identifiable change mapping. From a statistical perspective, this statement holds true as long as the frequency destiny is not estimated using a kernel, which enforces an extrapolation of density that extends one kernel half width beyond the range of the original data both below the minimum and above the maximum, introducing inflections in the frequency density at the tails (Lim *et al.*, 2010). In this study, however, the data was separated into logarithmic bins, and a log-log regression performed. Lim *et al.* (2010) constructed a magnitude-frequency plot from rockfall above the minimum detectable size, recorded using a TLS. The absence of any rollover in this inventory was interpreted to support the concept that previously created rollovers arose from methodological error. Despite this, physical explanations for the presence of a rollover in rockfall inventories are scarce.

While Lim *et al.* (2010) suggested that a rollover is unlikely to be the result of a physical process, here a rollover in the magnitude-frequency distribution is identified for inventories where $T_{int} > 21$ d. Only rockfall larger than the 0.03 m (LoD) × 0.15 m × 0.15 m

(the area of each cell, which exceeds the minimum point spacing) were analysed, which equates a volume of to 6.75×10^{-4} m^3. This implies that an undersampling of the small rockfall events did not occur at any interval due to methodological error and, therefore, undersampling of the smallest events at these intervals is likely to be the result of coalescence or superimposition of small failures $<$ *ca.* 0.01 m^3. As described in *Chapter 5*, the rollover shows an inversion with decreasing T_{int} such that an 'anti-rollover' becomes evident, in particular for $T_{int} < 3$ h. The value of T_{int} at which no rollover is observed is *ca.* 4 d – 7 d. As expected, monitoring at 4 d - 7 d resulted in the highest coefficients of determination for the regressions between log magnitude-log frequency. However, the fact that the regressions were strongest for monitoring at low T_{int} suggests that the nature of the rockfall size distribution is captured most accurately by high frequency monitoring, albeit with a higher percentage volume error.

The shifts in both the exponent and tail of each magnitude-frequency distribution can be used to infer two effects that operate in parallel. First, a power law exists such that the more the surface is monitored, the more rockfall are detected. From an anecdotal perspective, this fits with observations of the near-continuous sound of falling debris that can be heard when close by the rock face. In theory, this implies that an infinitesimally large number of small rockfall occur in the minutes and seconds prior to, and during, a collapse. To counter this, however, visual observations of rockfall and their deposits show that they retain a range of block sizes, rather than undergoing complete disintegration. A second hypothesis, therefore, is that the smaller events may in part both precede and relate to larger events. This suggests that rockfall fail by a process of fragmentation and that the precursors also scale in size to a power law fit in volume frequency. While a portion of rockfall events captured at anything greater than the finest monitoring frequency may be the sum of multiple smaller events, this relationship only holds to a minimum rockfall size (Figure 8.1).

The strength of a rock mass reduces with volume, since smaller volumes generally contain smaller cracks and the stress intensity at crack tips is proportional to the square root of crack length (Lockner, 2013; Siman-Tov *et al.*, 2017). An increase in sample lengths by an order of magnitude, for example from 0.1 m to 1 m, may lead to 70% decrease in rock strength for weathered diorite (Pratt *et al.*, 1972; Lockner, 2013). By implication, therefore, smaller fragments are likely to provide a larger resistance to the driving forces required to initiate movement. Furthermore, block strength at smaller scales is increasingly a function of tensile strength; this is invariably high as compared to rock mass strength, which typically includes jointing. A minimum volume must also exist where the size of a block is insufficient to yield the mass required for driving forces to exceed the frictional and cohesional resistance of the material, if the blocks we observe here occur as a function of rock failure. These effects may be offset by weathering at the surface, whereby block release is less related to conventional measures of rock strength. The anti-rollover effect highlights an increasing frequency density of

the smallest events, from which it can be inferred that small, more frequent rockfall would be detectable by monitoring at higher spatial and temporal resolutions. The minimum rockfall size therefore appears to be smaller than the minimum detectable size in this study. The analysis of pre-failure rockfall activity in *Chapter 7* supports this suggestion, given that multiple precursors at the periphery of developing rockfall appear to occupy the same 0.15 m raster cell.

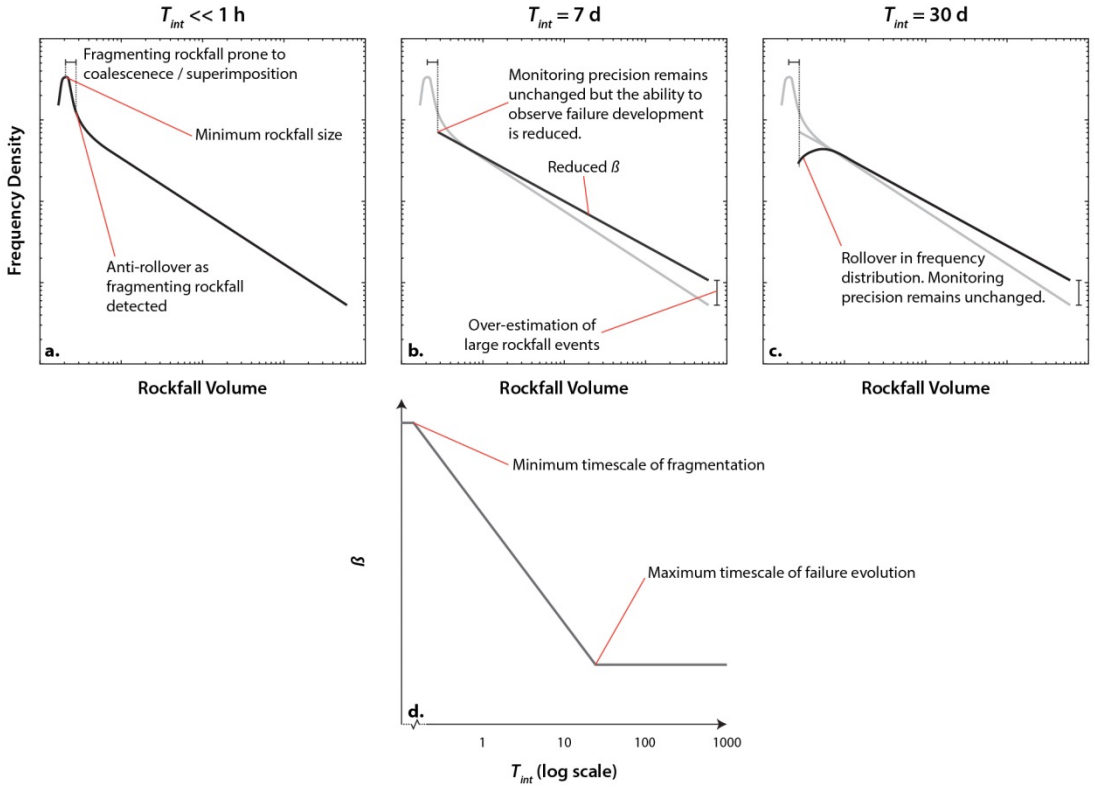

Figure 8.1: *Conceptual magnitude-frequency plots, based on data from monitoring over varying time epochs, T_{int}. (a) Rockfall monitoring using scan pairs separated by far shorter intervals than an hour. The anti-rollover effect highlights the high proportion of small rockfall observed over short intervals. The increase in very small events, only extends to a minimum rockfall volume, which represents the point at which the failing block is of insufficient mass for driving forces to exceeds the material's resistance to failure. (b) Monitoring with T_{int} = 7 d is undertaken at the same precision. However, due to coalescence and superimposition, the smallest events observed in (a) are not detectable. Furthermore, the overall proportion of small events within the detectable range is lower, and the proportion of large events is higher, resulting in a reduced value of β. (c) At monthly monitoring intervals, a rollover in the frequency density of the smallest events is observed, but the exponent remains the same. (d) Plot of the variation in exponent with T_{int}. With decreasing T_{int}, there is an exponential increase in the exponent (representing a large proportion of small rockfall). This applies until a minimum timescale of fragmentation.*

8.4.3 Rockfall timing in relation to environmental conditions

The database presented here is ideally, and arguably uniquely, suited to interpreting the nature of rockfall triggering by contemporaneous environmental conditions. While *in situ* instruments and ground-based radar systems can record changes to the slope more frequently, and at a frequency that is more comparable to timescales of variability in environmental conditions, these are less suited to the characterisation of material detachments from the slope than TLS at the scale at which they occur. Many studies have presented correlations between rockfall frequency and environmental drivers, often with data that is irregular and widely spaced through time, even up to multiple months (Rosser *et al.*, 2007a; Lim *et al.*, 2010; Delonca *et al.*, 2014; Strunden *et al.*, 2015; Vann Jones *et al.*, 2015; d'Amato *et al.*, 2016). The degree to which environmental conditions can be considered as preparatory factors or triggers of rockfall remains complex to address without high spatial and temporal resolution data. In this study, the high frequency of data collection has enabled an analysis of the degree to which near-contemporaneous environmental conditions act as triggers of failure. The regression analysis undertaken in *Chapter 6* shows that no significant relationship can be discerned using relatively simple pairwise correlation, even with the dataset presented here.

A simple explanation for this may be that the slope undergoes a lagged response to the effects of inclement weather conditions. However, this does not explain the very low coefficients of determination in relationships at all of the timescales considered (from 1 h – 30 d). Ultimately, a lagged response also fails to explain why some rainfall events resulted in above average rockfall occurrence, yet others of the same magnitude did not. While the strength of relationships between rockfall and rainfall, and rockfall and temperature did increase when considered at daily and weekly timescales, a significant proportion of rockfall have no apparent link to contemporaneous environmental conditions. A clear trend can only be observed when the rockfall signal for the entire monitoring period is aggregated at different scales, including diurnal and seasonal, which match the timescales of variation in environmental conditions, from storms to seasons. This has allowed rockfall to be considered in relation to tidal cycles, the time of day, and individual storm events, all of which require rockfall monitoring at low T_{int} and emphasise the importance of conditions in preparing the slope for failure.

The findings here suggest that no simple relationship may exist between the height of the tide and the occurrence of rockfall < 0.1 m^3. The probability of occurrence for larger rockfall (> 1 m^3), however, was more than double at high tide than at low tide. Vann Jones *et al.* (2015) found that the relationship between rockfall from the entire cliff correlated more strongly with marine conditions, as compared to rockfall sourced only from the inundated zone at the toe of the cliff. This was interpreted to support a hypothesis that the influence of marine-driven

erosion extends, albeit indirectly, above the inundated zone. This previous analysis is however forced to consider only monthly, and hence seasonal, variability. Here, however, it appears that small rockfall do not respond to marine forcing when considered at finer temporal resolution. Given that the rockfall inventory is dominated by small and frequent rockfall (minimum number of rockfall recorded in a scan here was one), they may be essentially constant and, as such, there may be no environmental link. Furthermore, since the cliff profile is not vertical, and the upper portion is set back from the foreshore platform and the ability for tension cracks to initiate at the cliff toe and propagate upward through the cliff is minimal (Styles *et al.*, 2011).

While temporal variations in rock slope deformation have been observed to correlate with changes in pore water pressure, recent studies have documented increased damage accumulated at specific times of the day, in temperatures above freezing. In this study, increased rockfall activity occurs through the day from sunset, with a peak in activity that corresponds to the greatest rate of air and rock temperature cooling (close to sunset). This bears significant resemblance to cracking events of a granite boulder, which showed a significant increase towards the mean time of sunset because of thermally induced tensile stress development (Eppes *et al.*, 2016).

As described in *Chapter 2*, the effects of thermomechanical stress on crack widening have been examined in a number of slopes (for example, Mufundirwa *et al.*, 2011; Collins and Stock, 2016). Gunzburger *et al.* (2005) showed that cooling during the night induced millimetre scale displacements of a block at the surface of a rock slope in southern France. This suggests that failure potential may be increased by a reduction in confining stresses during cooling, which cause the rock mass surrounding the failing block to contract. Gischig *et al.* (2011a) modelled a simplified slope based on the geometry and discontinuity sets of the Randa instability, Switzerland, which is subject to annual temperature cycles. This analysis showed that shear dislocation along discontinuities at depth can result in irreversible slip if a sufficient number of discontinuities are already critically stressed. Small temporal changes in stress were shown to develop by localised brittle damage and slip, resulting in damage that is accrued within the rock mass and manifest as apparent continued deformation. In winter, as blocks contract during cooling, normal stresses along steeply discontinuities decrease and slip can occur, whereas in summer, thermal expansion increases normal stresses, which inhibit slip. The net effect is one of fatigue within the rock mass, involving incremental sliding along critically stressed discontinuities. This modelling matched observed deformation by crack extensometers, and boreholes with inclinometers (Gischig *et al.*, 2011b). The Randa rockslide has a very low water table and, therefore, it is possible that thermomechanical stresses are of greater significance than in other settings. While the scale and mechanism of failure differs at East Cliff differs to the Randa rockslide, much of the exposed rock face exhibits dilated joints that promote drainage. It is therefore likely that freeze-thaw conditions during the winter months play a lesser role in

fatigue of the rock mass. However, given the low residence time of water on the cliff face, small strains due to thermal variation may be sufficient to general small-scale rockfall. The growth of microfractures at the near surface, observed by Eppes *et al.* (2016) during cooling of the rock mass, may therefore be significant. By examining the magnitude-frequency distribution of rockfall through time, an increase in the proportion of small rockfall events towards the summer is evident. During this period, the variations in rock face temperature are highest and, while rainfall accumulation is higher than during spring, it is not as high as during the winter. This suggests that variations in temperature may have an overriding influence on rockfall, driven by microfracture expansion and coalescence at the surface, and subsequent release of material through spalling.

While these conditions may not produce an obvious or instant trigger for rockfall, they may reflect the importance of thermal conditions in preparation for failure, by inducing irrecoverable widening of cracks or microfracture growth and, therefore, permanent damage to the rock mass. Cyclical forcing mechanisms have been shown to correspond to laboratory experiments of fatigue in rock samples. This fatigue enables catastrophic brittle fracture below the tensile strength, as a result of increasing stress-induced fracturing (Eberhardt *et al.*, 2016). While Gischig *et al.* (2011c) noted the importance of seasonal variations in temperature, this study has noted the importance of diurnal variations in temperature, as observed elsewhere (Vlcko *et al.*, 2008; Collins and Stock, 2016; Eppes *et al.*, 2016). This may imply that diurnal cycles of thermal stress development, and subsequent thermal-induced fragmentation, are superimposed on the overall progression of damage accumulation across a failing slope.

An analysis of the relationship between rockfall timing and the passage of rainfall events has shown that up to 30% of the largest 1 000 rockfall occurred during periods of rainfall, and 60% occurred within 24 h of rainfall. Cross-correlation of the time series of both rockfall and rain accumulation showed that rainfall only became significant between 3 h and 0 h in advance of the rockfall time series. While the specific nature of the intensity-duration characteristics shows that I-D exponents fit within a range of values outlined by Cepeda *et al.* (2010), the fact that the exponents differ very little between failures of loose material at the buttress and rockfall from the cliff face above suggests that these may be more closely related to the specific nature of rainfall events in this region, than they are to the triggering of different types of failure. However, when examined in *Chapter 7* with respect to the deformation of individual incipient rockfall blocks, the passage of individual rainfall events appears to induce an incremental but sustained increase in the rate of displacement. In the instances examined, rainfall did not actually occur at the time of failure but did correspond with the onset of acceleration towards failure. With respect to Bjerrum's (1967) model of the tertiary phase of failure, this supports the hypothesis that the growth of microcrack fractures within the slope can occur independently of environmental forcing and predispose a slope to failure, in this case over

a period of two hours. Attributing triggers to block detachment may therefore not be possible beyond the apparent correlations that emerge over longer time periods discussed previously.

The effect of water can be related to either ground water movement or the infiltration of rainfall. Water that occupies fractures reduces the effective normal stress acting on it, thereby reducing shear strength along the plane (Sjoberg, 1999). Eberhardt *et al.* (2016) note that hydromechanical fatigue of rock masses can be attributed to progressive failure, manifest as accelerated behaviour in rockslides following rainfall, even if increases in pore pressure are not exceptional relative to those before or after. However, hydromechaincal fatigue requires a groundwater flow regime at depth that results in significant pore pressure variation. Similarly, Jaboyedoff *et al.* (2004) noted that, prior to the Randa rockslide, weakening of material along discontinuities occurred through chemical weathering, allowing progressive reduction of shear resistance along joints without the development of pore pressure. Given that many of the rockfall in this study occur within exposed beds, rock mass fatigue could exist if increased water pressures are iteratively created and released by rainfall and drainage by seepage along bedding. However, since the rockfall are shallow and confining pressures are low, the likelihood of hydromechanical fatigue-driven failure is also low at the cliff surface where they primarily occur. However, the heavily jointed nature of East Cliff may promote dissolution of the sandstone along joints (Siman-Tov *et al.*, 2017) or the reduction of frictional resistance along these joints.

The density and width of fractures directly affects the infiltration capacity of the rock mass (Krähenbühl, 2004). However, the hydraulic conductivity of certain weak sedimentary rocks can allow a portion of the seepage through pores (Wyllie and Mah, 2004). The permeability of sandstone at East Cliff may result in the saturation of voids at the surface, reducing the tensile strength of the material but, more importantly, increasing the mass and crack propagation required for tensile failure. This conductivity may explain why a rockfall can occur at East Cliff at a scale and size below that defined by the joint network, but also relate to the occurrence of storm events.

Given that the strongest relationships have been observed between rockfall and temperature and rockfall and precipitation, it is possible that both may coincide to prepare the rock slope for failure, thereby allowing the increased rate and volume of material detachment that occurred from 8th November - 30th December. Contraction of the rock mass with cooling, while reducing the normal stress may also act to widen joints, allowing the infiltration of water and inducing greater spatial variation in pore pressures within the rock mass (Krähenbühl, 2004). Cooling introduces deviatoric stresses and reduced normal stress, which can result in the cracking of rock bridges, continuous loss of cohesion, and eventual failure (Watson *et al.*, 2004). A combination of progressive weakening of rock bridges near the surface and reduced resistance along joints due to water flow may have prepared the slope for larger failure events prior to the onset of stormy conditions at the end of the monitoring campaign. An important consideration

is the complex interplay of several factors that may all act to predispose failure. This was discussed in *Chapter 2* and is reflected in the proposed mechanisms above. The significance of external driving forces may change through time and only a more elaborate multivariate analysis may be suited to adequately describe the interplay between preparatory factors and triggers. The analysis presented in this study has highlighted that, while significant relationships can be derived over long-terms scales (e.g. 30 days), these relationships do not hold at finer scales and are therefore insufficient to adequately explain failure controls at finer scales.

8.5 Development of rockfall through time

A timescale of failure development of 4 d – 7 d has been inferred from the shift in rockfall volume frequency analysis of the entire inventory. However, monitoring of individual failures that develop through time is required to interpret the *in situ* processes that drive final failure. Analysis in *Chapter 7* provided examples of how the fragmentation of blocks for 30 rockfall developed through time. This showed that an increase in the number of small events, which coalesce and superimpose one another to ultimately form or precede the largest rockfall, can be observed over the same 4 d – 7 d timescale at which the inflection in the relationship between β and T_{int} is observed. Individual plots of these rockfall have shown that pre-failure rockfall occur at the periphery of incipient scars, typically at either the bottom or top, which may be indicative of small-scale failure of intact rock bridges beneath the surface or within the failing block itself. This may resemble a surface expression of Terzaghi's (1962) description of progressive failure by stress redistribution, which follows a loss of cohesion at a particular point on a slope. For the failure of a single coherent block, the highest stress and strain magnitudes would be expected on the perimeter, which may explain these precursor locations. Terzaghi also noted that discontinuities in natural settings are limited in persistence (Gischig, 2011c) and that some fracture propagation of intact rock bridges may be required for catastrophic failure.

As noted previously by Rosser *et al.* (2007b), there is a philosophical question as to what defines a precursor and what defines a final, or 'catastrophic', rockfall. Here, while rockfall are small relatively to comparable studies, final failure may refer to those rockfall that were preceded by hyperbolic accelerations in rockfall activity; however, precursors themselves also yield hyperbolic increases in activity (Voight, 1989, Crosta and Agliardi, 2003). Some work has previously been undertaken on the timing of how individual rock slope failures develop. Numerical modelling has elucidated temporal evolution of failures from kinematics (Allison and Kimber, 1998), strength degradation, structural control and undercutting (Styles *et al.*, 2011). In the field, precursors to final failure have been observed as spalling (Rosser *et al.*, 2007a;b), creep displacements (Royán *et al.*, 2015), and microseismicity (Senfaute *et al.*, 2009), which all imply an underlying time-dependent failure process. Amitrano *et al.* (2005) recorded a three order of

magnitude increase in seismic energy release in the 2 h leading to failure.

At East Cliff, both pre-failure deformation (creep) and pre-failure rockfall activity have been considered. The data generated implies that a similar pattern of acceleration may be manifest in disruptions to a failing slope surface. A hyperbolic increase in activity can often be considered similar to a homeostatic self-reinforcing process (Rosser *et al.*, 2013); the extent to which any rockfall acts to further destabilise a slope in itself raises questions as to whether the precursors presented a product of failure, as opposed to the cause. Pedrazzini *et al.* (2010) observed a decrease in the rate of small rockfall events, which implied that the slope had progressively stabilised itself as a result of the release of strain accumulated across it. Leroueil (2001) also noted that stress redistribution following local failure may create a new equilibrium state within the slope, rather than constituting an acceleration towards final failure. Accelerations in rockfall activity appeared to occur in the final hours of failure, similar to the seismic energy release monitored by Amitrano *et al.* (2005) and corresponding to displacement monitoring of brittle failure using ground-based radar (Dick, 2013). The period of this acceleration is far shorter than that observed by Royán *et al.* (2015), where the onset of acceleration began *ca.* 200 d prior to failure. The decrease in precursory creep with the size of final failure, found in this study, implies that this may be due to the fact that the failure observed by Royán *et al.* (1 012 m^3) was three orders-of-magnitude larger than the maximum detachment recorded here. However, it is also likely to relate, in part, to the much larger average T_{int} of 105 days.

Rose and Hungr (2007) presented inverse-velocity as a means of predicting large-scale ductile failures. Brittle mechanisms, in particular those within relatively small failures of strong rock, were shown to produce almost instantaneous failure and therefore prompted the suggestion that they were unsuited to prediction through displacement monitoring. Here, with what is arguably far more appropriate data, accelerations in creep observed during the final 2 h of failure suggest that while prediction of these failures is impossible using the current system, failure is not instantaneous and accelerated deformation is observable. An observation in this study, however, is that while pervious applications of this method (Zvelebil and Moser, 2001; Crosta and Agliardi, 2003), and specifically prior to rockfall (Royán *et al.*, 2015) have obtained best-fits in the tertiary phase of acceleration, even during the final hours of failure, this acceleration does not appear to be uniquely or purely hyperbolic. Rather, it appears to occur in multiple stages that superimpose onto a longer-term trend approximating a hyperbolic form. This is found for both slumping of material on the buttress, and for rockfall from the cliff above (for example, Figure 8.2).

The phases of deformation that occur during the tertiary phase of failure may represent the widening of joints, the occurrence of small rockfall events, breakage of rock bridges or self-reinforcing of failing blocks due to slip and subsequent interlocking of. Under shear, the

roughness of joints plays a time-dependent role, as interlocking can occur between asperities before microcracks in the asperities cause them to shear, forming a smooth rupture plane. Havaej *et al.* (2015) generated a discrete fracture network from terrestrial photogrammetry point clouds in order to simulate pentahedral wedge failures in a slate quarry, Cornwall, UK. Using a 3D distinct element simulation, perturbations in the downward trends of inverse velocity data, similar to those observed using the Reverse Cumulative Variance, were found prior to the failure of certain blocks. This was attributed to confinement and interlocking by surrounding blocks, which slow and constrained release.

Time-dependent deformation of discontinuities may also occur due to time-dependent breakage of intact rock bridges (Kemeny, 2005). The persistence of discontinuities contributing to slope failure is generally limited, requiring the failure of intact rock bridges to enable movement (Tuckey *et al.*, 2012; Havaej *et al.*, 2012; Stead and Wolter, 2015). These separate discontinuities and are required to fail in order for a block to become detached from a slope. Once failure has occurred, remnants of small previously intact rock are observable (Tuckey *et al.*, 2012; Tuckey and Stead, 2016). While the failure of rock bridges depends on the frictional and cohesional properties of the material, loading, and the geometry of the rock bridge relative to shear stress, their failure has been considered the result of sub-critical microcrack growth, the time-dependence of which dictates the timing and development of failure (Kemeny, 2005). Hamdi *et al.* (2015) also found perturbations in inverse velocity trends obtained from finite discrete element modelling of cave block failure. Similar to the results obtained by Havaej *et al.* (2015), cycles of acceleration and deceleration occurred prior to the onset of final failure, with each attributed to intact rock bridge failure within the model. The repetition of these cycles prior to the onset of final failure was suggestive of damage accumulation below the level of damage required to initiate final failure, which itself is associated with the continuous displacement and fracturing of the failing mass. In relation to this study, the time dependence of failure mechanisms, such as microcracking, may explain the hyperbolic increases in creep of a failing block. However, the iterative failure of intact rock bridges that occurs as a result of this may explain the multiple stages of acceleration that occur prior to failure.

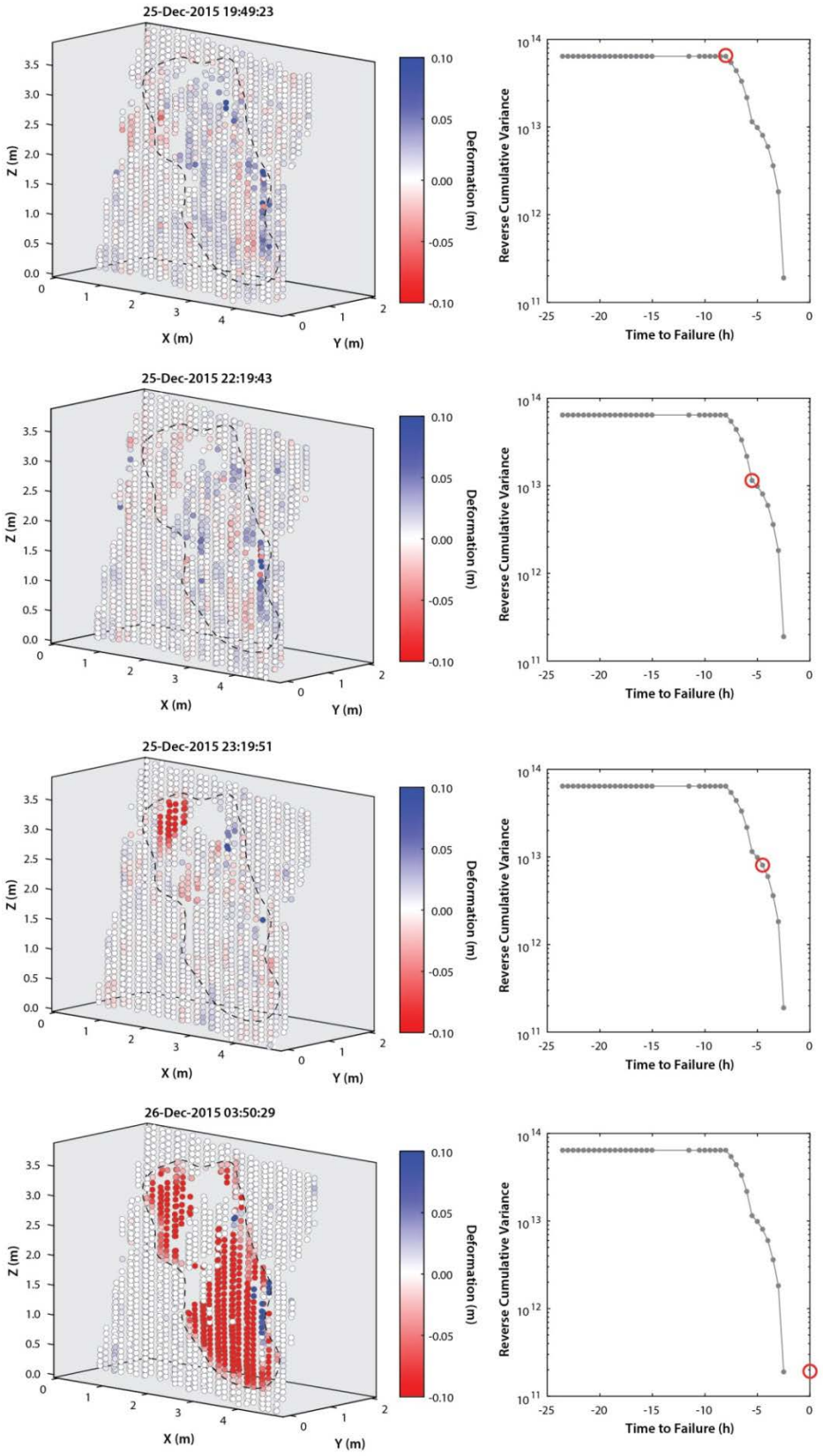

Figure 8.2: *Reverse cumulative variance shown for the 24 hours prior to a large rockfall. Inflections in the RCV appear to relate to pre-failure rockfall (red), but also small regions of forward movement (blue). Both may imply internal failure of rock bridges prior to failure, which ultimately result in the rock mass undergoing stages of acceleration prior to failure, rather than a simple hyperbolic acceleration. The accompanying video can be viewed in Appendix F.*

8.6 A new model of the controls on rockfall development

While patterns of acceleration prior to failure have been observed in this study, it is important to place these events within the context of the power-law behaviour of rockfall. By far the majority of rockfall ($> 99\%$) occurred without precursory activity, either because these detachments were too small or short-lived to detect, or because the size of the final failure was insufficient to yield the mass required for driving forces to exceed resisting forces. In such instances, the occurrence of a trigger is followed instantaneously by failure (Figure 8.3a). Here, the rockfall does not have the volume to fragment and internally fracture or the external trigger is of sufficient force to overcome any progressive mechanism. The result is that the rockfall does not exhibit precursors. These events represent quasi-continuous small scale mass wasting of the rock face, where rockfall are near-instantaneous, small, and essentially random in time and space. The size of these events is still sufficient to present a significant hazard and a significant agent in long term mass wasting, however, their timing is likely to be impossible to predict.

The second mode of observed failure presents an instantaneous rockfall as the result of a trigger, but requires some degree of preparation over time for the failure to occur. These rockfall are typically of medium size, defined here as $0.01 - 0.1$ m^3 (Figure 8.3b). Here, the onset of rainfall does not necessarily induce failure onset, but does increase the rate of observed deformation. This was observed in *Section 7.7* and may relate to a gradual reduction shear strength along joints; an increase in the mass of blocks that become saturated by rainwater and hence increase the driving forces; or the iterative breakage of rock bridges as a result of these processes.

Finally, for the largest events observed here, the onset of a trigger instigates internal deformation that is manifest on the surface as either ongoing and accelerating deformation, or the release of an increasing rate of precursory rockfall, that results in a distinct lag between the trigger and the failure itself (Figure 8.3c). While the fact that this acceleration towards failure occurs independently of external forcing supports previously observed relationships in the laboratory (for example, Petley *et al.*, 2005), here the calculation of the reverse cumulative variance has shown that, while elements of this trend may be hyperbolic, it may also be phased. For this type of event, the following observations apply:

(1) Failure *triggers* often do not necessarily coincide with the timing of the final failure itself; this implies that a block may reside close to a critical point and may only require infinitesimally small increases in stress to enter the final failure period. In this figure, the onset of acceleration occurs after a short period, which need not include any environmental forcing, such as rainfall.
(2) Some unstable parts of the slope may not collapse despite the passage of a large

external event. While rainfall events may accelerate the rate of deformation in a slope, this may be insufficient to result in failure. This implies that the rock mass must be prepared for failure, having accrued a sufficient amount of damage through fragmentation and weathering to instigate a later collapse.

(3) Rockfall from slopes have been shown to adhere to a power-law magnitude-frequency distribution, in which the many small events may actually be precursors to larger incipient events. Rockfall scars in (c) are preceded by smaller and more frequent rockfall in (b), which in turn are characterised by even more rockfall in (a). The ratio between these frequencies is apparently constant at any given site.

(4) The hyperbolic increase in rockfall activity, if detectable and distinguishable from background noise before collapse, may be conducive to failure prediction. This has been shown by Royán *et al.* (2015), but over a much longer timescale (several hundred days) for a larger rockfall. Here, significant accelerations in the rate of rockfall occur 2 h before failure. However, this stage may occur in phases, due to interlocking and subsequent shearing of asperities, joint widening, and shedding of material before collapse.

(5) The pattern of hyperbolic increase in deformation is only applicable for larger rockfall, which have sufficient volume to fragment and internally fracture.

8.7 Summary

This chapter has examined the findings produced from 4D monitoring of rockfall from a failing rock slope. Although monitoring of this type yields a number of unique considerations, these have been addressed in this study to enable the creation of an accurate rockfall inventory at sub-hourly intervals. Rockfall appear to develop through a process of fragmentation of the rock mass, inferred by examining the rockfall volume-frequency distribution measured at different monitoring intervals, and by identifying and characterising the timescales of pre-failure rockfall activity. This concept is indicative of quasi-continuous material loss from the rock face, which limits the potential for large rockfall to fail instantaneously. As a result, most rockfall at East Cliff are beneath the scale of joint persistence, which appears to provide an upper limit on failure size in this setting. The spatial and temporal scales of this process are hypothesised to extend down to a point where failure is purely driven by tensile strength, in which the mass of a block is the smallest required for failure to occur. Fragmentation is evident up to timescales of *ca.* 4 d – 7 d, supporting linear regression analysis that suggests that the relationship between the timing of final failure and external drivers is neither linear nor a direct cause-effect.

Small rockfall are driven by thermomechanically-induced stresses within the rock mass, in particular during cooling that occurs in the two hours prior to sunset. The slab-like shape and

shallow depth of these events emphasises the importance of near surface stress development that is independent of confining stresses. The increased proportion of small rockfall events towards the summer months (inferred from increases in the magnitude-frequency exponent of rockfall volumes during June and July) also highlights the sensitivity of the rock mass to temperature gradient.

The slope appears to respond to rainfall in a variety of ways. Intensity duration analysis and visual inspection of time series of rockfall and rainfall suggests that rainfall can act as a trigger, but only if sufficient preparation has occurred or if the rockfall is small (< 0.01 m^3). For large rockfall, the timing of rainfall is more closely related to the time of failure onset, rather than the failure itself, suggesting that rainfall may act to prepare the slope for failure. This is supported by the insignificant relationships obtained by linear regression, with the exception of some rainfall accumulation relationships, and the fact that rainfall induces a sustained increase in the overall rate of pre-failure deformation prior to rockfall. Temperature and rainfall may combine to predispose the slope for rockfall. For example, rainfall may reduce shear strength along joints, increase the mass of small fragments, but also act to cool the rock face, thereby inducing near-surface stress development and microcrack growth. Conversely, cooling may act to widen joints and increase infiltration of the rock mass. This enhanced preparation for failure may be the reason for the considerable increase in rockfall activity during the storms of November and December 2015.

In addition to pre-failure rockfall activity, pre-failure deformation of failing blocks has been detected. The acceleration towards final failure appears to occur in stages, rather than as a single hyperbolic acceleration; this is symptomatic of microcrack growth and coalescence. As shown in Figure 8.3, this reflects forward movement of the rock mass, which may be indicative of incremental, internal fracture of rock bridges, as well as pre-failure rockfall. Here, for the first time at such short intervals, both the pre-failure rockfall and pre-failure deformation have been shown to be present and accelerate prior to failure.

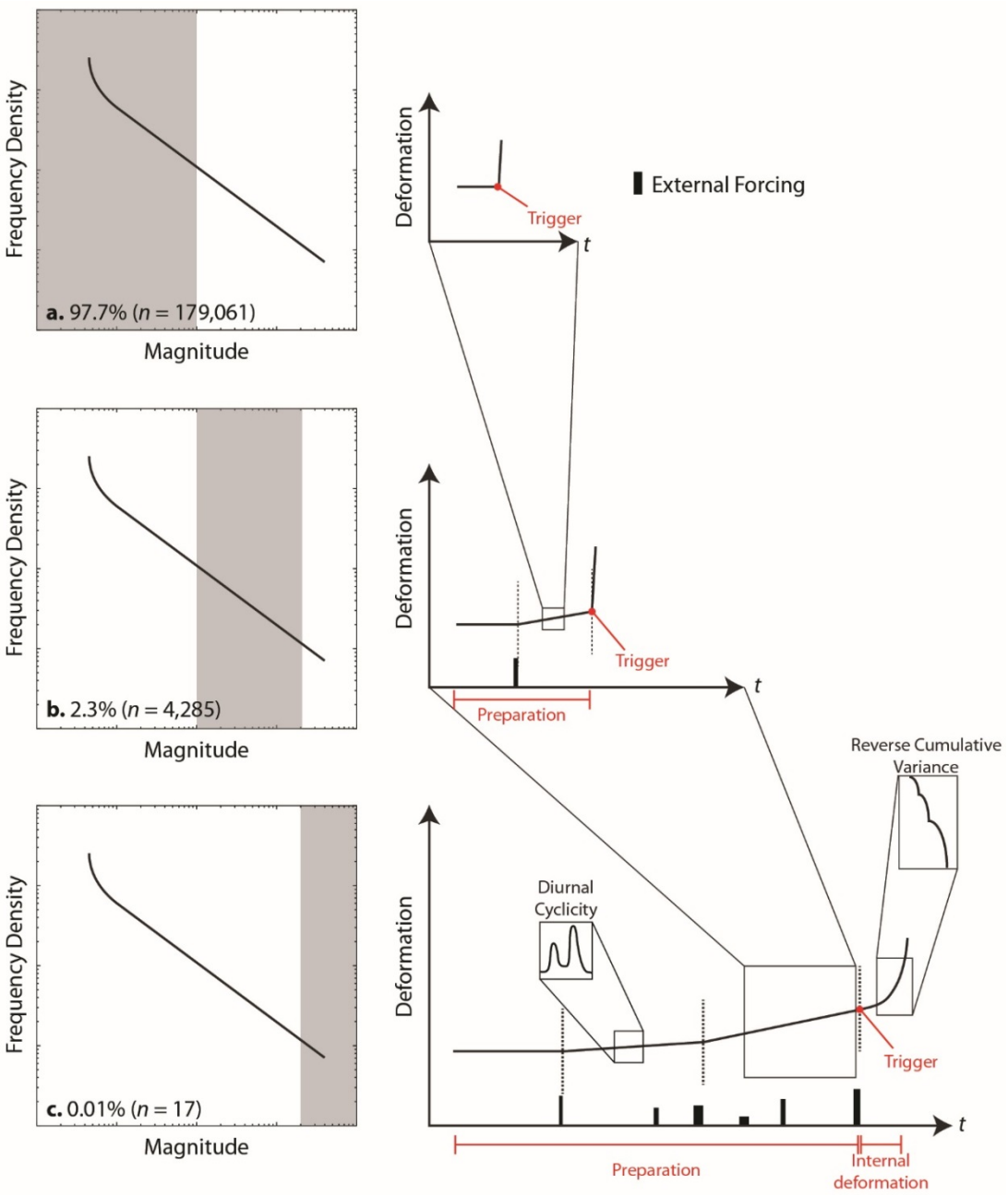

Figure 8.3: *Conceptual diagram of the possible paths to failure followed by rockfall observed in this study. For small rockfall, failure may occur instantaneously after a triggering event. This may be external or in-situ, such as the breaking of intact rock bridges. The culmination of these many, frequent rockfall contributes to the failure of larger, medium sized rockfall. These rockfall require preparation by weathering and precursory fragmentation, and may occur instantly following a trigger. Both small and medium sized rockfall precede larger scale rockfall. The path to failure that these events may take requires preparation by fragmentation of the rock mass. The rate of this damage accumulation may be increased by the passage of energetic external forcing events, such as rainfall, and may also superimpose diurnal cycles in the frequency of fragmentation. The passage of rainfall may act to trigger the onset of final failure, but the timing of final failure itself is independent of the timing of energetic environmental conditions. The acceleration towards failure may or may not be a hyperbolic increase in microfracture growth, since phased acceleration through interlocking and shearing of asperities, joint widening, or shedding of material may also occur.*

Chapter 9

Conclusions

9.1 Summary of thesis

In this chapter, the overarching aim and research questions introduced in *Chapter 1* are revisited. The development of a novel method, which handles and processes large volumes of scan data to create a reliable rockfall inventory, has underpinned the ability to answer the research questions posed at the outset of the thesis. These questions are outlined below, following a review of the approach to rockfall acquisition from 4D monitoring.

The method developed takes a series of ASCII files (n = 8 987), which contain the position, reflectance and deviation of each point in the point cloud, and proceeds to rotate, crop, filter, align, segment and detect change for each sequential scan pair. The resulting inventory contains > 180 000 rockfall that occurred over the 10-month monitoring period. While this monitoring period is shorter than those in previous studies undertaken over years (for example, Royán *et al.*, 2015) and decades (Rosser *et al.*, 2013), the number of scans acquired is between two and three orders of magnitude greater. Most importantly, the time interval between scans, T_{int}, is approximately two to three orders of magnitude smaller than previously, averaging *ca.* 0.5 hours.

The nature of these scans, in particular that they are captured from a single fixed position, has required a tailored approach to processing the data that minimises uncertainties, which have the potential to propagate within the dataset. While many of these arise from scanning from a single position, the approach developed to overcome these is also applicable to scans collected from multiple positions in other settings. The filters applied here are unique in that they estimate the proximity of a point to an edge by drawing on the topographic position and radiometric return of that point. Here, points that are close to edges have been shown to yield a lower precision between scans. The use of the structure of the radiometric return of the signal, or 'waveform', represents one of the first usages of this characteristic in applications of terrestrial LiDAR for monitoring. A number of approaches were tested to detect change between surfaces. The approach adopted compares surfaces in true 3D and is robust to the presence of edges in the dataset. The workflow presented here has been tested with subtle variations in the parameters and methods presented in *Chapter 4*, and was deemed to present the most realistic rockfall attainable. In this setting, this yielded lower LoDs than DEMs of Difference (DoDs) or the Multiscale Model to Model Cloud Comparison (M3C2; Lague *et al.*, 2013).

The results obtained have enabled unique insights into the mechanisms of rockfall development, the importance of factors that prepare the slope for failure, the timing of failure with respect to triggers, and the nature of the final phase of failure. The research questions in *Chapter 1* are now considered in light of the research undertaken in this thesis.

(1) Does the observed power-law behaviour of rockfall extend to its occurrence over short timescales?

Objectives 2, 3 and *4* have been completed in order to answer this research question. These include (a) assessing the use of 4D data in providing reliable volume estimates; (b) developing an understanding of the size distribution of rockfall, necessary to analyse the role of jointing (RQ2) and external drivers (RQ3) by rockfall volume; and (c) examining rockfall over a range of monitoring intervals to identify the timescales over which they evolve.

The pattern of rockfall adheres to a power law distribution similar to that in other studies. The exponent at 30 day intervals, $\beta = 1.78$, is within the range of previously observed estimates in this setting by Rosser *et al.* (2007a) and Barlow *et al.* (2012). In *Chapter 5*, the exponent β has been shown to be inversely proportional to the value of T_{int} for 1 h $< T_{int} <$ 106 h. At 1 h, therefore, the exponent $\beta = 2.27$, is higher than for previous studies in this setting. An additional consequence of this is that there is a three order of magnitude decrease in the frequency density of the largest rockfall events, purely because of more frequent monitoring. This has implications for hazard assessment and protection measures, such as rockfall net design, given that high frequency monitoring has yielded an increase in the relative probability of small rockfall. Deviations from the predicted exponent occur for small rockfall < 0.1 m^3. For rockfall identified between scan pairs at 30 d $< T_{int} <$ 90 d, this deviation is observed as a rollover in the dataset, in which the proportion of the smallest rockfall fall below the predicted frequency density of the power law. Conversely, an 'anti-rollover' in the distribution occurs for $T_{int} < 4$ d, in which the frequency of rockfall in the smallest volume bins is consistently (and increasingly) above the predicted density. Here, the same pre-processing and change detection techniques were applied to each set of T_{int} scan pairs, with the result that the LoD was the same. The fact that the smallest rockfall are under-represented in inventories where $T_{int} > 21$ d, suggests that these events do not represent methodological noise. As such, the anti-rollover effect observed in inventories where $T_{int} < 106$ h is not a function of erroneous pixels of change that are accumulated by more frequent scanning.

From a methodological perspective, the analysis implies that erosion monitoring at intervals more frequent than once per month, and the associated increase in cost, is unlikely to yield a significantly different pattern or inventory of rockfall. Furthermore, given that the uncertainty in volume estimation is largest for small detachments, less frequent monitoring (for

example, 30 days) can be considered reliable and representative of long-term erosion. However, surveys at $T_{int} <$ *ca.* 106 h are required for the purpose of monitoring failure development. The results show that a higher proportion of small rockfall are observed when monitoring at increasingly high frequencies, as long as this time interval does not exceed *ca.* 106 h. This suggests that failures in this setting occur through a process of fragmentation, in which precursors also tend to scale in size to a power law fit. This increase is, however, unlikely to extend to disintegration generating infinitesimally small rockfall, given that a sufficient mass is required to exceed the material's tensile strength.

(2) To what extent does the rock mass structure determine the permissible size of failures?

The scale of visible persistence have been extracted in 3D, using the recently developed *CloudCompare* plug-in *Facets* (Dewez *et al.*, 2016). Quantifying their dimensions in 3D has enabled a novel statistical approach to identifying their role in determining permissible failure size. This approach compares the distributions of facet widths and heights to distributions of rockfall depths, both of which are measured over the same range of lengths and are quantified in 3D. For each bed, the exponent of the distribution of facet lengths is higher than that of the rockfall depths. Detachments can therefore be considered to have occurred below the scale of the joint network. Nevertheless, when rockfall size distributions are compared, rockfall that originate from more closely jointed lithologies (for example, interbedded sandstone and siltstone) are dominated by smaller events, implying that the maximum rockfall size is often limited by the scale of persistence in the rock mass and that the rockfall monitored are unlikely to have failed across multiple discontinuities. This further confirms the concept of progressive fragmentation in rock masses. The shape of rockfall suggests that confining stresses are of significance in limiting the depth of rockfall; the average rockfall is slab-like, with the depth of the rockfall 0.156 times the length and breadth. This is suggestive of the importance of weathering of the surface of the cliff rock mass prior to failure, and highlights the potential significance of thermomechanical damage at the near-surface due to cooling.

(3) Are environmental conditions significant as triggers of rockfall occurrence and, if so, which conditions promote failure?

Analysis of the relationship between rockfall timing and environmental conditions is inherently complex. The dataset has presented tentative insights into direct links between rockfall and contemporaneous environmental conditions, yet no single control appears to dominate. An analysis of the seasonal trend of rockfall using high resolution monitoring suggests

that stormy conditions towards the winter months correlate with an overall increase in the rate and size of rockfall. An increase in rockfall size yields more block-like shapes, which fail to greater depths into the rock face. Their occurrence is therefore likely to reflect in part an increase in pore-water pressure within the highly permeable sandstone beds in the cliff studied.

Monitoring at $T_{int} < 1$ h shows that rainfall can act as an immediate trigger to rockfall, induce a delayed response, or result in no significant rockfall activity at all. In *Chapter 7*, the passage of rainfall events was shown to increase the rate of deformation within the footprint of yet-to-fail rockfall. This implies a reduction of frictional resistance along joints, and highlights the importance of weather conditions in preparing the slope for rockfall. For the rockfall examined in *Chapter 7*, rainfall coincided with the onset of accelerated failure but not with the timing of failure itself. This supports a hypothesis of exponentially increasing microfracture growth within the rock mass, which has been shown in laboratory experiments (Petley *et al.*, 2005), and which is independent of external conditions. While the infiltration of rain water reduces the resistance to failure along joints, saturation of the sandstone may also act to increase the mass of small, protruding blocks, which are otherwise of insufficient mass to fail.

Linear regressions between rockfall timing and single environmental conditions yielded insignificant relationships for rockfall of all volumes, and across the range of timescales applied. While some relationships were significant when conditions were averaged to a monthly timescale, the mechanisms that can be inferred from such relationships are limited, and a distinction between preparation and triggering of failure cannot be established. However, when rockfall timing was resampled according to the timescales of variability in environmental conditions, significant relationships were obtained. Rockfall frequency increased from sunrise throughout the day, but peaked for rockfall < 0.1 m^3 during the period of greatest cooling rate, between 1 h and 2 h before sunset. This implies that a slope may be prepared for failure by the occurrence of smaller rockfall, which occur due to thermomechanical stresses induced by cooling of the rock mass at the surface. The increase in the magnitude-frequency exponent of rockfall towards the summer months indicates that a higher proportion of smaller rockfall coincide with an overall increase temperature and an increase in temperature variability through the day. The latter is consistent with the sensitivity of rockfall to hourly temperature gradients, as shown in *Chapter 6*. The shallow depth of most failures highlights the importance of damage accumulation at the near surface, possibly as the result of microcrack growth and coalescence prior to failure. No relationship was found between tidal cycles and small rockfall, which may relate to the offset between the lower buttress and the upper near-vertical rock face that is located further away from and above the sea.

The relationships identified between temperature and rainfall, and the occurrence of failure may not be independent. The widening of joints at the surface may predispose infiltration of water, and hence the reduction of frictional resistance to failure, and the saturation of pores

within the material, increasing the probability of small-sale failures. Rainfall may also act to cool the rockface; prompting a spike of rockfall activity if this coincides with air temperature cooling. Exploring the interactions and combined effects of multiple environmental variables using this datasets is clearly an area for further research.

(4) Can 4D monitoring detect pre-failure rockfall or deformation of the rock mass at timescales below those previously observed for rockfall?

This research question draws upon the results of *Objective 6*, which was created with the aim of examining patterns of precursory activity within developing rockfall blocks, and relating this activity to environmental conditions. Only a small number of rockfall, in addition to slips of loose surficial material on the buttress, generated observable pre-failure deformation or pre-failure rockfall. An increase in pre-failure deformation with the volume of final failure goes some way to explaining this, since only 17 rockfall > 1 m^3 occurred. For both rockfall and slips on the buttress, pre-failure creep began to accelerate between 2 h and 6 h before failure, respectively. While previously considered a hyperbolic acceleration, the use of the reverse cumulative variance statistic has shown that this acceleration appears to be punctuated by the detachment of material prior to failure, and deformation of the rock mass indicative of progressive failure of intact rock bridges. The independence of this stage from environmental drivers, such as rainfall, supports previous hypotheses of microcrack growth, in which acceleration towards failure is irrecoverable and independent of changes in pore water pressure.

Pre-failure rockfall activity within the developing rockfall blocks was noticeable over timescales similar to the timescale of fragmentation inferred from magnitude-frequency analysis (*ca.* 100 h). For the largest 30 rockfall observed, the rate of rockfall activity showed an exponential increase towards final failure, conforming to observations of accelerating strain in the tertiary phases of other slope failures, and also to samples tested in the laboratory. In relation to rockfall in other settings, the material intact strength and persistence is likely to determine the ability to release small, fragmented rockfall in an accelerated pattern towards failure. In relation to the use of TLS in instability monitoring, this represents a considerable step-forward in the ability to monitor the development of failure.

9.2 Directions for further research

9.2.1 Methodological developments

The major methodological aim of this thesis was to develop a workflow capable of processing thousands of point clouds, in order to resolve the smallest possible rockfall. While the

minimum aerial extent of rockfall was fixed by the 0.15 m cell size, reducing the LoD determines the minimum resolvable depth, thereby influencing the ability to create a binary image of what is, and is not, detectable material loss or movement. With the reduction in point spacing, the system is now capable of resolving smaller aerial extents; however, an increase in precision of depth estimates (below the 0.03 m LoD in this study) can only arise with the application of new data treatment techniques. The application of 4D smoothing, either through surface smoothing or through smoothing the values of change measured between two point clouds (*Section 8.2*), is a logical next phase for the development of this system. The collection of a high frequency, sustained time series of scans makes this dataset suitable for reducing the width of the Gaussian distribution shown here, and by Kromer *et al.* (2015). This has the potential to enable a distinction between any creep of the rock mass and small-scale rockfall events.

A reduction in point spacing also introduces the potential to more finely resolve rockfall shapes in 3D. On a cliff scanned at a high incidence angle, this approach will only be a applicable for rockfall that are not in close proximity to zones of occlusion, in order to provide a closed hull of points and accurately resolve shape. The benefit of this approach is that it reduces the uncertainty associated with the interpolation of point data into a fixed grid, and therefore increases the suitability of inventories collected at low T_{int} for forecasting erosion rates in the long term. This would provide the additional benefit of drawing upon a representative range of rockfall sizes that does not suffer from superimposition or coalescence of small rockfall. Extracting the 3D rockfall shape also holds potential for accurate assessment of the kinematics of release relative to the joint network (Carrea *et al.*, 2012). Accelerations in pre-failure deformation have been observed to occur during the final 2 h before failure, with precursory rockfall activity visible in the *ca.* 106 h before failure. Hence, in this setting, a decrease in temporal resolution to 1 h and an increase in point spacing to a maximum of 0.10 m is arguably better suited to an understanding of the role of small rockfall in predisposing slope failure and the structural and external controls upon them than the current pattern.

A further methodological development is the developed use of the radiometric return of acquired points. Here, this has been used to remove points with high uncertainty based on their topographic position. However, monitoring changes to the recorded reflectance through time also holds several implications for examining the role of moisture across the rock mass in predisposing rockfall. The author has previously estimated the standard deviation of reflectance across the rock face through time. Based on monthly scans, this has provided a means of delineating the average area of cliff face inundated by the tide (see Appendix G) and for identifying points of seepage on the rockface. Half-hourly images of reflectance from a site at Staithes, 13 km north of East Cliff, have shown systematic wetting and drying of the rock mass within tidal cycles. The identification of the area impacted by tide is critical in accurately defining the role of marine conditions in generating shear stresses at the base of the cliff, and

their potential for vertical propagation (Wolters and Muller, 2008; Styles *et al.*, 2011). This technique has also allowed the identification of seepage from bedding planes, which provides some indication of the relative permeability of lithologies across the rock face, and the spatial correlation between ground water movement and rockfall occurrence. A final application of reflectance analysis is the retention of moisture on the cliff face following the passage of rainfall. This holds potential for examining the role of elevated pore pressures, but also the role of rainfall in cooling the rockface and generating damage through thermomechanical microfracture growth (Eppes *et al.*, 2016). For the database used in this study, the time between the passage of rainfall and a running 24 h background reflectance was acquired, highlighting that the 95th percentile of rainfall events induced higher than average wetting of the rock face for a 10 h period (see Appendix H). Variability in reflectance caused by the time of day, however, was not accounted for and would require further examination.

9.2.2 Developing the understanding of rockfall

Many of the findings in this study serve as a basis for future rockfall research. Beyond the visual observation of time series of rockfall and environmental conditions, as well as resampling of the rockfall data, limited relationships have been found by considering environmental conditions as rockfall triggers. Linear regressions between the two yielded broadly insignificant relationships, attributed to the fact that final failure has been observed to be apparently independent of external drivers. This analysis could, however, be developed by considering combinations of environmental conditions that act either concurrently or in specific sequences to promote rockfall occurrence. The relationship between temperature gradient and the occurrence of small rockfall, for example, may be enhanced by wetting of the cliff which increases the rate of surface cooling (for example, Eppes *et al.*, 2016). Conversely, cooling of the rock mass may cause contraction of blocks and subsequent widening of joints, increasing the infiltration of discontinuities and promoting slip along joints (for example, Krähenbühl, 2004). In essence, the application of statistical analysis techniques that describe more complex interactions between given conditions would be beneficial. These include, but are not limited to, the integration of decision tress, which identify specific combinations of environmental conditions.

While weather station data has been drawn upon here, there is also considerable potential to combine the TLS data with other datasets that have potential to improve the understanding of the relationship between environmental controls and rockfall. Thermal imaging and reflectance data would enable a spatial correlation to be established between rockfall and any regions of ground water seepage across the cliff (similar to Appendix H). It would also allow a developed appraisal of the relationship between environmental conditions, thermomechanical

stress development, and rockfall occurrence. This could constitute an assessment of the role of contemporaneous environmental conditions, such as simultaneous cooling during high tide, rainfall, and sunset. Previous relationships between rockfall timing and microseismic shaking, as a proxy for external forcing, have yielded significant correlations (Vann Jones *et al.*, 2015). However, these have drawn upon rockfall data that is cumulated over timescales considerably greater than the variability in cliff shaking and the frequency of microseismic monitoring.

The derivation of 3D change and its subsequent rasterisation has minimised many of the errors associated with DoDs. As such, and in part due to the considerable volumes of data already generated within this study, DEMs have not been created for each survey. However, DEMs generate the ability to easily interpret rockfall in relation to the topography of pre- and post-failure surfaces. This would enable an analysis of the spatial distribution of rockfall with respect to stress concentrations at convexities across the rock face, as well as the accentuation of these convexities by rockfall.

While pre-failure rockfall activity is frequently examined due to its relation to failure mechanisms and the timing of final failure, a dataset of this nature also has the potential to examine failures that occur after a large failure, rather than before. For example, the sudden removal of lateral support by large failures may result in elastic rebound, stress relief and dilation of the rock mass beneath (Zavodni and Broadbent, 1981). While at small scales this is unlikely to result in the creation of a defined surface, it has the potential to induce further detachments from the rock mass. Examples of this effect were observed in some instances within this research, and require further study. Failures scars in this setting rarely include single failure surfaces; rather, they comprise a combination of weathered joints and freshly broken rock, often with multiple sets of each. A more detailed analysis of scar fractography, which would be possible using the telephoto lens imagery applied in *Chapter 5* alongside more dense point cloud acquisition, would enable an appraisal of the role of rock bridge fracture prior to failure, and the influence of this upon the number of phases of acceleration during final failure.

9.3 Concluding remarks

This thesis has developed a novel workflow for processing large numbers of scans (10^3 - 10^4) to a high level of precision (LoD = 0.03 m). By detecting rockfall at a high spatial resolution and at intervals several orders of magnitude lower than in previous research, the significance of fragmentation of the rock mass has been discerned. A novel statistical approach for examining the control exerted by the joint network and the shape of the rockfall was undertaken, highlighting that rockfall occur beneath the scale of rock mass persistence and that rockfall are highly slab-like. Analysis of the relationship between environmental conditions and rockfall timing is complex, but the collection of high frequency scan data has shown the

potential for resampling the data according to cycles of environmental conditions. A peak in rockfall activity occurs in the final hours before sunset, during maximum cooling of the rock mass. This, combined with the shallow depth of rockfall, implies that near-surface thermomechanical microcrack growth drives many of the failures observed. An increase in the magnitude-frequency exponent during the summer months also suggests that high daily temperature fluctuations can generate a high proportion of small rockfall events. The generation of a high frequency rockfall inventory has shown a seasonal increase in rate and size with the onset of storms. When examined over shorter timescales, rainfall relates to rockfall timing in several ways. First, it induces a sustained increase in the rate of pre-failure deformation, without actually causing failure to occur. This can be considered as a preparation of the slope for failure and may constitute a reduction in resistance to shear along joints. Second, rainfall relates to the timing of small rockfall events, which may or may not constitute precursors to future, larger rockfall. These may occur due to cooling of the rock mass through wetting, or saturation of the sandstone to yield a mass sufficient to drive failure. Third, rainfall appears to trigger the onset of final failure but frequently does not coincide with the timing of failure. This supports laboratory analyses that have emphasised the role of exponential microcrack growth in defining the tertiary phase of failure, and the independence of this phase from external forcing. Pre-failure rockfall activity and pre-failure deformation have showed accelerations prior to rockfall, neither of which have been previously observed at such short timescales using TLS. Deformation prior to rockfall has presented linearity in inverse-velocity relationships; however, phases also appear to occur, which may reflect time-dependent breakage of rock bridges as the mass moves forwards.

The research presents a unique dataset that provides insight into relationships that have previously only been conceptualised by extrapolating findings of combined lower spatial and temporal resolution. In doing so, more questions have arisen about the controls on the nature and timing of rockfall that identify clear routes for future research in this field.

References

Abellán, A., Vilaplana, J.M. and Martínez, J., 2006. Application of a long-range Terrestrial Laser Scanner to a detailed rockfall study at Vall de Núria (Eastern Pyrenees, Spain). *Engineering Geology*, 88(3), pp. 136-148.

Abellán, A., Jaboyedoff, M., Oppikofer, T. and Vilaplana, J.M., 2009. Detection of millimetric deformation using a terrestrial laser scanner: experiment and application to a rockfall event. *Natural Hazards and Earth System Sciences*, 9(2), pp. 365-372.

Abellán, A., Calvet, J., Vilaplana, J.M. and Blanchard, J., 2010. Detection and spatial prediction of rockfalls by means of terrestrial laser scanner monitoring. *Geomorphology*, 119, pp. 162-171.

Abellán, A., Oppikofer, T., Jaboyedoff, M., Rosser, N.J., Lim, M. and Lato, M.J., 2014. Terrestrial laser scanning of rock slope instabilities. *Earth Surface Processes and Landforms*, 39(1), pp. 80-97.

Abellán, A., Derron, M.H. and Jaboyedoff, M., 2016. Use of 3D Point Clouds in Geohazards. Special Issue: Current Challenges and Future Trends. *Remote Sensing*, 8(2), pp. 130-138.

Afana, A., Hunter, G., Davis, J., Williams, J.G., Hardy, R.J. and Rosser, N.J., 2015. Integrating full-waveform terrestrial laser scanning into automated slope monitoring. *Markscheidewesen*, 122, pp. 16-22.

Agar, R., 1960. Post-glacial erosion of the North Yorkshire coast from the Tees estuary to Ravenscar. *Proceedings of the Yorkshire Geological and Polytechnic Society*, 32(4), pp. 409-427.

Agliardi, F., Crosta, G. and Zanchi, A., 2001. Structural constraints on deep-seated slope deformation kinematics. *Engineering Geology*, 59(1), pp. 83-102.

Akca, D., 2007. Matching of 3D surfaces and their intensities. *ISPRS Journal of Photogrammetry and Remote Sensing*, 62(2), pp. 112-121.

Alba, M., Fregonese, L., Prandi, F., Scaioni, M. and Valgoi, P., 2006. Structural monitoring of a large dam by terrestrial laser scanning. *International Archives of Photogrammetry, Remote Sensing and Spatial Information Sciences*, 36(5), 6 p.

Alda, J., 2003. Laser and Gaussian beam propagation and transformation. In Driggers, R.G. (ed.) *Encyclopedia of Optical Engineering*. New York: Marcel Dekker, Inc., pp. 999-1013.

Aleotti, P., 2004. A warning system for rainfall-induced shallow failures. *Engineering Geology*, 73(3), pp. 247-265.

Alexander, J. and Gawthorpe, R.L., 1993. The complex nature of a Jurassic multistorey, alluvial sandstone body, Whitby, North Yorkshire. *Geological Society, London, Special Publications*, 73(1), pp. 123-142.

Allan, J.C., Hart, R. and Tranquili, J.V., 2006. The use of Passive Integrated Transponder (PIT) tags to trace cobble transport in a mixed sand-and-gravel beach on the high-energy Oregon coast, USA. *Marine Geology*, 232(1-2), pp. 63-86.

Allison, R.J. and Kimber, O.G., 1998. Modelling failure mechanisms to explain rock slope change along the Isle of Purbeck coast, UK. *Earth Surface Processes and Landforms*, 23(8), pp. 731-750.

Amitrano, D., Grasso, J.R. and Senfaute, G., 2005. Seismic precursory patterns before a cliff collapse and critical point phenomena. *Geophysical Research Letters*, 32, L08314.

Amitrano, D., Gruber, S. and Girard, L., 2012. Evidence of frost-cracking inferred from acoustic emissions in a high-alpine rock-wall. *Earth and Planetary Science Letters*, 341-344, pp. 86-93.

Assali, P., Grussenmeyer, P., Villemin, T., Pollet, N. and Viguier, F., 2014. Surveying and modeling of rock discontinuities by terrestrial laser scanning and photogrammetry: Semi-automatic approaches for linear outcrop inspection. *Journal of Structural Geology*, 66, pp. 102-114.

Atanasiu, V., 2014. *Kernel smoothing density estimate for circular data*. Available at: https://uk.mathworks.com/matlabcentral/fileexchange/32614-kernel-smoothing-density-estimate-for-circular-data/content/circ_ksdensity.m (Accessed: 15 December 2016).

Avian, M., Kellerer-Pirklbauer, A. and Bauer, A, 2009. LiDAR for monitoring mass movements in permafrost environments at the cirque Hinteres Langtal, Austria, between 2000 and 2008. *Natural Hazards and Earth System Sciences*, 9(4), pp. 1087-1094.

Badoux, A., Graf, C., Rhyner, J., Kuntner, R. and McArdell, B.W., 2009. A debris-flow alarm system for the Alpine Illgraben catchment: design and performance. *Natural Hazards*, 49(3), pp. 517-539.

Bae, K.H., Belton, D. and Lichti, D., 2005. A framework for position uncertainty of unorganised three-dimensional point clouds from near-monostatic laser scanners using covariance analysis. *International Archives of Photogrammetry and Remote Sensing*, 36(3), pp. 7-12.

Bai, J.G., Lu, S. and Han, J., 2008. Importance of study of creep sliding mechanism to prevention and treatment of reservoir landslide. In Chen, Z., Zhang, J., Li, Z., Wu, F. and Ho, K. (eds.) *Landslides and Engineered Slopes: From the Past to the Future. Proceedings of the 10th International Symposium on Landslides and Engineered Slopes*. Xi'an, China, 30 June – 4 July. The Netherlands: CRC Press, pp. 1071-1076.

Bak, P., Tang, C. and Wiesenfeld, K., 1987. Self-organized criticality: An explanation of the 1/f noise. *Physical Review Letters*, 59(4), pp. 381-384.

Balakrishnan, N., Voinov, V. and Nikulin, M.S., 2013. *Chi-squared goodness of fit tests with applications*. Waltham, MA: Academic Press, 256 p.

Baltsavias, E.P., 1999. Airborne laser scanning: basic relations and formulas. *ISPRS Journal of Photogrammetry and Remote Sensing*, 54(2), pp. 199-214.

Bangen, S., Hensleigh, J., McHugh, P. and Wheaton, J., 2016. Error modeling of DEMs from topographic surveys of rivers using fuzzy inference systems. *Water Resources Research*, 52(2), pp. 1176-1193.

Barlow, J., Lim, M., Rosser, N., Petley, D., Brain, M., Norman, E. and Geer, M., 2012. Modeling cliff erosion using negative power law scaling of rockfalls. *Geomorphology*, 139, pp. 416-424.

Barrett, P.J., 1980. The shape of rock particles, a critical review. *Sedimentology*, 27(3), pp. 291-303.

Barron, A.J.M., Lott, G.K. and Riding, J.B., 2012. *Stratigraphical framework for the Middle Jurassic strata of Great Britain and the adjoining continental shelf.* Nottingham, UK: British Geological Survey, 177 p.

BBC, 2013. *Whitby landslip exposes human bones at 'Dracula graveyard'.* Available at: http://www.bbc.co.uk/news/uk-england-york-north-yorkshire-20970716 (Accessed: 8 July 2015).

Belton, D. and Lichti, D.D., 2006. Classification and segmentation of terrestrial laser scanner point clouds using local variance information. *The International Archives of the Photogrammetry, Remote Sensing and Spatial Information Sciences*, 36(5), pp. 44-49.

Benjamin, J., Rosser, N.J. and Brain, M.J., 2016. Rockfall detection and volumetric characterisation using LiDAR. In Aversa, S., Cascini, L., Picarelli, L. and Scavia, C. (eds.) *Landslides and Engineered Slopes. Experience, Theory and Practice: Proceedings of the 12th International Symposium on Landslides.* Napoli, Italy, 12 – 19 June. The Netherlands: CRC Press, pp. 389-395.

Benn, D.I. and Ballantyne, C.K., 1993. The description and representation of particle shape. *Earth Surface Processes and Landforms*, 18(7), pp. 665-672.

Besl, P.J. and Jain, R.C., 1988. Segmentation through variable-order surface fitting. *IEEE Transactions on Pattern Analysis and Machine Intelligence*, 10(2), pp. 167-192.

Besl, P.J. and McKay, N.D., 1992. Method for registration of 3-D shapes. In Schenker, P.S. (ed.) *Proc. SPIE 1611, Sensor Fusion IV: Control Paradigms and Data Structures.* Boston, MA, 30 April. Bellingham, WA: International Society for Optics and Photonics, pp. 586-606.

Bienert, A., Queck, R., Schmidt, A., Bernhofer, C. and Maas, H.G., 2010. Voxel space analysis of terrestrial laser scans in forests for wind field modelling. *International Archives of Photogrammetry, Remote Sensing and Spatial Information Sciences*, 38(5), pp. 92-97.

Bird, E.C., 2011. *Coastal geomorphology: an introduction.* 2nd ed. Princeton, Chichester: John Wiley & Sons., 310 p.

Bjerrum, L., 1967. Progressive failure in slopes of overconsolidated plastic clay and clay shales. *Journal of the Soil Mechanics and Foundations Division*, 93(5), pp. 1-49.

Blasone, G., Cavalli, M., Marchi, L. and Cazorzi, F., 2014. Monitoring sediment source areas in a debris-flow catchment using terrestrial laser scanning. *Catena*, 123, pp. 23-36.

Blott, S.J. and Pye, K., 2008. Particle shape: a review and new methods of characterization and classification. *Sedimentology*, 55(1), pp. 31-63.

Boehler, W., Vicent, M.B. and Marbs, A., 2003. Investigating laser scanner

accuracy. *The International Archives of Photogrammetry, Remote Sensing and Spatial Information Sciences*, 34(5), pp. 696-701.

Bonnaffe, F., Jennette, D. and Andrews, J., 2007. A method for acquiring and processing ground-based lidar data in difficult-to-access outcrops for use in three-dimensional, virtual-reality models. *Geosphere*, 3(6), pp. 501-510.

Boothroyd, R.J., Hardy, R.J., Warburton, J.W. and Marjoribanks, T.I., 2016. The importance of accurately representing submerged vegetation morphology in the numerical prediction of complex river flow. *Earth Surface Processes and Landforms*, 41(4), pp. 567-576.

Bozzano, F., Cipriani, I., Mazzanti, P. and Prestininzi, A., 2011. Displacement patterns of a landslide affected by human activities: insights from ground-based InSAR monitoring. *Natural Hazards*, 59(3), pp. 1377-1396.

Brain, M.J., Rosser, N.J., Norman, E.C. and Petley, D.N., 2014. Are microseismic ground displacements a significant geomorphic agent? *Geomorphology*, 207, pp. 161-173.

Brardinoni, F. and Church, M., 2004. Representing the landslide magnitude–frequency relation: Capilano River basin, British Columbia. *Earth Surface Processes and Landforms*, 29(1), pp. 115-124.

Brasington, J., Langham, J. and Rumsby, B., 2003. Methodological sensitivity of morphometric estimates of coarse fluvial sediment transport. *Geomorphology*, 53(3), pp. 299-316.

Brázdil, R., Šilhán, K., Pánek, T., Dobrovolný, P., Kašičková, L. and Tolasz, R., 2012. The influence of meteorological factors on rockfall in the Moravskoslezské Beskydy Mts. *Geografie*, 117(1), pp. 1-20.

Brideau M.-A. and Stead, D., 2009. The role of rear release surfaces, block size and lateral confinement on rock slope failure mechanisms. In *62nd Canadian geotechnical conference and 10th joint groundwater CGS/IAH-CNC conference*. Halifax, Canada, 20 – 23 September. Vancouver: The Canadian Geotechnical Society, pp. 489–496.

Brodu, N. and Lague, D., 2012. 3D terrestrial lidar data classification of complex natural scenes using a multi-scale dimensionality criterion: Applications in geomorphology. *ISPRS Journal of Photogrammetry and Remote Sensing*, 68, pp. 121-134.

Brückl, E. and Parotidis, M., 2005. Prediction of slope instabilities due to deep-seated gravitational creep. *Natural Hazards and Earth System Sciences*, 5(2), pp. 155-172.

Brunetti, M.T., Guzzetti, F. and Rossi, M., 2009. Probability distributions of landslide volumes. *Nonlinear Processes in Geophysics*, 16(2), pp. 179-188.

Bucci, F., Santangelo, M., Cardinali, M., Fiorucci, F. and Guzzetti, F., 2016. Landslide distribution and size in response to Quaternary fault activity: the Peloritani Range, NE Sicily, Italy. *Earth Surface Processes and Landforms*, 41(5), pp. 711-720.

Burjánek, J., Moore, J.R., Molina, F.X.Y. and Fäh, D., 2012. Instrumental evidence of normal mode rock slope vibration. *Geophysical Journal International*, 188(2), pp. 559-569.

Caine, N., 1980. The rainfall intensity: duration control of shallow landslides and debris flows.

Geografiska Annaler. Series A, Physical Geography, 62(1/2), pp. 23-27.

Callister, W.D. and Rethwisch, D.G., 2007. *Materials science and engineering: an introduction.* 7th ed. New York: Wiley, 832 p.

Cancelli, A. and Nova, R., 1985. Landslides in soil debris cover triggered by rainstorms in Valtellina (Central Alps-Italy). In *Proceedings of the 4th International Conference and Field Workshop on Landslides*. Tokyo, Japan, 23 – 31 August. Tokyo: The Japan Geological Society, pp. 267-272.

Carey, J.M., Moore, R., Petley, D. and Siddle, H.J., 2007. Pre-failure behaviour of slope materials and their significance in the progressive failure of landslides. In Mathie, E., McInnes, R., Fairbank, H. and Jakeways, J. (eds.) *Landslides and Climate Change: Challenges and Solutions. Proceedings of the International Conference on Landslides and Climate Change*. Ventnor, Isle of Wight, UK, 21 – 24 May 2007. London: Taylor & Francis, pp. 207-215.

Carrea, D., Abellán, A., Derron, M.H., Gauvin, N. and Jaboyedoff, M., 2012. Using 3D surface datasets to understand landslide evolution: from analogue models to real case study. In Eberhardt, E., Froese, C. and Turner, K. (eds.) *Landslides and Engineered Slopes: Protecting Society through Improved Understanding*. London: CRC Press, pp. 575-579.

Carrivick, J.L., Smith, M.W. and Quincey, D.J., 2016. *Structure from Motion in the Geosciences*. New York: John Wiley & Sons, 208 p.

Cepeda, J., Höeg, K. and Nadim, F., 2010. Landslide-triggering rainfall thresholds: a conceptual framework. *Quarterly Journal of Engineering Geology and Hydrogeology*, 43(1), pp. 69-84.

Ceriani, M., Lauzi, S. and Padovan, N., 1992. Rainfall and landslides in the Alpine area of Lombardia Region, central Alps, Italy. In *Proceedings of the INTERPRAVENT International Symposium 1992.* Bern, Switzerland, pp. 9-20.

Chau, K.T., Wong, R.H.C., Liu, J. and Lee, C.F., 2003. Rockfall hazard analysis for Hong Kong based on rockfall inventory. *Rock Mechanics and Rock Engineering*, 36(5), pp. 383-408.

Chaytor, J.D., Uri, S., Solow, A.R. and Andrews, B.D., 2009. Size distribution of submarine landslides along the US Atlantic margin. *Marine Geology*, 264(1), pp. 16-27.

Chen, Y. and Medioni, G., 1992. Object modelling by registration of multiple range images. *Image and Vision Computing*, 10(3), pp. 145-155.

Clark, J. and Robson, S., 2004. Accuracy of measurements made with a Cyrax 2500 laser scanner against surfaces of known colour. *Survey Review*, 37(294), pp. 626-638.

Collins, B.D. and Jibson, R.W., 2015. Assessment of existing and potential landslide hazards resulting from the April 25, 2015 Gorkha, Nepal earthquake sequence. *US Geological Survey Open-File Report 2015-1142*, 50 p.

Collins, B.D. and Sitar, N., 2010. Stability of steep slopes in cemented sands. *Journal of Geotechnical and Geoenvironmental Engineering*, 137(1), pp. 43-51.

Collins, B.D. and Stock, G.M., 2016. Rockfall triggering by cyclic thermal stressing of

exfoliation fractures. *Nature Geoscience*, 9(5), pp. 395-400.

Cox, N.J., 1999. *Transformations: an introduction*. Available at: http://www.stata.com/users/njc/topichlp/transint.hlp (Accessed: 2 December 2016).

Crosetto, M., Monserrat, O., Luzi, G., Cuevas-Gonzalez, M. and Devanthery, N., 2014. A noninterferometric procedure for deformation measurement using GB-SAR imagery. *IEEE Geoscience and Remote Sensing Letters*, 11(1), pp. 34-38.

Crosta, G.B. and Agliardi, F., 2003. Failure forecast for large rock slides by surface displacement measurements. *Canadian Geotechnical Journal*, 40(1), pp. 176-191.

Crozier, M.J., 2005. Multiple-occurrence regional landslide events in New Zealand: hazard management issues. *Landslides*, 2(4), pp. 247-256.

Dahal, R.K. and Hasegawa, S., 2008. Representative rainfall thresholds for landslides in the Nepal Himalaya. *Geomorphology*, 100(3), pp. 429-443.

Dai, F.C. and Lee, C.F., 2001. Frequency-volume relation and prediction of rainfall-induced landslides. *Engineering Geology*, 59, pp. 253-266.

Dai, F.C., Xu, C., Yao, X., Xu, L., Tu, X.B. and Gong, Q.M., 2011. Spatial distribution of landslides triggered by the 2008 Ms 8.0 Wenchuan earthquake, China. *Journal of Asian Earth Sciences*, 40(4), pp. 883-895.

D'Amato, J., Hantz, D., Guerin, A., Jaboyedoff, M., Baillet, L. and Mariscal, A., 2016. Influence of meteorological factors on rockfall occurrence in a middle mountain limestone cliff. *Natural Hazards and Earth System Sciences*, 16(3), pp. 719-735.

Davies, M.C., Hamza, O. and Harris, C., 2001. The effect of rise in mean annual temperature on the stability of rock slopes containing ice-filled discontinuities. *Permafrost and Periglacial Processes*, 12(1), pp. 137-144.

Decaulne, A. and Sæmundsson, Þ., 2007. Spatial and temporal diversity for debris-flow meteorological control in subarctic oceanic periglacial environments in Iceland. *Earth Surface Processes and Landforms*, 32(13), pp. 1971-1983.

Deganutti, A.M., Marchi, L. and Arattano, M., 2000. Rainfall and debris-flow occurrence in the Moscardo basin (Italian Alps). In Wieczorek, G.F. and Naeser, N.D. (eds.) *Debris-flow Hazard Mitigation: Mechanics, Prediction, and Assessment. Proceedings of the Second International Conference on Debris-flow Hazards Mitigation*. Taipei, Taiwan, 16 – 18 August. Rotterdam: A.A. Balkema, pp. 67-72.

Delonca, A., Gunzburger, Y. and Verdel, T., 2014. Statistical correlation between meteorological and rockfall databases. *Natural Hazards and Earth System Sciences*, 14(8), pp. 1953-1964.

Densmore, A.L., Ellis, M.A. and Anderson, R.S., 1998. Landsliding and the evolution of normal-fault-bounded mountains. *Journal of Geophysical Research: Solid Earth*, 103(B7), pp. 15203-15219.

Dewez, T.J.B., Girardeau-Montaut, D., Allanic, C. and Rohmer, J., 2016. Facets: A CloudCompare plugin to extract geological planes from unstructured 3D point clouds. *The International Archives of Photogrammetry, Remote Sensing and Spatial Information Science*, 41, B5.

Dick, G.J., 2013. *Development of an early warning time-of-failure analysis methodology for open pit mine slopes utilizing the spatial distribution of ground-based radar monitoring data*. Master's thesis. University of British Columbia. Available at: https://open.library.ubc.ca/cIRcle/collections/ubctheses/24/items/1.0166823 (Accessed: 7 February 2014).

Dick, G.J., Eberhardt, E., Cabrejo-Liévano, A.G., Stead, D. and Rose, N.D., 2014. Development of an early-warning time-of-failure analysis methodology for open-pit mine slopes utilizing ground-based slope stability radar monitoring data. *Canadian Geotechnical Journal*, 52(4), pp. 515-529.

Dieterich, J.H., 1978. Time-dependent friction and the mechanics of stick-slip. *Pure and Applied Geophysics*, 116(4-5), pp. 790-806.

Doyle, J.B. and Reese, J.D., 2011. Slope Monitoring and Back Analysis of the East Fault Failure, Bingham Canyon Mine, Utah. *Proceedings of Slope Stability 2011: International Symposium on Rock Slope Stability in Open Pit Mining and Civil Engineering*. Vancouver, BC, 18 – 21 September.

Duperret, A., Genter, A., Martinez, A. and Mortimore, R.N., 2004. Coastal chalk cliff instability in NW France: role of lithology, fracture pattern and rainfall. *Geological Society, London, Special Publications*, 20(1), pp. 33-55.

Durrieu, S., Allouis, T., Fournier, R., Véga, C. and Albrech, L., 2008. Spatial quantification of vegetation density from terrestrial laser scanner data for characterization of 3D forest structure at plot level. In Hill, R.A., Rosette, J. and Suárez, J. (eds.) *Proceedings of SilviLaser 2008: 8th International Conference on LiDAR Applications in Forest Assessment and Inventory*. Edinburgh, UK, 17 – 19 September. Edinburgh: SilviLaser, pp. 325-334.

Dussauge, C., Grasso, J.R. and Helmstetter, A., 2003. Statistical analysis of rockfall volume distributions: Implications for rockfall dynamics. *Journal of Geophysical Research: Solid Earth*, 108(B6), 11 p.

Dussauge-Peisser, C., Helmstetter, A., Grasso, J.R., Hantz, D., Desvarreux, P., Jeannin, M. and Giraud, A., 2002. Probabilistic approach to rock fall hazard assessment: potential of historical data analysis. *Natural Hazards and Earth System Sciences*, 2(1/2), pp. 15-26.

Earlie, C.S., Masselink, G., Russell, P. and Shail, R., 2013. Sensitivity analysis of the methodology for quantifying cliff erosion using airborne LiDAR – examples from Cornwall, UK. *Journal of Coastal Research: Special Issue 65 – International Coastal Symposium*, 1, pp. 470-475.

Eberhardt, E., Stead, D. and Stimpson, B., 1999. Quantifying progressive pre-peak brittle fracture damage in rock during uniaxial compression. *International Journal of Rock Mechanics and Mining Sciences*, 36(3), pp. 361-380.

Eberhardt, E., Stead, D., Coggan, J. and Willenberg, H., 2002. An intergrated numerical analysis approach applied to the Randa Rockslide. In Rybar, J., Stemberk, J. and Wagner, P. (eds.) *Proceedings of the First European Conference on Landslides*. Prague, Czech Republic, 24 – 26 June. Lisse: Balkema, pp. 335-362.

Eberhardt, E., Stead, D. and Coggan, J.S., 2004. Numerical analysis of initiation and progressive failure in natural rock slopes – the 1991 Randa rockslide. *International*

Journal of Rock Mechanics and Mining Sciences, 41(1), pp. 69-87.

Eberhardt, E., 2012. Landslide monitoring: The role of investigative monitoring to improve understanding and early warning of failure. In Clague, J.J. and Stead, D. (eds.) *Landslides: Types, Mechanisms and Modeling*. Cambridge: Cambridge University Press, pp. 222-234.

Eitel, J.U., Höfle, B., Vierling, L.A., Abellán, A., Asner, G.P., Deems, J.S., Glennie, C.L., Joerg, P.C., LeWinter, A.L., Magney, T.S. and Mandlburger, G., 2016. Beyond 3-D: The new spectrum of lidar applications for earth and ecological sciences. *Remote Sensing of Environment*, 186, pp. 372-392.

Elseberg, J., Borrmann, D. and Nüchter, A., 2011. Efficient processing of large 3d point clouds. In *Proceedings of the 23rd International Symposium on Information, Communication and Automation Technologies (ICAT)*. Sarajevo, Bosnia and Herzegovina, 27 – 29 October. IEEE, pp. 132-138.

Elseberg, J., Borrmann, D. and Nüchter, A., 2013. One billion points in the cloud–an octree for efficient processing of 3D laser scans. *ISPRS Journal of Photogrammetry and Remote Sensing*, 76, pp. 76-88.

Eppes, M.C., Magi, B., Hallet, B., Delmelle, E., Mackenzie-Helnwein, P., Warren, K. and Swami, S., 2016. Deciphering the role of solar-induced thermal stresses in rock weathering. *Geological Society of America Bulletin*, 128(9-10), pp. 1315-1338.

Farina, P., Leoni, L., Babboni, F., Coppi, F., Mayer, L. and Ricci, P., 2011. IBIS-M, an innovative radar for monitoring slopes in open-pit mines. In *Proceedings of Slope Stability 2011: International Symposium on Rock Slope Stability in Open Pit Mining and Civil Engineering*. Vancouver, BC, 18 – 21 September, pp. 18-21.

Federico, A., Popescu, M., Elia, G., Fidelibus, C., Internò, G. and Murianni, A., 2012. Prediction of time to slope failure: a general framework. *Environmental Earth Sciences*, 66(1), pp. 245-256.

Fell, R., Corominas, J., Bonnard, C., Cascini, L., Leroi, E. and Savage, W.Z., 2008. Guidelines for landslide susceptibility, hazard and risk zoning for land-use planning. *Engineering Geology*, 102(3), pp. 99-111.

Fowler A, France JI and Truong M., 2011. Applications of advanced laser scanning technology in geology. In *Proceedings of Slope Stability 2011: International Symposium on Rock Slope Stability in Open Pit Mining and Civil Engineering*. Vancouver, BC, 18 – 21 September.

Frayssines, M. and Hantz, D., 2006. Failure mechanisms and triggering factors in calcareous cliffs of the Subalpine Ranges (French Alps). *Engineering Geology*, 86(4), pp. 256-270.

Frisken, S.F. and Perry, R.N., 2002. Simple and efficient traversal methods for quadtrees and octrees. *Journal of Graphics Tools*, 7(3), pp. 1-11.

Froese, C.R., M. Charrière, F. Humair, M. Jaboyedoff and A. Pedrazzini, 2012. Characterization and management of rockslide hazard at Turtle Mountain, Alberta, Canada. In Clague, J.J. and Stead, D. (eds.), *Landslides: Types, Mechanisms and Modeling*. Cambridge: Cambridge University Press, pp. 310-322.

Froude, M.J., 2011. *Capturing and characterising pre-failure strain on failing slopes*. Masters

thesis. Durham University. Available at: http://etheses.dur.ac.uk/3272/1/mjfroudemscr.pdf (Accessed: 14 October 2012)

Fukuzono, T., 1985. A new method for predicting the failure time of a slope. In *Proceedings of the 4th International Conference and Field Workshop in Landslides*. Tokyo, Japan, 23 – 31 August. Tokyo: National Center for Disaster Prevention, pp. 145-150.

Fuyii Y. 1969. Frequency distribution of the magnitude of landslides caused by heavy rainfall. *Journal of the Seismological Society of Japan*, 22, pp. 244-247.

Gelfand, N., Ikemoto, L., Rusinkiewicz, S. and Levoy, M., 2003. Geometrically stable sampling for the ICP algorithm. In *Proceedings of the 4th International Conference on 3-D Digital Imaging and Modeling*. Banff, Canada, 6 – 10 October. IEEE, pp. 260-267.

Giannecchini, R., 2005a. Rainfall triggering soil slips in the southern Apuan Alps (Tuscany, Italy). *Advances in Geosciences*, 2, pp. 21-24.

Giannecchini, R., 2005b. Relationship between rainfall and shallow landslides in the southern Apuan Alps (Italy). *Natural Hazards and Earth System Sciences*, 6(3), pp. 357-364.

Gigli, G. and Casagli, N., 2011. Semi-automatic extraction of rock mass structural data from high resolution LIDAR point clouds. *International Journal of Rock Mechanics and Mining Sciences*, 48(2), pp. 187-198.

Girardeau-Montaut, D., Roux, M., Marc, R. and Thibault, G., 2005. Change detection on points cloud data acquired with a ground laser scanner. *The International Archives of Photogrammetry, Remote Sensing and Spatial Information Sciences*, 36(3), W19.

Gischig, V.S., 2011. *Kinematics and failure mechanisms of the Randa rock slope instability (Switzerland).* PhD thesis. ETH Zurich. Available at: http://e-collection.library.ethz.ch/eserv/eth:4487/eth-4487-02.pdf (Accessed: 5 January 2014).

Gischig, V.S., Moore, J.R., Evans, K.F., Amann, F. and Loew, S., 2011a. Thermomechanical forcing of deep rock slope deformation: 1. Conceptual study of a simplified slope. *Journal of Geophysical Research: Earth Surface*, 116(F4), 18 p.

Gischig, V.S., Moore, J.R., Evans, K.F., Amann, F. and Loew, S., 2011b. Thermomechanical forcing of deep rock slope deformation: 2. The Randa rock slope instability. *Journal of Geophysical Research: Earth Surface*, 116(F4), 17 p.

Glade, T., Crozier, M. and Smith, P., 2000. Applying probability determination to refine landslide-triggering rainfall thresholds using an empirical "Antecedent Daily Rainfall Model". *Pure and Applied Geophysics*, 157(6-8), pp. 1059-1079.

Goldstein, M.L., Morris, S.A. and Yen, G.G., 2004. Problems with fitting to the power-law distribution. *The European Physical Journal B-Condensed Matter and Complex Systems*, 41(2), pp. 255-258.

Gorte, B. and Pfeifer, N., 2004. Structuring laser-scanned trees using 3D mathematical morphology. *International Archives of Photogrammetry and Remote Sensing*, 35(B5), pp. 929-933.

Gorum, T., Fan, X., van Westen, C.J., Huang, R.Q., Xu, Q., Tang, C. and Wang,

G., 2011. Distribution pattern of earthquake-induced landslides triggered by the 12 May 2008 Wenchuan earthquake. *Geomorphology*, 133(3), pp. 152-167.

Graham, D.J., and Midgley N.G., 2000. Graphical representation of particle shape using triangular diagrams: An Excel spreadsheet method. *Earth Surface Processes and Landforms*, 25(13), pp. 1473-1477.

Greif, V., Sassa, K. and Fukuoka, H., 2006. Failure mechanism in an extremely slow rock slide at Bitchu-Matsuyama castle site (Japan). *Landslides*, 3(1), pp. 22-38.

Gunzburger, Y., Merrien-Soukatchoff, V. and Guglielmi, Y., 2005. Influence of daily surface temperature fluctuations on rock slope stability: case study of the Rochers de Valabres slope (France). *International Journal of Rock Mechanics and Mining Sciences*, 42(3), pp. 331-349.

Gutenberg, B.U. and Richter, C.F., 1954. *Seismicity of the earth and related phenomena*. 2nd ed. Princeton, NJ: Princeton University Press, 310 p.

Guthrie, R.H. and Evans, S.G., 2007. Work, persistence, and formative events: the geomorphic impact of landslides. *Geomorphology*, 88(3), pp. 266-275.

Guzzetti, F., Aleotti, P., Malamud, B.D. and Turcotte, D.L., 2002. Comparison of three landslide event inventories in central and northern Italy. In Romero, R. (ed.) *Proceedings of the 4th EGS Plinius Conference*, Mallorca, Spain, 2 – 4 October. Universitat de les Illes Balears (Spain).

Guzzetti, F., 2005. *Landslide Hazard and Risk Assessment*. PhD thesis. University of Bonn. Available at: http://hss.ulb.uni-bonn.de/2006/0817/0817.pdf (Accessed: 18 October 2012).

Guzzetti, F., Reichenbach, P., Cardinali, M., Galli, M. and Ardizzone, F., 2005. Probabilistic landslide hazard assessment at the basin scale. *Geomorphology*, 72(1), pp. 272-299.

Guzzetti, F., Peruccacci, S., Rossi, M. and Stark, C.P., 2007. Rainfall thresholds for the initiation of landslides in central and southern Europe. *Meteorology and Atmospheric Physics*, 98(3-4), pp. 239-267.

Guzzetti, F., Peruccacci, S., Rossi, M. and Stark, C.P., 2008. The rainfall intensity-duration control of shallow landslides and debris flows: an update. *Landslides*, 5(1), pp. 3-17.

Guzzetti, F., Ardizzone, F., Cardinali, M., Rossi, M. and Valigi, D., 2009. Landslide volumes and landslide mobilization rates in Umbria, central Italy. *Earth and Planetary Science Letters*, 279(3), pp. 222-229.

Guzzetti, F., Mondini, A.C., Cardinali, M., Fiorucci, F., Santangelo, M. and Chang, K.T., 2012. Landslide inventory maps: New tools for an old problem. *Earth-Science Reviews*, 112(1), pp. 42-66.

Hales, T.C. and Roering, J.J., 2007. Climatic controls on frost cracking and implications for the evolution of bedrock landscapes. *Journal of Geophysical Research: Earth Surface*, 112(F2), 14 p.

Hall, K., and Thorn, C.E., 2014. Thermal fatigue and thermal shock in bedrock: An

attempt to unravel the geomorphic processes and products. *Geomorphology*, 206, pp. 1 – 13, doi: 10.1016/j.geomorph.2013.09.022.

Hallet, B., Hunter, L. and Bogen, J., 1996. Rates of erosion and sediment evacuation by glaciers: A review of field data and their implications. *Global and Planetary Change*, 12(1), pp. 213-235.

Hallet, B., 2006. Why do freezing rocks break? *Science*, 314(5802), pp.1092-1093.

Hamdi, P., Stead, D., Elmo, D. and Töyrä, J., 2015. The Use of Numerical Methods in Simulating the Influence of Geological Structure on the Surface Subsidence Associated with Sub-Level Caving. In *49th US Rock Mechanics Symposium*, 28 June – 1 July, San Francisco, California. American Rock Mechanics Association, 15-571.

Handwerger, A.L., Rempel, A.W., Skarbek, R.M., Roering, J.J. and Hilley, G.E., 2016. Rate-weakening friction characterizes both slow sliding and catastrophic failure of landslides. *Proceedings of the National Academy of Sciences*, 113(37), pp. 10281-10286.

Harp, E.L. and Jibson, R.W., 1996. Landslides triggered by the 1994 Northridge, California, earthquake. *Bulletin of the Seismological Society of America*, 86(1B), pp. 319-332.

Harries, N., Noon, D., Pritchett, H. and Bates, D., 2009. Slope Stability Radar for Managing Rock Fall Risks in Open Cut Mines. In Diederichs, M. and Grasselli, G. (eds.) *Rock Engineering in Difficult Conditions. Proceedings of the 3rd Canada-US Rock Mechanics Symposium*. Toronto, Canada, 9 – 14 May. London: CRC Press, Paper 4279, 8 p.

Havaej, M., Coggan, J., Stead, D. and Elmo, D., 2016. A combined remote sensing–numerical modelling approach to the stability analysis of Delabole Slate Quarry, Cornwall, UK. *Rock Mechanics and Rock Engineering*, 49(4), pp. 1227-1245.

Havenith, H.B., 2014. Hazard and risk related to earthquake-triggered landslide events. In Sassa, K., Canuti, P. and Yin, Y. (Eds.) *Landslide Science for a Safer Geoenvironment. Volume 3: Targeted Landslides*. Switzerland: Springer International Publishing, pp. 197-203.

Helmstetter, A., Sornette, D., Grasso, J.R., Andersen, J.V., Gluzman, S. and Pisarenko, V., 2004. Slider block friction model for landslides: Application to Vaiont and La Clapiere landslides. *Journal of Geophysical Research: Solid Earth*, 109(B2), 15 p.

Helmstetter, A. and Garambois, S., 2010. Seismic monitoring of Séchilienne rockslide (French Alps): Analysis of seismic signals and their correlation with rainfalls. *Journal of Geophysical Research: Earth Surface*, 115(F3), 15 p.

Hemingway, J.E., Wilson, V. and Wright, C.W., 1968. *Geology of the Yorkshire Coast*. Colchester, England: Benham, 47 p.

Hengl, T., 2006. Finding the right pixel size. *Computers & Geosciences*, 32(9), pp. 1283-1298.

Hergarten, S., 2003. Landslides, sandpiles, and self-organized criticality. *Natural Hazards and Earth System Sciences*, 3(6), pp. 505-514.

Higgitt, D.L. and Allison, R.J., 1999. Clast exposure on boulder-covered desert

slopes. *Earth Surface Processes and Landforms*, 24(2), pp. 111-125.

Hodge, R., Brasington, J. and Richards, K., 2009. In situ characterization of grain-scale fluvial morphology using Terrestrial Laser Scanning. *Earth Surface Processes and Landforms*, 34(7), pp. 954-968.

Hodge, R.A., 2010. Using simulated terrestrial laser scanning to analyse errors in high-resolution scan data of irregular surfaces. *ISPRS Journal of Photogrammetry and Remote Sensing*, 65(2), pp. 227-240.

Hoek, E. and Bray, J.D., 1981. *Rock slope engineering*. 3rd edn. London: CRC Press, 368 p.

Höfle, B., Canli, E., Schmitz, E., Crommelinck, S., Hoffmeister, D. and Glade, T., 2016. 4D near real-time environmental monitoring using highly temporal LiDAR. In *EGU General Assembly Conference Abstracts*. Vienna, Austria, 17 – 22 April, 18, p. 11295.

Hong, Y., Hiura, H., Shino, K., Sassa, K., Suemine, A., Fukuoka, H. and Wang, G., 2005. The influence of intense rainfall on the activity of large-scale crystalline schist landslides in Shikoku Island, Japan. *Landslides*, 2(2), pp. 97-105.

Hong, Y., Adler, R. and Huffman, G., 2006. Evaluation of the potential of NASA multi-satellite precipitation analysis in global landslide hazard assessment. *Geophysical Research Letters*, 33(22), 5 p.

Hoover, A., Jean-Baptiste, G., Jiang, X., Flynn, P.J., Bunke, H., Goldgof, D.B., Bowyer, K., Eggert, D.W., Fitzgibbon, A. and Fisher, R.B., 1996. An experimental comparison of range image segmentation algorithms. *IEEE Transactions on Pattern Analysis and Machine Intelligence*, 18(7), pp. 673-689.

Hoppe, H., DeRose, T., Duchamp, T., McDonald, J. and Stuetzle, W., 1992. Surface reconstruction from unorganized points. *ACM SIGGRAPH Computer Graphics,* 26(2), pp. 71-78.

Hornung, A., Wurm, K.M., Bennewitz, M., Stachniss, C. and Burgard, W., 2013. OctoMap: An efficient probabilistic 3D mapping framework based on octrees. *Autonomous Robots*, 34(3), pp. 189-206.

Hovius, N., Stark, C.P. and Allen, P.A., 1997. Sediment flux from a mountain belt derived by landslide mapping. *Geology*, 25(3), pp. 231-234.

Hovius, N., Stark, C.P., Hao-Tsu, C. and Jiun-Chuan, L., 2000. Supply and removal of sediment in a landslide-dominated mountain belt: Central Range, Taiwan. *The Journal of Geology*, 108(1), pp. 73-89.

Huang, R.Q. and Li, A.W., 2009. Analysis of the geo-hazards triggered by the 12 May 2008 Wenchuan Earthquake, China. *Bulletin of Engineering Geology and the Environment*, 68(3), pp. 363-371.

Hungr, O. and Kent, A., 1995. Coal mine waste dump failures in British Columbia, Canada. *Landslide News*, 9, pp. 26-28.

Hungr, O., Evans, S.G. and Hazzard, J., 1999. Magnitude and frequency of rock falls and rock slides along the main transportation corridors of southwestern British Columbia. *Canadian Geotechnical Journal*, 36(2), pp. 224-238.

Hungr, O., McDougall, S., Wise, M. and Cullen, M., 2008. Magnitude–frequency relationships of debris flows and debris avalanches in relation to slope relief. *Geomorphology*, 96(3), pp. 355-365.

Illenberger, W.K., 1991. Pebble shape (and size!). *Journal of Sedimentary Research*, 61(5), 756-767.

Ioannou, Y., Taati, B., Harrap, R. and Greenspan, M., 2012. Difference of normals as a multi-scale operator in unorganized point clouds. In *Proceedings of the 2nd International Conference on 3D Imaging, Modeling, Processing, Visualization and Transmission*. Zurich, Switzerland, October 13 – 15. Washington DC: IEEE, pp. 501-508.

Issler, D., De Blasio, F.V., Elverhøi, A., Bryn, P. and Lien, R., 2005. Scaling behaviour of clay-rich submarine debris flows. *Marine and Petroleum Geology*, 22(1), pp. 187-194.

Iverson, R.M., 2000. Landslide triggering by rain infiltration. *Water Resources Research*, 36(7), pp. 1897-1910.

Iverson, R.M., 2005. Regulation of landslide motion by dilatancy and pore pressure feedback. *Journal of Geophysical Research: Earth Surface*, 110(F2), 16 p.

Jaboyedoff, M., Baillifard, F., Bardou, E. and Girod, F., 2004. The effect of weathering on Alpine rock instability. *Quarterly Journal of Engineering Geology and Hydrogeology*, 37(2), pp. 95-103.

Jaboyedoff, M., Metzger, R., Oppikofer, T., Couture, R., Derron, M.H., Locat, J. and Turmel, D., 2007. New insight techniques to analyze rock-slope relief using DEM and 3D-imaging cloud points: COLTOP-3D software. In Eberhardt, E., Stead, D. and Morrison, T. (eds.) *Rock Mechanics: Meeting Society's Challenges and Demands. Proceedings of the 1st Canada-US Rock Mechanics Symposium.* Vancouver, Canada, 27 – 31 May. London: CRC Press, pp. 61-68.

Jaboyedoff, M., Couture, R. and Locat, P., 2009. Structural analysis of Turtle Mountain (Alberta) using digital elevation model: toward a progressive failure. *Geomorphology*, 103(1), pp. 5-16.

Jaboyedoff, M., Oppikofer, T., Abellán, A., Derron, M.H., Loye, A., Metzger, R. and Pedrazzini, A., 2012. Use of LIDAR in landslide investigations: a review. *Natural Hazards*, 61(1), pp. 5-28.

Jahne, B., 2000. *Computer vision and applications: a guide for students and practitioners*. Orlando, FL: Academic Press, 679 p.

Kaasalainen S., Kukko A., Lindroos T., Litkey P., Kaartinen H., Hyyppa J., Ahokas E., 2008. Brightness measurements and calibration with airborne and terrestrial laser scanners. *IEEE Transactions on Geoscience and Remote Sensing*, 46, pp. 528–534.

Kaasalainen, S., Niittymaki, H., Krooks, A., Koch, K., Kaartinen, H., Vain, A. and Hyyppa, H., 2010. Effect of target moisture on laser scanner intensity. *IEEE Transactions on Geoscience and Remote Sensing*, 48(4), pp. 2128-2136.

Kalenchuk, K.S., Diederichs, M.S. and McKinnon, S., 2006. Characterizing block geometry in jointed rock masses. *International Journal of Rock Mechanics and Mining*

Sciences, 43(8), pp. 1212-1225.

Kasperski, J., Delacourt, C., Allemand, P., Potherat, P., Jaud, M. and Varrel, E., 2010. Application of a terrestrial laser scanner (TLS) to the study of the Séchilienne Landslide (Isère, France). *Remote Sensing*, 2(12), pp. 2785-2802.

Keefer, D.K., 2000. Statistical analysis of an earthquake-induced landslide distribution—the 1989 Loma Prieta, California event. *Engineering Geology*, 58(3), pp. 231-249.

Kemeny, J. and Turner, K., 2008. *Ground-based LiDAR: rock slope mapping and assessment.* Federal Highway Administration Report FHWA-CFL/TD-08-006. Available at: https://ntrl.ntis.gov/NTRL/dashboard/searchResults/titleDetail/PB2009111755.xhtml (Accessed: 8 October 2013).

Kemeny, J., 2005. Time-dependent drift degradation due to the progressive failure of rock bridges along discontinuities. *International Journal of Rock Mechanics and Mining Sciences*, 42(1), pp. 35-46.

Kemeny, J., Handy, J., Kraemer, D., and Norton, B., 2011. Accurate LIDAR Change Detection for Slope Stability and Rockfall Monitoring. In *Proceedings of Slope Stability 2011: International Symposium on Rock Slope Stability in Open Pit Mining and Civil Engineering*. Vancouver, BC, 18 – 21 September, 10 p.

Keqiang, H. and Sijing, W., 2006. Double-parameter threshold and its formation mechanism of the colluvial landslide: Xintan landslide, China. *Environmental Geology*, 49(5), pp. 696-707.

Kersten, T.P., Sternberg, H. and Mechelke, K., 2005, October. Investigations into the accuracy behaviour of the terrestrial laser scanning system Mensi GS100. In Grün, A. and Kahmen, H. (eds.) *Proceedings of the 7th International Conference in Optical 3D Measurement Techniques*. Vienna, Austria, 3 – 5 October, pp. 122-131.

Kilburn, C.R. and Petley, D.N., 2003. Forecasting giant, catastrophic slope collapse: lessons from Vajont, Northern Italy. *Geomorphology*, 54(1), pp. 21-32.

Kim, I.I., McArthur, B. and Korevaar, E.J., 2001. Comparison of laser beam propagation at 785 nm and 1550 nm in fog and haze for optical wireless communications. *Proceedings of SPIE, The International Society for Optical Engineering*, 4214, pp. 26-37.

Kirschbaum, D.B., Adler, R., Hong, Y., Kumar, S., Peters-Lidard, C. and Lerner-Lam, A., 2012. Advances in landslide nowcasting: evaluation of a global and regional modeling approach. *Environmental Earth Sciences*, 66(6), pp. 1683-1696.

Kogure, T. and Matsukura, Y., 2010. Critical notch depths for failure of coastal limestone cliffs: case study at Kuro-shima Island, Okinawa, Japan. Earth Surface Processes and Landforms, 35(9), pp. 1044-1056.

Korup, O., 2005. Distribution of landslides in southwest New Zealand. *Landslides*, 2(1), pp. 43-51.

Krähenbühl, R., 2004. Temperatur und Kluftwasser als Ursachen von Felssturz. *Bulletin für angewandte Geologie*, 7, pp. 19-35.

Krautblatter, M. and Moser, M., 2006. Will we face an increase in hazardous secondary

rockfall events in response to global warming in the foreseeable future? In Price, M.F. (Ed.) *Global Change in Mountain Regions*. Duncow: Sapiens, pp. 253-254.

Krautblatter, M. and Moser, M., 2009. A nonlinear model coupling rockfall and rainfall intensity based on a four-year measurement in a high Alpine rock wall (Reintal, German Alps). *Natural Hazards and Earth System Sciences*, 9(4), pp. 1425-1432.

Křemen, T., Koska, B. and Pospíšil, J., 2006. Verification of laser scanning systems quality. In *Shaping the Change: FIG XXIII Congress*. Munich, Germany, 8 – 13 October, pp. 1-16.

Kromer, R.A., Hutchinson, D.J., Lato, M.J., Gauthier, D. and Edwards, T., 2015a. Identifying rock slope failure precursors using LiDAR for transportation corridor hazard management. *Engineering Geology*, 195, pp. 93-103.

Kromer, R.A., Abellán, A., Hutchinson, D.J., Lato, M., Edwards, T. and Jaboyedoff, M., 2015b. A 4D filtering and calibration technique for small-scale point cloud change detection with a terrestrial laser scanner. *Remote Sensing*, 7(10), pp. 13029-13052.

Kromer, R.A., Abellán, A., Hutchinson, D.J., Lato, M., Chanut, M.-A., Dubois, L. and Jaboyedoff, M., 2017. Automated Terrestrial Laser Scanning with Near Real-Time Change Detection - Monitoring of the Séchilienne Landslide. *Earth Surface Dynamics*, doi:10.5194/esurf-2017-6.

Kuhn, M.R. and Mitchell, J.K., 1993. New perspectives on soil creep. *Journal of Geotechnical Engineering*, 119(3), pp. 507-524.

Kurz, T.H., Dewit, J., Buckley, S.J., Thurmond, J.B., Hunt, D.W. and Swennen, R., 2012. Hyperspectral image analysis of different carbonate lithologies (limestone, karst and hydrothermal dolomites): the Pozalagua Quarry case study (Cantabria, North-west Spain). *Sedimentology*, 59(2), pp. 623-645.

Kurz, T.H., Buckley, S.J. and Howell, J.A., 2013. Close-range hyperspectral imaging for geological field studies: workflow and methods. *International Journal of Remote Sensing*, 34(5), pp. 1798-1822.

Krautblatter, M. and Dikau, R., 2007. Towards a uniform concept for the comparison and extrapolation of rockwall retreat and rockfall supply. Geografiska Annaler: Series A, Physical Geography, 89(1), pp.21-40.

Lague, D., Brodu, N. and Leroux, J., 2013. Accurate 3D comparison of complex topography with terrestrial laser scanner: Application to the Rangitikei canyon (NZ). *ISPRS Journal of Photogrammetry and Remote Sensing*, 82, pp. 10-26.

Laine, S. and Karras, T., 2011. Efficient sparse voxel octrees. *IEEE Transactions on Visualization and Computer Graphics*, 17(8), pp. 1048-1059.

Lajtai, E.Z., Schmidtke, R.H. and Bielus, L.P., 1987. The effect of water on the time-dependent deformation and fracture of a granite. *International Journal of Rock Mechanics and Mining Sciences & Geomechanics Abstracts*, 24(4), pp. 247-255.

Lalonde, J.F., Unnikrishnan, R., Vandapel, N. and Hebert, M., 2005. Scale selection for classification of point-sampled 3D surfaces. In *Proceedings of the 5th International Conference on 3-D Digital Imaging and Modeling*. Ottowa, Canada, 13 – 16 June.

IEEE, pp. 285-292.

Lane, S.N. and Chandler, J.H., 2003. Editorial: the generation of high quality topographic data for hydrology and geomorphology: new data sources, new applications and new problems. *Earth Surface Processes and Landforms*, 28(3), pp. 229-230.

Larsen, I.J., Montgomery, D.R. and Korup, O., 2010. Landslide erosion controlled by hillslope material. *Nature Geoscience*, 3(4), pp. 247-251.

Larsen, M.C. and Simon, A., 1993. A rainfall intensity-duration threshold for landslides in a humid-tropical environment, Puerto Rico. *Geografiska Annaler. Series A. Physical Geography*, pp. 13-23.

Larsen, N.K. and Piotowski, J.A., 2005. Fabric pattern in a basal till succession and its significance for reconstructing subglacial processes - Reply. *Journal of Sedimentary Research*, 75(2), pp. 325-326.

Lato, M.J., Diederichs, M.S. and Hutchinson, D.J., 2010. Bias correction for view-limited Lidar scanning of rock outcrops for structural characterization. *Rock Mechanics and Rock Engineering*, 43(5), pp. 615-628.

Lato, M.J. and Vöge, M., 2012. Automated mapping of rock discontinuities in 3D lidar and photogrammetry models. *International Journal of Rock Mechanics and Mining Sciences*, 54, pp. 150-158.

Lefsky, M.A., Harding, D.J., Keller, M., Cohen, W.B., Carabajal, C.C., Del Bom Espirito-Santo, F., Hunter, M.O. and de Oliveira, R., 2005. Estimates of forest canopy height and aboveground biomass using ICESat. *Geophysical Research Letters*, 32(22).

Leroueil, S. 2001. Natural slopes and cuts: movement and failure mechanisms. *Géotechnique*, 51(3), pp. 197-243.

Li, G., West, A.J., Densmore, A.L., Jin, Z., Parker, R.N. and Hilton, R.G., 2014. Seismic mountain building: Landslides associated with the 2008 Wenchuan earthquake in the context of a generalized model for earthquake volume balance. *Geochemistry, Geophysics, Geosystems*, 15(4), pp. 833-844.

Li, G., West, A.J., Densmore, A.L., Hammond, D.E., Jin, Z., Zhang, F., Wang, J. and Hilton, R.G., 2016. Connectivity of earthquake-triggered landslides with the fluvial network: Implications for landslide sediment transport after the 2008 Wenchuan earthquake. *Journal of Geophysical Research: Earth Surface*, 121(4), pp. 703-724.

Lichti, D.D., Gordon, S.J. and Stewart, M.P., 2002. Ground-based laser scanners: operation, systems and applications. *Geomatica*, 56(1), pp. 21-33.

Licthi, D.D. and Franke, J., 2005. Self-calibration of the iQsun 880 laser scanner. In Grün, A. and Kahmen, H. (eds.) *Proceedings of 7th Conference in Optical 3D Measurement Techniques.* Vienna, Austria, 3 – 5 October, pp. 112-121.

Lichti, D.D., Gordon, S.J. and Tipdecho, T., 2005. Error models and propagation in directly georeferenced terrestrial laser scanner networks. *Journal of Surveying Engineering*, 131(4), pp. 135-142.

Lichti, D.D. and Jamtsho, S., 2006. Angular resolution of terrestrial laser scanners. *The*

Photogrammetric Record, 21(114), pp. 141-160.

Lichti, D.D., 2007. Error modelling, calibration and analysis of an AM–CW terrestrial laser scanner system. *ISPRS Journal of Photogrammetry and Remote Sensing*, 61(5), pp. 307-324.

Lichti, D.D. and Lampard, J., 2008. Reflectorless total station self-calibration. *Survey Review*, 40(309), pp. 244-259.

Lichti, D.D. and Skaloud, J., 2010. Registration and Calibration. Vosselman, G. and Maas, H.-G. (eds.) *Airborne and Terrestrial Laser Scanning*. Caithness, UK: Whittles Publishing, pp. 83-133.

Lim, M., Petley, D.N., Rosser, N.J., Allison, R.J., Long, A.J. and Pybus, D., 2005. Combined digital photogrammetry and time-of-flight laser scanning for monitoring cliff evolution. *The Photogrammetric Record*, 20(110), pp. 109-129.

Lim, M., Rosser, N.J., Allison, R.J. and Petley, D.N., 2010. Erosional processes in the hard rock coastal cliffs at Staithes, North Yorkshire. *Geomorphology*, 114(1), pp. 12-21.

Lim, M., Rosser, N.J., Petley, D.N. and Keen, M., 2011. Quantifying the controls and influence of tide and wave impacts on coastal rock cliff erosion. *Journal of Coastal Research*, 27(1), pp. 46-56.

Lockner, D.A., 1995. Rock failure. In Ahrens, T.J. (ed.) *Rock Physics & Phase Relations: A Handbook of Physical Constants*. Washington, D.C.: American Geophysical Union pp. 127-147.

Lucieer, A., de Jong, S. and Turner, D., 2014. Mapping landslide displacements using Structure from Motion (SfM) and image correlation of multi-temporal UAV photography. *Progress in Physical Geography*, 38(1), pp. 97-116.

Lukas, S., Benn, D.I., Boston, C.M., Brook, M., Coray, S., Evans, D.J., Graf, A., Kellerer-Pirklbauer, A., Kirkbride, M.P., Krabbendam, M. and Lovell, H., 2013. Clast shape analysis and clast transport paths in glacial environments: A critical review of methods and the role of lithology. *Earth-Science Reviews*, 121, pp. 96-116.

Main, I.G., 2000. A damage mechanics model for power-law creep and earthquake aftershock and foreshock sequences. *Geophysical Journal International*, 142(1), pp. 151-161.

Malamud, B.D., Turcotte, D.L., Guzzetti, F. and Reichenbach, P., 2004. Landslides, earthquakes, and erosion. *Earth and Planetary Science Letters*, 229(1), pp. 45-59.

Marques, F.M.S.F., 2008. Magnitude-frequency of sea cliff instabilities. *Natural Hazards and Earth System Sciences*, 8(5), pp. 1161-1171.

Martel, S.J., 2006. Effect of topographic curvature on near-surface stresses and application to sheeting joints. *Geophysical Research Letters*, 33(1), 5 p.

Martel, S.J., 2011. Mechanics of curved surfaces, with application to surface-parallel cracks. *Geophysical Research Letters*, 38(20), 6 p.

Martin, C.D. and Chandler, N.A., 1994. The progressive fracture of Lac du Bonnet granite. *International Journal of Rock Mechanics and Mining Sciences & Geomechanics Abstracts*, 31(6), pp. 643-659.

Matsuoka, N. and Sakai, H., 1999. Rockfall activity from an alpine cliff during thawing periods. *Geomorphology*, 28(3), pp. 309-328.

Matsuoka, N. and Murton, J., 2008. Frost weathering: recent advances and future directions. *Permafrost and Periglacial Processes*, 19(2), pp. 195-210.

Mathworks, 2017. *Parallel Computing Toolbox*. Available at: https://uk.mathworks.com/products/parallel-computing.html (Accessed: 3 March 2014)

Mazzanti, P., Bozzano, F., Cipriani, I. and Prestininzi, A., 2015. New insights into the temporal prediction of landslides by a terrestrial SAR interferometry monitoring case study. *Landslides*, 12(1), pp. 55-68.

McCoy, S.W., Kean, J.W., Coe, J.A., Staley, D.M., Wasklewicz, T.A. and Tucker, G.E., 2010. Evolution of a natural debris flow: In situ measurements of flow dynamics, video imagery, and terrestrial laser scanning. *Geology*, 38(8), pp. 735-738.

Met Office, 2015. *Storm Desmond*. Available at: http://www.metoffice.gov.uk/barometer/uk-storm-centre/storm-desmond (Accessed: 5 March 2016)

Meunier, P., Hovius, N. and Haines, J.A., 2008. Topographic site effects and the location of earthquake induced landslides. *Earth and Planetary Science Letters*, 275(3), pp. 221-232.

Milan, D.J., Heritage, G.L. and Hetherington, D., 2007. Application of a 3D laser scanner in the assessment of erosion and deposition volumes and channel change in a proglacial river. *Earth Surface Processes and Landforms*, 32(11), pp. 1657-1674.

Milan, D.J., Heritage, G.L., Large, A.R. and Fuller, I.C., 2011. Filtering spatial error from DEMs: Implications for morphological change estimation. *Geomorphology*, 125(1), pp. 160-171.

Miller, P.E., 2007. *A robust surface matching technique for coastal geohazard monitoring*. PhD thesis. Newcastle. Available at: https://theses.ncl.ac.uk/dspace/handle/10443/784 (Accessed: 11 December 2016).

Mitchell, J.K., Campanella, R.G. and Singh, A., 1964. Soil creep as a rate process. *Journal of the Soil Mechanics and Foundations Division, ASCE*, 94(1), pp. 231-253.

Mitra, N.J. and Nguyen, A., 2003. Estimating surface normals in noisy point cloud data. In *Proceedings of the 19th Annual Symposium on Computational Geometry*. San Diego, California, 8 – 10 June. New York: ACM, pp. 322-328.

Mitra, N.J., Gelfand, N., Pottmann, H. and Guibas, L., 2004. Registration of point cloud data from a geometric optimization perspective. In *Proceedings of the 2004 Eurographics/ACM SIGGRAPH Symposium on Geometry Processing*. Nice, France, 8 – 10 July. New York: ACM, pp. 22-31.

Moore, L.J., 2000. Shoreline mapping techniques. *Journal of Coastal Research*, pp. 111-124.

Monserrat, O. and Crosetto, M., 2008. Deformation measurement using terrestrial laser scanning data and least squares 3D surface matching. *ISPRS Journal of Photogrammetry and Remote Sensing*, 63(1), pp. 142-154.

Monserrat, O., Crosetto, M. and Luzi, G., 2014. A review of ground-based SAR

interferometry for deformation measurement. *ISPRS Journal of Photogrammetry and Remote Sensing*, 93, pp. 40-48.

Moreiras, S.M., 2006. Frequency of debris flows and rockfall along the Mendoza river valley (Central Andes), Argentina: Associated risk and future scenario. *Quaternary International*, 158(1), pp. 110-121.

Mufundirwa, A., Fujii, Y., Kodama, N. and Kodama, J.I., 2011. Analysis of natural rock slope deformations under temperature variation: A case from a cool temperate region in Japan. *Cold Regions Science and Technology*, 65(3), pp. 488-500.

Murad, M.A., Guerreiro, J.N. and Loula, A.F., 2001. Micromechanical computational modeling of secondary consolidation and hereditary creep in soils. *Computer Methods in Applied Mechanics and Engineering,* 190(15), pp. 1985-2016.

Murton, J.B., Peterson, R. and Ozouf, J.C., 2006. Bedrock fracture by ice segregation in cold regions. *Science*, 314(5802), pp. 1127-1129.

Navstar, 2015. *GeoExplorer Software*. Available at: http://www.navstar.com/products/software/ (Accessed: 17 May 2015).

Naylor, L.A., Stephenson, W.J. and Trenhaile, A.S., 2010. Rock coast geomorphology: recent advances and future research directions. *Geomorphology*, 114(1), pp. 3-11.

Nejati, H.R. and Ghazvinian, A., 2014. Brittleness effect on rock fatigue damage evolution. *Rock Mechanics and Rock Engineering*, 47(5), pp. 1839-1848.

Ni-Meister, W., Jupp, D.L. and Dubayah, R., 2001. Modeling lidar waveforms in heterogeneous and discrete canopies. *IEEE Transactions on Geoscience and Remote Sensing*, 39(9), pp. 1943-1958.

Niemi, N.A., Oskin, M., Burbank, D.W., Heimsath, A.M. and Gabet, E.J., 2005. Effects of bedrock landslides on cosmogenically determined erosion rates. *Earth and Planetary Science Letters*, 237(3), pp. 480-498.

Niethammer, U., Rothmund, S., Schwaderer, U., Zeman, J. and Joswig, M., 2011. Open source image-processing tools for low-cost UAV-based landslide investigations. *International Archives of the Photogrammetry, Remote Sensing and Spatial Information Sciences*, 38(1), pp. 161-166.

Norman, E.C., Rosser, N.J., Brain, M.J., Petley, D.N. and Lim, M., 2013. Coastal cliff-top ground motions as proxies for environmental processes. *Journal of Geophysical Research: Oceans*, 118(12), pp. 6807-6823.

Nurunnabi, A., Belton, D. and West, G., 2012. Diagnostic-robust statistical analysis for local surface fitting in 3D point cloud data. *ISPRS Annals of the Photogrammetry, Remote Sensing and Spatial Information Sciences*, 1-3, pp. 269-274.

Olsen, M.J., Kuester, F., Chang, B.J. and Hutchinson, T.C., 2010. Terrestrial laser scanning-based structural damage assessment. *Journal of Computing in Civil Engineering*, 24(3), pp. 264-272.

Oppikofer, T., Jaboyedoff, M. and Keusen, H.R., 2008. Collapse at the eastern Eiger flank in the Swiss Alps. *Nature Geoscience*, 1(8), pp. 531-535.

Oppikofer, T., Jaboyedoff, M., Blikra, L., Derron, M.H. and Metzger, R., 2009. Characterization and monitoring of the Åknes rockslide using terrestrial laser scanning. *Natural Hazards and Earth System Sciences*, 9(3), pp. 1003-1019.

Owen, L.A., Kamp, U., Khattak, G.A., Harp, E.L., Keefer, D.K. and Bauer, M.A., 2008. Landslides triggered by the 8 October 2005 Kashmir earthquake. *Geomorphology*, 94(1), pp. 1-9.

Parker, R.N., Densmore, A.L., Rosser, N.J., De Michele, M., Li, Y., Huang, R., Whadcoat, S. and Petley, D.N., 2011. Mass wasting triggered by the 2008 Wenchuan earthquake is greater than orogenic growth. *Nature Geoscience*, 4(7), pp. 449-452.

Pauly, M., Gross, M. and Kobbelt, L.P., 2002. Efficient simplification of point-sampled surfaces. In *Proceedings of the Conference on Visualization (VIS '02)*. Boston, MA, 27 October – 1 November. IEEE, pp. 163-170.

Pedrazzini, A., Oppikofer, T., Jaboyedoff, M., Chantry, R. and Stampfli, E., 2010. Assessment of rockslide and rockfall problems in an active quarry: case study of the Arvel quarry (western Switzerland). In *International Society for Rock Mechanics International Symposium – EUROCK 2010.* Lausanne, Switzerland, 15 – 18 June. London: Taylor & Francis, 4 p.

Pelletier, J.D., Malamud, B.D., Blodgett, T. and Turcotte, D.L., 1997. Scale-invariance of soil moisture variability and its implications for the frequency-size distribution of landslides. *Engineering Geology*, 48(3), pp. 255-268.

Perret, S., Stoffel, M. and Kienholz, H., 2006. Spatial and temporal rockfall activity in a forest stand in the Swiss Prealps - a dendrogeomorphological case study. *Geomorphology*, 74(1), pp. 219-231.

Pesci, A., Teza, G. and Ventura, G., 2008. Remote sensing of volcanic terrains by terrestrial laser scanner: preliminary reflectance and RGB implications for studying Vesuvius crater (Italy). *Annals of Geophysics*, 51(4), pp. 633-653.

Pesci, A., Teza, G. and Bonali, E., 2011. Terrestrial laser scanner resolution: numerical simulations and experiments on spatial sampling optimization. *Remote Sensing*, 3(1), pp. 167-184.

Petley, D.N., Bulmer, M.H. and Murphy, W., 2002. Patterns of movement in rotational and translational landslides. *Geology*, 30(8), pp. 719-722.

Petley, D.N., Higuchi, T., Petley, D.J., Bulmer, M.H. and Carey, J., 2005. Development of progressive landslide failure in cohesive materials. *Geology*, 33(3), pp. 201-204.

Petley, D.N. and Rosser, N.J., 2006. On the mechanics of a typhoon induced landslide. In *Proceedings of the 10th Taiwan Geography Conference*. Taipei, China: The Geographical Society of China, pp. 150-162.

Petley, D.N., Hearn, G.J., Hart, A., Rosser, N.J., Dunning, S.A., Oven, K. and Mitchell, W.A., 2007. Trends in landslide occurrence in Nepal. *Natural Hazards*, 43(1), pp. 23-44.

Petley, D.N., Petley, D.J. and Allison, R.J., 2008. Temporal prediction in landslides–understanding the Saito effect. In Chen, Z., Zhang, J., Li, Z., Wu, F. and Ho, K. (eds.)

Landslides and Engineered Slopes: From the Past to the Future. Proceedings of the 10th International Symposium on Landslides and Engineered Slopes. Xi'an, China, 30 June – 4 July. The Netherlands: CRC Press, pp. 865-871.

Petley, D.N., 2012. Global patterns of loss of life from landslides. *Geology*, 40(10), pp. 927-930.

Petrie, G. and Toth, C.K., 2009. Terrestrial laser scanners. In Shan, J. and Toth, C.K. (eds.) *Topographic Laser Ranging and Scanning: Principles and Processing*. Boca Raton, FL: CRC Press, pp. 87-128.

Pfeifer, N., Höfle, B., Briese, C., Rutzinger, M. and Haring, A., 2008. Analysis of the backscattered energy in terrestrial laser scanning data. *International Archives of the Photogrammetry, Remote Sensing and Spatial Information Sciences,* 37, pp. 1045-1052.

Phillips, M., Wolter, A., Lüthi, R., Amann, F., Kenner, R. and Bühler, Y., 2016. Rock slope failure in a recently deglaciated permafrost rock wall at Piz Kesch (Eastern Swiss Alps). *Earth Surface Processes and Landforms*, 13 p. doi: 10.1002/esp.3992.

Pottmann, H. and Hofer, M., 2003. Geometry of the squared distance function to curves and surfaces. In Hege, H.-C. and Polthier, K. (eds.) *Visualization and Mathematics III*. Berlin, Germany: Springer, pp. 221-242.

Powell, J.H., 2010. Jurassic sedimentation in the Cleveland Basin: a review. *Proceedings of the Yorkshire Geological Society*, 58(1), pp. 21-72.

Pratt, H.R., Black, A.D., Brown, W.S. and Brace, W.F., 1972. The effect of specimen size on the mechanical properties of unjointed diorite. *International journal of Rock Mechanics and Mining Science and Geomechanics Abstracts,* 9, pp. 513-529.

Putelat, T. and Dawes, J.H., 2015. Steady and transient sliding under rate-and-state friction. *Journal of the Mechanics and Physics of Solids*, 78, pp. 70-93.

Rabbani, T., Van Den Heuvel, F. and Vosselmann, G., 2006. Segmentation of point clouds using smoothness constraint. *International Archives of Photogrammetry, Remote Sensing and Spatial Information Sciences*, 36(5), pp. 248-253.

Rahardjo, H., Li, X.W., Toll, D.G. and Leong, E.C., 2001. The effect of antecedent rainfall on slope stability. *Geotechnical & Geological Engineering*. 19(3), pp. 371-399.

Reches, Z.E. and Lockner, D.A., 1994. Nucleation and growth of faults in brittle rocks. *Journal of Geophysical Research: Solid Earth*, 99(B9), pp. 18,159-18,173.

Riegl, 2015. *Data Sheet Riegl VZ-1000*. Available at: http://www.riegl.com/uploads/tx_pxpriegldownloads/DataSheet_VZ-1000_2015-03- 24.pdf (Accessed: 5 June 2016).

Riquelme, A.J., Abellán, A., Tomás, R. and Jaboyedoff, M., 2014. A new approach for semi-automatic rock mass joints recognition from 3D point clouds. *Computers & Geosciences*, 68, pp. 38-52.

Robinson, T.R., Davies, T.R.H., Wilson, T.M. and Orchiston, C., 2016. Coseismic landsliding estimates for an Alpine Fault earthquake and the consequences for erosion of the Southern Alps, New Zealand. *Geomorphology*, 263, pp. 71-86.

Rohmer, J. and Dewez, T., 2015. Analysing the spatial patterns of erosion scars using point

process theory at the coastal chalk cliff of Mesnil-Val, Normandy, northern France. *Natural Hazards and Earth System Sciences*, 15(2), pp. 349-362.

Rose, N.D. and Hungr, O., 2007. Forecasting potential rock slope failure in open pit mines using the inverse-velocity method. *International Journal of Rock Mechanics and Mining Sciences*, 44(2), pp. 308-320.

Rosser, N.J., Petley, D.N., Lim, M., Dunning, S.A. and Allison, R.J., 2005. Terrestrial laser scanning for monitoring the process of hard rock coastal cliff erosion. *Quarterly Journal of Engineering Geology and Hydrogeology*, 38(4), pp. 363-375.

Rosser, N.J., Lim, M., Petley, D.N., Dunning, S.A. and Allison, R., 2007a. Patterns of precursory rockfall prior to slope failure. *Journal of Geophysical Research: Earth Surface*, 112(F4), 14 p.

Rosser, N.J., Petley, D.N., Dunning, S.A., Lim, M. and Ball, S., 2007b. The surface expression of strain accumulation in failing rock masses. In Eberhardt, E., Stead, D. and Morrison, T. (eds.) *Rock Mechanics: Meeting Society's Challenges and Demands. Proceedings of the 1st Canada-US Rock Mechanics Symposium.* Vancouver, Canada, 27 – 31 May. London: CRC Press, pp. 113-120.

Rosser, N.J., Brain, M.J., Petley, D.N., Lim, M. and Norman, E.C., 2013. Coastline retreat via progressive failure of rocky coastal cliffs. *Geology*, 41(8), pp. 939-942.

Roth-Tabak, Y. and Jain, R., 1989. Building an environment model using depth information. *Computer*, 22(6), pp. 85-90.

Royán, M.J., Abellán, A. and Vilaplana, J.M., 2015. Progressive failure leading to the 3 December 2013 rockfall at Puigcercós scarp (Catalonia, Spain). *Landslides*, 12(3), pp. 585-595.

Rüeger, J.M., 2003. *Electronic Surveying Instruments: A Review of Principles, Problems and Procedures*. Sydney, Australia: University of New South Wales, 156 p.

Ruina, A., 1983. Slip instability and state variable friction laws. *Journal of Geophysical Research: Solid Earth*, 88(B12), pp. 10359-10370.

Rutzinger, M., Pratihast, A.K., Oude Elberink, S.J. and Vosselman, G., 2011. Tree modelling from mobile laser scanning datasets. *The Photogrammetric Record*, 26(135), pp. 361-372.

Saito, M., 1965. Forecasting the time of occurrence of a slope failure. In *Proceedings of the 6th International Congress of Soil Mechanics and Foundation Engineering*. Montreal, Canada, 8 – 15 September. Oxford: Pergamon Press, 2, pp. 537-541.

Salo, P., Jokinen, O. and Kukko, A., 2008. On the calibration of the distance measuring component of a terrestrial laser scanner. In Chen, J. (ed.) *Proceedings of the 21st ISPRS Congress: Silk Road for Information from Imagery*. Beijing, China, 3 – 11 July. 37(B5), pp. 1067-1072.

Sandrock, 2008. *Alchemyst/Ternplot.* Available at: https://uk.mathworks.com/matlabcentral/fileexchange/2299-alchemyst-ternplot (Accessed: 20 November 2015).

Sartori, M., Baillifard, F., Jaboyedoff, M. and Rouiller, J.D., 2003. Kinematics of the 1991 Randa rockslides (Valais, Switzerland). *Natural Hazards and Earth System Science*, 3(5), pp.423-433.

Sass, O. and Oberlechner, M., 2012. Is climate change causing increased rockfall frequency in Austria? *Natural Hazards and Earth System Sciences*, 12(11), pp. 3209-3216.

Scheidl, C., Rickenmann, D. and Chiari, M., 2008. The use of airborne LiDAR data for the analysis of debris flow events in Switzerland. *Natural Hazards and Earth System Sciences*, 8(5), pp. 1113-1127.

Schneider, D. and Schwalbe, E., 2008. Integrated processing of terrestrial laser scanner data and fisheye-camera image data. *International Archives of Photogrammetry, Remote Sensing and Spatial Information Science*, 37, pp. 1037-1044.

Scholz, C.H., 1968. Microfracturing and the inelastic deformation of rock in compression. *Journal of Geophysical Research*, 73(4), pp. 1417-1432.

Scholz, C.H., 1998. Earthquakes and friction laws. *Nature*, 391(6662), pp. 37-42.

Schürch, P., Densmore, A.L., Rosser, N.J., Lim, M. and McArdell, B.W., 2011. Detection of surface change in complex topography using terrestrial laser scanning: application to the Illgraben debris-flow channel. *Earth Surface Processes and Landforms*, 36(14), pp. 1847-1859.

Schuster, R.L. and Wieczorek, G.F., 2002. Landslide triggers and types. In Rybar, J., Stemberk, J. and Wagner, P. (Eds.) *Proceedings of the First European Conference on Landslides*. Prague, Czech Republic, 24 – 26 June. Lisse: Balkema, pp. 59-78.

Selby, M.J., 2005. *Hillslope Materials and Processes*. Oxford: Oxford University Press, 451 p.

Senfaute, G., Duperret, A. and Lawrence, J.A., 2009. Micro-seismic precursory cracks prior to rock-fall on coastal chalk cliffs: a case study at Mesnil-Val, Normandie, NW France. *Natural Hazards and Earth System Sciences*, 9(5), pp. 1625-1641.

Shea, W.T. and Kronenberg, A.K., 1992. Rheology and deformation mechanisms of an isotropic mica schist. *Journal of Geophysical Research: Solid Earth*, 97(B11), pp. 15201-15237.

Šilhán, K. and Pánek, T., 2010. Fossil and recent debris flows in medium–high mountains (Moravskoslezské Beskydy Mts, Czech Republic). *Geomorphology*, 124(3), pp. 238-249.

Siman-Tov, S., Katz, O. and Matmon, A., 2017. Examining the effects of ground motion and rock strength on the size of boulders falling from an overhanging cliff. *Engineering Geology*, 220, pp. 164-174.

Simard, M., Pinto, N., Fisher, J.B. and Baccini, A., 2011. Mapping forest canopy height globally with spaceborne lidar. *Journal of Geophysical Research: Biogeosciences*, 116(G4).

Slob, S., Hack, R. and Turner, A.K., 2002. An approach to automate discontinuity measurements of rock faces using laser scanning techniques. In *International Society for Rock Mechanics International Symposium – EUROCK 2002.* Madeira, Portugal, 25 – 27 November. London: Taylor & Francis, pp 87-94.

Snavely, N., Seitz, S.M. and Szeliski, R., 2008. Modeling the world from internet photo collections. *International Journal of Computer Vision*, 80(2), pp. 189-210.

Sneed, E.D. and Folk, R.L., 1958. Pebbles in the lower Colorado River, Texas, a study in

particle morphogenesis. *The Journal of Geology*, pp. 114-150.

Sornette, D., Helmstetter, A., Andersen, J.V., Gluzman, S., Grasso, J.R. and Pisarenko, V., 2004. Towards landslide predictions: two case studies. *Physica A: Statistical Mechanics and its Applications*, 338(3), pp. 605-632.

Soudarissanane, S., Lindenbergh, R., Menenti, M. and Teunissen, P.J.G., 2009. Incidence angle influence on the quality of terrestrial laser scanning points. In *Proceedings of the ISPRS Workshop on Laser Scanning*. Paris, France, 1 – 2 September. 38(W8), pp. 183-188.

Soudarissanane, S., Lindenbergh, R., Menenti, M. and Teunissen, P., 2011. Scanning geometry: Influencing factor on the quality of terrestrial laser scanning points. *ISPRS Journal of Photogrammetry and Remote Sensing*, 66(4), pp. 389-399.

Soudarissanane, S.S., 2016. *The geometry of terrestrial laser scanning; identification of errors, modeling and mitigation of scanning geometry*. Ph.D. Delft University of Technology. Available at: 10.4233/uuid:b7ae0bd3-23b8-4a8a-9b7d-5e494ebb54e5 (Accessed: 2 November 2012).

Stead, D. and Wolter, A., 2015. A critical review of rock slope failure mechanisms: The importance of structural geology. *Journal of Structural Geology*, 74, pp. 1-23.

Stilla, U. and Jutzi, B., 2008. Waveform analysis for small-footprint pulsed laser systems. In: Shan, J. and Toth, C. (eds.), *Topographic Laser Ranging and Scanning Principles and Processing*. CRC Press Taylor & Francis Group: Boca Raton, pp. 215-234.

Stock, G.M., Martel, S.J., Collins, B.D. and Harp, E.L., 2012. Progressive failure of sheeted rock slopes: the 2009–2010 Rhombus Wall rock falls in Yosemite Valley, California, USA. *Earth Surface Processes and Landforms*, 37(5), pp. 546-561.

Strunden, J., Ehlers, T.A., Brehm, D. and Nettesheim, M., 2015. Spatial and temporal variations in rockfall determined from TLS measurements in a deglaciated valley, Switzerland. *Journal of Geophysical Research: Earth Surface*, 120(7), pp. 1251-1273.

Stumpf, A., Malet, J.P., Allemand, P., Pierrot-Deseilligny, M. and Skupinski, G., 2015. Ground-based multi-view photogrammetry for the monitoring of landslide deformation and erosion. *Geomorphology*, 231, pp. 130-145.

Sturzenegger, M., Yan, M., Stead, D. and Elmo, D., 2007. Application and limitations of ground-based laser scanning in rock slope characterization. In Eberhardt, E., Stead, D. and Morrison, T. (eds.) *Rock Mechanics: Meeting Society's Challenges and Demands. Proceedings of the 1st Canada-US Rock Mechanics Symposium.* Vancouver, Canada, 27 – 31 May. London: CRC Press, pp. 29-36.

Sturzenegger, M. and Stead, D., 2009a. Quantifying discontinuity orientation and persistence on high mountain rock slopes and large landslides using terrestrial remote sensing techniques. *Natural Hazards and Earth System Sciences*, 9(2), pp. 267-287.

Sturzenegger, M. and Stead, D., 2009b. Close-range terrestrial digital photogrammetry and terrestrial laser scanning for discontinuity characterization on rock cuts. *Engineering Geology*, 106(3), pp. 163-182.

Styles, T.D., Coggan, J.S. and Pine, R.J., 2011. Back analysis of the Joss Bay Chalk Cliff Failure using numerical modelling. *Engineering Geology*, 120(1), pp. 81-90.

Suwa, H., Hirano, M. and Okunishi, K., 1991. Rock failure of a cut slope in the Kyusyu Shimanto Geologic Belt, Japan. In *Annals of the Disaster Prevention Research Institute*. Kyoto, Japan: Kyoto University, 34(B1), pp. 139-151.

Suwa, H., Mizuno, T., Suzuki, S., Yamamoto, Y. and Ito, K., 2008. Sequential processes in a landslide hazard at a slate quarry in Okayama, Japan. *Natural Hazards*, 45(2), pp. 321-331.

Ten Brink, U.S., Geist, E.L. and Andrews, B.D., 2006. Size distribution of submarine landslides and its implication to tsunami hazard in Puerto Rico. *Geophysical Research Letters*, 33(11), 4 p.

Terzaghi, K., 1950. Mechanism of landslides. In Paige, S. (ed.) *Application of Geology to Engineering Practice (Berkeley Volume).* Washington DC: Geological Society of America, pp. 83-123.

Teza, G., Galgaro, A., Zaltron, N. and Genevois, R., 2007. Terrestrial laser scanner to detect landslide displacement fields: a new approach. *International Journal of Remote Sensing*, 28(16), pp. 3425-3446.

Tonini, M. and Abellan, A., 2014. Rockfall detection from terrestrial LiDAR point clouds: A clustering approach using R. *Journal of Spatial Information Science*, 2014(8), pp. 95-110.

Travelletti, J., Oppikofer, T., Delacourt, C., Malet, J.P. and Jaboyedoff, M., 2008. Monitoring landslide displacements during a controlled rain experiment using a long-range terrestrial laser scanning (TLS). *International Archives of the Photogrammetry, Remote Sensing and Spatial Information Sciences*, 37, pp.485-490.

Trenhaile, A.S., 1987. *The geomorphology of rock coasts*. Oxford University Press, USA, 84 p.

Tuckey, Z., Stead, D., Sturzenegger, M., Elmo, D. and Terbrugge, P., 2012. Towards a methodology for characterizing intact rock bridges in large open pits. In *Proceedings of 46th US Rock Mechanics Symposium and 5th U.S.-Canada Rock Mechanics Symposium*, 24 – 27 June, Chicago, Illinois. American Rock Mechanics Association, 12-251.

Tuckey, Z. and Stead, D., 2016. Improvements to field and remote sensing methods for mapping discontinuity persistence and intact rock bridges in rock slopes. *Engineering Geology*, 208, pp. 136-153.

Turcotte, D.L., Malamud, B.D., Guzzetti, F. and Reichenbach, P., 2002. Self-organization, the cascade model, and natural hazards. *Proceedings of the National Academy of Sciences*, 99(1), pp. 2530-2537.

Turcotte, D.L. and Malamud, B.D., 2004. Landslides, forest fires, and earthquakes: examples of self-organized critical behavior. *Physica A: Statistical Mechanics and its Applications*, 340(4), pp. 580-589.

Turner, D., Lucieer, A. and de Jong, S.M., 2015. Time series analysis of landslide dynamics using an unmanned aerial vehicle (UAV). *Remote Sensing*, 7(2), pp. 1736-1757.

Tymkow, P., Borkowski, A. and Norwida, C.K., 2010. Vegetation modelling based on

TLS data for roughness coefficient estimation in river Valley. *International Archives of the Photogrammetry, Remote Sensing and Spatial Information Science*, 38(8), pp. 309-313.

UCLA Statistics Consulting Group, 2016. *Regression with Stata*. Available at: http://www.ats.ucla.edu/stat/stata/webbooks/reg/chapter1/statareg1.htm (Accessed: 1 December 2016).

Valagussa, A., Frattini, P. and Crosta, G.B., 2014. Earthquake-induced rockfall hazard zoning. *Engineering Geology*, 182(B), pp. 213-225.

Vallianatos, F., 2013. On the statistical physics of rockfalls: a non-extensive view. *Europhysics Letters*, 101(1), 4 p.

Van Westen, C.J., Castellanos, E. and Kuriakose, S.L., 2008. Spatial data for landslide susceptibility, hazard, and vulnerability assessment: an overview. *Engineering Geology*, 102(3), pp. 112-131.

Vann Jones, E.C., Rosser, N.J., Brain, M.J. and Petley, D.N., 2015. Quantifying the environmental controls on erosion of a hard rock cliff. *Marine Geology*, 363, pp. 230-242.

Varnes, D.J., 1978. Slope movement types and processes. In Schuster, R.L. and Krizek, R.J. (eds.) *Landslides: Analysis and Control. Transportation Research Board Special Report 176*. Washington DC: National Academy of Science, pp. 11-33.

Vauchez, A., Tommasi, A. and Barruol, G., 1998. Rheological heterogeneity, mechanical anisotropy and deformation of the continental lithosphere. *Tectonophysics*, 296(1), pp. 61-86.

Verrecchia, E.P., Freytet, P., Julien, J. and Baltzer, F., 1997. The unusual hydrodynamical behaviour of freshwater oncolites. *Sedimentary Geology*, 113(3), pp. 225-243.

Viero, A., Teza, G., Massironi, M., Jaboyedoff, M. and Galgaro, A., 2010. Laser scanning-based recognition of rotational movements on a deep seated gravitational instability: The Cinque Torri case (North-Eastern Italian Alps). *Geomorphology*, 122(1), pp. 191-204.

Viles, H.A. and Goudie, A.S., 2003. Interannual, decadal and multidecadal scale climatic variability and geomorphology. *Earth-Science Reviews*, 61(1), pp. 105-131.

Viles, H.A, Ehlmann, B., Wilson, C.F., Cebula, T., Page, M. and Bourke, M., 2010. Simulating weathering of basalt on Mars and Earth by thermal cycling. *Geophysical Research Letters*, 37(18), 5 p.

Viles, H.A., 2013. Linking weathering and rock slope instability: non-linear perspectives. *Earth Surface Processes and Landforms*, 38(1), pp. 62-70.

Vlcko, J., Greif, V., Grof, V., Jezny, M., Petro, L. and Brcek, M., 2009. Rock displacement and thermal expansion study at historic heritage sites in Slovakia. *Environmental Geology*, 58(8), pp. 1,727-1,740.

Vöge, M., Lato, M.J. and Diederichs, M.S., 2013. Automated rockmass discontinuity mapping from 3-dimensional surface data. *Engineering Geology*, 164, pp. 155-162.

Voight, B., 1989. A relation to describe rate-dependent material failure. *Science*, 243(4,888), pp. 200-203.

Voisin, S., Foufou, S., Truchetet, F., Page, D. and Abidi, M., 2007. Study of ambient light influence for three-dimensional scanners based on structured light. *Optical Engineering*, 46(3), 4 p.

Vosselman, G., Gorte, B.G., Sithole, G. and Rabbani, T., 2004. Recognising structure in laser scanner point clouds. *International Archives of Photogrammetry, Remote Sensing and Spatial Information Sciences*, 46(8), pp. 33-38.

Wehr, A., 2009. LiDAR Systems and Calibration. In: Shan, J. and Toth, C. (eds.), *Topographic Laser Ranging and Scanning Principles and Processing*. CRC Press Taylor & Francis Group: Boca Raton, pp. 129-172.

Wheaton, J.M., Brasington, J., Darby, S.E. and Sear, D.A., 2010. Accounting for uncertainty in DEMs from repeat topographic surveys: improved sediment budgets. *Earth Surface Processes and Landforms*, 35(2), pp. 136-156.

Whitby Gazette, 2012. *Historic homes doomed by landslide*. Available at: http://www.whitbygazette.co.uk/news/historic-homes-doomed-by-landslide-1-5172749 (Accessed: 7 July 2015).

Wieczorek, G.F., and Snyder, J.B., 2009. Monitoring slope movements. In Young, R., and Norby, L. (eds.) *Geological Monitoring*. Boulder, CO: Geological Society of America, pp. 245-271.

Williams, J.G., Rosser, N.J., Afana, A., Hunter, G. and Hardy, R.J. 2013. Can full-waveform technology enhance the use of terrestrial laser scanning to monitor rock slope deformation? In Dight, P. (ed.) *Proceedings of the 2013 Symposium on Slope Stability in Open Pit Mining and Civil Engineering*. Brisbane, Australia, 25 – 27 September. Perth: Australian Centre for Geomechanics, pp. 763-775.

Wolman, M.G. and Miller, J.P., 1960. Magnitude and frequency of forces in geomorphic processes. *The Journal of Geology*, 68(1), pp. 54-74.

Wolters, G. and Müller, G., 2008. Effect of cliff shape on internal stresses and rock slope stability. *Journal of Coastal Research*, pp. 43-50.

Woo, H., Kang, E., Wang, S. and Lee, K.H., 2002. A new segmentation method for point cloud data. *International Journal of Machine Tools and Manufacture*, 42(2), pp. 167-178.

Wyllie, D.C. and Mah, C., 2004. *Rock slope engineering*. 4th edn. New York: Taylor & Francis, 456 p.

Xu, C., Xu, X., Yao, X. and Dai, F., 2014. Three (nearly) complete inventories of landslides triggered by the May 12, 2008 Wenchuan Mw 7.9 earthquake of China and their spatial distribution statistical analysis. *Landslides*, 11(3), pp. 441-461.

Xu, C., Xu, X. and Shyu, J.B.H., 2015. Database and spatial distribution of landslides triggered by the Lushan, China Mw 6.6 earthquake of 20 April 2013. *Geomorphology*, 248, pp. 77-92.

Yanites, B.J., Tucker, G.E., Mueller, K.J. and Chen, Y.G., 2010. How rivers react to

large earthquakes: Evidence from central Taiwan. *Geology*, 38(7), pp. 639-642.

Young, A.P., Guza, R.T., O'Reilly, W.C., Flick, R.E. and Gutierrez, R., 2011. Short-term retreat statistics of a slowly eroding coastal cliff. *Natural Hazards and Earth System Sciences*, 11(1), pp. 205-217.

Zavodni, Z.M., 2000. Time-dependent movements of open-pit slopes. In Hustrulid, W.A., McCarter, M.K. and Van Zyl, D.J.A. (eds.) *Slope Stability in Surface Mining*. Colorado, USA: Society for Mining, Metallurgy, and Exploration, pp. 81-87.

Zêzere, J.L., Trigo, R.M. and Trigo, I.F., 2005. Shallow and deep landslides induced by rainfall in the Lisbon region (Portugal): assessment of relationships with the North Atlantic Oscillation. *Natural Hazards and Earth System Sciences*, 5(3), pp. 331-344.

Zhang, Z., 1994. Iterative point matching for registration of free-form curves and surfaces. *International Journal of Computer Vision*, 13(2), pp. 119-152.

Zvelebill, J., 1985. Time prediction of a rockfall from a sandstone rock slope. In *Proceedings of the 4th International Symposium on Landslides*. Toronto, Canada, 16 – 21 September. Toronto: University of Toronto Press, 3, pp. 93-96.

Zvelebill, J. and Moser, M., 2001. Monitoring based time-prediction of rock falls: Three case-histories. *Physics and Chemistry of the Earth, Part B: Hydrology, Oceans and Atmosphere*, 26(2), pp. 159-167.

Appendices

Appendix A

Magnitude-frequency power laws for monitoring over the same period, but with different time intervals between scans, T_{int}.

Table A.1.1: *Intercept and exponent data used in Figure 5.27a and Figure 5.27c*

T_{int}	s	β
< 1 h	-4.020	-1.311
3 h	-3.445	-1.147
6 h	-3.175	-1.064
12 h	-2.872	-0.984
24 h	-2.641	-0.921
96 h	-2.212	-0.819
7 d	-2.010	-0.777
14 d	-1.988	-0.794
21 d	-1.984	-0.767
30 d	-1.888	-0.769
90 d	-1.652	-0.663

Table A.1.2: *Intercept and exponent data used in Figure 5.27b and Figure 5.27d*

T_{int}	T_{int}	T_{int}
< 1 h	0.671	-1.239
3 h	0.716	-1.060
6 h	0.205	-0.990
12 h	0.704	-0.920
24 h	0.679	-0.868
96 h	0.655	-0.812
7 d	0.661	-0.775
14 d	0.522	-0.833
21 d	0.589	-0.794
30 d	0.479	-0.822
90 d	0.528	-0.752

Table A.1.3: *Intercept and exponent data used in Figure 5.27c and Figure 5.27f*

T_{int}	T_{int}	T_{int}
< 1 h	1.185	-2.273
3 h	1.221	-2.090
6 h	1.224	-2.011
12 h	1.235	-1.925
24 h	1.210	-1.868
96 h	1.184	-1.800
7 d	1.169	-1.769
14 d	1.052	-1.806
21 d	1.065	-1.803
30 d	1.003	-1.778
90 d	1.102	-1.695

Appendix B

Video of failures from the rockface that occurred during the 10-month monitoring period.

https://www.youtube.com/watch?v=K4s_TJS0bAk

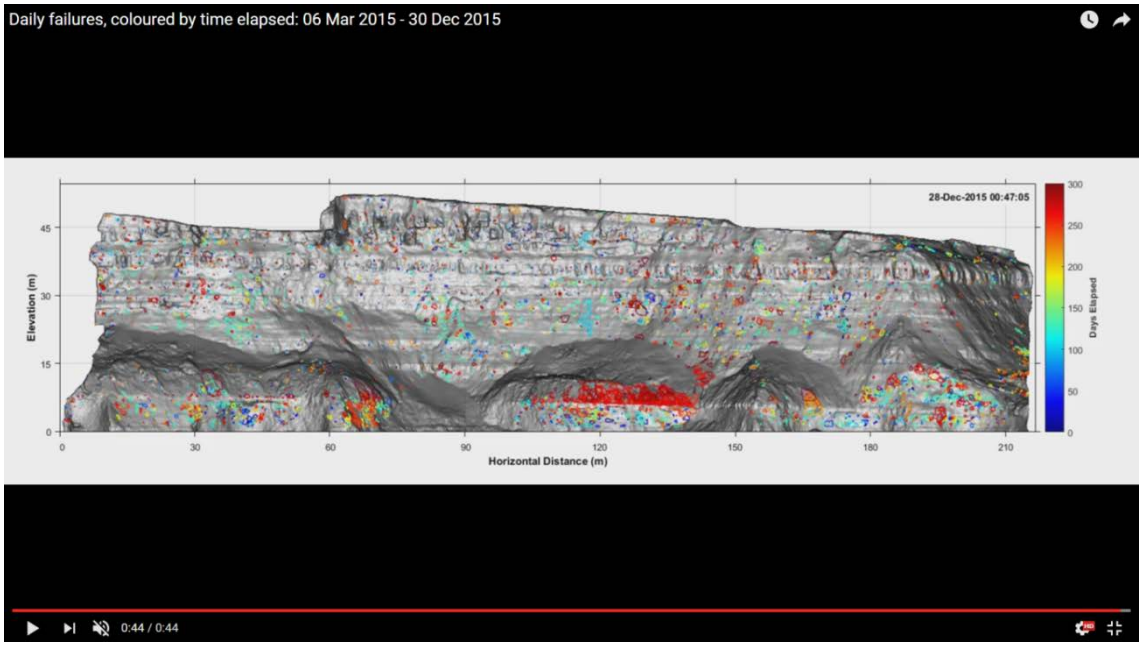

Appendix C

Further examples of the relationship between area of pre-failure activity recorded and the T_{int} of monitoring. Some failures are near-instantaneous and, therefore, the area does not change with monitoring interval. For others, pre-failure events are only distinguishable from high-frequency monitoring.

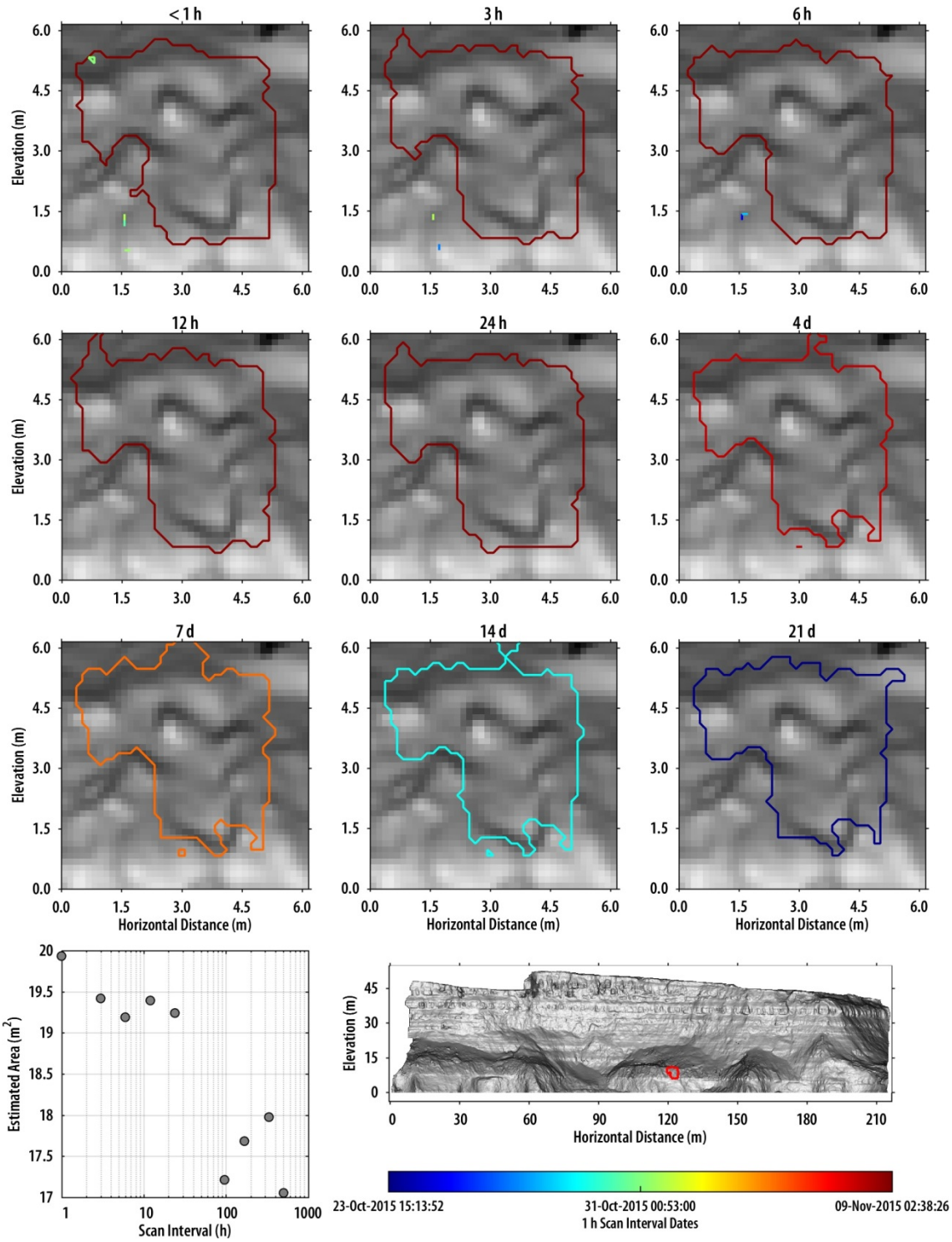

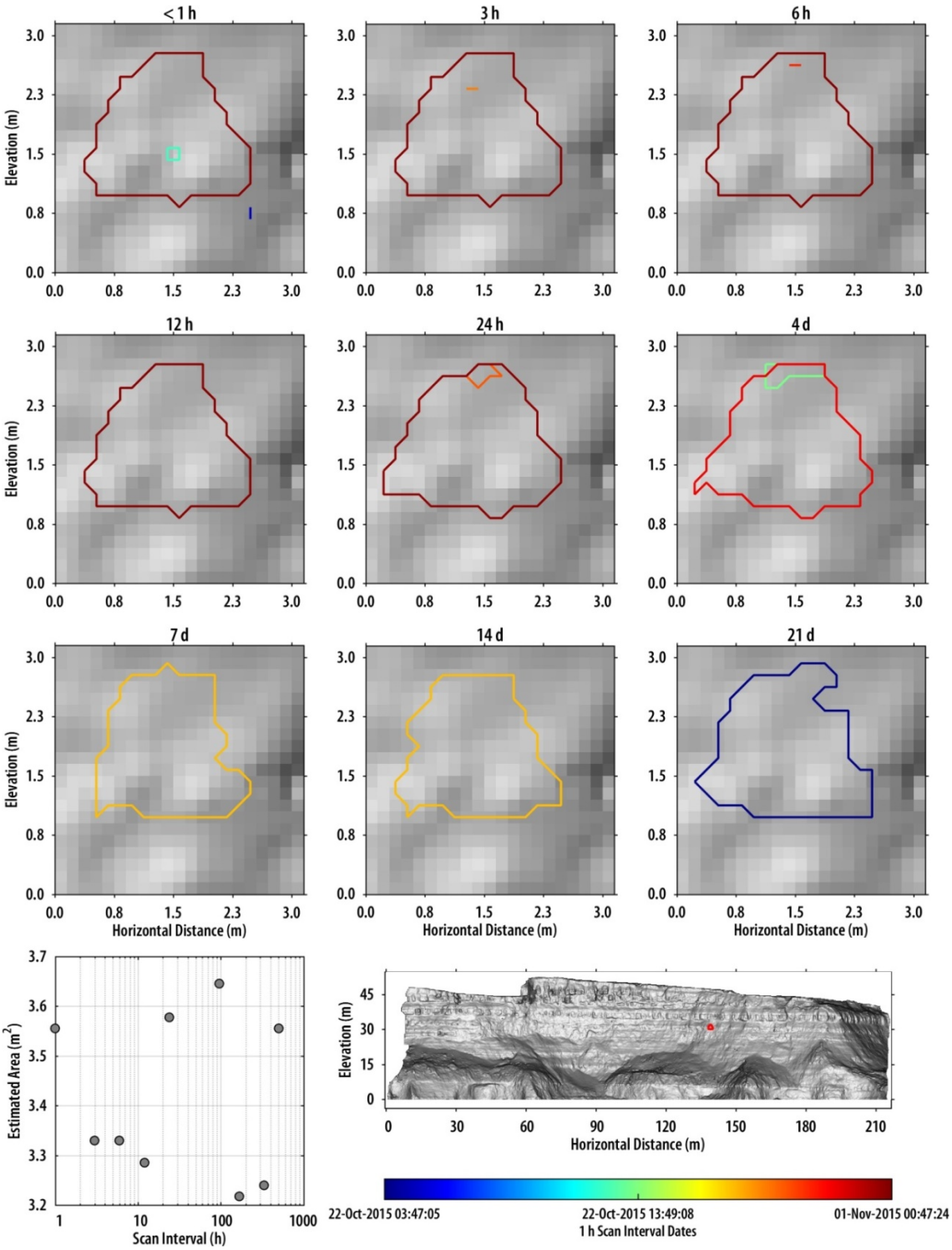
< 1 h
3 h
6 h
12 h
24 h
4 d
7 d
14 d
21 d
Elevation (m)
Horizontal Distance (m)
Estimated Area (m²)
Scan Interval (h)
22-Oct-2015 03:47:05
22-Oct-2015 13:49:08
01-Nov-2015 00:47:24
1 h Scan Interval Dates

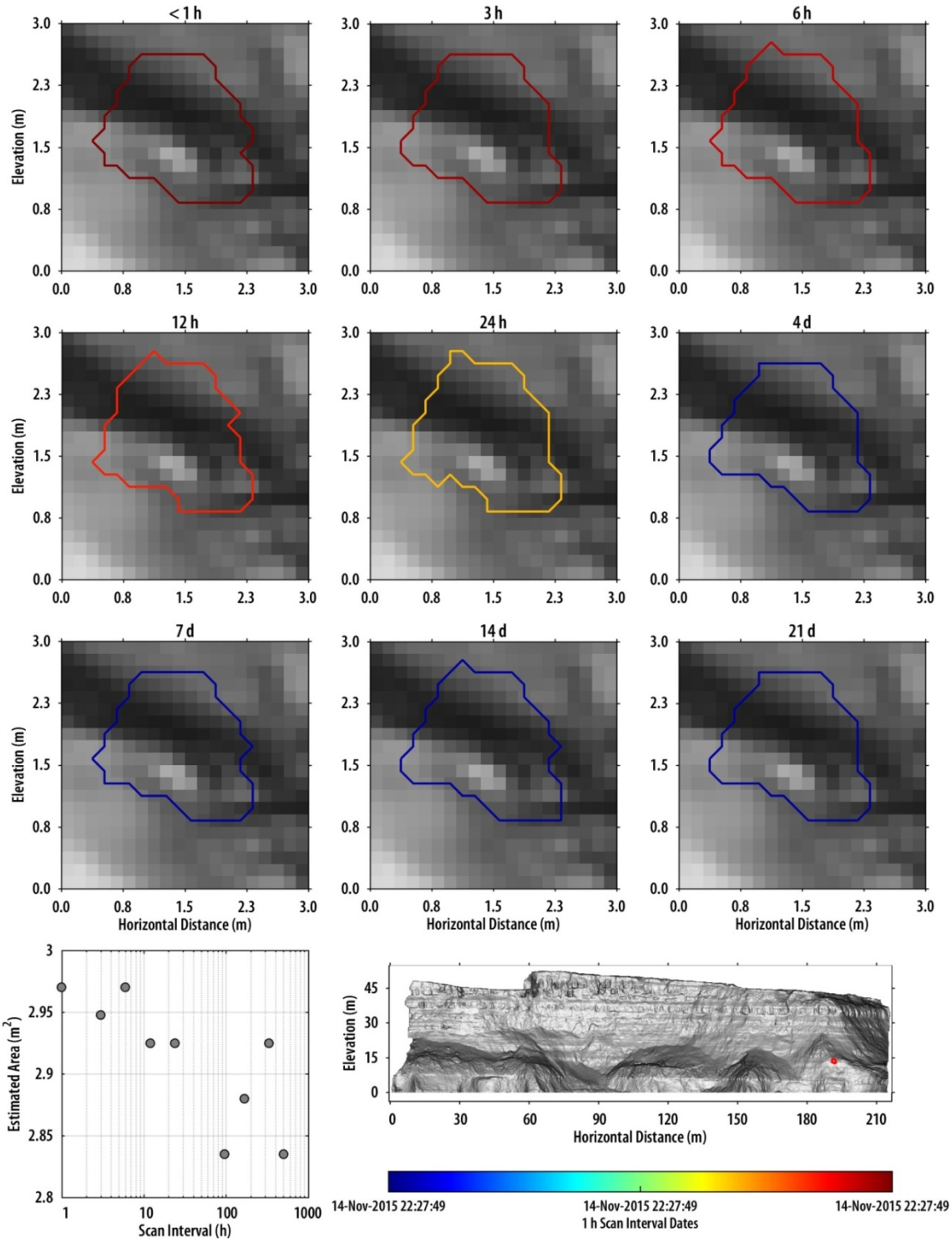
< 1 h
3 h
6 h
12 h
24 h
4 d
7 d
14 d
21 d
Elevation (m)
Horizontal Distance (m)
Estimated Area (m²)
Scan Interval (h)
Elevation (m)
Horizontal Distance (m)
14-Nov-2015 22:27:49
14-Nov-2015 22:27:49
1 h Scan Interval Dates
14-Nov-2015 22:27:49

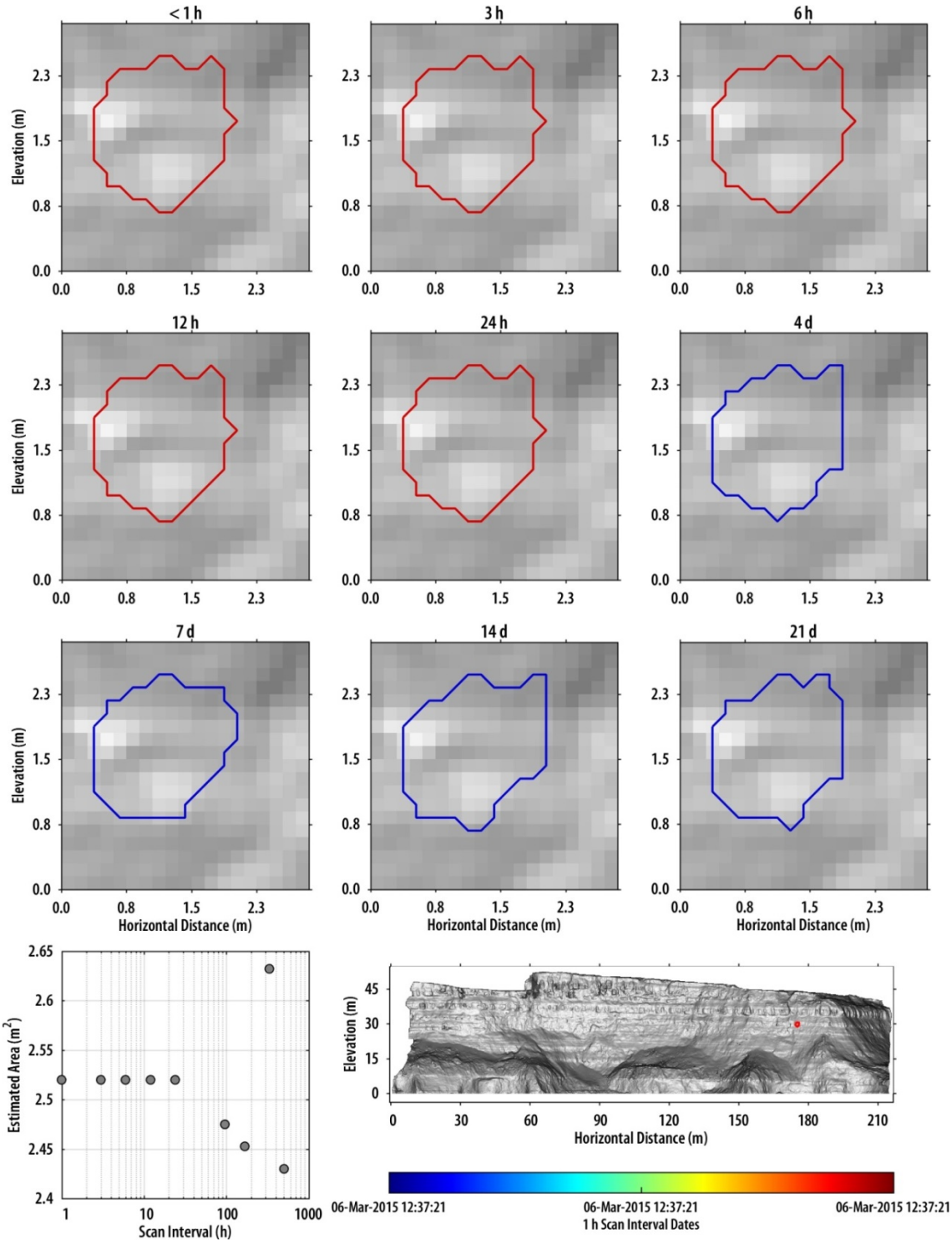
< 1 h
3 h
6 h
12 h
24 h
4 d
7 d
14 d
21 d
Elevation (m)
Horizontal Distance (m)
Estimated Area (m²)
Scan Interval (h)
Elevation (m)
Horizontal Distance (m)
06-Mar-2015 12:37:21
06-Mar-2015 12:37:21
1 h Scan Interval Dates
06-Mar-2015 12:37:21

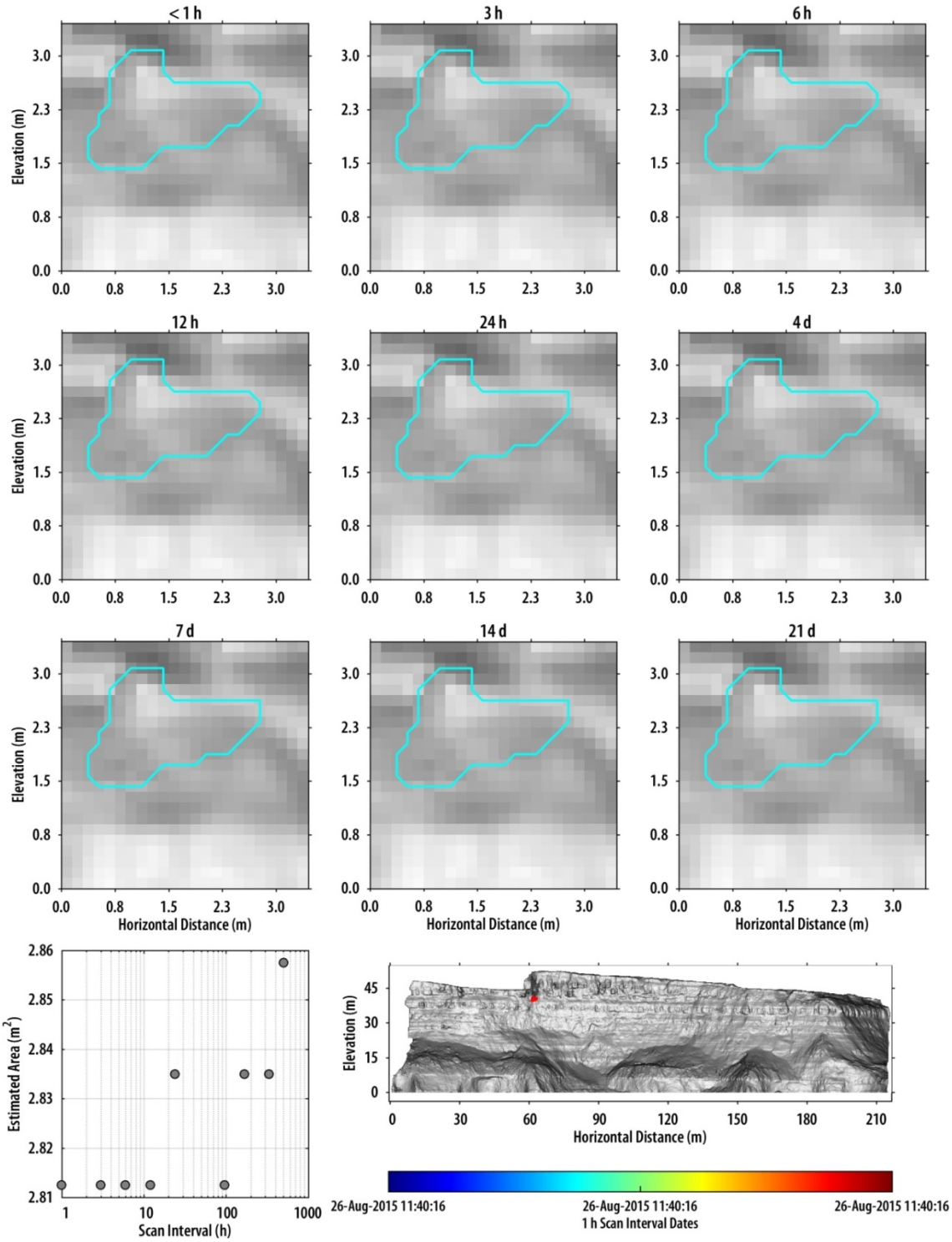
< 1 h
3 h
6 h
12 h
24 h
4 d
7 d
14 d
21 d
Elevation (m)
Horizontal Distance (m)
Estimated Area (m²)
Scan Interval (h)
26-Aug-2015 11:40:16
26-Aug-2015 11:40:16
1 h Scan Interval Dates
26-Aug-2015 11:40:16

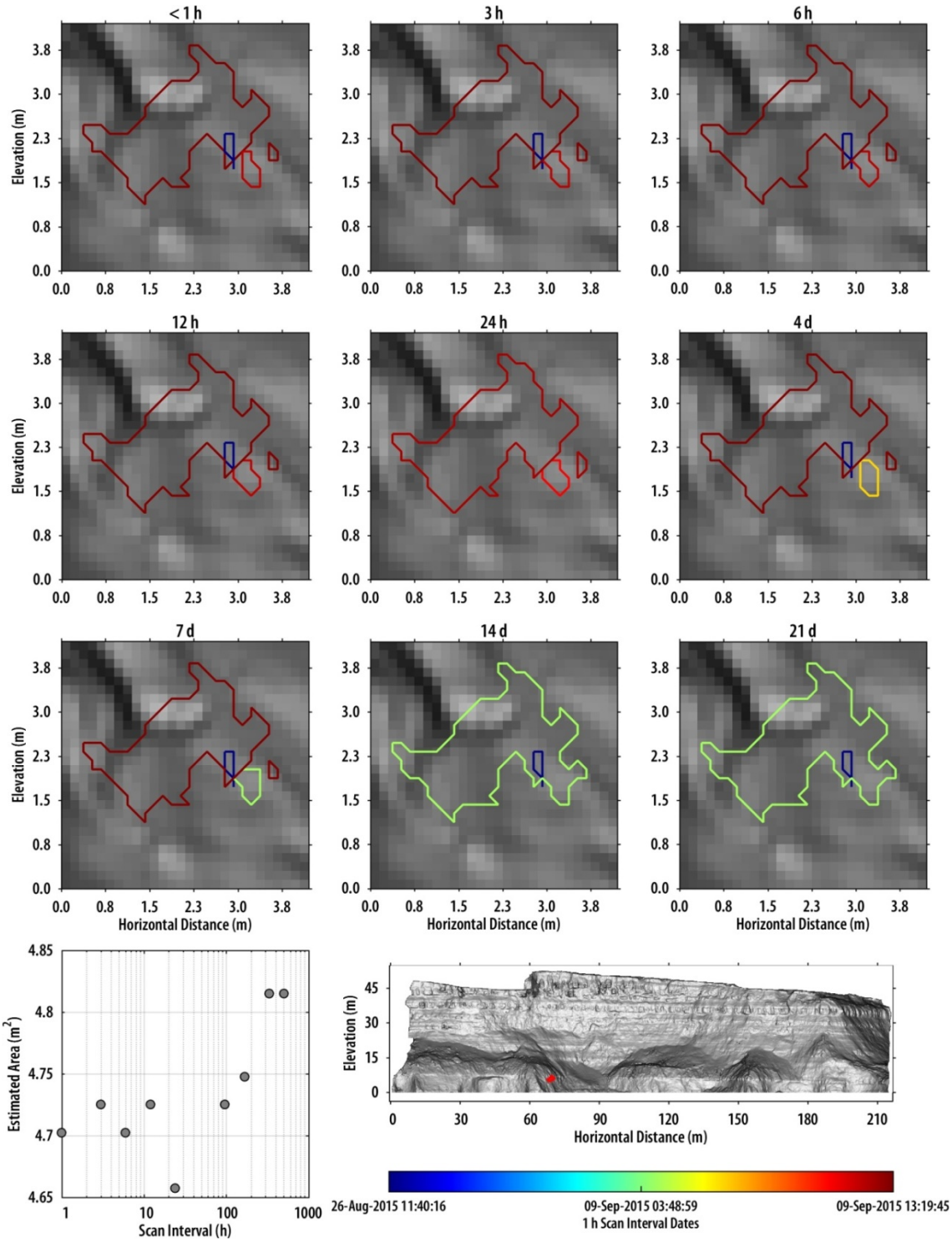
< 1 h
3 h
6 h
12 h
24 h
4 d
7 d
14 d
21 d
Elevation (m)
Horizontal Distance (m)
0.0
0.8
1.5
2.3
3.0
3.8
Estimated Area (m²)
4.65
4.7
4.75
4.8
4.85
Scan Interval (h)
1
10
100
1000
Elevation (m)
0
15
30
45
0
30
60
90
120
150
180
210
Horizontal Distance (m)
26-Aug-2015 11:40:16
09-Sep-2015 03:48:59
09-Sep-2015 13:19:45
1 h Scan Interval Dates

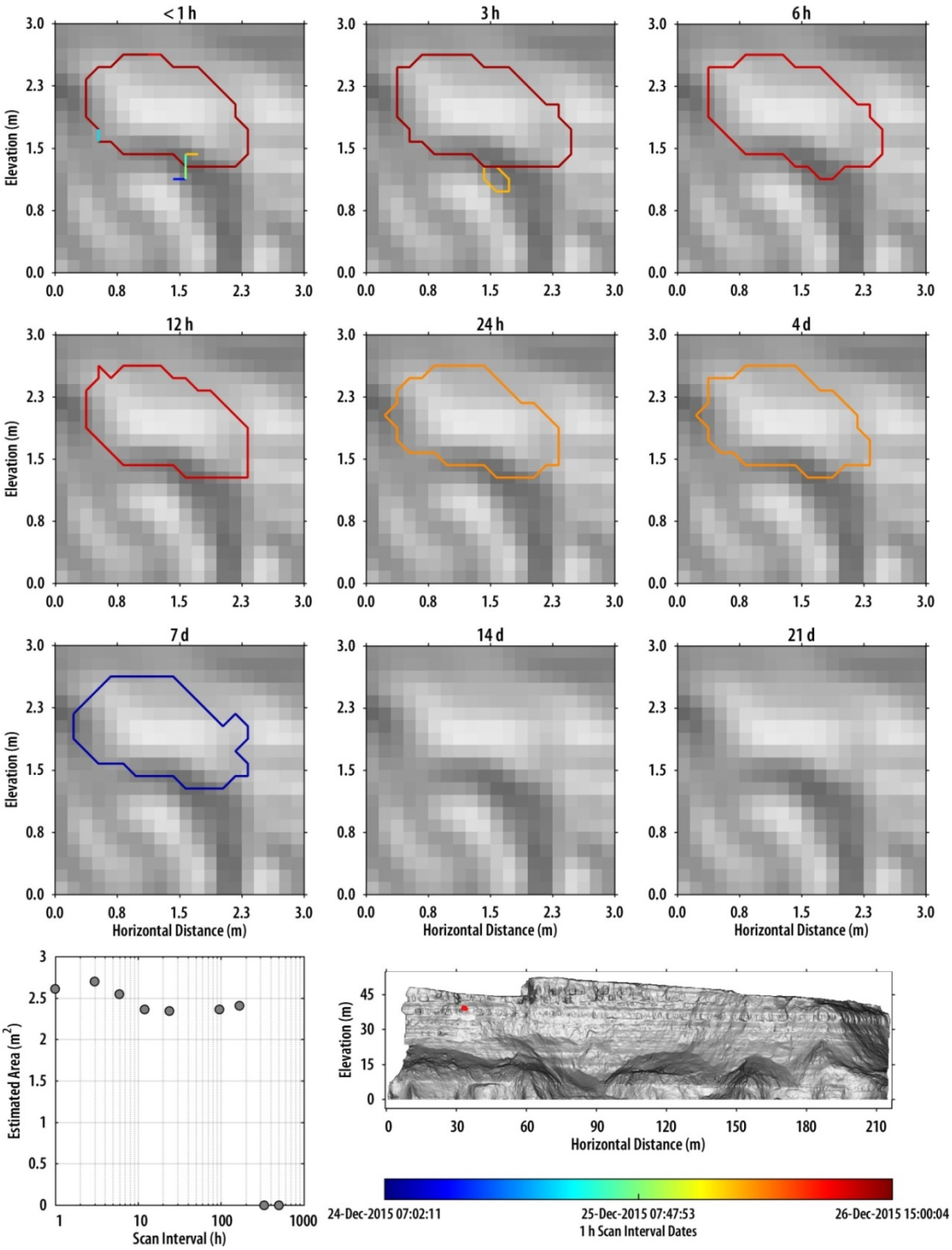
< 1 h
3 h
6 h
12 h
24 h
4 d
7 d
14 d
21 d
Elevation (m)
Horizontal Distance (m)
Estimated Area (m²)
Scan Interval (h)
24-Dec-2015 07:02:11
25-Dec-2015 07:47:53
26-Dec-2015 15:00:04
1 h Scan Interval Dates

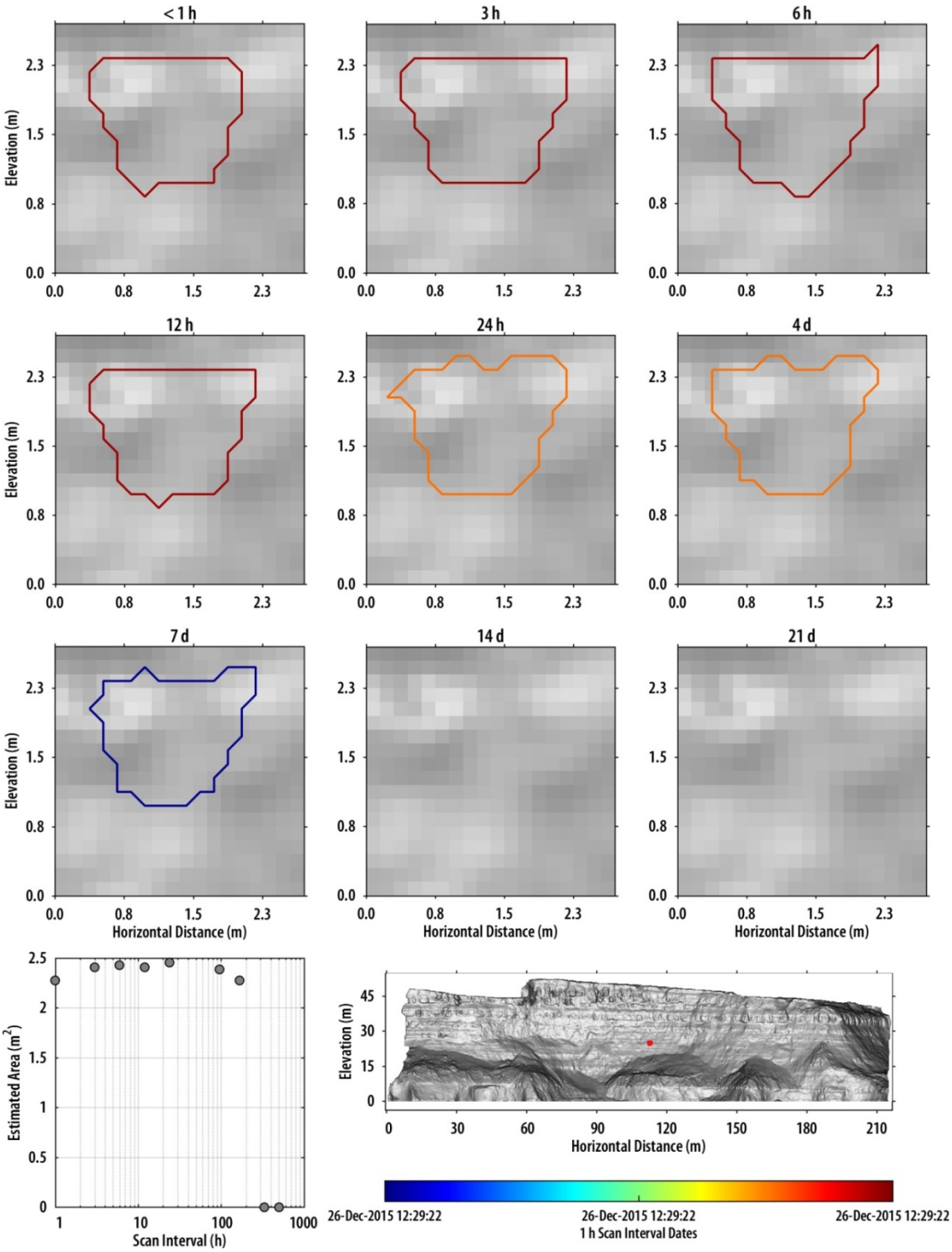
< 1 h
3 h
6 h
12 h
24 h
4 d
7 d
14 d
21 d
Elevation (m)
Horizontal Distance (m)
Estimated Area (m²)
Scan Interval (h)
Elevation (m)
Horizontal Distance (m)
26-Dec-2015 12:29:22
26-Dec-2015 12:29:22
1 h Scan Interval Dates
26-Dec-2015 12:29:22

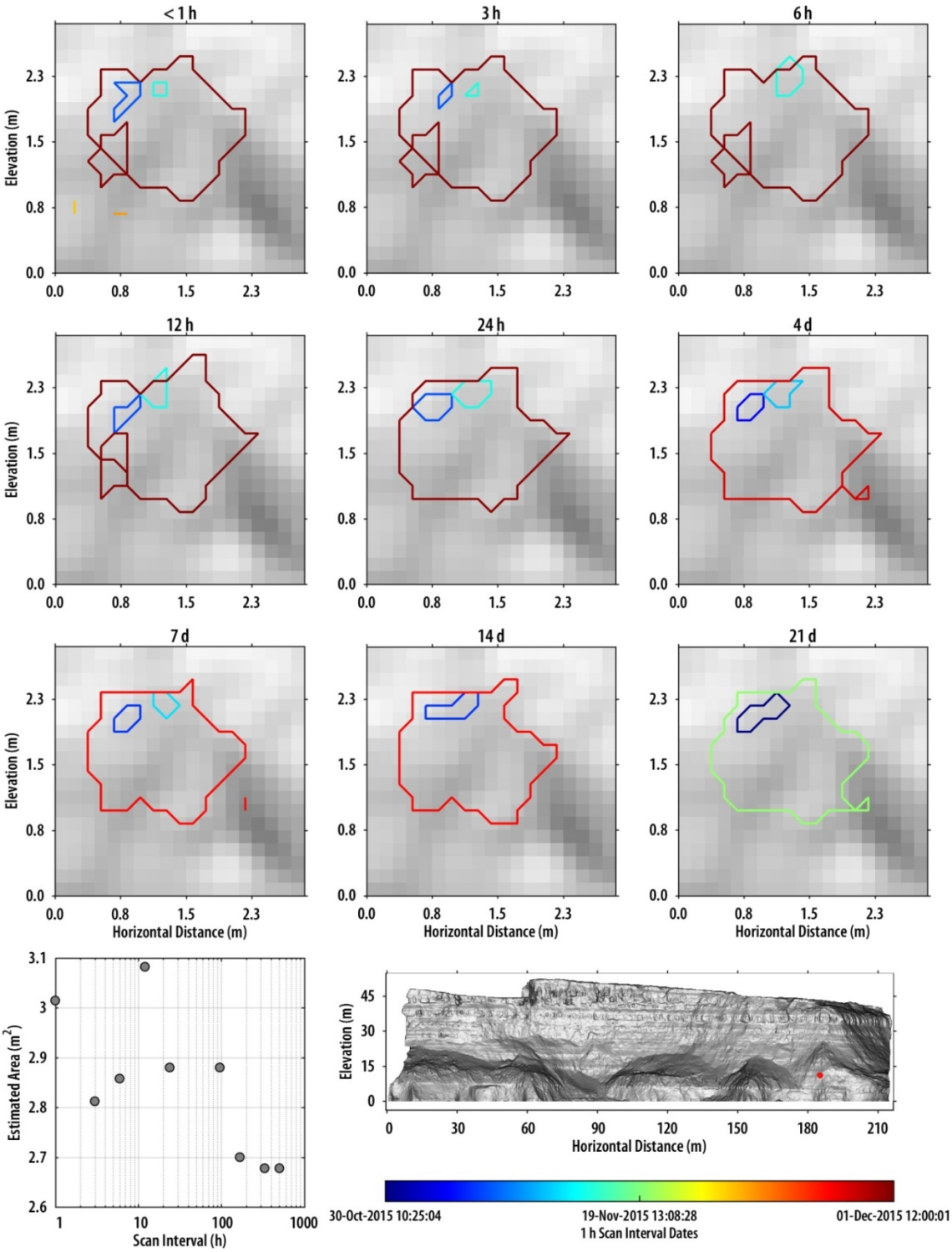
< 1 h
3 h
6 h
12 h
24 h
4 d
7 d
14 d
21 d
Elevation (m)
Horizontal Distance (m)
Estimated Area (m²)
Scan Interval (h)
Elevation (m)
Horizontal Distance (m)
30-Oct-2015 10:25:04
19-Nov-2015 13:08:28
01-Dec-2015 12:00:01
1 h Scan Interval Dates

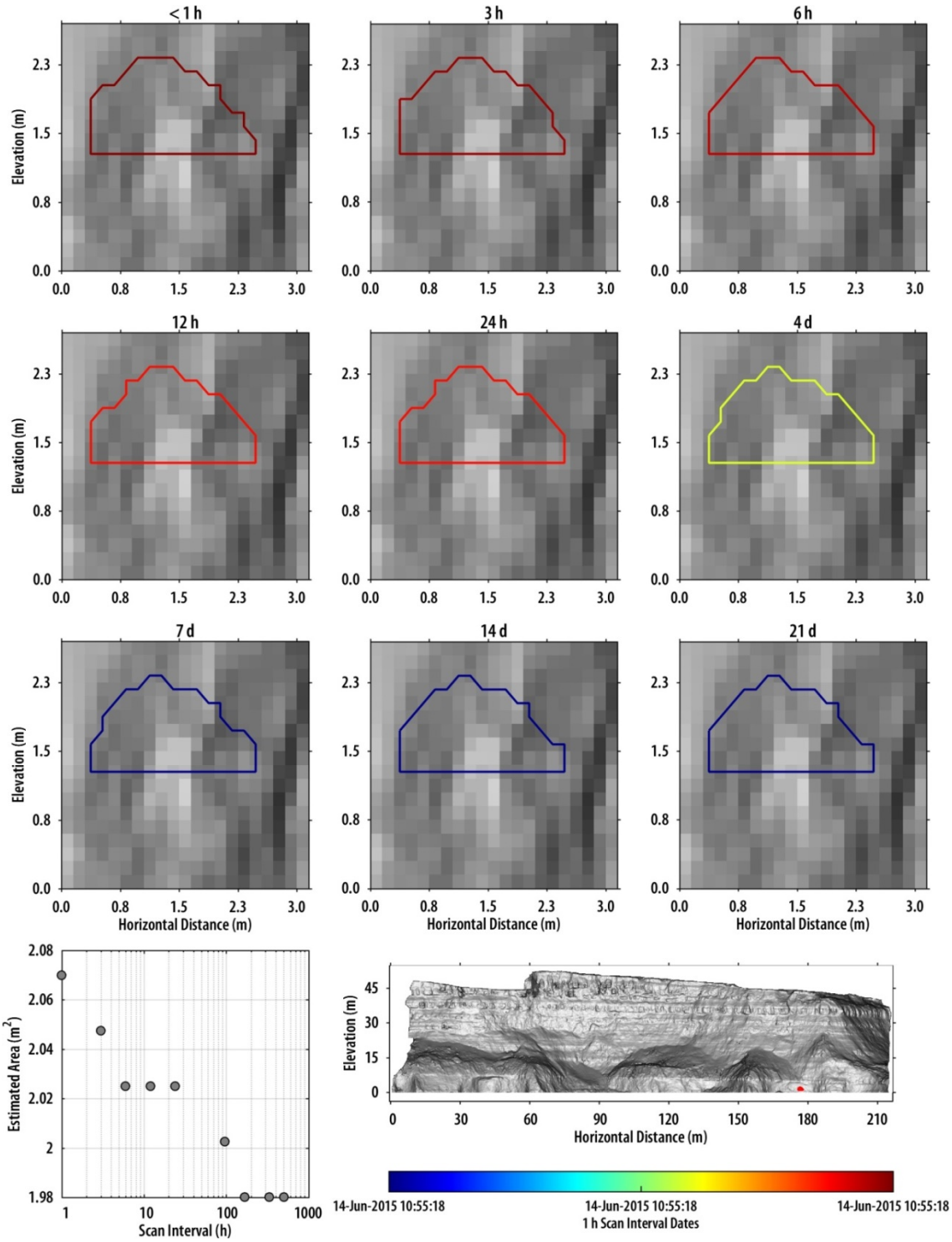
< 1 h
3 h
6 h
12 h
24 h
4 d
7 d
14 d
21 d
Elevation (m)
Horizontal Distance (m)
Estimated Area (m²)
Scan Interval (h)
Elevation (m)
Horizontal Distance (m)
14-Jun-2015 10:55:18
14-Jun-2015 10:55:18
1 h Scan Interval Dates
14-Jun-2015 10:55:18

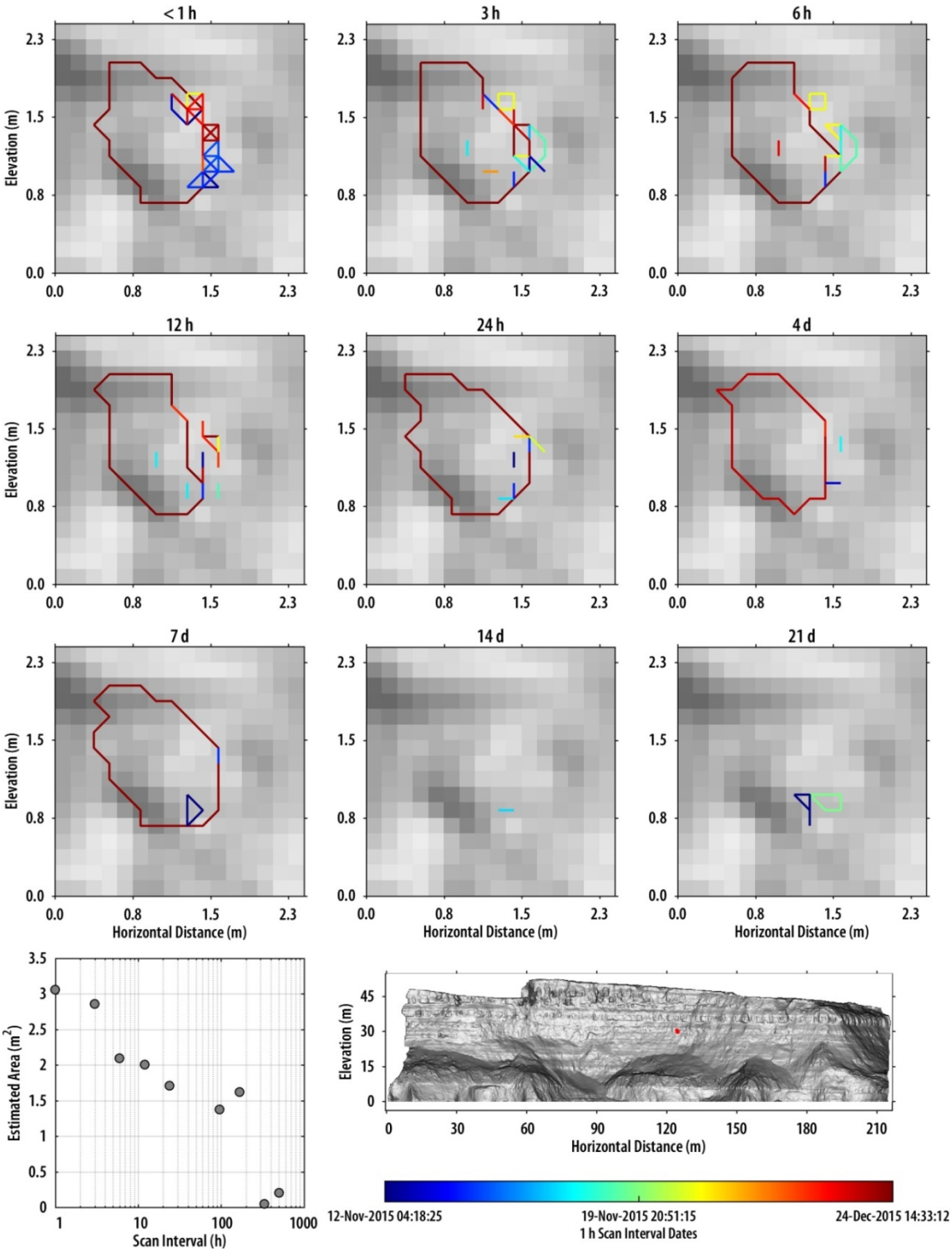
< 1 h
3 h
6 h
12 h
24 h
4 d
7 d
14 d
21 d
Elevation (m)
Horizontal Distance (m)
Estimated Area (m²)
Scan Interval (h)
12-Nov-2015 04:18:25
19-Nov-2015 20:51:15
24-Dec-2015 14:33:12
1 h Scan Interval Dates

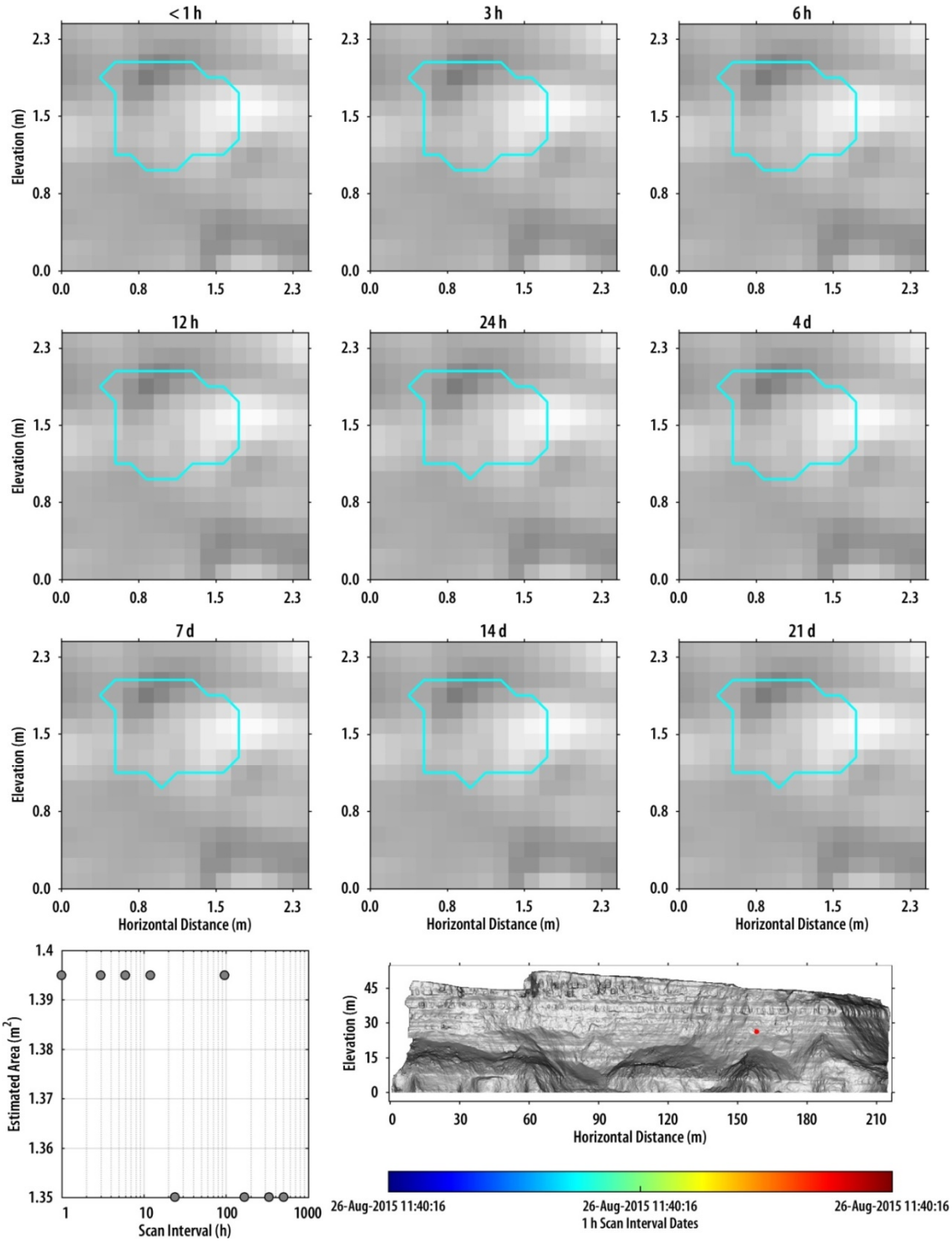
< 1 h
3 h
6 h
12 h
24 h
4 d
7 d
14 d
21 d
Elevation (m)
Horizontal Distance (m)
Estimated Area (m²)
Scan Interval (h)
26-Aug-2015 11:40:16
26-Aug-2015 11:40:16
1 h Scan Interval Dates
26-Aug-2015 11:40:16

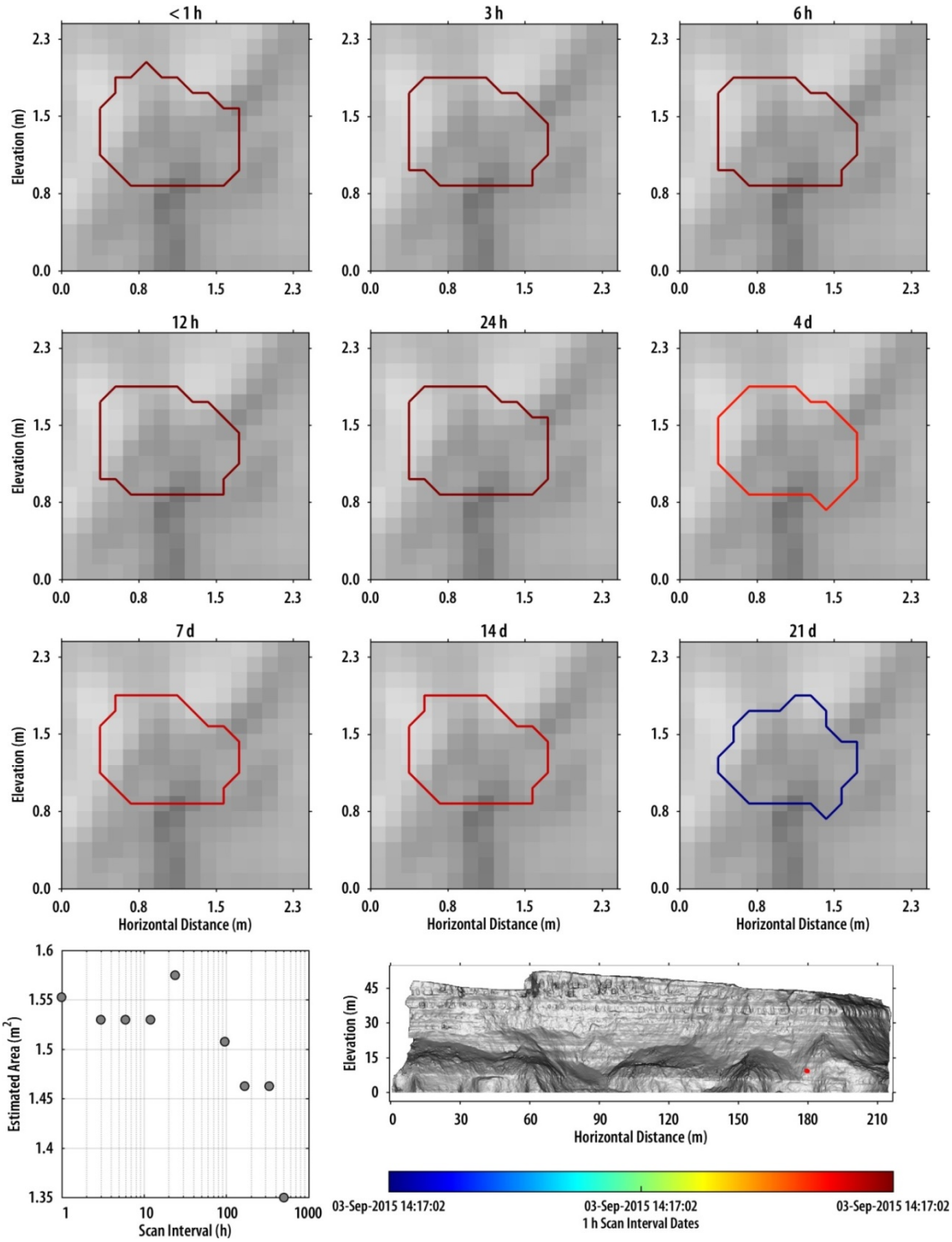
< 1 h
3 h
6 h
12 h
24 h
4 d
7 d
14 d
21 d
Elevation (m)
Horizontal Distance (m)
Estimated Area (m²)
Scan Interval (h)
Elevation (m)
Horizontal Distance (m)
03-Sep-2015 14:17:02
03-Sep-2015 14:17:02
1 h Scan Interval Dates
03-Sep-2015 14:17:02

Appendix D

An example of pre-failure deformation. Here, a forward movement of material prior to failure is indicative of toppling of failure.

https://www.youtube.com/watch?v=rWL06JhxYeI

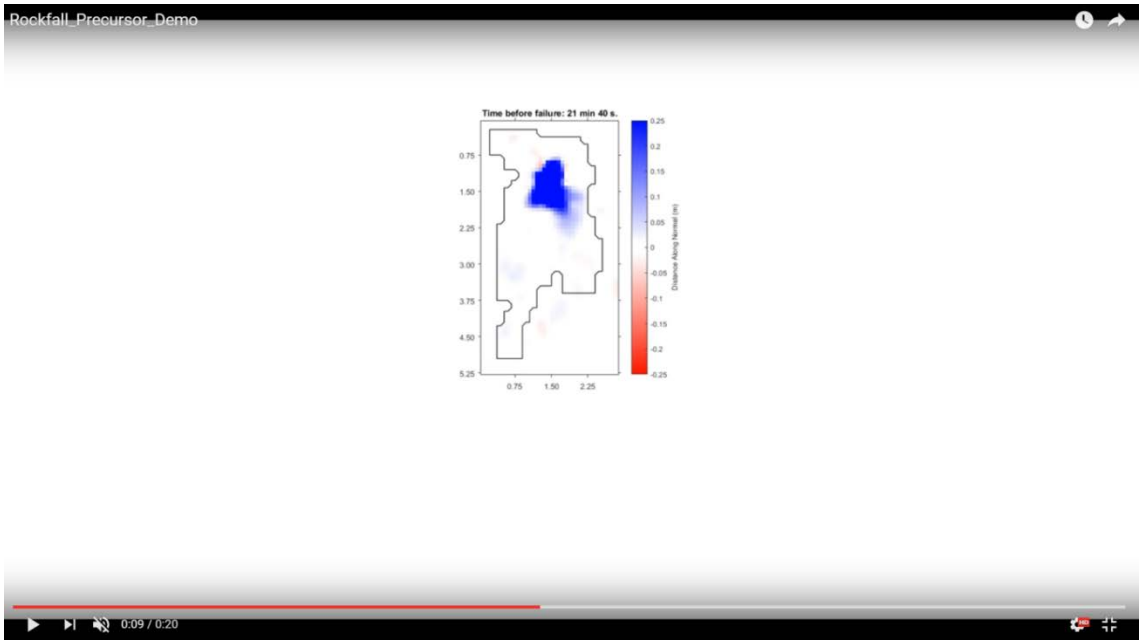

Appendix E

This appendix provides basic details of the 4D smoothing approach that is being developed for integration into the DAN VCL change detection described in *Chapter 4*.

The code takes a series of ICP-aligned point clouds and stacks them on top of one another. For each point in the most recent point cloud, referred to as the query point, q_P, a neighbourhood of points is defined within a fixed radius. This process is described in simple terms in Figure A.E.1. From this neighbourhood, a local reference plane is generated that minimises the sum of square distances (Pauly *et al.*, 2002). The orthogonal projection of the query point onto the least-squares plane, q_H, is then calculated. A bivariate polynomial surface is then created using points from all 10 point clouds within a user-defined radius of the projected query point. The creation of this surface is weighted by the spatial and temporal position of neighbouring points, and the 'smoothed' position of the query point is its orthogonal projection onto the surface, q_{MLS}.

The polynomial surface is created by applying two weightings to points that neighbour the query point's projection onto the least-squares plane. First, a spatial weighting is applied that is based upon the distance between each point and q_H. A Gaussian kernel determines the importance of points that are close to q_H relative to those that are further away. A sensitivity analysis has been undertaken to define this kernel, which can be viewed as a low-pass filter such that features smaller than the kernel size will be smoothed out. Second, a weighting was applied to each point based on the point cloud to which it belonged, such that a higher weighting is given to points belonging to the most recent, and therefore realistic, surface. Both the temporal weighting and spatial weighting can be tailored to the timescale and aerial extent of the process under examination. As long as the window of temporal averaging (determined by the temporal weighting) is below the timescale of change, the noise in change detection estimates can be reduced without smoothing out real movement. Similarly, the spatial weighting should ensure that the points that are used do not span an area greater than the scale of examined movement. The relative importance of a point's position in the spatial domain, compared to its position in time, is also addressed. The effect of this method is not to produce a more realistic surface, because it is averaged, or 'smoothed', across the topography. However, the surface that is produced is optimised for change detection (Figure A.E.2).

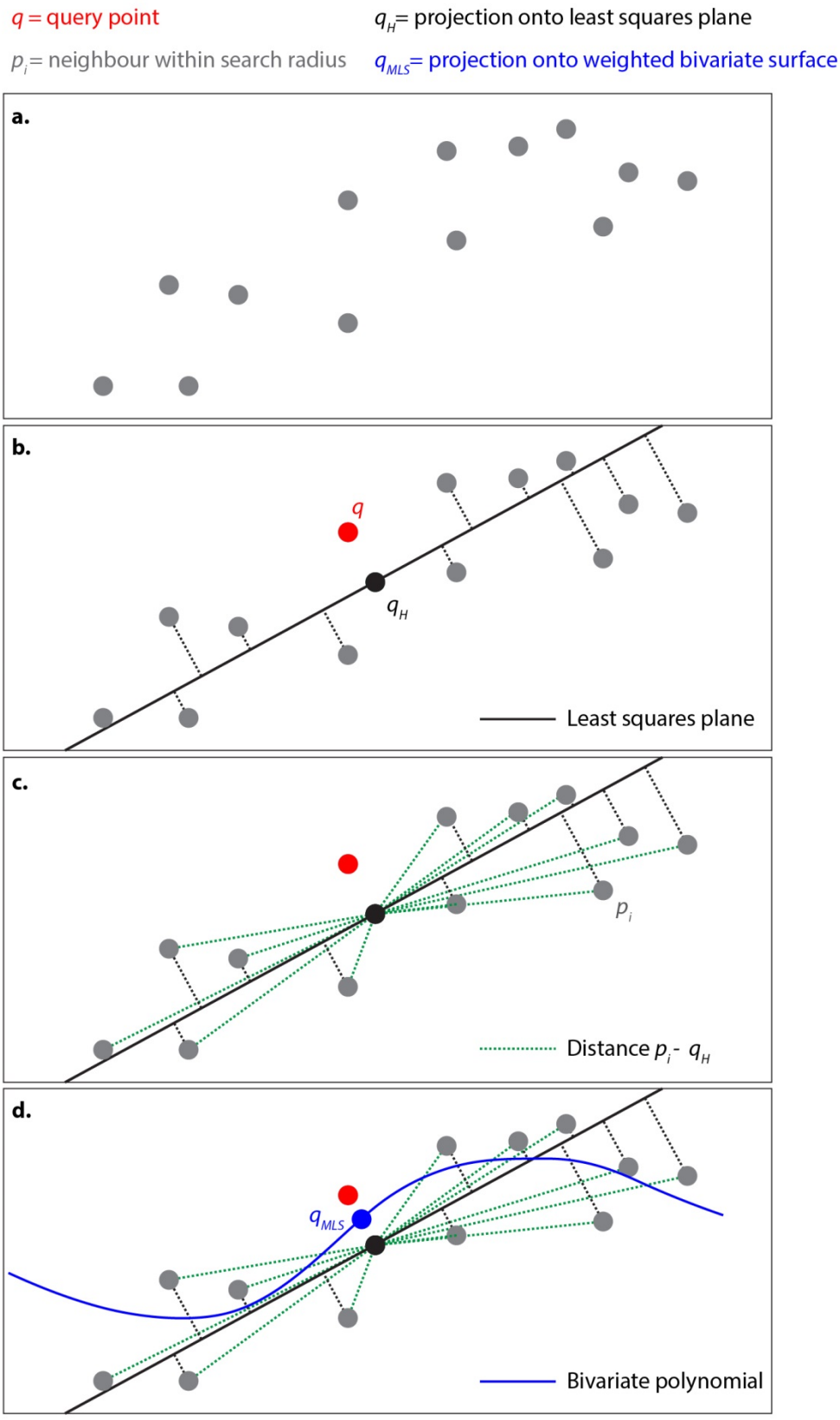

Two parameters vary for MLS 3D:

(1) Neighbourhood search radius from query point q

(2) Weighting of distance p_i - q_H where $w = e^{-D\hat{}2/\lambda\hat{}2}$

For MLS 4D, weighting of distance p_i - q_H combined with $w = 1/(ScanID^{\tau})$

Figure A.E.1: *Schematic diagram of the stages of 3D MLS. For 4D MLS, the neighbourhood of points includes the ten previous point clouds.*

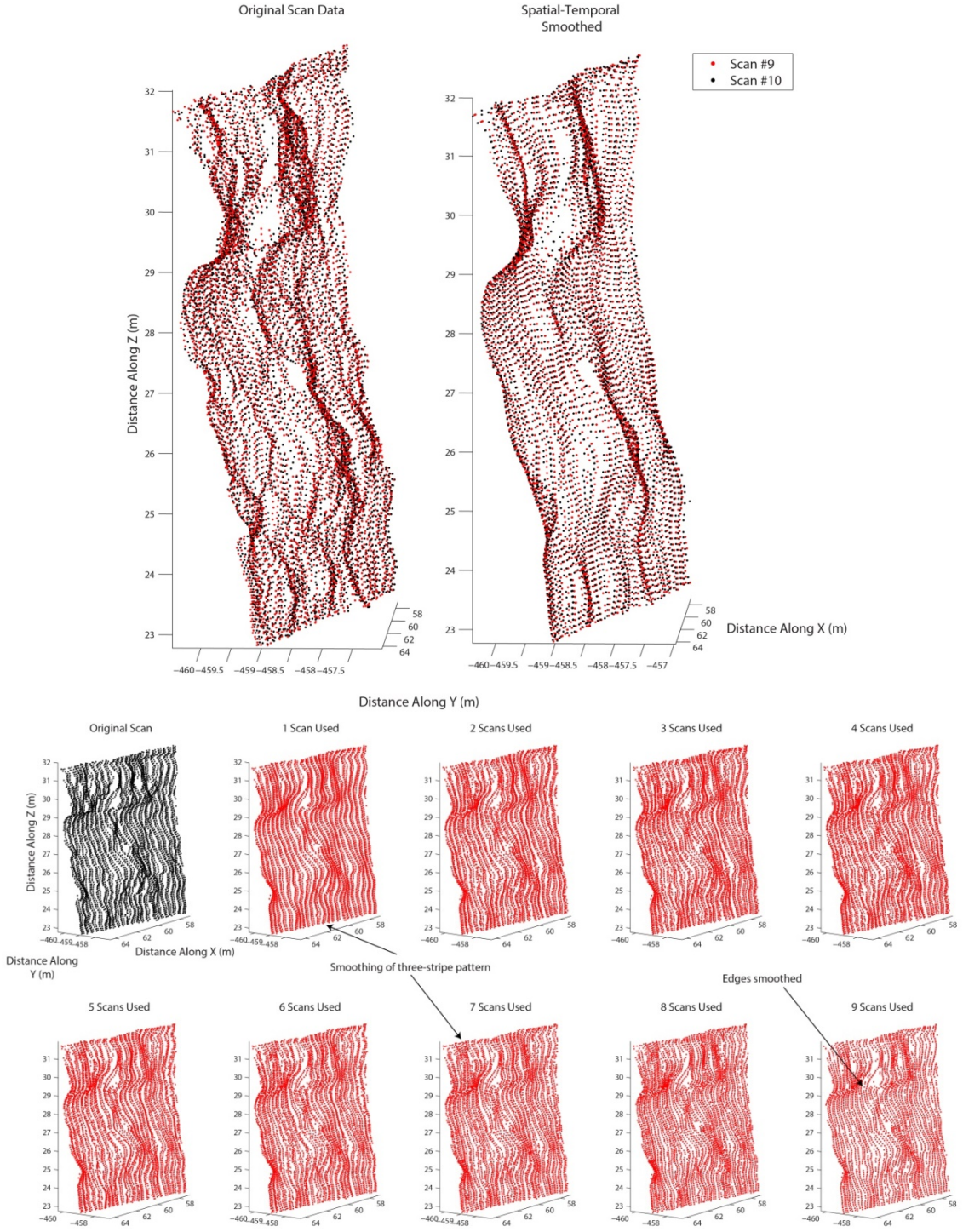

Figure A.E.2: *Top: Example of a 4D MLS smoothed surfaces. While neither surface is as topographically realistic once smoothed, the offset between the surfaces is smaller, thereby optimising these surfaces for change detection of very small movements over wider areas. Bottom: Averaging between multiple scans reduces artefacts in the data that reduce measurement precision, such as the triple-striping of Riegl systems, and edges.*

This analysis was first undertaken upon a series of planar boards, positioned at 100 m intervals over 1,000 m (Figure A.E.3). Reductions of the order of 30% in the orthogonal distance between

measured points and a least-squares plane, representative of the board, were recorded (Figures A.E.4 and A.E.5). A DAN VCL change detection was subsequently applied to successive scans of the board, resulting in a decrease from the centimetre LoD scale, to the millimetre LoD scale at all distances. This approach was also shown to reduce the LoD between scans of East Cliff, from 0.030 m to 0.005 m. For an open-pit high-wall using a different instrument (Riegl VZ-4000), the data ensured that the percentage of points within a 10 mm theoretical minimum precision, quoted by the manufacturer, increased from 18% to 85% of the point cloud (LoD 0.053 m to LoD 0.015 m; Figure A.E.6).

Figure A.E.3: *Targets distributed at 100 m intervals between 100 m and 1,000 m on a disused former WWII airfield. The targets were repeatedly scanned at 30 minute intervals over a 24 h period.*

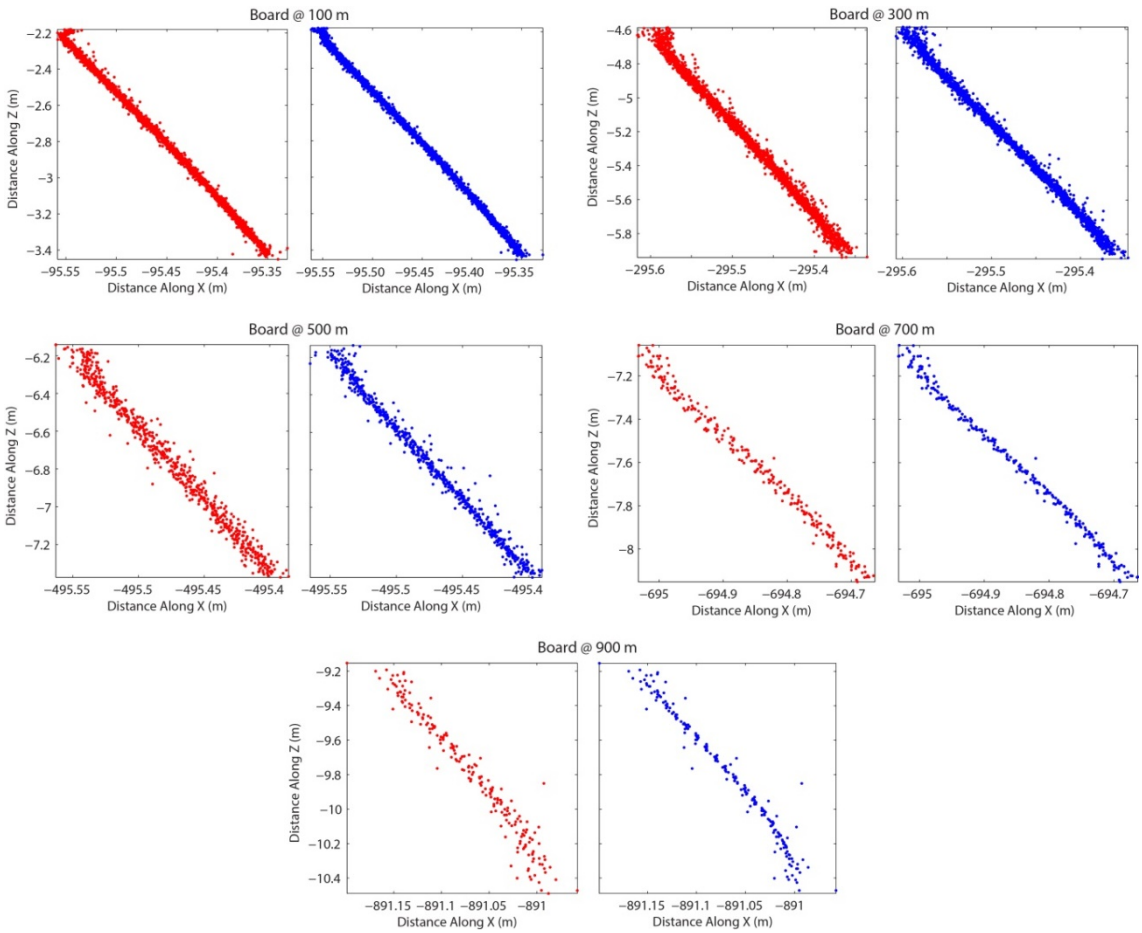

Figure A.E.4: *Reduction in the point-to-plane distance for boards using data from multiple scans, smoothed using 4D MLS*

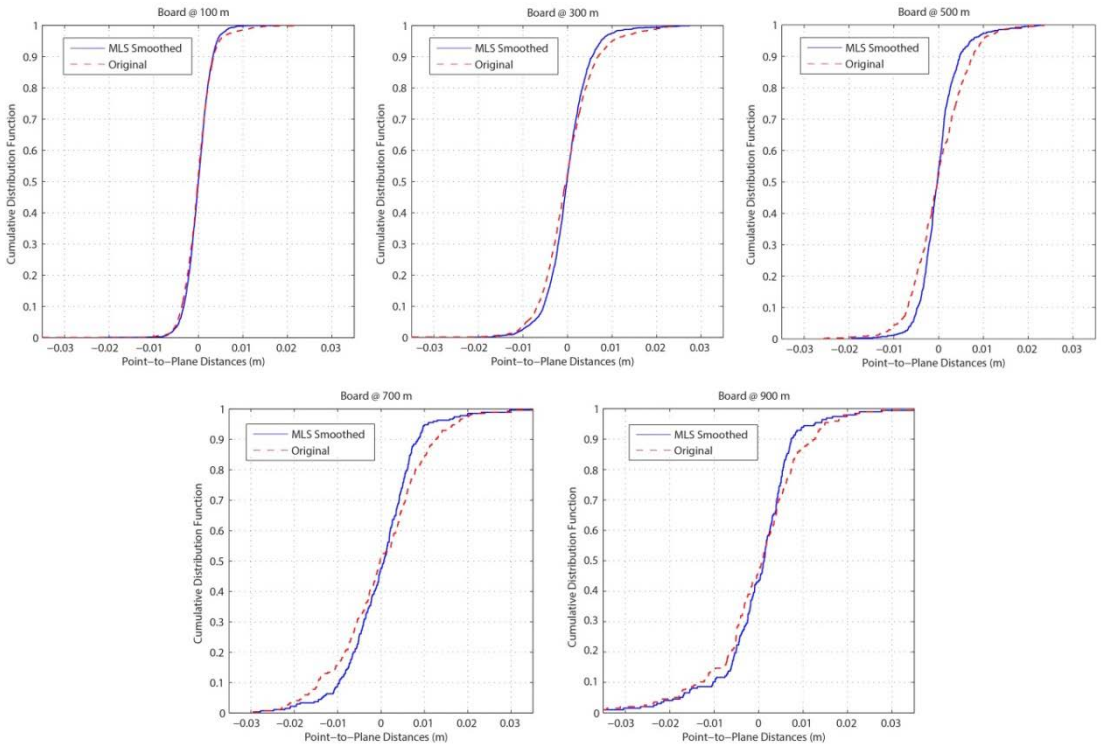

Figure A.E.5: *Cumulative distribution of cloud-to-cloud change detections show a lower precision after 4D MLS is applied.*

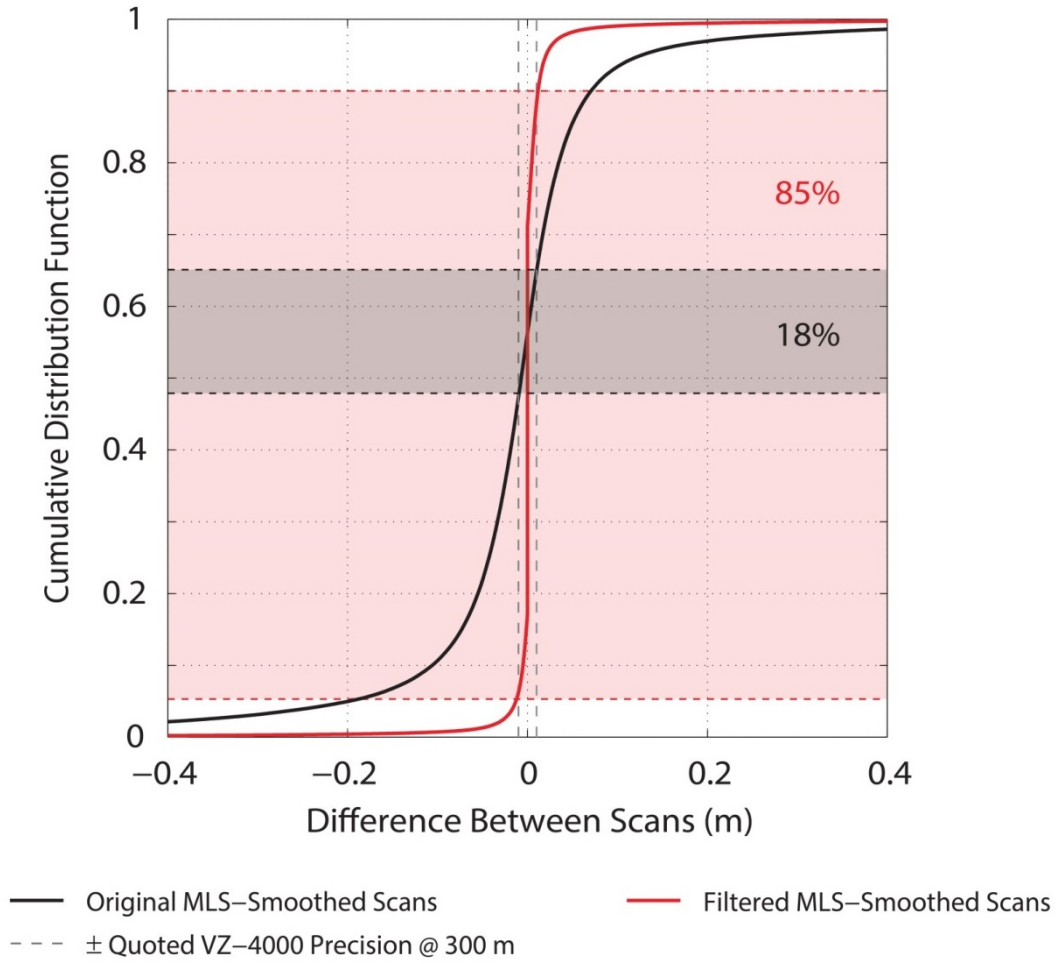

Figure A.E.6: *Change detection between two scans of an open-pit high wall, between which no change occurred. Here, 3D MLS shows an improvement in precision, such that 85% of the point clouds fall within Riegl's quoted precision under test conditions at the minimum target range (300 m). This is increased from 18% using the raw point cloud data.*

Appendix F

Video of reverse cumulative variance, RCV, development during the final 24 h before failure alongside point clouds of change. Deformation (forward movement) in blue, is evident within the entire developing rockfall block, resulting in inflections in the RCV. This is also illustrated in Figure 8.3. Bottom: area of the rockface from which points are used.

https://www.youtube.com/watch?v=XxB2cbBQVkw

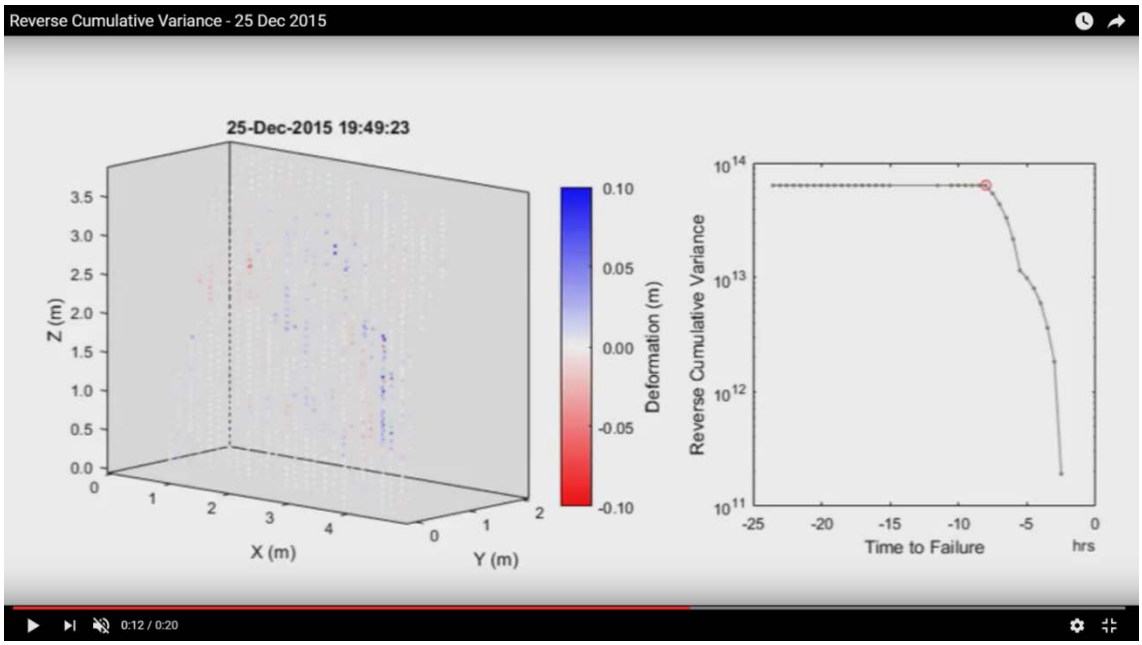

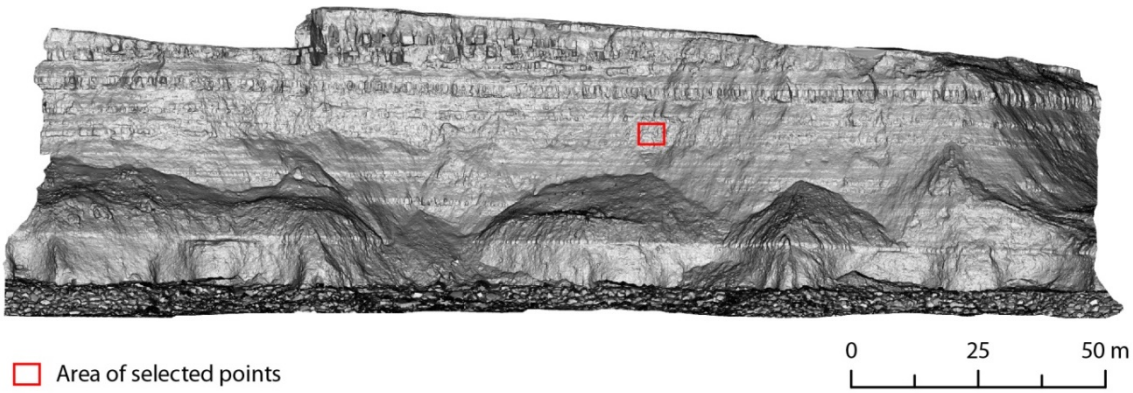

Appendix G

This appendix provides basic details of the 4D smoothing approach that is being developed for integration into the DAN VCL change detection described in *Chapter 4*.

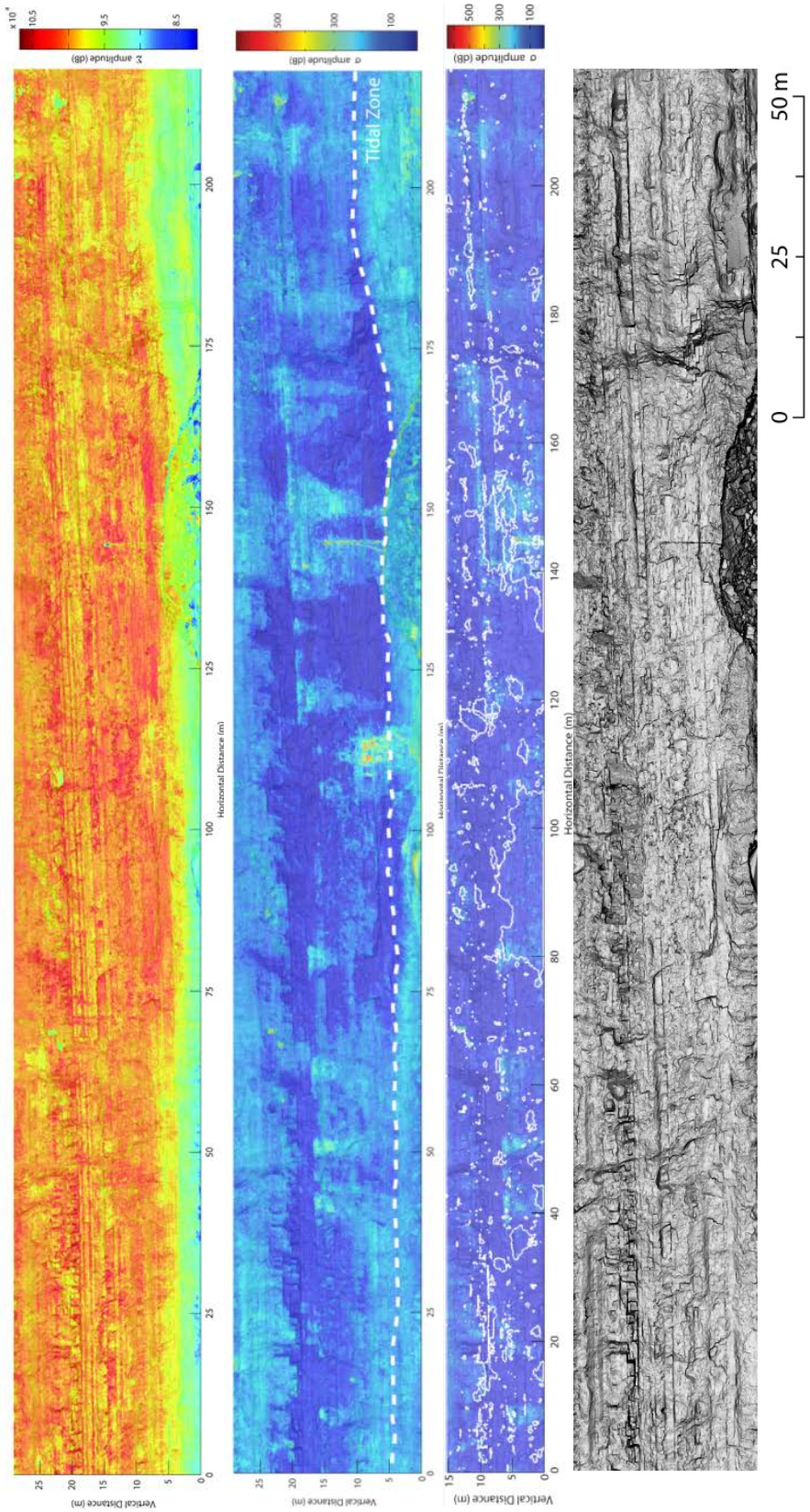

Figure A.G.1: *Top: An image of the sum of reflectances from a cliff at Staithes, North Yorkshire. The constituent reflectance images were acquired from monthly TLS surveys over an 18-month period. At the base of the cliff, the reduction in the total reflectance provides an estimate of the zone that is either inundated by the tide or subjected to wetting by waves. Middle: The same reflectance images have been used to estimate the standard deviation of surface reflectance. This again allows a delineation of the tidal zone. Notably, however, an additional feature is the presence of zones of high variability. These appear to constitute seepage from sub-horizontally bedded sedimentary rocks. In the lower image, the white polygons delineate rockfall that occurred during this period, which bears a considerable spatial correlation to the zones of seepage. Bottom: Slope model of the cliff where white colours are face-on to the viewing angle.*

Appendix H

This appendix highlights the potential use of the radiometric return of the laser (here defined as reflectivity of the surface), in order to understand the time over which the rock face remains wet after rainfall. This has the potential to inform the timescale over which rainfall can trigger slope failure.

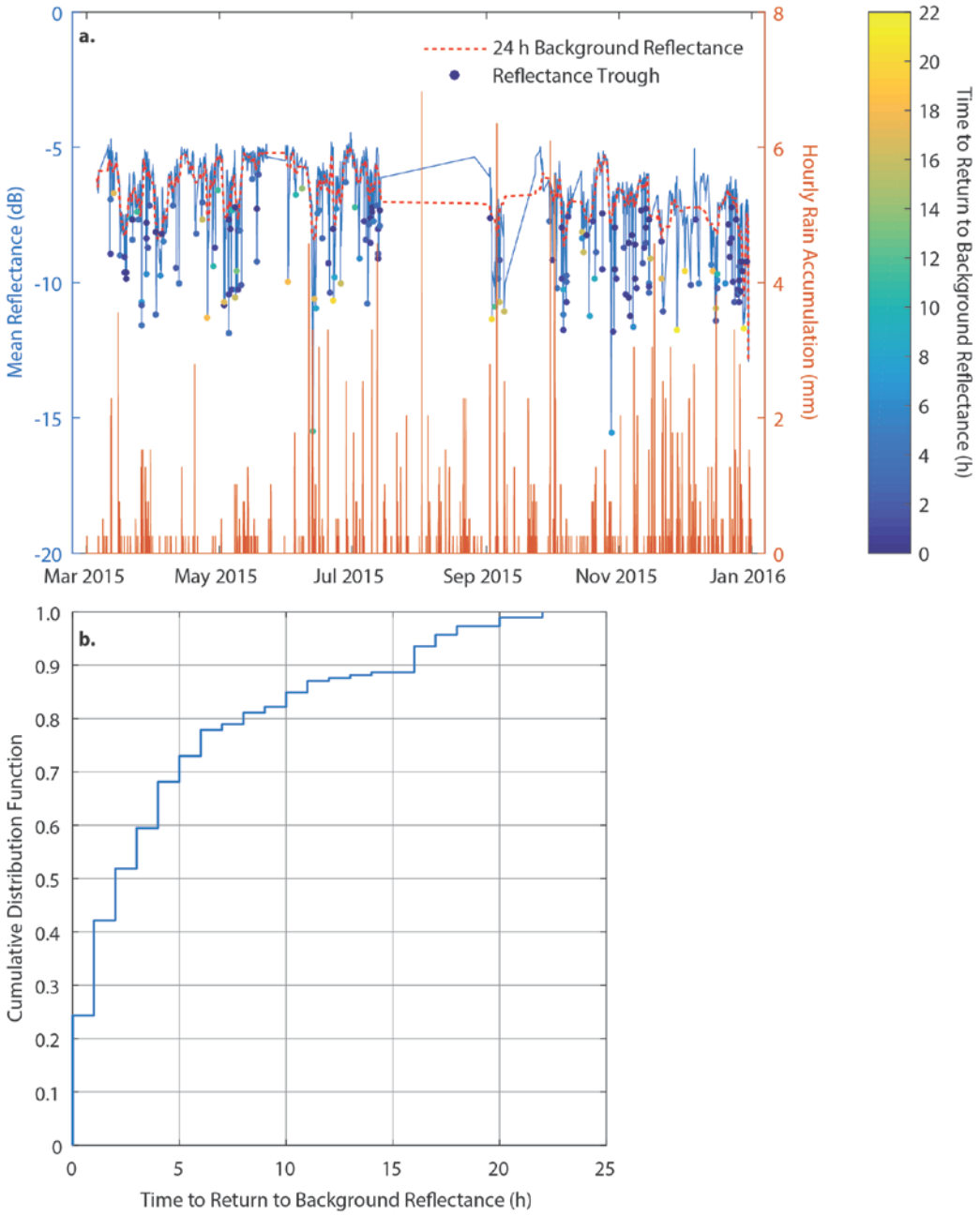

Figure A.H.1: *(a) Mean reflectance for each of the 8,987 point clouds plotted for the entire monitoring period (blue). Troughs are identified based on a user-defined deviation from previous reflectances (circles). From visual observation, it is clear that a relationship exists between the timing of rainfall events (orange line) and troughs in reflectance. The colour of these circles represents the time taken to return to a background rate, defined as the 24 h average. (b) This time taken is plotted as a cumulative distribution function for each of the identified troughs. This suggests that the cliff remains wet for a maximum of 24 h following a rainfall event. Notably, this is similar to the offset in timing of the largest 1,000 rockfall relative to the most recent storm events. However, this technique requires more thorough sensitivity analysis and testing.*